Organic Free Radicals for Molecular Electronics and Spintronics

Carlos Franco Pujante

Tesis doctoral
Programa doctorado de Ciencia de Materiales

Directores
Prof. Concepció Rovira Angulo
Dr. Marta Más Torrent

Tutora
Adelina Vallrivera Massó

Departament de Química
Facultat de Ciències

2016

Memoria presentada para aspirar al Grado de Doctor por:

Carlos Franco Pujante

Dr. Marta Más Torrent   Prof. Concpeció Rovira Angulo

Bellatera, 22 de septiembre de 2016

La Prof. **Concepció Rovira**, investigadora principal, y la Dr. **Marta Más**, científica titular del CSIC en el Instituto de Ciencia de Materiales de Barcelona (CSIC-ICMAB)

CERTIFCAN

Que Carlos Franco Pujante, licenciado en Química, ha realizado el trabajo de investigación que tiene como título "Organic Free Radicals for Molecular Electronics and Spintronics", y que este trabajo se ha desarrollado en el marco del programa de doctorado de Ciencia de Materiales del Departamento de Química de la Universidad Autonoma de Barcelona.

y para que así conste, firman el presente certificado

Dr. Marta Más Torrent   Prof. Concpeció Rovira Angulo

Bellaterra, 20, de septiembre de 2016

Chapter 1:
# Introduction and objectives

Introduction and Objectives

1. Introduction

Nanotechnology industry has maintained for four decades, a rapid pace of miniaturization of the semiconductor silicon-based devices, as predicted by Intel co-founder Gordon Moore in 1965.[1] However, in the last years it has been observed that size reduction doubles every 18 months, even though the current fabrication techniques are reaching a features size-limit, after the vertiginous progress seen in developing novel device fabrication and characterization techniques.[2]

In general nanotechnology is based in two main approaches for device fabrication: *top-down* and *bottom-up* methodologies (Figure 1). The *top-down* techniques depart from big objects to obtain smaller ones, sculpting them, and are the most commonly used in standard inorganic-based electronics, while *bottom-up* approaches use small building units that are assembled to form more complex structures.[3]
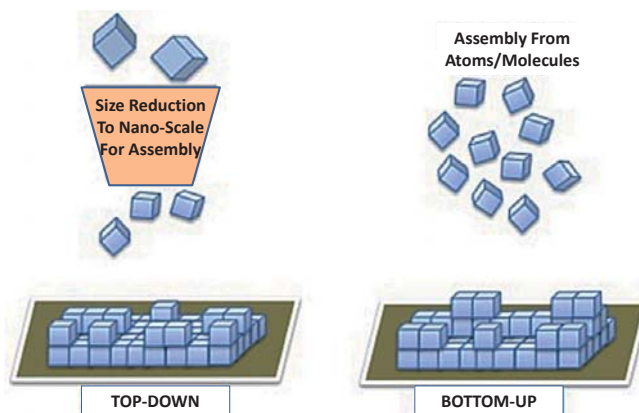
Figure 1: Approaches for devices fabrication in nanotechnology: bottom-up and top-down.

The first to realize in the importance of control thing at small scale was Richard Feynman, which exposes his ideas in the conference of 1959 entitled "*There´s plenty of room at the bottom*".[4] Following this philosophy, bottom-up methods appeared as a promising alternative to top-down technologies. On this basis, molecules are very good candidates to act as building blocks to construct more complex architectures and therefore, chemistry have been started to play an important role in nanotechnology. This concept has led to birth of *molecular electronics science.*

1.1 Molecular electronics

The concept of "*molecular electronics*" was born in the latest 1900s as a branch of nanotechnology related with the study and application of molecular building blocks for the fabrication of electronic components at molecular scale. From a general perspective, molecular electronics settles over two main pillars: first the search of novel molecular materials with tailored properties and functionalities for specific application (i.e. rectifiers, wires, switches, etc.); and second, the continuous development of fabrication, manipulation and characterization techniques for the implementation of the novel molecular materials in real devices.

The process of charge transfer through organic molecules is one of the most attractive topic of molecular electronic because a deep knowledge of the operating mechanism involved in this charge transfer process could open the door to understand some biological phenomena, as for example photosynthesis.[5] Electron transfer (ET) processes have been extensively studied over the last 60 years both experimentally and theoretically, by using different approaches. Since the early 1970s, many experimental studies have been dedicated to measuring the ET processes through organic molecules in D-B-A systems in solution, where D and A are respectively electron donor and acceptor molecular units, covalently linked by a molecular bridge, B.[6] These studies revealed the importance of the electronic structure of the bridge in ET between D and A. Based on these studies, the scientific community started to employ the expression "molecular wire" to refer to the bridge, and discuss its ability to "conduct" electrons.

In 1971 an experimental work of Kuhn[7,8] compared the ET studies carried out on D-B-A systems in solution with the ones measuring current flowing through fatty acids organized in Langmuir-Blodgett films when sandwiched between two metal electrodes. After that pioneer work, in 1974 the theoretical studies of Aviram and Ratner proposed the use of organic molecules sandwiched between two electrodes to obtain the function of an electronic rectifier.[9] Based on the Aviram-Ratner studies in 1990, Ashwell and Sambles[10, 11] and later on Metzger[12] reported experimental results that proved the rectification effect theoretically predicted by using junctions incorporating Langmuir-Blodgett films based on hexadecylquinolinium tricyanoquinodimethanide.

In the latest 1990s, the combination of nanofabrication, [13] a more familiar use of scanning probe microscopies,[14,15] and the ability to form stable chemical bonds between molecules and metal surfaces motivated the fabrication of the metal-molecules-metal junctions, giving rise to the starting of experimental molecular electronics. The first significant work attempting to measure single-molecule transport came from Mark Reed and James Tour.[16] Their works in the late 1990s and early 2000s advanced on the understanding of how such measurements could be performed, and provided insights about the transport properties of different molecules. The success of these early measurements ignited broad interest worldwide, and significant review articles appeared in 2000[17] and in 2001[18], giving place to the true beginning of molecular electronics.

Experimentally, a large variety of different Metal-Bridge-Metal (M-B-M) junctions has been proposed to investigate the electronic properties of molecules. Figure 1 summarizes the most commonly used techniques, which have been classified according to the number of contacted

molecules. Thus there are junctions that only contact one molecule (Break-Junctions and STM); other that contact a set of molecules in small number (CP-AFM and Cross-Wires); and finally junctions that contact a large organized aggregates of molecules as self-assembled monolayer (SAM). In relation with these techniques, Break-junctions and STM are the junctions which provide the most informative data for fundamental molecular-level resolution. At the opposite, the large area junctions are able to characterize the electrical behaviour of large groups of organic molecules, complementing the results extracted from single-molecule experiments and giving useful information for applications of organic electronic devices.
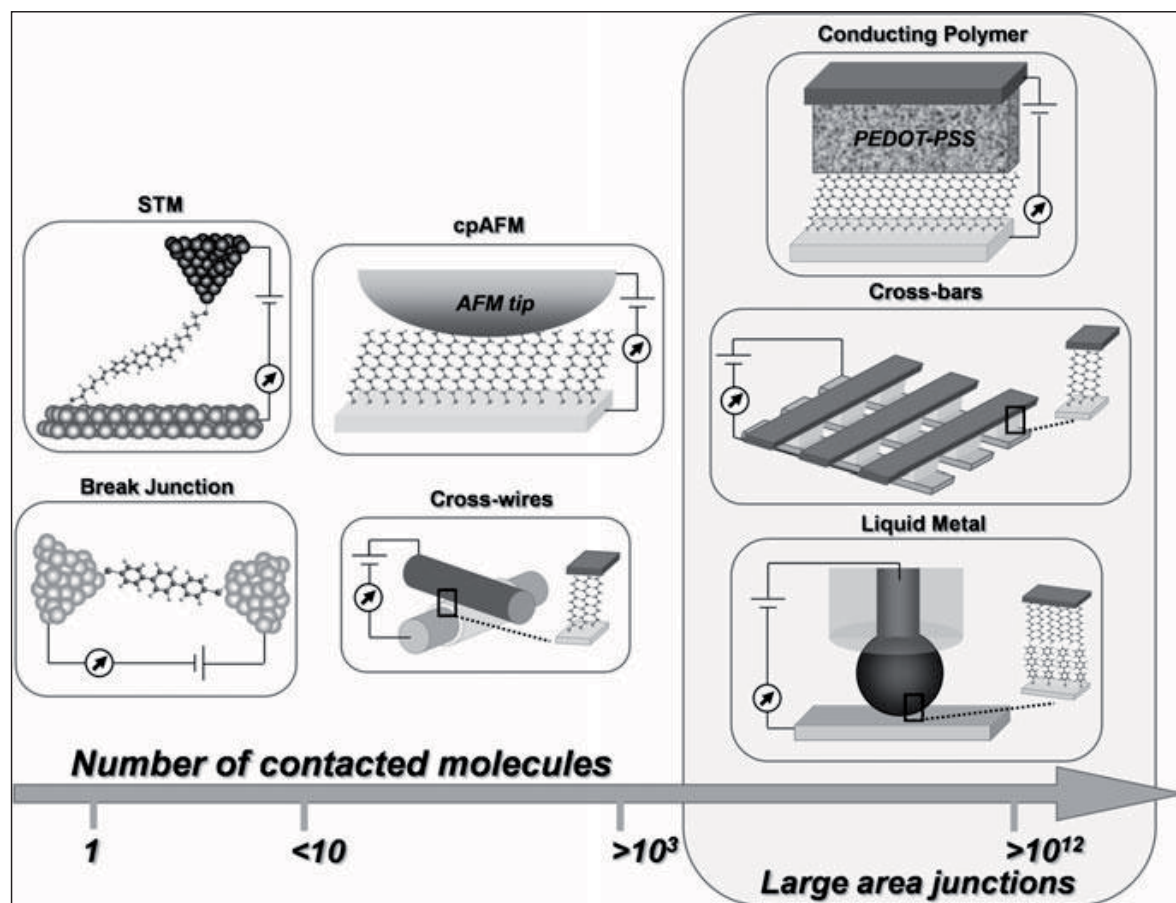
Figure 2: Schematic representation of the most commonly used molecular electronic junctions ordered fo the number of contacted molecules.[19]

In the last years there has been much interest in exploiting not only the electronic properties of the molecular devices but also the magnetic properties. This field is known as molecular spintronics or spin- based electronics, which aims at controlling the interaction between the electron spin of the molecules and the conduction electrons in order to inject, manipulate and detect the electron spin into solid state systems.[20] In this area, organic free radicals are very promising molecules due to their magnetic properties deriving of the unpaired electrons and the fact that the spin-orbit and hyperfine interaction are weak, favoring long spin relaxation times and

coherent spin propagation. Although organic free radicals are known for their high reactivity, several persistent and isolable radicals have been described in the last decades.[21, 22]

1.2 Polychlorotriphenylmethyl radicals (PTM) for electronic devices.

1.2.1 PTM molecule

Molecules combining diverse magnetic, optical, and electric properties in the same structural unit have an increased value as components in the denominated multifunctional materials. An example of such compounds is the family of polychlorotriphenylmethyl (PTM) radicals that have been studied for several decades for their interesting properties. Their multifunctionality and versatility as organic materials makes them promising candidates to be implemented in molecular electronics.

The polychlorotriphenylmethyl (PTM) radicals are composed by three partially or totally chlorinated benzene rings connected to a central carbon with sp2 hybridization, known as α carbon, and are characterized by their great chemical and thermal stability (Figure 3).[23,24] Such stability arises from the six bulky chlorine atoms in *orto* positions providing steric shielding to the α carbon, where the spin density is mostly localized. Chlorine atoms in para positons have also a hindering effect towards aromatic substitutions in such positions.
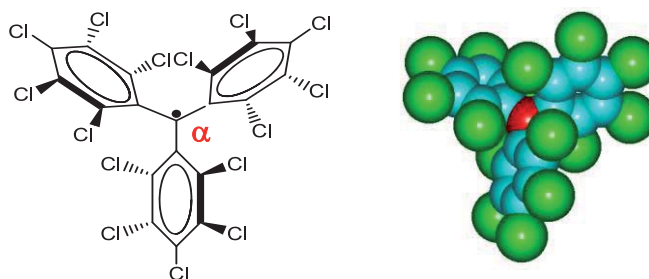
Figure 3: PTM radical molecular formula (left) and three dimensional model (right).

In solution, these compounds are stable to oxygen and to solvents and acids and are unstable only under white light. When radicals are irradiated in solution, *orto* chlorine atoms loss occurs, degenerating in ring closure and formation of fluorenil radical species.[25]

The high stability of the PTM radicals allows purifying them by standard techniques without significant decomposition. Additionally, in solid state these radicals show higher stability, being completely stable to moisture, oxygen and light, decomposing without melting around 300 ^{0}C.

1.2.2 Synthesis

PTM radical show a versatile chemistry due to the ability to functionalize *meta* and *para* positions of the aromatic rings without losing their magnetic properties and stability. The preparation of PTM radical starts with the synthesis of the polychlorinated triphenylmethane skeleton, also

known as αH-PTM, with a hydrogen in the α carbon. To obtain the radical, the αH-PTM is first treated with a strong base, giving the anion form. The PTM anion is then oxidized to its corresponding PTM radical, usually with iodine, *p*-chloranil or silver nitrate (Figure x).
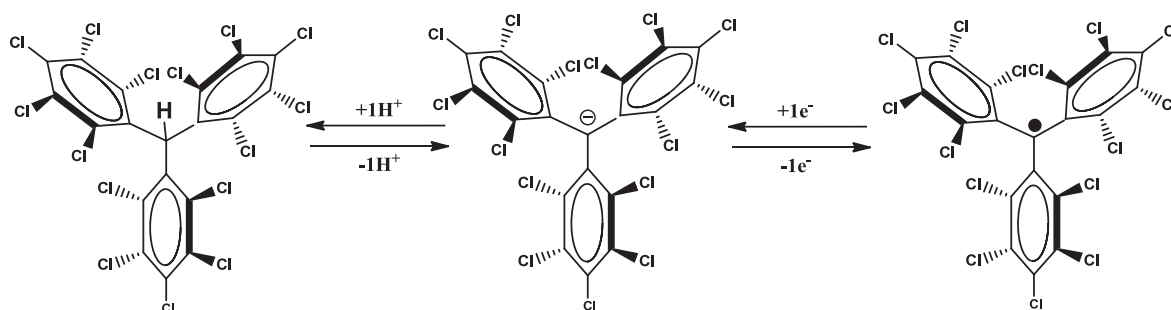

Figure 4: Conversion of αH-PTM to its corresponding PTM radical.

This is also the most common strategy followed to synthesize PTM derivatives, which implies the formation of the radical in the last step of the synthesis of those derivatives, nevertheless the high stability of this radical also permits to perform reactions when the radical is formed. Actually it have been reported different PTM derivatives with a large variety of functional groups,[22] making the PTM chemistry very wide and with a lot of possibilities to design derivatives adapted to concrete functions.

Many radical derivatives have been obtained and used as building blocks to prepare materials with specific properties and functions. Thus, PTM radicals have been reported to behave as switches in solution,[26,27] and to take part in non-linear optics systems,[28] porous molecular based magnets,[29, 30] and mixed-valence systems with intramolecular charge transfer.[31,32]

1.2.3 Electroactivity

The α carbon steric protection is also responsible for the stability of the derived cationic and anionic species of these radicals. In the cyclic voltamperometry (CV) of PTM radicals in solution it is seen two reversible redox waves corresponding to the oxidation of the PTM radical to the cation form and reduction to the corresponding anion form (Figures 5 and 6). The latter process is of particular interest since occurs at very low voltage.
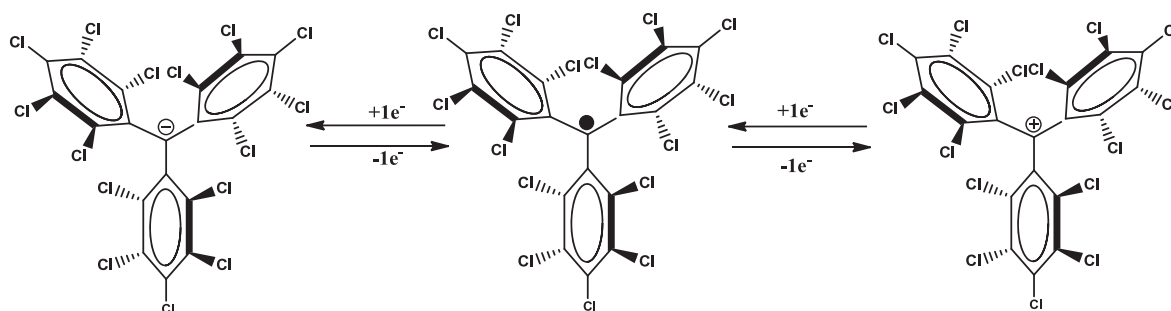
Figure 5: Redox equilibria for PTM radical.
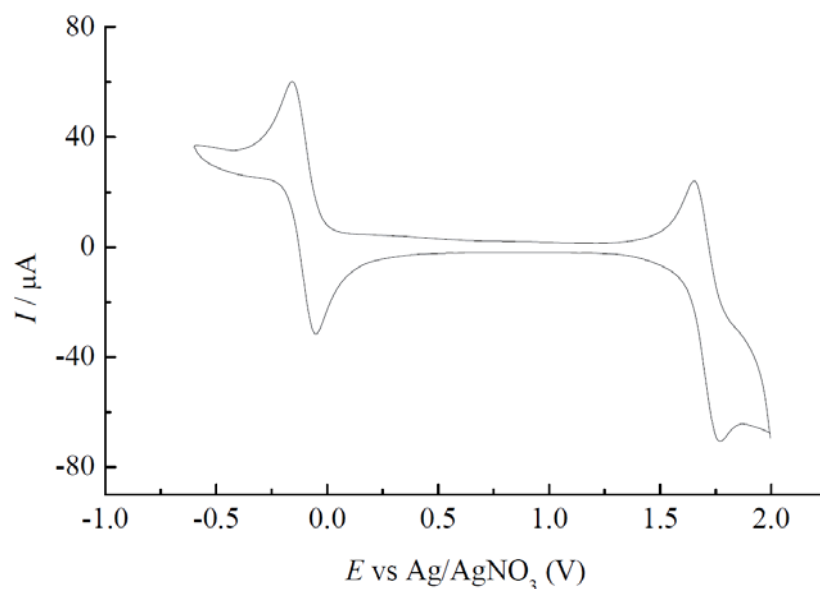
Figure 6: Top: redox pair resulting from the oxidation and reduction of PTM radical. Bottom: PTM radical CV versus Ag/AgNO₃, using a platinum wire as counter electrode and electrolyte solution of 0.1M tetrabutyl ammonium hexafluorophospate in dichloromethane.

The PTM derivatives can act in D-A systems as donor or acceptor when they are in their anion or radical form, respectively. For these unique characteristics, PTM radicals derivatives have been used either as electron-donor or as electron-acceptor dyads to study Intramolecular Electron Transfer (IET) phenomena, or behave as molecular switches for memory devices.

Their electron acceptor character has been used in the preparation of PTM-Ferrocene[33,34] and PTM-TTF dyads,[35] and also linked to different amine donor moieties.[36]

Eventually, the electrochemical amphotericity of the PTM radicals has been used to prepare symmetric biradical derivatives that can form mixed-valence radical-anion systems exhibiting IET along different phenyl based bridges.[37,31,32]

1.2.4 Paramagnetism

The Electron Paramagnetic Resonance (EPR) spectra of PTM radical, at room temperature an in deoxygenated solution, is characterized by a single and narrow (less than 1 Gauss) line centered at a g value between very close to the value of the free electron (g = 2.0023) due to the low spin orbit interaction[38] (Figure 7).
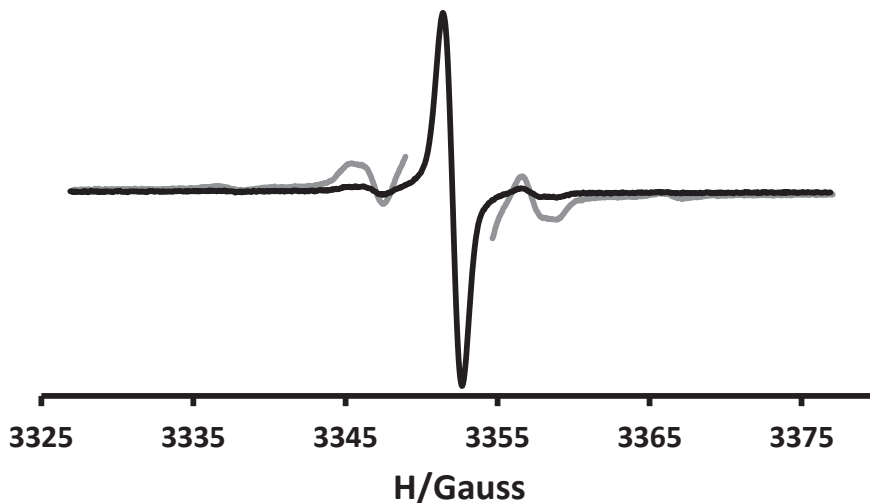
Figure 7: EPR spectrum of PTM radical recorded at room temperature in deoxygenated CH2Cl2 (g = 2.0023). In grey the same spectrum recorded with a higher power to better appreciate the ^{13}C hyperfine coupling.

Apart from the central line, the EPR spectrum shows a small equidistant pair of lines on both sides of the main line as well as a more separated and broad doublet. These signals corresponds to the coupling of the free electron, with the ^{13}C nuclei (I = 1/2, natural abundance 1 %) of the triphenylmethyl skeleton. The magnitude of the hyperfine coupling depends on the extent of the electron delocalization on the different positions of the trityl skeleton, hence being the larger one (29.75 G) due to the coupling with the central carbon nucleus, while the hyperfine coupling of 13.43 and 10.57 Gauss corresponds to the coupling with the three equivalent *ipso* and the six equivalent *ortho* [13]C nuclei.[38] When one or more chlorine atoms in either the *meta* or *para* positions are substituted, the couplin of the electron with EPR active nuclei of such functional group can also be observed.[39,40]

1.2.5 Optical properties

Interestingly, the PTM anion unambiguously shows different optical properties compared to the PTM radical. The two species have different colour, absorbing at different wavelengths, the most significant absorption band for appearing at 385 nm for the radical and at 515 nm for the anion. Furthermore, contrary to the PTM radical, which is fluorescent in the red region (λ = 650 nm), the corresponding PTM anion is a non-fluorescent specie.

In a chronoamperometric experiments (Figure 8), ten oxidations reduction cycles of PTM radical in solution were carried out electrochemically and each state was monitored by the UV-Vis. The reversibility of the system was elucidated by the fact that the absorbance of each species was recovered completely after each cycle and an isosbestic point in the UV-Vis spectra is observed.
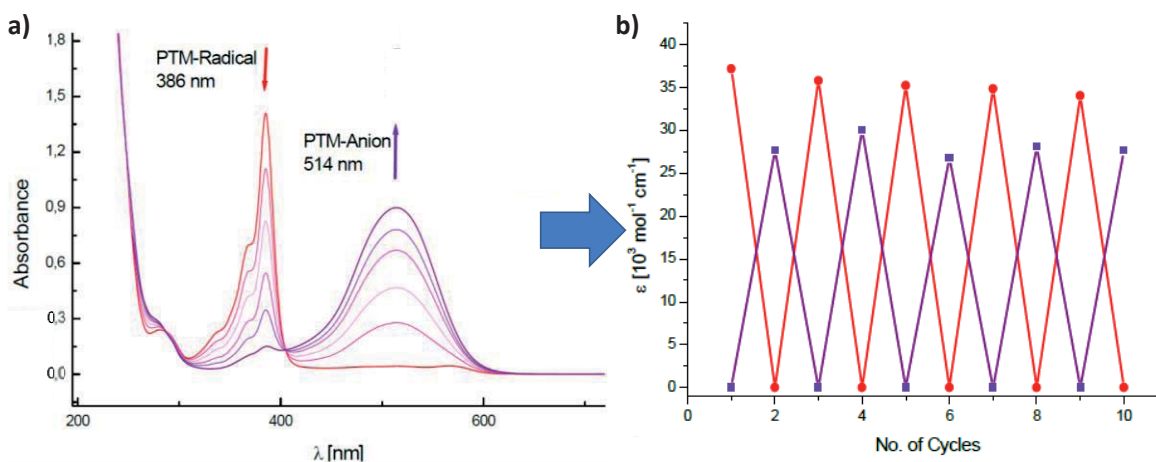
Figure 8: a) UV-Vis absorbance spectra showing the bands evolution upon interconversion from the PTM radical to the PTM anion in a CH_2Cl_2. b) Molar absorptivity of the radical (red 385 nm) and anion (purple, 515 nm) absorption bands in the different cycles of the electrochemical interconversion.

1.2.6 PTM radicals on surfaces

The possibility to use redox molecular switchable molecule to functionalize solid surfaces makes PTM radicals promising candidates for application in molecular spintronics. To investigate their electronic and spin transport properties at the molecular level several studies have been carried out to anchor and organize PTM derivatives by means of physisorption and chemisorption.

Physisorption

The supramolecular organization of a PTM radical bearing three long alkyl chains has been reported on High Ordered Graphite (HOPG),[41] leading to a multilayer organization which is influenced by the HOPG substrate symmetry. The observed nanostructures are sustained by different intermolecular interactions such as Cl···Cl, Cl···Ph, π–π, van der Waals, and CH···π interactions.
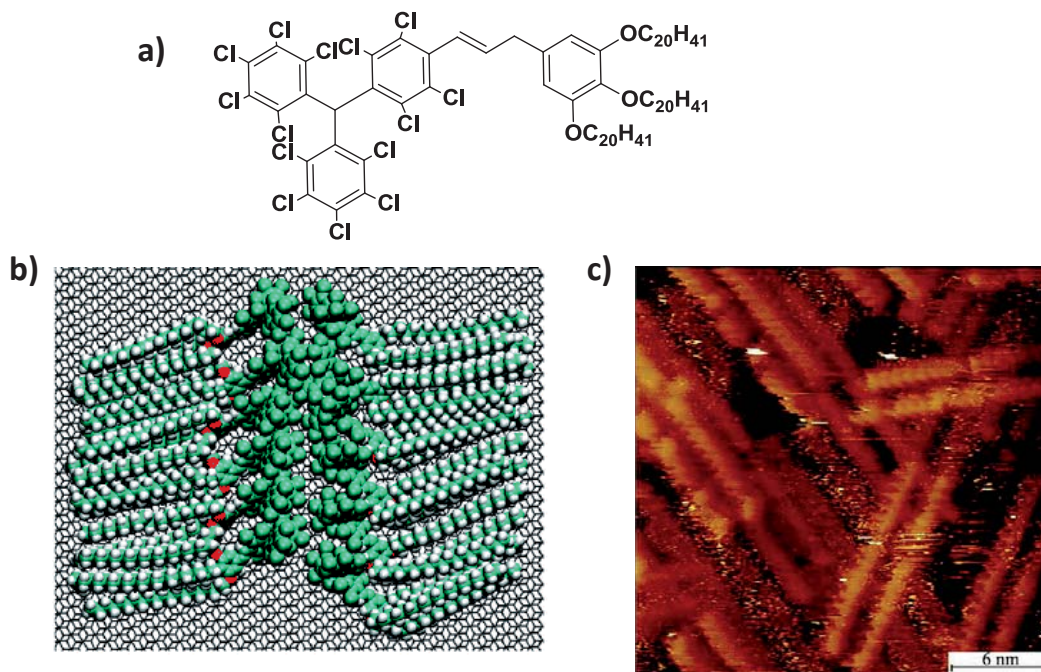
Figure 9: a) Structure of the designed PTM radical to br physisorben on HOPG. b) Simulation of the assembly of the radical on HOPG. c) STM image of the multilayer hierarchical organization.[41]

Chemisorption

Additionally, the immobilization of PTM radicals on surfaces by a covalent bond was carried out through different approaches. Self-assembled monolayers (SAMs) of PTM radicals have been reported on silicon oxide,[42] indium tin oxide (ITO)[43] and gold substrates,[44] and their characterization proved that their magnetic, electrochemical and optical properties are preserved on surface.
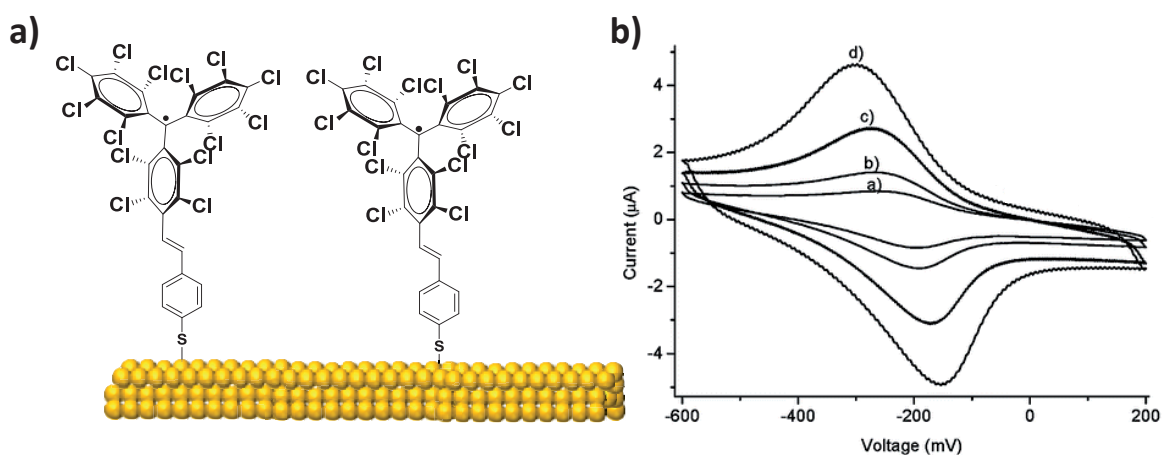
Figure 10: a) PTM radical SAM on gold substrate. b) CV of the PTM radical SAM on gold, using the SAM as working electrode, versus Ag/AgCl and a platinum wire as counter electrode, in 0.1 M tetrabutylammonium hexafluorophosphate solution in CH_2Cl_2, at different scan rate: 50 (a), 100 (b), 300 (c) and 400 (d) mV/s.[44]

Interestingly, the transport characteristics of PTM SAMs on gold were studied by conductive probe atomic force microscopy (CP-AFM). The resistivity of the junction Au/PTM/AFM, using both the PTM radical and its corresponding close-shell αH-PTM form was measured. It was observed that the PTM radicals exhibited a conductivity of two orders of magnitude higher compared to αH-PTM.[45,46]
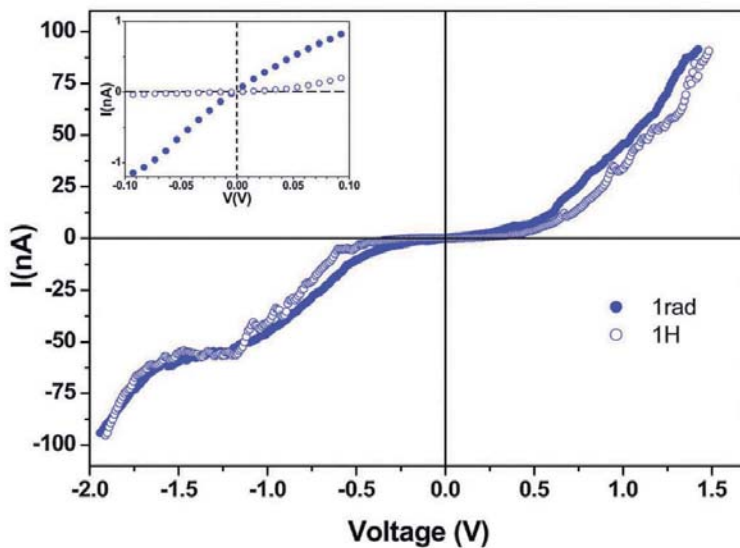
Figure 11: *I–V* curves as a function of the applied load for the PTM rad (blue dots) and αH (white dotos) Inset: magnification of the linear region at low voltages.[46]

Taking into account the described PTM radicals properties, we can conclude that these are suitable materials to be used as building blocks in molecular electronics.

2. Objectives

The present Doctoral thesis is centered in the development of new molecular electronic devices and studies the electron transfer phenomena associated to them. We want to exploit the properties of PTM molecules to explore the charge transfer mechanism involved in systems containing PTM derivatives.

The objectives proposed in this work are:

1) Study the charge transfer process over different conjugated linear oligomers acting as molecular wires. For that purpose, we want to exploit the amphotericity of the PTM radical in order to connect these wires to two PTM radicals, generate the mixed-valence species, and study the intramolecular electron transfer through the wires in solution.

2) To elucidate the charge transfer mechanisms operating when the current flows through the PTM radical molecules. Thus, we planned to synthesize a family of PTM molecules with different length, form SAMs with them and study the conductance through PTM molecular junction devices. Also we proposed to study the conductance of PTM molecules in their different redox states, in order to develop a conductive switch.

3) To exploit the magnetic properties of PTM radicals in spintronics. For that, we proposed to generate single PTM molecule devices and study their electronic and magnetic properties.

References

[1] G. Moore, *Electronics*, 1965, **38**, 114.

[2] C. B. Gorman, R. L. Carroll, *Angew. Chem. Int. Ed.,* 2002, **41**, 4378.

[3] A. C. V. Balzani, M. Venturi, *Molecular Devices and Machines – A Journey into the Nano World, WILEY/CVH Verlag GmbH & Co. KGaA, Weinheim*, 2003.

[4] R. P. Feynman, *Engineering and Science*, 1960, **23**, 22.

[5] M. E. Brederode, M. R. Jones, R. Van Grondelle, *Biochemistry*, 1997, **36**, 6855-6861.

[6] L. de Cola, *Molecular wires: from desing to properties. In: Topics in Current Chemistry 257. Springer, Heidelberg*, 2005.

[7] B. Mann, H. Khun *J. Appl. Phys.*, 1971, **42**, 4398-4406.

[8] H. Khun, *Thin Solid Films*, 1989, **178**, 1-16.

[9] A. Aviram, M. A. Ratner, *Chem. Phys. Lett.,* 1974, **29**, 277-283.

[10] G. J. Ashwell, J. R. Sambles, A. S Martin, W. G. Parker, M. J. Szablewski, *J. Chem. Soc. Chem. Commu.,* 1990, **19**, 1374-1376.
[11] A. S. Martin, J. R. Sambles, G. J. Ashwell, *Phys. Rev. Lett.,* 1993, **70**, 218-221.

[12] R. M. Metzger, B. Chen, U. Hopfner, M. V. Lakshmikantham, D. Vuillaume, T. Kawai, X. Wu, H. Tachibana, T. V. Hughes, H. Sakurai, J. W. Baldwin, C. Hosch, M. P. Cava, L. Brehmer, G. J. Ashwell, *J. Am. Chem. Soc.*, 1997, **119**, 10455-10466.

[13] Z. Ci, *Nanofabrication: principles, capabilities and limits. Springer, Heidelberg*, 2008.

[14] M. Browker, P. R. Dacie, *Scanning tunneling microscopy in Surface science and catalysis. Wiley-VCH, Weinheim*, 2010.

[15] F. C. Simeone, C. Albonetti, M. Caballini, *J. Phys.Chem. C*, 2009, **113**, 18987-18994.

[16] M. A. Reed, C., Zhou, C. J. Muller, T. P. Burgin, J. M Tour, *Science,* 1997, **278**, 252–254.

[17] C. Joachim, J. K. Gimzewski, A. Aviram, *Nature*, 2000, **408**, 541–548.

[18] A. Nitzan, *Annu. Rev. Phy. Chem.*, 2001, **52**, 681–750.

[19] B. Branchi, C. Herrman, K. W. Hipps, M. Hliwa, C. Joachim, C. Li, D. L. Mattern, R. M. Metzger, A. Mishchenko, M. A. Rampi, M. A. Ratner, N. Renaud, F. C. Simeone, G. C. Solomon, T. Wandlowski, *Unimolecular and Supramolecular Electronics II: Chemistry and Physisc Meet at Metal-Molecule Interfaces, Topics in Current Chemistry* 2012, **313**.

[20] a) S. Sanvito, *Chem. Soc. Rev.*, 2011, **40**, 3336; b) S. Sanvito, A. R. Rocha, *J. Comput. Theor. Nanosci.*, 2006, **3**, 624; c) W. Wernsdorfer, *Int. J. Nanotechnol.*, 2010, **7**, 497.

[21] R. G. Hicks, *Org. Biomol. Chem.*, 2007, **5**, 1321.

[22] I. Ratera, J. Veciana*, Chem. Soc. Rev.*, 2012, **41**, 303.

[23] M. Ballester, J. Riera, J. Castañer, C. Badia, J. M. Monso, *J. Am. Chem. Soc.*, 1971, **93**, 2215.

[24] M. Ballester, *Acc. Chem. Res.*, 1985, **18**, 380.

[25] M. A. Fox, E. Gaillard, C. C. Chen, *J. Am. Chem. Soc.*, 1987, **109**, 7088.

[26] C. Sporer, I. Ratera, D. Ruiz-Molina, Y. Zhao, J. Vidal-Gancedo, K. Wurst, P. Jaitner, K. Clays, A. E. Persoons, C. Rovira, J. Veciana, *Angew, Chem. Int. Ed.*, 2004, **43**, 5266.

[27] I. ratera, D. Ruiz-Molina, J. Vidal-Gancedo, k. Wurst, N. Daro, J. F. Letard, C. Rovira, J. Veciana, *Angew, Chem. Int. Ed.*, 2001, **40**, 919.

[28] I. Ratera, S. Marcen, D. Ruiz-Molina, C. Rovira, J. Veciana, J. F. Letard, E. Freysz, *Chem. Phys. Lett.,* 2002, **363**, 245.

[29] D. Maspoch, D. Ruiz-Molina, K. Wurst, J. Tejada, C. Rovira, J. Veciana*, J. Am. Chem. Soc.,* 2004, **126**, 730–731.

[30] D. Maspoch, D. Ruiz-Molina, K. Wurst, N. Domingo, M. Cavallini, F. Biscarini, J. Tejada, C. Rovira, J. Veciana, *Nature Materials*, 2003, **2**, 190.

[31] J. Sedo, D. Ruiz-Molina, J. Vidal-Gancedo, C. Rovira, J. Bonvoisin, J. P. Launay, J. Veciana, *Adv. Mater.*, 1996, **8**, 748.

[32] J. Bonvoisin, J. P. Launay, C. Rovira, J. Veciana, *Angew, Chem. Int. Ed.*, 1994, **33**, 2106.

[33] I. Ratera. D. Ruiz-Molina, F. Renz, J. Ensling, K. Wurst, C. Rovira, P. Gutlich, J. Veciana, *J. Am. Chem. Soc.*, 2003, **125**, 1462.

[34] I. Ratera, C. Sporer, D. Ruiz-Molina, N. Ventosa, J. Baggerman, A. M. Brouwer, C. Rovira, J. Veciana, *J. Am. Chem. Soc.*, 2007, **129**, 6117.

[35] a) J. Guash, L. Grisanti, V. Lloveras, J. Vidal-Gancedo, M. Souto, D. Morales, M. Vilaseca, C. Sissa, A. Painelli, I. Ratera, C. Rovira, J. Veciana, *Agew. Chem. Int. Ed*., 2012, **51**, 1-6. b) J. Guash, L. Gristani, S. Jung, D. Morales, G. D'Avino, M. Souto, X. Fontrodona, A. Painelli, F. Renz, I. Ratera, J. Veciana. *Chem. Mater*., 2013, **25**, 808-814. c) J. Guash, L. Grisanti, M. Souto, V. Lloveras, J. Vidal-Gancedo, I. Ratera, A. Painelli, C. Rovira, J. Veciana *J. Am. Chem. Soc.,* 2013, **135**, 6958-6967.

[36] A. Heckmann, C. Lambert, *J. Am. Chem. Soc*., 2007, **129**, 5515.

[37] V. Llovera, J. Vidal-Gancedo, D. Ruiz Molina, T. M. Figueria-Duarte, J. F. Neirengarten, J. Veciana, C. Rovira, *Faraday Discussions*, 2006, **131**, 291. + JACS 2011

[38] O. Armet, J. Veciana, C. Rovira, J. Riera, J. Castañer, E. Molins, J. Rius, C. Miravilles, S. Olivella, J. Brichfeus, *J. Phys. Chem*., 1987, **91**, 5608.

[39] M. Ballester, J. Riera, J. Castaner, A. Rodriguez, C. Rovira, J. Veciana, *J. Org. Chem.*, 1982, **47**, 4498–4505.

[40] M. Souto, D. Morales, J. Guash, I. Ratera, C. Rovira, A. Pailli, J. O. Jeppesen, C. Rovira, J. Veciana, *Chem. Eur. J.,* 2015, **21**, 8816-8825.

[41] N. Crivilles, S. Fukurawa, A. Minoia, A. V. Heyen, M. Mas-Torrent, C. Sporer, M. Linares, A. Volodin, C. Van Haesendonck, M. Van der Auweraer, R. Lazzaroni, S. De Feyter, J. Veciana, C. Rovira, *J. Am. Chem. Soc*, 2009, **131**, 6246.

[42] N. Crivilles, M. Mas-Torrent, S. Perruchas, N. Roques, J. Vidal-Gancedo, J. Veciana, C. Rovira, L. Bsabe-Desmonts, B. J. Ravoo, M. Crego-Calama, D. N. Reinhoudt, *Agew. Chem. Int. Ed*., 2007, **46**, 2215.

[43] C. Simao, M. Mas-Torrent, N. Crivillers, V. Lloveras, J.-M. Artes, P. Gorostiza, J. Veciana, C. Rovira, *Nature Chemistry*, 2001, **1**, 1.

[44] N. Crivillers, M. Mas-Torrent, J. Vidal-Gancedo, J. Veciana, C. Rovira, *J. Am. Chem. Soc.,* 2008, **130**, 5499.

[45] N. Crivillers, C. Munuera, M. Mas-Torrent, C. Simao, S. T. Bromley, C. Ocal, C. Rovira, J. Veciana, *Adv. Mater.*, 2009, **21**, 1177.

[46] N. Crivillers, M. Paradinas, M. Mas-Torrent, S. T. Bromley, C. Rovira, C. Ocal, J. Veciana, *Chem. Commun*., 2011, **47**, 4664–4666.

Chapter 2:
Molecular Wires

MOLECULAR WIRES

One of the first to coin the term ''molecular wire'' was the 1988 Nobel Prize winner J.-M. Lehn who described a caroviologen molecule that could be incorporated into vesicle membrane and act as a transmembrane electron channel.[1] The use of single-molecule electronic components is very interesting to achieve the smallest scale in circuits, but it is challenging since they have to be connected by conducting wires of the same (molecular) dimensions. One of the major issues in molecular electronics is the measurement, and understanding of the current voltage response of an electronic circuit in which molecular systems act as conducting elements. Before incorporating molecules in nanoscale circuits, it is necessary to understand the conductivity behavior of the proposed molecular wires in bulk.
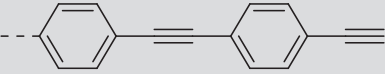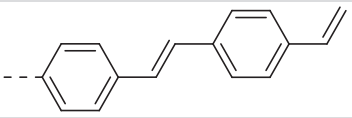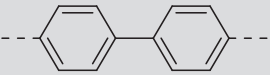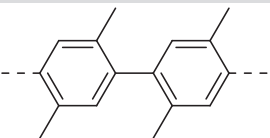
1. Molecular Wires
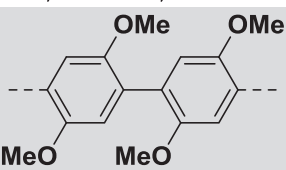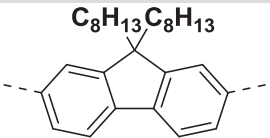
A molecular wire should be able to act as a charge (electrons or holes) transport element, and function as an elementary building block for nanoscale devices.

There are different molecular structures that have been investigated as molecular wires as for example conjugated chains (Table 1), porphyrin oligomers,[2] carbon nanotubes[3] or DNA.[4]

Most of the investigated molecular wires are conjugated linear oligomers. In general, these kinds of molecules can be readily synthesized in good yield giving a family of oligomers with different length. The π conjugation of multiple bonds gives rise to a delocalized π molecular orbital, in which the charge can be easily transported.
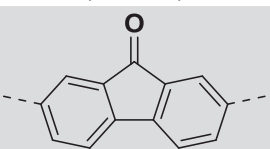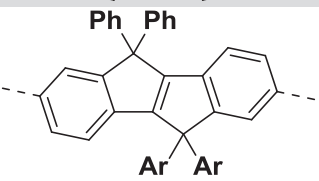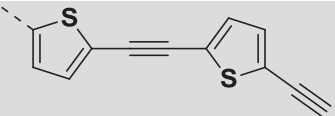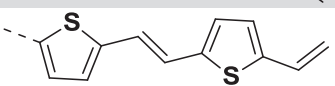
Traditionally oligo-(*p*- phenylene ethynylenes) **OPPE**[5,6,7] derivatives have been deeply studied due to the fact that they can be synthesized easily in a good yield and oligomers with large length can be achieved. Nevertheless, due to the torsion angle between the phenyl rings and the triple bonds, the conjugation is not very effective. By contrast, the oligo-*p*-phenylene vinylenes **OPPV**[8,9] in which the triple bond is changed by a double bond, have an increased flexibility and conjugation between the aromatics rings. Other wires that have demonstrated their efficacy in electron transport are oligo-*p*-phenylene (**ph_n**),[10] oligo-*p*-xylene (**xy_n**)[11] and oligo-*p*-dimethoxybenzene bridges (**dmb_n**).[11] Other very interesting oligomers are those based on fused aromatic rings as oligofluorene (**fl_n**),[12,13] oligo-2,7-fluorenone (**FN_*n***)[14] and fused oligo-*p*-phenylene vinylene (**COPV**) due to the higher π-conjugation.[15] Molecular wires derived from polythiophenes have also revealed good properties as hole transporters.[16,17,18]Oligo-(2,5-thiophene ethynylenes) (**OTE**)[16] and oligo-thiophene vinylene (**nTV**)[17,18] have been also studied and demonstrated to efficiently transport holes.

Table 1: Conjugated hydrocarbonate structures most commonly used as molecular wires.

Acronym	Structure	Group/ref
OPPE		Albinsson,[5] Guldi,[6] Tour[7]
OPPV		Wasielewski,[8] Guldi[9]
ph_n		Wasielewski[10]
xy_n		Wenger[11]
dmb_n		Wenger[11]
fl_n		Wasielewski,[12] Martin[13]
FN_n		Wasielewski[14]
COPV		Nakamura[15]
OTE		Tour[16]
nTV		Langa,[17] Roncali[18]

# 2. Characterization techniques

As described above, a molecular wire is a structure through which charges can be transported/transferred from one end to the other. But in order to determine the conductivity of a molecular wire it is necessary to induce the charge transfer through the molecules. For this purpose, two different types of experiments are employed. On one side, some techniques are able

to directly measure the conductivity through the molecule integrated between located two electrodes when a bias voltage is applied. For instance, single molecule break junctions or sandwiched SAMs might provide a wealth of information. On the other hand, an easier and technologically less demanding methodology is to perform the studies in solution by inducing an intramolecular-electron-transfer (IET) reaction between a donor and acceptor moieties linked at each end of the molecular wire.

2.1 In junctions

One of the first examples of conduction measurements directly through a molecular wire linked to two electrodes was published in 1996 by J.M. Tour and P.S. Weiss.[19] In this work they studied the conductivity of SAMs of *n*-dodecanthiol and **OPPE**-thiol on gold, using a scanning tunneling microscope (STM). It was found that the conjugated molecule **OPPE** is better conductor than dodecanethiol.

Many examples have been published since then as the two representative ones mentioned below. In 2010, N. Tao and co-workers published a study of the charge transport characteristics of a family of long **fl$_n$** molecular wires using the scanning tunneling microscope break junction technique on gold (Figure 1).[20] They determined that the two shortest wires (n= 1, 2) show strong length dependence and temperature invariant conductance behavior, whereas the longer two wires (n= 3, 4) show weak length dependence and temperature variation conductance behavior. This tendency is consistent with a model where conduction occurs by two different mechanisms: superexchange in the shorter molecules and hopping in the longer wires (these mechanisms will be explained in the next section).
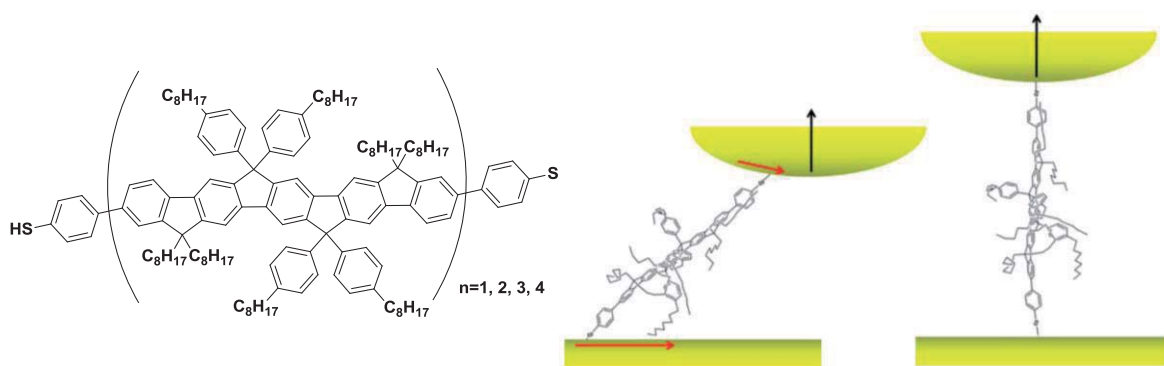
Figure 1: Molecular structure of the wires used in the study from N. Tao *et al.* and schematic illustration of proposed molecular junction evolution. As the tip retracts, the molecule slides along the surface of the substrate so that it is pulled upright.[20]

Another interesting example of single molecular wires conductance was performed by L. Venkataraman and co-workers in 2015. In this work, they demonstrate that charge carriers in STM

single-molecule junctions (STEM-BJ) can be tuned within a family of molecular wires that contain electron-deficient thiophene-1,1-dioxide (**TDO**) building blocks. By performing thermopower measurements they extract the Seebeck coefficient and they show that the dominant charge carrier changes from holes to electrons as the number of **TDO** units is increased, thus, the conductivity transport can be tuned from p- to n-type (Figure 2).[21]
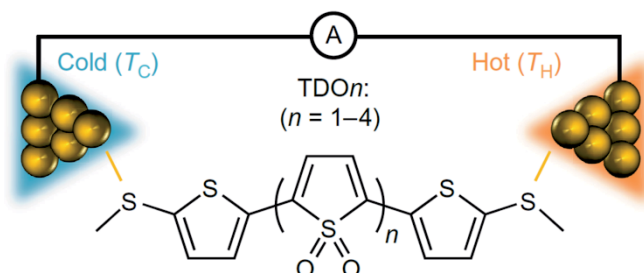

Figure 2: Schematic representation of the STM-BJ set-up to measure the Seebeck coefficient of a family of molecules, **TDOn** (n = 1–4, TDO4 is shown in the lower panel). The STM-BJ gold substrate is heated with the gold tip maintained at room temperature.[21]

Although over the last years there have been technological breakthroughs on the development and improvement of techniques to measure molecular wires conductivity in metal junctions, there are still reproducibility difficulties and much work is still needed.

2.2 In solution

An alternative method to determine the charge transport through a molecular wire is to create a donor acceptor dyad (D-A) in which the molecular wire acts as a bridge connecting the donor and the acceptor units. In these systems an electron transfer can be thermally o photochemically induced. Therefore, electron donor-bridge-acceptor (D-B-A) structures (Scheme 1) could serve as model systems to probe intramolecular electron transfer (IET) processes through the bridge in solution.
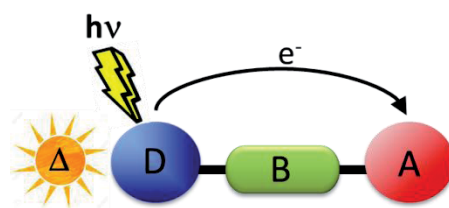
Scheme 1

Scheme 2 shows a representation of the different types of IET processes that can take place. Mainly, there are two classes of IET: one that involves the excited states of the molecule in the electron transfer process (Scheme 2.i), and other that takes place on the ground state (Scheme 2.ii and 2.iii).
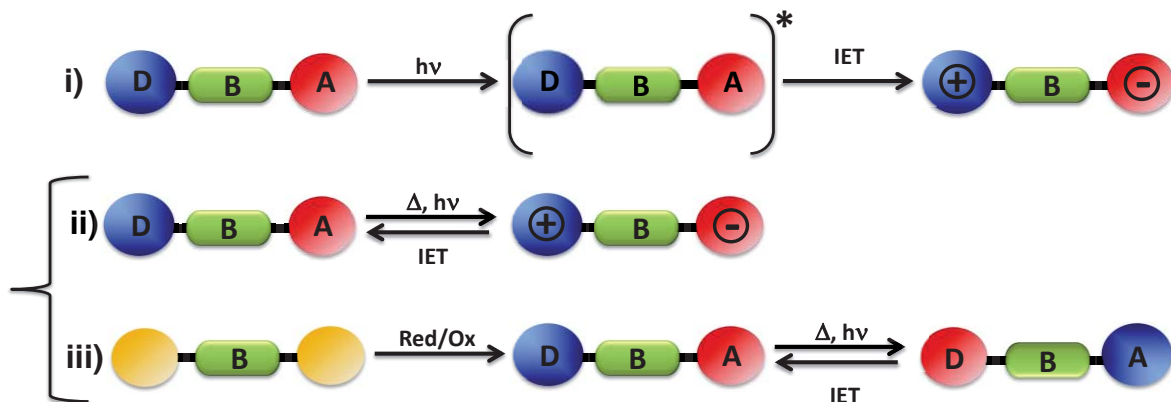
Scheme 2

The energetic pathway of the process i) is represented in Scheme 3. Here the electron transfer occurs after the molecule is brought to an electronic excited state through the absorption of one photon ($h\nu$). In that way, the donor/acceptor capacity of the system increases facilitating the IET that produces a charge separation state (D^+-B-A^-). This process is described by a constant rate k_{cs}. This charge separation state evolves through a charge recombination pathway (described in Scheme 3 by k_{cr}) to the original state. By transient spectroscopy methods, the rate constant of both charge separation and charge recombination processes can be determined.[22]
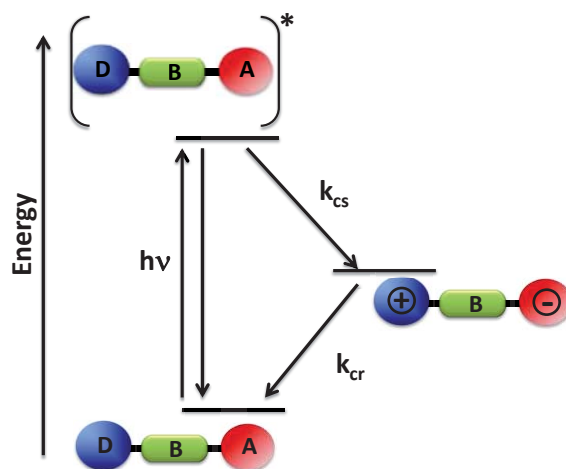
Scheme 3

In the processes identified in Scheme 2 as ii) and iii), the IET occurs in the ground sate induced by direct excitation ($h\nu$) or through thermal excitation.

These mechanisms take place in D-A dyads where the charge separated state is accessible directly from the ground state (process ii); or as it is represented in process iii, systems with two redox centers in different oxidation state, also known as mixed valence species. In mixed valence

systems, the crucial feature is the exchange of valence between the two centers (Scheme 4). The charge interconversion leads to an internal and external reorganization energies, which are related with the activation energy of IET. The fundamental aspects of the mixed valence systems and D-A dyads are developed in the next section.
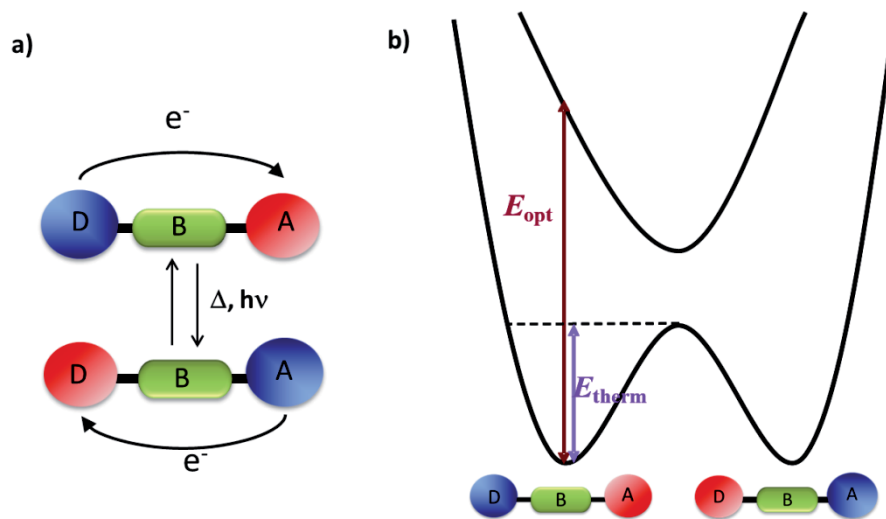
Scheme 4

3. Mixed Valence Systems and D-A dyads

3.1 Introduction

Organic Mixed-Valence (MV) systems are highly relevant due to their optical and charge transport properties.[23] However, the importance of these systems lies in the fact that they are excellent models to study the intramolecular electron transfer phenomenon, of great relevance in biophysics processes, such as photosynthesis or in molecular electronic devices.[24]

It is not easy to give a straightforward definition of the MV compounds as well as their differences with the D-A systems composed of two different units. To address these issues it is necessary to consider the similarities of these two classes of systems (MV and D-A): (i) both consist of two or more redox centers, one acting as an electron donor and the other as an electron acceptor; (ii) in both compounds an electron transfer IET or charge transfer ICT can take place between the donor and the acceptor moieties. In general, the IET refers to a general intramolecular electronic exchange, while ICT denotes the partial charge transfer optically induced.[25]

As shown in Figure 3 the IET generates, for MV (Figure 3a) a new ground state with different spin and charge distribution, while for D-A (Figure 3b) supposes a new electronic excited state. As a result, the MV systems could be defined as an open-shell systems associated to the ground state. On the contrary, the D-A are close-shell systems in the ground state, except when the acceptor or the donor unit is a neutral radical in the ground state (Figure 3b).[26]
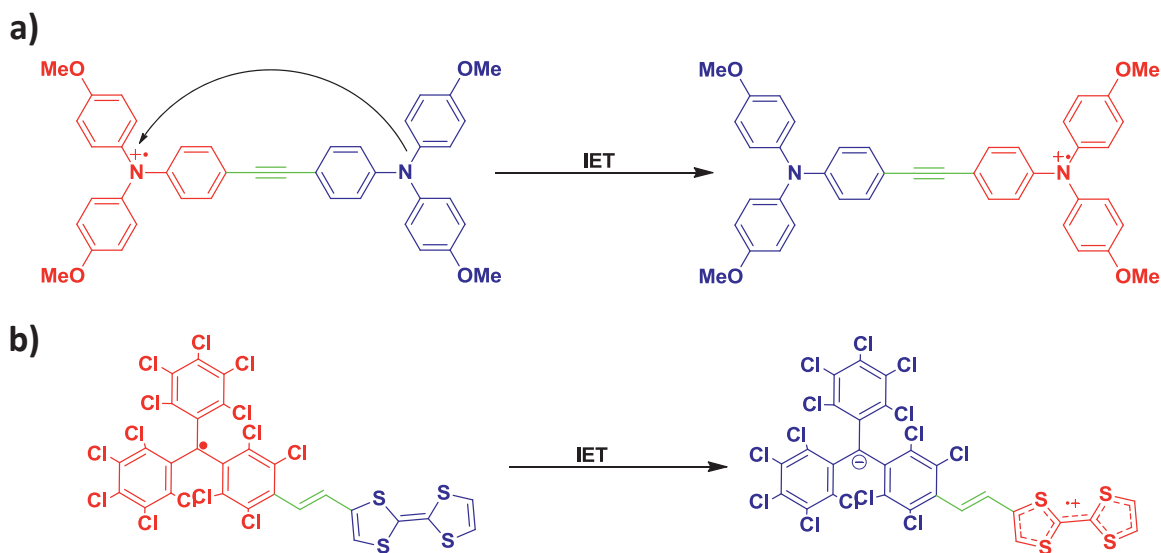

Figure 3: Example of a) MV system, b) D-A system. The blue molecules correspond to electron donors and the red ones to the electron acceptors.- Bridges are colored in green.

3.2 Marcus Theory

The first fundamental and generally accepted quantification of IET reactions in solution was developed by R. A. Marcus in 1950.[27] Despite this theory emerged on investigations of "self-exchange reactions" and "cross-reactions" of metal ions in solution,[28] the principal concepts are applicable to IET processes in organic and inorganic MV systems.

3.2.1 Diabatic treatment: Classical Marcus Theory

In agreement with Marcus Theory,[24b, 29, 30, 31] the free-energy surfaces of a MV system with two redox centers can be reduced to two diabatic one-dimensional parabolic profiles along a reaction coordinate x. Profile representing the reactant and the product state after the IET process takes place. According to the nature of the redox centers, the MV systems can be classified in two types: (i) degenerated, if the two redox centers are the same, and therefore product and reactant are energetically equivalents (Figure 4a); and (ii) non-degenerated, if the redox centers are different and therefore have different energy (Figure 4b). In this latter case, ΔG^{00} is the free-energy difference between A and B states.
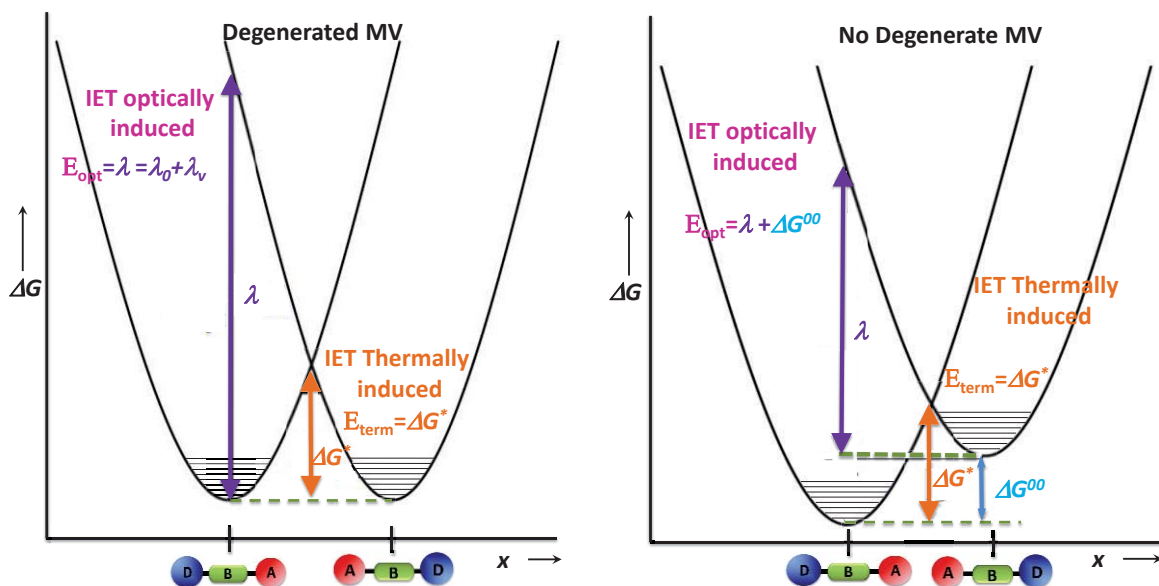
Figure 4: Diabatic free energy surfaces (blue lines) of a MV compound with a) degenerated MV states and b) non-degenerated MV states, and the two possible pathways for IET: Optically induced IET and thermally induced IET.

The IET occurs, regardless of the MV type, through two possible pathways: (i) thermally induced IET along the reaction coordinate x from the free-energy minimum of the reactant to the free-energy minimum of the product with the free activation energy (ΔG^*); and (ii) optically induced IET which, through vertical excitation and according to the Franck-Condon principle, from the minimum of the reactant to the product surface. For degenerated MV systems, the energy necessary for the optically induced exchange, is known as reorganization energy of Marcus λ (Figure 4a). λ depends of two factors: (i) the solvent reorganization energy λ_0, which considers the reorientation of the solvent molecules, near the MV system, after IET has taken place, and (ii) λ_v which takes into account the changes of bond lengths and bond angles at the redox centers while

changing their oxidation states. For non-degenerated MV systems, the energy necessary to promote the optically IET is the total of ΔG^{00} and λ (Figure 4b).

The mathematic expression for the thermally induced pathways can be described as follows:

The outersphere reorganization energy λ_0 can be calculated by using a dielectric continuum model. In this model, the donor and acceptor redox centers are assumed to have spherical geometries with the radius r_1 and r_2 and a center to center distance of r_{12}. The solvent reorganization energy can then be calculated by equation (1), where n is the refraction index and D is the permittivity of the solvent.[27a, 32] The inner reorganization energy λ_v depend on the molecular nature of the MV system and therefore is different for each case.

$$\lambda_0 = \frac{e^2}{4\pi\varepsilon_0}\left[\frac{1}{2r_1}+\frac{1}{2r_2}+\frac{1}{r_{12}}\right]\left[\frac{1}{n^2}-\frac{1}{D}\right] \tag{1}$$

The rate constant k of electron transfer is given by an Arrhenius-type Equation (Eq(2)), where k_B is the Boltzmann constant, T is the temperature, and ΔG^* is the free energy of activation needed to thermally induce the electron transfer. The pre-exponential factor A, depends on the nuclear motion frequency through the transition state (v_n), and the electron transmission coefficient κ_{el}, which is equal to one in the classical treatment.

$$k = Ae^{\frac{-\Delta G^*}{k_BT}} \quad \text{with} \quad A = v_n\kappa_{el} \tag{2}$$

Within a classical treatment, the diabatic free energy surfaces for product and reactant are parabolas with identical λ values. A simple algebraic analysis leads to Equation 3 for the calculation of ΔG^*.

$$\Delta G^* = \frac{(\lambda+\Delta G^{00})^2}{4\lambda} \tag{3}$$

Combining equations 2 and 3 the Marcus Equation of thermally induced IET (Eq(4)) is obtained.

$$k = Ae^{\frac{(\lambda+\Delta G^{00})^2}{4\lambda k_BT}} \tag{4}$$

The classical Marcus Theory (diabatic) assumes that the electronic coupling between the donor and acceptor centers, V_{ab}, is much lower than the thermal energy (k_BT). So the standard Marcus Theory is only applicable to MV compounds with only small electronic interaction.

3.2.2 Adiabatic Treatment: Marcus-Hush/Muliken-Hush Theory

The Marcus-Hush theory[33, 34] represents an extension of the classical Marcus theory, that allows its application to MV systems in which the electronic communication between the donor and acceptor (V_{ab}) is large compared to the thermal energy k_BT, and therefore the introduction of an adiabatic effect is required.

Figure 5 represents the adiabatic free energy surfaces of a MV system with non-degenerated states (degenerated states would correspond to a system where ΔG^{00} = 0). According to this, the combination of the two diabatic harmonic potential with a free energy of V_{aa} and V_{bb} which interact trough the electronic coupling (V_{ab}), generates two new adiabatic free energy surfaces (ground state and excite state). The free energy difference between ground and excited at the intersection of the two diabatic free energy surfaces, is equivalent to twice the value of the electronic coupling ($2V_{ab}$). If $2V_{ab} \ll \lambda$ (the reorganization energy), the ground state presents two minimum associated to reagent and product.
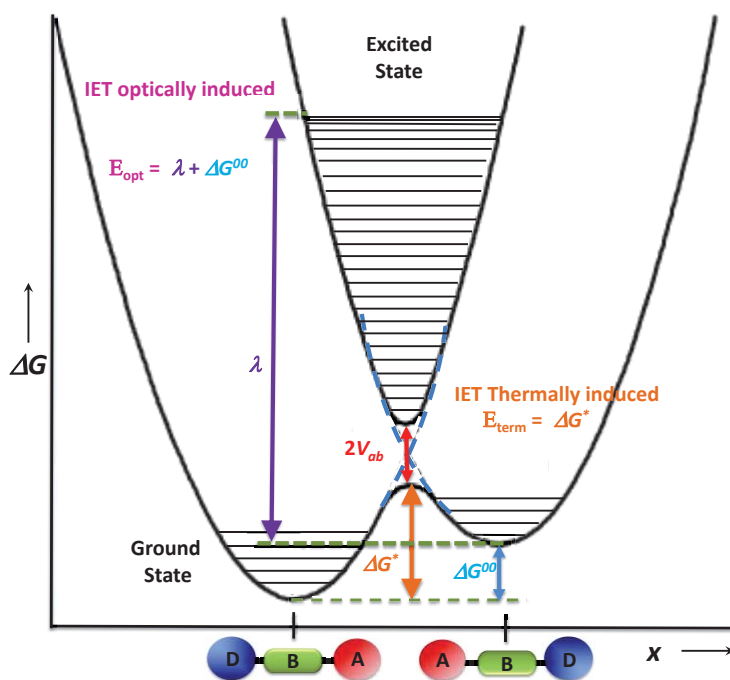
Figure 5: Adiabatic free energy surfaces (black solid lines) of a MV compound with non-degenerated MV states. The free energy difference between the electronic ground and excited states at the intersection point of the diabatic free energy surfaces (blue dashed lines) is equivalent to $2V_{ab}$.

As it can be seen in Figure 5, the separation of the two diabatic curves implies an increment of the V_{ab}. Also if V_{ab} increases, the adiabatic minima of the ground state are getting close according to the resonant factor V_{ab}^2/λ. Therefore, as the barrier of the thermally induced IET process (ΔG^*) depends of the V_{ab} and λ, ΔG^* for the adiabatic treatment can be calculated by introducing this

condition in equation 3 obtaining the general expression to calculate ΔG^* (equation 5), which is simplified in the equation 6 for a degenerated MV system.

$$\Delta G^* = \frac{(\lambda - 2V_{ab})^2 + \Delta G^{00}(\Delta G^{00} + 2\lambda)}{4\lambda} \tag{5}$$

$$\Delta G^* = \frac{(\lambda - 2V_{ab})^2}{4\lambda} \tag{6}$$

According to equations 5 and 6, an increase of V_{ab} to the situation when $V_{ab} \gg \lambda$, implies that the energy barrier is zero ($\Delta G^* = 0$). Hence the adiabatic free energy surface of the ground state is reducing to a minimum, as a result of the large electronic coupling between the two redox centers. Therefore, product and reactant cannot be distinguished generating a new state totally delocalized.

The contribution of Hush to the adiabatic theory was the development of a method for V_{ab} calculation through the UV-Vis-NIR absorption spectrum of MV and D-A systems.[29, 35] Hush was based on the Intervalence Charge-Transfer (IV-CT) band originated from the optically induced Intervalence Charge-Transfer (ICT), which always appears in NIR region of the electronic absorption spectrum. The optically induced ICT proceeds from the Boltzmann weighted vibrational states of one minimum of the electronic ground state G, according to the Frank-Condon principle, into the vibrational manifold of the exited electronic state E. Relaxation from the exited state yields the product state with the charge being transferred. The Boltzmann-weighted population of vibrational states is a necessary condition for the validity of the Marcus-Hush approach. This condition is only fulfilled at the high-temperature limit (HTL) where $h\tilde{v} \ll k_b T$. In that situation, the energetic separation of the different vibronic states is small enough to populate all of them.

The formation of an IV-CT band is represented in Figure 6a for a degenerated MV system. In that case the most probable transition from the ground state to excited state occurs at $\tilde{v}_{max} = \lambda$, that coincide with the maximum absorption of the IV-CT band. As in that situation the electronic coupling is weak, the band presents a symmetric Gaussian profile due to the population of the vibrational states is weighted. Thus, in the high-temperature limit (HTL), the band width $\tilde{v}_{1/2}$ can be calculated by equation 7.

$$\tilde{v}_{(1/2)}(HTL) = \sqrt{16 ln2 k_b T \tilde{v}_{max}} \tag{7}$$

This band is often used to identify an IV-CT process. The IV-CT band gets more asymmetric as the electronic coupling V_{ab} increases. This situation is represented in Figure 6b. The asymmetric character is a result of a cut-off of the transitions at the energy $2V_{ab}$, which is the smallest energy possible for an electronic transition.
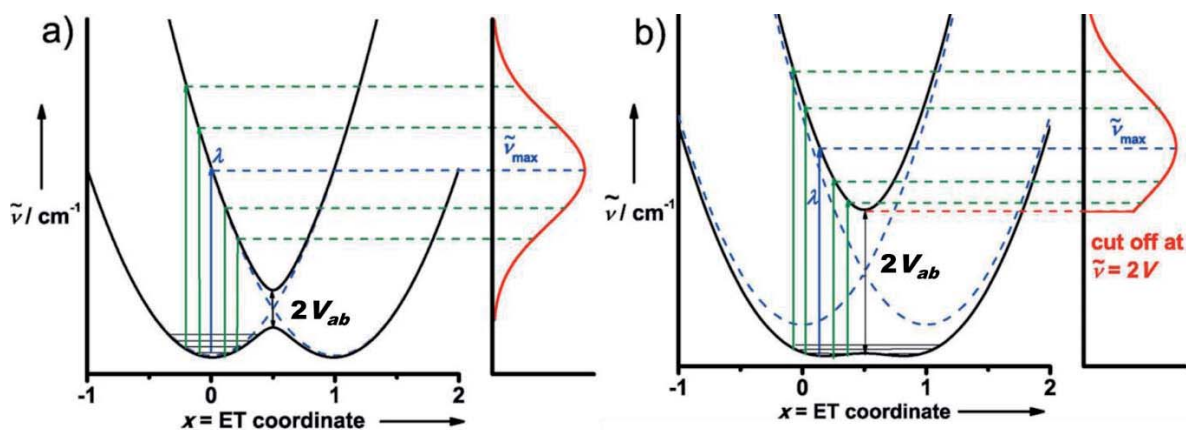
Figure 6: Formation of a IV-CT bands in MV compounds with a relatively small electronic coupling (V_{ab}): (a) with relatively strong coupling (b). Both figures reflect the situation for MV systems with degenerated MV states $0 < V < \lambda/2$. The vibrational levels have been omitted in order to simplify the figure.[36]

But the most important achievement of Marcus-Hush[29, 35, 37] theory is the possibility to extract the electronic coupling through IV-CT band analysis. Hence, applying a more rigorous mathematic derivation the equation 8 is obtained which is known as general Marcus-Hush theory or Muliken-Hush theory.[38] Where $\tilde{v}_{max}$ and $\tilde{v}_{1/2}$ are the energy and the width at half height of IV-CT band (in cm^{-1}), ε_{max} is the maximum molar absortion (M^{-1}·cm^{-1}) and R is distance between the two redox centers (Å). Nevertheless, when the IC-TV is quite asymmetric, (as for example in Figure 6b), V_{ab} can be calculated through the maximum energy transition (Eq. 9)

$$V_{ab} = \frac{2.06x10^{-2}\sqrt{\varepsilon_{max}\bar{v}_{max}\bar{v}_{1/2}}}{R} \qquad (8)$$

$$V_{ab} = \bar{v}_{max}\big/2 \qquad (9)$$

3.3 Robin-Day classification of the MV and D-A systems

The adiabatic profiles of free energy shape depend on the ratio of electronic coupling V_{ab} and the Marcus reorganization energy λ. In the 60's Robin and Day classified MV and D-A systems into three classes considering these two factors (Figure 7).[39]

The D-A compounds where no electronic coupling (V_{ab} = 0) between donor and acceptor centers exists belong to class I (Figure 7a). The two redox centers do not influence each other and may be considered as isolated moieties. Therefore, no IET or ICT can take place in such compounds, neither optically or thermally. The explanation to this fact could be related to two factors: (i) the distance between the two redox centers are very large; or (ii) the interaction between donor and acceptor through the bridge is forbidden.

The D-A compounds where the electronic coupling between D and A is smaller than half the Marcus reorganizations energy $0 < V_{ab} < \lambda/2$ belong to Class II (Figure 7b). Here the diabatic free energy shapes are split in two adiabatic free energy shapes corresponding to excited and ground

states, where the ground state presents a double minimum. The charge is mainly localized in one redox center, but can be transferred (thermally or optically induced) to the other redox center.

In class III systems (Figure 7c) the interaction between the two redox centers is so strong that makes impossible to distinguish two minimum in the adiabatic ground state. As a consequence, the charge is totally delocalized over both redox centers. In this case $V_{ab} \geq \lambda/2$ and the activation energy is zero ($\Delta G^* = 0$).
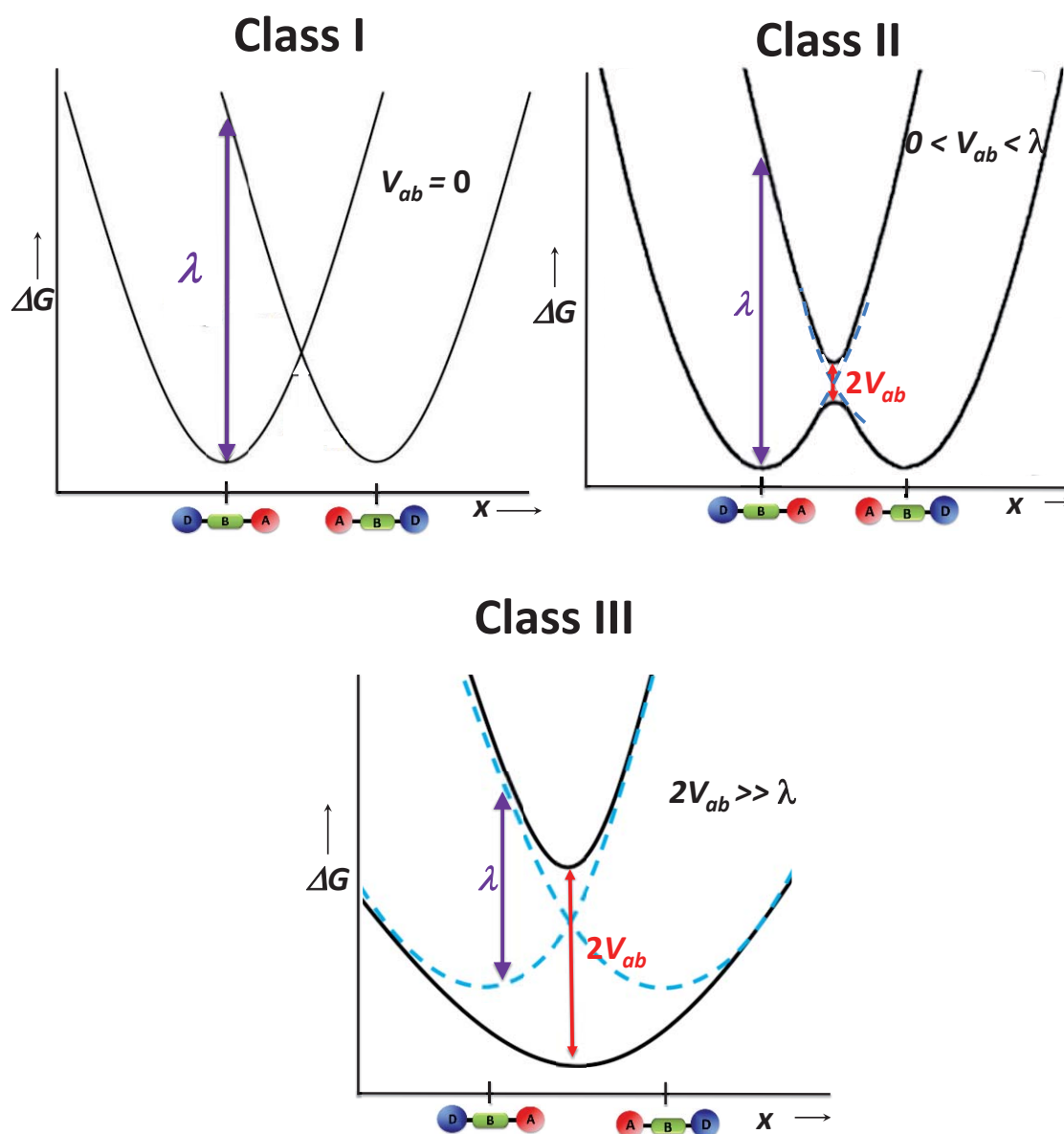
Figure 7: Calculated diabatic (blue dashed lines) and adiabatic (solid black lines) free energy shapes of class I-III MV systems with degenerate states. a) class I, b) class II, and c) class III.

3.4. IET studied by Electron Paramagnetic Resonance

Until now we have described that, according to the Marcus theory, the IET reactions in organic MV systems can be optically studied by analyzing the Intervalence Charge-Transfer band, which, as already stated, appears in the NIR region of the absorption spectrum. So, this methodology implies the study of the IET process induced by optical energy ($h\nu$). Nevertheless, as we mentioned in previous sections we can thermally induce the IET process in the ground state, but then the processsshould be analyzed by another methodology different from the optical spectroscopy. In this regard, variable temperature electron paramagnetic resonance (VT-EPR) spectroscopy has been extensively used.

VT-EPR experiments are based on the application of temperature to reach a dynamic process whereby the environment of a paramagnetic center can be affected modifying the line-shape of the EPR spectrum, causing an inhomogeneous line broadening. Such processes are hindered rotation, tumbling of the molecule, interaction with other paramagnetic species, chemical reaction and also IET processes. The line broadening arises from dynamic fluctuations in the local field at the unpaired electron(s). If changes occur sufficiently slowly, it is possible to observe lines assignable to distinct species. However, as the rate of fluctuations increases, the EPR lines broaden and finally coalesce into a single line (or set of lines), the position of which is the weighted average of the original line positions.

Consider an unpaired electron that can exist in either of two distinct forms or environments, (*a* and *b)* and each one has a distinctive EPR spectrum. For the sake of simplicity, assume that the probabilities for these forms are f_a and f_b (where $f_a + f_b = 1$) and that each form gives rise to a single EPR line of Lorentzian shape, one at resonance field B_a and the other at a higher field B_b. The line separation is $\Delta B_0 = B_b - B_a$.

In Figure 8a, the system is in the limit of slow exchange velocity ($k = 0$). In that point, the half-life of both states is very high ($\tau \rightarrow \infty$), and therefore there are two narrow lines corresponding to the two states. When the velocity exchange of the dynamic process is moderate (Figure 8b), the half-life of the two states is low, and hence the linewidth starts to increase. In figure 8c, the velocity exchange increases causing a further increase of the linewidth and a decrease of the ΔB_0. Figure 8d shows the coalescence of the two signals. In that point $\Delta B_0 \rightarrow 0$ and the broad signal is centered in the middle point $(B_b + B_a)/2$. When the limit of fast exchange velocity ($k \rightarrow \infty$) is reached (Figure 8e the half-life of the *a* and *b* states are very low ($\tau = 0$), appearing one narrow line corresponding to the sum of the two states.
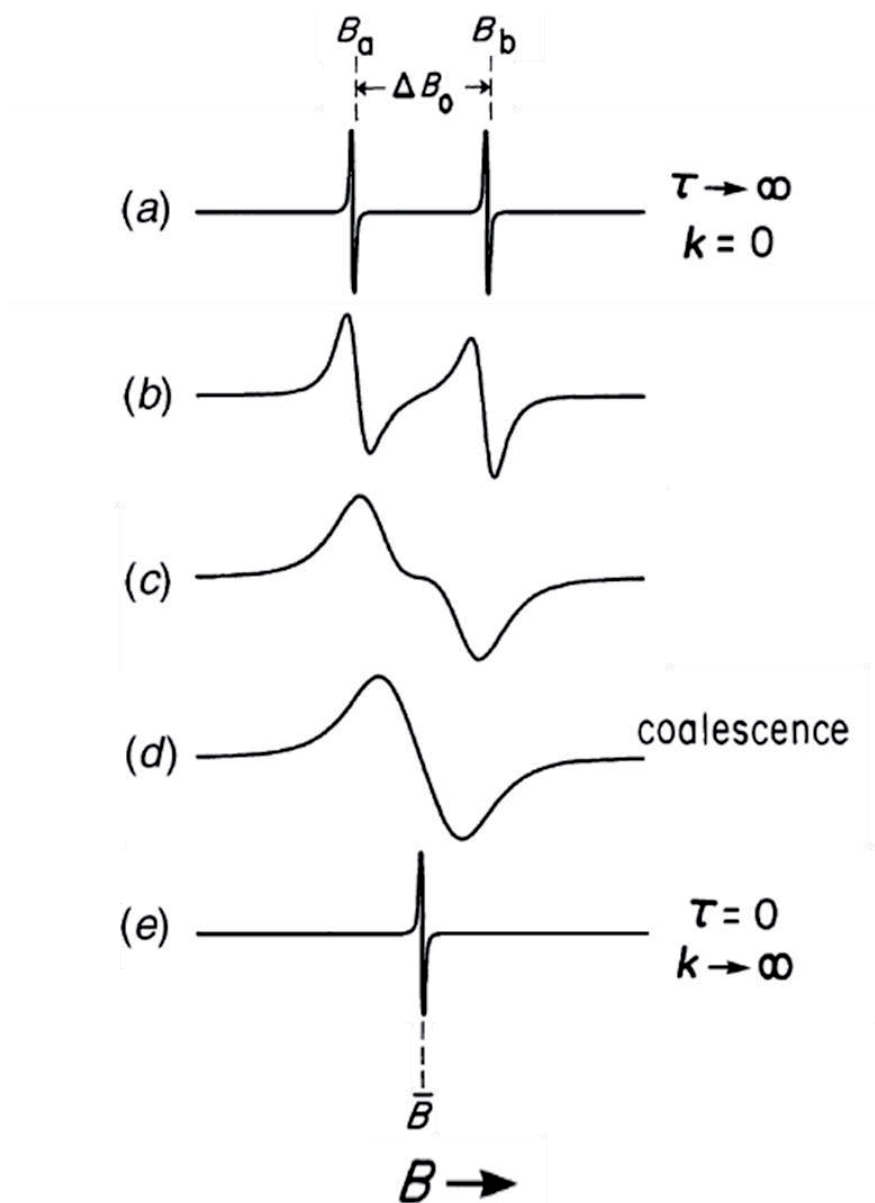
Figure 8: Simulated EPR spectra showing the effect of the increasing rate of interconversion between species *a* and *b* of an unpaired electron species. a) Slow rate limit ($\tau \rightarrow \infty$); b) moderately slow rate; c) faster rate showing spectral lines shifts; d) coalescence point; e) faster rate limit ($\tau = 0$).reference[40]

Thus, studying the dynamic IET process caused by temperature variation in a MV system, it is possible to determine the rate constant and the thermodynamic parameters involved. To be analyzed by EPR spectroscopy, the charge-transfer rate in MV compounds should be relatively low and should fall into the 10^7-10^9 s^{-1} region. Thus, MV systems with weak V_{ab} and/or high reorganization energy that slows down charge- transfer rates are particularly interesting.

One representative example to illustrate this methodology is the MV species studied by N Gautier *et. al*.[41] In this work they studied the thermally activate IET rate between a *p*-benzoquinone radical-anion ($\mathbf{Q^{\bullet-}}$) acting as an electron donor, and a *p*-benzoquinone acting as electron acceptor

(**Q**) connected through a tetrathiafulvalene (**TTF**) molecule acting as a bridge. This MV system can be in two equivalent states depending on the benzoquinone center where the radical is located. The two states can be interconverted between each other by overcoming an energetic barrier that corresponds to the activation energy of the IET process (Scheme 5). In that MV compounds, the radical has two equivalent groups of hydrogens, H_a H_b, which can be coupled to the unpaired electron in different way depending on the IET rate.
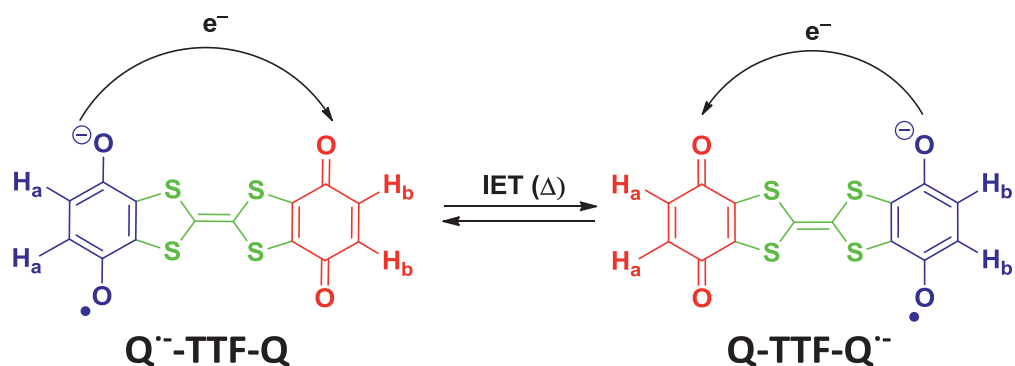
Scheme 5

In the situation where the electronic transfer is slower than the EPR time scale (slow exchange), the unpaired electron appears as localized in one of the benzoquinone centers, and it is only coupled with the two hydrogens of the corresponding aromatic ring (H_a or H_b). As the nuclear spin of hydrogens is $I = \frac{1}{2}$, there are three possible transitions, which as a result would generate three lines with intensity 1:2:1 in the EPR spectrum. This is the spectrum observed at the lowest temperature (260K) in Figure 9.

By contrast, in the situation where the electronic transfer is very fast (fast exchange), the unpaired electron is moving between the two benzoquinone centers, getting an average state where the unpaired electron appears to be in the two benzoquinone centers at the same time. Therefore the unpaired electron is coupling with both H_a and H_b hydrogens, and as the two states are equivalents, H_a and H_b hydrogens became equivalents. Therefore, the EPR spectrum would consist in five lines with intensity 1:4:6:4:1, accordingly with an electron coupled with four equivalents hydrogens as observed in the spectrum at 340K in Figure 9.

In the intermediate region, as the temperature is gradually lowered from 340 to 260K, the alternate lines broaden and disappear due to the change in the dynamic electron exchange rate between both of the benzoquinone centers through the **TTF** bridge.

The lowest temperature spectrum demonstrate that the unpaired electron is localized on one particular benzoquinone unit on the EPR time scale, and as the temperature is raised the activation energy barrier is overcome, which promotes a faster IET process between the two benzoquinone moieties. The dynamic of the intramolecular exchange process can be theoretically

simulated[42] (Figure 9b), obtaining the rate constants for the thermally activated IET process, and consequently the thermodynamic parameters.
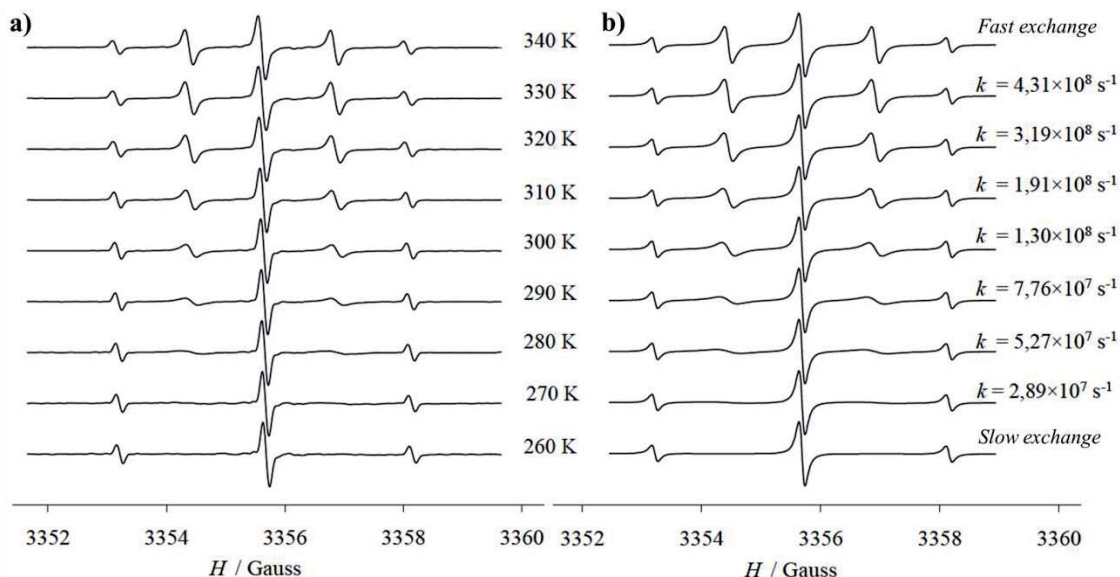
Figure 9: Experimental (a) and simulated (b) EPR spectra of **Q$^{\bullet-}$-TTF-Q** MV at different temperatures.[41]

The variable-temperature EPR methodology has been useful to study the thermally induced IET through different bridges in Mixed-Valence systems and elucidate the charge transfer mechanism using different redox centers as for example: tetraalkylhydrazines,[43] dinitroaromatic radical anions[44], bis(triarylamine) radical cations[45], bis(1,4-dimethoxybenzene) radical cations[46] and also PTM radicals,[47] that are the ones used in this work.

3.5 Transport Mechanisms in intramolecular electron transfer

The frontier orbitals of the redox centers of the MV systems and the bridge units have an important impact on the IET/ICT behavior. Thus, modification of molecular orbital overlap between the redox centers and bridges or their relative orientation influences the IET rate. In this context, three different mechanisms can take place: superexchange (SE), flickering (FR) and hopping (HOP). In most cases, not a single mechanism occurs but rather the operative mechanism is a mixture of them, although in general one is predominant.

Superexchange model: in the coherent SE mechanism (Figure 10a) the charge is at no time located on the bridge but is transferred by tunneling processes, meditated by virtual states, from the donor to the acceptor. The electron tunneling is caused by the thermal fluctuation in the donor and acceptor energy levels that originate a resonance between them. The SE mechanism relies on the assumption that the gap between HOMO/LUMO of the bridge and the redox active levels of the donor and acceptor is large compared to the electronic coupling between donor/acceptor and the bridge.[48]

The SE IET rate is given by the exponential equation 10. Where R is the overall distance over which the charge is transferred, r is the distance between two neighboring bridges units, ΔA is the free energy difference for IET from D to A, and β is the decay constant. Hence in this mechanism the transfer rate decreases exponentially whit the donor-acceptor distance.

$$k_{SE} = \frac{2\pi}{\hbar} \frac{V_{ab}^2}{\sqrt{4\pi\lambda k_B T}} e^{-\beta(R-r)} e^{-\frac{(\Delta A+\lambda)^2}{4\lambda k_B T}} \tag{8}$$

Filckering resonance model: This model applies to a situation that arises when IET occurs along a chain where donor, acceptor, and bridge levels are similar in energy. In the FR model the bridge acts as chain of redox sites, each of which can accept and donate electrons or holes (Figure 10b). IET from donor to acceptor is assumed to take place when thermal fluctuations of active energy levels of donor, bridge and acceptor are simultaneously in resonance. The charge moves with very little or no nuclear relaxation through the energy-aligned redox states.[49]

The FR rate is given by the equation 11, where Θ is a decay factor and ΔA_{BD} is the free energy difference for IET form donor to bridge.

$$k_{FR} = \frac{2\pi}{\hbar} \frac{V_{ab}^2}{\sqrt{4\pi\lambda k_B T}} \frac{\sqrt{2}}{\pi R/r} e^{-\Theta(R-r)} e^{-\frac{(\Delta A_{BD}+(\lambda-\Delta A)/2)^2}{2\lambda k_B T}} e^{-\frac{(\Delta A+\lambda)^2}{4\lambda k_B T}} \tag{9}$$

Charge Hopping model: Both SE and FR models do not describe properly the IET on longer bridges, thus charge hopping (Figure 10c) is an alternative to that situation. In this model charge hopping occurs in an incoherent transport channel where a localized excess electron or charge is assumed to hop between consecutive sites *i* and *j* with hopping rates k_{ij} to k_{ji}, where after each hop there is a relaxation. The time dependent site populations of the charge, p_i, in a system of N bridges units, are given by a system of coupled first order differential equations:

$$
\begin{aligned}
p_D &= -k_{1D}p_D + k_{D1}p_1 \\
p_1 &= k_{1D}p_D - (k_{D1} + k_{21})p_1 + k_{12}p_2 \\
&\;\;. \\
&\;\;. \\
p_N &= k_{NN-1}p_{N-1} - (k_{N-1N} + k_{AN})p_N + k_{NA}p_A \\
p_A &= k_{AN}p_N - k_{NA}p_A
\end{aligned}
\tag{10}
$$

The assumption of first order kinetics is justified when the charge population on the bridge remains small. Thus the bridge levels are energetically well separated from the donor/acceptor levels. Hence, solving the set of equation 12 the kinetic equation for this model (equation 13) can be obtained:

$$k_{HOP} = \cfrac{e^{-\frac{\Delta A_{BD}}{k_B T}}}{\cfrac{1}{k_{AN}} + \cfrac{1}{k_{D1}} + \cfrac{\frac{R}{r} - 2}{k_{BB}}}$$

<div style="text-align: right">(11)</div>

The hopping kinetic constant (k_{HOP}) can be interpreted as an effective rate constant for hopping from the donor to the acceptor via the bridge sites. The hopping model predicts that the effective hopping rate decrease linearly with the number of bridge sites, in contrast to the exponential distance dependence of the SE and FR rates.
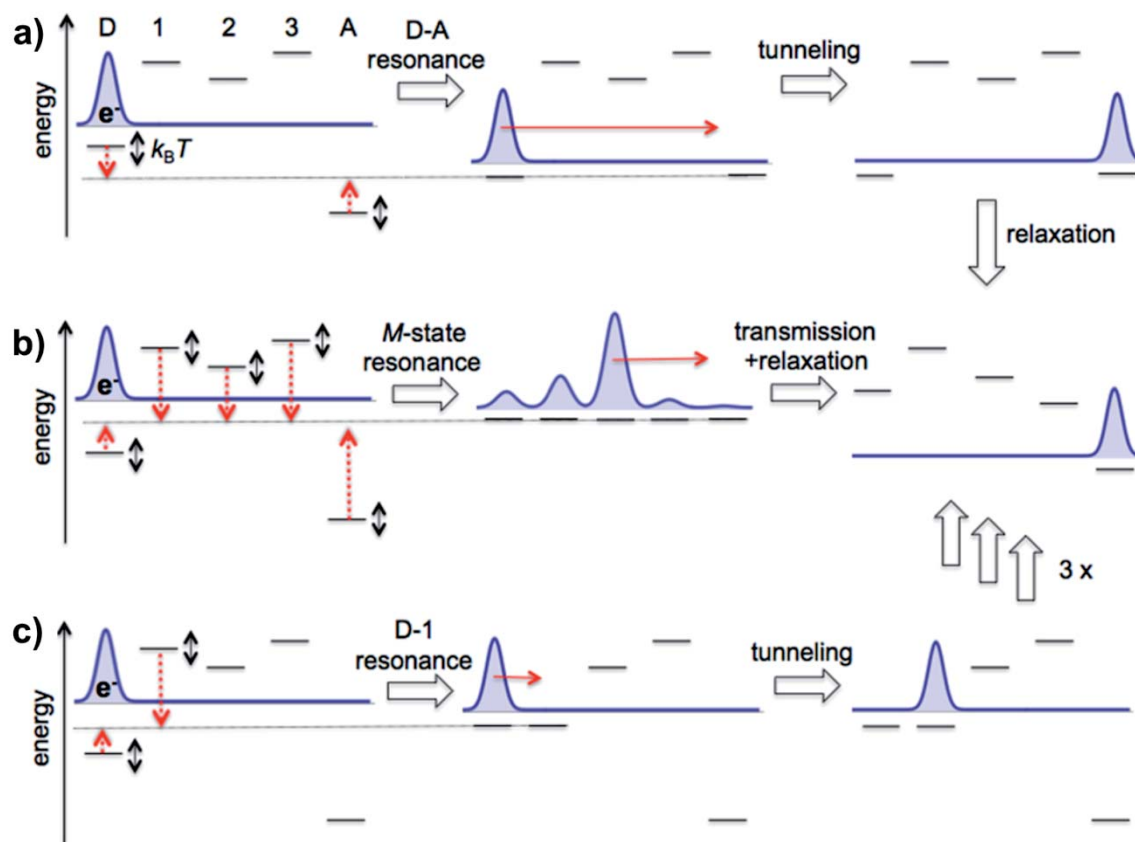

Figure 10: (a) Superexchange (SE), (b) flickering resonance (FR), and (c) hopping (HOP) models for IET along a chain of 5 redox active molecular sites. The first site is the electron donor (D), the last site is the acceptor (A), and there are three bridge sites (1, 2, 3) between D and A. One-electron energy levels are drawn in black lines for each site. The excess electron is indicated by a Gaussian function, initially localized at site D.[50]

The kinetic rate of IET in a MV system not only depends on the distance between the donor/acceptor redox centers and the temperature, but there are other factors that contribute to it. (i) One is the nature and structure of the bridge since in general rigid bridges have more conductance than flexible ones as a consequence of a better electronic coupling between donor/acceptor. (ii) Also the polarity of the media influences in the Marcus reorganization energy. Generally in polar solvents the IET is slower than in the non-polar ones, because the polar solvents increase the reorganization energy.

4. Precedents

Our group has a long experience in the study of molecular wires using MV systems based on PTM radical as electroactive redox center to promote the IET process through different wires. In 2011 a study about the IET process in the ground state on PTM radical/anion MV systems linked by *p*-phenylenevynilene (**nOPPV** n = 1-5) bridges was published. The PTM radical acts as acceptor, and the PTM anion as electro donor (Figure 11).[51]

In this **PTM⁻-nOPPV-PTM•** MV family the thermally induced IET was analyzed with the kinetic parameters obtained through the rate constant, k_{IET}, attained from VT-EPR measurements. The thermal k_{IET} dependence revealed the presence of two competing regimes for IET: at high temperature the predominant mechanism is hopping while at low temperature the principal mechanism is the superexchange. Both mechanisms occur to different extents depending on the length of the MV compounds (Figure 11b). Therefore the length of the **OPPVs** has an influence on the activation energy barriers of the hopping processes, diminishing the barriers as the length increases.
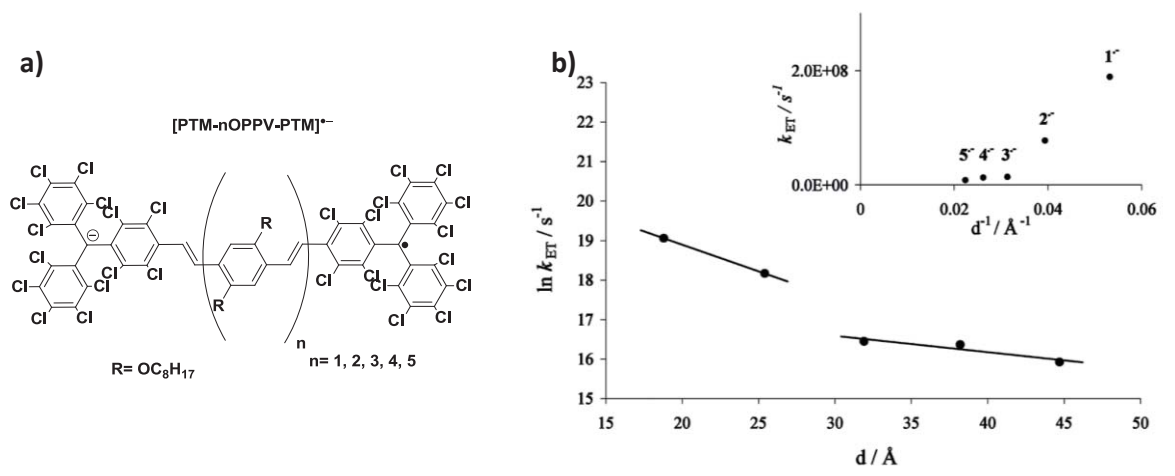
Figure 11: a) **[PTM-nOPPV-PTM]•⁻** MV family. b) Dependence of the IET rate constants on the bridge lengths for **[PTM-nOPPV-PTM]•⁻** in 1,2-dichlorobenzene at 300 K. Inset: Dependence of k_{ET} vs 1/d for such compounds.[51]

Oligothiophenes represent a well-known family of organic molecules, broadly applied as bulk semiconductors but also as molecular wires. In 2012 F. Langa and J. Casado studied a family of Mixed-Valence compounds with oligo-thiophene vinylene oligomers (**nTV** n =2, 4, 6, 8) as a bridge of two end-capping ferrocenes.[52] They studied the delocalization/localization of charge into the **nTV** molecular wire inducing the IET by the effect of the temperature in the **[Fc-nTV-Fc]•⁺** MV systems. The electronic ground state was analyzed by resonance Raman spectroscopy focusing on the C=C/C-C vibrational Raman modes. They observed that (i) the shorter members of the family (n = 2 and 4) are a fully delocalized charge MV system; (ii) in the longest one (n = 8), the charge is localized at the bridge center; (iii) the hexamer (n = 6) is at delocalized-to-localized turning point between the two limiting structures, which is corroborated by tuning the delocalized/localized

equilibrium with the modification of solvent and temperature. The explanation of this behavior is due to an efficient inter-ferrocene coupling which is modulated by the length of the bridge (Figure 12), demonstrating that **nTV** are good wires to promote the IET.
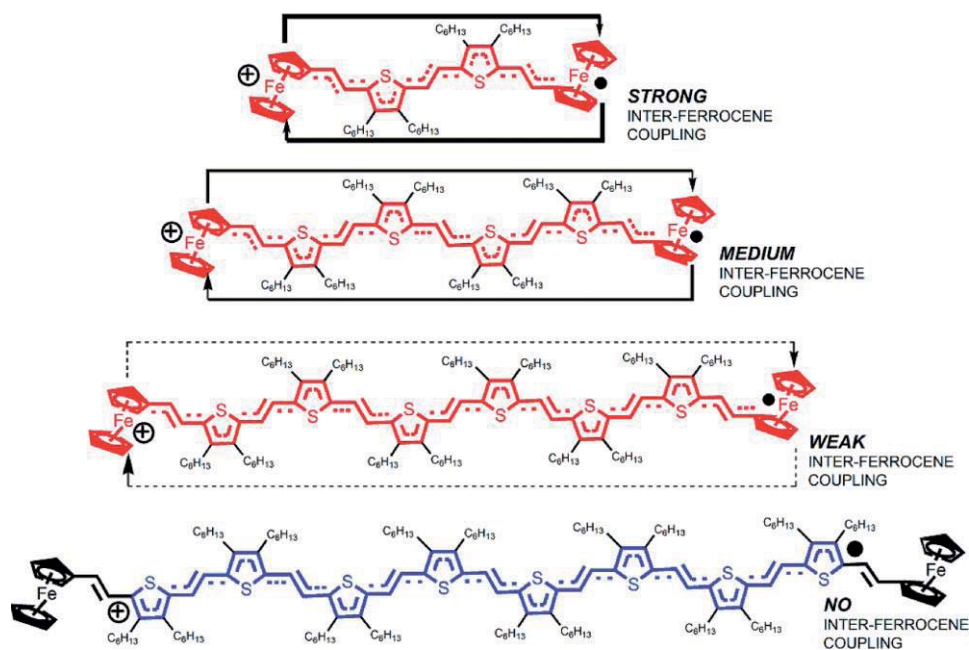
Figure 12: Schematic representation of the delocalized to localized hypothesis of **[Fc-nTV-Fc]**$^{\bullet+}$.[52]
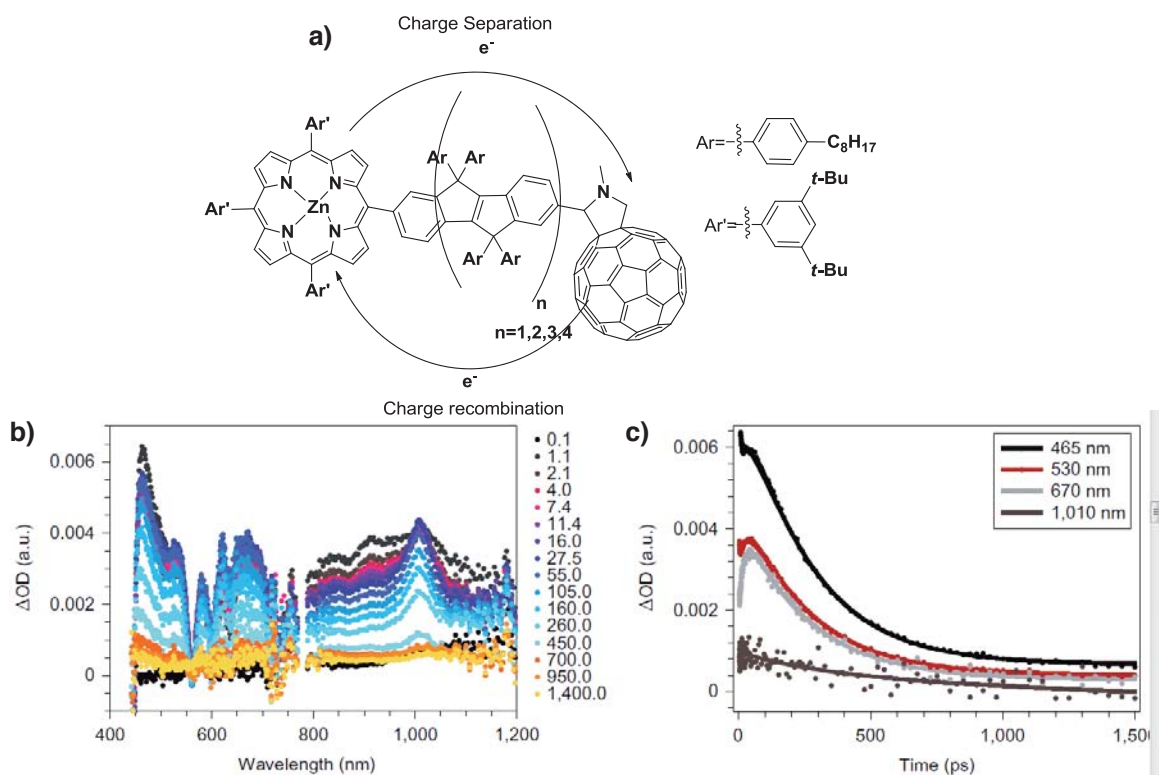
On the other hand, **COPV** bridges planarize the **OPPVs** (Scheme 6) and as consequence it is expected that their efficiency acting as molecular wires should be superior, allowing that the intramolecular charge transfer occurs at long distance. Thus, Sukegawa *et al.* implemented the **COPV** bridges in D-B-A systems, and studied the photoinduced ICT with zinc porphyrin (**ZnP**) group acting as electron donor and fullerenes (**C$_{60}$**) as acceptor (Figure 13a).[53]

nOPPV **nCOPV**
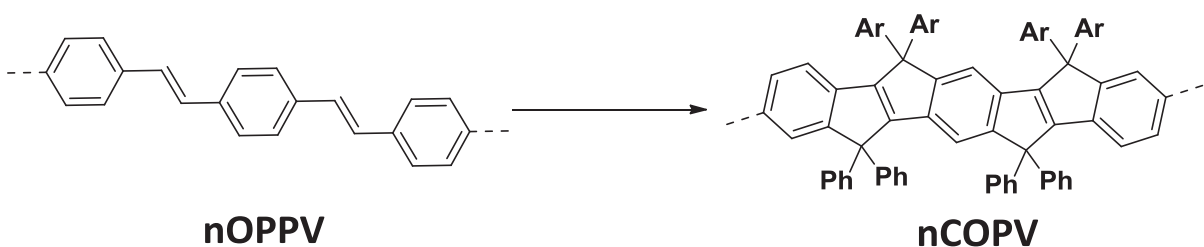
Scheme 6

First, through photon absorption, the **ZnP** group is excited increasing in that way the donor capacity. In that excited sate, the charge transfer occurs over the conjugated bridges to the acceptor, leading to a charge separation (CS) state or D$^+$-B-A$^-$, in which **ZnP** unit has a positive charge and the **C$_{60}$** has a negative charge. Figure 13b shows the spectra of the transient species, in which bands of both **ZnP$^{+\bullet}$** and **C$_{60}$$^{-\bullet}$** are observed. Afterwards a charge recombination (CR) process takes place and a decay to the fundamental state from this transient D$^+$-B-A$^-$ state occurs (Figure 13c).

Analyzing both charge separation and charge recombination processes through the **COPV** wires, they found that the charge transfer mechanism was superexchange as opposed to the hopping one determined for the longer wires of the flexible **OPPV**. These results were associated to the high electron coupling between donor and acceptor, and also to the vibrational molecular coupling between the π-conjugated skeleton and the intramolecular charge transfer.


Figure 13: a) Structures of the compounds used in this study. **ZnP–C$_{60}$** conjugates linked by **nCOPV** that possess a rigid and planar structure. **ZnP** and **C$_{60}$** moieties serve as electron donor and acceptor, respectively, and **COPV** serves as a molecular wire to mediate the charge transfer. b) Steady-state spectra and femtosecond flash photolysis in THF at room temperature. Differential absorption spectra of **ZnP–1COPV–C$_{60}$** (387 nm, 200 nJ) with several time delays between 0.1 and 1,400 ps. Absorptions at 465, 530 and 670 nm indicate the formation of **ZnP$^{\bullet+}$** and that at 1,010 nm indicates the formation of **C$_{60}$$^{\bullet-}$** as a result of CS. c) Time–absorption profiles at 465, 530 and 670 nm (**ZnP$^{\bullet+}$**),and 1,010 nm (**C$_{60}$$^{\bullet-}$**). The decay constant of these bands corresponds to the CR rate.[53]

5. Objectives

In view of the exposed precedents, our goal in this part of the thesis was to synthesize and study MV system formed by vinyl-thiophene oligomers of increasing length as a bridge, and two end-capping PTMs radical/anion as electron injector/collector. We planned to study the charge conduction behavior in ground state for the **[PTM-nTV-PTM]**$^{\bullet-}$ MV family (Figure 14a) by different and complementary techniques (i.e., variable temperature EPR, UV-Vis-NIR and Raman spectroscopy). Furthermore, due to the interesting electrochemical properties of oligo-thiophene vinylene oligomers, we proposed to study the electronic and magnetic properties of the derivatives formed by the oxidation of the **nTV** bridges (Figure 14b).

On the other hand, with the aim of comparing the influence of the bridge flexibility in these MV systems, we set out the study by variable temperature EPR of the intramolecular charge transfer through rigid **COPV** wires in ground state. We used a MV system constituted for two PTMs radical/anion as donor/acceptor **[PTM-nCOPV-PTM]**$^{\bullet-}$ (Figure 14c),tocompare the results with the previous results achieved with flexible **nOPPV** wires.
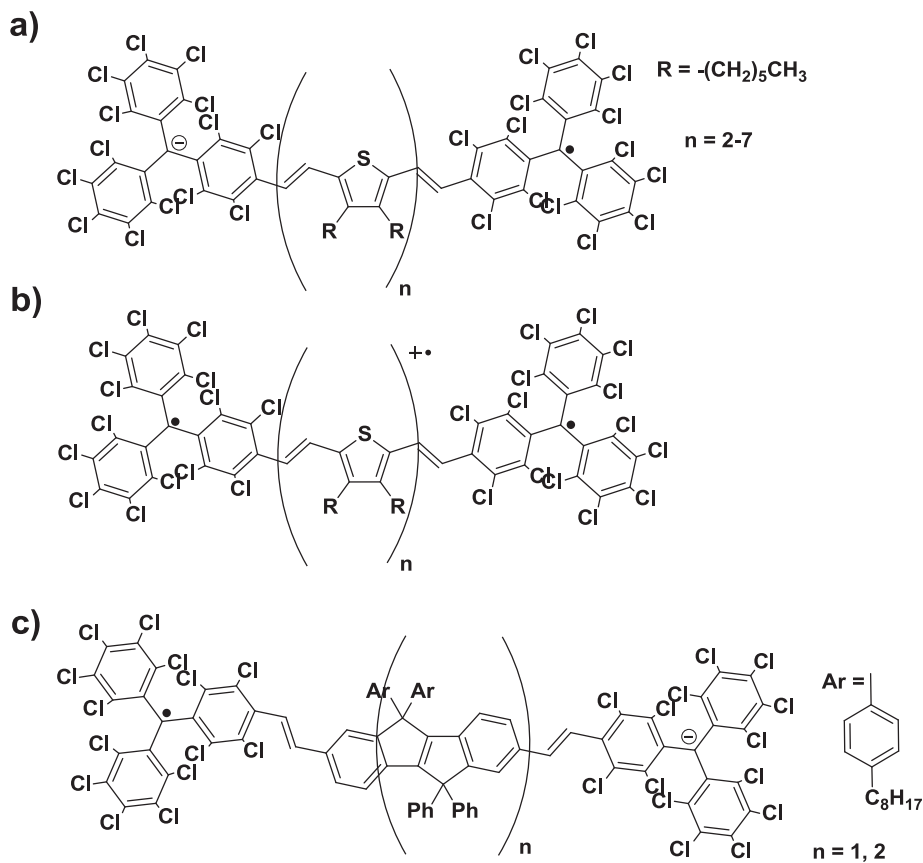
Figure 14: Scheme of the different species studied. a) **[PTM-nTV-PTM]**$^{\bullet-}$ Mixed-Valence, b) oxidized species **[PTM-nTV-PTM]**$^{\bullet+}$, and c) the planar **COPV** MV **[PTM-nCOPV-PTM]**$^{\bullet-}$.

6. Results and Discussion

6.1 Mixed valence systems with flexible wires

6.1.1 Design and Synthesis

To achieve our goal to study a series of **nTV** wires with the mixed valence approach using the PTM as redox center, a family of **PTM-nTV-PTM** biradical molecules with **nTV** wires of different length was needed in order to have a complete picture of the phenomena involved on the electron transfer process.

The retro-synthetic pathway to prepare the **PTM-nTV-PTM** is represented in Scheme 7. The target birradicals **PTM-nTV-PTM** can be synthesized by the corresponding **(αH-α'H)PTM-nTV-PTM**, which can be obtained by the reaction of the PTM phosphonate and dialdehyde **nTV** derivative (**CHO-nTv-CHO**)
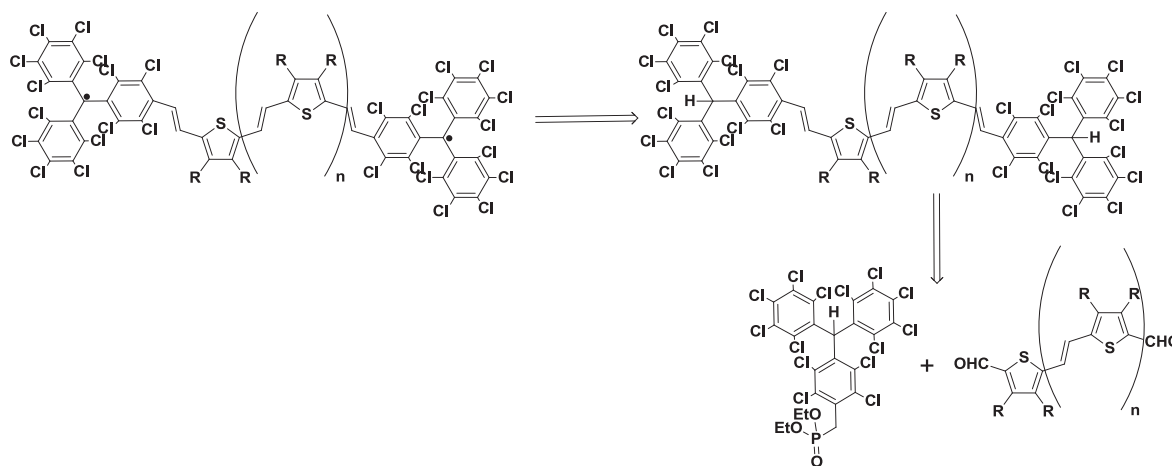
Scheme 7

Thereby, the first step was to synthesize a series of **CHO-nTV-CHO** (n = 2-7)[*] following the strategy developed by Roncali.[18,54] Once obtained the dialdehyde wires, we synthesized the **(αH, α'H)-PTM-nTV-PTM**, through a Witting-Horner olefination between the PTM phosponate[55] and the appropriate dialdehyde **CHO-nTV-CHO**. This reaction gives in a very good yield the bisubstituted compounds (more than 60%), in contrast with the substitution of the **OPPV** dialdheyde, that gives a mixture of the mono and bisubstituted compounds.[51] Treatment with an excess of tetrabutylammonium hydroxide (Bu₄NOH) gives the corresponding biscarbanions **[PTM-nTV-PTM]⁻²**, which were subsequently oxidized with silver nitrate to give the target biradicals **PTM-nTV-PTM** (Figure 15).

---

[*] Molecules provided by F. Langa group.

Following the same strategy, we also we synthesized a monoradical derivative (**PTM-2TV**), in order to be used as a model system. All synthetic details and characterization spectra are in the article "*On the Operative Mechanisms of Hole Assisted Negative Charge Motion in Ground States of Radical-anion Molecular Wires*" (submitted).
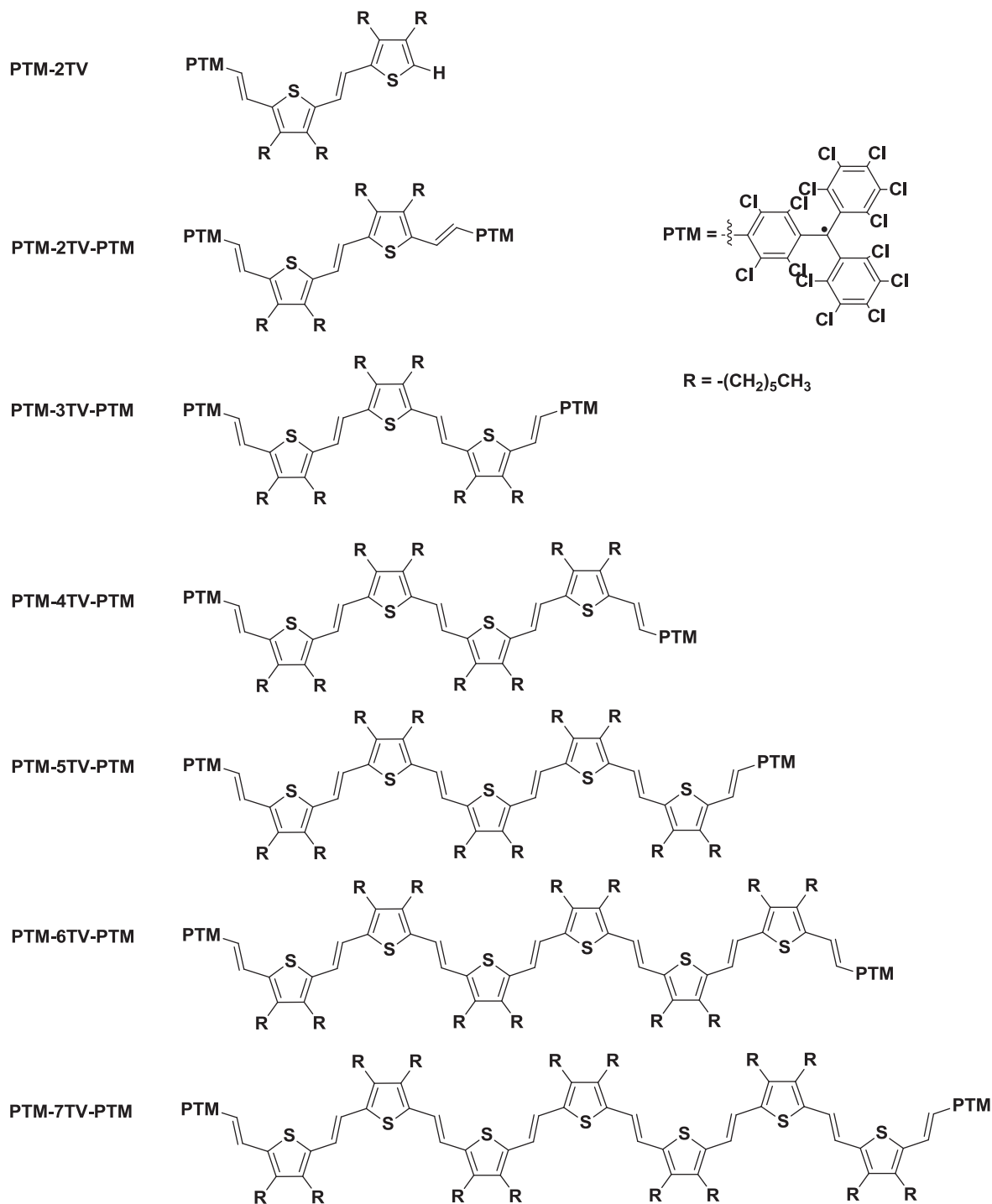

Figure 15: Chemical structures of the **PTM-nTV-PTM** family and the model compound **PTM-2TV**.

6.1.2 Characterization of Biradicals PTM-nTV-PTM

Electrochemical study (cyclic voltammetry)

The electrochemical characterization of the biradicals was performed by cyclic voltammetry and the results are summarized in Table 2. In the table, it can be observed that the two PTM moieties have the same reduction potential, which is constant for all the family. This fact is an indication of the weak electronic coupling between the PTM units. We also observed the increase in the number of oxidation waves when the number of **TV** in the oligomers rises.

The **PTM-2TV-PTM** shows two reversible oxidation states attributable to the oxidation of the two **TV** rings. In the free **2TV** bridges these oxidation states are irreversible,[18a] thus the attachment of the two bulk acceptor groups to the wire, stabilizes the oxidation states of the **2TV** oligomer.

From CV data we also estimated the HOMO-LUMO gap, defined as the difference between the reduction potential and the first oxidation potential ($\Delta E_{(Ox1-Red)}$). As expected, the HOMO-LUMO gap decreases when the wire length increases, such that the increment of **TV** units in the oligomers makes the bridge oxidation easier.

Table 2: Half-wave electrochemical potential (in V *vs.* Ag/AgCl) of the **PTM-nTV-PTM** series obtained through cyclic voltammetry measurements with $TBAPF_6$ (0.1M in CH_2Cl_2) as electrolyte, Pt wires as working and counter electrodes at scan rate of 100 mV/S

Compound	$E^{1/2}_{Red}$	$E^{1/2}_{Ox1}$	$E^{1/2}_{Ox2}$	$E^{1/2}_{Ox3}$	$E^{1/2}_{Ox4}$	$E^{1/2}_{Ox5}$	$E^{1/2}_{Ox6}$	$\Delta E_{(Ox1-Red)}$
	(V)	(V)	(V)	(V)	(V)	(V)	(V)	(V)
PTM-2TV	-0.17	0.80	1.54					0.97
PTM-2TV-PTM	-0.18	0.78	1.37					0.96
PTM-3TV-PTM	-0.17	0.65	1.07					0.82
PTM-4TV-PTM	-0.16	0.57	0.83	1.34				0.73
PTM-5TV-PTM	-0.19	0.51	0.68	1.14	1.48			0.70
PTM-6TV-PTM	-0.17	0.51	0.61	0.99	1.61	1.74		0.68
PTM-7TV-PTM	-0.15	0.51	0.51	0.86	1.11	1.42	1.69	0.66

Figure 16 shows the UV-Vis-NIR absorption spectra in CH_2Cl_2 of the **PTM-nTV-PTM** biradicals. Besides the chlorinated aromatic bands, an intense band at $\lambda_{max} \approx 390$ nm corresponding to the PTM radical, and the band of the π-conjugated oligo-vinylenethiophene structure are observed. As expected, when increasing the lenght of the **nTV** chain, the corresponding band moves to higher wavelength (447 → 580 nm), which is related to the increase of the conjugated π-system as a consequence of the larger number of **TV** units. Also, the molar absorptivity of the **nTV** band gradually rises on increasing the bridge length.

In the NIR region appears a broad band corresponding to the intramolecular charge transfer between the donor bridge and the acceptor PTM radicals. These broad bands also show a red shift with the elongation of the bridge. In shorter compounds (**PTM-2TV-PTM** and **PTM-3TV-PTM**), the CT band is clearly observed, nevertheless for the rest of compounds this bands are overlapped with the tail of the intense **nTV** absorption bands.
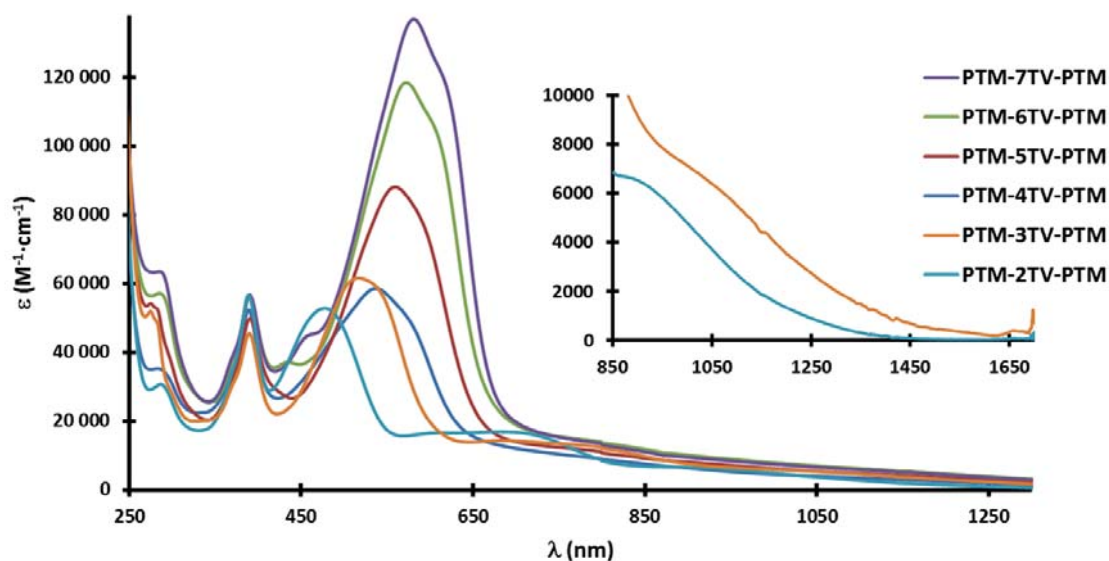

Figure 16: UV-Vis-NIR spectra in CH_2Cl_2 at room temperature of the **PTM-nTV-PTM** series. Inset: enlargement of the NIR region of the absorption spectra of **PTM-2TV-PTM** and **PTM-3TV-PTM.**

Table 3: UV-Vis-NIR data of the **PTM-nTV-PTM** series.

Compound	λ(nm);Logε (L·mol^{-1}·cm^{-1})				
PTM-2TV	391;(4.51)	436;(4.48)	580;(3.83)	633;(3.83)	802; (3.31)
PTM-2TV-PTM	389;(4.66)	478;(4.61)	613;(3.84)	683;(3.85)	1032[a]
PTM-3TV-PTM	390;(4.66)	515;(4.79)	683;(4.15)	795;(4.10)	1091[a]
PTM-4TV-PTM	389;(4.71)	537;(4.76)			1136[a]
PTM-5TV-PTM	390;(4.69)	554;(4.94)			1168[a]
PTM-6TV-PTM	390;(4.67)	569;(4.99)			1212[a]
PTM-7TV-PTM	390;(4.66)	580;(5.05)			1213[a]

a) *Values obtained by deconvolution of the spectral bands of concentrated solutions.*

To analyze in deep the electronic transitions of these molecules, we measured the UV-Vis-NIR spectra at different temperatures. Figure 17 shows the absorption spectra obtained at variable temperature (300 → 78 K) in a solution of 2Me-THF for **PTM-2TV-PTM** and **PTM-5TV-PTM** as representatives of the shorter and longer compounds, respectively. In these spectra we observed that the wide absorption band associated to **nTV** in all of cases evolves to a sharper resolved band at low temperatures. This effect is owing to the wide distribution of molecular conformers existing at room temperature, as a consequence of the free torsion of the dihedral angle around the vinylthiophene group. The populations of the accessible conformers decrease on lowering the temperature, populating the lower energy conformer which corresponds to the flatter structure, which is more rigid, what explains the vibrational resolution. So, these experiments reveal the existence of a number of different geometric conformations of the **nTV** bridges at room temperature as expected for a flexible wire.
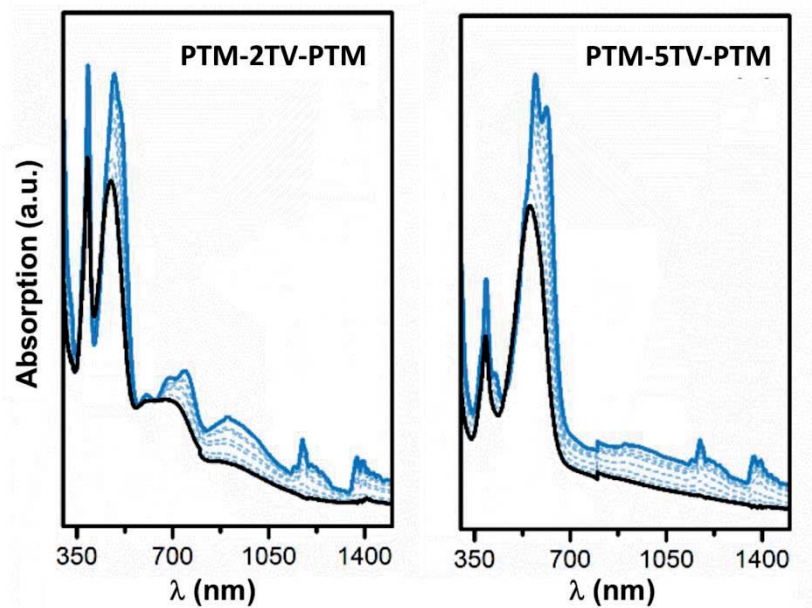
Figure 17: UV-Vis-NIR spectra of **PTM-2TV-PTM** and **PTM-5TV-PTM** in 2Me-THF solution, from room temperature (black line) to 78K (blue bold line) at intervals of 50K (dashed lines)

Raman Spectroscopy

To understand better the influence of the acceptor group radical PTM on the **nTV** bridges, we analyzed the resonant Raman spectra of the **PTM-nTV-PTM** family, focusing on the $v(C=C)$ region. Figure 18 shows the Raman spectra for these compounds registered at room temperature in a CH_2Cl_2 solution. Here three main regions of transitions can be observed:

At 1610-1570 cm^{-1} a band that moves from 1587 cm^{-1} for **PTM-2TV-PTM** to 1576 cm^{-1} for **PTM-7TV-PTM** appears. These bands (blue) can be attributed to $v(C=C)_{vinyl}$, and its displacement is associated to the progressive increase of the π-conjugation in the ground state. In the shorter compounds this band presents a second component (green) that moves to lower frequencies by increasing the number of π-conjugated units. From **PTM-5TV-PTM** the second component disappears merging with $v(C=C)_{vinyl}$. That component should correspond with $v(C=C)$ of the vinyl groups linked to the PTM unit $v(C=C)_{vinyl-PTM}$.

A second region is found at around 1510 cm^{-1} (black). Here only in the shorter members of the family the bands are observed. These bands correspond to the PTM radical $v(C=C)_{PTM}$.[56]

Finally in the 1395-1385 cm^{-1} region appears the band associated to the C=C vibration of the thiophene rings $v(C=C)_{Th}$ (pink), that moves from 1394 cm^{-1} in **PTM-2TV-PTM** to 1386 cm^{-1} in **PTM-7TV-PTM**.

Finally we compared our results with those previously obtained for **nTV** bridges without PTM end groups.[57] We detected that the $\nu(C=C)_{Vinyl}$ and $\nu(C=C)_{Th}$ move to lower frequency by the effect of the incorporation of the acceptor PTM group. Consequently, the integration of PTM groups in **TV** wires improves the electronic π-conjugation.
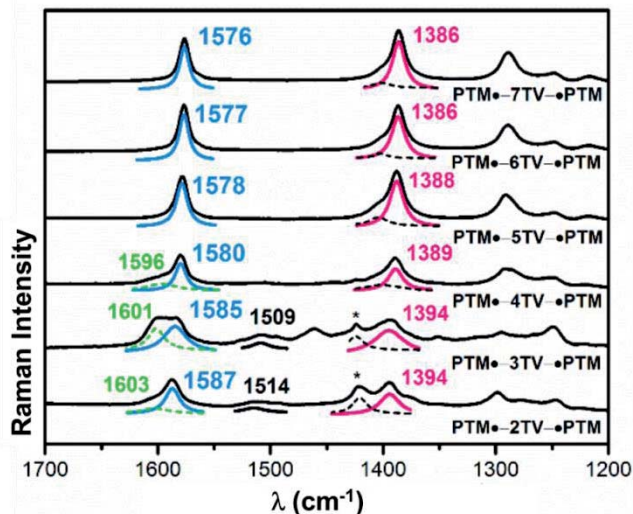

Figure 18: Normalized Raman Spectra of the **PTM-nTV-PTM** series, at room temperature in CH_2Cl_2 under resonant conditions (λ_{exc} = 633 nm unless for **PTM-2TV-PTM**, λ_{exc} = 532 nm). The frequencies values were assigned through deconvolution. $\nu(C=C)_{vinyl}$ (blue), $\nu(C=C)_{vinyl-PTM}$ (green), $\nu(C=C)_{PTM}$ (black) and $\nu(C=C)_{Th}$ (pink). * correspond to solvent bands.

EPR spectroscopy

The **PTM-nTV-PTM** compounds are open-shell molecules due to the two PTM radicals. Thus the magnetic behavior of these molecules can be studied by electron paramagnetic resonance.

Solution EPR spectra under isotropic conditions at low temperature of all diradicals in CH_2Cl_2/Toluene (1/1) consist of six overlapped main lines assigned to the coupling of the unpaired electrons with two sets of two equivalent hydrogens from the two **TV** units closer to the PTM moieties (In Figure 19b and 19c the EPR spectra for **PTM-2TV-PTM** and **PTM-5TV-PTM** are shown as representative examples). The observation of two sets of isotropic hyperfine coupling constants, a_i, in diradicals **PTM-nTV-PTM** that are half of those observed for the segmental model monoradical **PTM-2TV**, (Figure 19a), indicates the existence of a magnetic interaction between the two unpaired free electrons in all the diradical series with magnetic exchange constants, J, that fulfill the condition $|J| \gg |a_i|$.

To evaluate the intramolecular PTM-PTM magnetic interaction, we measured the half-field transition. This is a forbidden transition which is a signature of the triplet state when ferromagnetic coupling between two free electrons occurs. As the probability of this transition exponentially decreases with the distance, in our systems it could just be seen in the **PTM-2TV-PTM** (Figure 19c) and **PTM-3TV-PTM** compounds.
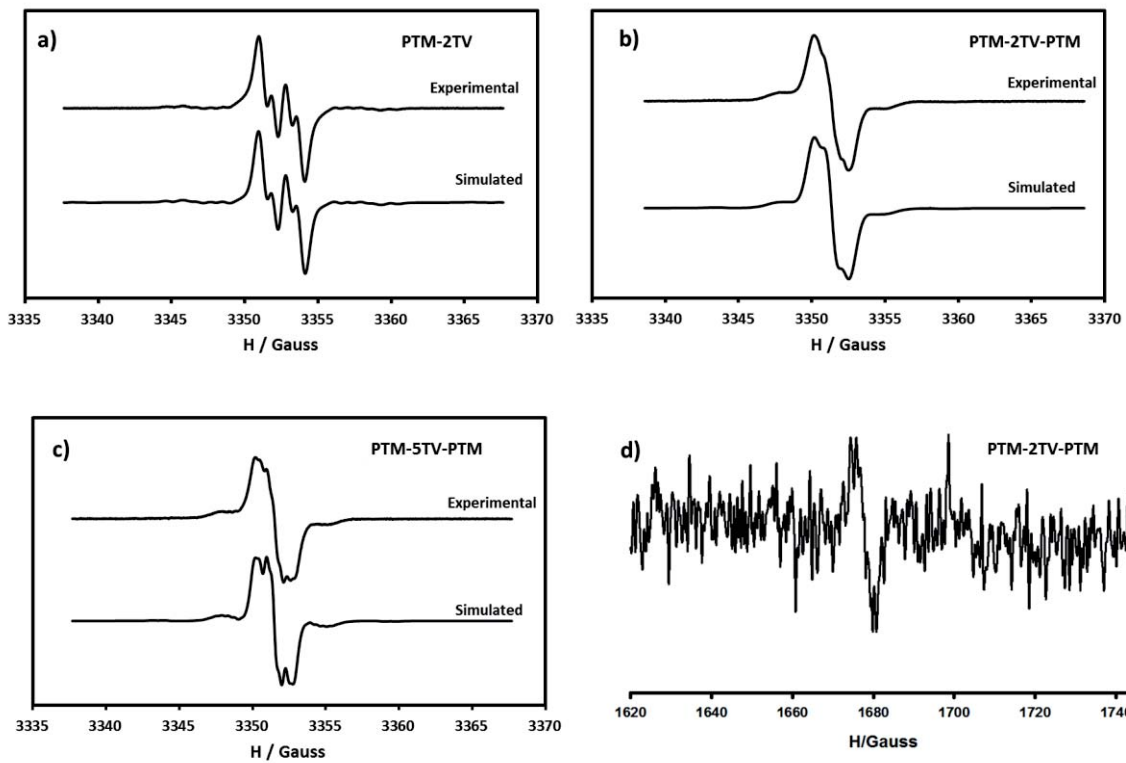
Figure 19: Experimental and simulated isotropic solution EPR spectra in CH_2Cl_2 at 240 K of a) **PTM-2TV**, b) **PTM-2TV-PTM**, c) **PTM-5TV-PTM**. d) $\Delta Ms = 2$ transition of **PTM-2TV-PTM** in Toluene/ CH_2Cl_2 (1/1) at 120K.

6.1.3 Mixed-Valence [PTM-nTV-PTM]•− family

After study the molecular and electronic properties of the **PTM-nTV-PTM** birradicals, we generated the corresponding MV radical-anions **[PTM-nTV-PTM]•−** to induce the IET process through the wires. In the article "*On the Operative Mechanisms of Hole Assisted Negative Charge Motion in Ground States of Radical-anion Molecular Wires*" we describe the study of the IET process in the ground state by variable-temperature EPR (Figure 20a and 20b) and complementary techniques as UV-Vis-NIR and resonant Raman spectroscopies. To support the experiments quantum chemical modeling was also performed.

This multi-fold information of the spin/charge exchange rate in the ground electronic states serves to propose for the longer oligomers (**nTV**; n = 4-7) a biased bidirectional symmetrical charge hopping mechanism through the **nTV** bridge imparted by two reflecting PTM sites at opposite ends. The initial step of the mechanism is the oxidation of the donor wire by the acceptor PTM radical subunit forming a symmetric charge separated state with a positive polaron in the bridge flanked by two PTM anions. After the formation of this transitory species positive charge may hop through the bridge finally decaying by an electron-hole annihilation that restores the **nTV** radical-anion with the charges in opposite ends. This finding is rather unusual since transport of negative charge (**PTM-nTV-PTM**) through bridges most of the times occurs through empty "conduction" states able to accommodate an excess of negative charge rather than mediated by positive charges (Figure 20c). On the contrary, in the shorter radical-anions (**nTV**; n = 2,3) the operative mechanism for the spin/charge exchange seems to be the flickering mechanism favored by the higher rigidity (or quinoidization) of their bridges.
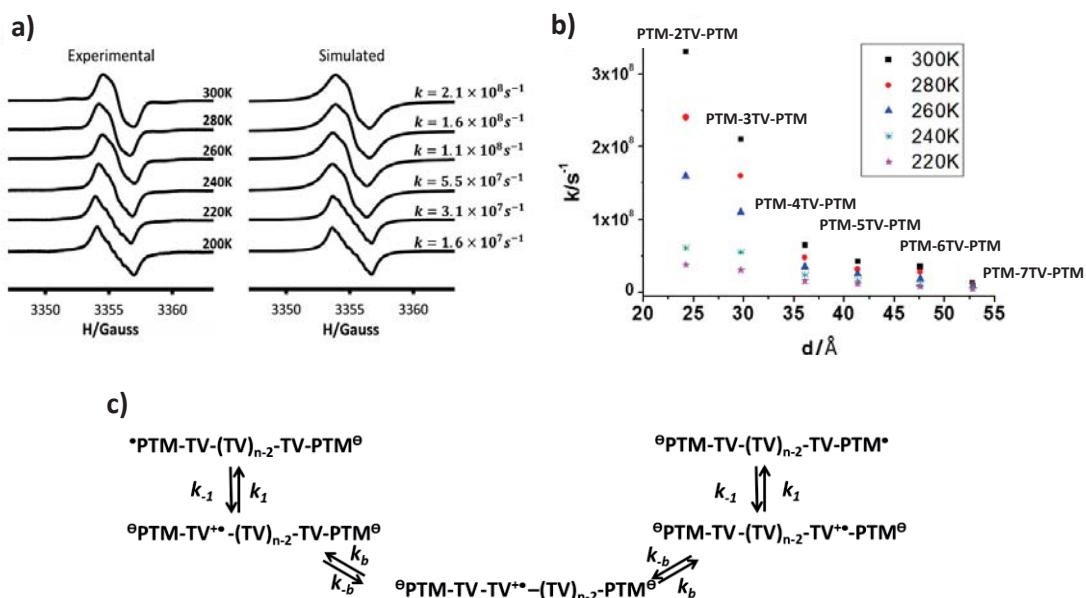
Figure 20: a) Temperature-dependent changes in the EPR spectrum of **[PTM-3TV-PTM]•−** solution in CH_2Cl_2 (left), and simulated spectra (right) with different spin/charge exchange rates. b) Distance dependences of spin/charge exchange rates, k, of **[PTM-nTV-PTM]•−** radical-anions in the temperature range 220-300 K. c) Proposed mechanism of the spin/charge exchange process in the larger radical-anions **[PTM-nTV-PTM]•−** for n>3 where a hole is stepwise transported along the **nTV** molecular wire.

6.1.4 Oxidized species: Characterization of [PTM-nTV-PTM]$^{+\bullet}$ and [PTM-nTV-PTM]$^{2+}$

The electronic structure of successive redox states of a series of oligo-thiophene vinylene oligomers without end substituent groups was previously investigated in detail by UV-Vis-NIR and EPR spectra in solution.[58] In this thesis we planned to explore the influence of the PTM radical substituent on the electronic and magnetic properties of oxidized oligo-thiophene vinylene molecular wires.

The oxidized species can be generated by two methodologies:

(i) Chemically, through the addition of equivalent amounts of an oxidant. For vinyl-thiophenes the best choice is $FeCl_3$, because it is a soft oxidant soluble in organic solvents and the reduced form ($FeCl_2$) is non-reactive and precipitates in most organic solvents. However, the most interesting characteristic is that both ($FeCl_3$ and $FeCl_2$) do not absorb in the Vis-NIR of the electromagnetic spectrum, allowing to visualize the evolution of the oxidized vinyl-thiophene.

(ii) Electrochemically, by applying a continuous voltage in an electrolyte media.

UV-Vis-NIR Spectroscopy

Figure 21 shows the oxidation process of the **PTM-nTV-PTM** family followed by UV-Vis-NIR spectroscopy. The spectra were registered in a spectro-electrochemical cell at constant potential interval of ±15 mV in a 1 mM CH_2Cl_2/0.1M $TBAPF_6$ solution. By the addition of a known concentration of a solution of $FeCl_3$ in CH_2Cl_2, we also chemically generated the cations that show the same UV-Vi-NIR spectra as those from Figure 21.

In all cases the oxidation of the neutral birradical **PTM-nTV-PTM** (black line) implies the disappearance of the **nTV** bands, and the appearance of two bands corresponding to the **[PTM-nTV-PTM]$^{+\bullet}$** (red line) in the Vis-NIR region. Upon further oxidation of the longer compounds (n = 4-7) the **[PTM-nTV-PTM]$^{+\bullet}$** radical-cation bands evolve to one structured broad band corresponding to the dication[59] species **[PTM-nTV-PTM]$^{2+}$** (blue line). The band at 390 nm attributed to the PTM radical remains unchanged except for the **PTM-2TV-PTM** compound, in which the intensity decreases around 50%. For the model **PTM-2TV** compound the band at 390 nm disappears upon oxidation. Thus the presence of the thiophene radical cation does not affect the PTM radical, except for the shorter member of the family **PTM-2TV-PTM** and the model **PTM-2TV**.
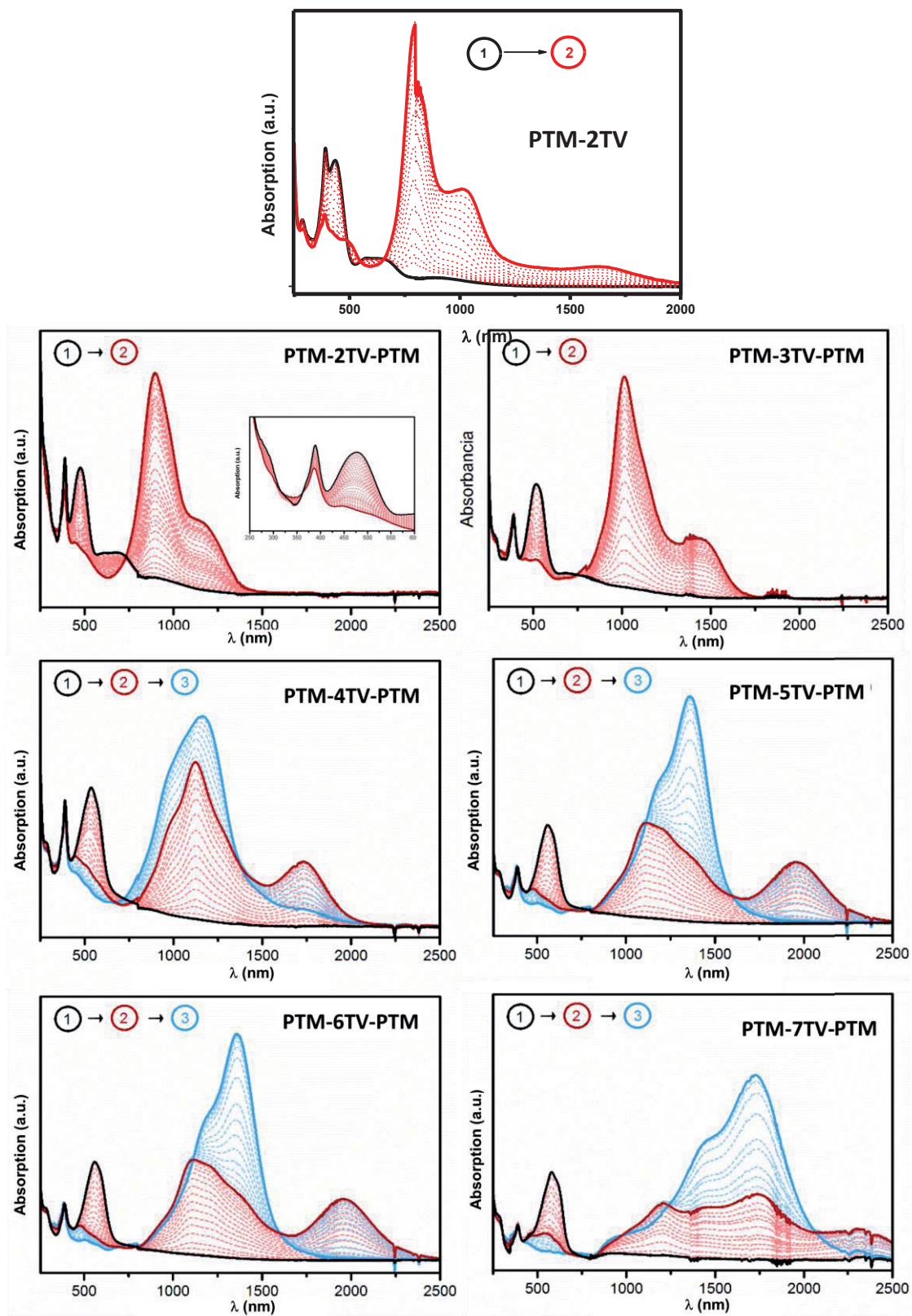
Figure 21: Absorption spectra obtained through UV-Vis-NIR spectro-electrochemistry measurements for all **PTM-nTV-PTM**. Black line corresponds to neutral **PTM-nTV-PTM**, red line to **[PTM-nTV-PTM]$^{+\bullet}$** and blue line to **[PTM-nTV-PTM]$^{2+}$**.

Figure 22 represents the FT-Raman spectra (λ_{exc} = 1064 nm) of a) **[PTM-nTV-PTM]$^{+\bullet}$** and b) **[PTM-nTV-PTM]$^{2+}$** in a CH_2Cl_2 solution at room temperature, generated by the addition of incremental amounts of a $FeCl_3$ solution.

The **[PTM-nTV-PTM]$^{+\bullet}$** Raman spectra are characterized by a band assigned to $v(C=C)_{vinyl}$ vibration around 1550-1540 cm^{-1}. Comparing the Raman spectra of the neutral **PTM-nTV-PTM** biradicals with the one of **[PTM-nTV-PTM]$^{+\bullet}$** we notice that the generation of a radical-cation implies the displacement of the $v(C=C)_{vinyl}$ band to lower frequencies. This effect can be attributed to the formation of a quinoidal structure on the thiophene rings causing the weakness of the vinyl bond (see Figure 23).

In the FT-Raman spectra of **[PTM-nTV-PTM]$^{2+}$**, we detected a medium intensity band at 1570-1540 cm^{-1} associated to $v(C=C)_{vinyl}$ vibration. In that situation the quinoidal segment in the bridge increases and stabilizes a second positive charge. The fact that the $v(C=C)_{vinyl}$ band does not change in comparison with the radical-cation could be attributed to a quintuplet radical form, where the radical cations and the PTM radicals do not interact with each other (Figure 23).
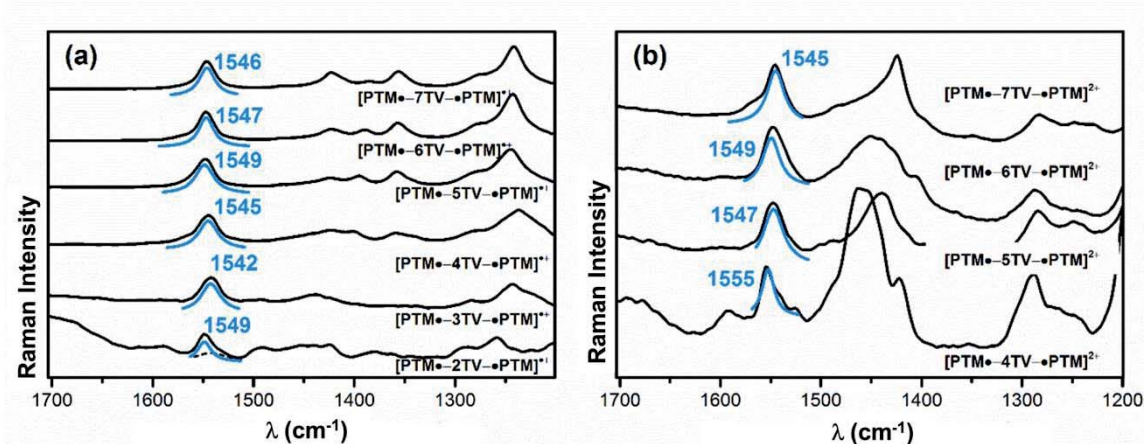
Figure 22: a) FT-Raman spectra in CH_2Cl_2 (λ_{exc} = 1064 nm) of **[PTM-nTV-PTM]$^{+\bullet}$**. b) FT-Raman spectra (λ_{exc} = 1064 nm) of **[PTM-nTV-PTM]$^{2+}$**. All spectra were registered in CH_2Cl_2 at room temperature. The frequency values have been assigned by band deconvolution. $v(C=C)_{vinyl}$ blue.
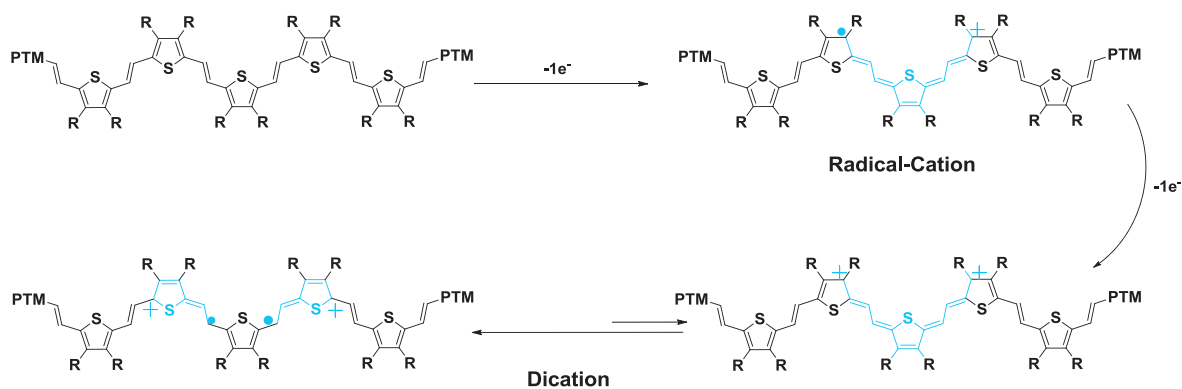
Figure 23: Schematic representation of the structural evolution of the oxidized species using **PTM-5TV-PTM** as a representative example.

EPR Spectroscopy

To check our hypothesis deduced by Raman spectroscopy, we performed EPR analysis of the radical cation and dication species for all family of compounds (Figure 24).

First EPR spectra of Figure 24 corresponds to the **PTM-2TV** radical before (black) and after adding one equivalent of $FeCl_3$ (red). As evidenced by these spectra, the EPR signal of the PTM radical disappears when the cation radical of the thiophene is formed, which is in agreement with the vanishing of the UV-Vis band at 390 associated to the PTM radical. This result is in accordance with the coupling of the radical-cation of thiophene with the PTM radical forming a quinoidal structure.

The EPR spectrum of the **PTM-2TV-PTM** biradical shows 3 overlapped main lines (black spectrum of Figure 25) due to the magnetic coupling of both PTM radicals with two equivalent vinyl hydrogens. When the compound is oxidized to the **[PTM-2TV-PTM]$^{•+}$**, the spectrum shows instead 2 overlapped lines (red spectrum of Figure 25), owing to the coupling of one PTM radical with one vinyl hydrogen, and has a lower intensity. This observation is in accordance with the coupling of one of the two PTM radical moieties of the molecule with the generated thiophene monocation radical (Scheme 8).This is in agreement with the halving of the UV-Vis band at 390 associated to the PTM radical.
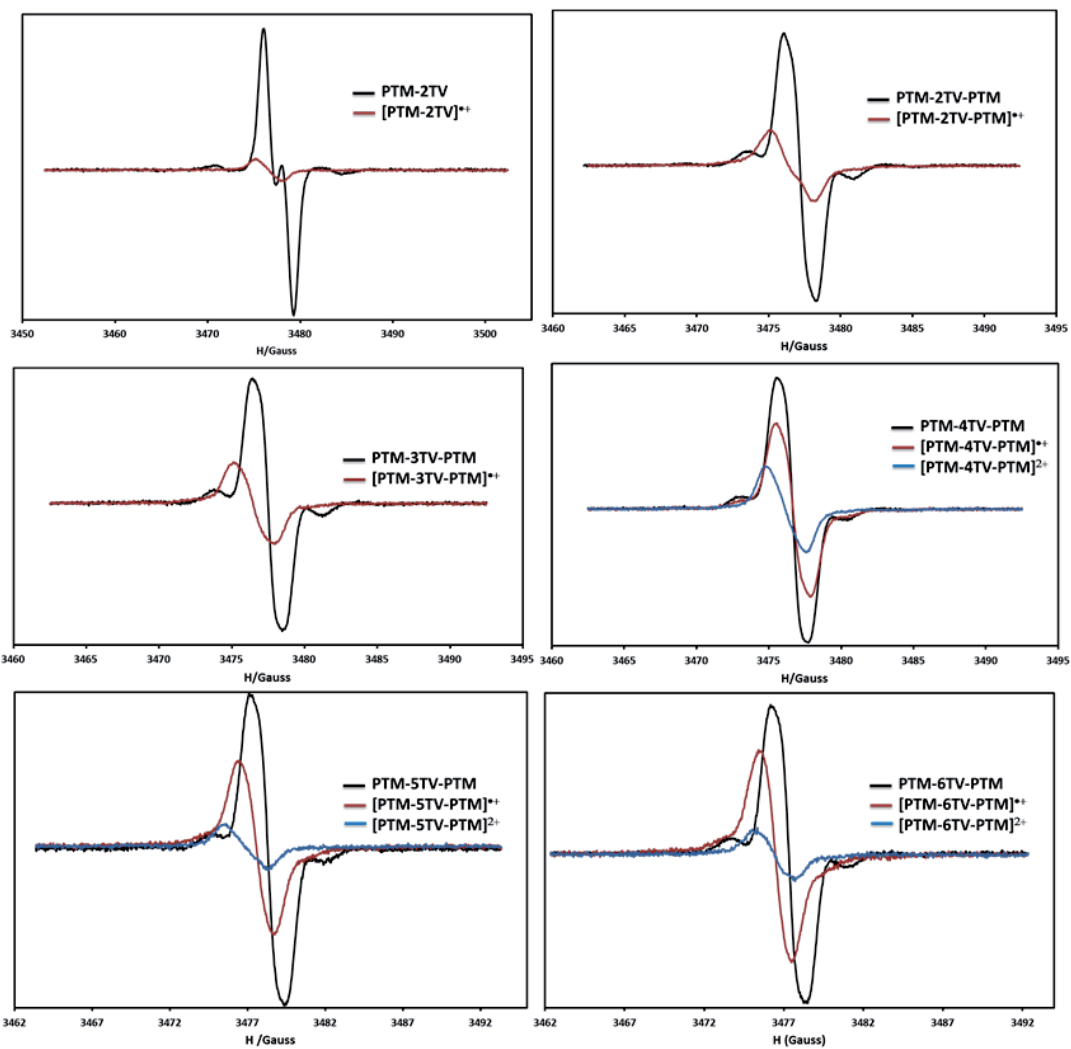
[PTM-2TV-PTM]

-1e⁻

[PTM-2TV-PTM]•⁺
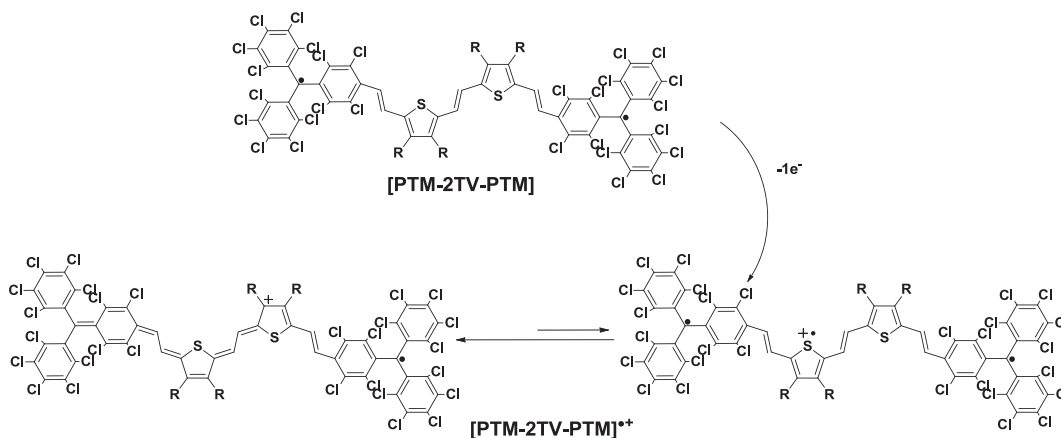
Scheme 8

The EPR spectrum of **[PTM-3TV-PTM]•⁺** shows a clear decay of the intensity of the PTM radical signal with respect to the starting biradical, but in contrast to the previous case, the EPR signal does not show two overlapped lines but one broad line. It seems that there is also an interaction between one PTM radical and the thiophene radical-cation, but we cannot discard that the formation of the monocation radical takes place in the central thiophene ring and the observed signal corresponds to the triradical species.

In the corresponding EPR spectra of the oxidized species of **PTM-4TV-PTM** we observed that when the monocation radical is formed, the initial signal of the neutral biradical (black line) decreases in intensity (red line) but the shape of the signal is very similar. This can be explained by the fact that the thiophene radical cation can be located either in the two central rings or in the ones interacting with the PTM radical and then a triradical species is formed. When the dication is formed (blue line) the signal intensity decreases even more. In this situation the molecule has two thiophene cation radicals that seem to interact more with the two PTM radicals.

For the rest of longer compounds the EPR spectra of the oxidized species have the same characteristics than the ones of **PTM-4TV-PTM**, and therefore the interpretation of the radical interactions that can be extracted from the EPR spectra are the same.

We demonstrated that, except for **PTM-2TV-PTM** and **PTM-2TV**, the oxidized compounds are high spin species where the PTM radical and the thiophene radical cation have a magnetic interaction that could be parallel or antiparallel, leading to a singlet or a high spin ground state. As the EPR signal do not disappear completely, but just decrease in intensity, it can be suggested that the ground state is a mixture of singlet states, in which spins are antiparallel implying the signal cancelation, and high spin states where the spin are parallel and EPR active.

Figure 24: EPR spectra of radical **PTM-2TV** and **PTM-nTV-PTM** biradicals (black lines), **[PTM-nTv-PTM]**[•+] generated after addition of one equivalent of FeCl$_3$ (red lines), and **[PTM-nTv-PTM]**[2+] generated after addition of two equivalents of FeCl$_3$ (blue lines). All EPR spectra were registered in CH$_2$Cl$_2$ solution at room temperature. The oxidation processes were followed by UV-Vis-NIR.

6.2 Mixed-Valence systems with rigid wire

6.2.1 Synthesis

In order to study the IET through **nCOPV** rigid wires in the ground state, we synthesized two **PTM-nCOPV-PTM** (n =2, 3) compounds (Scheme 9) following the same procedure described for the synthesis of the **PTM-nTV-PTM** family.

The preparation of **PTM-nCOPV-PTM** compounds starts with the synthesis of the corresponding hydrogenated (**αH α'H- PTM-nCOPV-PTM**) derivatives through a Wittig-Horner reaction, using the αH-PTM-phosphonate and bisaldehyde-**COPV**[†] as reagents. This reaction provides a mixture of two PTM-COPV derivatives, the mono-substituted and the bis-substituted compounds which were easily separated by flash chromatography. Then, the bis-substituted derivatives were treated with an excess of tetrabutylammonium hydroxide to remove the acidic polychloro-triphenylmethane protons to give the corresponding bis-anion derivatives, which were subsequently oxidized in situ with *p*-chloranil to obtain the corresponding birradical compounds **PTM-nCOPV-PTM** (n =2, 3). Radical-anion Mixed-Valence systems was prepared by partial reduction of the biradical with tetrabutylammonium hydroxide.
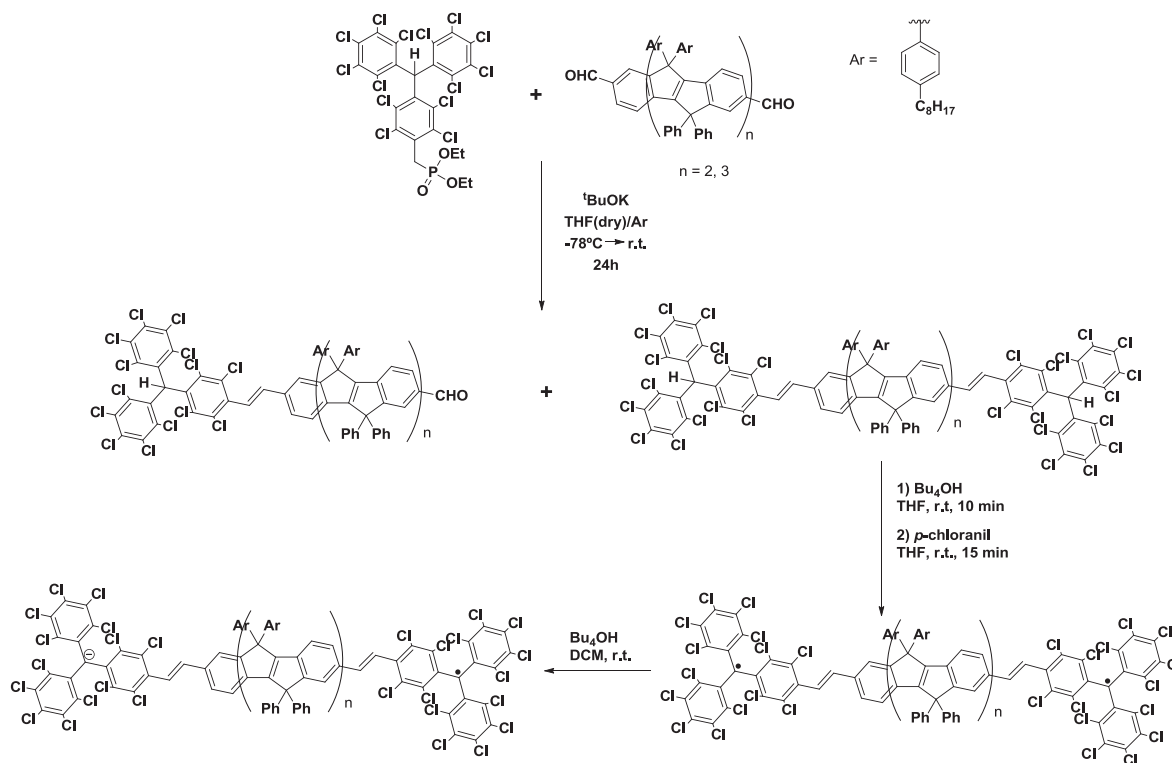
**Scheme 9:** Synthetic pathway for obtaining **PTM-2COPV-PTM** and **PTM-3COPV-PTM** molecules.

[†] Molecules provided by Prof. E. Nakamura from Tokyo University.

6.2.2 Spectroscopic chracterization

UV-Vis-NIR spectroscopy

The UV-Vis-NIR spectra of the biradical species in CH_2Cl_2 (Figure 25 black line) shows: i) one intense band at 390 nm and two weak bands at 570 and 655 nm which are characteristic of PTM radicals, ii)two intense additional bands with maxima at 447-469 nm for **PTM-2COPV-PTM** and 466-497 nm for **PTM-3COPV-PTM,** which correspond to the **COPV** bridge, and iii) a weak band centered at 788 and 855 nm for **PTM-2COPV-PTM** and **PTM-3COPV-PTM,** respectively, attributed to an intramolecular charge-transfer process between the bi-radical (acceptor) and the bridge (donor). By adding incremental amounts of a solution of Bu_4NOH in $CH_2Cl_2$the radical is reduced to the anion and, as a consequence, the bands associated to the PTM-radical and the intramolecular charge-transfer band begin to disappear and new bands attributed to the PTM-anion appear around 604nm (green plots of Figure 25). No bands corresponding to a charge transfer (V_{ab}) between the PTM anion and PTM radical can be observed in the spectra of concentrated solutions of the MV systems.
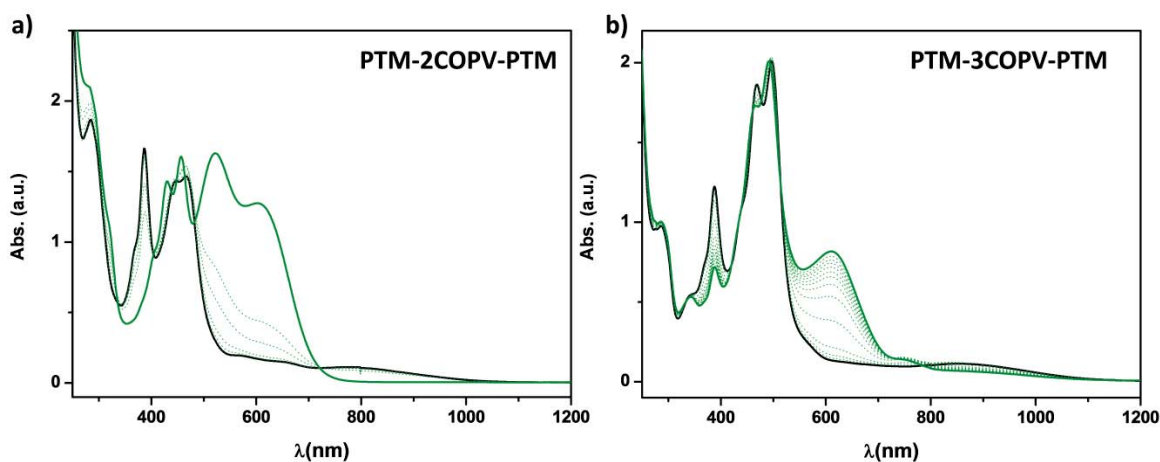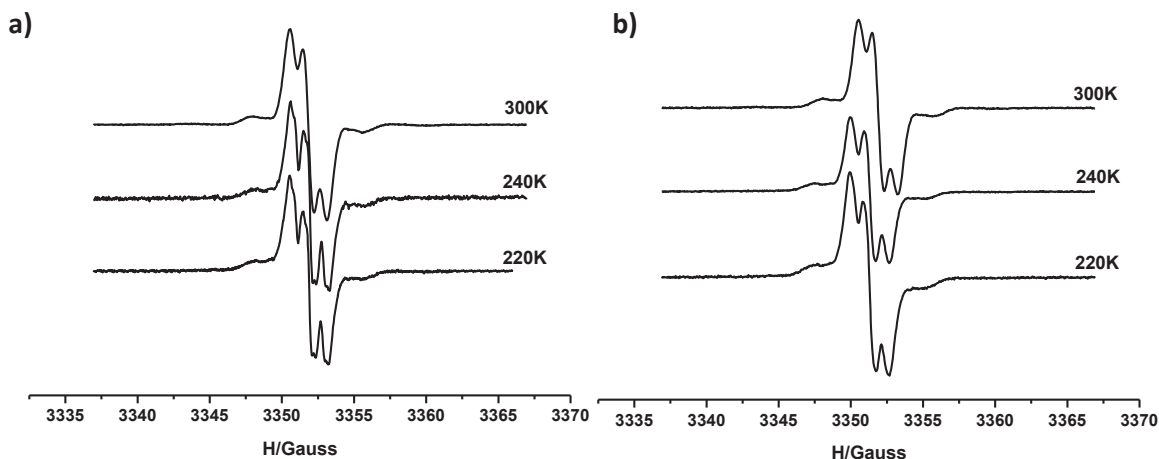

Figure 25: UV-Vis-NIR spectra of compound a) **PTM-2COPV-PTM** and b) **PTM-3COPV-PTM** upon stepwise reduction with Bu_4NOH. Black line represents the **PTM-nCOPV-PTM** birradical and green line the corresponding radical anion **[PTM-nCOPV-PTM]$^{\bullet-}$.** All spectra were recorded in CH_2Cl_2 solution at room temperature

EPR spectra of Biradicals.

Solution EPR spectra under isotropic conditions at room temperature of **PTM-nCOPV-PTM** compounds in CH_2Cl_2 (Figure 26a) consist of three overlapped lines, which correspond to the coupling of the unpaired electrons with the two sets of two equivalent vinyl-hydrogens closest to PTM moieties. In the spectra at low temperature (220K) is shown in Figure 26. It is possible to observe six overlapped lines due to the coupling with the other vinyl-hydrogens. The coupling constant values are half of the ones shown for related monoradicals, meaning that the two

electrons are magnetically interacting, fulfilling the condition that $J \gg a$. This means either that the ground state of **PTM-nCOPV-PTM** compounds is the triplet state with a J value higher than the hydrogen coupling constants or that if the singlet is the ground state, the triplet state is very close in energy and can be thermally populated at low temperature.
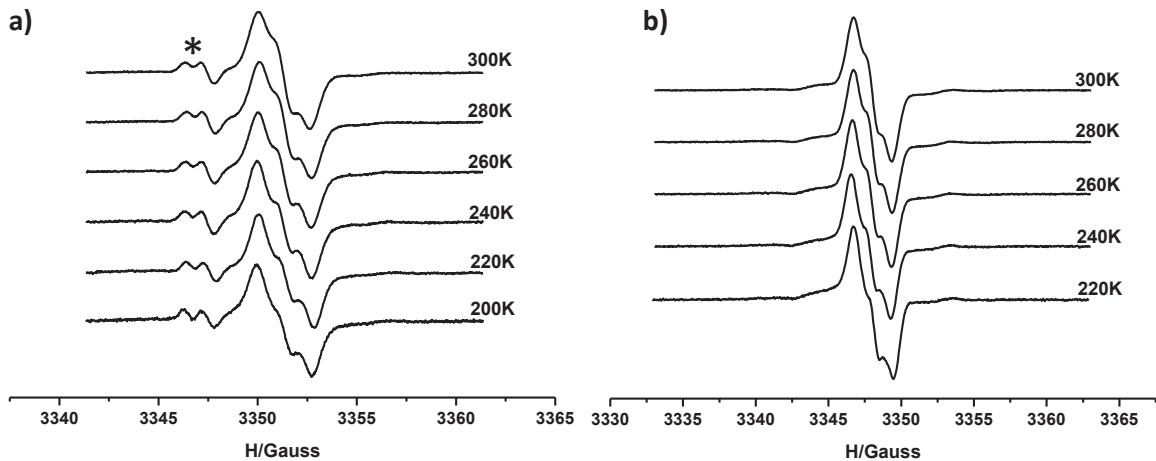

Figure 26: EPR spectra of compound a) **PTM-2COPV-PTM** and b) **PTM-3COPV-PTM** in CH_2Cl_2 solution at different temperatures.

EPR of Mixed Valence species

To generate the MV derivatives, we used the same methodolgy described before. Since the bi-anion species are not active in EPR, we have reduced the biradical **PTM-nCOPV-PTM** compound with a solution of Bu_4NOH until the anion bands were very intense in the UV-Vis-NIR spectrum and only a small proportion of mixed valence radical anion is observed. In that way we can assume that the comproportonation equilibrium between all species, birradical, radical anion and dianion is shifted giving a mixture of mixed-valence and bi-anion in solution. The registered EPR spectra will then correspond only to the **[PTM-nCOPV-PTM]**•⁻ mixed valence species.

The room temperature EPR spectrum of **[PTM-nCOPV-PTM]**•⁻ compounds consists of 3 overlapped lines (Figure 27) which correspond to the coupling of the electron with two hydrogens of the vinyl closest to both PTM units. This means that in the mixed-valence species the intramolecular electron transfer (IET) rate between the PTM radical and the PTM anion is in the "fast-exchange" regime at room temperature. When the temperature decreases the spectra does not show significant changes, although it can be observed that the central line decreases somewhat indicating that the exchange rate constant is decreasing a little bit. If we compare these spectra with the ones of the parent mixed valence compounds with flexible phenylene vinylene bridges of the same length (Figure 28), in the temperature range between 300K and 200K, [51] it is clear that the charge is much more delocalized in **[PTM-nCOPV-PTM]**•⁻ as expected because of the rigidity of the **nCOPV** bridge.

Figure 27: EPR spectra of mixed valence species generated from a) **PTM-2COPV-PTM** and b) **PTM-3COPV-PTM** upon stepwise addition of a solution of BU$_4$OH in CH$_2$Cl$_2$. The spectra were recorded in CH$_2$Cl$_2$ solution at different temperatures. *(* This small signal is due to an impurity which is not observed in the biradical counterpart).*

PTM-4OPPV-PTM **PTM-3COPV-PTM**
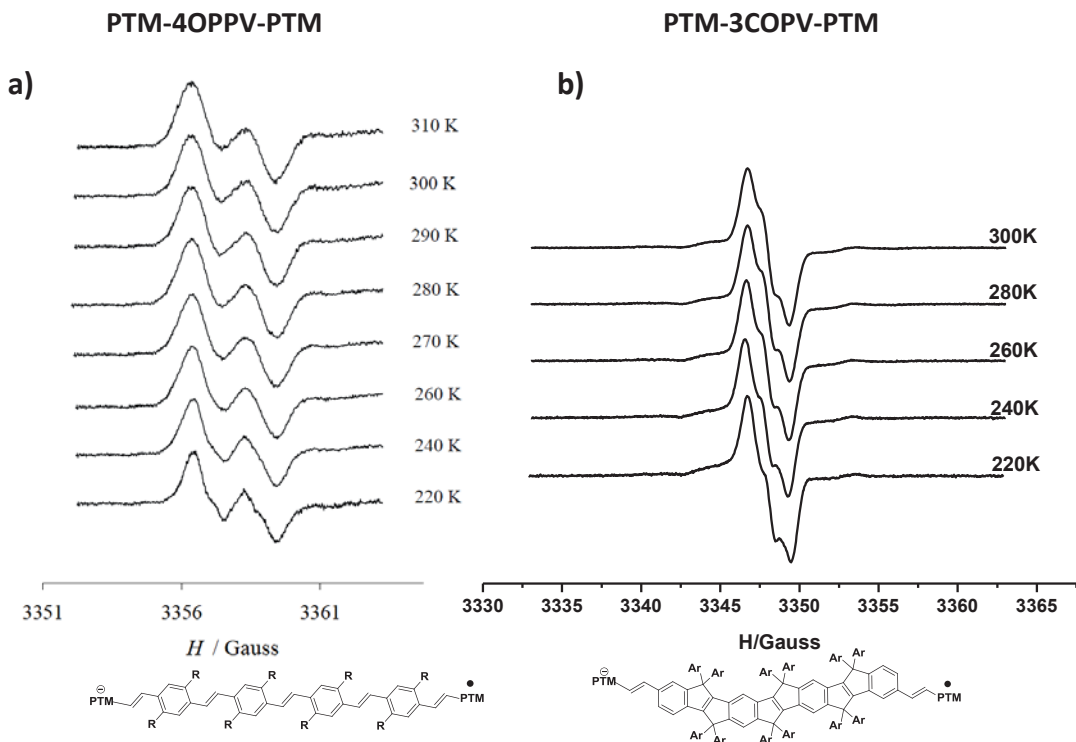
Figure 28: Comparison of IET, analyzed by EPR spectroscopy, of two MV composed by a) flexible wire **4OPPV** and b) rigid wire **3COPV**, which have similar length.

These interesting results are still preliminary and we have to repeat the EPR experiments, in order to obtain clean spectra without impurities. Further, we want to study by Raman spectroscopy the mixed valence compounds. Additionally, we plan in the near future to synthesize and study a more extended **PTM-nCOPV-PTM** mixed valence family, in order to analyzed the IET in longer **COPV** wires and compare the results with the mixed valence **PTM-nOPPV-PTM** family with flexible bridges.

60

7. Summary

We have achieved the proposed goal to synthesize MV systems formed by different conjugated bridges of increasing length acting as a molecular wires connecting two PTMs radical/anion as electron injector/collector. In these MV systems we have studied the electron transfer processes through the wires.

First, a family of molecular wires of vinylene-thiophene with a long range of lengths (**nTV** n = 2-7), having two PTM radicals at the ends of the wires (**PTM-nTV-PTM**) were synthesized and their electrochemical, optical and magnetic properties studied by different and complementary techniques (CV, UV-Vis-NIR, Raman and EPR spectroscopy).

The MV species of the **PTM-nTV-PTM** family were generated through the reduction of one PTM radical to the PTM anion (**[PTM-nTV-PTM]$^{\bullet-}$**), which allowed us to study the Intramolecular-Electron-Transfer (IET) through the **nTV** wires using the MV approach. The IET process through these wires in the ground state was studied by variable-temperature EPR, UV-Vis-NIR, and resonant Raman spectroscopy. We demonstrated that the longer **nTV** wires (n = 4-7) have a biased bidirectional charge hopping mechanism, where the driving force of the process is the formation of a positive polaron in the wire. However, in the shorter **nTV** wires (n = 2, 3) the flickering mechanism is dominant because the quinoidization of the wires is more favored.

Besides we were able to obtain the oxidized species of the **PTM-nTV-PTM** family through the oxidation of one thiophene (mono radical cation **[PTM-nTV-PTM]$^{+\bullet}$**), or two thiophenes (dication **[PTM-nTV-PTM]$^{2+}$**). We studied the oxidized **PTM-nTV-PTM** species by different techniques: UV-Vis-NIR, Raman and EPR spectroscopy. We demonstrated that, except for the shorter compound (**PTM-2TV-PTM**), the oxidized **PTM-nTV-PTM** species are high spin compounds where PTM radicals and thiophene radical cations are not interacting strongly.

We have also synthesized a family of rigid molecular wires with two PTM radicals at the ends (**PTM-nCOPV-PTM**, n = 2, 3). These **PTM-nCOPV-PTM** were studied by UV-Vis-NIR and EPR spectroscopy.

We generated the MV by the reduction of one PTM radicals (**[PTM-nCOPV-PTM]$^{\bullet-}$**), and studied the IET process through the COPV wires by variable-temperature EPR spectroscopy. In the preliminary studies realized with the **[PTM-nCOPV-PTM]$^{\bullet-}$** MV systems, we found that IET is more efficient thorough these planar wires compared with the **OPPV** flexible wires of the same length.

References

[1] T. S. Arrhenius, M. Blanchard-Desce, M. Dvolaitzky, J.-M. Lehn, *Proc. Natl. Acad. Sci. USA,* 1986, **83**, 5355–5359.

[2] a) M. J. Crossley, P. L. Burn, *J. Chem. Soc. Chem. Commun.* 1987, **39**. b) M. J. Crossley, P. L. Burn, *J. Chem. Soc. Chem. Commun.* 1991, 1569. c) J. R. Reimers, L. E. Hall, M. J. Crossley, N. S. Hush, *J. Phys. Chem. A* 1999, **103**, 4385. d) F. Barigelletti, L. Flamigini, *Chem. Soc. Rev.* 2000, **29**, 1. e) S. Fraysse, C. Coudret, J.-P. Launay, *J. Am Chem. Soc*. 2003, **125**, 5880.

[3] a) C. Journet, W. K. Maser, P. Bernier, A. Loiseau, M. L. de la Chapelle, S. Lefrant, P. Deniard, R. Lee, J. E. Fischer, *Nature* 1997, **388,** 756. b) T. W. Ebbessen, H. J. Lezec, H. Hiura, J. W. Bennet, H. F. Ghaemi, T. Thio, *Nature* **2000**, *382*, 54. c) J. Kong, N. R. Franklin, C. W. Zhou, M. G. Peng, K. J. Cho, H. J. Dai, *Science* 2000, **287**, 622. d) M. S. Dresselhaus, G. Dresselhaus, P. C. Eklund, *Science of Fullerenes and Carbon Nanotubes*, Academic Press, San Diego, 1996. e) M. S. Dresselhaus, G. Dresselhaus, P. Avouris, *Carbon Nanotubes: Synthesis, Structure, Properties, and Applications*, Springer, Berlin, 2001.

[4] 32. H. Fink, C. Schonenberg, *Nature* 1999, **398**, 407. b) A. J. Storm, J. van Noort, S. De Vries, C. Dekker, *Appl. Phys. Lett.* 2001, **79**,3881.

[5] a) K. Pettersson, J. Wiberg, T. Ljungdahl, J. Martensson and B. Albinsson, *J. Phys. Chem. A*, 2005, **110**, 319. b) K. Kilså, J. Kajanus, A. N. Macpherson, J. Mårtensson and B. Albinsson, *J. Am. Chem. Soc.*, 2001, **123**, 3069; c) J. Wiberg, L. Guo, K. Pettersson, D. Nilsson, T. Ljungdahl, J. Mårtensson and B. Albinsson, *J. Am. Chem. Soc.*, 2006, **129**, 155.

[6] C. Atienza, N. Martin, M. Wielopolski, N. Haworth, T. Clark and D. M. Guldi, *Chem. Commun.,* 2006, 3202.

[7] L. Jones, J.S. Schumm, J.M. Tour, *J. Org. Chem*. 1997, **62,** 1388.

[8] W. B. Davis, W. A. Svec,M. A. Ratner andM. R.Wasielewski, *Nature*, 1998, **396**, 60.

[9] F. Giacalone, J. L. Segura, N. Martin and D. M. Guldi, *J. Am. Chem. Soc.*, 2004, **126,** 5340.

[10] a) E. A. Weiss, M. J. Ahrens, L. E. Sinks, A. V. Gusev, M. A. Ratner and M. R. Wasielewski, *J. Am. Chem. Soc*., 2004, **126**, 5577. b) E. A. Weiss, M. J. Tauber, R. F. Kelley, M. J. Ahrens, M. A. Ratner and M. R. Wasielewski, *J. Am. Chem. Soc.*, 2005, **127**, 11842.

[11] D. Hanss, M. E. Walther and O. S. Wenger, *Coord. Chem. Rev*., 2010, **254**, 2584.

[12] a) R. H. Goldsmith, L. E. Sinks, R. F. Kelley, L. J. Betzen, W. H. Liu, E. A. Weiss, M. A. Ratner and M. R. Wasielewski, Proc. Natl. Acad. Sci. U. S. A., 2005, **102**, 3540. b) T. Miura, R. Carmieli and M. R. Wasielewski, *J. Phys. Chem. A*, 2010, **114**, 5769.

[13] C. Atienza-Castellanos, M. Wielopolski, D. M. Guldi, C. van der Pol, M. R. Bryce, S. Filippone and N. Martin, *Chem. Commun*., 2007, 5164.

[14] A. B. Ricks, K. E. Brown, M. Wenninger, S. D. Karlen, Y. A. Berlin, D. T. Co and M. R. Wasielewski, *J. Am. Chem. Soc.*, 2012, **134**, 4581.

[15] X. Zhu, C. Mitsui, H. Tsuji, E. Nakamura *J. Am. Chem. Soc.*, 2009, **131 (38)**, 13596–13597.

[16] a) D. L. Pearson, J. M. Tour, *J. Org. Chem.* 1997, **62**, 1376. b) J. M. Tour, *Polymer News.* 2000, **25**, 329.

[17] F. Oswald, D.-M. Shafiqul Islam, M. E. El-Khouly, Y. Araki, R. Caballero, P. de la Cruz, O. Ito, F. Langa, *Phys. Chem. Chem. Phys,* 2014, **16**, 2443-2451-

[18] a) I. Jestin, P. Frere, N. Mercier, E. Levillain, D. Stievenard, J. Roncali, *J. Am. Chem. Soc.* 1998*, 120,* 8150-8158. b) j. Roncali, Acc. Chem. Res. 2000, 33, 147.

[19] L. A. Bumm, J. J. Arnold, M. T. Cygan, T. D. Dunbar, T. P. Burgin, L. Jones II, D. L. Allara, J. M. Tour, P. S. Weiss, *Science* 1996, **271**, 1705.

[20] T. Hines, I. Diez-Perez, J. Hihath, H. Liu, Z. S. Wang, J. Zhao, G. Zhou, K. Müllen, and N. Tao*, J. Am. Chem. Soc.* 2010, **132**, 11658–11664.

[21] E. J. Dell, B. Capozzi, J. Xia, L. Venkataraman and L. M. Campos, *Nat. Chem*. 2015, **7**, 209.

[22] M. Gilbert, B. Albinsson, *Chem. Soc. Rev* 2015, **44**, 845.

[23] a) R. J. Mortimer, *Electrochim. Acta*. 1999, **44**, 2971. b) D. R. Rosseinsky, R. J. Mortimer, *Adv. Mater*. 2001, **13**, 783. c) M. Green, *Chem. Ind.* 1996, **641**. d) *Chem. Rev*. 2004, **104** (11), 4887. e) G. Saito, Y. Yoshida, *Bull. Chem. Soc. Jpn.* 2007, **80**, 1. f) E. Gomar-Nadal, L. Mugica, J. Vidal-Gancedo, J. Casado, J. T. Lopez Navarrete, J. Veciana, C. Rovira, D. Amabilino, *Macromolecules* 2007, **40,** 7521. 5. g) Y. T. Tao, C. H. Chuen, C. W. Ko, W. Peng, *J. Chem. Mater*. 2002, **14**, 4256. h) S. Schols, S. Verlaak, C. Rolin, D. Cheyns, J. Genoe, P. Heremans, *Adv. Funct. Mater.* 2007, **18** (1), 136. i) S. Mohamed, D. Demeter, J.-A. Laffitte, J.-A. P. Blanchard,J. Roncali, *Scientific Reports* 2015, **5**, 9031.

[24] a) S. S. Isied, M. Y. Ogawa, J. F. Wishart, *Chem. Rev.* 1992, **92**, 381. b) R. A. Marcus, N. Sutin, *Biochim. Biophys. Acta Rev. Bioenerg.* 1985, **811**, 265. c) D. M. Adams, L. Brus, C. E. D. Chidsey, S. Creager, C. Creutz, R. Kagan, P. V. Kamat, M. Lieberman, S. Lindsay, R. A. Marcus, R. M. Metzger, M. E. Michel-Beyerle, J. R. Miller, M.D. Newton, D. R. Rolison, O. Sankey, K. S. Schanze, J. Yardley, X. Zhu, *J. Phys. Chem. B* 2003, **107**, 6668.

[25] A. Heckmann, C, Lambert, *Angew. Chem. Int. Ed*. 2012, **51** (2), 326.

[26] J. Guasch, L. Grisanti, V. Lloveras, J. Vidal-Gancedo, M. Souto, D. C. Morales, M. Vilaseca, C. Sissa, A. Painelli, I. Ratera, C. Rovira, J. Veciana, *Angew. Chem. Int*. *Ed.* 2012, **51**, 11024 −11028

[27] a) R.A. Marcus, *J. Chem. Phys.* 1956, **24**, 966. b) R. A. Marcus, *Rev. Mod. Phys.* 1993, **65**, 599.

[28] K. Wieghardt, *Chem. Unserer Zeit* 1979, **13**, 118.

[29] B. S. Brunschwig, N. Sutin, *Coord. Chem. Rev.* 1999, **187**, 233.

[30] R. A. Marcus, *Discuss. Faraday Soc*. 1960, **29**, 21.

[31] R. A. Marcus, *J. Chem. Phys.* 1965, **43**, 679.

[32] B. S. Brunschwig, S. Ehrenson, N. J. Sutin, *Phys. Chem.* 1986**, 90**, 3657.

[33] a) N. S. Hush, *Coord. Chem. Rev.* 1985**, 64**, 135. b) N. S. Hush, *Electrochim. Acta* 1968, **13**, 1005.

[34] C. Creutz, M. D. Newton, N. Sutin, *J. Photochem. Photobiol. A* 1994**, 82**, 47.

[35] B. S. Brunschwig, C. Creutz, N. Sutin, *Chem. Soc. Rev.* 2002**, 31**, 168.

[36] C. Lambert, G. Noll, *J. Am. Chem. Soc.* 1999**, 121**, 8434.

[37] a) R. J.Cave, M. D. Newton, *Chem. Phys. Lett.* 1996, **249**, 15. b) S. F. Nelsen, M. D. Newton, *J. Phys. Chem. A,* 2000***, 104, 10023.*

[38] N. S. Hush, *Prog. Inorg. Chem.* 1967**, 8**, 391.

[39] M. B. Robin, P. Day, *Adv. Inorg. Chem. Radiochem.* 1967, **9**, 247.

[40] J. A. Weil, J. R. Bolton, J. E. Wetz, *Electron Paramagnetic Resonance*, 1994.

[41] N. Gautier, F. Fumur, V. Lloveras, J- Vidal-Gancedo, J. Veciana, C. Rovira, P Hudhomme, *Angew. Chem. Int. Ed*. 2003, **42**, 2765-2768.

[42] a) J. Heizner, *Mol. Phys*. 1971, **22**, 167. b) *Quantum Chemistry Program Exchange* 1972, **No. 209**.

[43] a) S. F. Nelsen, P. J. Hintz, J. M. Buschek, G. R. Weisman, *J. Am. Chem. Soc*. 1975, **97**, 4933-4936. b) S. F. Nelsen, H. Chang, J. J. Wolff, J. Adamus, *J. Am. Chem. Soc* 1993, **115**, 12276-12289.

[44] J. Telo, S. F Nelsen, Y. Zhao, *J. Phys. Chem. A* 2009, **113**, 7730-7736.

[45] K. Lancaster, S. A. Odom, S. C. Jones, S. Thayumanavan, S. R. Marder, J.-L. Bredas, V. Coropceanu, S. Barlow, *J. Am. Chem. Soc.* 2009, **131**, 1717-1723.

[46] S. V. Rosokha, D. K. Sun, J. K. Kochi, *J. Phys. Chem. A,* 2002, **106**, 2283,-2292.

[47] a) J. Bonvoisin, J.-P. Launay, C. Rovira, J. Veciana, *Angew. Chem*.1994, **106,** 2190–2193; *Angew. Chem. Int. Ed.* 1994, **33**, 2106–2109; b) V. Lloveras, J. Vidal-Gancedo, D. Ruiz-Molina, T. M. Figueira-Duarte, J.-F. Nierengarten, J. Veciana, C. Rovira, *Faraday Discuss*. 2006, **131**, 291–305.

[48] A. Nitzan, *Chemical Dynamics in Condensed Phases; Oxford University Press: New York*, 2006.

[49] Y. Zhang, C. Liu, A. Balaeff, S. Skourtis, D. N. Beratan. *Proc. Natl. Acad. Sci. U. S. A*. 2014, **111**, 10049–10054

[50] J. Blumberger, *Chem. Rev*. 2015, **115**, 11191 - 11238.

[51] V. Lloveras, J. Vidal-Gancedo, T. M. Figueria-Duarte, J.-F. Nierengarten, J. J. Novoa, F. Mota, N. Ventosa, C. Rovira, J. Veciana, *J. Am. Chem. Soc.*, 2011, **133**, 5818.

[52] S. Rodríguez-González, M. C. Ruiz-Delgado, R. Caballero, P. De la Cruz, F. Langa, J. T. López-Navarrete, J. Casado, *J. Am. Chem. Soc.*, 2012, **134**, 5675.

[53] J. Sukegawa, C. Schubert, X. Zhu, H. Tsuji, D. M. Guldi, E. Nakamura, *Nat. Chem.* 2014, **6**, 899.

[54] F. Oswald, D.-M. Shafiqul Islam, Y. Araki, V. Troiani,P. de la Cruz, A. Moreno, O. Ito, F. Langa, *Chem. Eur. J.* 2007, **13**, 3924 – 3933

[55] C. Rovira, D. Ruiz-Molina, O. Elsner, J. Vidal-Gancedo, J. Bonvoisin, J.-P. Launay, J. Veciana, *Chem. Eur. J.* 2001, **7**, 240.

[56] S. R. González, B. Nieto-Ortega, R. González Cano, V. Lloveras, J. J. Novoa, F. Mota, J. Vidal-Gancedo, C. Rovira, J. Veciana, E. del Corro, M. Taravillo, V. G. Baonza, J. T. Lopez-Navarrete, J. Casado, *J. Chem. Phys.*, 2014, **140 (16)**, 164903.

[57] P. Mayorga-Burrenzo, B. Pelado, R. Ponce-Ortiz, P. De la Cruz, J. T. Lopez-Navarrete, F. Langa, J. Casado, *Chem. Eur. J.* 2015, **21 (4)**, 1713 – 1725.

[58] J. J. Apperloo, J.-M. Raimundo, P. Frere, J. Roncali. R. A. J. Janssen, *Chem. Eur. J.* 2000, **6**, 1698-1707.

[59] a) J. L. Bredas, G. B. Street, *Acc. Chem. Res.* 1985, **18**, 309. b) J. A. E. H. van Haare, E. E: Havinga, J. L. J. van Dongen, R. A. J. Janssen, J. Cornil, J. L. Bredas. *Chem. Eur. J*. 1998, **4**, 1509.

Publication 1

Title	On the Operative Mechanisms of Hole Assisted Negative Charge Motion in Ground States of Radical-anion Molecular Wires
Authors	Franco, Carlos; Burrezo, Paula; Lloveras, Vega; Caballero, Ruben; Alcon, Isaac; Bromley, Stefan; Mas-Torrent, Marta; Langa, Fernando; López Navarrete, Juan T.; Rovira, Concepcio; Casado, Juan; Veciana, Jaume
Publication	Submitted to J. Am. Chem. Soc

On the Operative Mechanism of Hole Assisted Negative Charge Motion in Ground States of Radical-anion Molecular Wires

Carlos Franco,[†] Paula Mayorga Burrezo,[§] Vega Lloveras,[†] Rubén Caballero,[⊥] Isaac Alcón,[∥] Stefan Bromley,*[,∥,‡] Marta Mas-Torrent,[†] Fernando Langa,[⊥] Juan T. López Navarrete,[§] Concepciò Rovira,*[,†] Juan Casado,*[,§] and Jaume Veciana*[,†]

[†] Department of Molecular Nanoscience and Organic Materials, Institut de Ciència de Materials de Barcelona (CSIC), Campus Universitari de Bellaterra, E-08193, Cerdanyola, Barcelona, Spain.

[§] Department of Physical Chemistry, University of Malaga, Campus de Teatinos s/n, 29071 Malaga, Spain.

[⊥] Instituto de Nanociencia, Nanotecnología y Materiales Moleculares (INAMOL), University of Castilla-La Mancha, Campus de la Fábrica de Armas, 45072 Toledo, Spain.

[∥] Department of Physical Chemistry, Faculty of Chemistry, University of Barcelona, Av. Diagonal, 647, 08028-Barcelona, Spain.

[‡] Catalan Institution of Research and Advanced Studies (ICREA), 08010-Barcelona Spain.

ABSTRACT: (Charge transfer/transport in molecular wires over varying distances is a subject of great interest in the field of molecular electronics. The transport mechanisms in these systems have been generally accounted for on the basis of tunneling or superexchange charge transfer operating over small distances which progressively gives way to hopping assisted transport over larger distances. The underlying molecular sequential steps that likely take place during hopping and the operative mechanism occurring at intermediate distances have received much less attention given the difficulty in assessing detailed molecular-level information. We describe

here the operating mechanisms for unimolecular electron transfer/transport in the ground state of radical-anion mixed-valence derivatives occurring between their terminal perchlorotriphenylmethyl/ide groups through thiophene-vinylene oligomers that act as conjugated wires of increasing length up to 30 Å. The unique finding here is that the net transport of the electron in the larger molecular wires is initiated by an electron-hole dissociation intermediated by hole delocalization (conformationally assisted and thermally dependent) forming mobile polaronic states in the bridge that terminate by an electron-hole recombination at the other wire extreme. On the contrary for the shorter radical-anions our results suggest that a flickering resonance mechanism which is intermediate between hopping and superexchange is the operative one. We support these mechanistic interpretations by applying the pertinent biased kinetic models of the charge/spin exchange rates determined by electron paramagnetic resonance and by molecular structural level information obtained from UV-Vis and Raman spectroscopies and by quantum chemical modelling.

The main mechanisms used to describe charge transfer/transport processes across a chain of ionizable molecular subunits bridge are charge hopping (CH), flickering resonance (FR), and superexchange (SE).[1] CH is a thermally activated incoherent process where a localized charge excess is assumed to hop between consecutive sites on the bridge where relaxation take place previous to each hop. In this model "real" wire states (i.e., excited, conformational, charged, hot vibrational, etc.) take an active part in the charge transport and for this reason this mechanism is operative even for long bridges. On the contrary, in the SE mechanism thermal fluctuations bring the energy levels of the two terminal subunits into degeneracy (resonance) causing the charge to tunnel from one extreme of the wire to another without residing on the
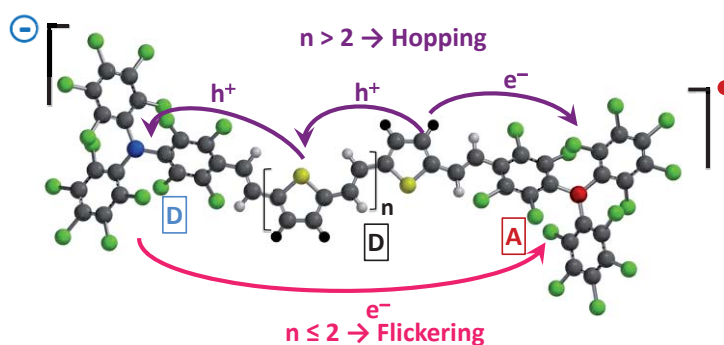
bridge. Thereby this mechanism is operative only for the shorter wires. Finally, the recently proposed FR[1] mechanism can be thought of as a compromise between CH and SE where the energy levels of the two terminal subunits and those of the bridge subunits became all in resonance due to thermal fluctuations. Then, the charge moves ballistically, without nuclear relaxation, through the energy-aligned states to become trapped at the end of the wire. Given the inherent nature of charge transfer/transport, it combines and competes with many other molecular processes thus giving rise to a panoply of scenarios. In order to understand such complex phenomena, which are particularly relevant in molecular electronics and biological systems, detailed knowledge from a range of experimental and theoretical probes is of vital importance.

The most commonly employed protocol for mechanistic studies of charge transport is the measurement of electrical currents through molecular junctions.[2-9] However, complementary *in-situ* spectroscopic studies are difficult given the nanometer resolution often required. For analogous studies in solution, molecular charge transport is usually evaluated is by photoexcitation by inducing an energetically downhill movement of excitons through the wire, whereby the dynamics can be studied by time-resolved spectroscopies[10]. Unfortunately, these photoactivated transient methods also contain coupling terms among the excited states thus potentially "masking" the intrinsic charge transport characteristics in the ground state.[11,12] It turns out that "clean" insights into the intrinsic conduction mechanisms are obtained in the "unperturbed" ground electronic state for which mixed valence (MV) systems are very good choices. Among these, radical MV systems are ideal candidates for this purpose since they can be studied by means of Electron Paramagnetic Resonance (EPR) in solution[13] which, in addition, facilitates the use of complementary *in situ* spectroscopic techniques, like UV-Vis-NIR and Raman, providing further rich molecular level cross-information.

Perchlorotriphenylmethyl radicals (PTM) are persistent and stable open-shell derivatives with good electron accepting properties and have been successfully used as redox centers in MV radical-anion systems, allowing the study of electron transfer/transport through different bridges.[14-16] Bridges based on thiophene-vinylene oligomers (nTV) have been recently demonstrated to perform as one of the most efficient π–conjugated extended molecular wires.[17-19] Given their electronic rich donor nature, these nTV bridges are typically considered as hole (positive charge) transmitters.[17-19] Conversely, nTV bridges have never been used to promote charget transfer/transport between negatively charged terminal groups.

In this work, a series of six electron-donor nTV oligomers substituted at their terminal sites with two PTM radical groups, •PTM-nTV-PTM• (1-6, Scheme 1), properly reduced to radical-anion MV species are studied. The excess charge conduction behavior in the resulting

mixed-valence [PTM-nTV-PTM]•⁻ species is studied by variable-temperature EPR complemented by *in situ* UV-Vis-NIR and resonant Raman spectroscopies and supported by electronic structure calculations. This multi-fold information of the spin/charge exchange rate in the ground electronic states serves to propose for the longer oligomers (nTV; n = 4-7) a biased bidirectional symmetrical charge hopping mechanism through the nTV bridge, imparted by two reflecting PTM sites at opposite ends. The initial step of the mechanism is the thermally activated intramolecular oxidation of the wire by the "neutral" PTM• subunit forming a symmetric charge separated state with a mobile positive polaron in the bridge flanked by two PTM⁻ anions. After the formation of this transitory species where charge may hop among the TV units, and that finally decays by an electron-hole annihilation that restores the neutral nTV radical-anion. This finding is rather unusual since charge transport of negative charge (PTM•⁻→PTM•) through hole-transmitter bridges (nTV) most of the times occurs through empty "conduction" states able to accommodate an excess of charge rather than mediated by positive charges. On the contrary, in the shorter radical-anions (nTV; n = 2,3) the operative mechanism for the spin/charge exchange seems to be the FR mechanism favored by the higher rigidity (or quinoidization) of their bridges.
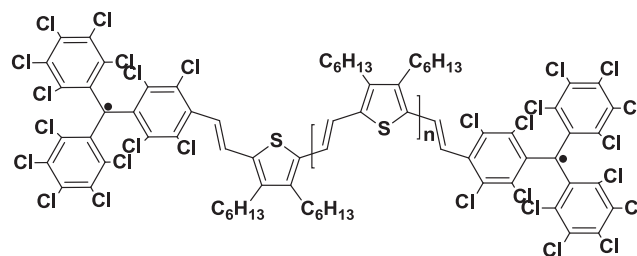

1, n = 1; **2**, n= 2; **3**, n= 3; **4**, n= 4; **5**, n= 5; **6**, n = 6

Scheme 1.

Results and discussion

Synthesis and characterizations. The synthesis of diradicals **1-6** starts with the preparation of the corresponding by hydrogenated derivatives, **(αH,α'H)-PTM-nTV-PTM**, through a Witting-Horner olefination between the polychlorotriphenylmethane phosponate derivative[20] and the suitable nTV dialdehydes (see SI). Treatment with an excess of base gives the corresponding biscarbanions [PTM-nTV-PTM]⁻² that are subsequently oxidized to **1-6**. Diradicals **1-6** were completely characterized with usual spectroscopic techniques, like IR, UV-Vis (Table S1), Raman, and MALDI-TOF MS (see SI). Cyclic voltammetries of diradicals **1-6** show well resolved two-electron reduction peaks and reversible oxidations resulting in amphoteric redox behaviors of **1-6** (Table S1). Solution EPR spectra of diradicals **1-6** (Table S3) consist of four overlapped main lines from which two isotropic hyperfine coupling constants, a_i, that are half of those observed for the segmental model monoradical **PTM-2TV** (see SI), have been determined. Such results indicate the

existence of a magnetic interaction between the two unpaired electrons through the diamagnetic bridge, which are additionally confirmed by frozen solution EPR spectra of **1** and **2** that show $\Delta M_s = 2$ half-field forbidden transitions due to thermally accesible triplet states (Figures S65-S70). Generation of radical-anions [**PTM-nTV-PTM**]$^{\bullet-}$ was achieved by a stepwise chemical or electrochemical reduction of diradicals **1-6** (Figure S1).
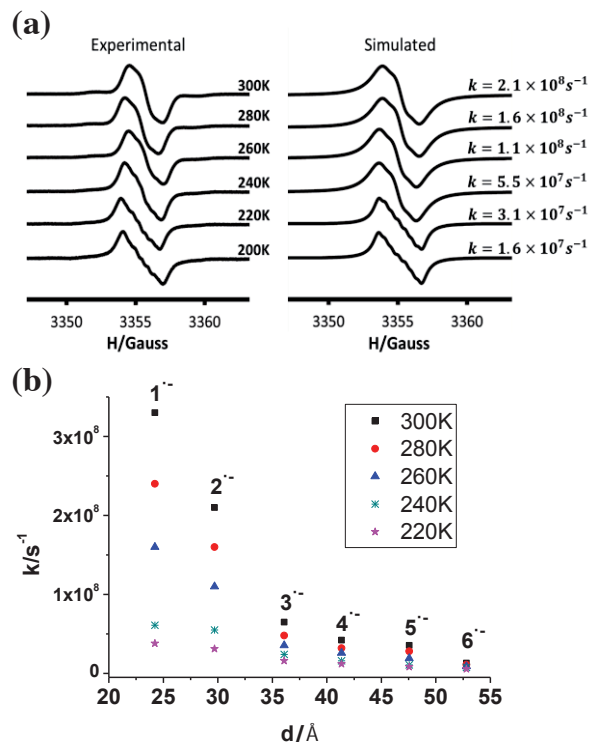
Figure 1: a) Temperature-dependent changes in the EPR spectrum of **2**$^{\bullet-}$ solution in CH_2Cl_2 (left), and simulated spectra (right) with different spin/charge exchange rates. b) Distance dependences of spin/charge exchange rates, k, of radical-anions (**1**$^{\bullet-}$–**6**$^{\bullet-}$) in the temperature range 220-300 K.

***In situ* spectroscopic studies**. Intramolecular spin/charge transfer in radical-anions [**PTM-nTV-PTM**]$^{\bullet-}$ was examined by variable-temperature EPR measurements. In all these radical-anions the EPR line shapes changed with the temperature going from four to three overlapped lines when the temperature is increased (in the range 200-300 K), indicating a passage from the slow to fast exchange regime at the EPR time-scale. The first-order rate constants (k) for spin/charge exchange between the two PTM sites in each compound were determined by simulation of the experimental EPR spectra using the ESR-EXN software[21] (Figures 1a and S2-S7). The comparison at a given temperature for all radical anions demonstrates that k decreases with the increasing of the nTV bridge lengths (Figure 1b). For a given compound, k also exhibits a net dependence with the temperature (Figure 1b) disclosing that a thermally activated intramolecular dynamic spin/charge exchange occurs between the two terminal PTM sites for all radical-anions. From the dependence of k values was deduced that for the shorter

compounds the operating mechanism is strongly dependent on the temperature as well as on the length of the bridge, whereas for the longer ones both thermal and size variations are considerably smaller. Such different behaviors between shorter (nTV; n= 2, 3) and longer (nTV; n=4-7) bridges point to the presence of two distinct mechanisms. The question therefore arises about the particular electron transfer/transport mechanism which operates in these MV radical-anions.
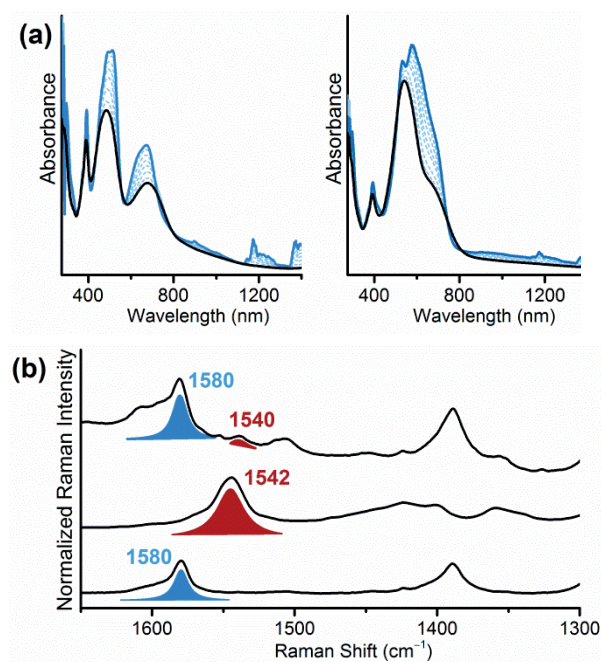

Figure 2: a) Evolution of UV-Vis-NIR spectra of the **1**$^{\bullet-}$ and **4**$^{\bullet-}$ as a function of the temperature. Black line corresponds to UV-Vis-NIR at room temperature and blue line at 77K. b) Comparison of 633nm Raman spectra in DCM of **3**$^{\bullet-}$ (top), **3**$^{\bullet+}$ (medium) and **3** (bottom).

Variable-temperature UV-Vis-NIR electron absorption spectroscopy under the same conditions as the EPR measurements, were performed for all radical-anions. Spectra at room temperature (Figure 2a and S8) show three well-distinguished kinds of bands: a band at around 390 nm, characteristic of **PTM**$^{\bullet}$ radical chromophore, another set of very intense bands at 485-573 nm, due to the conjugated nTV bridges, and finally absorption bands with medium intensity at 678-720 nm, assigned to the negatively charged **PTM**$^{-}$ partially spreading out in the bridge (i.e., forming the PTM&nTV segment). Worth noticing is the intervalence charge transfer (IVT) band exhibited by **1**$^{\bullet-}$ at 1372 nm (Figure S1 inset) which is not detected for the rest of radical-anions. This result is consistent with the typical exponential decay of the intensity (accompanied by a blue-shift) of IVT bands with increasing molecular lengths. Interestingly, the nTV centered bands of radical-anions clearly show a red-shift with the enlargement of the bridge from 485 to 573 nm, while the PTM&nTV absorption is less altered with the size (i.e., from 678 nm for **1**$^{\bullet-}$ to 720 nm in **6**$^{\bullet-}$). Furthermore, the nTV bands are broad and ill-resolved at

room temperature but they evolve into a clear vibronic structure at 77 K more pronounced in the larger compounds (Figure 2a and S8). Conversely, the rest of the bands (PTM and PTM&nTV bands) are minimally affected by cooling. The detection of vibrational resolution in the absorption spectra on cooling might reveal the existence of an ample distribution of molecular conformers at room temperature formed by distortions among the repeating units around the thiophene vinylene C-C bonds. By removing thermal energy the population of the most planar, rigid and energetically stable conformer is increased providing the vibronic components. Furthermore, this indicates the flatness or flexibility of the ground electronic state potential energy curve against conformational distortions in the larger MV radical-anions, an aspect of relevance for the further discussion.

Resonant Raman spectra of radical-anions [**PTM-nTV-PTM**]$^{\bullet-}$ at room temperature (Figure 2b (top) and S9) taken with the excitation laser at 633 nm, in resonance with one of the absorption bands, provide unique vibrational fingerprints of the radical-anions. In comparison with the Raman spectra of the neutral diradicals (Figure 2b, bottom and S10), radical-anions (Figures 2b, top and S9) exhibit resonant Raman bands emerging from the different domains of the radical-anions: i) the bands at >1600 cm^{-1}, due to PTM-nTV fragments mostly supporting the excess of negative charge, and ii) the bands at 1580-1590 cm^{-1} corresponding to the molecular fraction of the bridge without an excess of negative charge. Nevertheless, the most significant finding in these resonant Raman spectra, is the detection of bands with medium-low intensities around 1540 cm^{-1}, together with several other weaker bands in the region of 1390-1460 cm^{-1}. In Figure 2 the spectrum of the radical cation of **3**, **3**$^{\bullet+}$ (generated by addition of one equivalent of a FeCl$_3$ solution), is also shown which presents the most prominent band at 1540 cm^{-1} accompanied be weaker features in the same interval of 1390-1460 cm^{-1}, such as **3**$^{\bullet-}$. In the **3**$^{\bullet+}$ the charge is confined in the middle of the nTV moiety (the electro-deficient **PTM**$^{\bullet}$ at each extreme repels and get away the positive charge), and the thiophene get quinoidal whereas the vinylenes are correspondingly strained, overall planarizing the bridge. Indeed, the resemblance between the 1540/1390-1460 cm^{-1} bands in **3**$^{\bullet+}$/**3**$^{\bullet-}$ reveals common structural features.
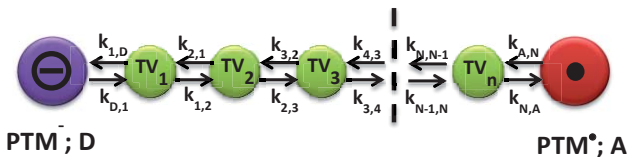
Scheme 2.

Mechanistic analysis. To elucidate the mechanism of electron transfer, one often refers to the interpretation of the k values within the framework of the classical Marcus theory which includes the role of the temperature in connection with microscopic parameters of relevance such as reorganization energies, electronic couplings and driving forces.

We propose that the mechanism of the spin/charge exchange process, at least in the larger radical-anions **3**$^{\bullet-}$, **4**$^{\bullet-}$, **5**$^{\bullet-}$ and **6**$^{\bullet-}$ proceeds as shown in Scheme 2 (see also Scheme S1) where a hole is stepwise transported by a hopping mechanism along the nTV molecular wire. The election of this sequential mechanism is first justified since takes into account the electron acceptor capability of PTM radical unit and the donor ability of nTV bridges to easily stabilize the positive charge within the bridge as revealed by their amphoteric redox behaviour. This redox property supports the simultaneous presence of the negative and positive charges in the molecule. Assuming a hole in the nTV bridge, this simplified kinetic scheme can be described as a biased bidirectional symmetrical positive charge hopping process with two reflecting sites at the opposite molecular ends where the rates of site-to-site hopping inside the nTV toward ($k_1=k_{2,1}$) and away ($k_2=k_{1,2}$) from the PTM$^{\bullet}$ radical are different among them but identical to those rates of the other wire extreme ($k_1=k_{2,1}= k_{N-1,N}$ and $k_2=k_{1,2} = k_{N,N-1}$) due to the molecular symmetry (see SI for more details). In particular we assume that $k_1 > k_2$[22] because the rate of a hole moving toward a negatively charged PTM site must be larger than in the opposite direction due to electrostatic attraction. In addition we assume that the hopping rates backward and forward inside the wire are similar ($k_{N-1,N-2}= k_{N-2,N-1} = k_3; \forall\ N \geq 4$) because the hopping hole is far from the charged termini. According to the classical Marcus theory and previous considerations on related systems,[23,24] the apparent spin/charge exchange rate, k_{ET} is given by (see SI):

$$k_{ET} \simeq \frac{\pi}{\hbar} \frac{|V_{D1}|^2}{\sqrt{4\pi\lambda_D k_B T}} e^{-\frac{(\Delta E_{BD} + \lambda_{D1})^2}{4\lambda_{D1} k_B T}} e^{-\beta(R-R_0-2r)} (Eq.\,1)$$

where ΔE_{BD} is the energy change corresponding to an electron injection from the TV bridge site nearest to PTM$^{\bullet}$ radical to the latter site (transition TV1 $\rightarrow$ PTM$^{\bullet}$), λ_{D1} ($=\lambda_{AN}$) is the reorganization energy of such a transition and $|V_{D1}|$ ($=|V_{AN}|$) denotes the coupling of the PTM$^{\bullet}$ to the corresponding terminal unit of the bridge, k_B the Boltzman's constant, T the absolute temperature, R (in Å) is the overall distance over which the spin/charge is transferred, R_o corresponds to the distance between the PTM units separated by a single-bridging TV unit (17.9 Å), r is the distance between two neighboring TV units (4.6 Å^{-1}), and the decay factor, β (in Å^{-1}). R and R_o values for all radical anions were determined as the distances between the central carbon atoms of PTM units, obtained from optimized geometries from quantum chemical calculations. The solution of Eq. [1] is linked to the underlying mechanism by means of ΔE_{BD} which is therefore inserted in the equation as a phenomenological parameter characteristic of the proposed mechanism. In our case, ΔE_{BD} represents the energy cost for the formation of an intermediate species which should contain a positive polaron in the mid-

dle of the nTV structure and therefore flanked by two PTMs each one with a negative charge. Assuming this, the barrier is accounted by the free energy required to form the dianion-cation charge separate state which is provided by the Weller formalism[25] by considering the cathodic and anodic redox potentials for the independent formation of a radical cation and a radical-anion directly taken from the CV data (see SI). This approximation gave ΔE_{BD} values from -1.13 eV for the shorter (n = 2) to -0.83 eV for the larger (n= 7) radical anion (see SI). Finally, fittings the experimental k data of **[PTM-nTV-PTM]**$^{\bullet-}$ (n = 4-7) to Eq. 1 using the latter ΔE_{BD} values gave the following parameters: $\lambda_{D_I} = \lambda_{AN} \approx 0.5$ eV, $|V_{D_I}| = |V_{AN}| \approx 0.07$ eV and a decay factor β of 0.25 Å^{-1}. These values are fully consistent with our experimental observations: i) since $\lambda_{IA} > |V_{IA}|$ therefore all radical-anion systems can be classified as class II MV systems and ii) the moderate decay factor value is in consonance with the capacity of the wire of transmitting the charge through large distances between the redox centers by means of a hopping mechanism. It must be highlighted that this mechanism conciliates the amphoteric redox behavior, the detection in the Raman spectrum of the anion radical species of weak features due to the radical cation (or dianion-cation species) and the rigidity at low temperatures of the bridge snice the contributions of the thieno-quinoidal polarons.

Theoretical modelling. To provide more insight in the underlying charge transfer phenomena density functional theory (DFT) calculations were performed on **1**$^{\bullet-}$ where the spectator C_6H_{13} side chains of the TV units were replaced by methyl groups to improve computational tractability. Previous studies of molecular MV systems have recommended using functionals 50% of Hartree-Fock-like exchange (HFLE),[26] or 35 % HFLE together with a continuum treatment of solvation.[27] We found that both approaches yielded stable charge localised states and here, unless otherwise stated, we report results obtained using the PBE functional[28] with 50% HFLE (referred to as PBE-50) employing the Gaussian 09 code.[29] Unfortunately, similar calculations on larger radical-anions were untractable due to the large sizes of molecules. The optimised structure of **1**$^{\bullet-}$ (Figure 3a) displays the 2TV bridge with a planar conformation and each PTM twisted by 40° with respect to the 2TV plane. To assess the behaviour of **1**$^{\bullet-}$ at finite temperatures we performed an *ab initio* molecular dynamics simulation (AIMD) at 300K using the FHI-AIMS code.[30] From 18 sample "snapshots" of thermally activated conformations taken over a 3ps period from these runs we calculated the spin distribution using the PBE-50 method described above. As indicated in Figure 4b (top) during the thermal motion at 300K the spin distribution fluctuates between being either localized on one of the two PTM units (←,→) or fully delocalized over the entire molecule (○). Figure 4b plots the variation of φ between each PTM unit and the 2TV wire. During the first 1.5ps φ present large values, typical of highly twisted

structures, and the spin distribution in **1**$^{\bullet-}$ tends to be localized on either one PTM unit (← or →). Conversely, for the latter 1.5ps, φ values are much smaller (i.e. flatter conformation) and the spin distribution tends to delocalize over the entire molecular skeleton. Therefore, it seems that the spin density (and thus the negatively charged density) well follows the thermally activated rotational fluctuations of **1**$^{\bullet-}$, in accordance with previous studies on single PTMs.[31] To investigate the 0K potential energy landscape underlying the thermally perturbed conformers, we fully optimized the structures of the 18 snapshots which all collapse into localized solutions. This suggests that the thermally excited structures with delocalized electronic states correspond to transitional conformations. The 0K delocalized solution obtained from a highly symmetric structure is found to lay 0.15 eV above all obtained localized solutions, providing a thermally accessible energy barrier between the localised electronic configurations (Figure 3c). Moreover, we have found that the calculated optical IVT energy depends on the degree of localization/delocalization of the ground electronic state, ranging from 1.1 eV for the localized solutions to 0.4 eV for the transitional delocalized states, reproducing quite well the observed band appearing at 0.7 eV (i.e. 1372 nm). We further note that the experimental IVT value is also consistent with typical β-HOMO/β-SUMO gap values found for the 18 thermally activated snapshots.

According to the DFT results, the charge transfer mechanism for **[PTM-2TV-PTM]**$^{\bullet-}$ appears not to involve a net bridge polaron state, but a transition state dependent on a resonance between the two PTM units, a situation more reconcilable with a SE mechanism. In pure SE, however, the bridge plays no part in the charge transfer, whereas from our analysis the degree of coupling between the PTM units and the bridge (via the torsion angles, φ) plays an essential role. Thus, a pure SE interpretation does not fully capture our theoretical findings. Between SE and hopping, the FR model aims to reconcile bridge participation without the presence of localised polarons on the bridge. We feel that for **[PTM-2TV-PTM]**$^{\bullet-}$ the FR mechanism is a reasonable alternative while for longer molecules the bridge will increasingly have more conformational freedom potentially allowing for charge/structure localisation (i.e. polaron formation). In turn this allows polaronic hopping to become increasingly prominent with respect to FR for bridges of n≥3 in **[PTM-nTV-PTM]**$^{\bullet-}$.
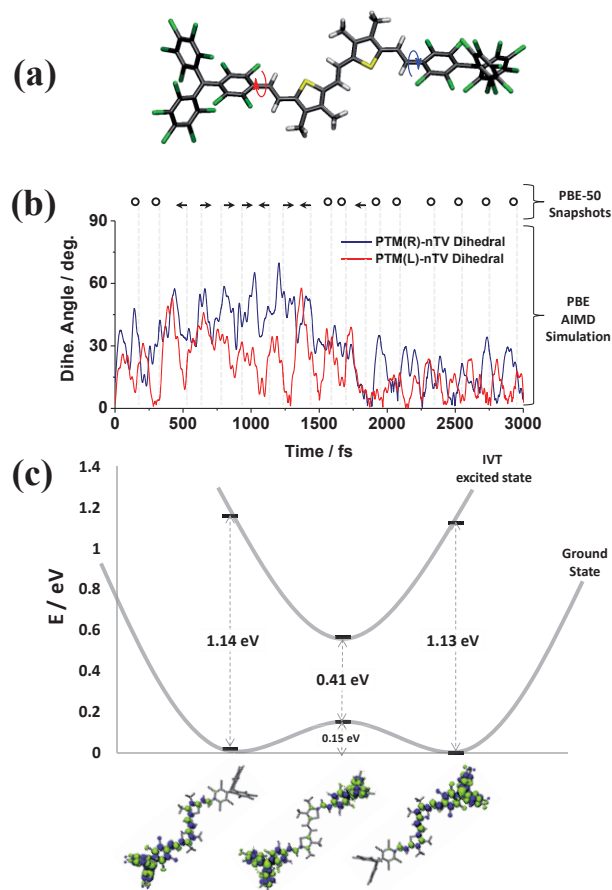
Figure 3: a) Optimized structure of **1**•⁻. The helical arrows indicate the dihedral angles (*φ*) between each PTM unit and the 2TV wire. b) Variation of the indicated dihedral angles in a) during 3 ps of an AIMD simulation of **1**•⁻ at 300K using the PBE functional. The left/right arrows and circles indicate left/right localization or delocalization of spin density respectively for particular snapshots, c) Relative energies for each studied electronic configuration (left-localized, delocalized and right-localized). The calculated energies of the optical IVT for each case are also provided. The structures of each configuration with the corresponding highlighted spin densities are provided below the x axis.

Conclusions

The use of a multi-technique approach, based on variable-temperature EPR, UV-Vis-NIR, and resonant Raman spectroscopies and on theoretical calculations, allowed us to thoroughly investigate the charge transfer mechanisms in the ground state of a series of six radical-anions [**PTM-nTV-PTM**]•⁻ (n=2-7) of distinct lengths. For the shortest 2TV-bridged molecule we propose that charge transfer occurs through a flickering resonance type mechanism. On the contrary for molecules with bridges with 4 or more TV units we propose that the exchange of the negative spin/charge occurs through a thermally activated incoherent biased bidirectional symmetrical charge hopping mechanism of positive charge. In this latter mechanism the polaron formation inside the bridge and the hopping of holes among the bridging TV units participate in the spin/charge exchange from one negatively charged

(reduced) PTM site to the other PTM radical (neutral) site. The reported results show that a bridge with an electronically rich donor nature, that are typically considered as an efficient hole transmitter, can also be used to promote charge transfer/transport between neutral negatively charged terminal groups of molecular wires in their ground states.

ASSOCIATED CONTENT

(Word Style "TE_Supporting_Informati**on**"). **Supporting Information**. A brief statement in nonsentence format listing the contents of material supplied as Supporting Information should be included, ending with "This material is available free of charge via the Internet at http://pubs.acs.org." For instructions on what should be included in the Supporting Information as well as how to prepare this material for publication, refer to the journal's Instructions for Authors.

AUTHOR INFORMATION

Corresponding Author

* (Word Style "FA_Corresponding_Author_Footnote"). Give contact information for the author(s) to whom correspondence should be addressed.

Present Addresses

†If an author's address is different than the one given in the affiliation line, this information may be included here.

Author Contributions

The manuscript was written through contributions of all authors. / All authors have given approval to the final version of the manuscript. / ‡These authors contributed equally. (match statement to author names with a symbol)

Funding Sources

Any funds used to support the research of the manuscript should be placed here (per journal style).
Notes
Any additional relevant notes should be placed here.

ACKNOWLEDGMENT

(Word Style "TD_Acknowledgments"). Generally the last paragraph of the paper is the place to acknowledge people (dedications), places, and financing (you may state grant numbers and sponsors here). Follow the journal's guidelines on what to include in the Acknowledgement section.

ABBREVIATIONS

CCR2, CC chemokine receptor 2; CCL2, CC chemokine ligand 2; CCR5, CC chemokine receptor 5; TLC, thin layer chromatography.

REFERENCES

(1) Blumberger,J.. *Chem. Rev.*, **2015**, *115*, 11191–11238.
(2) A. Nitzan, M. A. Ratner, *Science*, **2003**, *300*, 1385.
(3) S. H. Choi, B. Kim, C. D. Frisbie, *Science*, **2008**, *320*, 1482.
(4) Q. Lu, K. Liu, H. Zhang, Z. Du, X. Wang, F. Wang, *ACS Nano*, **2009**, *3*, 3861.

(5) P. Moreno-García, M. Gulcur, D. Z. Manrique, T. Pope, W. Hong, V. Kaliginedi, C. Huang, A. S. Batsanov, M. R. Bryce, C. Lambert, T. Wandlowski, *J. Am. Chem. Soc.*, **2013**, *135*, 12228.

(6) V. Kaliginedi, P. Moreno-García,. H. Valkenier, W. Hong, V. M. García-Suárez, P. Buiter, J. L. H. Otten, J. C. Hummelen, C. J. Lambert, T. Wandlowski, *J. Am. Chem. Soc.*, **2012**, *134*, 5262.

(7) L. Luo, S.H. Choi, C. D. Frisbie, *Chem. Mater.*, **2011**, *23*, 631.

(8) S. H. Choi, C. Risko, M. C. Ruiz-Delgado, B. Kim, J. L. Brédas, C. D. Frisbie, *J. Am. Chem. Soc.*, **2010**, *132*, 4358 (2010)

(9) T. Hines, I. Diez-Perez, J. Hihath, H. Liu, Z. S. Wang, J. Zhao, G. Zhou, K. Müllen, N. Tao, *J. Am. Chem. Soc.*, **2010**, *132*, 11658 (2010).

(10) J. Sukegawa, C. Schubert, X. Zhu1, H. Tsuji, D. M. Guldi, E. Nakamura1 *Nat. Chem.*, **2014**, *6*, 899.

(11) A. B. Ricks, K. E. Brown, M. Wenninger, S. D. Karlen, Y. A. Berlin, D. T. Co, M. R. Wasielewski, *J. Am. Chem. Soc.*, **2012**, *134*, 4581.

(12) M. Gilbert, B. Albinsson, *Chem. Soc. Rev.,* **2015**, *44*, 845.

(13) A. Heckmann, C. Lambert, *Angew. Chem. Int. Ed.*, **2012**, *51*, 326.

(14) J. Sedó, D. Ruiz, J Vidal-Gancedo, C. Rovira, J Bonvoisin, J.P. Launay, J. Veciana. *Adv. Mater*, **1996**, *748*.

(15) O. Elsner, D. Ruiz-Molina, J. Vidal-Gancedo, C. Rovira, J. Veciana, *Nano Letters,* **2001**, *1,* 117.

(16) V. Lloveras, J. Vidal-Gancedo, T. M. Figueira-Duarte, J.-F. Nierengarten, J. J. Novoa, F. Mota, N. Ventosa, C. Rovira, J. Veciana, *J. Am. Chem. Soc.*, **2011**, *133*, 5818.

(17) I. Jestin, P. Frère, P. Blanchard, J. Roncali, *Angew. Chem., Int. Ed.,* **1998***, 37,* 942.

(18) F. Oswald, D.-M. Islam, M. E. El-Khouly, Y. Araki, R. Caballero, P. de la Cruz, O. Ito, F. Langa, *Phys.Chem.Chem.Phys*, **2014**, *16*, 2443.

(19) S. Rodríguez-González, M. C. Ruiz-Delgado, R. Caballero, P. de la Cruz, F. Langa, J. T. López-Navarrete, J. Casado, *J. Am. Chem. Soc.,* **2012**, *134,* 5675.

(20 C. Rovira, D. Ruiz-Molina, O. Elsner, J. Vidal-Gancedo, J. Bonvoisin, J-P. Launay, J. Veciana, *Chem. Eur. J.*, **2001**, *7, 240.*

(21) J. Heinzer, *Mol. Phys.*, **1971**, *22*, 167; *Quantum Chemistry Program Exchange* 1972, Nº 209. We thank Prof. A. Lund for a copy of this program.

(22) A. Butler Ricks, K. E. Brown, M. Wenninger, S. D. Karlen, Y. A. Berlin, D. T. Co, M. R. Wasielewski, J. Am. Chem Soc., **2012**, *134*, 4581.

(23) Y.A. Berlin, M. A. Ratner, *Rad. Phys. Chem.*, **2005**, *74*, 124.

(24) E. G. Petrov, Ye. V. Shevchenko, V. May, *Chem. Phys.*, **2003**, *288*, 269.

(25) A. Weller, *Z. Phys. Chem.*, **1982**, *133*, 93.

(26) A. Kubas, F. Hoffmann, A. Heck, H. Oberhofer, M. Elstner, J. Blumberger, *Phys. Chem. Chem. Phys.*, **2015**, *17*, 14342.

(27) M. Renz, K. Theilacker, C. Lambert, M. Kaupp, *J. Am. Chem. Soc*, **2009**, *131*, 16292.

(28) J. P. Perdew, K. Burke, and M. Ernzerhof, *Phys. Rev. Lett.*, **1996**, *77*, 3865.

(29) Frisch, M. J.; Trucks, G. W.; Schlegel, H. B.; Scuseria, G. E.; Robb, M. A.; Cheeseman, J. R.; Scalmani, G.; Barone, V.; Mennucci, B.; Petersson, G. A.; Nakatsuji, H.; Caricato, M.; Li, X.; Hratchian, H. P.; Izmaylov, A. F.; Bloino, J.; Zheng, G.; Sonnenberg, J. L.; Hada, M.; Ehara, M.; Toyota, K.; Fukuda, R.; Hasegawa, J.; Ishida, M.; Nakajima, T.; Honda, Y.; Kitao, O.; Nakai, H.; Vreven, T.; Montgomery, J. A., Jr.; Peralta, P. E.; Ogliaro, F.; Bearpark, M.; Heyd, J. J.; Brothers, E.; Kudin, K. N.; Staroverov, V. N.; Kobayashi, R.; Normand, J.; Raghavachari, K.; Rendell, A.; Burant, J. C.; Iyengar, S. S.; Tomasi, J.; Cossi, M.; Rega, N.; Millam, N. J.; Klene, M.; Knox, J. E.; Cross, J. B.; Bakken, V.; Adamo, C.; Jaramillo, J.; Gomperts, R.; Stratmann, R. E.; Yazyev, O.; Austin, A. J.; Cammi, R.; Pomelli, C.; Ochterski, J. W.; Martin, R. L.; Morokuma, K.; Zakrzewski, V. G.; Voth, G. A.; Salvador, P.; Dan-

nenberg, J. J.; Dapprich, S.; Daniels, A. D.; Farkas, Ö.; Ortiz, J. V.; Cioslowski, J.; Fox, D. J. *Gaussian 09, revision A.08; Gaussian, Inc.: Wallingford, CT,* **2009**.

(30) V. Blum, R. Gehrke, F. Hanke, P. Havu, V. Havu, X. Ren, K. Reuter, and M. Scheffler, *Computer Phys. Commun.*, **2009**, **180**, 2175.

(31) I. Alcón and S. T. Bromley, *RSC Adv.*, **2015**, 5, 98593.

On the Operative Mechanism of Hole Assisted Negative Charge Motion in Ground States of Radical-anion Molecular Wires

Carlos Franco[1], Paula Mayorga Burrezo[2], Vega Lloveras[1], Rubén Caballero[3], Isaac Alcón[4], Stefan Bromley[4], Marta Mas-Torrent[1], Fernando Langa[3], Juan T. López Navarrete[2], Concepciò Rovira*[,1], Juan Casado*[,2], Jaume Veciana*[,1]

[1]Department of Molecular Nanoscience and Organic Materials, Institut de Ciència de Materials de Barcelona (CSIC), Campus Universitari de Bellaterra, E-08193, Cerdanyola, Barcelona, Spain.

[2]Department of Physical Chemistry, University of Malaga, Campus de Teatinos s/n, 29071 Malaga, Spain.

[3]Instituto de Nanociencia, Nanotecnología y Materiales Moleculares (INAMOL), University of Castilla-La Mancha, Campus de la Fábrica de Armas, 45072 Toledo, Spain.

[4]Department of Physical Chemistry, Faculty of Chemistry, University of Barcelona, Av. Diagonal, 647, 08028-Barcelona, Spain.

E-mails: cun@icmab.es (CR); casado@uma.es (JC), vecianaj@icmab.es (JV).

Supporting Information

Contents

General Remarks.

All the chemicals and solvents were purchased form Sigma-Aldrich or Acros Organics and were used as received. Anhydrous solvents, where indicated were dried using standard techniques. Chromatographic purifications were performed using silica gel 60 SDS (particle size 0.040-0.063 mm). Analytical thin-layer chromatography was performed using Merck TLC silica gel 60 F254. ^{1}H NMR spectra were recorded as CDCl$_3$ solutions on a Brüker-Topspin AV 400 instrument. Chemical shifts are given as δ values. Residual solvent peaks being used as the internal standard (CHCl3; δ = 7.27 ppm). ^{13}C NMR chemical shifts are reported relative to the solvent residual peak (CDCl3, 77.00 ppm). FT Infrared spectra were recorded on a AVATAR 370 FTIR Thermo Nicolet and on a Spectrum One FT-IR Spectroscopy instruments using an ATR accessory. Mass spectra (MALDI-TOF) were recorded on a VOYAGER DETM STR mass spectrometer using dithranol as matrix and in a Bruker Ultraflex LDI-TOF. Spectrometer. Steady State UV-Vis measurements were carried out on a Shimadzu UV 3600 and a Cary 5000E Varian spectrophotometers. For extinction coefficient determination, solutions of different concentration were prepared in CH$_2$Cl$_2$, HPLC grade, with absorption between 0.1-1 of absorbance using a 1 cm UV cuvette. ESR spectra were performed with a Bruker ESP 300 E equipped with a rectangular cavity T102 that works with an X-band (9.5 GHz). The solutions were degassed by argon

bubbling before the measurements. Cyclic voltammetry measurements were obtained with a potentiostat Autolab/PGSTAT204 Metrohm in a standard 3 electrodes cell.

The synthesis of oligothyenilenevinylenes bisaldehydes with 2, 4, and 6 thiophene units, dithyenilenevinylene monoaldehyde and that of the phosphonate PTM derivative was performed according to procedures previously described.[1, 2]

Synthesis of nTV Bridges
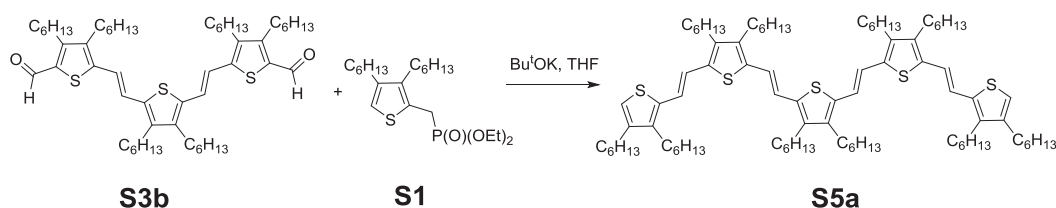
Scheme S1

Synthesis of S5a. Under argon atmosphere potassium *tert*-butoxide (130 mg, 1.16 mmol) is added in small portions over a stirred solution of **S3** (200 mg, 0.23 mmol) and diethyl-(3,4-dihexiltienyl)-methylphosponate (**S1**)1[b] (280 mg, 0.7 mmol) in dry tetrahydrofuran (20 mL). The mixture is stirred at room temperature for 16 hours. Then water and dichloromethane are added. The aqueous phase is extracted with dichloromethane and the organic phases are dried ($MgSO_4$) and evaporated. The crude obtained is purified by column chromatography (SiO_2, Hexane) affording **S5a** as a dark purple solid (263 mg, 83 %). ^{1}H-NMR (400 MHz, $CDCl_3$) δ/ppm: 6.99 (m, 8H), 6.77 (s, 2H), 2.60 (m, 16H), 2.49 (t, 4H, ^3J = 7.5 Hz), 1.75-1.20 (m, 80H), 0.92 (m, 30H).^{13}C-NMR (100 MHz, $CDCl_3$) δ/ppm: 143.4, 141.6, 141.5, 141.4, 141.3, 140, 137.1, 135.2, 135, 134.9,119.8, 119.4, 119.3, 119.2, 117.9, 31.7, 31.6, 31.5, 31.2, 31.1, 30.9, 29.7, 29.6, 29.4, 29.3, 29.2, 29.0, 27.0 26.9, 22.6, 14.2, 14.1´14.11, 14.0. FT-IR (KBr) υ / cm^{-1}: 2923, 2951, 2844, 2363, 2322, 11470, 1264, 919, 716,701. UV-Vis (CH_2Cl_2), λ_{max}/nm (log ε): 524 (4.63). EM (m/z) (MALDI-TOF): calculated for $C_{88}H_{140}S_5$: 1350.96 ; found: 1351.44 (M+H).

---

[1] a) I. Jestin, P. Frere, N. Mercier, E. Levillain, D. Stievenard, J. Roncali, *J. Am. Chem. Soc.* **1998**, *120*, 8150–8158. b) J. Roncali, *Acc. Chem. Res.* **2000**, *33*, 147–56. c) E. M. Barea, R. Caballero, F. Fabregat-Santiago, P. De la Cruz, F. Langa, J. Bisquert, *Chemphyschem* **2010**, *11*, 245–50. d) S. Rodríguez González, M. C. Ruiz Delgado, R. Caballero, P. De la Cruz, F. Langa, J. T. López Navarrete, J. Casado, *J. Am. Chem. Soc*. **2012**, *134*, 5675–81.
[2] C. Rovira, D. Ruiz-Molina, O. Elsner, J. Vidal-Gancedo, J. Bonvoisin, J-P. Launay, J. Veciana, *Chem. Eur. J.* **2001**, *7,* 240
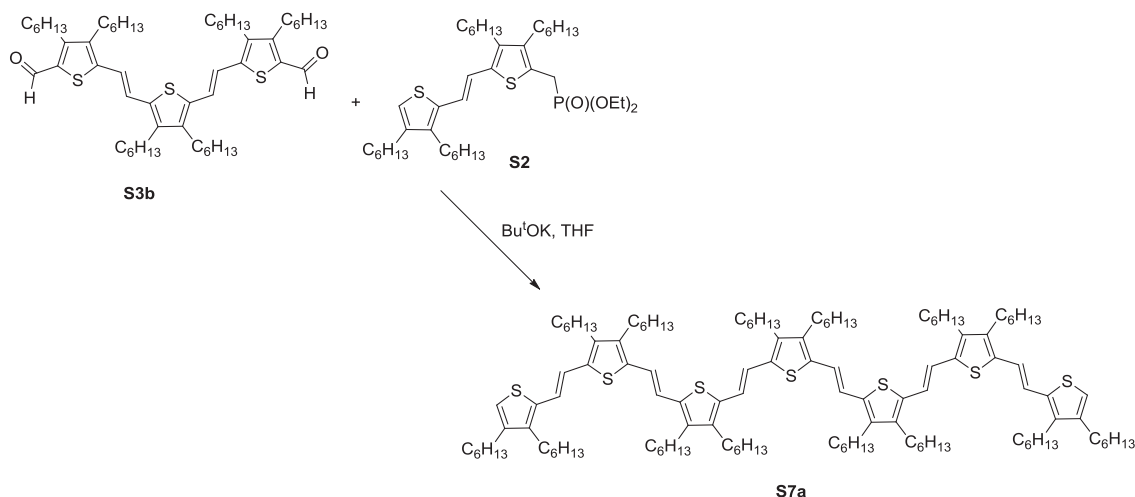
Scheme S2

Synthesis of S7a. Under argon atmosphere potassium *tert*-butoxide (121 mg, 1.04 mmol) is added in small portions over a stirred solution of **S3** (200 mg, 0.23 mmol) and phosphonate **S2**1[a] (470 mg, 0.70 mmol) in dry tetrahydrofuran (20 mL). The mixture is stirred at room temperature for 16 hours. Then water and dichloromethane are added. The aqueous phase is extracted with more dichloromethane and the organic phases are dried (MgSO$_4$) and evaporated. The crude obtained is purified by column chromatography (SiO$_2$, Hexanes) to obtain **S7a** as a dark blue solid (387 mg, 87 %). ^{1}H-NMR (400 MHz, CDCl$_3$) δ/ppm: 6.99 (m, 12H), 6.77 (s, 2H), 2.61 (m, 24H), 2.50 (t, 4H, ^3J = 7.6 Hz), 1.70-1.16 (m, 112H), 0.92 (m, 42H). ^{13}C-NMR (100 MHz, CDCl$_3$) δ/ppm: 143.3, 141.7, 141.5, 140.0, 137.1, 135.2, 135.0, 119.9, 117.9, 31.8, 31.7, 31.6, 31.5, 31.4, 31.2, 30.9, 27.7, 29.4, 29.3, 29.2, 29,0 27.0, 29.9, 22.6, 14.2, 14.1, 14.0. FT-IR (KBr) v/cm^{-1}: 2952, 2926, 2847, 2366, 2316, 1364, 1382, 1296, 1261, 922, 869, 723. UV-Vis (CH$_2$Cl$_2$), λ_{max}/nm (log ε): 562 (2.17). EM (m/z) (MALDI-TOF): calculated for C$_{124}$H$_{196}$S$_7$: 1909.34; found: 1911.63 (M+H).
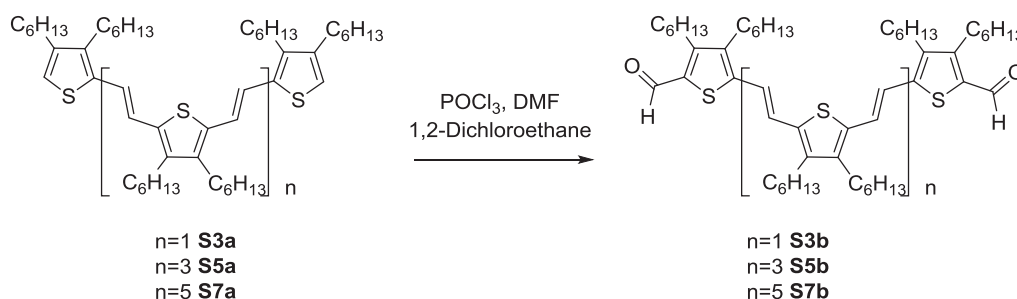
Scheme S3

General Procedure for Vilsmeier-Hack formylation. Under Argon atmosphere, phosporus oxychloride is added dropwise over a stirred solution of dimethylformamide

and the corresponding nTV oligomer in 1,2-dichloroethane at 0°C and the solution is refluxed overnight. The reaction mixture is poured in a concentrated solution of sodium acetate in water and stirred for 1 hour. The phases are separated, the aqueous phase is extracted with dichloromethane and the organic phases dried (MgSO$_4$) and evaporated. The crude obtained is purified by column chromatography (SiO$_2$, Hexanes:Dichlorometane 1:2).

Synthesis of S3b. According to the general procedure, from **S3a** (316 mg, 0.39 mmol), dimethylformamide (0.2 mL, 2.5 mmol), and phosporus oxychloride (0.2 mL, 1.52 mmol) in 1,2-dichloroethane (30 mL). **S3b** is obtained as a dark red solid (216 mg, 64%).^{1}H-NMR (400 MHz, CDCl$_3$) δ/ppm: 9.99 (s, 2H), 7.26 (d, 2H, ^3J=15.4 Hz), 6.98 (d, 2H, ^3J=15.4 Hz), 2.86 (t, 4H, ^3J=7.6 Hz), 2.62 (m 8H), 1.65-1.55 (m, 4H), 1.55-1.48 (m, 8H), 1.45-1.20 (m, 48H), 1.0-0.8 (m, 18H). ^{13}C-NMR (100 MHz, CDCl$_3$) δ/ppm: 182.4, 153.5, 147.4, 144.6, 142.4, 136.2, 135.5, 124.1, 119.6, 32.9, 32.2, 32.1, 32.1, 31.7, 30.3, 30.0, 29.9, 29.8, 27.7, 27.0, 23.2, 14.7, 14.6. FT-IR (KBr) v/cm^{-1}: 2923, 2853, 2361, 1643, 1591, 1510, 1463, 1404, 1281, 1246, 1211, 1120, 1038, 933, 714, 669. UV-Vis (CH$_2$Cl$_2$), λ_{max}/nm (log ε): 254 (4.51), 283 (4.34), 483 (4.65). EM (m/z) (MALDI-TOF): calculated for C$_{54}$H$_{84}$O$_2$S$_3$: 860.57; found: 861.39 (M+H).

Synthesis of S5b. According to the general procedure from **S5a** (260 mg, 0.19 mmol), dimethylformamide (0.1 mL, 1.30 mmol), and phosporus oxychloride (0.1 mL, 1.1 mmol) in 1,2-dichloroethane (30 mL). **S5b** is obtained as a dark purple solid (220 mg, 80%).^{1}H-NMR (400 MHz, CDCl$_3$) δ/ppm: 9.98 (s, 2H), 7.27 (d, 2H, ^3J =15.6 Hz), 7.05 (d, 2H, ^3J =15.4 Hz), 6.98 (d, 2H, J =15.4 Hz), 6.95 (d, 2H, ^3J =15.6 Hz), 2.86 (t, 4H, ^3J=7.7Hz) 2.61 (m, 16H), 1.65-1.2 (m, 90H), 0.93 (m, 30H). ^{13}C-NMR (100 MHz, CDCl$_3$) δ/ppm: 181.8, 153.4, 147.3, 144.1, 142.1, 141.8, 141.4, 137.0, 135.4, 134.6, 134.0, 123.7, 120.2, 119.3, 118.0, 32.3, 316, 31.5, 31.4, 31.2, 31.1, 31.0, 29.4, 29.3, 29.2, 29.1, 27.2, 27.1, 27.0, 26.9, 26.3, 22.7, 22.6, 22.5, 22.4, 14.2, 14.1, 14.0. FT-IR (KBr) v/cm^{-1}: 2952, 2930, 2853, 1644, 1594, 1461, 1397, 1378, 1286.54, 1255, 1204, 919, 707, 666. UV-Vis (CH$_2$Cl$_2$), λ_{max}/nm (log ε): 557 (5.05). EM (m/z) (MALDI-TOF): calculated for C$_{190}$H$_{140}$O$_2$S$_5$:1412.95; found: 1412.48 (M+).

Synthesis of S7b. According to the general procedure, from **S7a** (260 mg, 0.14 mmol), dimethylformamide (0.06 mL, 0.82 mmol), and phosporus oxychloride (0.05 mL, 0.54 mmol) in 1,2-dichloroethane (20 mL). **S7b** is obtained as a dark blue solid (233 mg, 76%).^{1}H-NMR (400 MHz, CDCl$_3$) δ/ppm: 9.99 (s, 2H), 7.28 (d, 2H, ^3J =14.9 Hz), 7.04 (d, 2H, ^3J =15.5 Hz), 7.0 (m, 4H), 6.98 (d, 2H, ^3J =14.9 Hz), 6.69 (d, 2H, ^3J =15.5 Hz), 2.86 (t, 4H, ^3J =7.5 Hz), 2.62 (m, 24H), 1.65-1.30 (m, 112H), 0.94 (m, 42H). ^{13}C-NMR

(100 MHz, CDCl$_3$) δ/ppm: 181.8, 153.0, 147.3, 144.1, 142.2, 141.8, 141.7, 141.4, 137.2, 135.74, 135.31, 135.0, 134.5, 134.0, 123.8, 120.4, 120.3, 119.6, 119.3, 119.1, 117.9, 32.3, 31.6, 31.5, 31.2, 31.1, 31.0, 30.1, 29.7, 29.4, 29.3, 29.2, 29.1, 27.2, 27.1, 27.0, 26.3, 22.6, 22.5, 14.2, 14.1, 14.0. FT-IR (KBr) v/cm^{-1}: 2961, 2923, 2860, 1651, 1594, 1581, 1454, 1394, 1378, 1290, 1245, 1207, 925, 703, 666. UV-Vis (CH$_2$Cl$_2$), λ_{max}/nm (log ε): 582 (5.15). EM (m/z) (MALDI-TOF): calculated for C$_{126}$H$_{196}$O$_2$S$_7$: 1965.33; found: 1966.00 (M+H).

General procedure for the synthesis of (αH,α'H)-PTM-nTV-PTM and (αH)-2TV-PTM. Witting-Horner olefination.

Under Argon, potassium *tert*-butoxide is added in small portions over a stirred solution of **PTM-P(O)(OEt)$_2$** in dry tetrahydrofuran at -78°C and the mixture is stirred at this temperature for 0.5 hours, then a solution of the corresponding oligomer aldehyde in dry THF is added and the mixture is allowed to warm to room temperature in the dark. The resulting mixture is stirred at room temperature for the indicated time. After solvent evaporation the crude is purified by column chromatography.
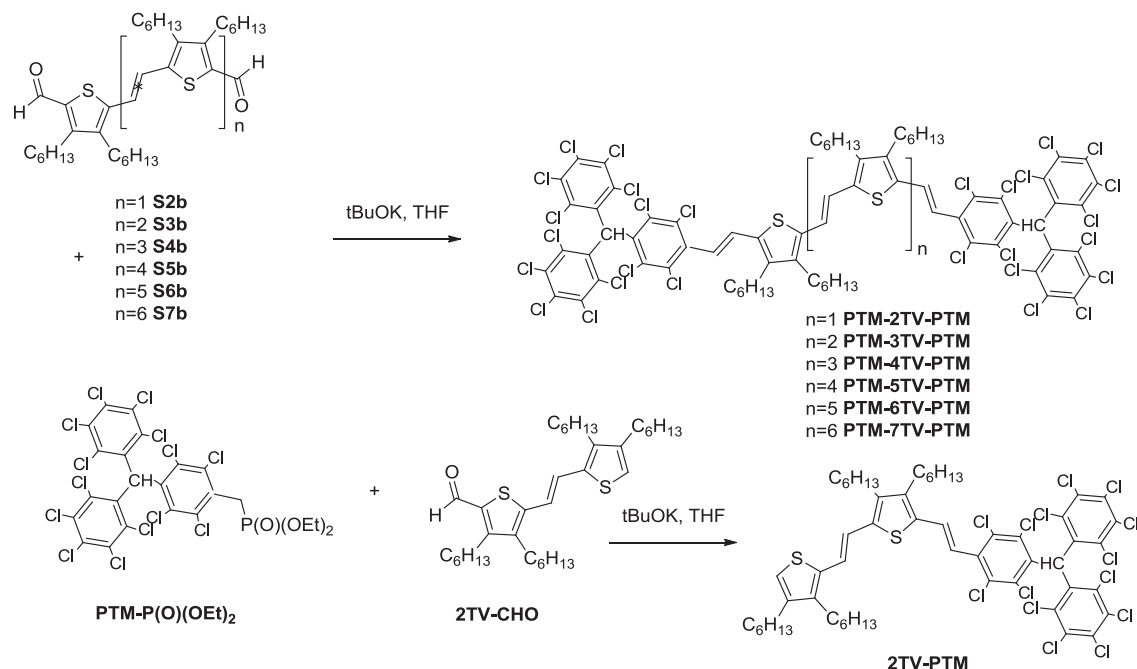
Scheme S5

Synthesis of (αH)-2TV-PTM. According to the general procedure, from **2TV-CHO**[1] (100 mg, 0.180 mmol), PTM-P(O)(OEt)$_2$ (236 mg, 0.269 mmol), potassium *tert*-butoxide

(40.3 mg, 0.359 mmol) and 15 mL of THF. The reaction mixture is stirred for 96 hours, and the crude obtained is purified by column chromatography (SiO$_2$, Hexane:Dichloromethane 9:1) to obtain **(αH)-2TV-PTM** as orange solid. (141 mg, 62%). ^{1}H-NMR (400 MHz, CDCl$_3$) δ/ppm: 7.35 (d, 1H, ^{3}J=16.1 Hz), 7.06 (d, 1H, ^{3}J=15.5 Hz), 7.03 (s, 1H), 6.98 (d, 1H, ^{3}J=15.5 Hz), 6.83 (d, 1H, ^{3}J=16.1 Hz), 2.71-2.47 (m, 8H), 1.61-0.62 (m, 44H).^{13}C-NMR (100 MHz, CDCl$_3$) δ/ppm: 144.28, 143.50, 141.17, 140.64, 137.48, 137.27, 136.73, 136.64, 136.62, 135.36, 135.15, 135.02, 134.85, 133.98, 133.93, 133.57, 133.55, 133.51, 133.45, 133.11, 132.74, 132.45, 132.41, 132.00, 30.48, 121.15, 120.66, 118.82, 118.38, 56.64, 31.74, 31.69, 31.62, 31.59, 31.21, 31.00, 29.70, 29.68, 29.46, 29.37, 29.30, 29.27, 29.04, 27.25, 27.02, 26.95, 22.63, 14.17, 14.10, 1.03. FT-IR v/cm^{-1}: 2924.6, 2854.4, 1611.4, 1535.2, 1460.3, 1365.3 1337.9, 1297.0, 1239.8, 1136.9, 1117.5, 929.9, 852.4, 828.1, 807.7, 715.3, 690.1, 647.7, 614.8. UV-Vis (CH$_2$Cl$_2$), λ_{max}/nm (log ε): 429 (4.51). EM (m/z) (MALDI-TOF): calculated for C$_{55}$H$_{58}$Cl$_{14}$S$_2$: 1277.9; found: 1278.2 (M+).

Synthesis of (αH,α'H)-PTM-2TV-PTM. According to the general procedure, from **S2b** (60 mg, 0.102 mmol), PTM-P(O)(OEt)$_2$ (224 mg, 0.256 mmol), potassium *tert*-butoxide (35 mg, 0.308 mmol) and 10 mL of THF. The reaction mixture is stirred for 22 hours, and the crude obtained is purified by column chromatography (SiO$_2$, Hexane:Dichloromethane 9:1) to obtain **(αH,α'H)-PTM-2TV-PTM** as orange solid. (75 mg, 36%). ^{1}H-NMR (400 MHz, CDCl$_3$) δ/ppm: 7.34 (d, 2H, ^{3}J=16.1 Hz), 7.03 (s, 2H), 7.01 (s, 2H), 6.83 (d, 2H, ^{3}J=16.1 Hz), 2.71-2.47 (m, 8H), 1.61-0.62 (m, 44H).^{13}C-NMR (100 MHz, CDCl$_3$) δ/ppm: 144.9, 143.6, 137.7, 137.2 137.1 135.6, 134.5, 134.1, 134.0, 133.9, 121.6, 120.8, 57.2, 32.6, 32.2, 32.1, 31.8, 30.2, 30.0, 29.8, 27.8, 27.6, 23.2, 14.7, 14.6, 1.56, 1.21. FT-IR v/cm^{-1}: 2920.8, 2850.0, 1602.7, 1533.6, 1462.0, 1361.8, 1338.4, 1296.2, 1263.1, 1239.1, 1136.6, 1115.7, 1021.8, 948.4, 921.6, 859.3, 807.9, 714.6, 679.0, 647.9. UV-Vis (CH$_2$Cl$_2$), λ_{max}/nm (log ε): 474 (4.66). EM (m/z) (MALDI-TOF): calculated for C$_{76}$H$_{60}$Cl$_{28}$S$_2$: 2030.10; found: 2030.32 (M+).

Synthesis of (αH,α'H)-PTM-3TV-PTM. According to the general procedure, from **S3b** (59 mg, 0.07 mol), PTM-P(O)(OEt)$_2$ (150 mg, 0.17 mmol), potassium *tert*-butoxide (25 mg, 0.2 mmol) and 25 mL of THF. The reaction mixture is stirred for 22 hours, and the crude obtained is purified by column chromatography (SiO$_2$, Hexane:Dichloromethane 9:1) to obtain **(αH,α'H)-PTM-3TV-PTM** as a dark solid. (103 mg, 64%). ^{1}H-NMR (400 MHz, CDCl$_3$) δ/ppm: 7.37 (d, 2H, ^{3}J=16.2 Hz), 7.07 (d, 2H, ^{3}J=15.5 Hz), 7.02 (s, 2H), 7.07 (d, 2H, ^{3}J=15.5 Hz), 6.85 (d, 2H, ^{3}J=16.2 Hz), 2.61 (m, 12H), 1.64-1.20 (m, 48H), 0.93 (m, 18H).^{13}C-NMR (100 MHz, CDCl$_3$) δ/ppm: 144.4, 142.3, 141.5, 137.2, 136.6, 136.5, 135.3, 135.1, 134.9, 134.8, 133.9, 133.9, 133.6, 133.5, 133.5, 133.1, 132.4,

132.4, 131.9, 130.4, 120.8,, 120.6, 119.2, 56.6, 31.7, 31.7, 31.6, 31.5, 31.2, 31.2, 29.5, 29.3, 29.3, 27.2, 27.0, 22.6, 14.1, 14.1, 11.4. FT-IR (KBr) v/cm^{-1}: 2927, 2854, 2366, 2322, 2290, 1603, 1533, 1454, 1359, 1337, 1296, 1249, 1128, 1021, 922, 808, 707, 647. UV-Vis (CH$_2$Cl$_2$), λ_{max}/nm (log ε): 392 (4.26), 514 (4.81). EM (m/z) (MALDI-TOF): calculated for C$_{94}$H$_{88}$Cl$_{28}$S$_3$: 2304.72; found: 2305.83 (MH+).

Synthesis of (αH,α'H)-PTM-4TV-PTM. According to the general procedure, from **S4b** (80 mg, 0.07 mol), PTM-P(O)(OEt)$_2$ (150 mg, 0.17 mmol), potassium *tert*-butoxide (25 mg, 0.2 mmol) and 20 mL of THF. The reaction mixture is stirred for 24 hours, and the crude obtained is purified by column chromatography (SiO$_2$, Hexane:Dichloromethane 9:1) to obtain **(αH,α'H)-PTM-4TV-PTM** as a dark solid. (128 mg, 71%). ^{1}H-NMR (400 MHz, CDCl$_3$) δ/ppm: 7.37 (d, 2H, ^{3}J=16.1 Hz), 7.07 (d, 2H, ^{3}J=15.4 Hz), 7.03 (s, 2H), 7.01 (s, 2H), 6.99 (d, 2H, ^{3}J=14.7 Hz), 2.61 (m, 16H), 1.54-1.26 (m, 64H), 0.94 (m, 24H).^{13}C-NMR (100 MHz, CDCl$_3$) δ/ppm: 144.33, 142.28, 141.76, 141.34, 137.63, 137.17, 136.56, 136.54, 135.62, 135.30, 135.08, 134.96, 134.92, 134.80, 133.90, 133.87, 133.51, 133.49, 133.44, 133.39, 133.04, 132.96, 132.39, 132.35, 131.92, 130.36, 120.68, 120.59, 119.53, 118.99, 56.57, 31.70, 31.64, 31.54, 31.53, 31.52, 31.22, 31.15, 31.12, 29.65, 29.61, 29.42, 29.38, 29.27, 29.26, 27.19, 26.98, 26.94, 22.57, 14.13, 14.08, 14.05. FT-IR v/cm^{-1}: 2923.9, 2854.5, 1736.9, 1606.4, 1633.8, 1460.9, 1361.7, 1338.4, 1294.9, 1136.6, 1117.2, 1019.7, 950.9, 920.7, 859.1, 807.9, 764.4, 713.9, 686.1, 648.5. UV-Vis (CH$_2$Cl$_2$), λ_{max}/nm (log ε): 379 (4.29), 542 (4.96). EM (m/z) (MALDI-TOF): calculated for C$_{112}$H$_{116}$Cl$_{28}$S$_4$: 2583.06; found: : 2583.6 (M+).

Synthesis of (αH,α'H)-PTM-5TV-PTM. According to the general procedure, from **S5b** (100 mg, 0.07 mol), PTM-P(O)(OEt)$_2$ (153 mg, 0.18 mmol), potassium *tert*-butoxide (24 mg, 0.21 mmol) and 30 mL of THF. The reaction mixture is stirred for 48 hours, and the crude obtained is purified by column chromatography (SiO$_2$, Hexane:Dichloromethane 9:1) to obtain **(αH,α'H)-PTM-5TV-PTM** as a dark solid. (150 mg, 75%). ^{1}H-NMR (400 MHz, CDCl$_3$) δ/ppm: 7.37 (d, 2H, ^{3}J=16.0 Hz), 7.03 (s, 2H), 7.00 (m, 8H), 6.85 (d, 2H, ^{3}J=16.0 Hz), 2.62 (m, 20H), 1.77-1.22 (m, 80H), 0.94 (m, 30H). ^{13}C-NMR (100 MHz, CDCl$_3$) δ/ppm: 144.4, 142.3, 141.8, 141.4, 137.7, 137.3, 136.6, 135.7, 135.3, 135.1, 134.9, 133.9, 133.5, 133.1, 132.4, 31.97, 130.4, 120.7, 119.6, 119.4, 118.9, 56.6, 31.6, 31.2, 29.7, 29.5, 29.3, 27.0, 22.6, 14.2, 14.1. FT-IR (KBr) v/cm^{-1}: 2920, 2850, 1603, 1454, 1382, 1334, 1293, 1249, 926, 802, 710, 653. UV-Vis (CH$_2$Cl$_2$), λ_{max}/nm (log ε): 400 (4.82), 559 (5.32). EM (m/z) (MALDI-TOF): calculated for C$_{130}$H$_{144}$Cl$_{28}$S$_5$: 2859.10; found: 2860.88 (MH+).

Synthesis of (αH,α'H)-PTM-6TV-PTM. According to the general procedure, from **S6b** (100 mg, 0.06 mol), PTM-P(O)(OEt)$_2$ (129 mg, 0.15 mmol), potassium *tert*-butoxide (22 mg, 0.18 mmol) and 15 mL of THF. The reaction mixture is stirred for 20 hours, and the crude obtained is purified by column chromatography (SiO$_2$, Hexanes:Dichloromethane 9:1) to obtain **(αH,α'H)-PTM-6TV-PTM** as a dark solid. (95 mg, 50%). ^{1}H-NMR (400 MHz, CDCl$_3$) δ/ppm: 7.38 (d, 2H, [3]J=16.0 Hz), 7.04 (s, 2H), 7.01 (m, 10H), 6.85 (d, 2H, [3]J=16.0 Hz), 2.62 (m, 24H), 1.64-1.20 (m, 96H), 0.94 (m, 36H). ^{13}C-NMR (100 MHz, CDCl$_3$) δ/ppm: 144.4, 142.3, 141.7, 141.4, 137.7, 137.2, 136.6, 136.5, 135.7, 135.3, 135.1, 135.0, 134.8, 133.9, 133.9, 133.6, 133.5, 133.5, 133.4, 133.1, 132.9, 132.4, 132.3, 131.9, 130.4, 120.7, 119.4, 118.9, 56.6, 31.7, 31.7, 31.6, 31.2, 29.5, 29.3, 27.2, 27.0, 22.6, 22.4, 14.2, 14.1. FT-IR (KBr) v/cm^{-1}: 2949, 2930, 2914, 2857, 2357, 1606, 1461, 1340, 1296, 1258, 1093, 1024, 919, 808, 688. UV-Vis (CH$_2$Cl$_2$), λ_{max}/nm (log ε): 436 (5.03), 572(5.50). EM (m/z) (MALDI-TOF): calculated for C$_{148}$H$_{172}$Cl$_{28}$S$_6$: 3135.96; found: 3138.10 (MH+).

Synthesis of (αH,α'H)-PTM-7TV-PTM. According to the general procedure, from **S7b** (102 mg, 0.05 mol), PTM-P(O)(OEt)$_2$ (113 mg, 0.13 mmol), potassium *tert*-butoxide (18 mg, 0.16 mmol) and 20 mL of THF. The reaction mixture is stirred for 72 hours, and the crude obtained is purified by column chromatography (SiO$_2$, Hexane:Dichloromethane 8:1) to obtain **(αH,α'H)-PTM-7TV-PTM** as a dark solid. (122 mg, 71%). ^{1}H-NMR (400 MHz, CDCl$_3$) δ/ppm: 7.37 (d, 2H, [3]J=15.8 Hz), 7.02 (s, 2H), 7.00 (m, 12H), 6.85 (d, 2H, [3]J=15.8 Hz), 2.62 (m, 28H), 1.70-1.15 (m, 112H), 0.94 (m, 42H). ^{13}C-NMR (100 MHz, CDCl$_3$) δ/ppm: 144.4, 142.4, 141.8, 141.4, 140.9, 137.7, 137.2, 136.6, 135.8, 135.4, 135.4, 135.1, 135.0, 134.8, 133.9, 133.9, 133.6, 133.5, 133.1, 132.9, 132.5, 132.4, 131.9, 130.4, 126.9, 124.4, 120.7, 119.7, 119.5, 56.6, 34.9, 31.9, 31.7, 31.6, 31.5, 31.4, 31.2, 30.3, 30.1, 29.7, 29.5, 29.3, 27.2, 27.1, 22.6, 14.2, 14.1. FT-IR (KBr) v/cm^{-1}: 3015, 2920, 2857, 1613, 1527, 1458, 1369, 1334, 1296, 1252, 922, 808, 713, 650, 615. UV-Vis (CH$_2$Cl$_2$), λ_{max}/nm (log ε): 368 (4.79), 455 (5.05), 582 (5.57). EM (m/z) (MALDI-TOF): calculated for C$_{166}$H$_{200}$C$_{l28}$S$_7$: 3409.48; found: 3413.54.

General procedure for the synthesis of biradicals •PTM-nTV-PTM• (1-6) and radical •PTM-2TV.

To a solution of **(αH,α'H)-PTM-nTv-PTM** (0,03mmol) in THF (10ml), an excess (0.1 ml, 0.22 mmol) of tetrabutylammonium hydroxide (40% in water) was added. The resulting violet mixture was stirred for 15min and then AgNO$_3$ (56 mg, 0.33 mmol)) was added and the mixture stirred for 2 min. The solution changed the color to dark brown while

the silver (Ag^0) precipitated. Then, the solution was filtered to eliminate the silver and evaporated under reduced pressure. The obtained product was filtered through silica gel with CH_2Cl_2 to yield a dark brown powder in almost quantitative yield (96-98%).

All obtained radicals are stable in the solid state at ambient conditions. PTM radicals have their open-shell centers sterically shielded by six bulky chlorine atoms which ensure their persistency and thermal and chemical stabilities.[3]

Characterizations

·PTM-2TV

IR ν(cm^{-1}): 2923, 2853, 1735, 1662, 1501, 1589, 1458, 1394, 1334, 1248, 1117, 964, 929, 816, 734, 709, 652, UV-Vis (CH_2Cl_2), λ(nm) log(ε)(L·mol^{-1}·cm^{-1})·10^{-3}: 391(4.51), 436 (4.48), 580 (3,83), 633(3.83, 802 (3.31). EM (m/z) (MALDI-TOF): calculated for $C_{55}H_{57}Cl_{14}S_2$: 1276.96; found: 1277.2 (M+). EPR,(Table S1) CV (Table S2)

·PTM-2TV-PTM·

IR ν(cm^{-1}): 2923, 2853, 1735, 1591, 1503, 1452, 1402, 1333, 1247, 1117, 940, 816, 768, 734, 708, 651. UV-Vis (CH_2Cl_2), λ(nm) log(ε)(L·mol^{-1}·cm^{-1})·10^{-3}: 389(4.64), 478(4.61), 613(3.84), 683(3.85), 870(3.76), 1058(3.33). EM (m/z) (MALDI-TOF): calculated for $C_{76}H_{58}Cl_{28}S_2$: 2027.51; found: 2026.36 (M+). EPR,(Table S1) CV (Table S2)

·PTM-3TV-PTM·

IR ν(cm^{-1}): 2922, 2854, 1586, 1493, 1461, 1397, 1333, 1245, 1117, 924, 815, 734, 708, 651. UV-Vis (CH_2Cl_2), λ(nm) log(ε)(L·mol^{-1}·cm^{-1})·10^{-3}: 390(4.66), 515(4.79), 683(4.15), 795(4.10), 1050(3.67), 1268(3.11). EM (m/z) (MALDI-TOF): calculated for $C_{94}H_{86}Cl_{28}S_3$: 2304.70; found: 2304.2 (M+). EPR,(Table S1) CV (Table S2)

·PTM-4TV-PTM·

IR ν(cm^{-1}): 2919, 2851, 1737, 1657, 1582, 1502, 1460, 1394, 1334, 1247, 1117, 1091, 942, 922, 816, 766, 734, 709, 651. UV-Vis (CH_2Cl_2), λ(nm) log(ε)(L·mol^{-1}·cm^{-1})·10^{-3}: 389(4.71), 537 (4.76). EM (m/z) (MALDI-TOF): calculated for $C_{112}H_{114}Cl_{28}S_4$: 2580.89; found: 2580,36 (M+). EPR,(Table S1) CV (Table S2)

·PTM-5TV-PTM·

IR ν(cm^{-1}): 2919, 2851, 1737, 1657, 1582, 1502, 1460, 1394, 1334, 1247, 1117, 1091, 942, 922, 816, 766, 734, 709, 651. UV-Vis (CH_2Cl_2), λ(nm) log(ε)(L·mol^{-1}·cm^{-1})·10^{-3}:

[3] (a) M. Ballester, *Adv. Phys. Org. Chem.* 1989. **25**, 267. (b) D. Maspoch, N. Domingo, D. Ruiz-Molina, K. Wurst, J. Tejada, C. Rovira, J. Veciana *J. Am. Chem. Soc.* 2004, **126**, 730.

390(4.69), 554 (4.94). EM (m/z) (MALDI-TOF): calculated for $C_{130}H_{142}Cl_{28}S_5$: 2857.02; found: 2856.54 (M+). EPR,(Table S1) CV (Table S2)

•PTM-6TV-PTM•

IRν(cm^{-1}): 2924, 2854, 1737, 1578, 1501, 1460, 1379, 1334, 1246, 1117, 922, 817, 734, 709, 652.. UV-Vis (CH$_2$Cl$_2$), λ(nm) log(ε)(L·mol^{-1}·cm^{-1})·10^{-3}: 390 (4.67) 569,(4.99). EM (m/z) (MALDI-TOF): calculated for $C_{148}H_{170}Cl_{28}S_6$: 3133.27; found: 3133.29 (M+). EPR,(Table S1) CV (Table S2)

•PTM-7TV-PTM•

IRν(cm^{-1}): 2920, 2852, 1735, 1595, 1462, 1379, 1336, 1251, 1117, 942, 921, 815, 712, 652. UV-Vis (CH$_2$Cl$_2$), λ(nm) log(ε)(L·mol^{-1}·cm^{-1})·10^{-3}: 390 (4.66), 580 (5.05). EM (m/z) (MALDI-TOF): calculated for $C_{166}H_{198}Cl_{28}S_7$: 3410.49; found: 3410.26 (M+). EPR,(Table S1) CV (Table S2).

Table S1: UV-Vis data for diradicals **1-6** and monoradical **•PTM-2TV** in CH$_2$Cl$_2$ solution

Compound	λ(nm);Logε (L·mol^{-1}·cm^{-1})				
•PTM-2TV	391;(4.51)	436;(4.48)	580;(3.83)	633;(3.83)	802; (3.31)
•PTM-2TV-PTM• (1)	389;(4.66)	478;(4.61)	613;(3.84)	683;(3.85)	1032[a]
•PTM-3TV-PTM• (2)	390;(4.66)	515;(4.79)	683;(4.15)	795;(4.10)	1091[a]
•PTM-4TV-PTM• (3)	389;(4.71)	537;(4.76)			1136[a]
•PTM-5TV-PTM• (4)	390;(4.69)	554;(4.94)			1168[a]
•PTM-6TV-PTM• (5)	390;(4.67)	569;(4.99)			1212[a]
•PTM-7TV-PTM• (6)	390;(4.66)	580;(5.05)			1213[a]

a) Values obtained by deconvolution of spectral bands of concentrated solutions.

Table S2. CV data of diradicals **1-6** and monoradical •**PTM-2TV** in a solution of Bu_4NPF_6 0,1M in CH_2Cl_2. Working electrode Pt wire, reference electrode Ag/AgCl, counter electrode Pt wire. Scan rate 0.1 V/s

Compound	$E^{1/2}_{Red}$ (V)	$E^{1/2}_{Ox1}$ (V)	$E^{1/2}_{Ox2}$ (V)	$E^{1/2}_{Ox3}$ (V)	$E^{1/2}_{Ox4}$ (V)	$E^{1/2}_{Ox5}$ (V)	$E^{1/2}_{Ox6}$ (V)	$\Delta E_{(Ox1-Red)}$ (V)
•**PTM-2TV**	-0.17	0.80	1.54					0.97
•**PTM-2TV-PTM•** (1)	-0.18	0.78	1.37					0.96
•**PTM-3TV-PTM•** (2)	-0.17	0.65	1.07					0.82
•**PTM-4TV-PTM•** (3)	-0.16	0.57	0.83	1.34				0.73
•**PTM-5TV-PTM•** (4)	-0.19	0.51	0.68	1.14	1.48			0.70
•**PTM-6TV-PTM•** (5)	-0.17	0.51	0.61	0.99	1.61	1.74		0.68
•**PTM-7TV-PTM•** (6)	-0.15	0.51	0.51	0.86	1.11	1.42	1.69	0.66

Table S3: EPR data for diradic als **1-6** and monoradical •**PTM-2TV** in CH_2Cl_2/Toluene (1:1) solution.

Compound	T/K	g_{iso}	a_H	$a_{C,\alpha}$	$a_{C,arom}$	ΔH_{pp}
•**PTM-2TV**	220	2.0029	1.73(1H) 0.78(1H)	29.1	12.7;10.2	0.74
•**PTM-2TV-PTM•** (1)	220	2.0028	0.88(2H); 0.32(2H)	14.3	5.1;6.1	0.65
•**PTM-3TV-PTM•** (2)	220	2.0032	0.85(2H); 0.38(2H)	14.2	5.1;6.1	0.50
•**PTM-4TV-PTM•** (3)	220	2.0030	0.85(2H); 0.38(2H)	14.4	5.1;6.1	0.50
•**PTM-5TV-PTM•** (4)	220	2.0029	0.87(2H); 0.38(2H)	14.3	5.1;6.1	0.52
•**PTM-6TV-PTM•** (5)	220	2.0030	0.86(2H); 0.38(2H)	14.4	5.1;6.1	0.50
•**PTM-7TV-PTM•** (6)	220	2.0034	0.90(2H); 0.36(2H)	13.4	5.1;6.1	0.74

Constants: g_{iso}, isotropic Lande factor (±0.0003); a_i, hyperfine coupling constants with i nuclei (in Gauss) obtained by simulation (WinEPR); ΔH_{pp}, peak-to-peak line width (in Gauss).

Generation of the anion-radicals [PTM-nTV-PTM]•−

The formation of the radical-anions was performed by chemical reduction of the corresponding diradicals with Bu_4NOH followed by UV-Vis. Upon stepwise addition of the reducing agent, the intense band at 385 nm associated with the radical character

(SOMO to LUMO transition) diminishes and the broad band around 650 corresponding to the anion increases. Formation of radical-anions **[PTM-nTV-PTM]•–** was also performed by electrochemical reduction of diradicals following its evolution along time (Figure S1).
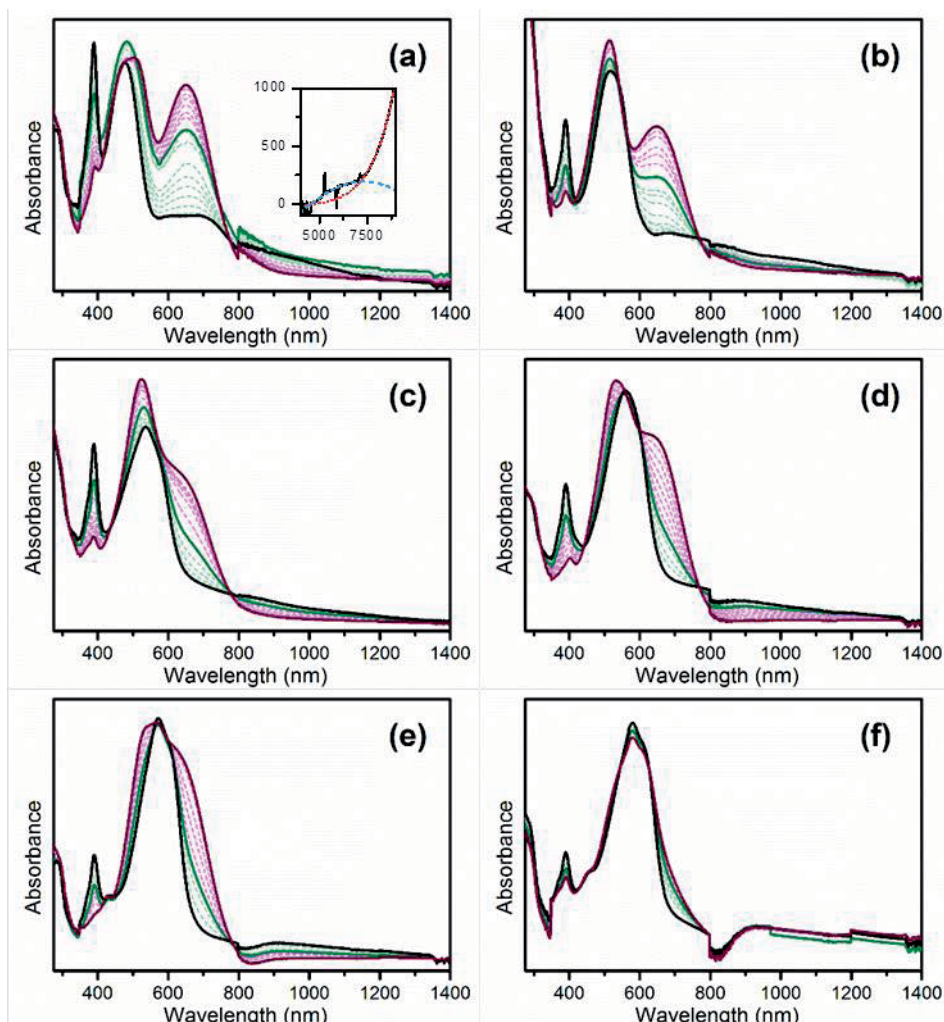
Figure S1: Time evolution of the UV-Vis spectrum of (a) **1,** (b) **2**, (c) **3**, (d) **4**, (e) **5** and (f) **6**, upon electrochemical reduction at -0.2 V in CH_2Cl_2/ 0.1 M nBu4NPF6 at 22 ºC. Neutral: solid black line, radical anion: solid green line and dianion: solid purple line.

For the VT-EPR experiments, the reduction of diradicals **1- 6** was performed until an almost complete reduction to the dianions **1^{2-}- 6^{2-}** was achieved. This procedure is advantageous because it avoids interferences from the diradical precursors since the resulting solutions contain, besides a small concentration of the desired mixed-valence **[PTM-nTV-PTM]•–** species, a large concentration of the ESR-silent dianion species, thereby providing good spectral resolutions.

For Raman experiments the studied solutions were also those with a small amount of the mixed valence species.

Variable-temperature EPR spectra of radical-anions [PTM-nTV-PTM]$^{\bullet-}$

The experimental VT-EPR spectra were simulated using the ESR-EXN program The hyperfine coupling constants of the segmental model radical $^{\bullet}$PTM-2TV were taken as initial inputs for the simulations of VT-EPR spectra of **[PTM-nTV-PTM]$^{\bullet-}$** and then adjusted, along with the exchange rate, to obtain the best fit to each experimental spectrum. This fitting was repeated three times for each spectrum to obtain the average exchange rate and its error. Solvents with different nature and polarity were tested and only CH_2Cl_2 was appropriate to see an acceptable resolution of the lines that permits to observe the IET process from slow to fast rate exchange regimes. The resolution of the spectra was not good enough to simulate all acquired data, but in most cases 5 spectra at distinct temperatures for each compound were good enough to get the kinetic data for the thermodynamic studies.
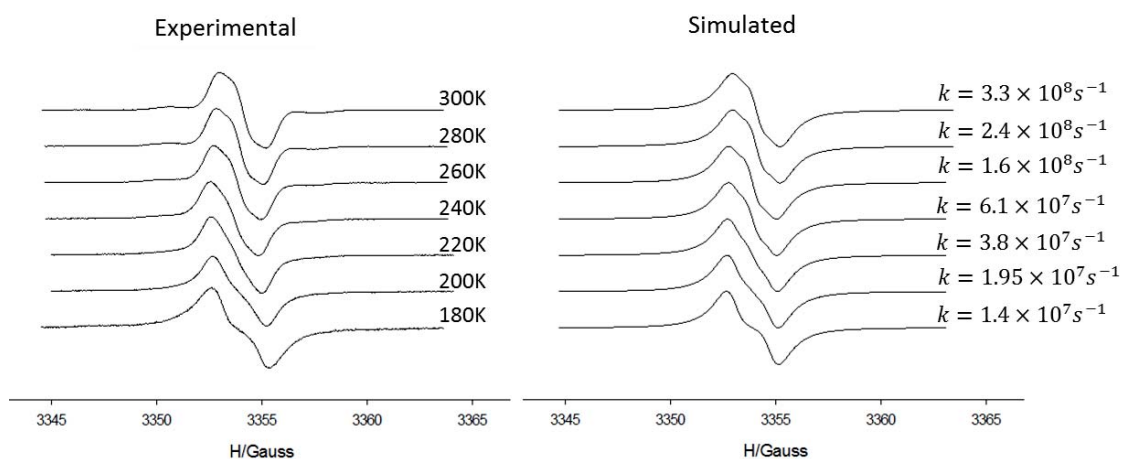
Figure S2: VT-ESR spectra of **[PTM-2TV-PTM]$^{\bullet-}$** in CH_2Cl_2. Experimental spectra in the temperature range of 180-300K (left) and simulated spectra (right) with different IET rates, k_{ET}, rates.
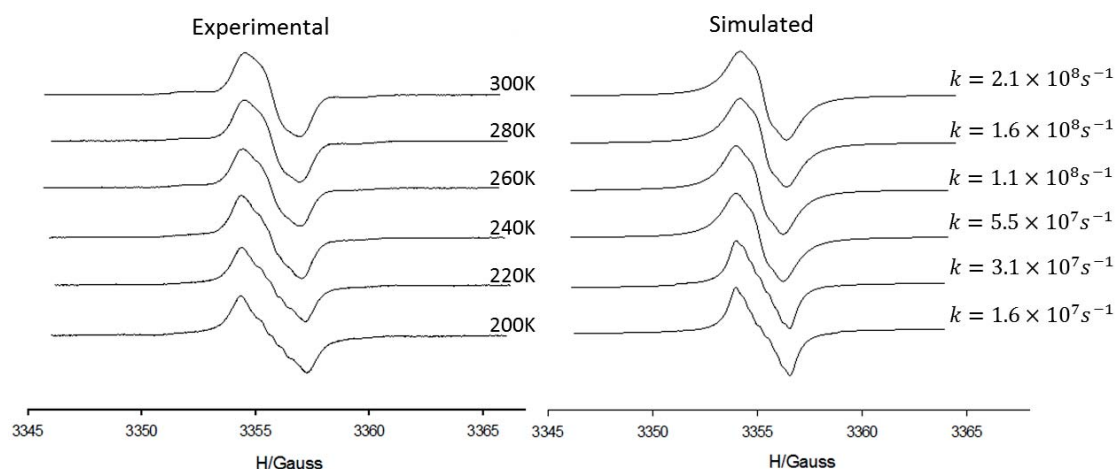
Figure S3: VT-ESR spectra of **[PTM-3TV-PTM]$^{\bullet-}$** in CH_2Cl_2. Experimental spectra in the temperature range of 200-300K (left) and simulated spectra (right) with different **IET**, k_{ET}, rates.
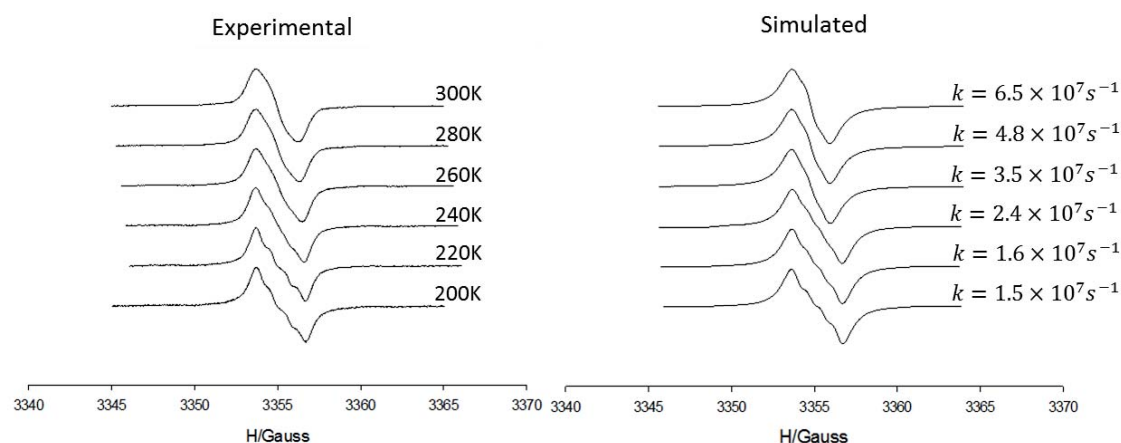
Figure S4: VT-ESR spectra of **[PTM-4TV-PTM]**$^{\bullet-}$ in CH_2Cl_2. Experimental spectra in the temperature range of 200-300K (left) and simulated spectra (right) with different **IET**, k_{ET}, rates.
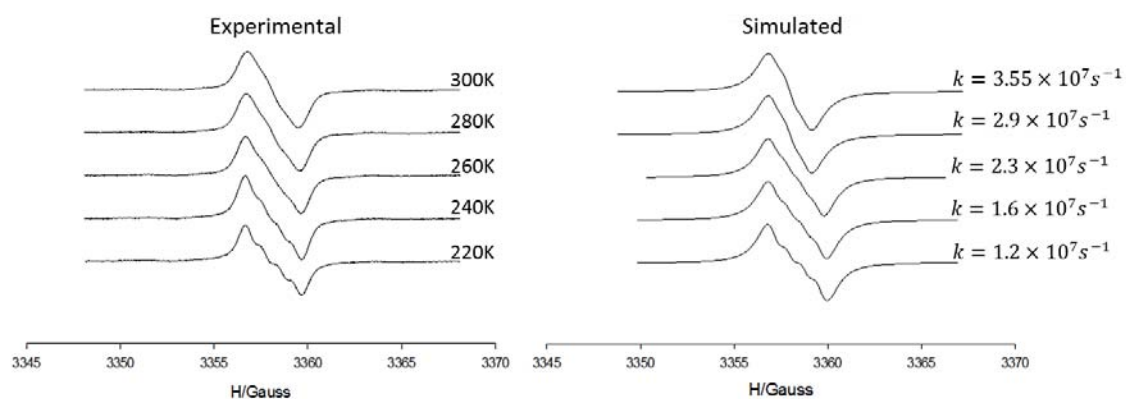
Figure S5: VT-ESR spectra of **[PTM-5TV-PTM]**$^{\bullet-}$ in CH_2Cl_2. Experimental spectra in the temperature range of 220-300K (left) and simulated spectra (right) with different **IET**, k_{ET}, rates.
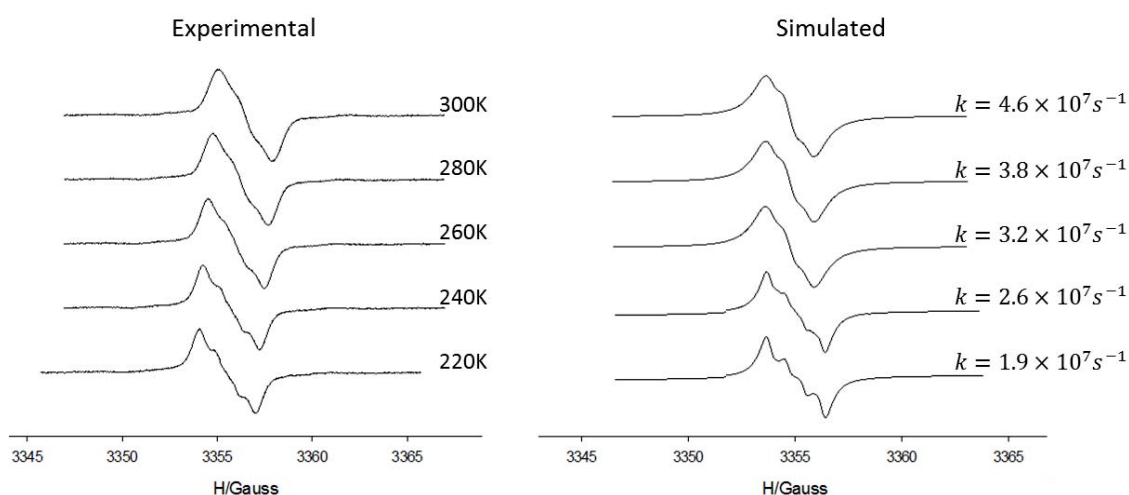
Figure S6: VT-ESR spectra of **[PTM-6TV-PTM]**$^{\bullet-}$ in CH_2Cl_2. Experimental spectra in the temperature range of 220-300K (left) and simulated spectra (right) with different **IET**, k_{ET}, rates.
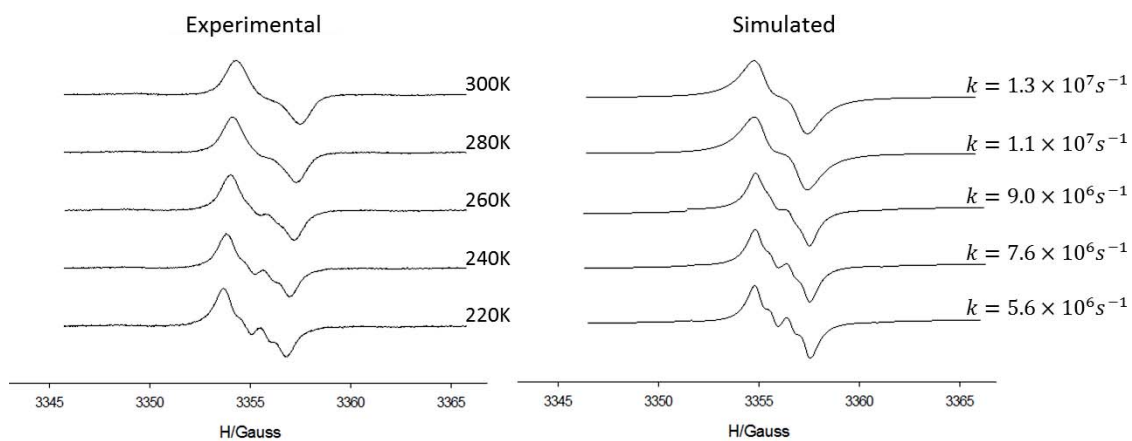
Figure S7: VT-ESR spectra of **[PTM-7TV-PTM]**$^{\bullet-}$ in CH_2Cl_2. Experimental spectra in the temperature range of 220-300K (left) and simulated spectra (right) with different **IET**, k_{ET}, rates.
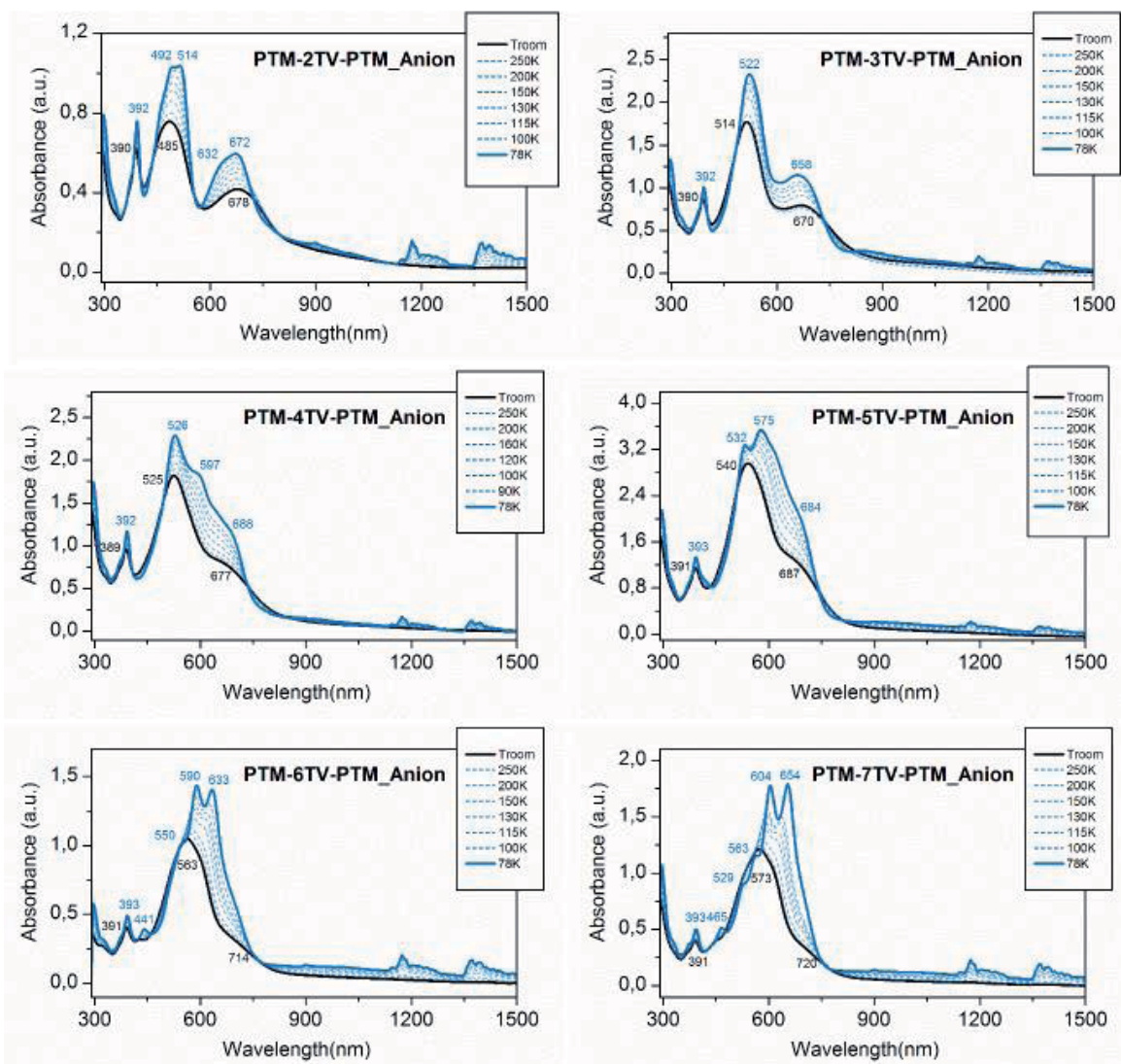
Figure S8. UV-Vis-NIR spectra of the radical- anions **[PTM-nTV-PTM]**$^{\bullet-}$ in Me-THF as a function of the temperature.
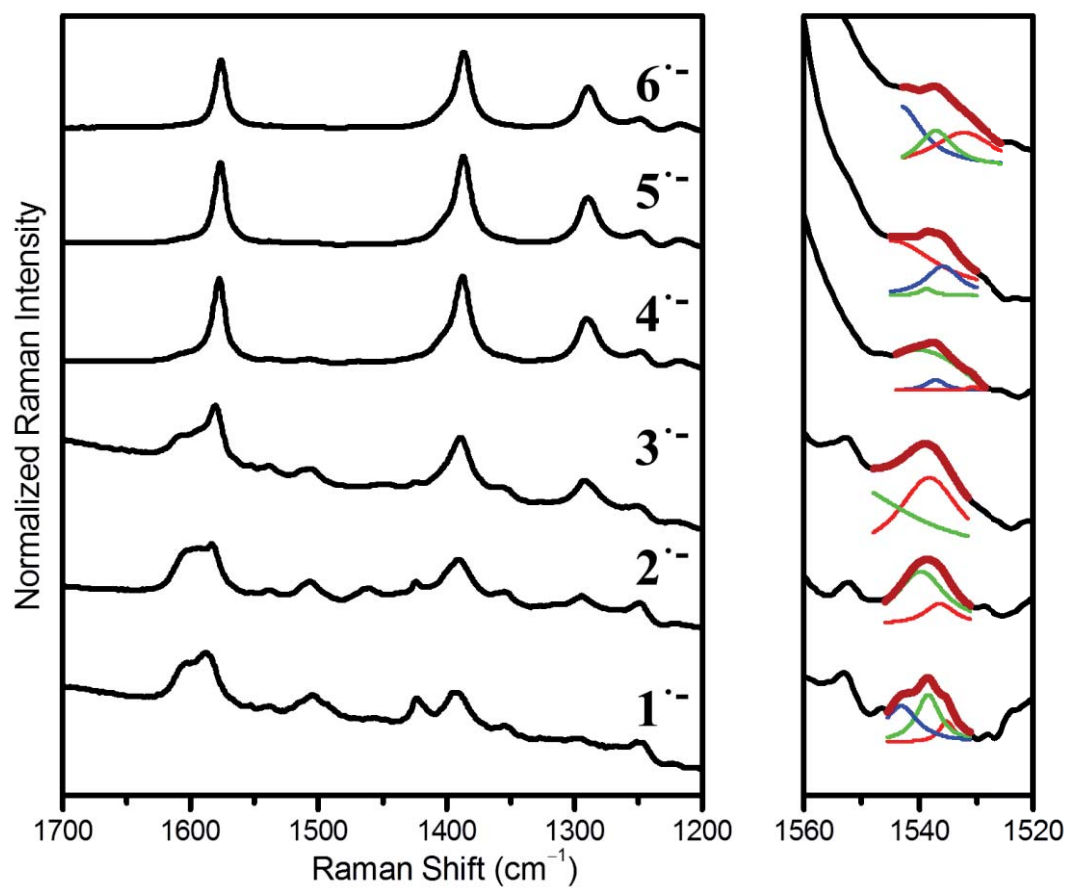
Figure S9. 633 nm Raman spectra of the radical-anions **[PTM-nTV-PTM]**$^{\bullet-}$ in CH_2Cl_2 at room temperature
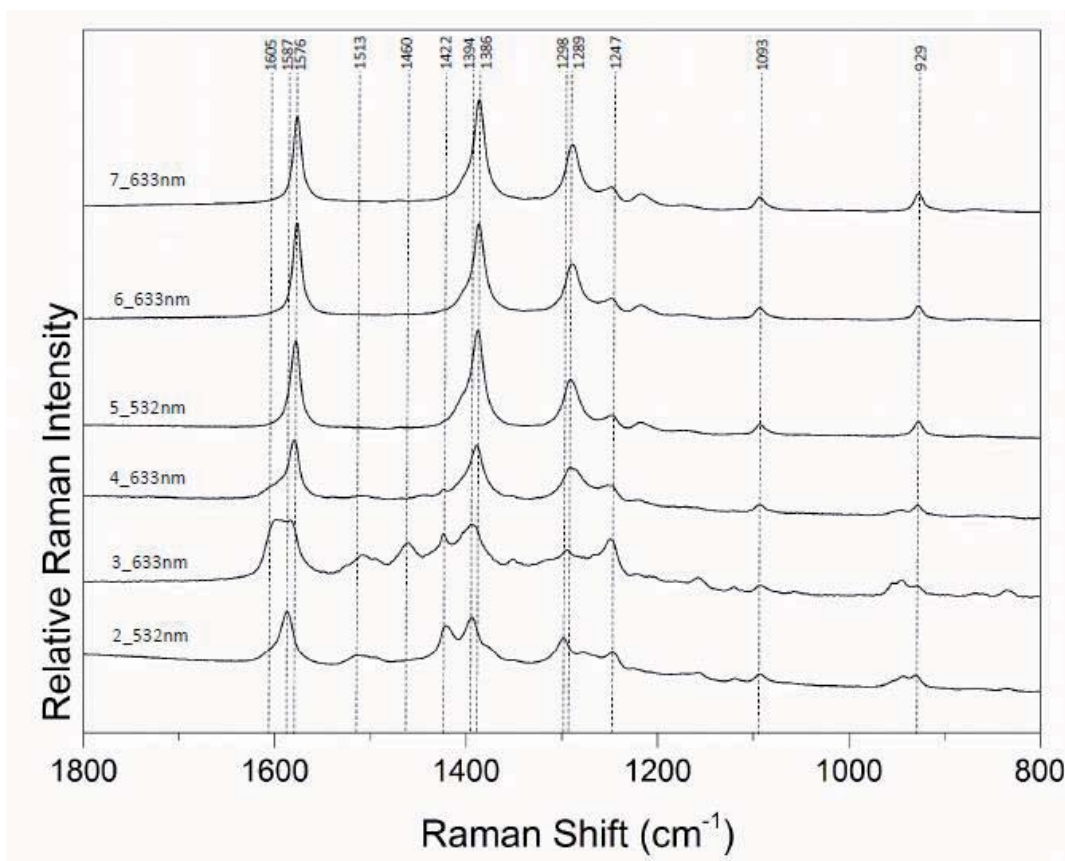
Figure S10. Raman spectra of diradicals **•PTM-nTV-PTM•** (**1-6**) in CH₂Cl₂ at room temperature. From bottom to top **1** to **6**

Table S4: Average ln k_{ET} values with their standard deviations obtained from simulations of EPR of radical-anions **[PTM-nTV-PTM]**•− (n=2-7) in CH_2Cl_2 at temperatures between 300 and 220 K.

Radical-Anion R, in Å	T, in K	300	280	260 Ln k_{ET}	240	220
PTM-2TV-PTM•− 24.22 Å		19.61±0.53	19.30±0.55	18.89±0.55	17.93±0.40	17.45±0.25
PTM-3TV-PTM•− 29.70 Å		19.16±0.52	18.89±0.47	18.52±0.38	17.82±0.38	17.25±0.37
PTM-4TV-PTM•− 36.09 Å		17.99±0.50	17.69±0.44	17.38±0.37	16.99±0.25	16.59±0.25
PTM-5TV-PTM•− 41.35 Å		17.55±0.19	17.28±0.21	17.07±0.19	16.53±0.19	16.30±0.17
PTM-6TV-PTM•− 47.56 Å		17.38±0.45	17.15±0.37	16.76±0.33	16.19±0.32	15.92±0.41
PTM-7TV-PTM•− 52.80 Å		16.38±0.08	16.21±0.09	16.01±0.23	15.84±0.20	15.54±0.37

R_0 (**PTM-1TV-PTM**)•− = 17.92 Å; R, distance from central C atom of PTM unit to the center of TV unit, r = 4.63 Å
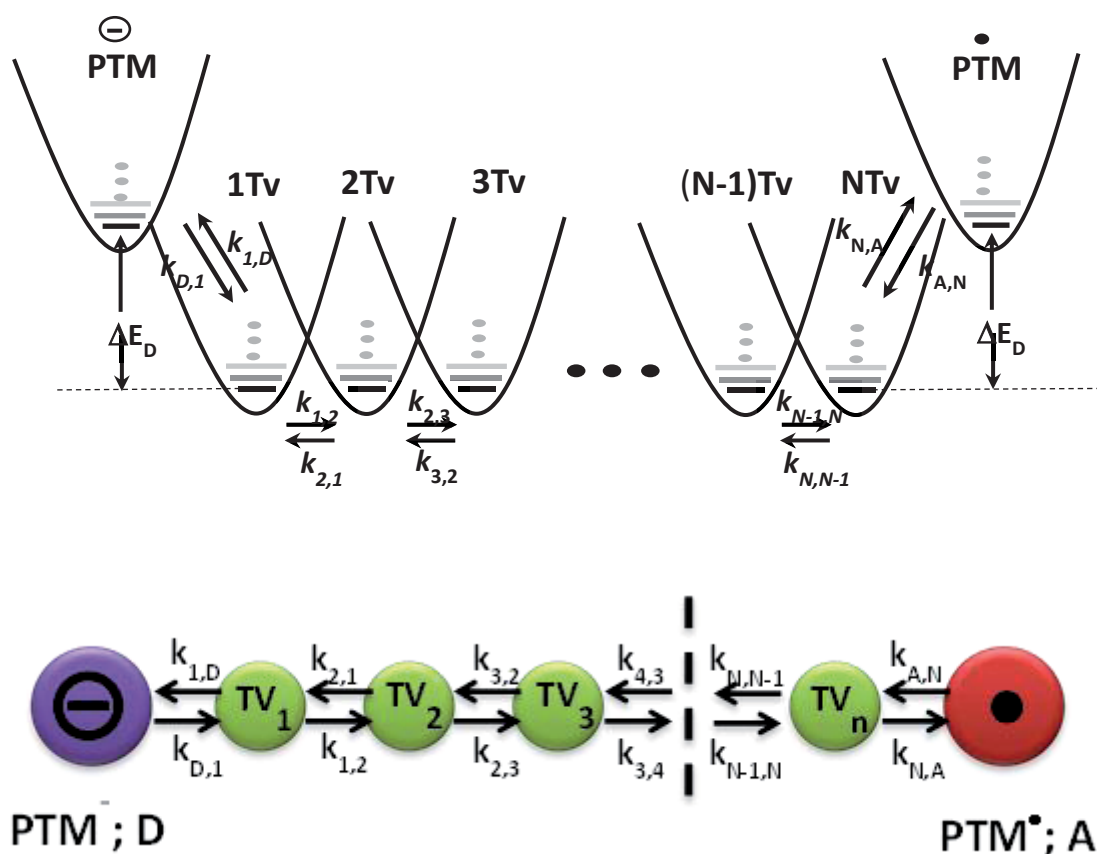
Scheme S5

Estimation of ΔE_D values

The rate determinant step and its associate energy values, ΔE_{BD}, were calculated with the Weller equation [1],

$$\Delta E_{BD} = e(E_{ox} - E_{red}) - \left(\frac{1}{4\pi\epsilon_0}\right)\left(\frac{e^2}{R_{D1}\epsilon_s}\right) \qquad \text{(Eq. S1)}$$

using ε_s (CH$_2$Cl$_2$) = 8.9, R_{D1} = 9.47 Å and the following reduction and oxidation potentials:

E_{red} (in Volts): $^\bullet$PTM-TV$_1$-(TV)$_{n}$-$_1$PTM$^\ominus$ + 1e$^-$ $\rightarrow$ $^\ominus$PTM-TV$_1$-(TV)$_n$-PTM$^\ominus$, given by the second reduction potential of diradicals $^\bullet$PTM-TV$_1$-(TV)$_n$-PTM$^\bullet$.

E_{ox} (in Volts): $^\ominus$PTM-TV$_1$-(TV)$_{n}$-$_1$PTM$^\ominus$ $\rightarrow$ $^\ominus$PTM-TV$_1^\oplus$-(TV)$_{n}$-$_1$PTM$^\ominus$ + 1e$^-$, which can be estimated in a first approximation to the oxidation potential of diradicals $^\bullet$PTM-TV$_1$-(TV)$_{n}$-$_1$PTM$^\bullet$.

Derivation of rate constants, *k*, for a thermally activated biased bidirectional symmetrical charge hopping process and its application to spin/charge exchange process for radical-anions [PTM-nTV-PTM]$^{\bullet-}$ (n=4-7).

The rate equation for a general multistep hopping process, using the flux conservation method [2,3], lead to Eq. S2, which is valid for a bidirectional symmetrical charge hopping process, as reported by Petrov et al. [4].

$$k_{ET} = \frac{\frac{k_{1,D}}{k_{D,1}}\Psi}{\frac{1}{k_{N,A}} + \frac{\Psi}{k_{1,D}} + \frac{1+\Phi}{K_{N,N-1}}} = \frac{e^{-\frac{\Delta E_{BD}}{k_B T}}}{\frac{1}{k_{N,A}} + \frac{\Psi}{k_{1,D}} + \frac{1+\Phi}{K_{N,N-1}}} \qquad (Eq.\,S2)$$

Where Ψ and Φ are functions of hopping rates only and are given by:

$$\Psi = \prod_{q=1}^{N-1} \frac{k_{q,q+1}}{k_{q+1,q}} \qquad (Eq.\,S3)$$

$$\Phi = \sum_{s=1}^{N-2}\left(\prod_{q=s}^{N-2} \frac{k_{q+1,q+2}}{k_{q,q+1}}\right) \qquad (Eq.\,S4)$$

For our system the mechanism for the charge transfer in the longer compounds can be described as a biased sequential hopping. As these molecules are symmetric, the rate constants are equal at both sides of the molecules related by a symmetry plane. For example for the **[PTM-4Tv-PTM]**$^{\bullet-}$ (**3**$^{\bullet-}$), $k_{1,D}=k_{4,A}$; $k_{D,1}=k_{A,4}$; $k_{1,2}=k_{4,3}=k_1$ and $k_{2,1}=k_{3,4}=k_2$. Assuming that the rate constants in the middle of the bridge are practically equal ($k_{2,3}=k_{3,2}=k_3$), the Eqs. S3 and S4 can be rewritten as:

$$\Psi = 1 \qquad (Eq.\ S5)$$

$$\Phi = 1 + (N-3)\frac{k_1}{k_3} \qquad (Eq.\ S6)$$

The substitution in the general Eq. S2 gives

$$k_{ET} = \frac{k_d e^{-\frac{\Delta E_{BD}}{k_B T}}}{1 + \frac{k_d}{k_2}\left[2 + \frac{k_1}{k_3}\left(\frac{R'}{r} - 2\right)\right]} \qquad (Eq.\,S7)$$

where $k_d = k_{1,D}k_{N,A}/(k_{1,D} + k_{N,A}) = k_{1,D}/2$ and $(N-1)=R'/r$; where $R'=R-R_0$ being R' the overall distance between the two terminal PTM groups, R_0 corresponds to the distance between the PTM units separated by a single-bridging unit TV(17.92 Å) and r is the distance between two consecutive TV units (4.63 Å). For these systems we can assume that the determining rate step is the $k_{1,D}$ and $k_d \ll k_2$. Therfore, Eq. S7 can be approximated to:

$$k_{ET} \simeq k' e^{-\frac{\Delta E_{BD}}{k_B T}} e^{-\beta R'} \qquad (Eq.\,S8)$$

where

$$\beta = \frac{k_1 k_{1,D}}{2 k_2 k_3 r}; \; k' = \frac{k_{1,D}}{2} e^{-\frac{k_{1,D}}{k_2}} e^{\frac{k_{1,D} k_1}{k_3 k_3}} \simeq \frac{k_{1,D}}{2} e^{\frac{k_{1,D} k_1}{k_2 k_3}} \simeq \frac{k_{1,D}}{2} e^{2\beta r}$$

Replacing the latter expressions in Eq. S8 gives

$$k_{ET} \simeq \frac{k_{1,D}}{2} e^{-\frac{\Delta E_{BD}}{k_B T}} e^{-\beta(R - R_0 - r)} \qquad \textit{(Eq. S9)}$$

Finally, using the rate constants $k_{1,D}$ and $k_{D,1}$ in the Marcus form [4] Eq. S9 is transformed into:

$$k_{ET} \simeq \frac{\pi}{\hbar} \frac{|V_{D1}|^2}{\sqrt{4\pi \lambda_D k_B}} e^{-\frac{(\Delta E_{BD} + \lambda_{D1})^2}{4 \lambda_{D1} k_B T}} e^{-\beta(R - R_0 - 2r)} \qquad (Eq. \, 10)$$

where $\lambda_{D,1}$ is the reorganization energy of the transition $D \rightarrow 1$, $|V_{D1}|$ is the electronic coupling of the PTM unit and the contiguous TV unit of the bridge and k_B is the Boltzman's constant.

[1] A. Weller, *Z. Phys. Chem.*, **1982**, *133*, 93.

[2] Y.A. Berlin, M. A. Ratner, *Rad. Phys. Chem.*, **2005**, *74*, 124.

[3] A. Butler Ricks, K. E. Brown, M. Wenninger, S. D. Karlen, Y. A. Berlin, D. T. Co, M. R. Wasielewski, *J. Am. Chem Soc.*, **2012**, *134*, 4581.

[4] E.G. Petrov Ye. V. Shevchenko, V. May, *Chem. Phys.*, **2003**, *288,* 269.

^{13}C-, and ^1H-NMR, FT-IR, MALDI-MS, EPR spectra of new compounds
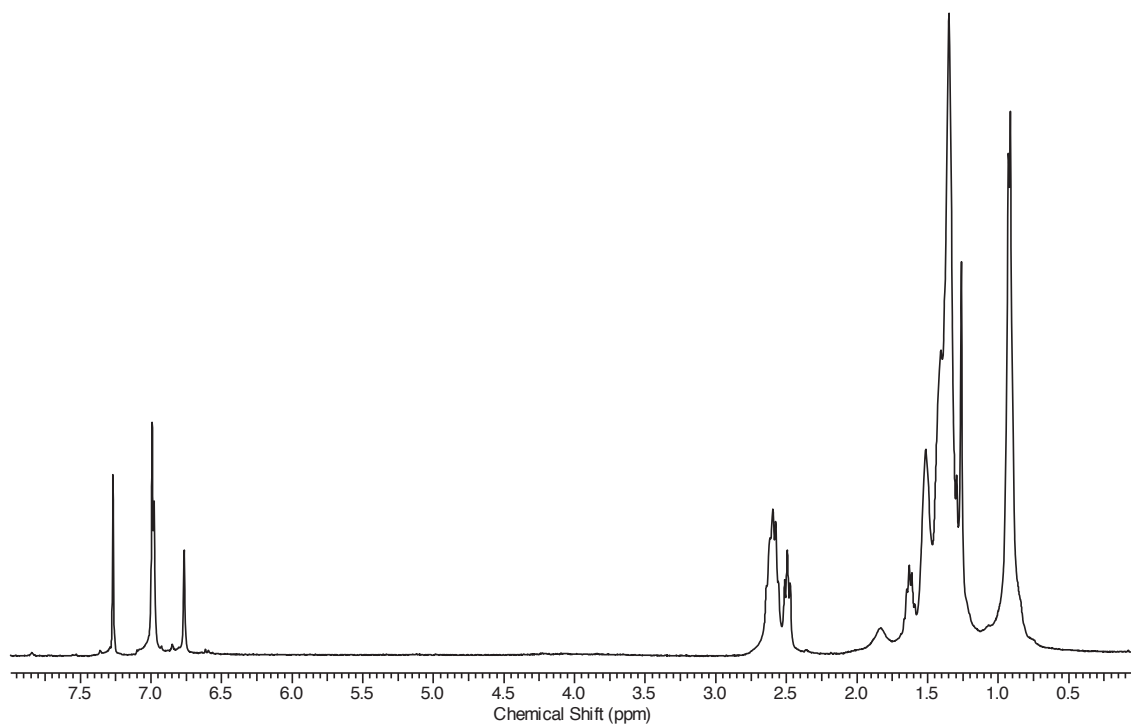
Figure S11. ^1H-NMR spectrum of compound **S5a**.
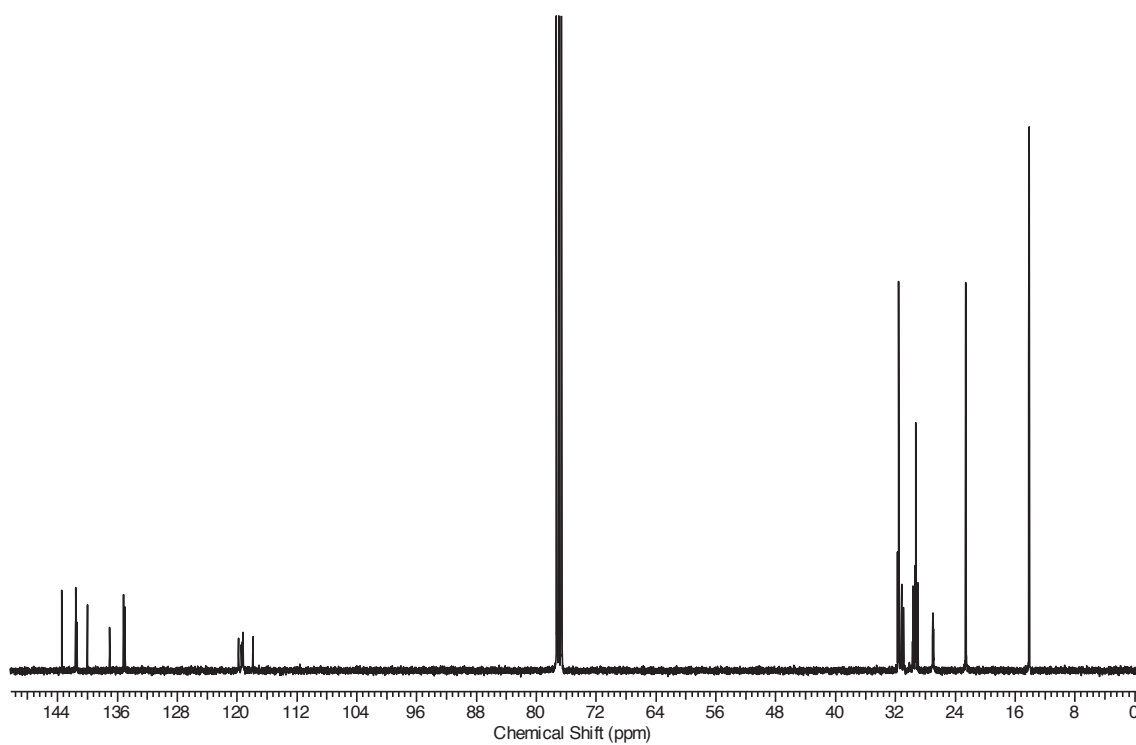
Figure S12. ^{13}C-NMR spectrum of compound **S5a**.
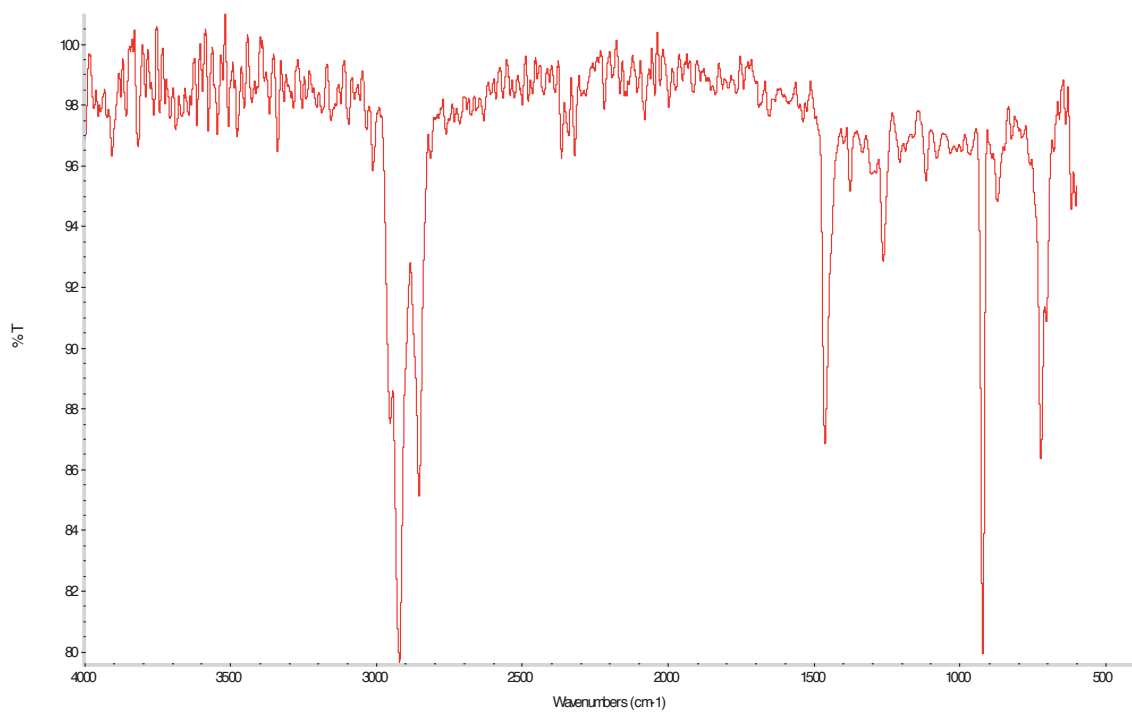
Figure S13. FT-IR spectrum of compound **S5a**.
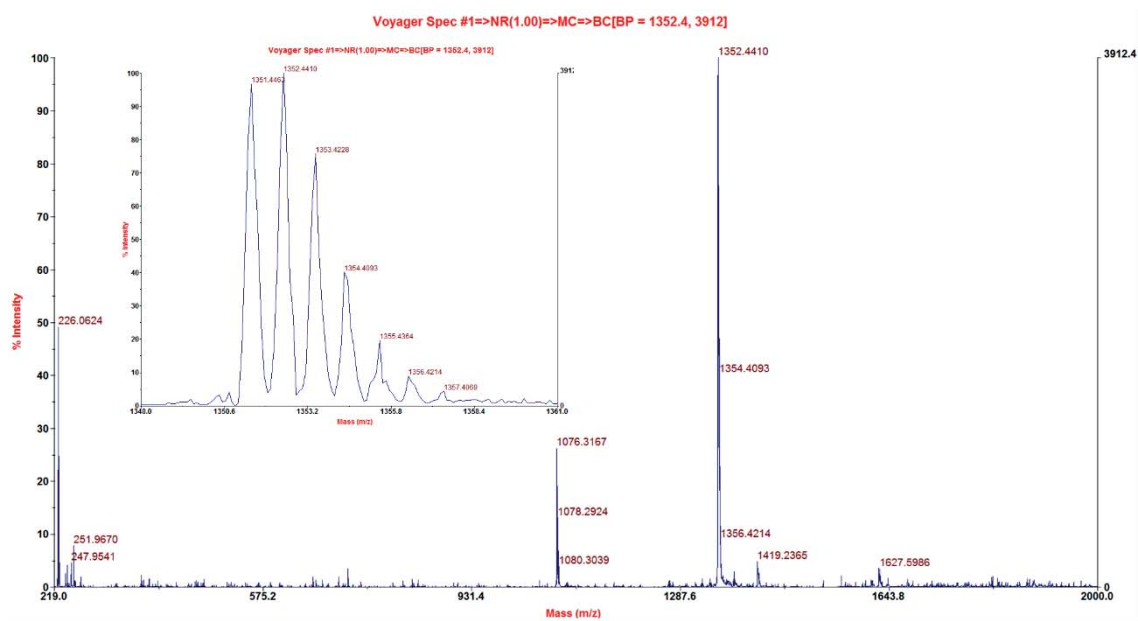
Figure S14. Mass spectrum of compound **S5a**.
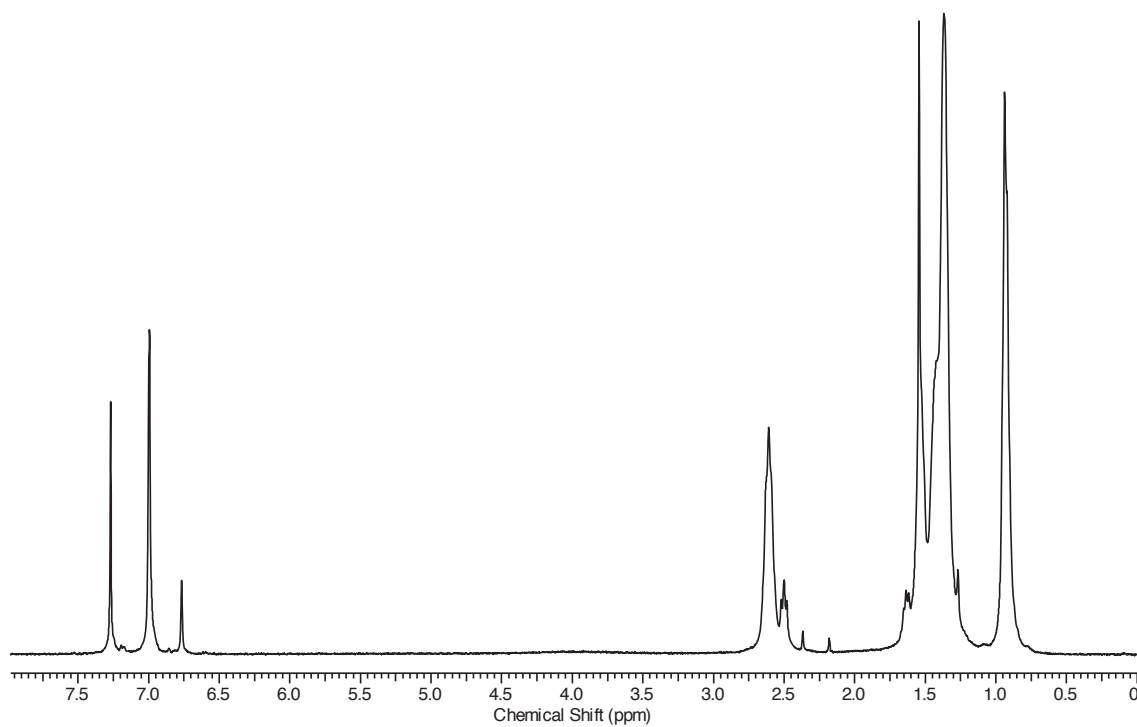
Figure S15. ^{1}H-NMR spectrum of compound **S7a**.
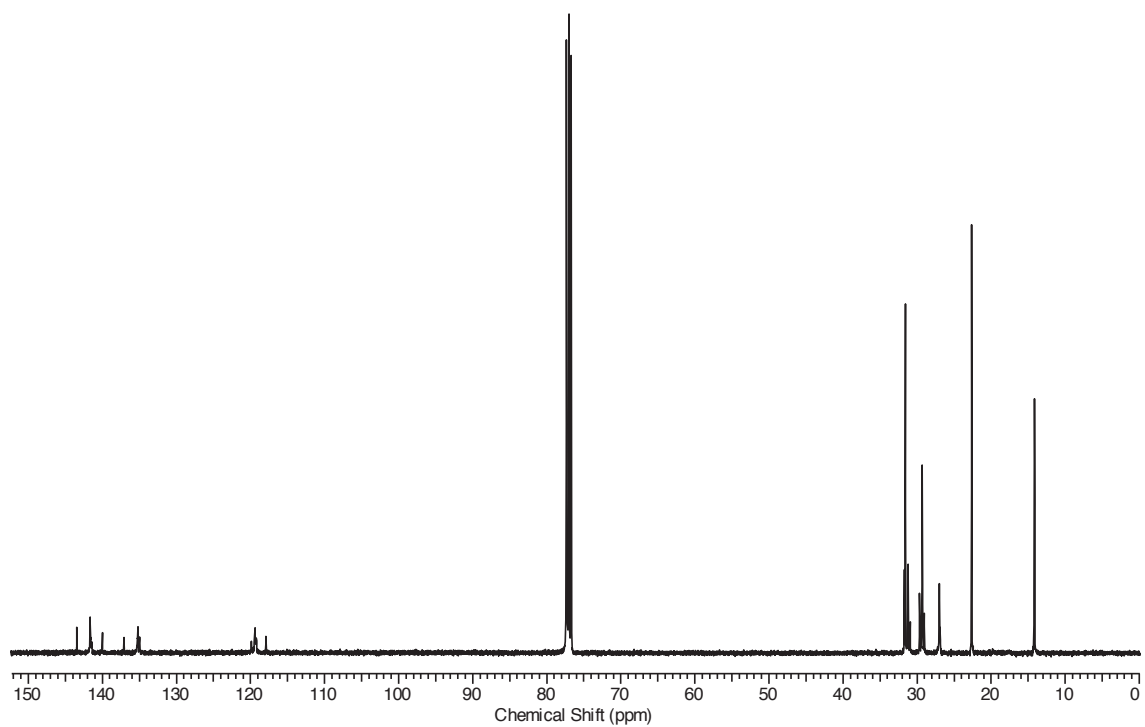
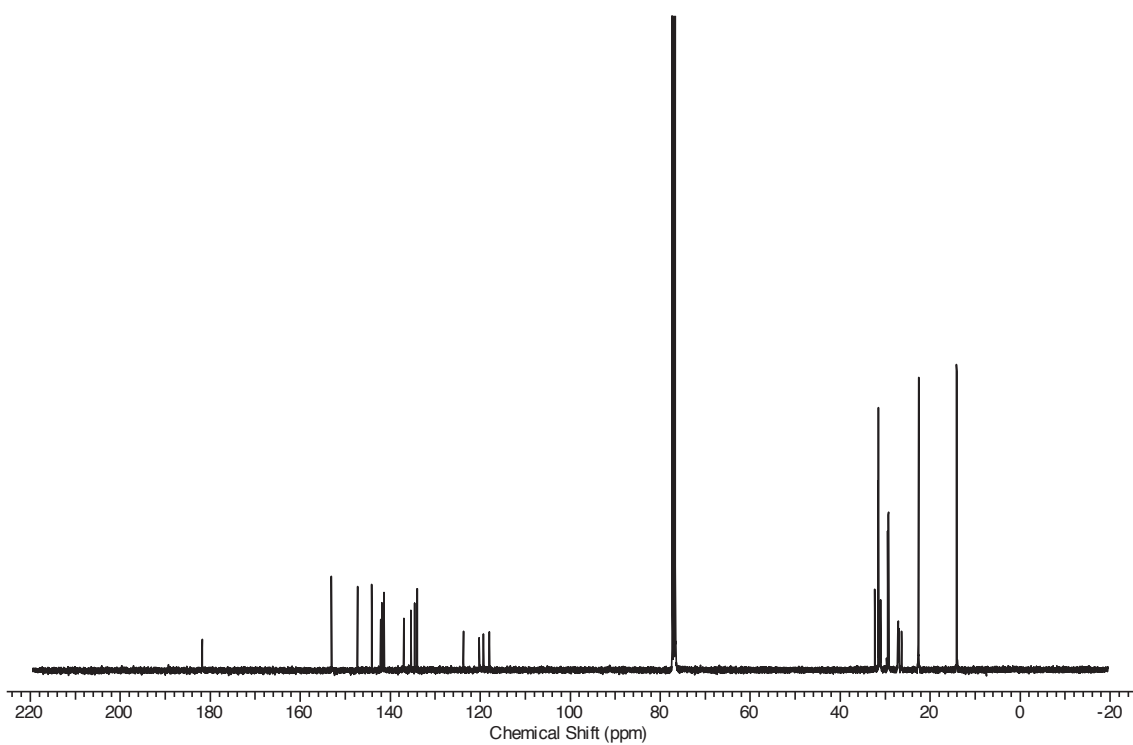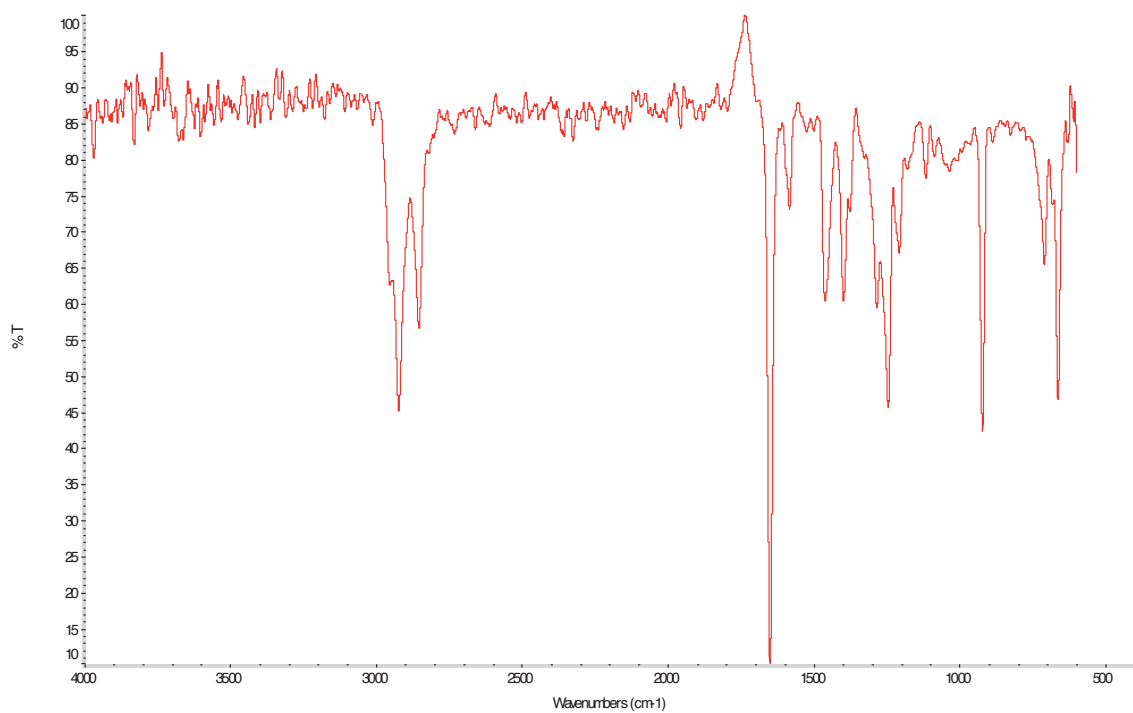**Figure S16.** ^{13}C-NMR spectrum of compound **S7a**.
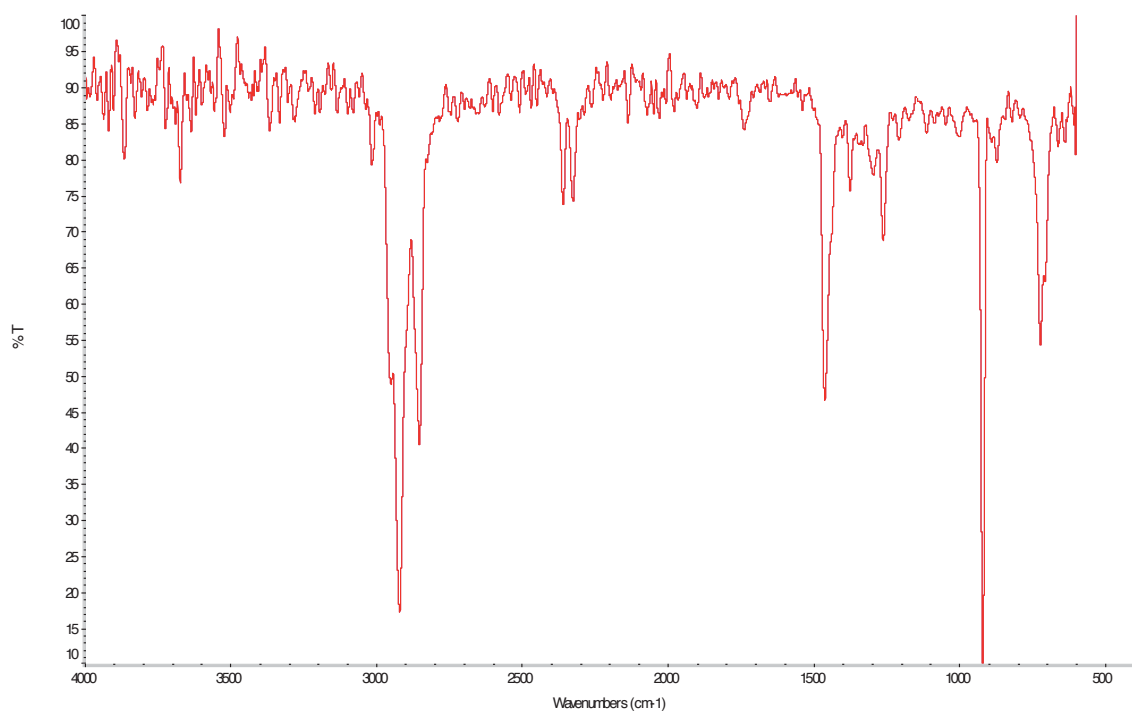
Figure S17. FT-IR spectrum of compound **S7a**.
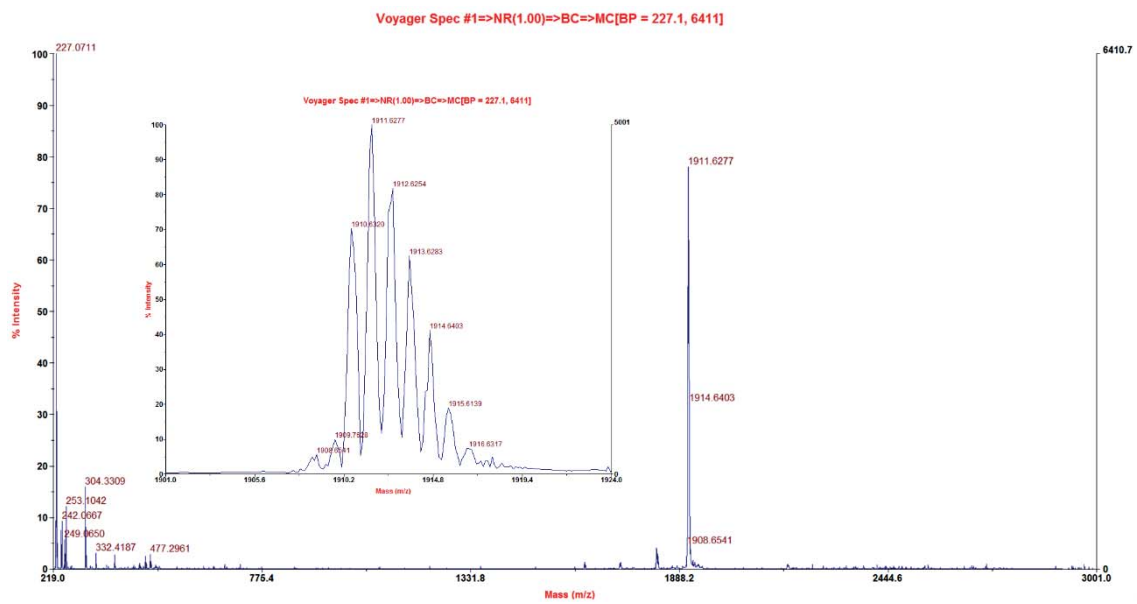
Figure S18. Mass spectrum of compound **S7a**.
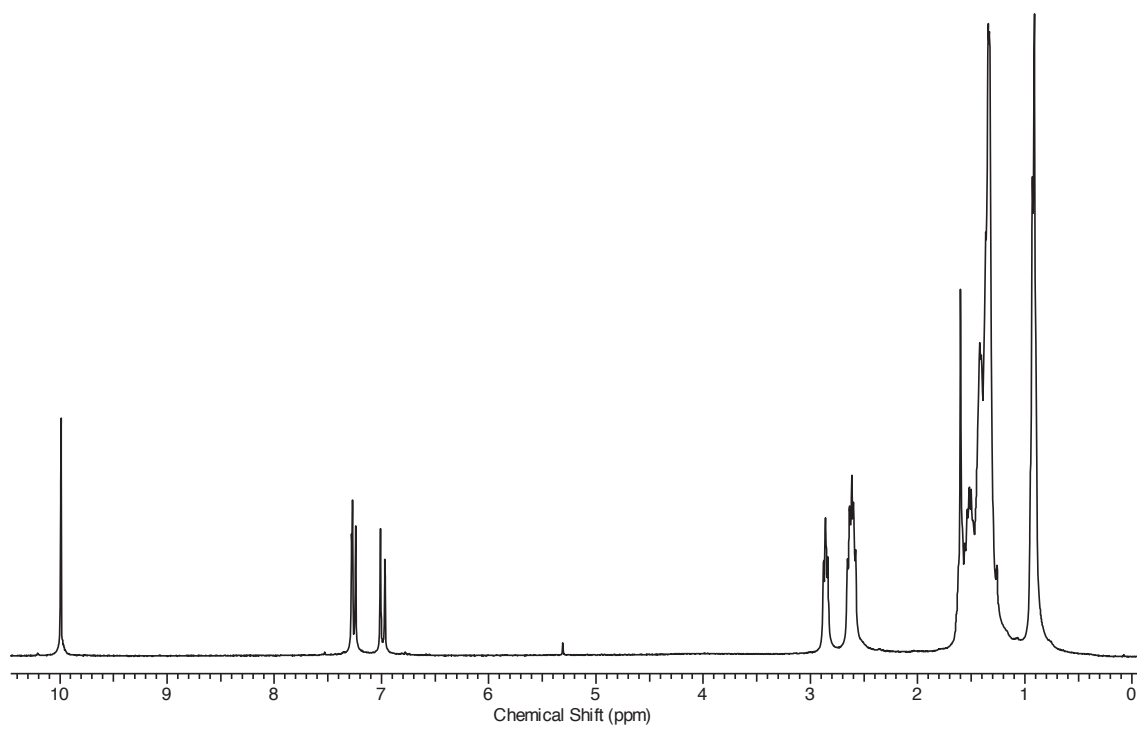
Figure S19. ^{1}H-NMR spectrum of compound **S3b**.
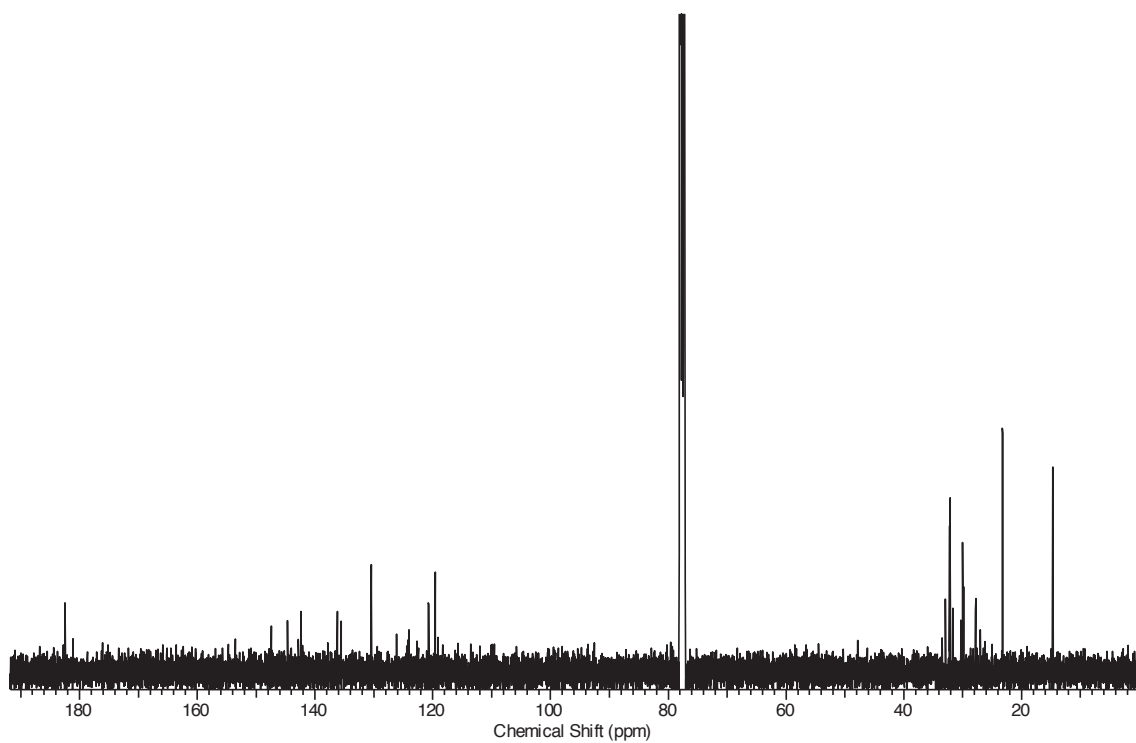
Figure S20. ^{13}C-NMR spectrum of compound **S3b**.
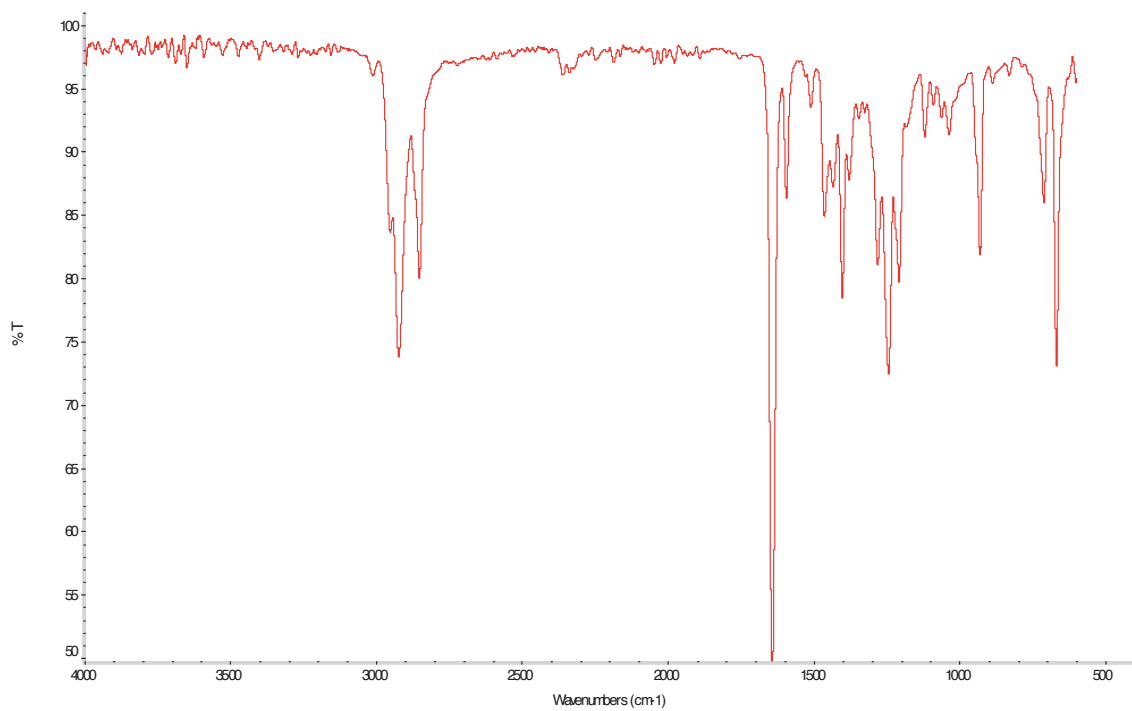
Figure S21. FT-IR spectrum of compound **S3b**.
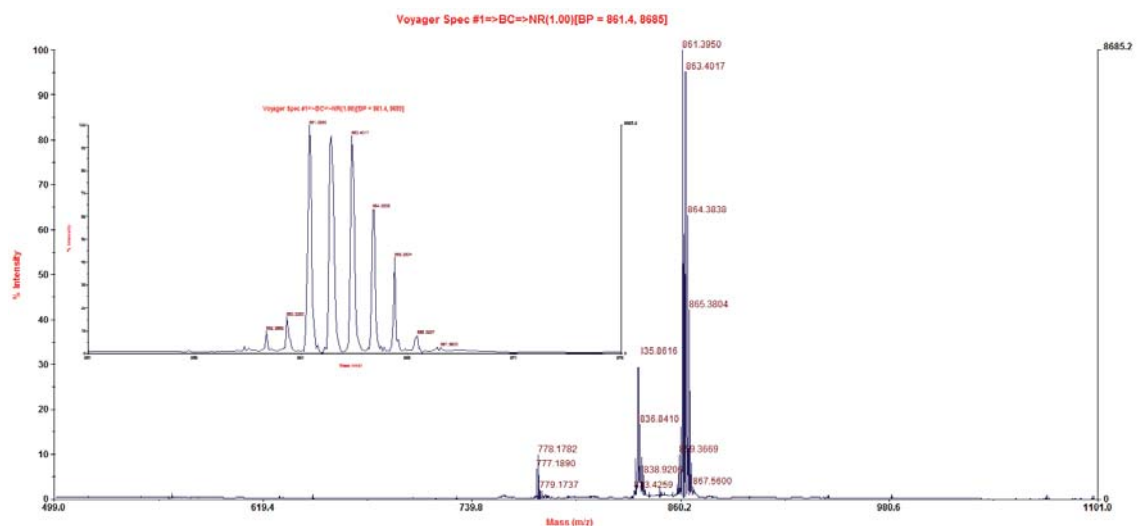
Figure S22. Mass spectrum of compound **S3b**.
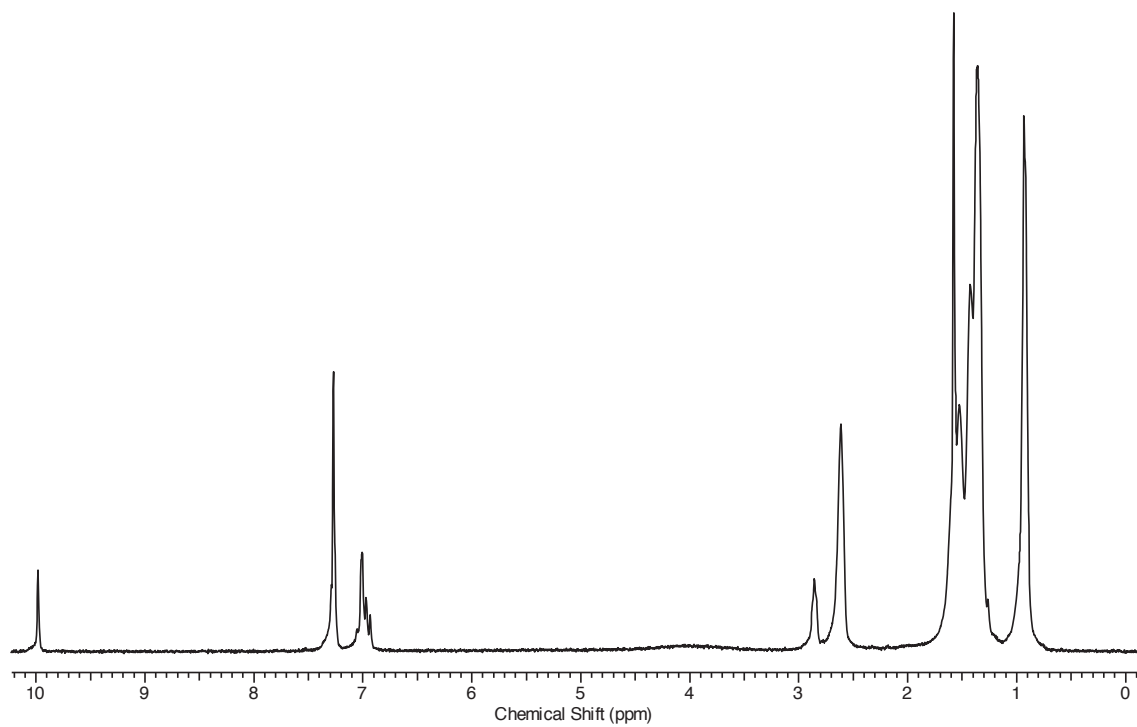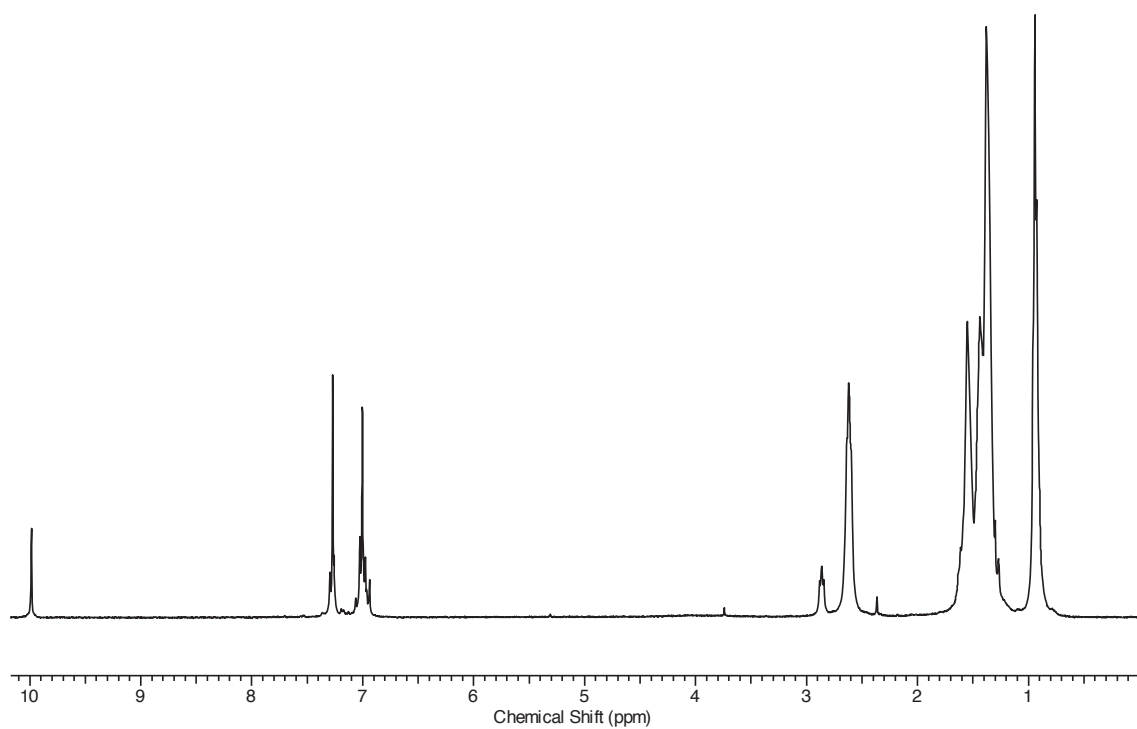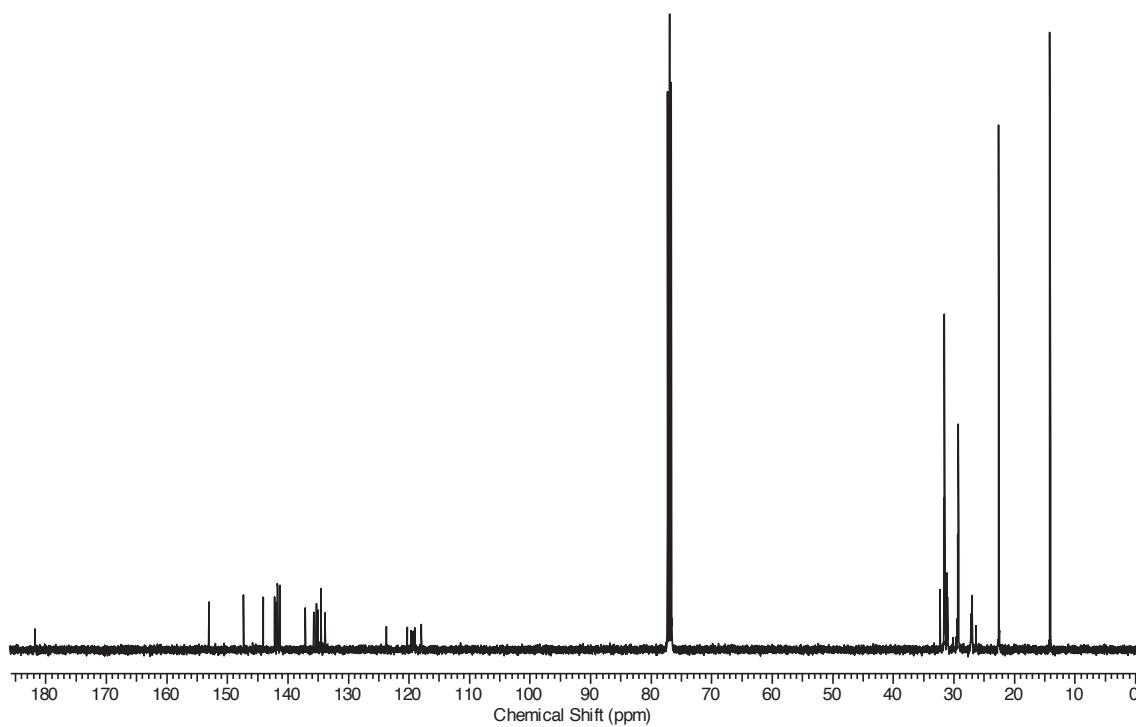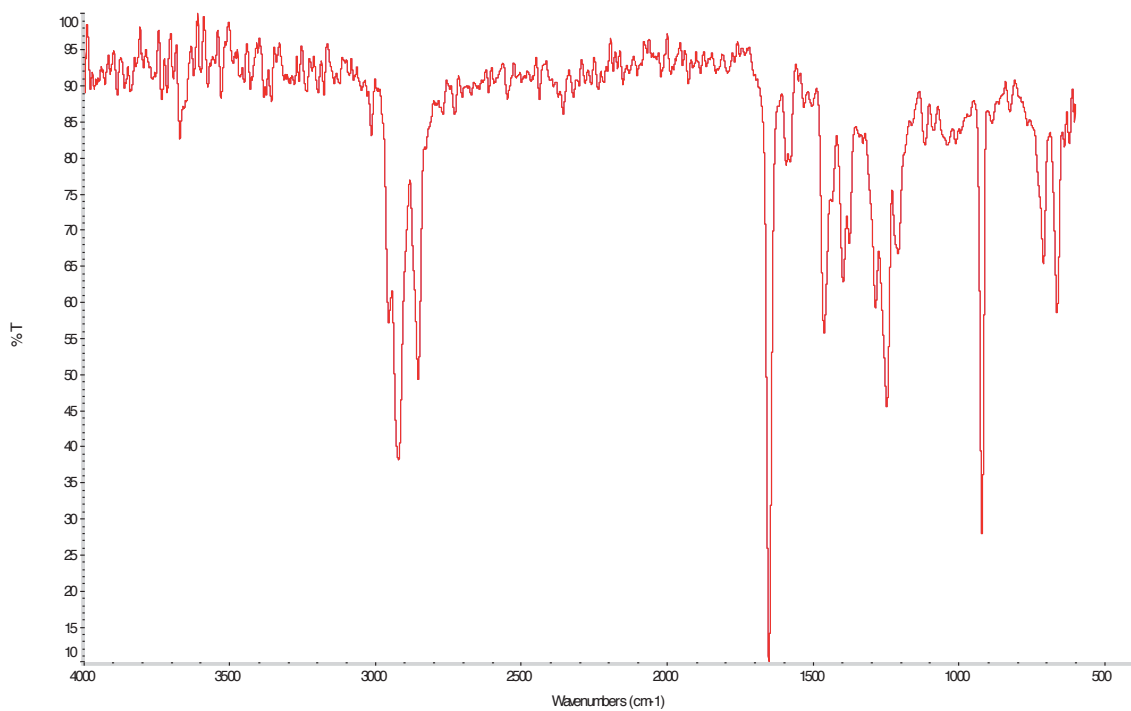

Figure S23. ^{1}H-NMR spectrum of compound **S5b**.

Figure S24. ^{13}C-NMR spectrum of compound **S5b**.

Figure S25. FT-IR spectrum of compound **S5b**.
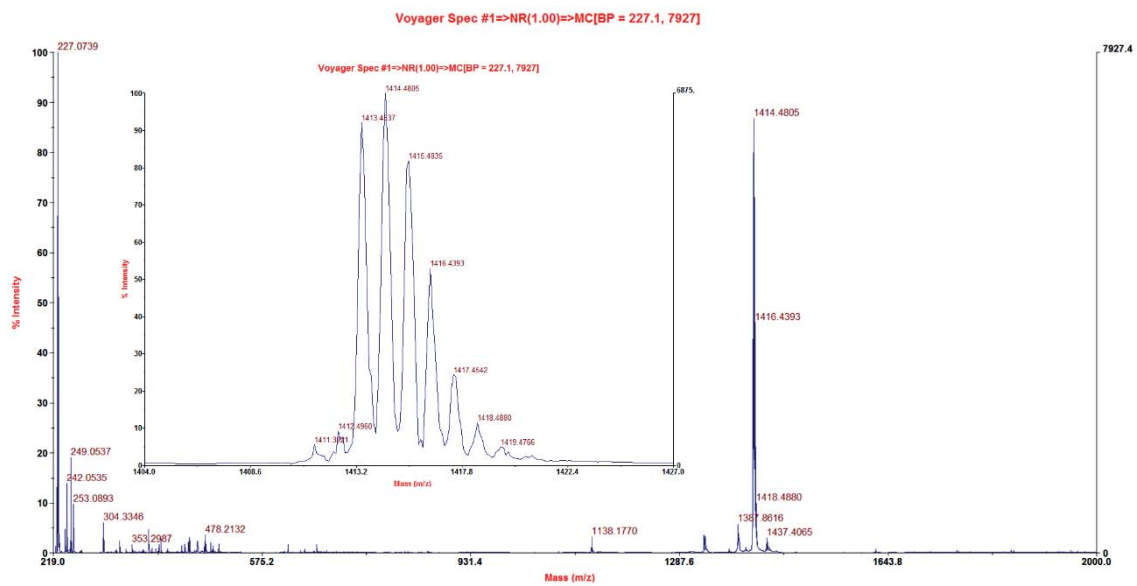
Figure S26. Mass spectrum of compound **S5b**.

Figure S27. ^{1}H-NMR spectrum of compound **S7b**.
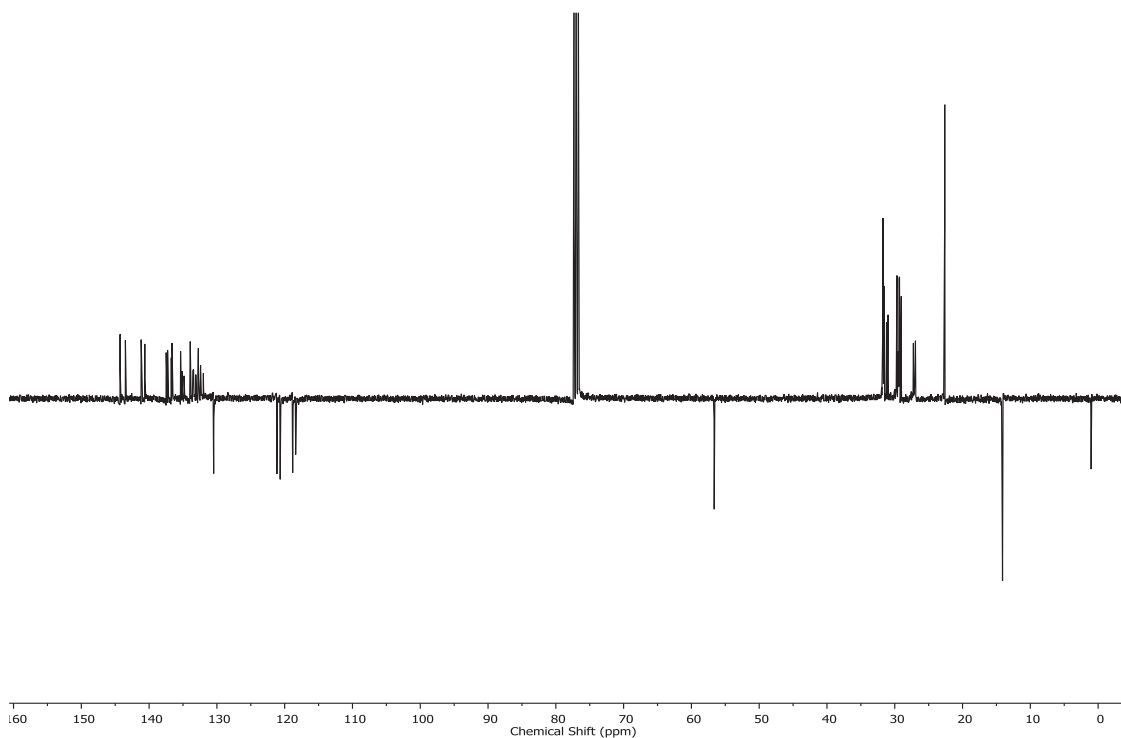
Figure S28. ^{13}C-NMR spectrum of compound **S7b**.

Figure S29. FT-IR spectrum of compound **S7b**.
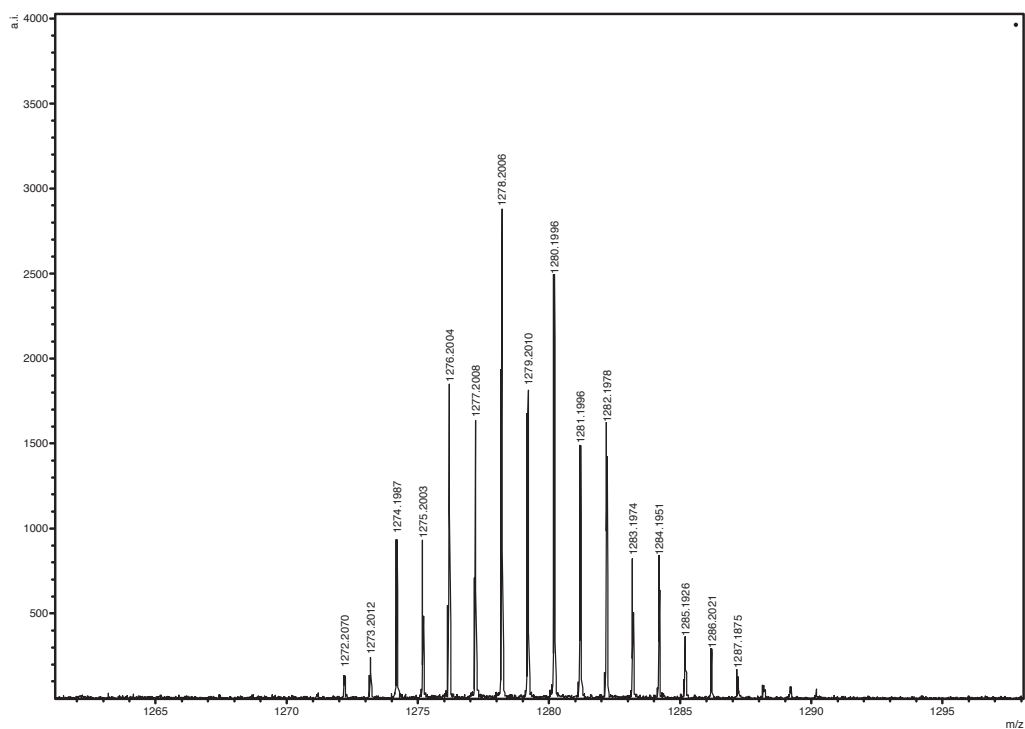
Figure S30. Mass spectrum of compound **S7b**.
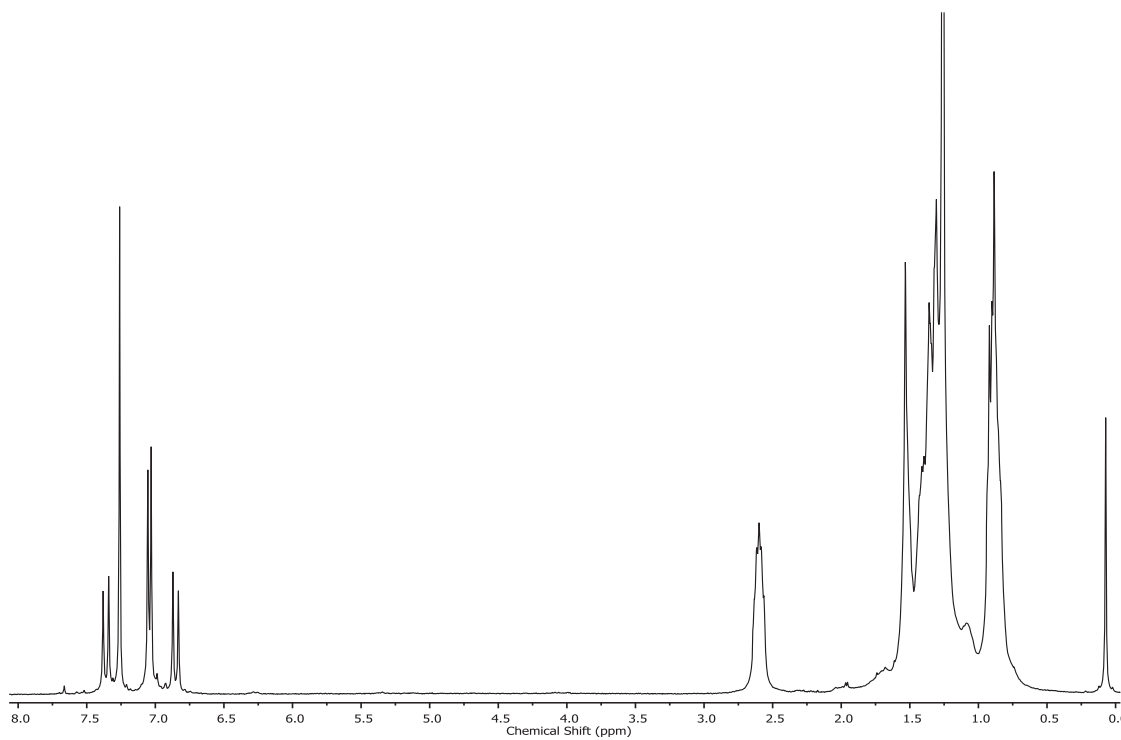

Figure S31. ^{1}H-NMR spectrum of compound **(αH)-2TV-PTM**

Figure S32. ^{13}C-NMR spectrum of compound **(αH)-2TV-PTM**
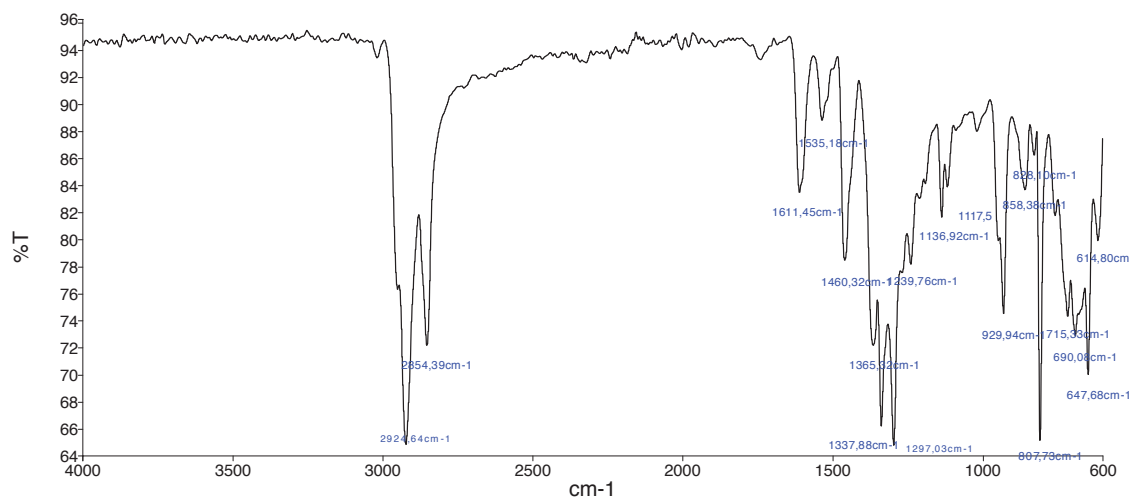
Figure S33. FT-IR spectrum of compound **(αH)-2TV-PTM**

Figure S34. Mass spectrum of compound **(αH)-2TV-PTM**

Figure S35. ^{1}H-NMR spectrum of compound **(αH,α'H)-PTM-2TV-PTM**
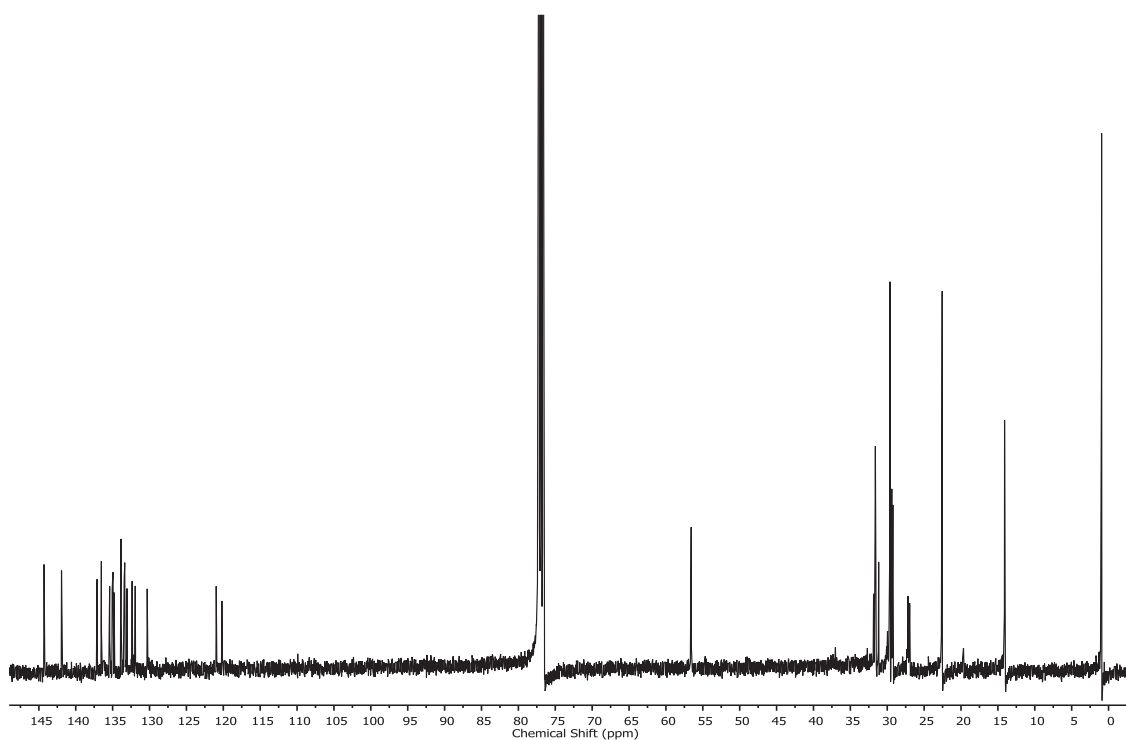
Figure S36. ^{13}C-NMR spectrum of compound **(αH,α'H)-PTM-2TV-PTM**
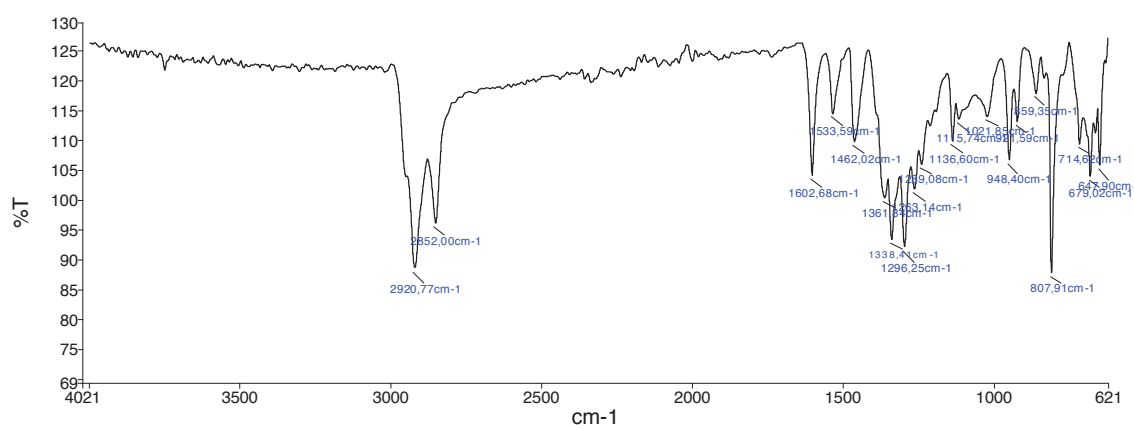
Figure S37. FT-IR spectrum of compound **(αH,α'H)-PTM-2TV-PTM**
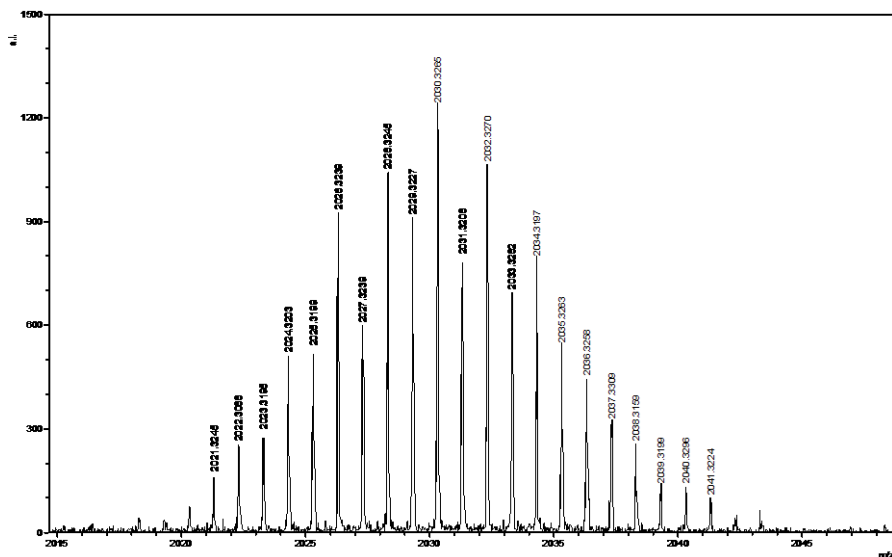
Figure S38. Mass spectrum of compound **(αH,α'H)-PTM-2TV-PTM**

Figure S39. ^{1}H-NMR spectrum of compound **(αH,α'H)-PTM-3TV-PTM**
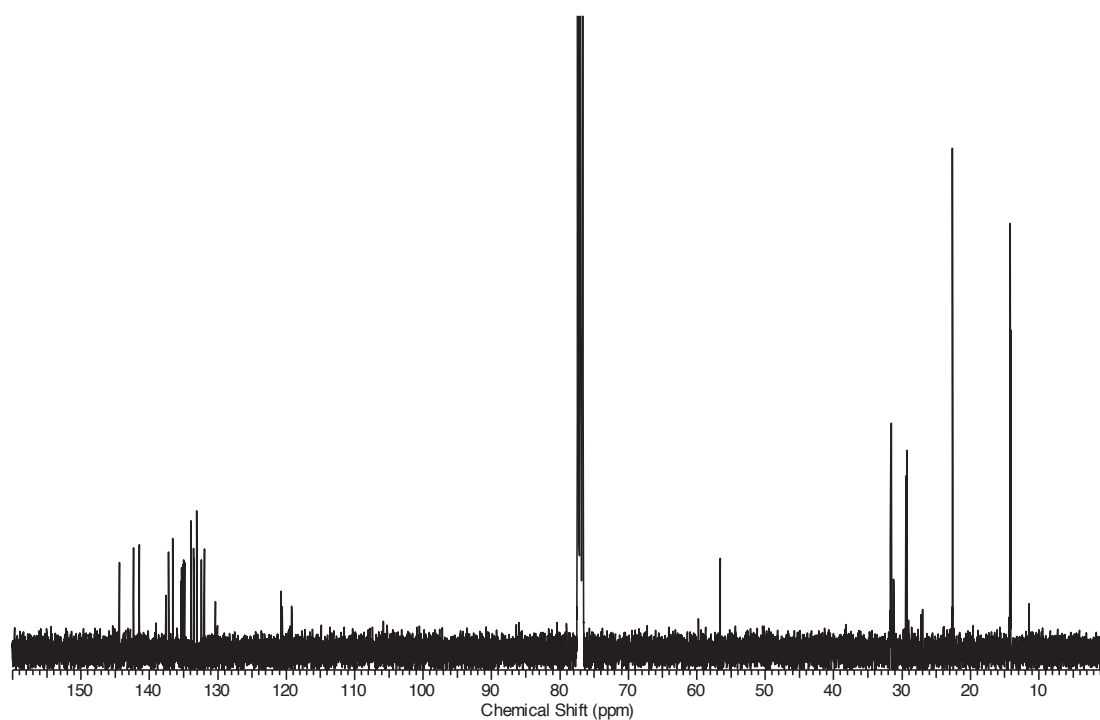
Figure S40. ^{13}C-NMR spectrum of compound **(αH,α'H)-PTM-3TV-PTM**
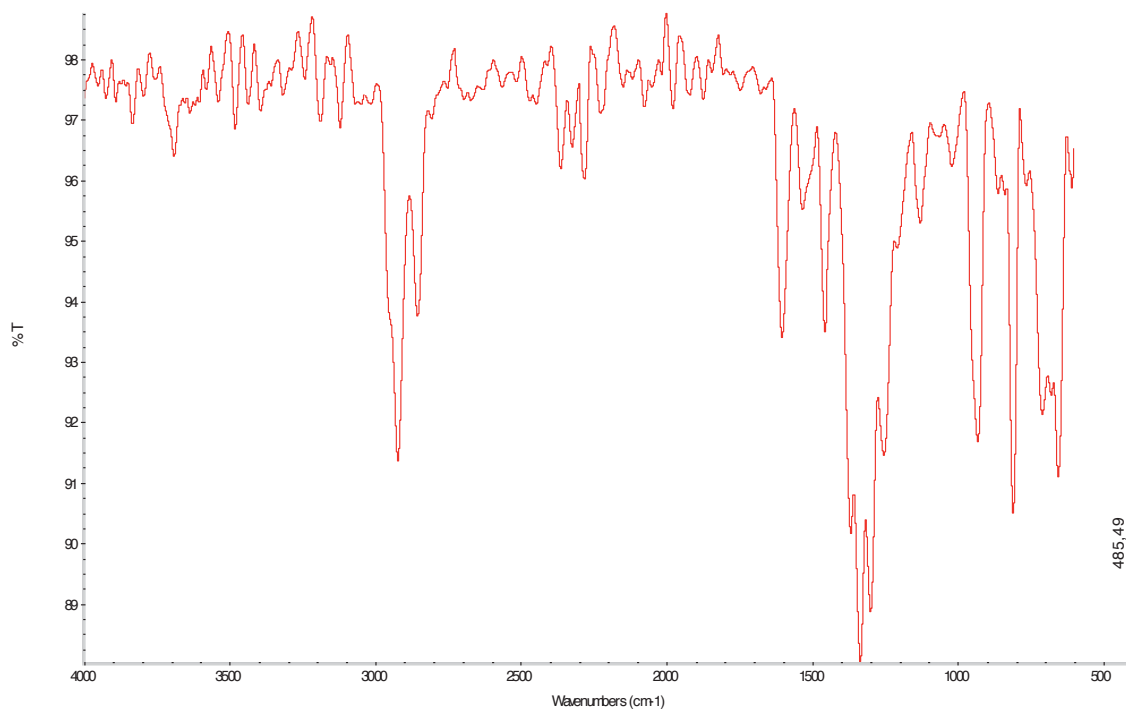
Figure S41. FT-IR spectrum of compound **(αH,α'H)-PTM-3TV-PTM**

Figure S42. Mass spectrum of compound **(αH,α'H)-PTM-3TV-PTM**

Figure S43. ^{1}H-NMR spectrum of compound **(αH,α'H)-PTM-4TV-PTM**
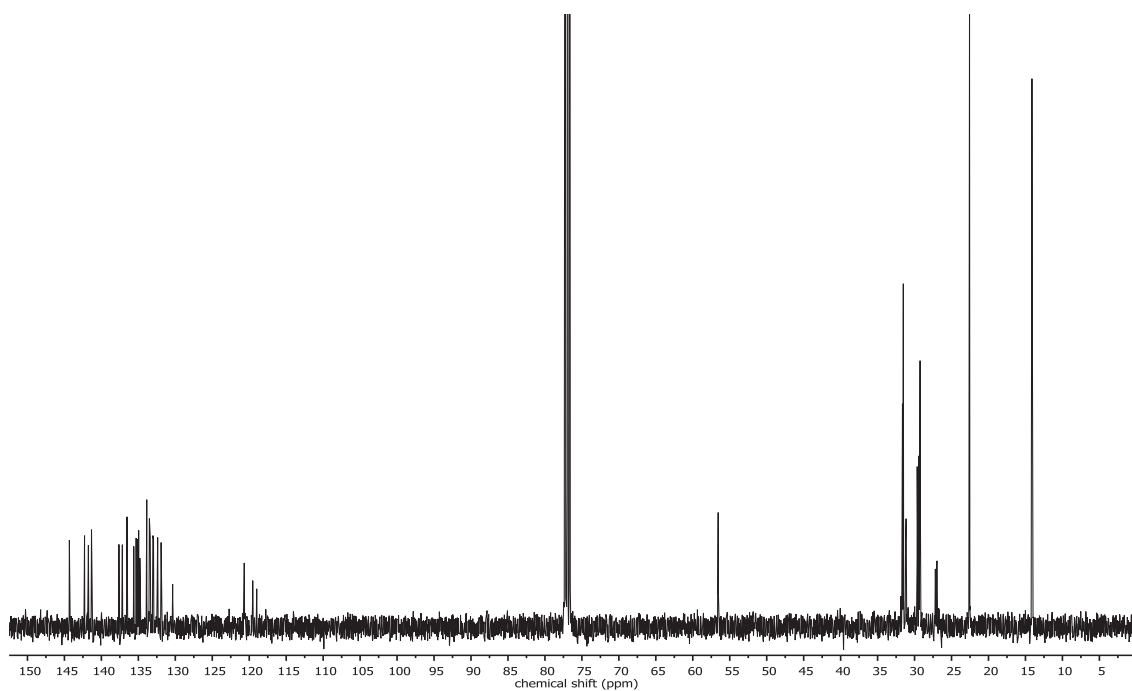
Figure S44. ^{13}C-NMR spectrum of compound **(αH,α'H)-PTM-4TV-PTM**
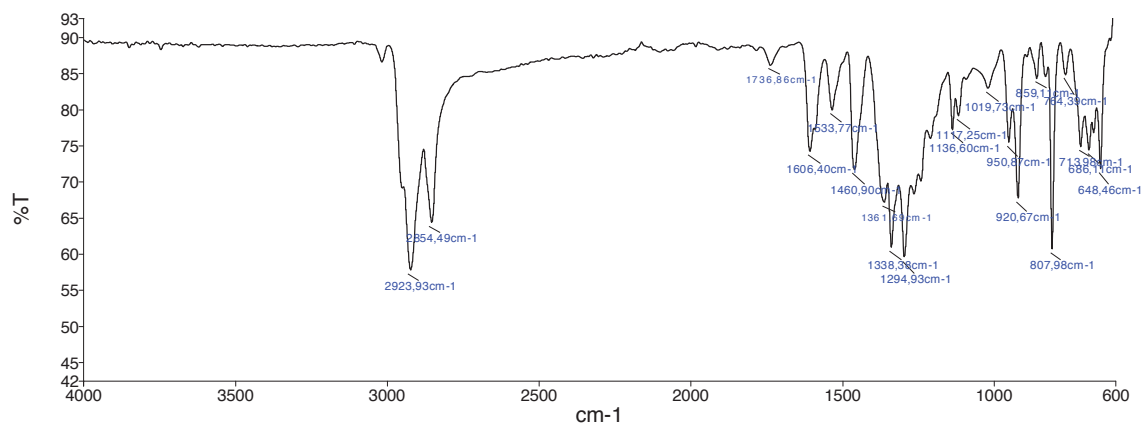
Figure S45. FT-IR spectrum of compound **(αH,α'H)-PTM-4TV-PTM**
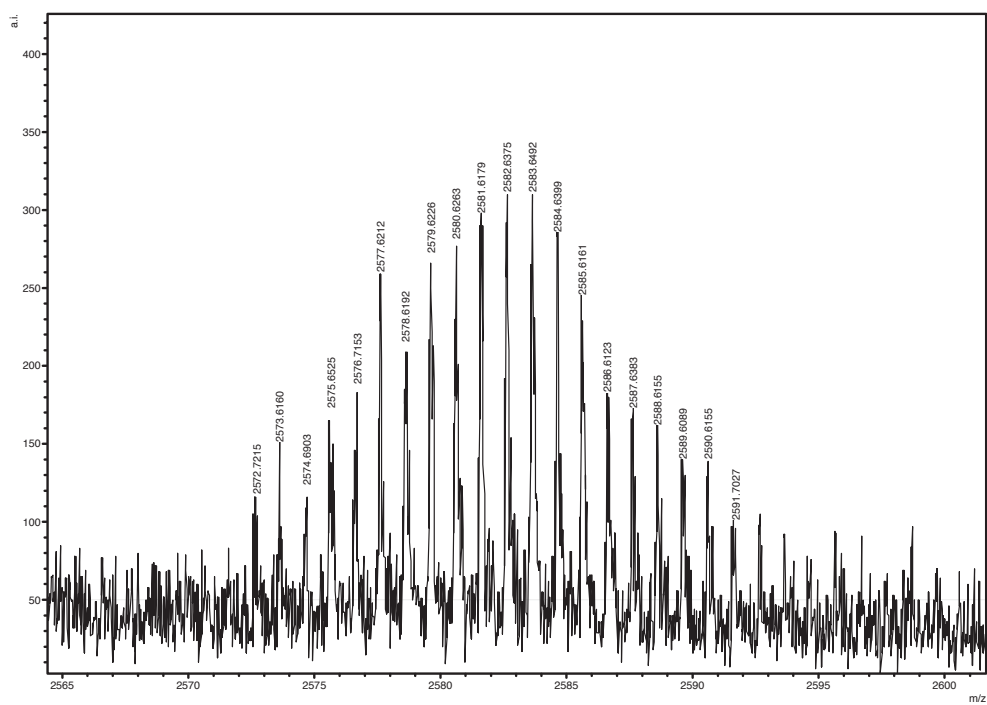
Figure S46 Mass spectrum of compound **(αH,α'H)-PTM-4TV-PTM**
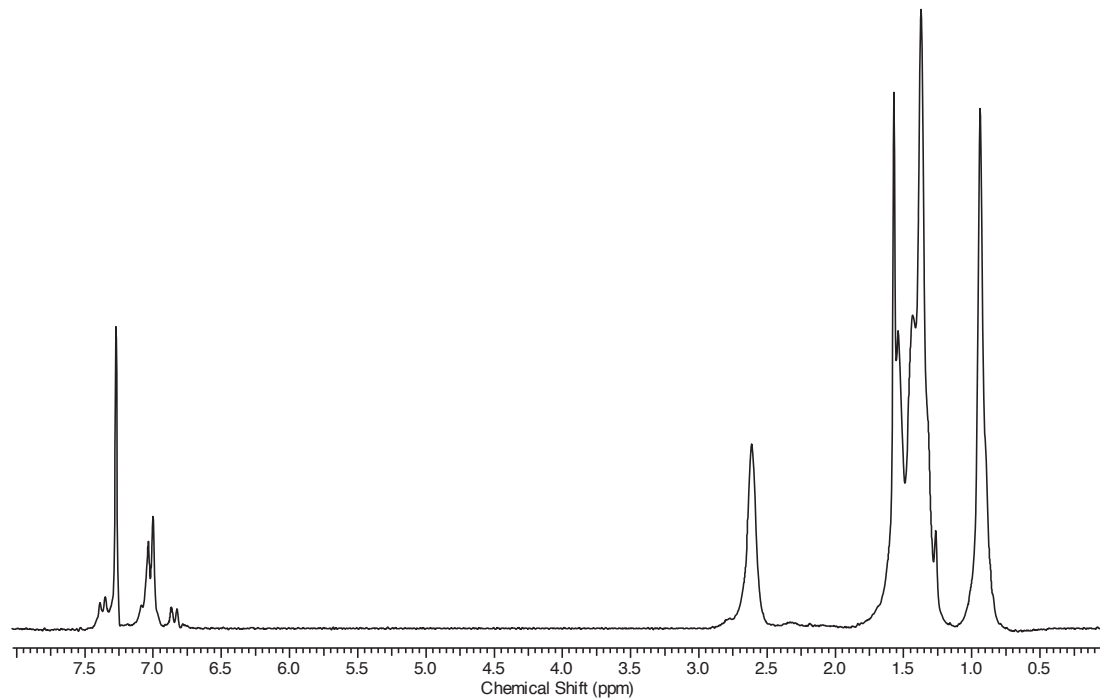
Figure S47. ^{1}H-NMR spectrum of compound **(αH,α'H)-PTM-5TV-PTM**
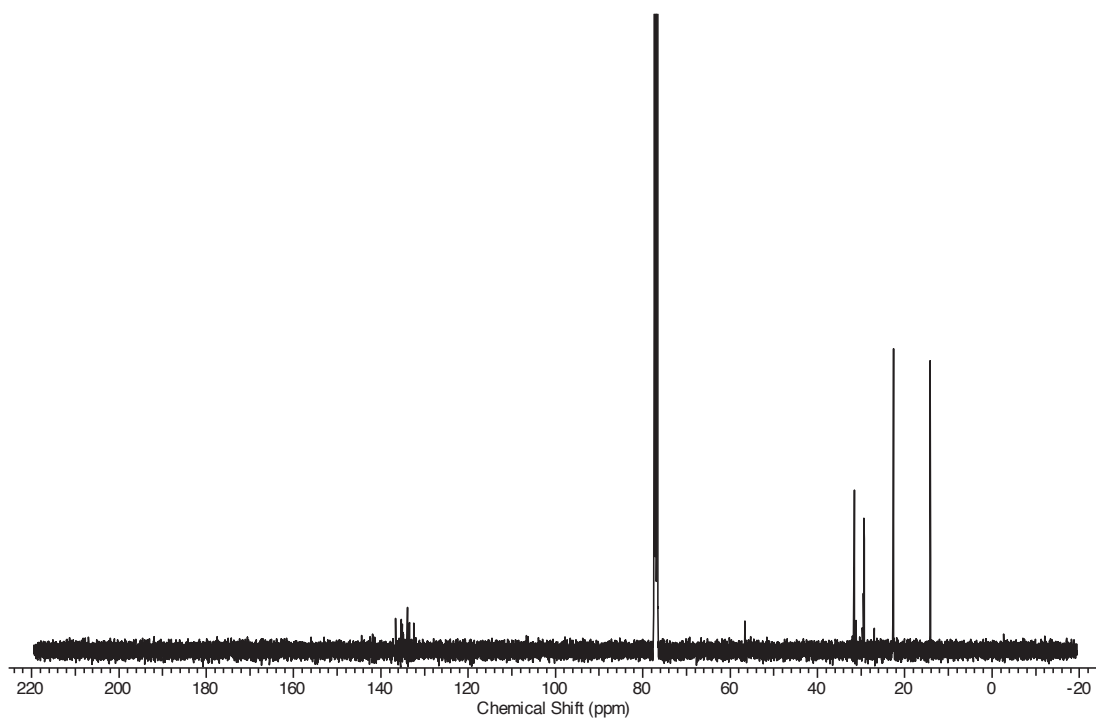
Figure S48. ^{13}C-NMR spectrum of compound **(αH,α'H)-PTM-5TV-PTM**
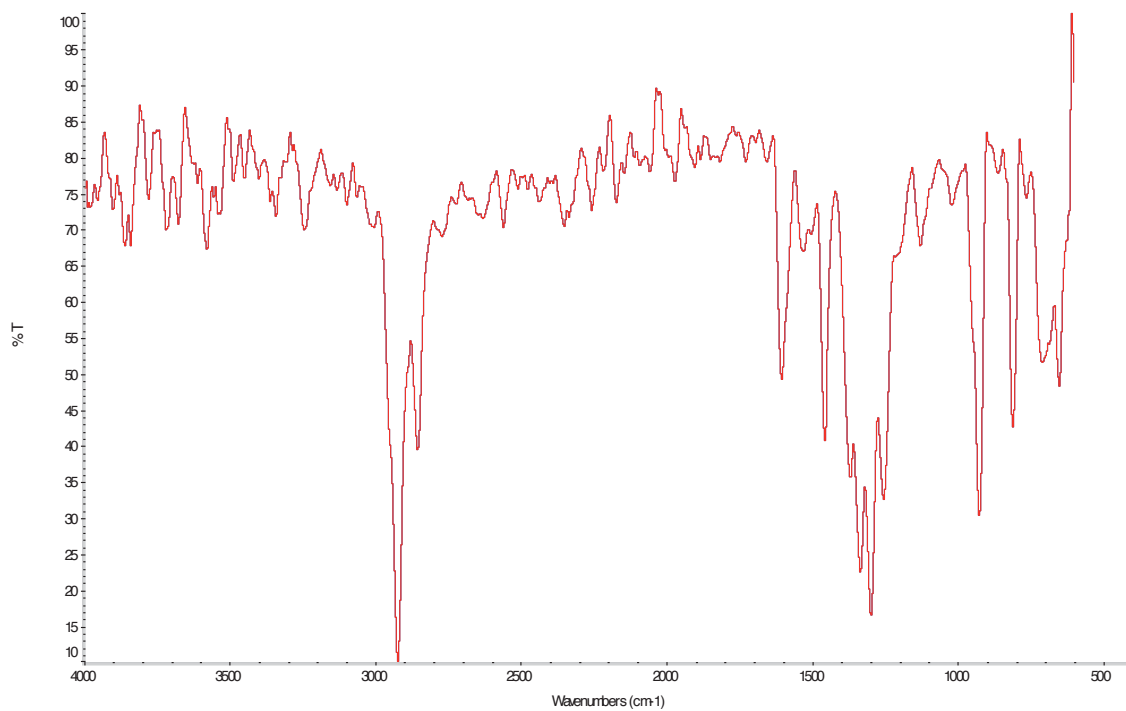
Figure S49. FT-IR spectrum of compound **(αH,α'H)-PTM-5TV-PTM**
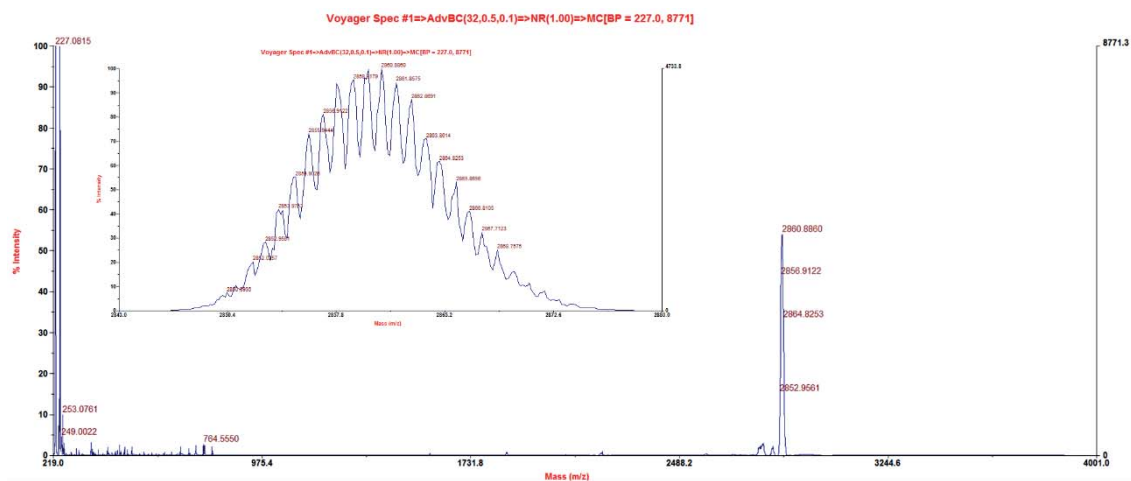
Figure S50. Mass spectrum of compound **(αH,α'H)-PTM-5TV-PTM**
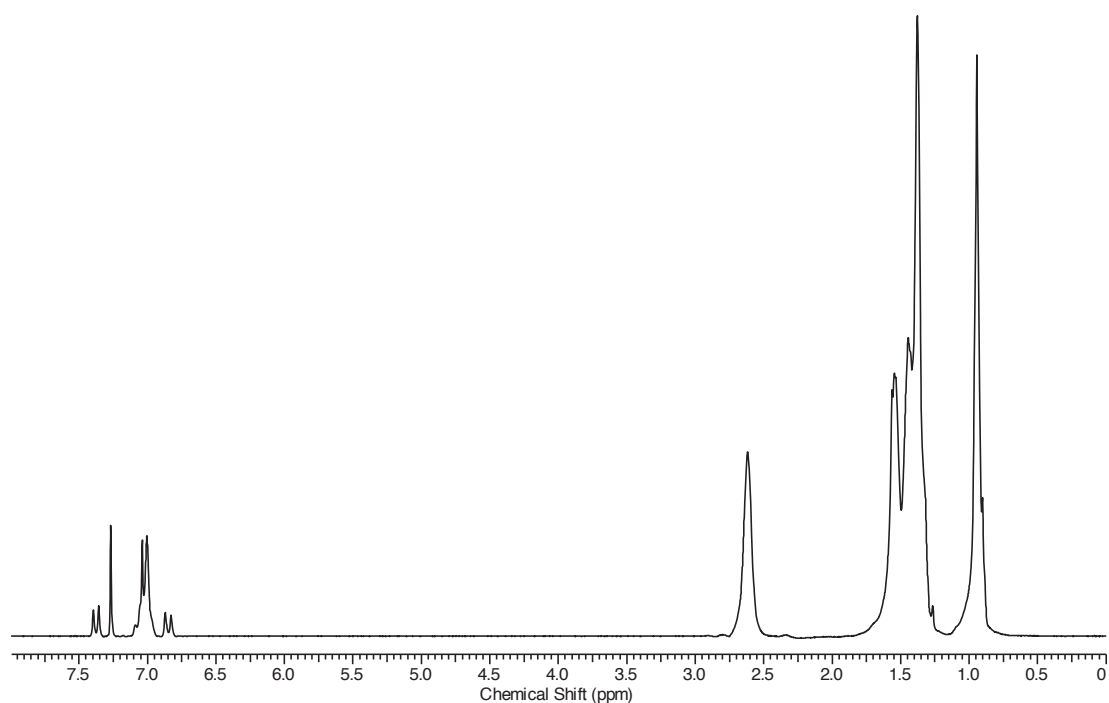
Figure S51. ^{1}H-NMR spectrum of compound **(αH,α'H)-PTM-6TV-PTM**
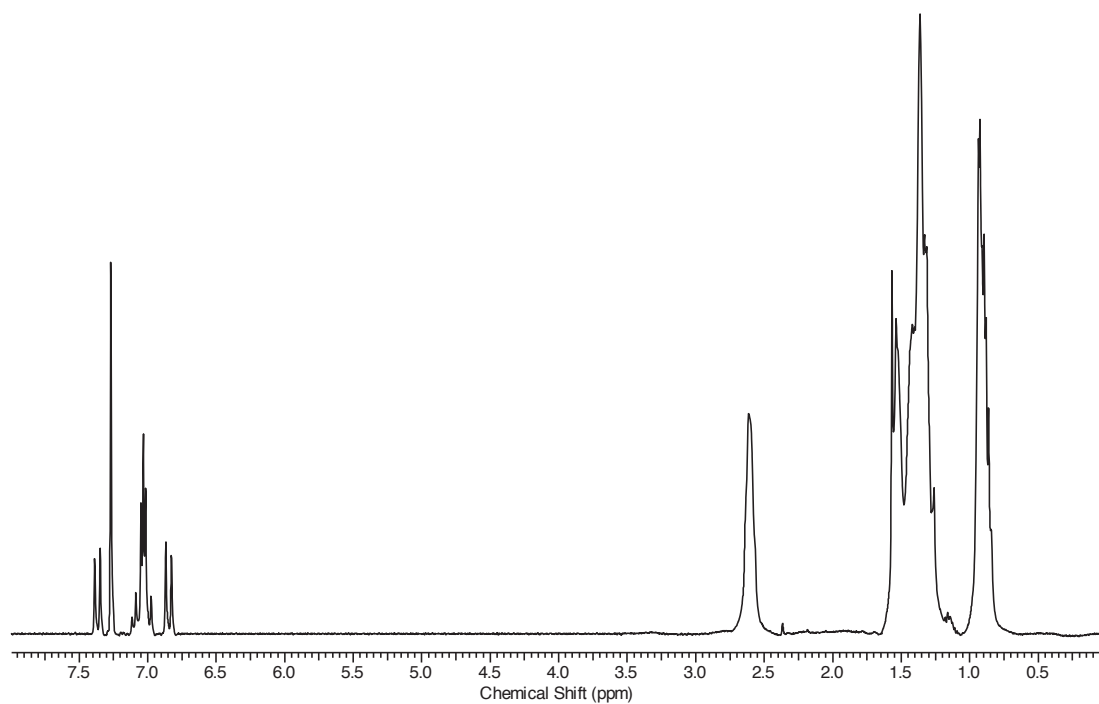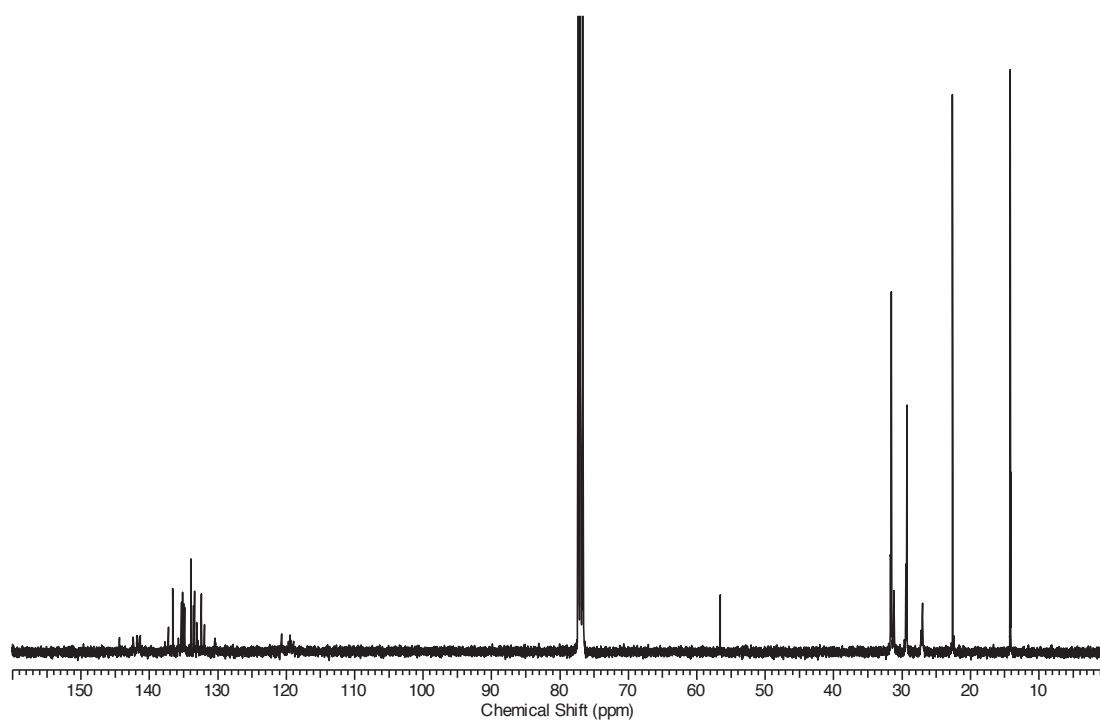
Figure S52. ^{13}C-NMR spectrum of compound **(αH,α'H)-PTM-6TV-PTM**

Figure S53. FT-IR spectrum of compound **(αH,α'H)-PTM-6TV-PTM**
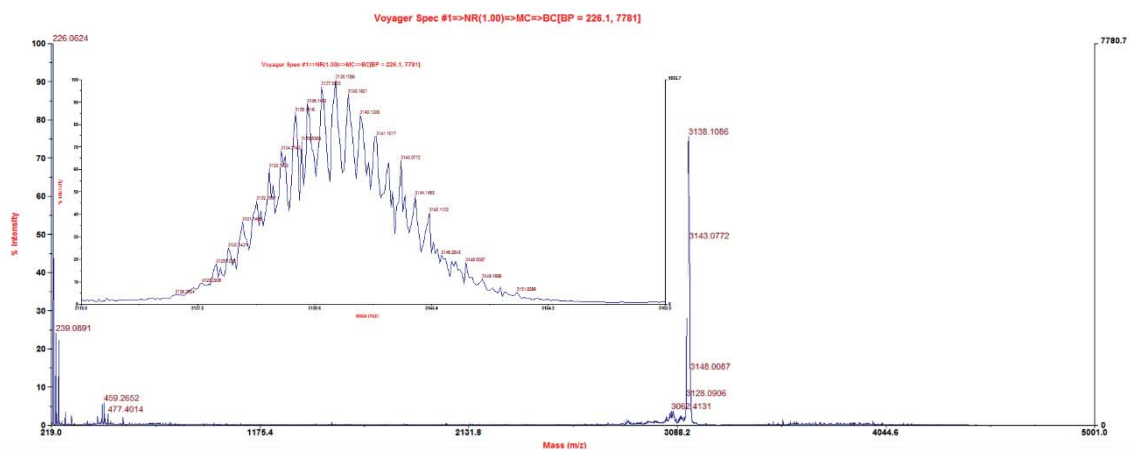
Figure S54. Mass spectrum of compound **(αH,α'H)-PTM-6TV-PTM**
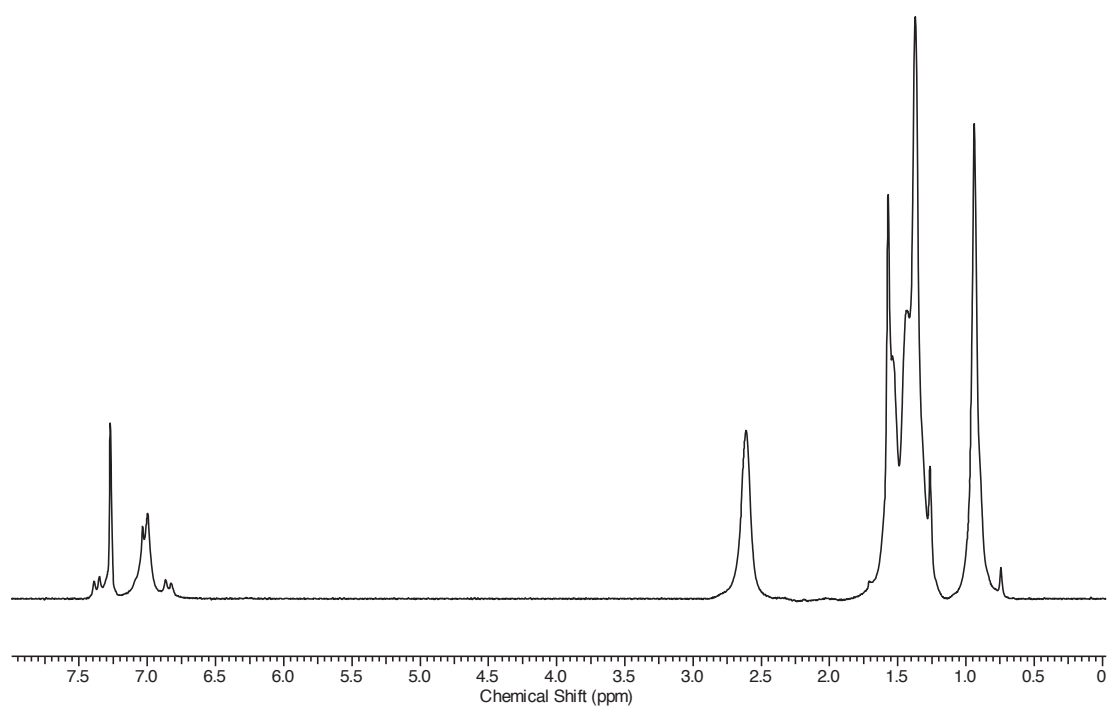
Figure S55. ¹H-NMR spectrum of compound **(αH,α'H)-PTM-7TV-PTM**
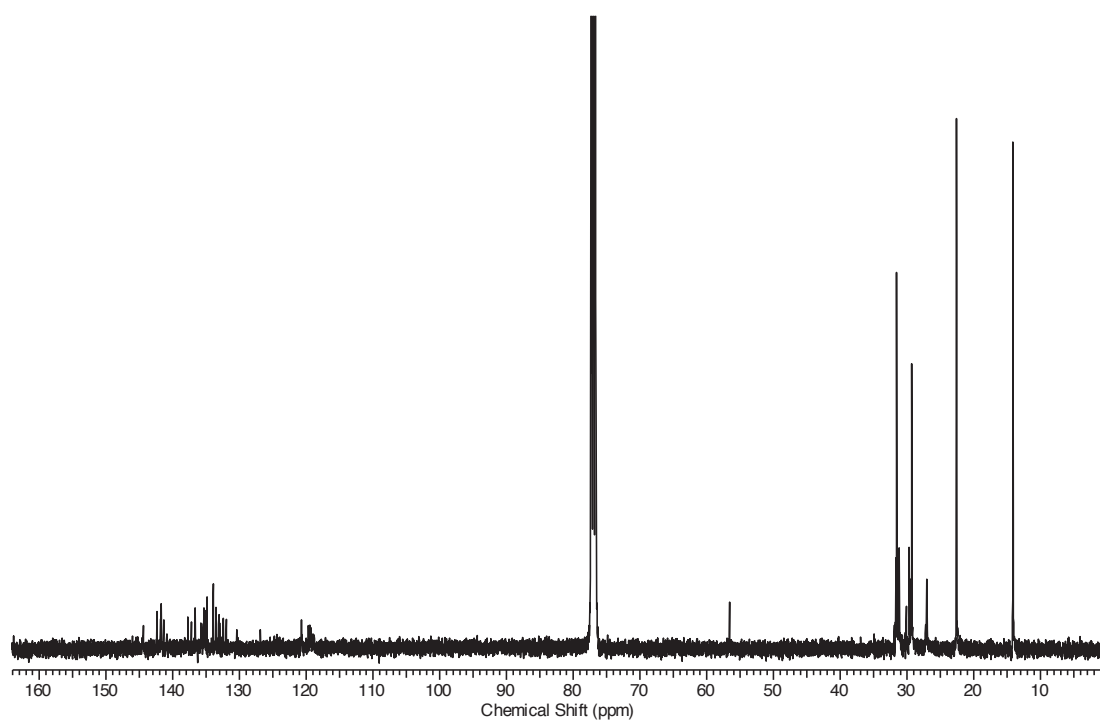
Figure S56. ^{13}C-NMR spectrum of compound **(αH,α'H)-PTM-7TV-PTM**
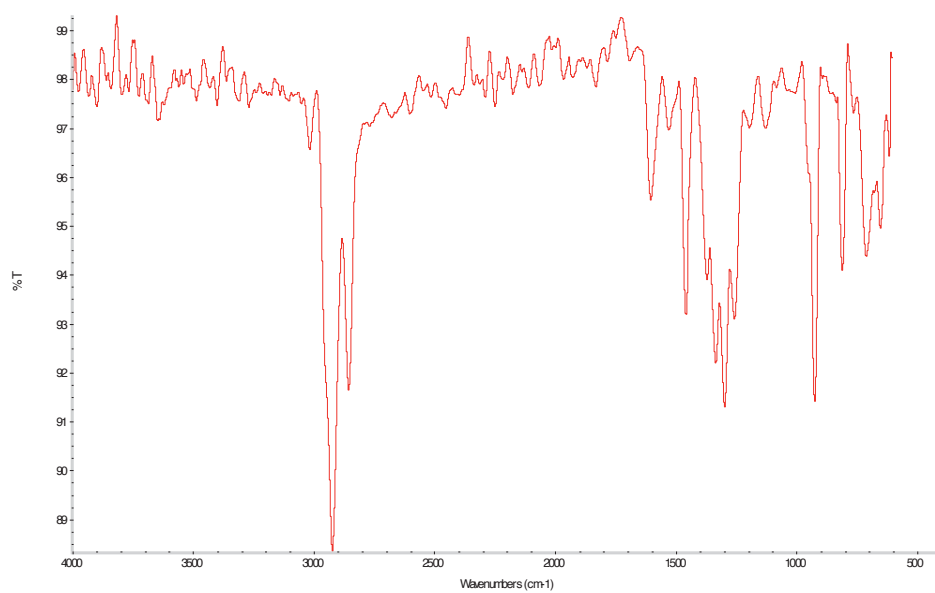
Figure S57. FT-IR spectrum of compound **(αH,α'H)-PTM-7TV-PTM**
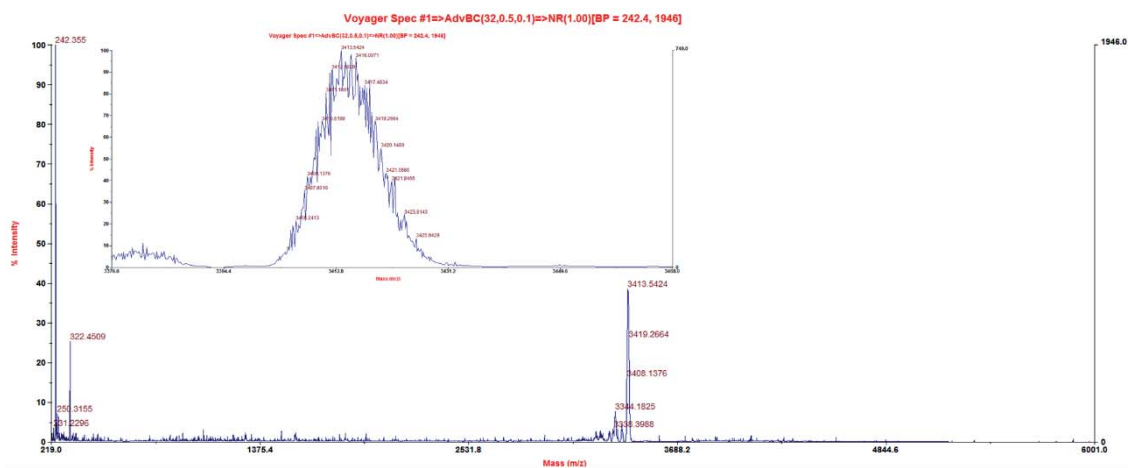
Figure S58. Mass spectrum of compound **(αH,α'H)-PTM-7TV-PTM**

H / Gauss
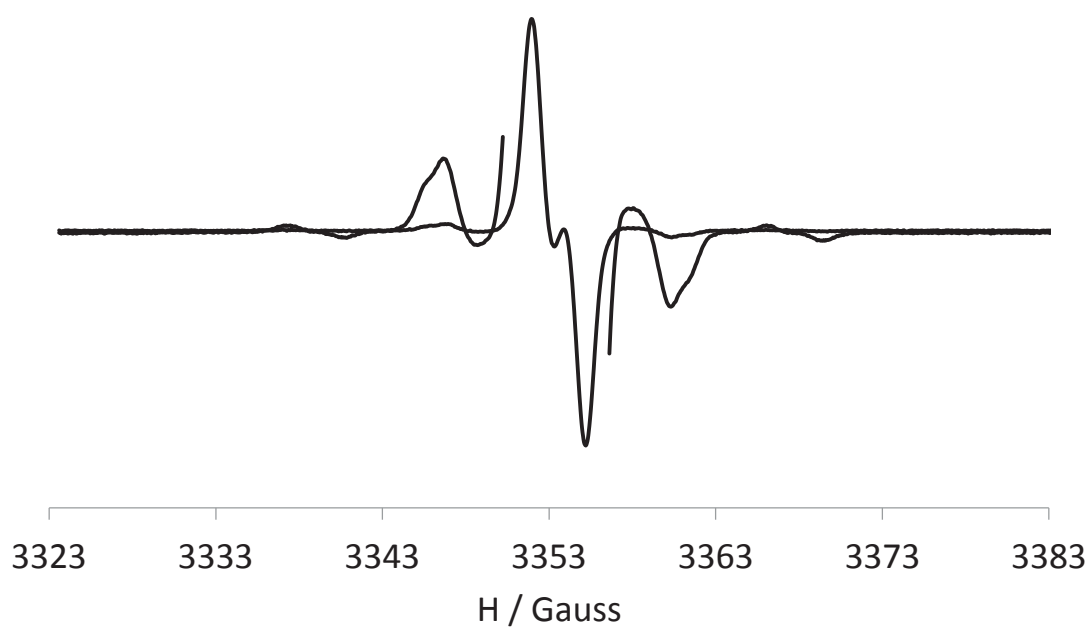
Figure S59. Isotropic solution EPR spectra of radical **•PTM-2TV** in Toluene/CH$_2$Cl$_2$ (1/1) at 300K.
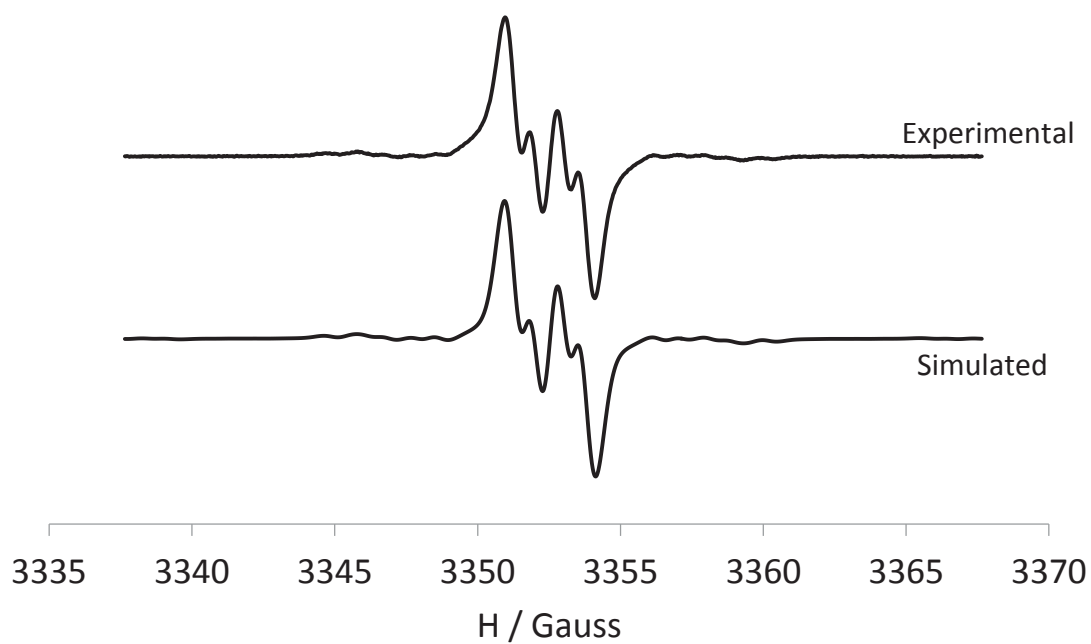
Figure S60. Experimental and simulated isotropic solution EPR spectra of radical •**PTM-2TV** in Toluene/CH_2Cl_2 (1/1) at 240K
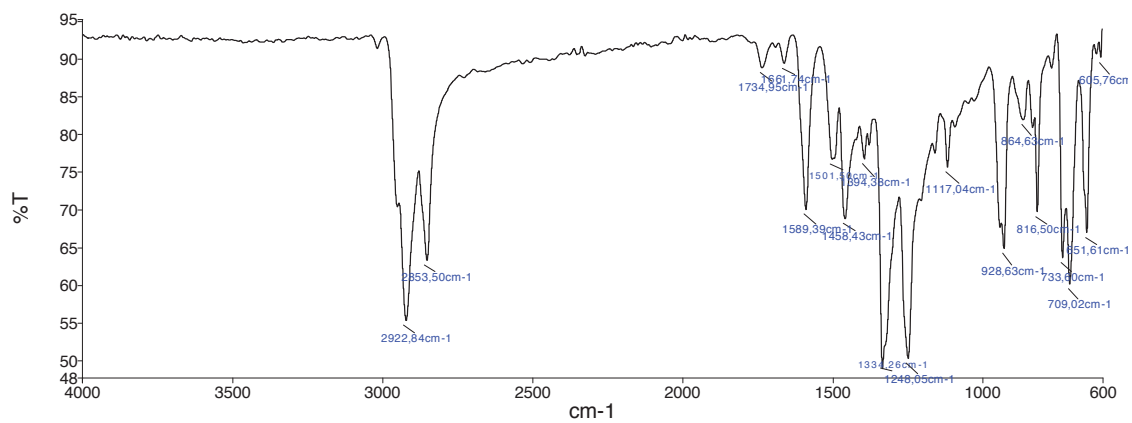
Figure S61. FT-IR spectrum of radical •**PTM-2TV**.
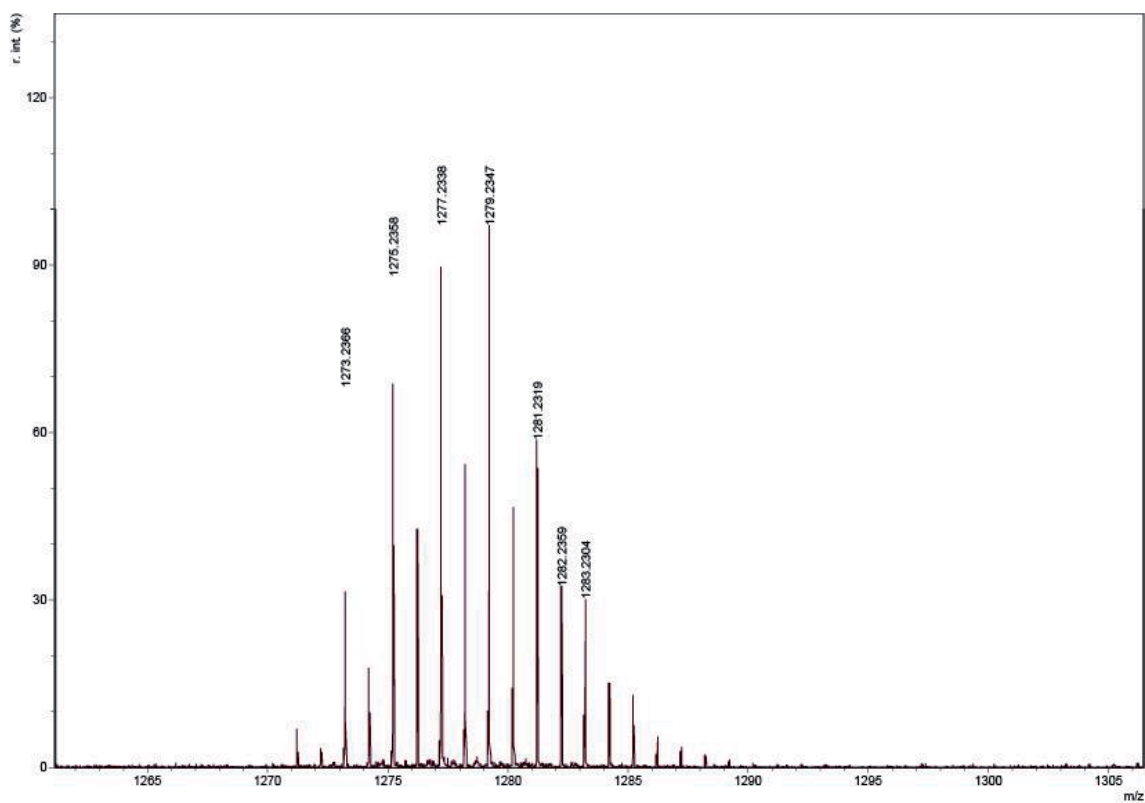
Figure S62. Mass spectrum of radical •**PTM-2TV**.

H / Gauss
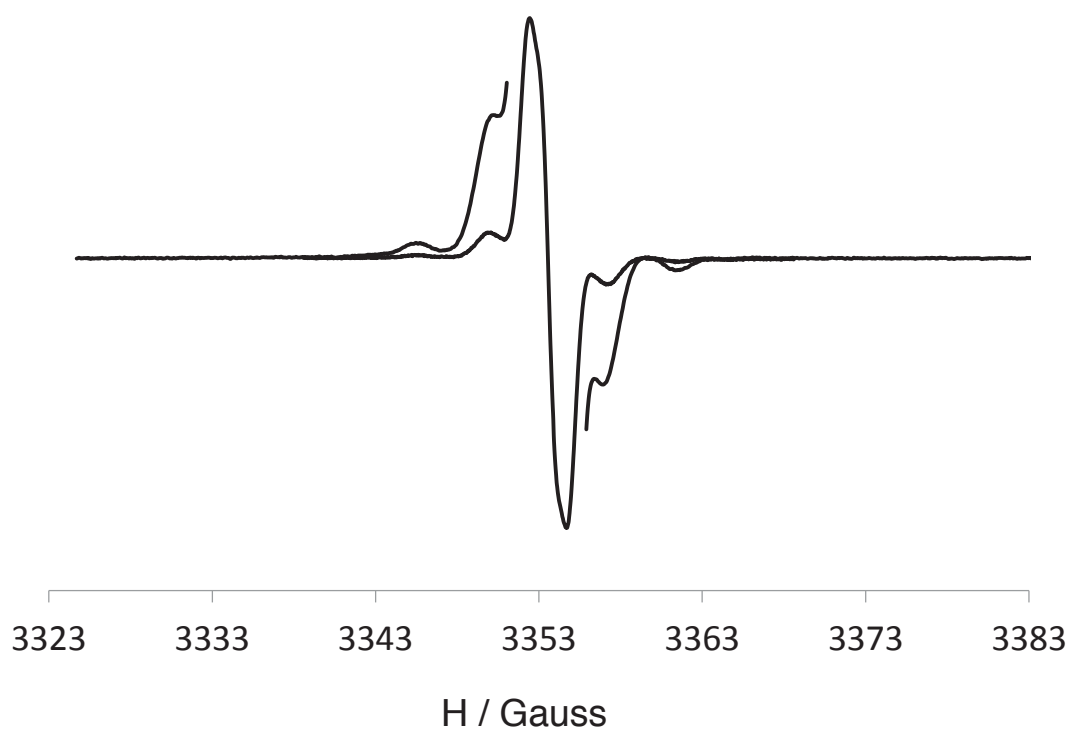
Figure S63. Isotropic solution EPR spectra of diradical •**PTM-2TV-PTM**• (**1**) in Toluene/CH$_2$Cl$_2$ (1/1) at 300K.
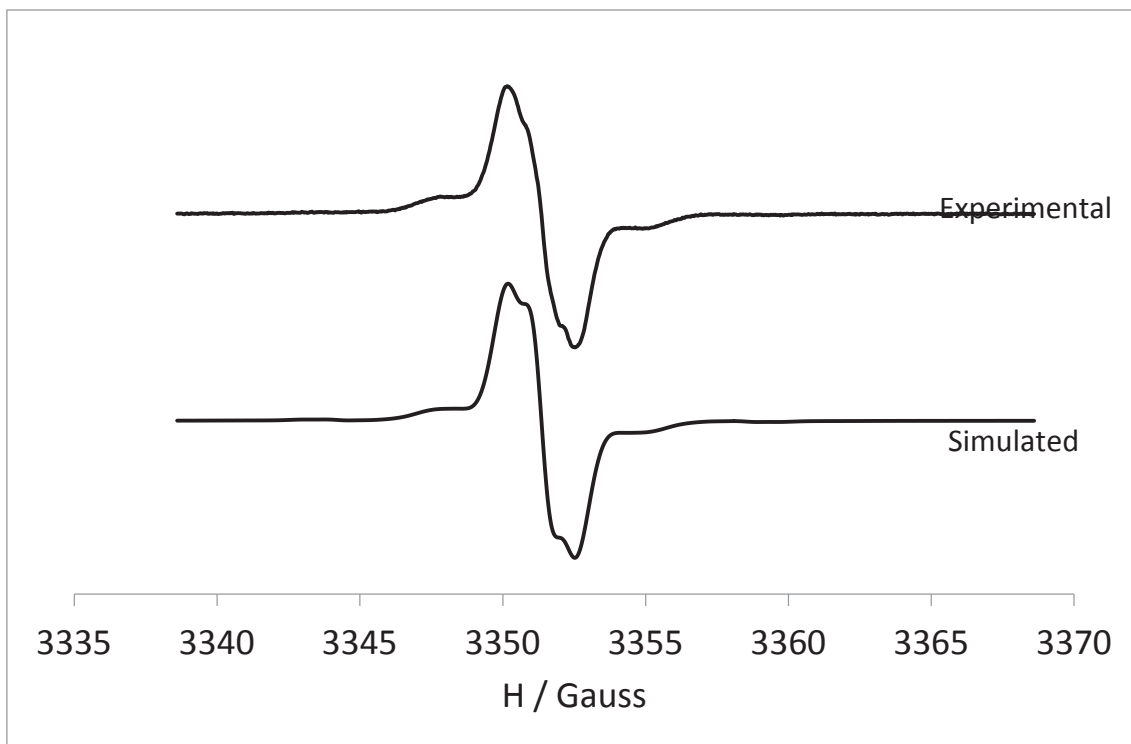
Figure S64. Experimental and simulated isotropic solution EPR spectra of biradical •**PTM-2TV-PTM**• (**1**) in Toluene/CH₂Cl₂ (1/1) at 220K
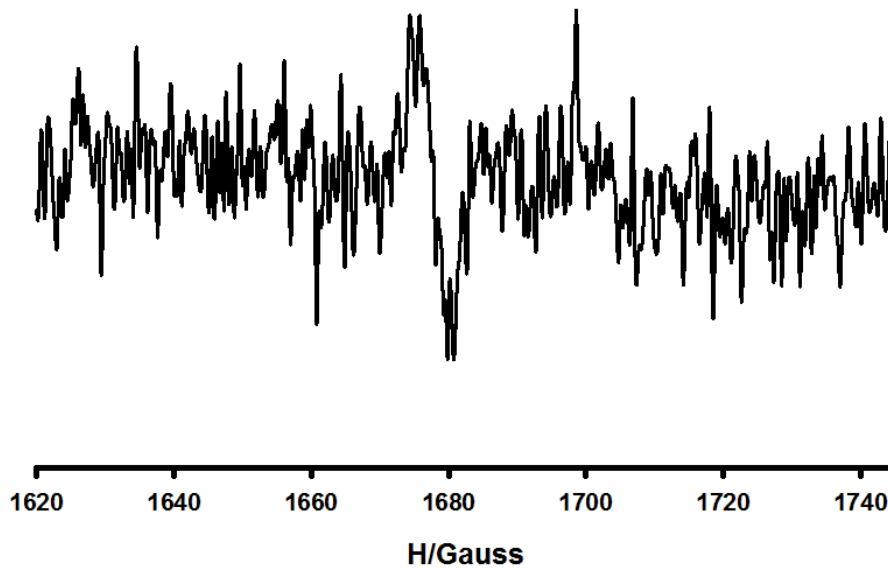
Figure S65. $\Delta M_s=2$ transition of diradical •**PTM-2TV-PTM**• (**1**) in Toluene/CH₂Cl₂ (1/1) at 120K
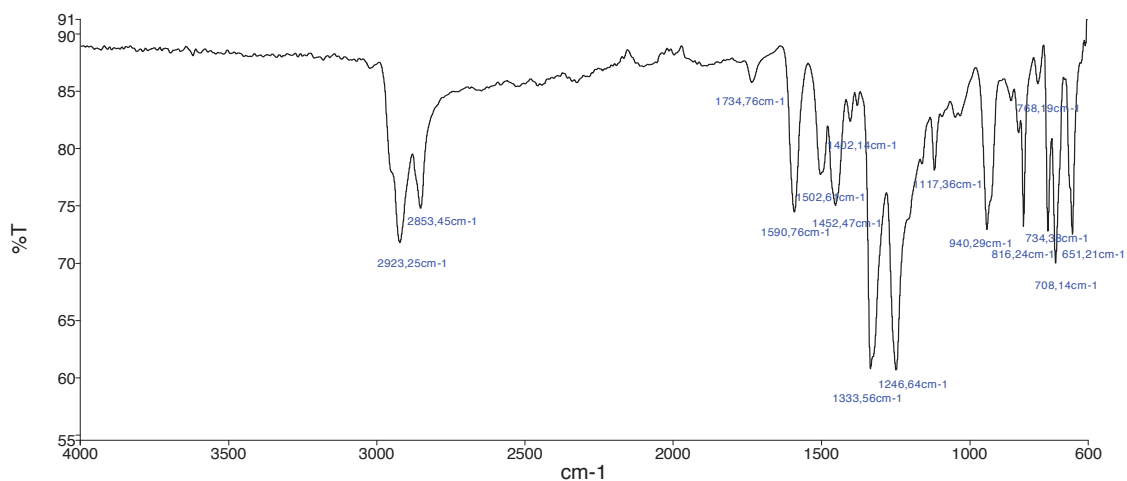
Figure S66. FT-IR spectrum of diradical •**PTM-2TV-PTM**• (**1**)
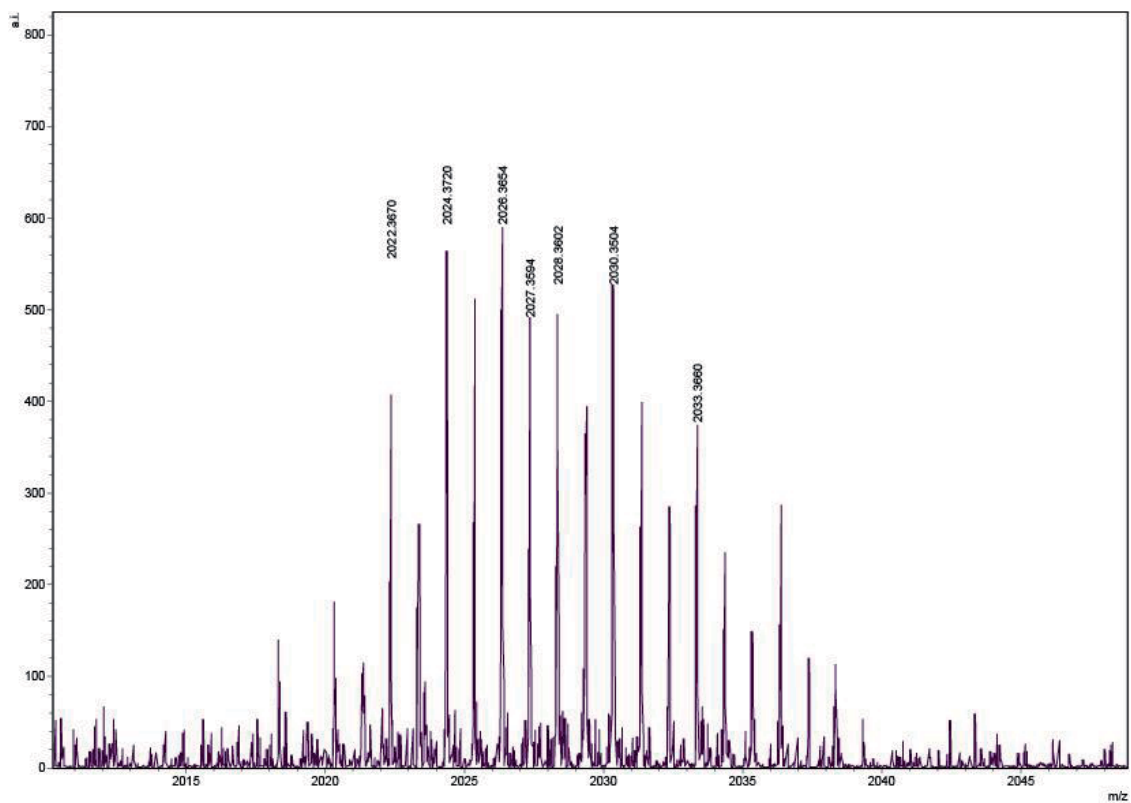
Figure S67. Mass spectrum of diradical •**PTM-2TV-PTM**• (**1**)
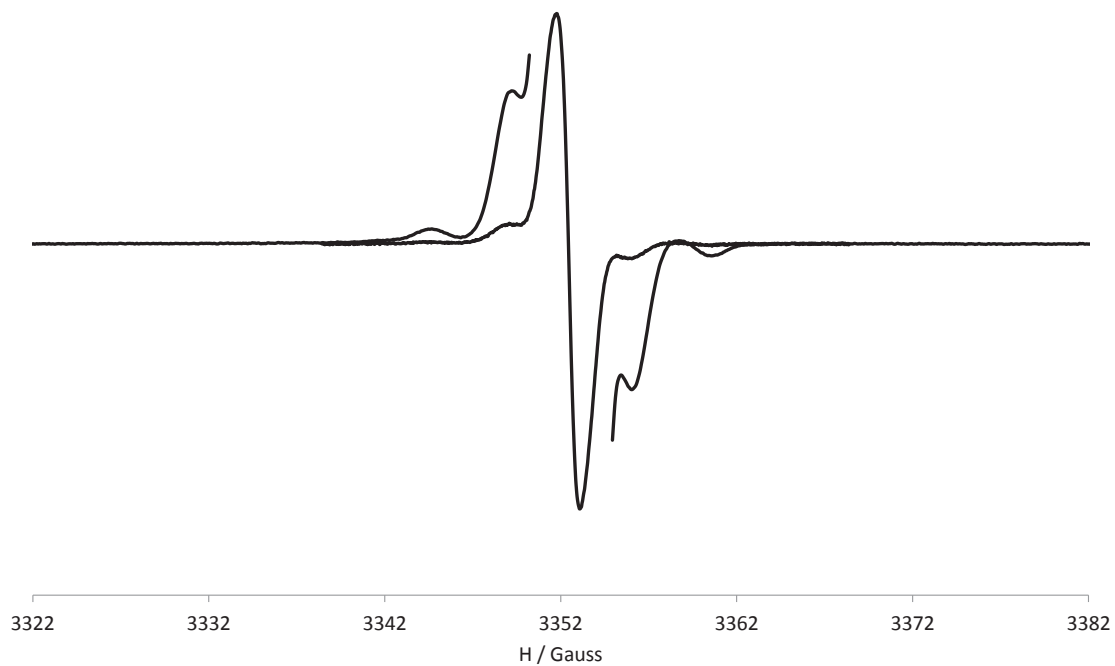
Figure S68. Isotropic solution EPR spectra of diradical •**PTM-3TV-PTM**• (**2**) in Toluene/CH_2Cl_2 (1/1) at 300K.

Experimental
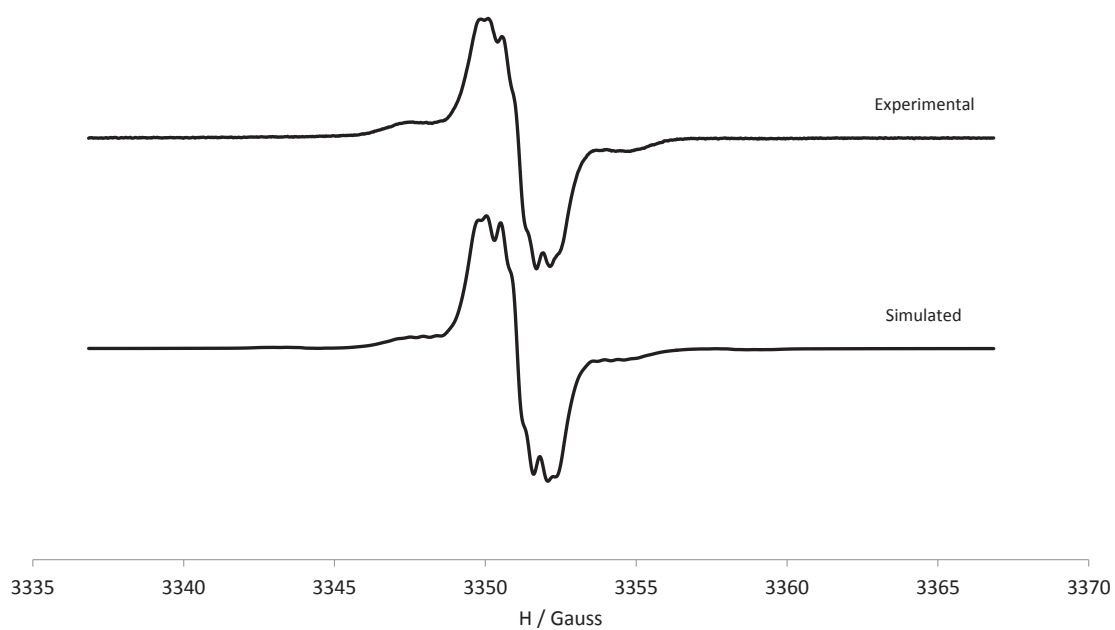
Simulated

Figure S69. Experimental and simulated isotropic solution EPR spectra of diradical •**PTM-3TV-PTM**• (**2**) in Toluene/CH_2Cl_2 (1/1) at 220K
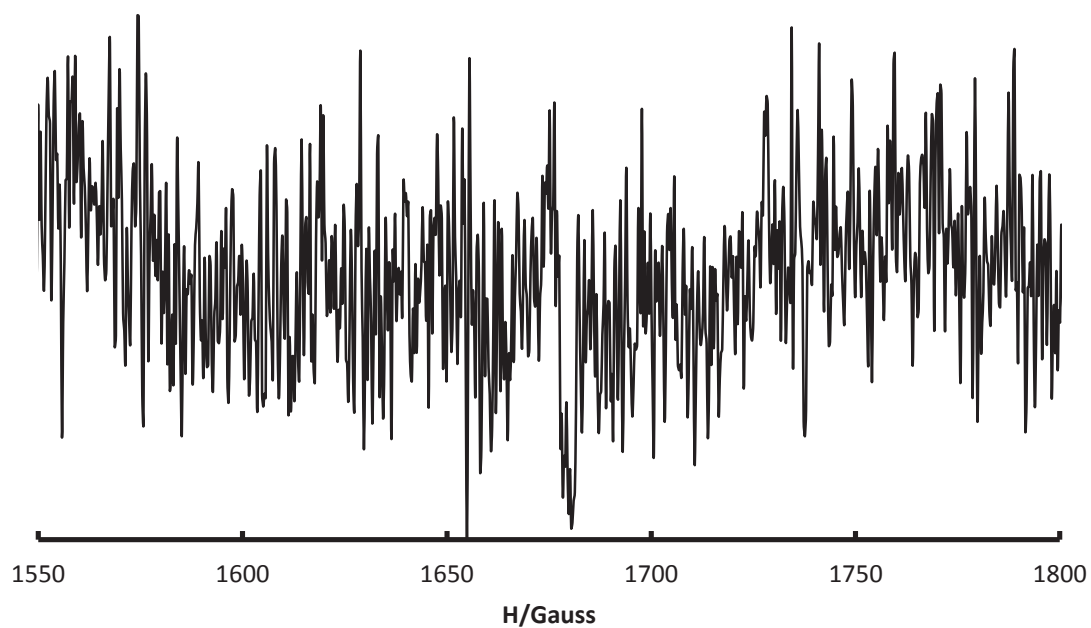
Figure S70. $\Delta M_s=2$ transition of diradical **°PTM-3TV-PTM°** (**2**) in Toluene/CH$_2$Cl$_2$ (1/1) at 120K
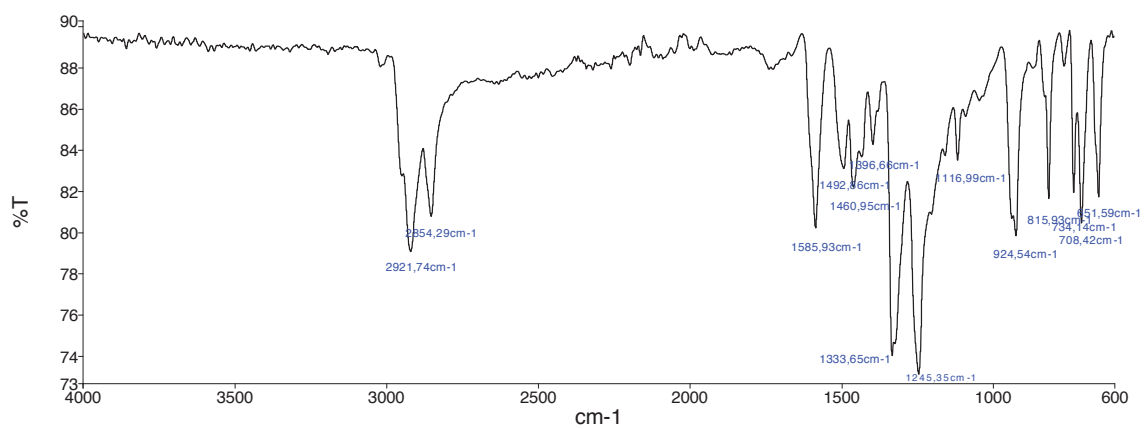
Figure S71. FT-IR spectrum of diradical **°PTM-3TV-PTM°** (**2**)
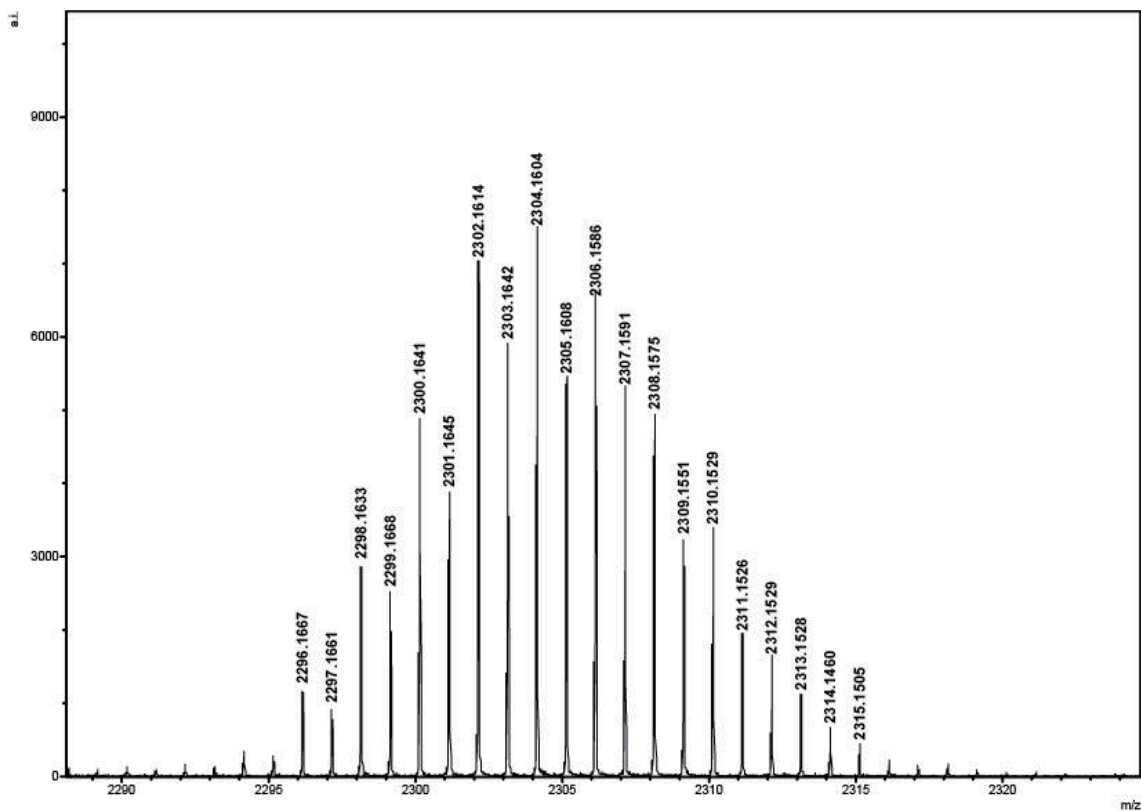
Figure S72. Mass spectrum of diradical •**PTM-3TV-PTM**• (**2**)
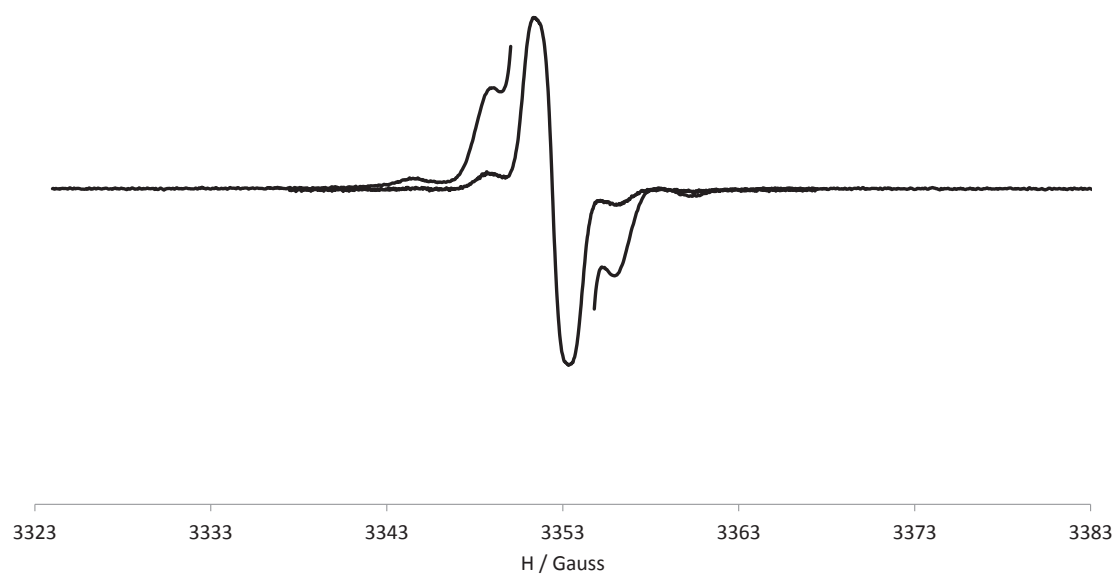
Figure S73. Isotropic solution EPR spectra of diradical •**PTM-4TV-PTM**• (**3**) in Toluene/CH$_2$Cl$_2$ (1/1) at 300K
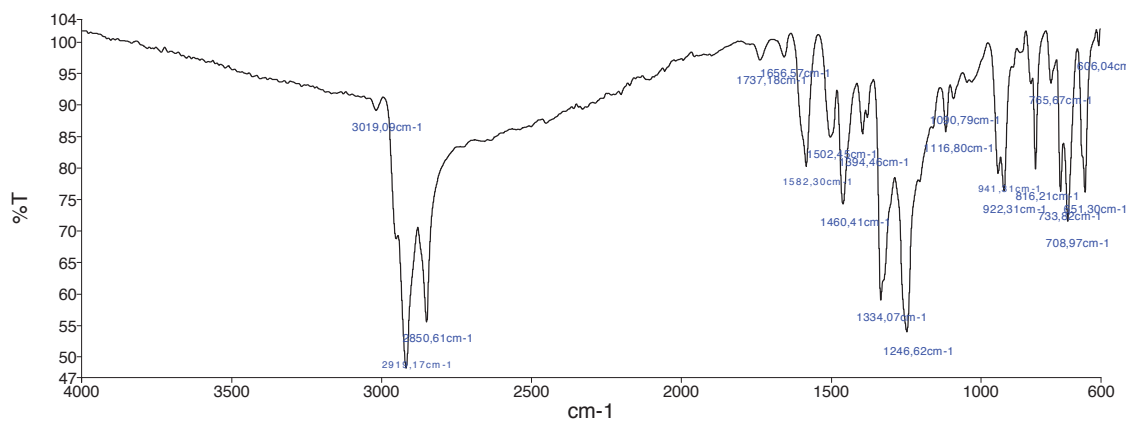
Figure S74. FT-IR spectrum of diradical •**PTM-4TV-PTM**• (**3**)
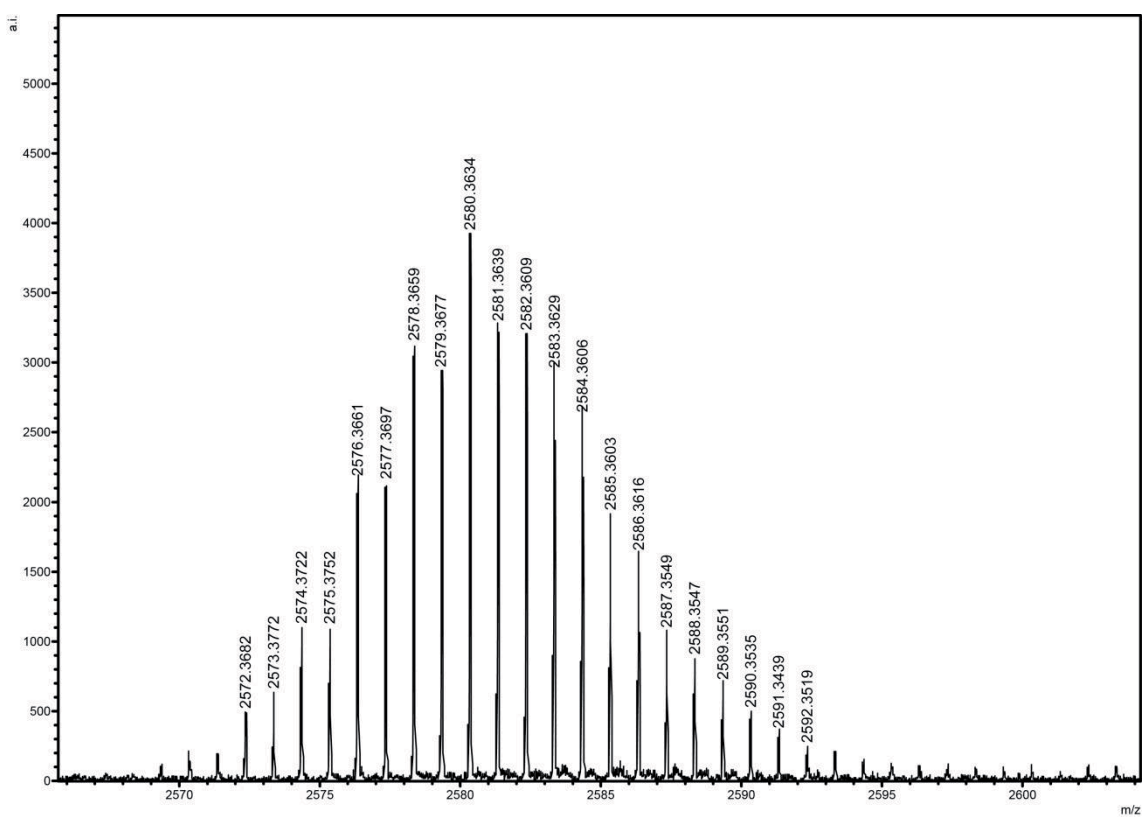
Figure S75. Mass spectrum of diradical •**PTM-4TV-PTM**• (**3**)
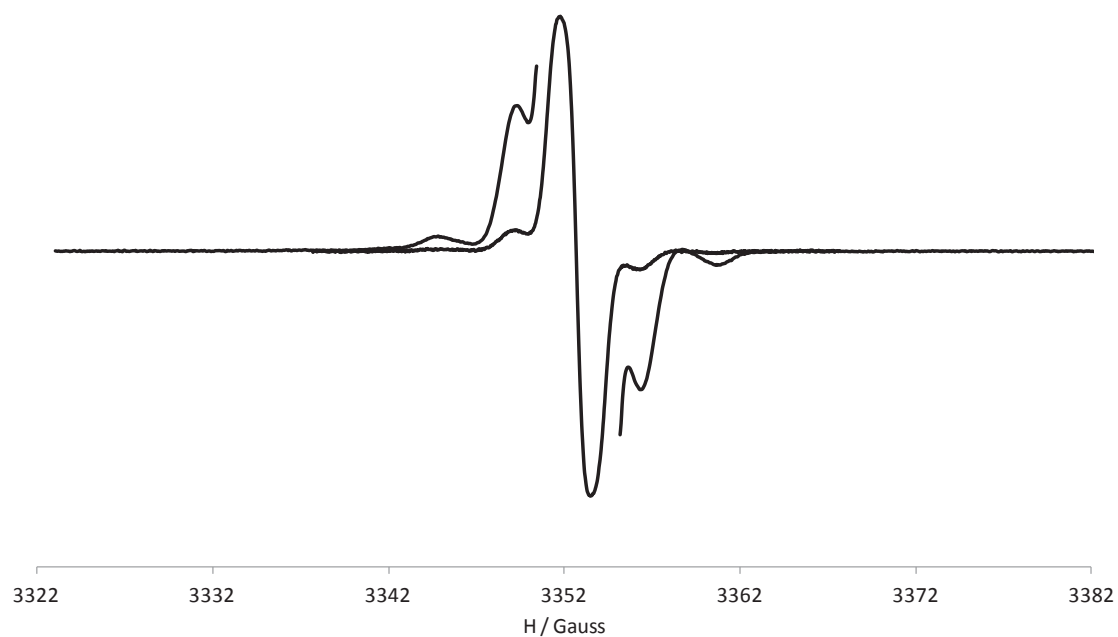
Figure S76. Isotropic solution EPR spectra of diradical $^\bullet$**PTM-5TV-PTM**$^\bullet$ (**4**) in Toluene/CH$_2$Cl$_2$ (1/1) at 300K
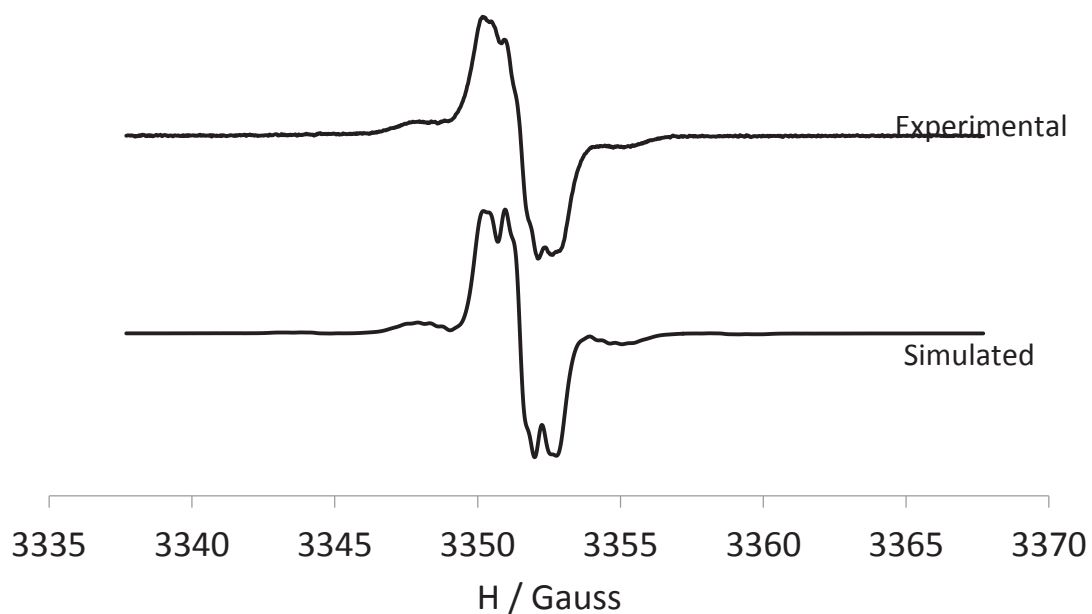
Figure S77. Experimental and simulated isotropic solution EPR spectra of diradical $^\bullet$**PTM-5TV-PTM**$^\bullet$ (**4**) in Toluene/CH$_2$Cl$_2$ (1/1) at 220K
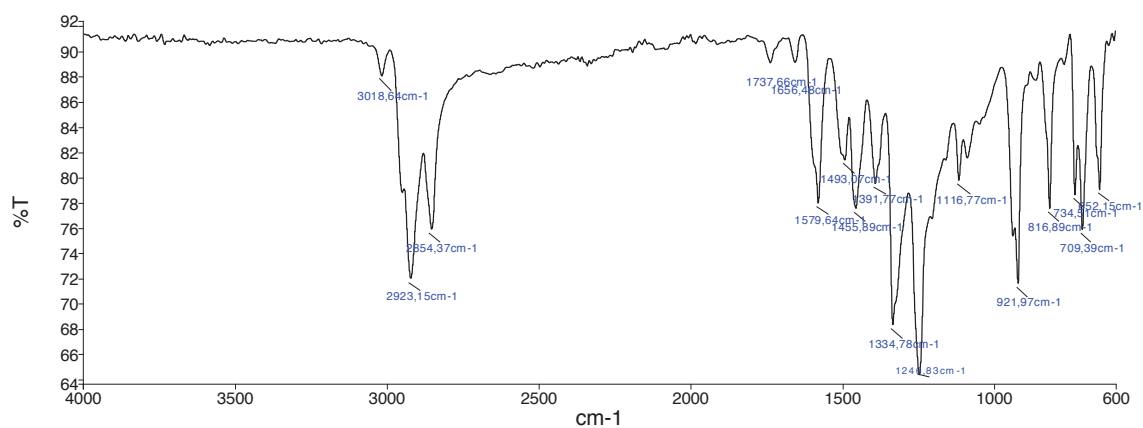
Figure S78. FT-IR spectrum of compound •**PTM-5TV-PTM**• (**4**)
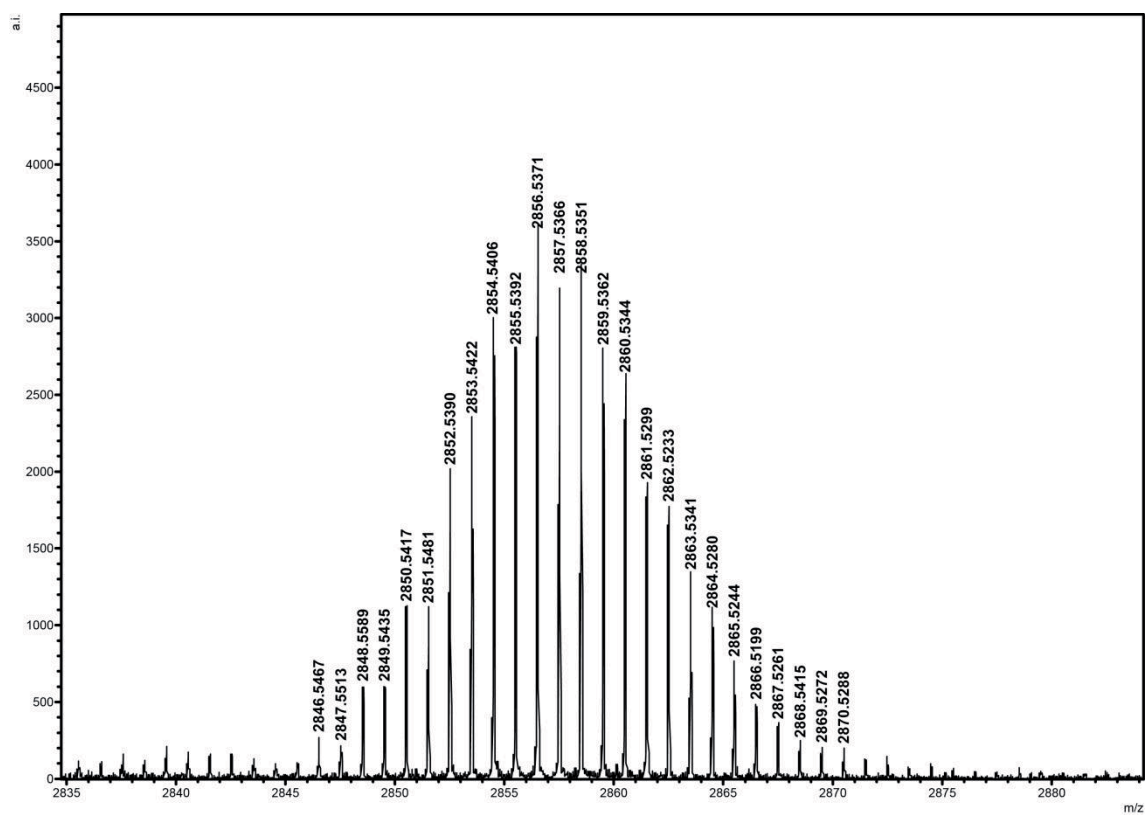
Figure S79. Mass spectrum of diradical •**PTM-5TV-PTM**• (**4**)
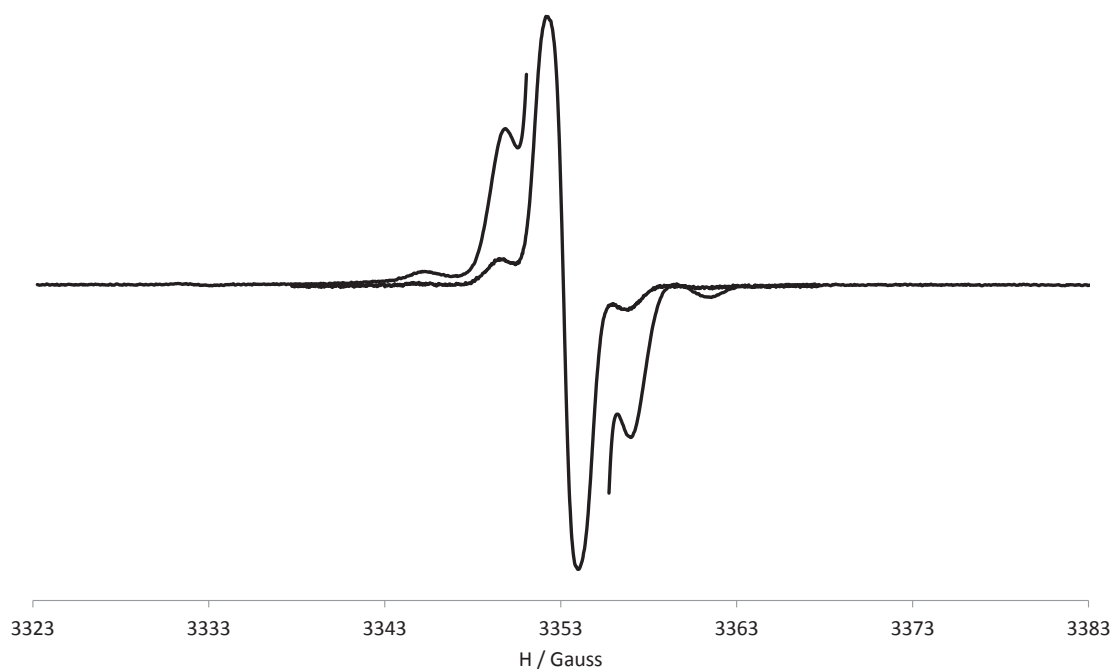
Figure S80. Experimental isotropic solution EPR spectra of diradical •**PTM-6TV-PTM**• (**5**) in Toluene/CH₂Cl₂ (1/1) at 300K
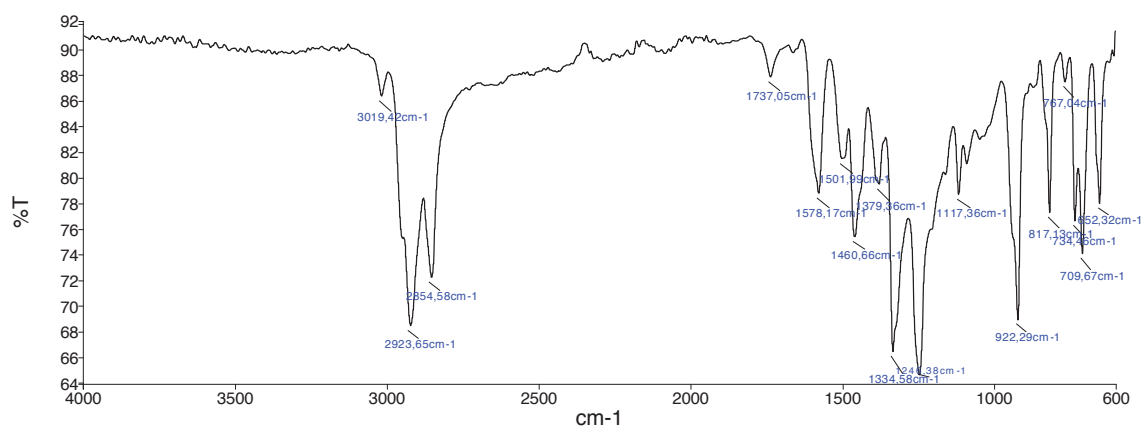
Figure S81. FT-IR spectrum of diradical •**PTM-6TV-PTM**• (**5**)
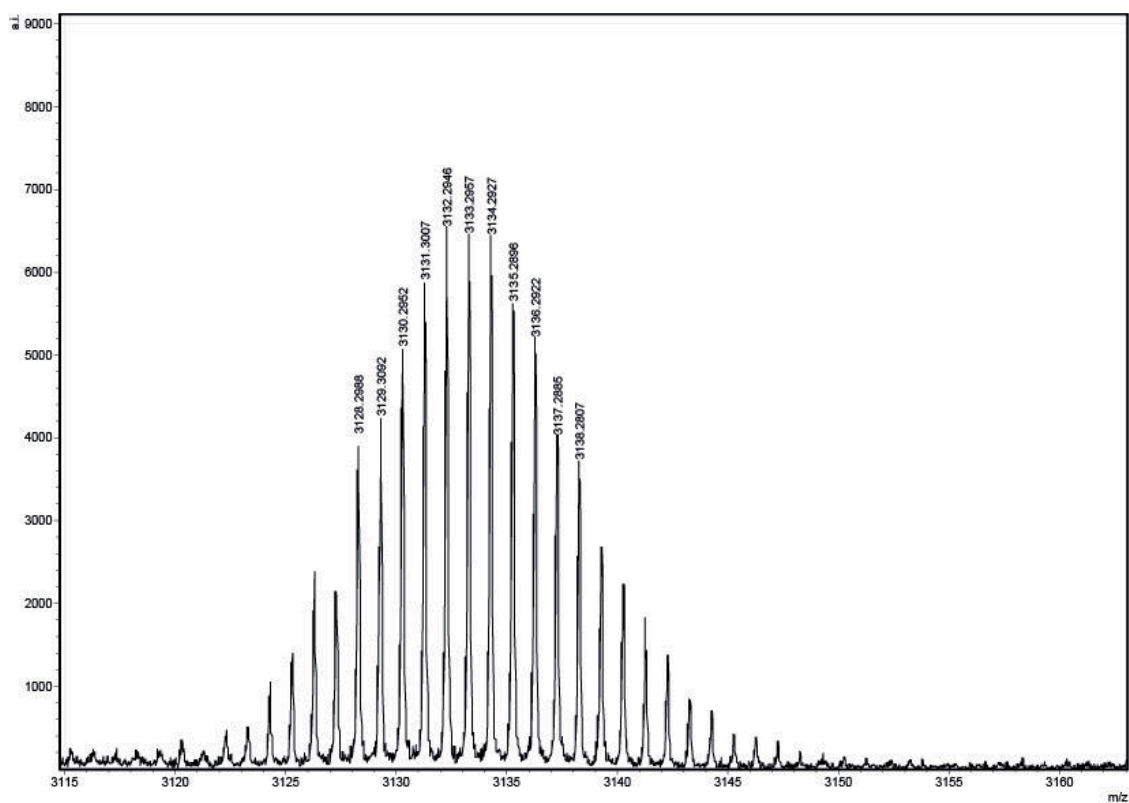
Figure S82. Mass spectrum of diradical •**PTM-6TV-PTM**• (**5**)
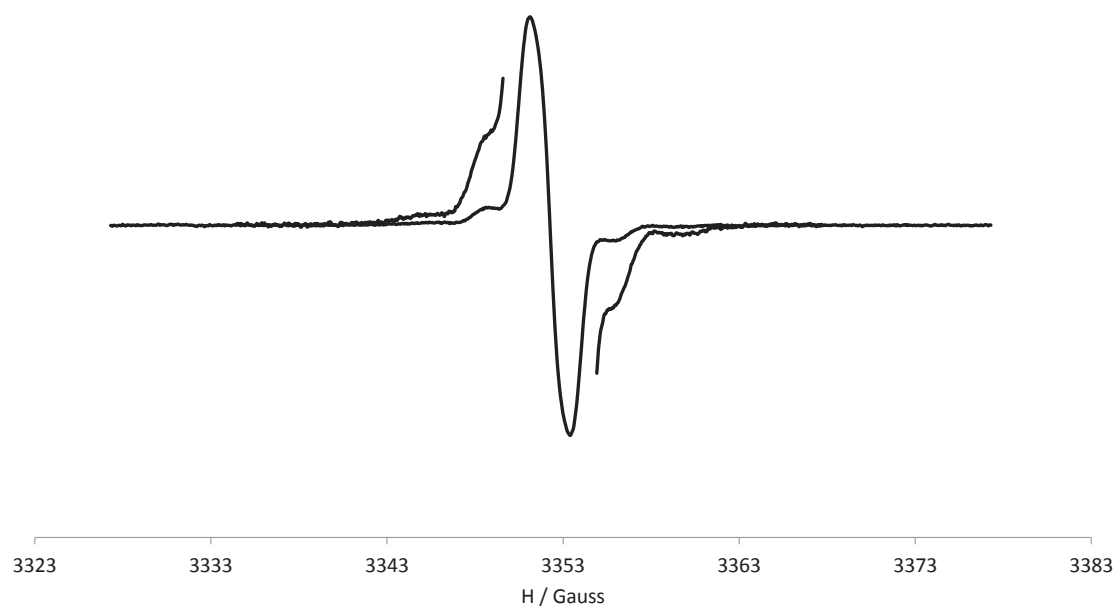
Figure S83. Experimental isotropic solution EPR spectra of diradical •**PTM-7TV-PTM**• (**6**) in Toluene/CH$_2$Cl$_2$ (1/1) at 300K
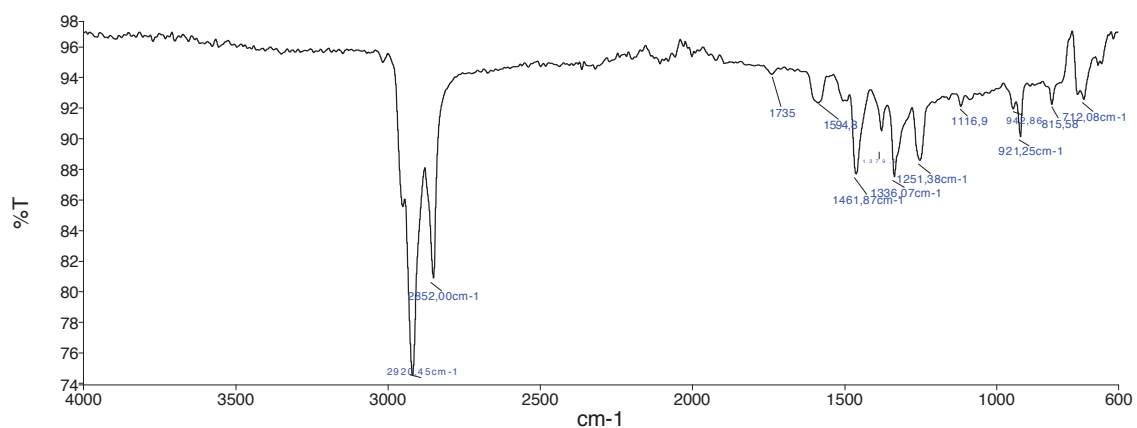
Figure S84. FT-IR spectrum of diradical •**PTM-7TV-PTM**• (**6**)
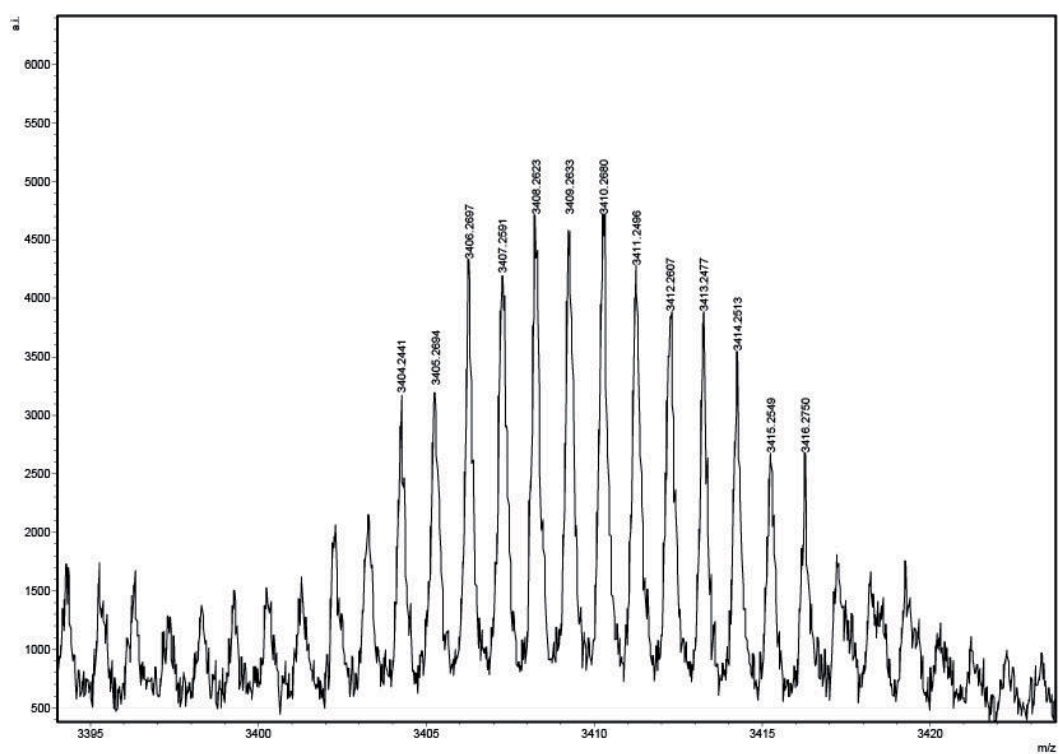
Figure S85. Mass spectrum of diradical •**PTM-7TV-PTM**• (**6**)

Chapter 3:
Self-Assembled Monolayers

Self-Assembled Monolayers (SAMs)

In the field of molecular electronics, besides designing molecules with the correct properties to act as functional components of molecular devices, there are many other important factors to take into account as the development of reliable methodologies for positioning, connect and measure the electronic properties of those molecules. Actually different techniques for measuring the conductivity of the molecules have been proposed as,[1] for example, scanning tunneling microscopy (STM),[2] conductive atomic force microscope (CP-AFM)[3] or break junctions (BJ).[4-5] However for study the molecules by these methodologies it is necessary to immobilize them in a solid support in order to maintain its properties isolated for the rest of the media. One of the most versatile tools to address molecules on surfaces is through the preparation of self-assembled monolayers (SAMs) by covalent bonding to a surface.[6]

1. Introduction

In the last years, the design and construction of hybrid materials based on solid substrates functionalized with organic molecules, which are disposed in an organized monolayer (SAM), has obtained great relevance.[7] This great interest is based in the number of different applications in which they can be exploiting, as for example: (i) organic reaction on surfaces;[8] (ii) development of new catalysts;[9] (iii) development of new photochemistry and electrochemistry sensors;[10,11] (iv) design and construction electronic devices at nonmetric scale;[12,13] (v) reduction of the metals corrosion;[14,15] (vi) and also study of electronic transfer processes.[16,17,18]

The formation of a SAM is based in the absorption of active molecules in substrate's surface resulting in a monolayer of those molecules with a defined packing and orientation. To form a SAM is necessary that molecules react with the substrate resulting in a covalent bond between molecules and substrate. Besides the bond energy molecule-surface, for the SAM formation must be taking into account the non-covalent molecule-molecule interaction (Van der Walls interactions, hydrogen bonds… etc.), and the molecule-solvent interactions.[19]

In a SAM, three main features can be considered (Figure 1). First, the terminal group, which will define the new properties of the surfaces, and usually has a great impact in the SAMs ordering if any steric or electrostatic hindrance exists.[20] Secondly, the spacer group, commonly an alkane backbone, which has revealed to have striking importance in the SAMs packing.[21] And finally the anchoring group that is the responsible to binding between the surface and the molecule.
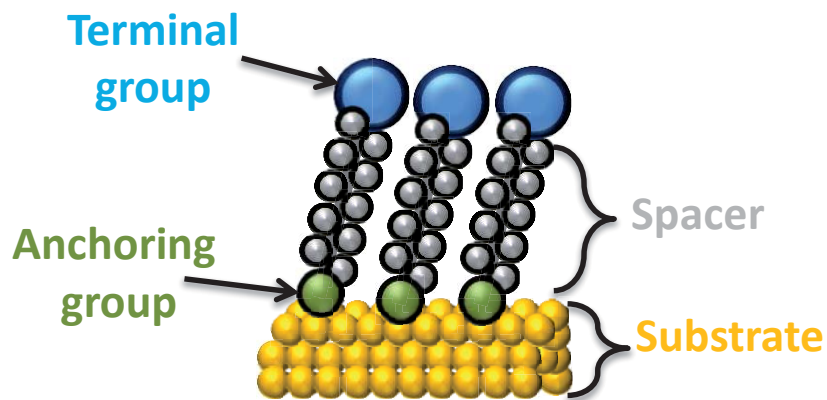
Figure 1: Schematic illustration of the different parts of a SAM

There are many different anchoring groups which are able to react with diverse substrate. The most extensively studied are: thiols over gold,[22,23,24,25] silver,[26,27,] copper,[26] palladium,[28,29] platinum,[30] and mercury;[31] and the silanes over silicon oxide,[32] or indium tin oxide (ITO).[33] Recently with the discovery of graphene, have been investigated some anchoring group able to react with graphene surfaces.

1.1 SAM preparation

The SAMs can be prepared from spontaneously absorption of molecules in solution or in vapor phase. In that work we only focused in the solution method.

The most used protocol to prepare SAMs through a solution is the immersion method (Figure 2). This consists in an immersion of a clean substrate in an organic solution of the target compound for several hours at controlled temperature in inert atmosphere. In this methodology the reaction between the molecules and the surface is very quick, getting highly packed surfaces in short time, but the reorganization process is slower, and for that, it is necessary immersion time of several hours in order to maximize the molecular density and minimize the SAM defects.
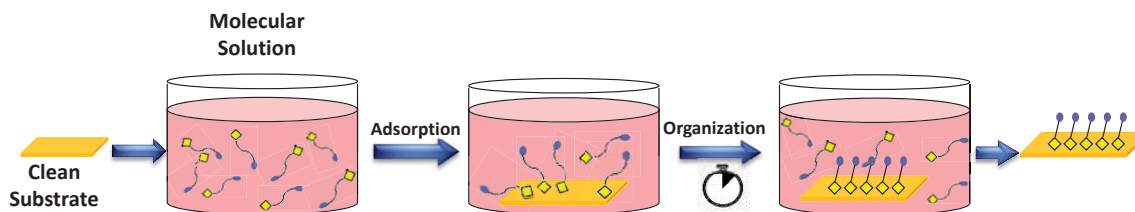
Figure 2: SAM preparation through the immersion methodology.

Also, other factors must be taking into account in SAM structuration:

Solvent. The solvent affects to thermodynamics and kinetics of the assembly process, due to the solvent-substrate and solvent-molecule interactions.

Temperature. The temperature is directly related with kinetics of the SAM formation and the number of the SAM defects. Some studies suggested that the effect of the temperature is crucial during the first minutes of the SAM formation.[34]

Molecular concentration and immersion time. These two parameters are inversely related, because at low concentrations is necessary high immersion times.[35,36]

Molecular purity. In general is necessary high purity degree of the SAM formed molecules, but nevertheless some experiments suggested that impurity traces less of 5% do not affect to the formation and structure of the SAM. [28,35]

Oxygen in solution. Some works suggested that degas the solvent with an inert gas improvement the reproducibility of the SAMs properties.[26,28]

Substrate activation. One of the most important steps in the preparation of a SAM is the substrate pretreatment that concerns both specific cleaning and activation procedures for the appropriate anchoring of the molecules. Two cleaning procedures are commonly used according to the surface an can involve dry (oxygen plasma, UV/ozone plasma) or wet (piranha bath, hydrofluoric acid, aqua-regia) chemistry.

In order to verify the appropriate SAM formation and that the molecular system are persevered on surfaces, appropriate techniques are requires to characterize these systems. The common techiques that are used to characterize physically and chemically the SAMs and that were used on this thesis are summarized in Table 1, where the SAM property related to each technique are disclosed.

Table 1: SAM characterization techniques employed in the present thesis.

	SAM property	Technique employed
Chemical and structural properties	Hydrophobicity	Contac angle
	Structure and order	Scanning Tunneling Microscopy (STM)
	Elemental composition	X-Ray Photoelectron Spectroscopy (XPS)
	Structural Composition	Ultraviolet photoelectron spectroscopy (UPS)
		Near edge X-ray adsorption fine structure spectroscopy (NEXAFS).
Physical Properties	Electric	Cyclic Voltamperometry
		I-V measurements in junctions (STS and Egain)
	Magnetic	Electro Paramagnetic Resonance (EPR)

2. Conductivity through SAMs

2.1 Introduction

The last few years, the study of charge transport processes through single organic molecules by using molecular junctions has generated great attention, both from a fundamental point of view and by the possibility of developing molecular electronic devices to be implemented somehow into current silicon-based technology.[37] But the study of the charge transport processes is still a challenge due to the different parameter that influences in them such as: the charge transport through the molecules, the transport mechanism from electrodes to the molecules, and the nature of the electrode-molecule contact.[38] However large molecular junctions (i.e. SAMs) present two main advantages in comparison with the single molecular junction: (i) a simpler assembly, requiring less sophisticated fabrication; and (ii) a higher versatility towards potential application in organic electronics.

In this chapter we first will focus in the different techniques to contact SAMs with a top electrode, then we will describe the different theoretical aspect of the charge transfer processes in metal/molecule/metal systems, and finally we will summarize and compare few experimental results developed for different SAMs.

2.2 Experimental Testbeds for molecular junctions

Electronic test structures are the basis for charge transport studies through organic SAMs with varying structure and chemistry. There are many different techniques to contact SAMs, which characteristics are summarized in Table 2. Basically the various techniques differs in the efficacy of the contact, the number of contacted molecules, and if the contact with top electrode is permanent or not.

Table 2: Comparison of commonly used test structures and their characteristics.

Technique	Yield	Contacted Molecules	Permanent structure	Resistance per molecule	Reference
STM	High	1	No	10^4	40
Conducting AFM	High	10^2-10^3	No	10^4-10^7	42, 43, 44
Liquid Metal	High	10^{11}	No	10^8	45-49
Metal evaporation	Low	10^3-10^{10}	Yes	10^6	39
Nanopore	Moderate	10^3-10^4	Yes	10^6	50-53
Polymer protected	High	10^8-10^{10}	Yes	10^8-10^{12}	54-56

2.2.1 Scanning tunneling microscopy

Scanning tunneling microscopy (STM) (Figure 3) has been commonly used to study different aspects of the SAMs (morphology, order...), as well as to explore the charge transport phenomena

through them. This system is quite interesting because allows to analyze the SAM morphology and the electrical characteristics simultaneously. The setup is composed by a sharp STM tip contacted to the substrate, which acts as the top electrode approaching the area of interest (without contacting it) and some bias voltage is applied between the tip and the substrate. In that way, tunneling current is monitored along with height revealing surface morphology and electrical characteristics. [40]
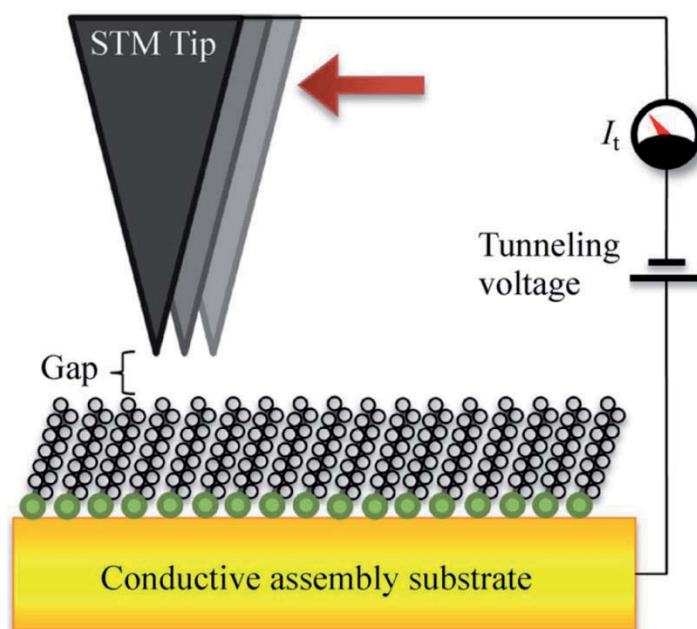
Figure 3: STM illustration. A sharp tip is scanned over the SAM surface and the small tunneling current is amplified and analyzed.[41]

2.2.1 Conducting probe atomic force microscopy

The conducting probe atomic force microscopy (CP-AFM) is an evolution of conventional atomic force microscopy, and is one of the most commonly used techniques to characterize SAMs and to investigate their electrical properties.[42] In a CP-AFM setup (Figure 4), a conducting AFM tip is directly brought in contact with the molecules in the SAM under controlled loading force. A sweeping voltage is applied between the tip and the substrate in stationary mode to carry out electrical current-voltage (*I-V*) measurements.

Compared with the STM technique, the CP-AFM has some advantages as for example that the direct contact of AFM tip with the SAM can prevent the current reduction caused by the additional tunneling gap that exists in STM.[43,44] Another important advantage is that this technique does not require the use of a device patterning process. However, variations in the AFM tip radius and bottom electrodes roughness induce some uncertainty in the number of molecules in the junction, resulting in a large variation in the measured *I-V* characteristics.
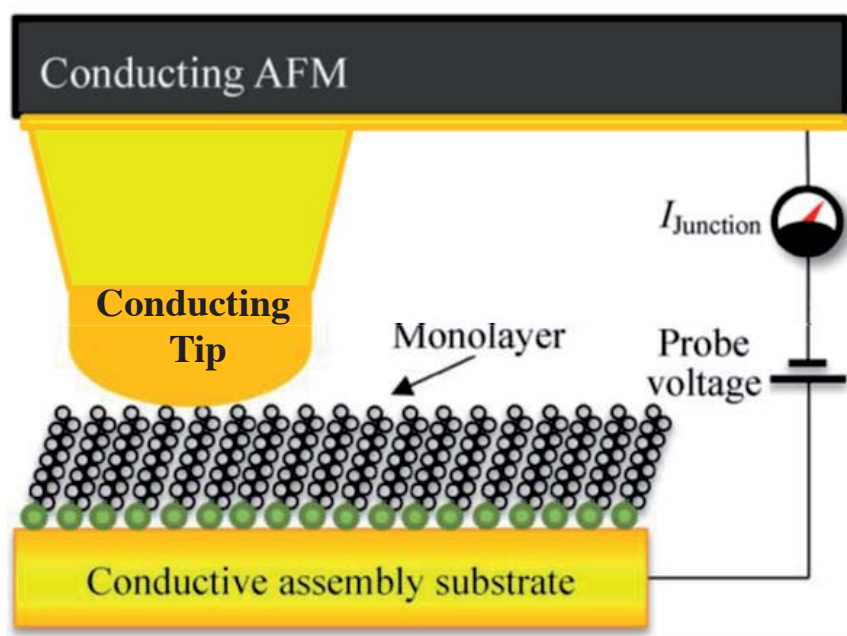
Figure 4: An illustration of conducting probe AFM for SAMs measurement where a metal coated AFM tip is brought into contact with the SAM decorated surface. Because of the relatively large size of the tip, this measurement technique measures current through multiple adsorbed molecule.[41]

2.2.3 Liquid metal

Liquid metal contacts were among the first used to study the charge transport through organic monolayers.[45] Mercury has been used to contact SAM in Hg-SAM-SAM-metal junctions, fabricated by controlling the contact of a drop of SAM-coated Hg with a second metal surface that contains another SAM (Figure 5).[46] The mercury electrode presets some advantages with respect to the other techniques. First the soft Hg drop adapt better to the surface and there is less risk of abrasion or compression of the SAM. Also, when contact occurs through a liquid, the pinholes have lower incidence, thus providing a better scenario for electrical conduction studies.[47]

Therefore, the simplicity of this technique will ensure the validity of statistical analysis of the data and enable the understanding of charge transport mechanisms. However the junction yields are low and the junctions may be unstable because Hg is easily amalgamated with Au bottom electrodes[48] during repeated *I-V* measurements leading to a subsequent deterioration, which could derive in a short circuit.[49]

To overcome the problems presented when using a Hg drop, other metals and metal alloys which are liquid at room temperature can be used. One of the most commonly used metal alloys to contact SAMs is eutectic gallium-indium (EGaIn), which will be discussed in depth in next section.
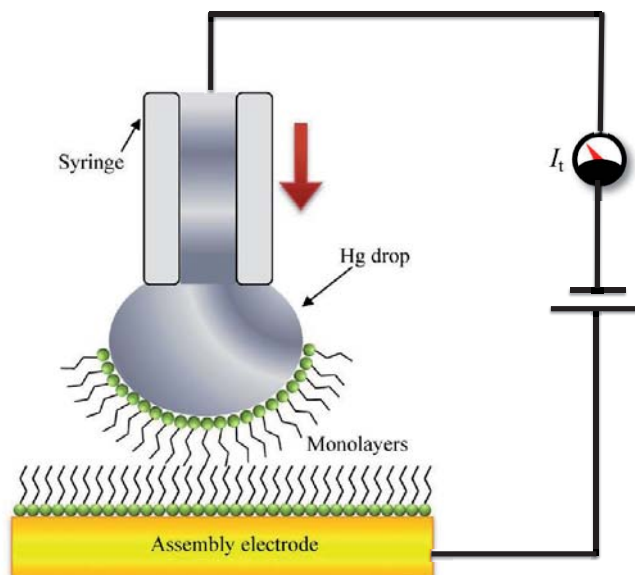
Figure 5: Illustration of a liquid metal setup. A syringe containing a liquid metal (here mercury) is brought into contact with a surface in solution.[41]

2.2.5 Nanopore

This junction is based in create by electron beam lithography and reactive ion etching, a single pore in the substrate with a diameter of approximately ten nanometers through the suspended isolating layers in SiO_2 or Si_3N_4. After the SAM formation on the created pore, the device is covered on the top by evaporated metal to complete the molecular junction (Figure 6). [50] To avoid the thermal damage to the SAM layer, liquid nitrogen is flowing, and the evaporation rate is kept very low. Despite this the yield of the nanopore device is low due to the high possibility of short circuit formation.[51] However, this technique allows temperature variable experiments, which are very interesting to analyze the charge transport mechanism through the SAM.[52] Also this junction technique is a useful platform for create functional device applications, such as non-volatile memory devices and diodes.[53]
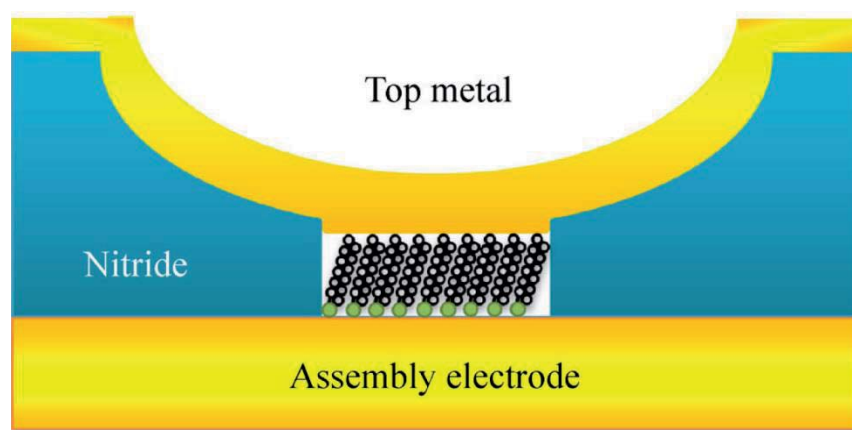
Figure 6: Illustration of a nanopore junction.[41]

2.2.6 Polymer protected junctions

This technique involves the deposition of a polymeric conductive layer between the SAM and the metallic top electrode to isolate the attached molecules, and achieve good contact which prevents the degradation of the device in ambient conditions.[54] To achieve the junction, first the SAM on the substrate is formed, then a water-based suspension of the conducting polymer PEDOT:PSS (poly-(3,4-ethylenedioxythiophene) stabilized with poly-(4-styrenesulfonic acid)) is spin-coated on the top of the SAM covering it. Subsequently the metal top electrode is deposited on top of the PEDOT:PSS layer (Figure 7). This technique provides a high yield of devices and stable junctions in ambient conditions.[55] Nevertheless, the use of a conductive polymer has some limitations and presents some doubts as a universal platform for physical-organic studies because the properties of the interface between the polymer layer and the molecules are not well understood.[56]
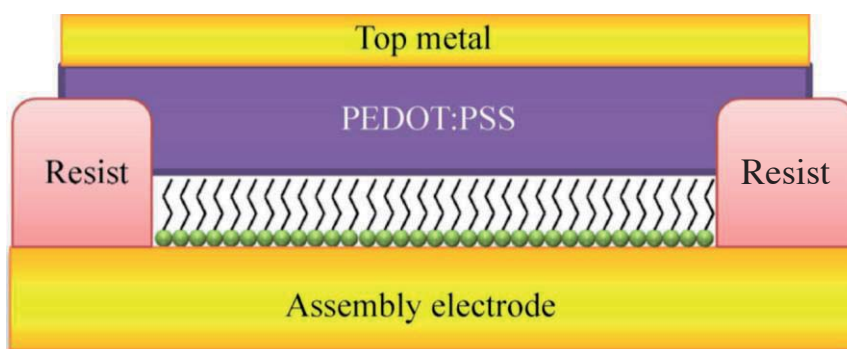
Figure 7: Illustration of a fabricated device with a SAM protected by a conductive polymer. The polymer protects the SAM from damage during subsequent metal evaporating, thus reducing the incidence of the shorts and permitting the formation of junctions of large area.[41]

2.3 Charge Transfer Mechanism

The charge transfer through molecular junctions can be described using the D-B-A model described in the previous chapter, with the difference that donor and acceptor are substituted by two electrodes (M-B-M'). In that way the charge transfer go from one electrode (M) to the other (M') mediated by the bridge (B). The nature of the mechanism involved in these processes depends in first approximation on the difference in energy between M/M' and the closest molecular orbitals to the metals.

In molecular junctions, non-resonant tunneling is the most often observed mechanism.[57] The most simple model to describe the tunneling behavior in M-B-M' systems can be defined as a finite potential barrier through which electrons travel. Simmons[58] described a model, which relates the probability of transport (in one dimension) to give current density (J_{DT}) with dielectric thickness (d), barrier height of potential barrier (ϕ), electron charge (q), voltage applied (V), electron mass (m), and Planck's constant (h) (equation 1). This model can be seen graphically in Figure 8, where the barrier limits electrons traveling to the opposing metal.

$$J_{DT} = \frac{q^2 V}{h^2}\sqrt{2m\phi}\; e^{\frac{-4\pi d}{h}\sqrt{2m\phi}} \tag{1}$$
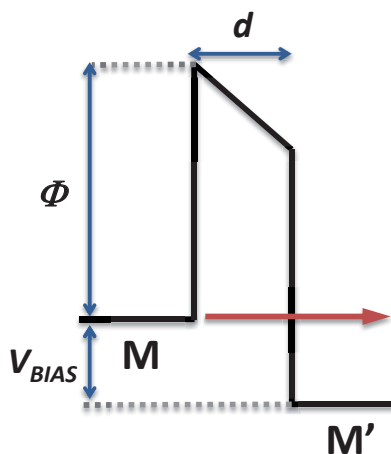
Figure 8: Schematic representation of the Simmons model

However, the presence of molecules inside the tunnel gap decreases the tunnel barrier, and the molecular HOMO-LUMO gap can also influence in the electron transport. For these reasons the Simmons approach is incomplete, since this model does not take into account the discrete spacing between the energy levels of the molecules inside the metal. So, a more refined model that takes into account the active role played by the molecule and introduces the coupling of the tunneling electron with the off-resonance electronic states of the molecule is necessary. The model that best fits these requirements is superexchange coupling, which was previously described in section 3.5 of the chapter 2 for D-B-A systems. In this model, the rate of the charge transport process depends on the ΔE offset between the energy levels of D/A units and those of the bridge, while in a molecular junction the transport process depends on the difference between the electrodes Fermi

levels and the molecular levels. Consequently, when the HOMO is closer than LUMO to electrodes Fermi levels the holes transport is favored; while if the closer one is the LUMO the charge transfer will occur via electrons.

Therefore the rate of charge transfer in molecular junctions can be described in function of the current flow I (Equation 2) or in function of the resistance (Equation 3)

$$I = I_0 e^{-\beta d} \tag{2}$$
$$R = R_0 e^{\beta d} \tag{3}$$

where d is the length of the molecule and β is a decay factor that depends on the nature of the molecular structure and the bias voltage. So, in the Simmons model $\beta \propto \phi^{1/2}$, while in the superexchange treatment $\beta \propto \ln(\Delta E)$, where $\Delta E = E_{LUMO} - E_F$.

There are a few cases where the molecular orbitals of the molecules are close in energy to the Fermi levels of the M and M'.[42a,59] In those cases, the electron transfer occurs by incoherent hopping[60] between the localized states of the molecules, which, as we mentioned in the previous chapter, shows a low dependence with the molecular length but high temperature reliance.

2.4 Charge Transfer in Molecular Junctions

The most studied issues in molecular electronics, are how the molecular length, structure and contact nature influence in charge transfer process. For that purpose, the current voltage (I-V) characteristics have been thoroughly investigated for large number of molecular junctions with a variety of platforms and techniques.

In this regard alkanethiols have been extensively studied as standards systems, since their structure and configuration are well characterized,[61] and because the thiol group permits their reaction with standard metal substrates (Au, Ag, Pt …) in high yields. There are two kind of alkanethiols which are commonly used, alkanemonothiols ($CH_3(CH_2)_{n-1}SH$, **Cn**) where one thiol is located at the end of molecule, and alkanedithiols ($HS(CH_2)_nSH$, **DCn**) where thiols are located at both ends of the molecule and can form covalent bond with top and bottom electrodes. These molecules present a superexchange regime when they are integrated in junctions with two metallic electrodes, due to the large HOMO-LUMO gap of approximately 8 eV.[62]

2.4.1 Contact dependence

The statistical analysis of **Cn** and **DCn** SAMs devices, contacted by gold evaporated electrodes, are shown in Figure 9. Figure 9 (a-f) represents the histograms of the current densities for alkanemonothiols of different of length (**C8**, **C12** and **C16**) and alkanedithiols (**DC8**, **DC9** and **DC10**) at 1.0 V with the most probable positions indicated with arrows.[63] The conduction mechanism through the alkyl chains in these devices is the superexchange, which was demonstrated by its temperature-independent I-V characteristics and the exponential dependence of its transport characteristics on molecular length. In Figure 9g, can be also observed that the alkanedithiols

junctions have higher conductance than the alkanemothiols. This observation relies in the different metal-molecule contact nature (physisorbed or chemisorbed) with the gold evaporated electrode.
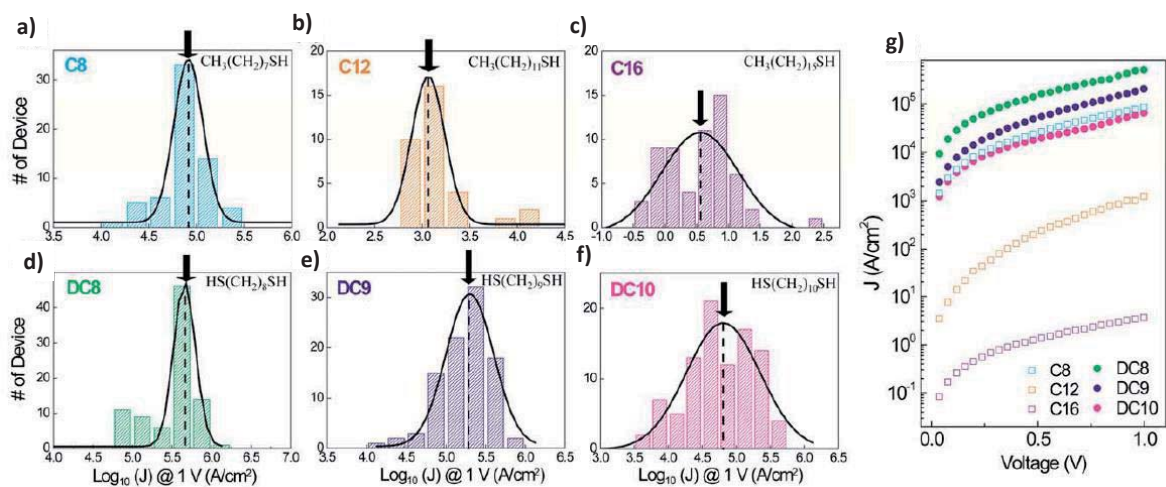
Figure 9: Statistical histograms of log *J* measured at 1.0 V for a) **C8**, b) **C12**, c) **C16**, d), **DC8**, e) **DC9** and f) **DC10**. The data are fitted to a Gaussian function and the mean positions are indicated with arrows. g) *J-V* characteristics of these devices from the mean positons of the fitted Gaussian function.[63]

2.4.2 Molecular structure dependence

Both the backbone structure and anchoring group of the molecules have influence in the conductivity of the junctions.

The attenuation factor β, which is determined by taking the linear fit of a logarithmic plot of the resistance *vs* different molecular length, is used to evaluate the tunnel barrier to promote the tunneling charge transfer through the molecular structure. Figure 10 compare the β values obtained for alkanethiols junctions, with those found for different oligophenylenethiols junctions. Here the β for alkanethiols was found to be ~ 0.92 Å^{-1} which is higher than that of oligo phenylenethiol ones (which β values are in the range of 0.2-0.6 Å^{-1}) The small HOMO-LUMO gap for π-bonded molecules (3-5 eV),[42b,62] compared with that of alkanethiol molecules (8 eV), explains the large difference in β values. These comparisons provide a clear indication that alkanethiol molecules in molecular junctions have a considerably higher tunneling barrier height that does π-bonded ones.

Other parameter than can be extracted from these measurements is the contact resistance R_0, which is used to investigate the effective metal-molecule resistance that depends on the anchoring groups. R_0 can be defined in the limit when molecular length approaches to zero. The plots in Figure 10 indicate that (i) R_0 for alkanedithiols is smaller than R_0 for alkanemothiols by an order of magnitude due to the different properties of chemisorbed and physisorbed contacts;[63] (ii) R_0 for oligoacene-SH is smaller than R_0 for oligoacene-NC due to the presence of a higher tunneling barrier at the contact for isocyanide (CN)- linked molecules than for thiol (S)-linked ones;[42f] (iii) R_0 for *p*-phenylenedithiols and R_0 for *p*-phenylenemonothiols have similar values since in this case

the top electrode has a PEDOT-PSS layer that contact with the molecules and the second thiol group of the dithiols do not contact directly with the gold coinciding with the junction resistance without SAM.[64]
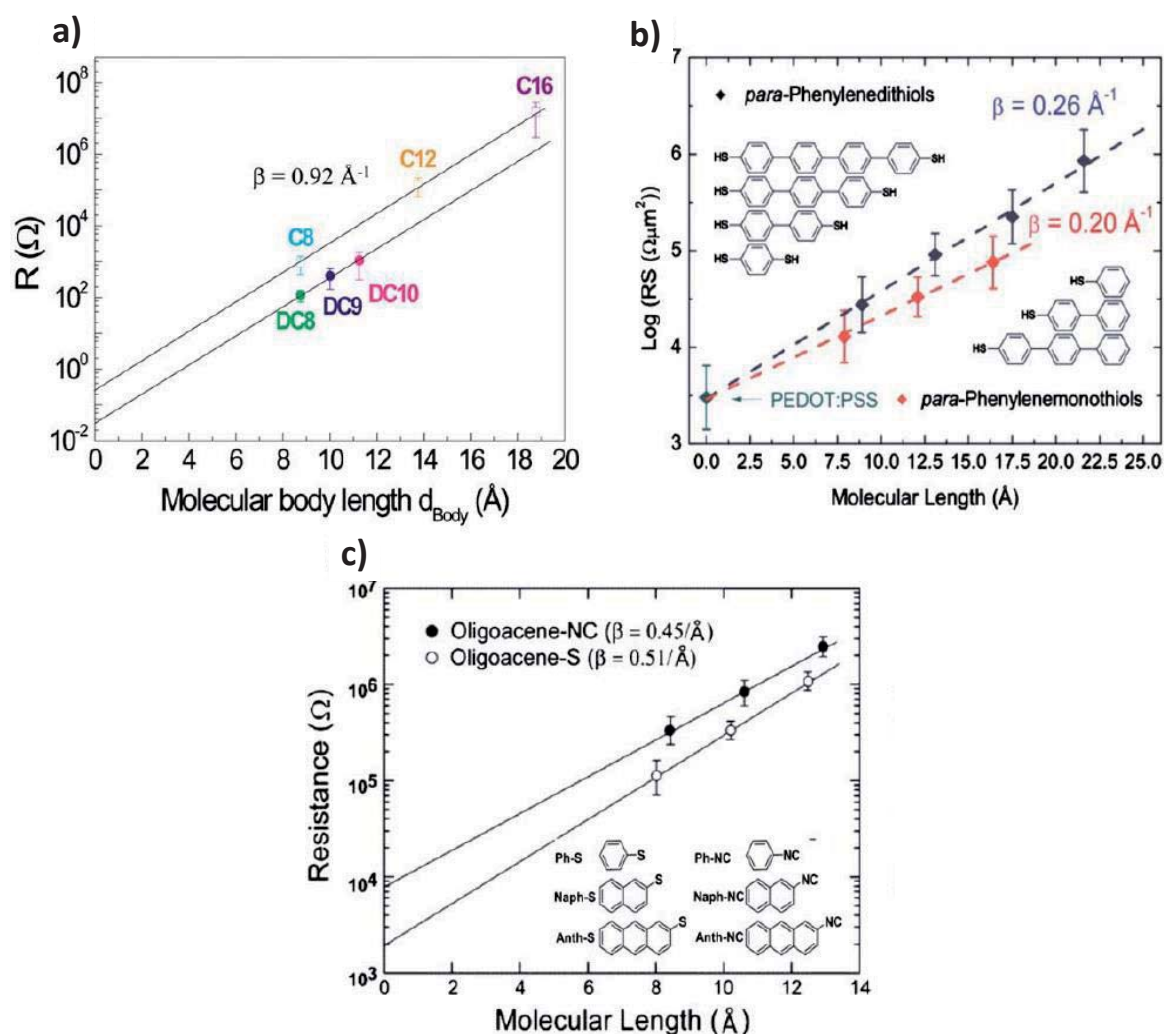
Figure 10: a) Graphical plot of *R vs* length for alkanemonothiol and alkanedithiol junctions.[63] b) Normalised resistance *vs* molecular length plot for **P1DT**-**P4DT** and **P1MT**-**P3MT** in PEDOT:PSS-based molecular junctions.[64] c) Semilog plot of *R vs* molecular length for oligoacene-S and oligoacne-NC in CP-AFM.[42f]

2.4.3 Electrode structure dependence

We can also obtain information about the influence of electrode nature and structure analyzing the β and R_0 values for alkanethiols with different junction structures. As shown in Figure 11a no trends were found in the measured β values with work function for contact electrodes.[42e] Besides, the β values with standard deviations obtained from different testbeds junctions are in the same range values (Figure 11b).[55,65] However, the R_0 values were observed to decrease when the work function of the contact metal increased (Figure 11c).[42e] This trend suggest a hole-type transport in alkanethiols molecular junctions, whereby the HOMO level more closely aligns with the Fermi level of the metal than LUMO level. In that way, the Fermi level approaches the HOMO level as the

metal work function increases, thereby decreasing the contact barrier height to transport through the junction and reducing R_0.
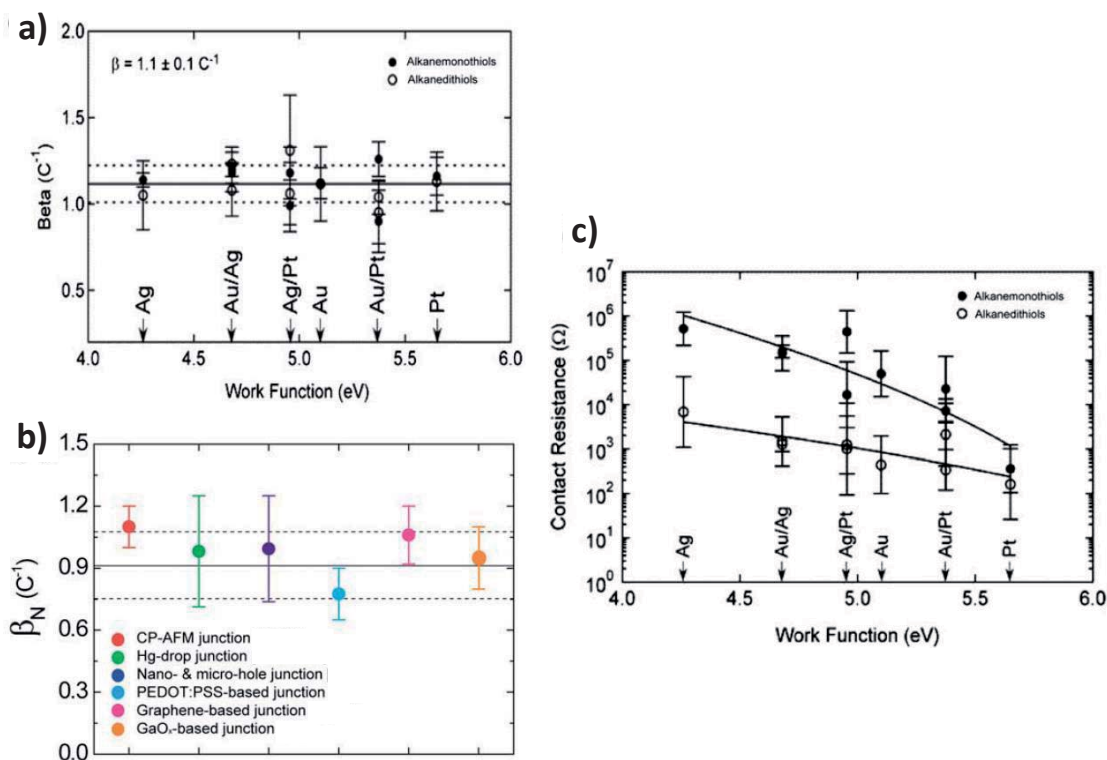
Figure 11 a) β values as function of electrode metal work functions for alkanemothiols and alkanedithiols in a CP-AFM junction.[42e] b) β values of alkyl-based molecular junctions in different testbeds.[66] c) R_0 as a function of electrode metal work function for alkanemothiols and alkanedithiols in CP-AFM junctions.[42e]

2.5 Molecular Junctions with tunable molecules

Until now, only non-active molecular junctions have been described showing that the electrical properties of these junctions are generally dominated by non-resonant tunneling mechanism. However the electronic properties of molecular junctions can be modified by functionalization of the attached molecules with an appropriate chemical active group, whose electronic structure can be changed by external magnetic, electromagnetic or electrochemical inputs. Thus the molecular junctions may allow the realization of more practical device applications as can be rectifiers, memory devices or switches.

2.5.1 Rectifier molecular junctions.

Nijhuis et al. report a comparison of SAMs of alkanethiolates with ferrocene active group ($SC_{11}Fc$) and SAMS of alkanethiolates without ferrocene moiety ($SC_{10}CH_3$ and $SC_{14}CH_3$) on silver, contacted by EGaIn electrode.[65, 67] They observed by measuring the current density J, versus applied voltage V, that the molecular junctions containing ferrocene units were able to rectify current with large rectifications ratios R ≈ 1.0 x 10^2 (R = $|J(-V)|/|J(V)|$ at ± 1 V). In contrast, junctions formed only with alkanethiol SAMs did not rectify the current (Figure 12a and 12b). To understand better these

rectification effects, they studied the *J-V* characteristics at different temperatures. Figure 13c shows that the *J* values depend on temperature at negative voltage (between -1.0 V and -0.6 V) but are independent of temperature at positive voltage. This variation clearly indicates that the charge transfer mechanism operating at negative voltage is hopping and, while at positive voltage is tunneling. Based on the temperature variable *I-V* measurements, the authors suggested that the rectification mechanism across ferrocene SAM junctions may be related to the charge transport processes that change with the bias polarity from tunneling (positive voltages) to hopping (negative charge).
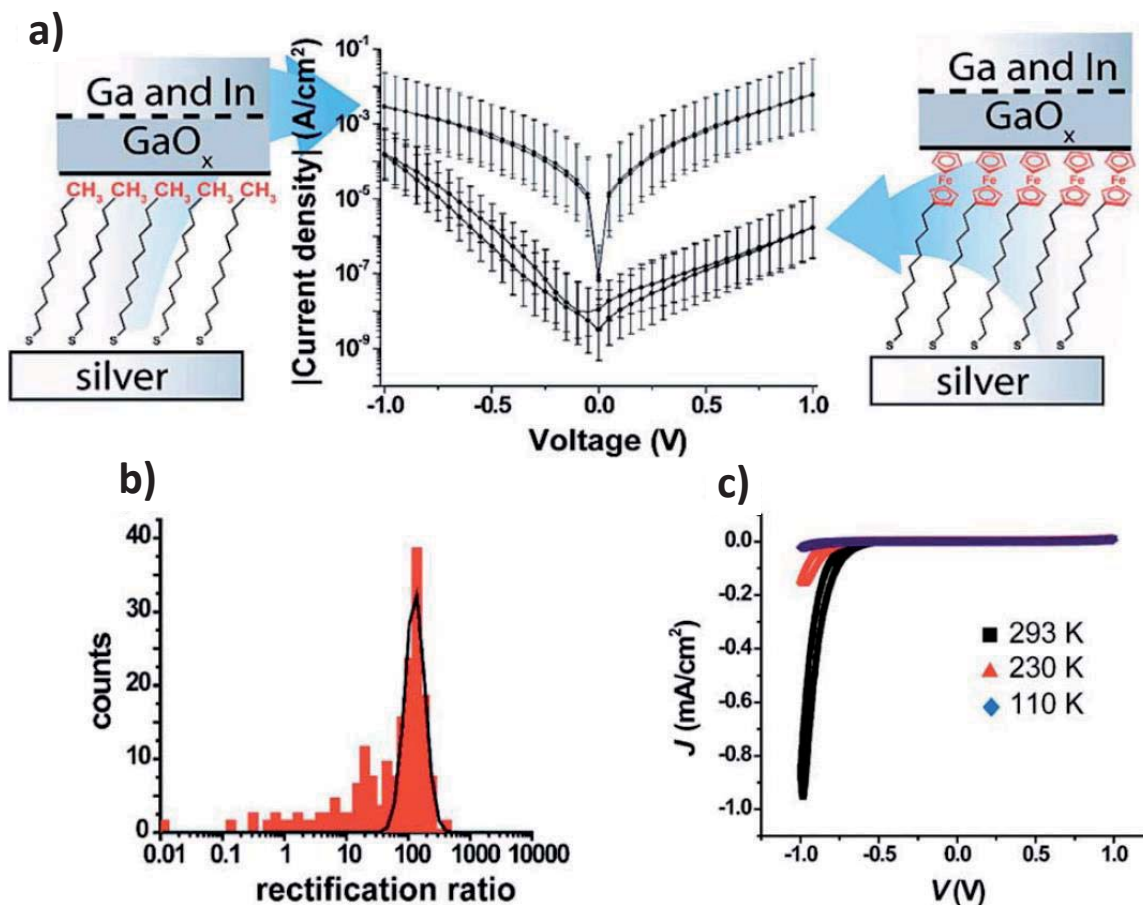
Figure 12: a) *J-V* characteristics for $SC_{11}Fc$ (right) and $SC_{10}CH_3$ (left) in EGaIn junctions. b) Histograms of rectification ratios for $SC_{11}Fc$ molecular junctions with a Gaussian fit. c) *J-V* characteristics for $SC_{11}Fc$ molecular junctions measured at different temperatures. [65, 67]

2.5.3 Molecular-junctions as switches

A very interesting application of molecular junctions implementing active molecules, is the possibility to switch the current flow through them by external stimuli. This can be realized by changing the energy difference (*ΔE*) between the LUMO (or HOMO) of the attached active molecule and the Fermi level of the electrodes by an external trigger. Generally two kind of molecules have been used for that purpose: photo-active molecules, allowing optical triggered switches; and electroactive molecules, allowing redox switches.

Optical switches are based on the fact that the light can induce a change in the electronic structure of the molecules, and consequently a variation of ΔE. Therefore, in molecular junctions incorporating photoactive molecules, light can be used as external trigger to tune the current flow For a molecular junction to behave as a photoswitch, three condition are required: (i) the geometry of the molecule in the junction must be appropriate, (ii) irradiation of the active molecule must produce isomers of different conductance and (iii) the excited state of the molecule should not be quenched by the metal electrodes.[68]

Until now, two types of photoactive molecules have been successfully used in molecular junctions: diarylethenes and azobenzene derivatives.

Diarylethenes based molecules have to different states, the conjugated one (ring-closed) and the non-conjugated (ring-open), which can be reversibly interconverted by exposure to different wavelength ranges. The ring-closed form exists under irradiation in ultraviolet region (λ = 300-350 nm), while the ring open form occurs under irradiation in the visible region (λ = 500-600 nm). Figure 13 shows the *J-V* characteristic of the open and closed isomers of a diarylethene in a PEDOT:PSS-based junctions.[69] In these junctions the tunneling current through the closed state is higher than the one through the open state. This is because the open and close forms exhibit a different degree of conjugation, and therefore different HOMO-LUMO gaps. Thus, the barrier for a tunneling charge in the more conjugatedclosed state is lower than in the open form.
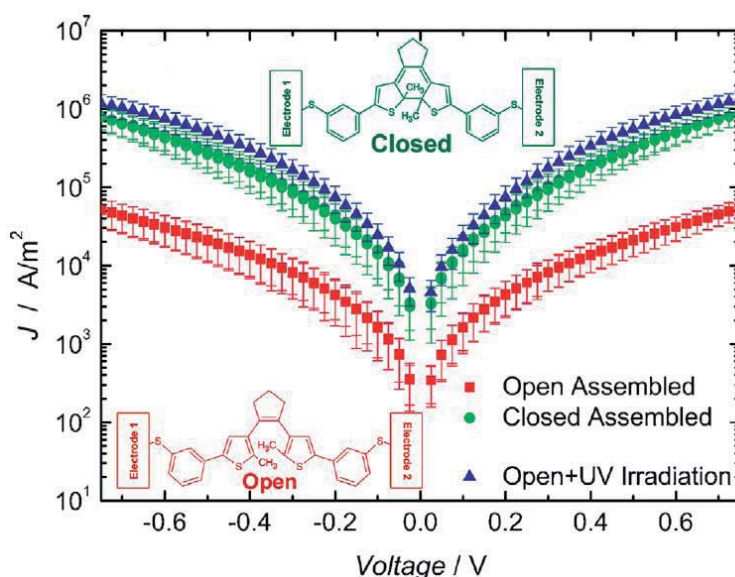
Figure 13: *J–V* characteristics of the closed (green) and open (red) isomers as self-assembled in the molecular junctions and *J–V* characteristics of the junctions with the open isomer self-assembled and subsequently photoisomerized to the closed isomer with UV irradiation (blue).[69]

Azobenze derivatives can reversibly interconvert from *trans-* to *cis-* isomer form under photo illumination at different wavelength.[70] The *trans*-isomer shown in Figure 14 can be isomerized to

cis-isomer applying an irradiation of 365 nm, while the *cis*-isomer can be interconverted to trans-isomer at 450nm.[70] Therefore, the conductance of the *trans-* and *cis-* isomer is expected to differ as a result of the conformational change. Figure 14 shows the *I-V* curves for *trans-* and *cis*-isomers from an azobenze-based junction,[70a] employing a CP-AFM approach. From linear fits of the *I-V* data it was found that the resistance of the trans-isomer was higher than the cis-isomer. This effect can be explained by the expected decrease in the tunneling barrier width, as a result of the conformational change.
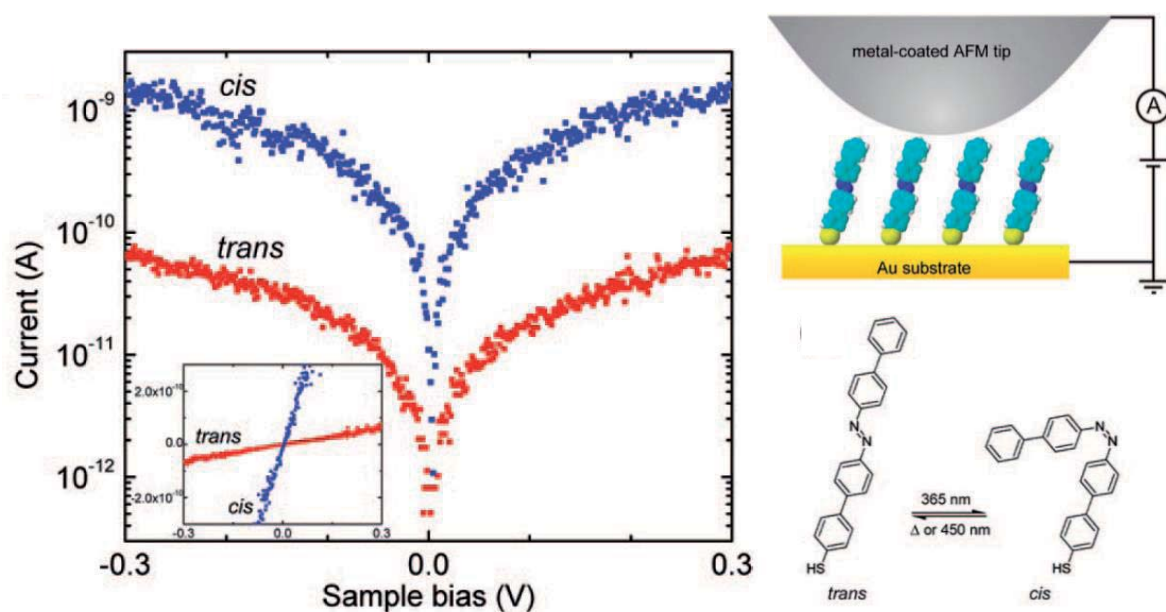
Figure 14: Representative *I-V* traces (semilog scale) recorded before and after UV irradiation showing larger currents following photoisomerization into the cis conformation (linear scale in inset). Right: structure of the *trans* and *cis* isomers of the light-switchable azobenzene derivative considered in this study and a schematic of the setup used for performing C-AFM measurements on azobenzene SAMs.[70a]

Electrochemical switches

The conductance of junctions incorporating electroactive molecules shows dependence with the redox state of the molecules. This characteristic can be exploited to fabricate nonvolatile molecular junctions.

Lee et al. exploited the redox properties of Ru^{II} complexes in gold SAM junctions composed by Ru^{II} terpyridine complexes with thiol-terminated alkyl spacer, contacted by PEDOT:PSS-gold electrode.[71] Analyzing the *I-V* SAM characteristics (Figure 15) it is remarkable that at negative voltage there is a reproducible hysteresis (bottom inset of Figure 15b). The authors proposed that the hysteresis is the result of charging/discharging Ru^{II} terpeyridine complex in the SAM. They also elucidate the charge transfer mechanism through studying the *I-V* temperature dependence. Due to the temperature-independent *I-V* characteristics, they concluded that the conduction mechanism is a direct tunneling that may contain at least two-step tunneling process for electron reduction and oxidation through the metal-ligand complex center.

Subsequently, they performed write-read-erase-read (WRER) cycles in the junctions to check the response of the system as non-volatile molecular memory devices. Figure 15c shows the WRER cycles, demonstrating that the system is quite robust for more than 300 cycles, and its potential applicability as non-volatile memory device.
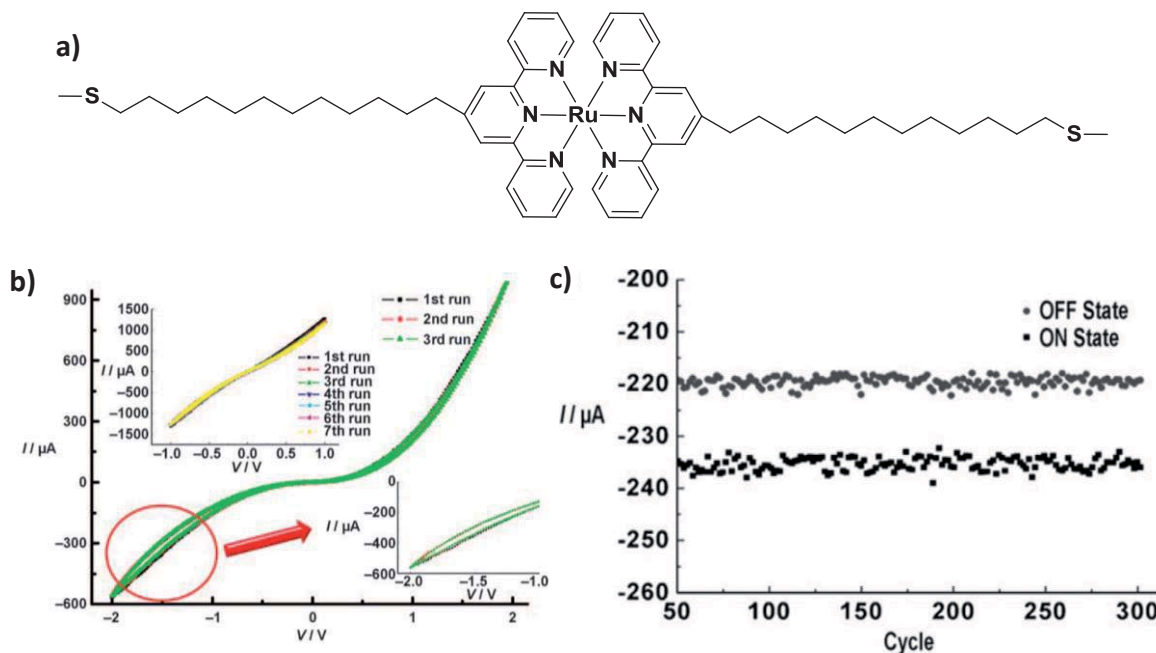
Figure 15: a) Ruthenium complex used for SAMs fabrication. b) Hysteric I-V characteristics for the ruthenium complex SAMs in PEDOT:PSS-based junctions. Top inset shows I-V characteristics in the junction without ruthenium SAMs. Bottom inset shows the magnification of the I-V curve in the hysteric region. c) Current ON/OFF states as a function of the number of WRER cycles.[71]

The redox state of the electroactive molecules can also be changed and their conductance measured using electrochemical junctions. In an electrochemical junction the Fermi level of the electrodes can be changed relatively to the redox potential of the electroactive species by an applied potential measured against an external reference electrode. Therefore, the Fermi level of the electrodes can be tuned and aligned with the molecular orbitals. In these systems the reference electrode acts as a gate, while the two electrodes (substrate and contact electrode) are the source and drain.[72]

It has been reported a number of studies how control the current via an external reference electrode in electrochemical STM incorporating electroactive molecules as violagens,[73] oligophenlyne ethylenes,[74] porphyrins,[75] oligo-anilines, thiophenes,[76] metal transition complexes,[77] carotenes,[78] ferrocenes,[79] perylene tetracarboxylic bismide,[80] and redox active proteins.[81]

3. Precedents

Summarizing what was mentioned in the previous section, there are three factors that influence the SAMs conductivity: the alignment of the molecular levels with the metals Fermi levels, the nature of the metal/molecule top electrode contacts, and the electronic structure of the molecules. Nevertheless, other aspects, such as sample preparation techniques, the SAM quality, and the reproducibility of the contact method, play an important role on the reliability and understanding of resulting transport measurements, and might be the origin of some errors in the conductance data.[62,82] One way to minimize these problems and reduce the dependence of the results on the experimental conditions is to rely on comparative transport measurements, in which individual molecular parameters are modified. Examples of this methodology are the studies of the dependence of the electron transport on the molecular length,[83] which has been widely investigated in different molecules. Another example is the study performed in 2009 in our group comparing the transport properties of two SAMs based on polychlorotriphenylmethyl (PTM) derivatives that strongly differ in their electronic configuration (Figure 16).[84]
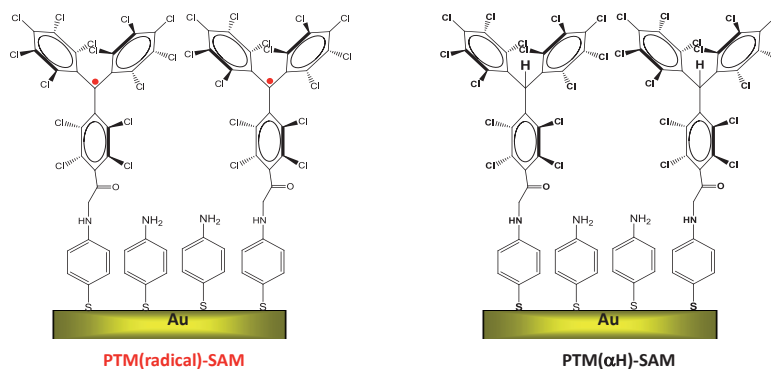
Figure 16: Scheme of the open-shell PTM radical SAM (PTM(radical)-SAM) and closed-shell PTM derivative SAM (PTM(αH)-SAM).[84]

In that work, N. Crivillers *et al* reported the investigation of the transport properties performed by conducting AFM on SAMs based on open-shell PTM radicals and closed-shell PTM or αH-PTM derivatives on gold. These two systems give rise to SAMs with no significant structural molecular variations, but with extremely different electronic structures. They found that the PTM(radical)-SAM shows a junction resistance (10-40 MΩ) one order of magnitude smaller than that of the PTM(αH)-SAM (200-300 MΩ) (Figure 17).
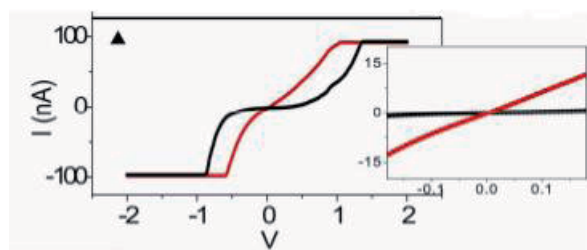
Figure 17: *I-V* characteristics for gold of PTM(radical)-SAM (red line) and PTM(αH)-SAM (black line) in CP-AFM junctions. Inset: linear region of the *I-V* curves used to calculate the junction resistance. [84]

It was thought that the conductance difference is associated to the distinct PTMs electronic structure what was rationalized by density functional theory calculations (Figure 18). The PTM (αH) has a large energy HOMO-LUMO gap (~ 5 eV), while for the PTM radical the energy gap between the singly occupied molecular orbital (SOMO) and the singly unoccupied molecular orbital (SUMO), is considerably smaller. Also the energy of the SUMO orbital of PTM radical is significantly closer to the Fermi level of the AFM tip than the energy of the LUMO of non-radical PTM (αH). This result suggest that the electronic differences between PTM (αH) and PTM (radical) with respect to their electron-accepting orbitals may play an important role in enhancing the conduction in the PTM(radical)-SAM. Therefore in view of these results, the authors suggest that the SUMO orbital assists the electron transport in PTM(radical)-SAM diminishing the tunnel barrier or contributing to a resonant tunneling mechanism.
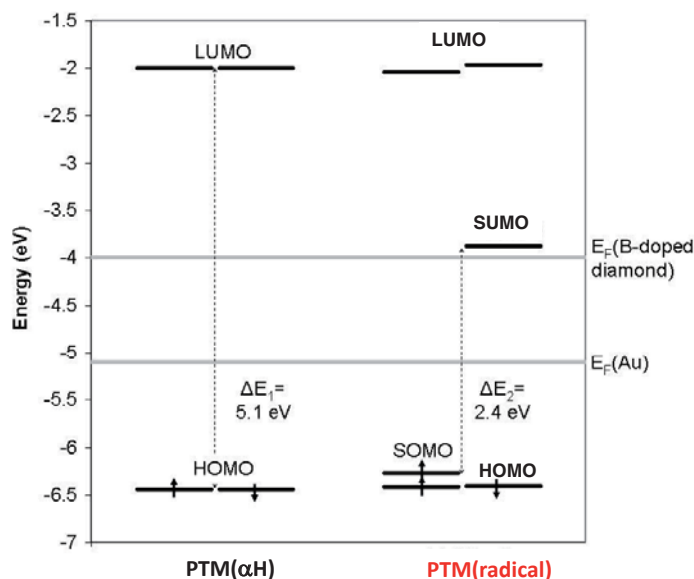
Figure 18: Energy levels of PTM(αH) and PTM(radical) derivatives obtained from DFT calculation. [84]

88

4. Objectives

As exposed in precedents, the SUMO orbital seems to play an important role in the charge transport processes through PTM radical molecules, but the transport mechanism involved is not clear. Since it is known that the conductance dependence with distance varies with the transport mechanism, to clarify which is the operative mechanism it is necessary to analyze the conductance in molecules which differ only in the length between the active group and the substrate.

Therefore our goal in this thesis was to synthesize a family of PTM derivatives, both radical and non-radical molecules, which only differ in the length of the chain linking the anchoring group and the PTM, and analyze the charge transport features of the corresponding SAMs. We proposed to synthesize a family of PTMderivatives with alkyl chains of different lengh and as anchoring group a sulfur derivative capable to form SAMs on gold (Figure 19). The technique that we have chosen to prepare and measure the junctions is the EGaIn electrode.[*]
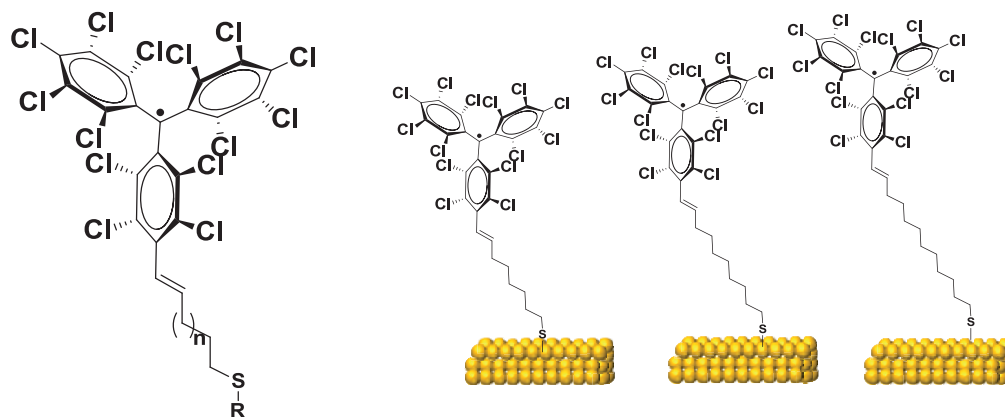
Figure 19: Scheme of the PTM radical family proposed in that thesis and the illustration of those on gold substrates.

By other hand, PTM radical is an electroactive molecule that presents a low reduction potential to the corresponding PTM anion, which is a very interesting characteristic in the field of redox switches. In addition, PTM radical and PTM anion structures are almost identical, which derives in low inner reorganization energy associated with the structural change upon reduction/oxidation. Furthermore, bulky redox systems, as PTM, show low outer-sphere reorganization energy associated with the surrounding solvent which derives in high current enhancement efficiency in redox-active molecular junctions. In view of this, we expected that the PTM radical will be a very good redox mediator.

Therefore, we planned to study the conductance of PTM radical SAMs in its different redox states, using electrochemical junctions.[†]

---

[*] This work has been done in collaboration with Professor Christian A. Nijhuis of Singapore University.
[†] This study has been done in collaboration with Dr. Alexander Rudnev of Bern University.

5. Conductivity through PTM SAMs contacted by EGaIn electrode

5.1 EGaIn electrode

As we mentioned before one of the best techniques to contact SAMs is to use a liquid metal electrodes, principally because the liquid metal gives soft contacts with the SAM reducing the incidence of the defects in the SAM. One of the most used is the EGaIn electrode (Figure 20).[85]

The abbreviation of EGaIn corresponds to an electrode formed by a fluid metal eutectic, which is composed by a 75% of Ga and 25% of In. EGaIn has a melting point of 15.5 ^{0}C[86] and therefore it is a liquid at room temperature; it also presents a high electrical conductivity (3.4 x 10^4 S cm^{-1});[87] and due to the high superficial tension it can form metastable non-spherical structures as cones and filaments with diameters $\geq$ 1 μm.
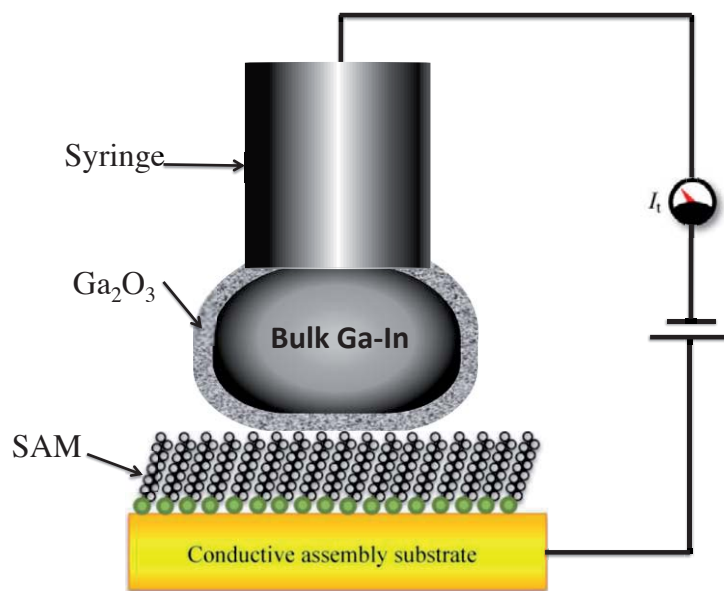
Figure 20: Illustration of a EGaIn setup. A syringe containing the mixture of Ga and In is brought into contact with the SAM surface. Electrical characterization is carried out using the back of the syringe as top electrode.

Spectroscopy measurements of EGaIn in air show that its surface is principally composed of gallium oxide, which is an n-type semiconductor.[87] Several experiments demonstrated that there are not observable changes in the average magnitude or range of J when EGaIn is left in air for extended periods before to be deposited over a conductive surface; therefore the contribution of the surface oxide to J is constant.[85]

To form the EGaIn contact electrodes, a drop of EGaIn is suspended from a metal syringe bringing the drop into contact with a surface, and retracting the needle slowly. The drop of EGaIn adopt a hour-glass shape until it is bifurcated into two structures, one conical attached to the syringe and

one attached to bare surface (which is discarded). In that way, a conical tip of EGaIn is produced with diameters ranging from 1 to 100 µm (Figure 21). The size of the cone depends of the diameter of the needle and the speed the syringe is raised. Then using a micromanipulator the EGaIn tip is brought into contact with a SAM, thereby obtaining the *J-V* characteristics.

Figure 21: A sequence of images to show the formation of the EGaIn conical tip.[85]

To demonstrate the effectiveness of this electrode, it is used to contact different Ag SAMs of alkanethiols with diverse length.[85] The obtained data demonstrated that, under ambient conditions, the 90% of the EGaIn junctions survived by more than 30 *J-V* traces. So, due to high yield of the junctions, the EGaIn allows generating a large statistic of complete *J-V* traces, permitting carry out studies relating organic structure to transport mechanism in SAMs. The ability to acquire statistically large number of data is a necessary step for the physical modeling of transport through ensembles of molecules that include defects.

Summarizing, EGain i) makes conformal, nondamaging contacts at room temperature, ii) can be molded into nonspherical shapes with micrometer-scale, or larger dimensions, iii) is commercially available, iv) can be deposited with a pipette or syringe without high temperatures or vacuum, v) has a low vapor pressure, vi) is nontoxic, and vii) allows large statistics. All these characteristics, makes EGaIn a good candidate for incorporation into functional organic devices, and specifically in that thesis the EGaIn electrode was used to analyze PTM SAM devices.

5.2 Results and Discussion

5.2.1 Design and synthesis of the molecules

To obtain a family of PTM derivatives able to form SAM on gold substrate it is necessary that the molecules have a correct functional group capable to give stable junction with gold metal. Sulfur derivatives are commonly used for that purpose because they react with gold forming stable covalent bonds, being the thiol group (-SH) the most commonly employed. Nevertheless thiol group has a low oxidation potential giving disulfide derivatives and could reduce the PTM radical to PTM anion. Therefore, before designing a synthetic pathway to obtain a family of PTM derivatives with a thiol group, it is crucial to check if the PTM radical is stable in presence of thiol

group. Hence, we mixed a solution of PTM radical without any functionalization with a commercial alkylthiol in CH_2Cl_2 for several days following the process by UV-Vis spectroscopy. During this time, the UV-Vis spectra of the PTM radical does not changed and any band corresponding to the PTM anion can be observed, so we concluded that both PTM radical and alkanethiol are stable under standard conditions.

Other problem associated to the stability of the thiol group came from the methodology commonly used to synthesize PTM. This synthetic pathway implies deprotonation of the α-carbon of the αH-PTM with a base to form the anion and subsequent oxidation to the radical. In this last step the thiol group could be also oxidized. To prevent this lateral reaction we decided to protect the thiol group deprotecting when the PTM radical is formed. The most common way to protect thiols is through the formation of a thioester, which can be deprotected to the thiol using a base, but this methodology is not applicable for our molecules, because the PTM radical is reduced by bases. So we need a protective group resistant to bases and oxidant reagents and that can be deprotected under acidic media. With these conditions, the trityl group could be a good candidate for the synthesis of our PTM family.

Taking into account all these considerations we proposed the retro-synthetic pathway shown in Scheme 1 for obtaining the proposed family of radical and nonradical PTM derivatives with alkyl chains of different lengths ending in a thiol group (**HSC$_n$PTM^R** and **HSC$_n$PTM^{NR}** n = 8, 10 and 12). The molecules **HSC$_n$PTM^R** and **HSC$_n$PTM^{NR}** could be respectively obtained thorough the deprotection of thiol group of the corresponding protected molecules with a strong organic acid. The molecules **10**, **11**, and **12** could be obtained from the corresponding αH derivatives (**7**, **8**, and **9**) in two steps: first the reaction with a strong base as tetrabutylammonium hydroxide, will promote the elimination of the acidic proton in α position giving the corresponding carbanion; and as second step the oxidation of this carbanion to the equivalent radical. The **7**, **8**, and **9** molecules could be synthesized by Wittig-type coupling between the appropriate trityl carboxaldehyde derivative and the known αH-PTM phosphonate derivative. These trityl carboxaldehyde derivatives (**4**, **5**, and **6**) could be synthesized by the oxidation of the corresponding trityl alcohols (**1**, **2**, and **3**), which could be obtained by a typical SN2 reaction between commercial bromoalkylalcohols and tritylthiol.
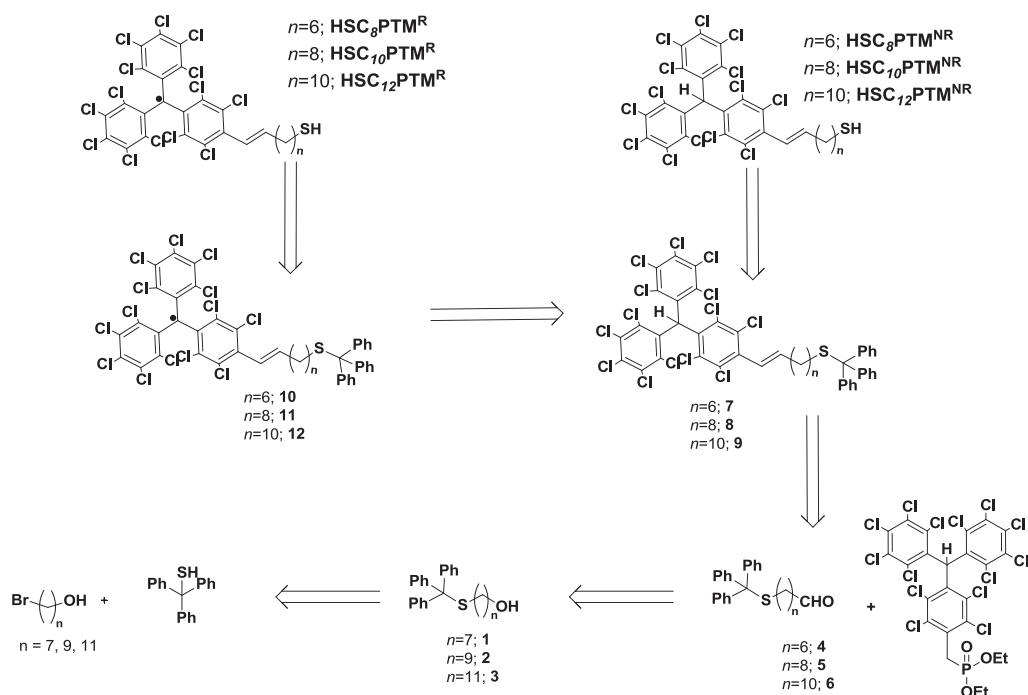
Scheme 1

Following the proposed synthetic pathway, we obtained, in a good yield, two families of molecules one with PTM radicals (**HSC$_n$PTM^R**) and other with αH-PTM (**HSC$_n$PTM^{NR}**) which have an alkyl chain with different lengths and a thiol at the end of the alkyl chain as a anchoring group. All new compounds were characterized by the usual techniques applied to organic molecules and, in addition, the electrical and magnetic properties of the radicals were also characterized by cyclic voltammetry (CV) and electron paramagnetic resonance spectroscopy (EPR), respectively. All synthetic details and characterization spectra are in the SI of the article *Chemical control over the energy level alignment in a two-terminal junction* (DOI:10.1038/ncomms12066).

Subsequently we investigated the conditions to prepare good SAMs with the family of radical and non-radical PTMs on gold substrate employing the immersion methodology. We examined the different parameters as concentration of the PTM derivatives, solvents, immersion time and temperature. After several tests we found that the best conditions to prepare the SAMs were using freshly template-stripped Au surfaces with ultra-flat topography, which were immersed in 0.5 mM solutions of the target compound in toluene for 24h at 40 ^{0}C and then for an additional 24h at room temperature. We characterized the SAMs employing CV and angle-resolved X-ray photoelectron spectroscopy (ARXPS). Furthermore we determined the electronic structure of the SAMS by ultraviolet photoelectron spectroscopy (UPS) and near edge X-ray adsorption fine structure spectroscopy (NEXAFS). This characterization permitted to determine experimentally the scheme of the energetic levels (Figure 22). All results and details are in the above mentioned article.

5.2.2 Electrical characterization of the SAMs

We have performed a systematic investigation of the transport thorough the SAMs of radical PTM derivatives (**HSC$_n$PTM^R**) on gold surfaces by employing the EGaIn electrode. Measurements on the junctions formed with the close-shell αH PTM derivatives (**HSC$_n$PTM^{NR}**) were also performed as reference .

Through the statistical *J-V* measurements realized for the different Au^{TS}-SC$_n$PTM$^{R/NR}$//GaO$_x$^{cond}/EGaIn junctions both at room and variable temperature, we demonstrate that the mechanism of charge transport is coherent tunneling for both the PTM radical and PTM αH. Also we observed that in all PTM derivatives of different length, the radical specie is 100 times more conductive than the PTM αH, which is due to the smaller SOMO-SUMO gap with respect to the HOMO-LUMO gap of the α-H derivatives. Importantly, it has been demonstrated that the hypothesis of different mechanisms for charge transfer in radical and non-radical SAMS proposed as possible in previous works[84] is not correct since the reported results demonstrate that the increased conductance of the PTM radical based SAMs is not due to a resonant tunneling mechanism but instead due to a SUMO assisted coherent non-resonant tunneling. All details are described in the article *Chemical control over the energy level alignment in a two-terminal junction* (DOI:10.1038/ncomms12066).
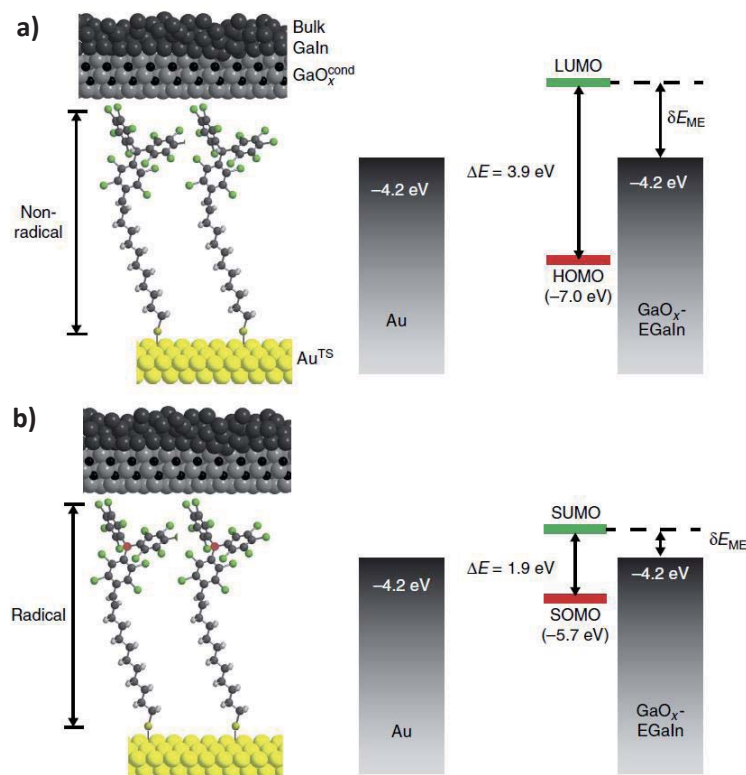
Figure 22: Schematic representations of the PTM gold junctions contacted by EGaIn and the corresponding energy level diagrams for a) PTM αH or non-radical and b) PTM radical.

6. Electrochemically gated charge transport measurements of PTM SAMs

6.1 Electrochemical gating

The fabrication of SAMs with the functions of common electronic units, such as rectifiers, switches or transistors, is one of the most attractive aspects of molecular electronics. In that field, switching is a basic function in logic gate and memory devices, thus, it is highly attractive to design SAMs revealing a switching behavior in their conductance between ON and OFF states. For that, it is required the modulation of the energy levels of the systems (Fermi level of electrodes plus molecular level of the active molecule) in SAM by the incursion of a third electrode, able of tune the energy levels by the application of a gate bias voltage. The gate voltage (V_g) can be used to tune wave functions and particularly redox energy states of the molecules with respect to the contacts, with consequent control over the junction conductance. But the positioning of the third electrode in SAM devices is challenging. This has been achieved for planar devices with a metal gate electrode underlying and separated from the source-drain contact pair by a thin dielectric film.[88]

An alternative approach to the solid-state gating is to use an electrochemical gate. In this setup the energy levels of the system are controlled through the electrochemical potential for the device immersed in an electrolyte solution relative to a reference electrode. This is achieved in a four-electrode electrochemical setup with counter- and reference electrodes serving alongside the source and drain electrodes. An electrified liquid interface also has the advantage that two potentials can be controlled simultaneously: the bias voltage E_{bias} between two working electrodes (source and drain) and the potential drop between each individual working electrode and the reference electrode.[89]

The classic scanning tunneling spectroscopy (STS) with an STM tip under electrochemical condition has been widely used to contact SAMs. In this setup, the STM tip and the substrate act as source/drain electrodes *vs* an external reference and counter electrode. The electrochemical STS (EC-STS) (Figure 23) requires the insulation of the STM tip by a non-conductive material except for the very end of the tip in order to minimize electrochemical leakage currents and also capacitive current components to no more than 1 pA. If excess the pA range, the overlapping current between the components can mask the tunneling current through the junction.[90]
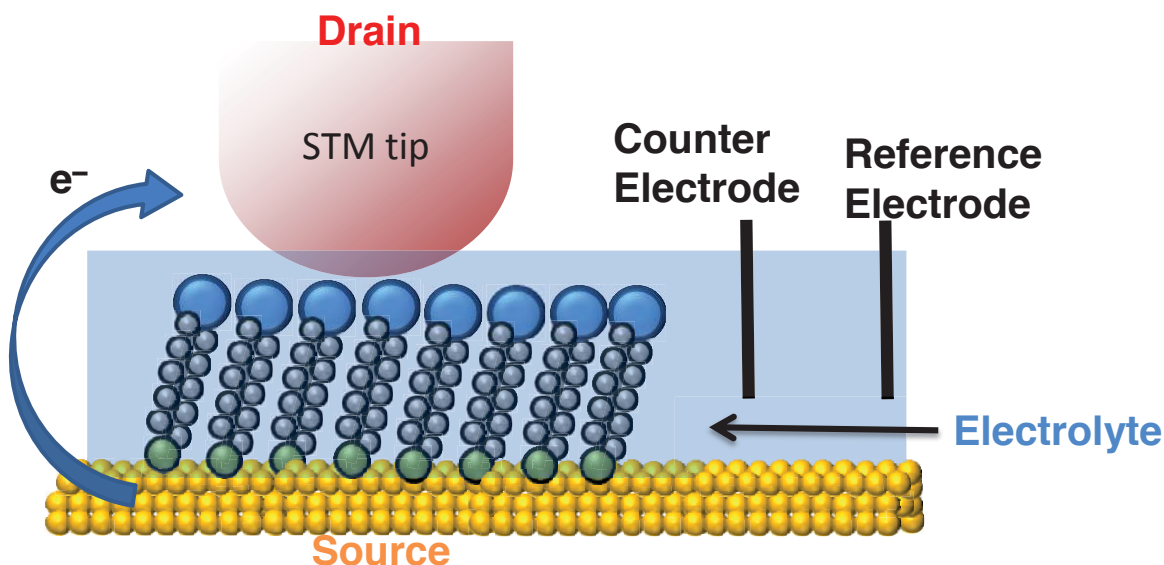
Figure 23: Schematic representation of electrochemical scanning tunneling microscopy (EC-STM)

Redox-active molecules represent a particular unique family of switches. Due to their properties, they can reduce or oxidize upon the application of an electrochemical gate field and that is why they are very interesting in order to achieve the in situ electrochemical gate-controlled charge transport.[91] The first to employ the concept of electrochemical gating with redox active molecules was Tao and coworkers in 1996. They used a scanning tunneling microscopy (STM) to study tunneling through Fe(III)–protoporphyrin (**FePP**) adsorbed flat on a highly ordered pyrolytic graphite (HOPG) electrode.[92] At the electrode potential where **FePP** was reduced, an increase of tunneling current was observed (Figure 25a) to flow between the tip and substrate through adsorbed **FePP**. This resonance condition was interpreted as arising from alignment of the Fermi level of the metal electrode with the lowest unoccupied molecular level (LUMO) of **FePP**.

More recently in 2006, T. Wandlowsky and coworkers published a study of the redox properties of a viologen (**V**) derivative (4, 4'- bipyridinium), immobilized on Au (111) using a gold STM tip.[93] They observed that, at variable substrate potential and at constant bias voltage, a sigmoidal potential dependence attributed to electronic structure changes of the viologen moiety during the one electron reduction/re-oxidation process $V^{2+} \leftrightarrow V^{+\bullet}$. Also they notice that the tunneling *vs* voltage curve shows a maximum located at the equilibrium potential of the $V^{2+} \leftrightarrow V^{+\bullet}$ redox process (Figure 25b).
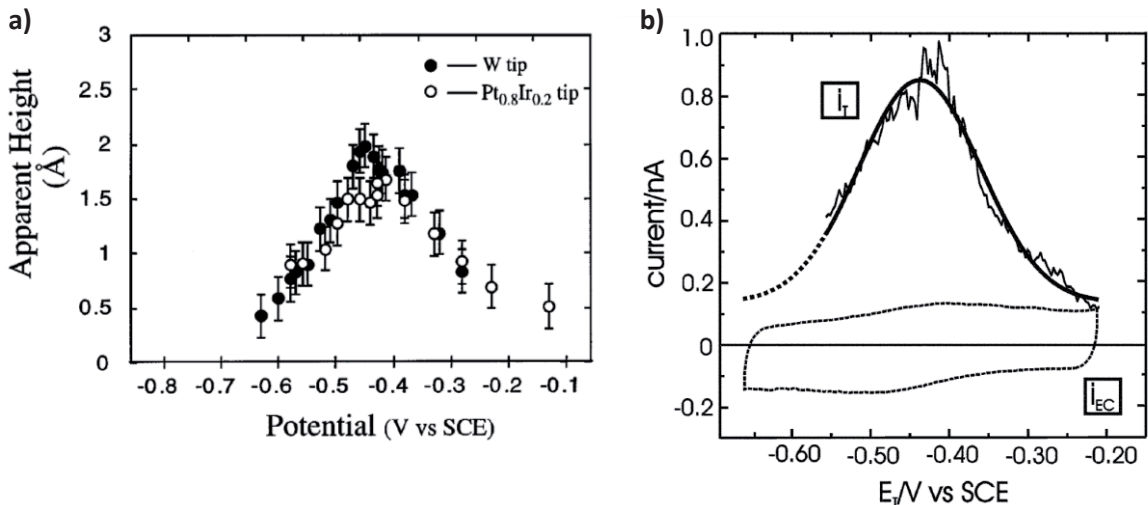
Figure 24: a) Apparent height of **FePP** relative to **PP** as a function of the substrate potential. The data obtained with the $Pt_{0.8}-Ir_{0.2}$ tip and with the W tip are represented by open circles and filled circles, respectively.[92] b) Tunneling current versus tip potential recorded in 0.05 M $KClO_4$ at pH 7 for a junction Au(T)/**V**/Au(S) at fixed bias (E_T - E_S) = 0.100 V. The solid black trace represents the average of 20 independent half cycles recorded when scanning the tip potential between -0.650 V and -0.200 V The thick solid and dotted lines represent the result of aGaussian fit to the redox-molecule-gated tunneling junction.[93]

Other systems studied with electrochemical gating technique have included oligophenylene-ethynylenes,[94] various perylene tetracarboxylic diimide derivatives,[95] oligo-anilines,[96] and a pyrrolo-tetrathiafulvalene (pTTF) derivative.[97]

6.1.1 Theoretical modeling

These systems, the in situ electrochemically gated EC-STS configuration can be modeled in terms of the redox active molecules positioned within the nanogap between the substrate and STS tip. The conductive response of this junction while the electrochemical potential is swept can be understood by considering the relative positions of the Fermi levels of the electrode contacts and the oxidized and reduced states of the PTM molecule. One of the models which describe better the tunneling switches performed with electrochemical active molecules is the two-step tunneling with partial vibrational relaxation model developed by Kuznestov, Ulstrup, and colleagues.[98]

According with K-U model, a molecule with discrete electronic levels is located between a metal substrate and a probe electrode (i.e. a STM tip), both providing continuously distributed electronic levels. The energetic levels of the molecule are broadened by interactions of the redox-center with the electrolyte and with the substrate. In that setup, there is a direct off-resonant tunneling current between the tip and the substrate with respect to the Fermi levels (ε_F) of the adjacent electrodes, while the energy levels of the solvated molecule are constantly fluctuating due to the variations of the solvation energy.

At a first step the LUMO orbital of the redox specie may decreases its energy due to fluctuations, and approach to the Fermi level of the substrate electrode causing the first electron transfer

(Figure 25 left). As consequence of this resonance between the Fermi level and the molecular orbital an enhancement of the tunneling current is produced.

After the first step, the energy of the occupied LUMO* decreases due to the vibrational relaxation and the second electron transfer step occurs between the LUMO* and the Fermi level of the tip. The second step happens before the LUMO orbital complete its vibrational relaxation and before the energy of the LUMO level overpasses de Fermi level of the tip electrode (Figure 25 right). Subsequently, the empty LUMO starts to relax toward higher energies and may accept another electron from the substrate electrode repeating the cycle.
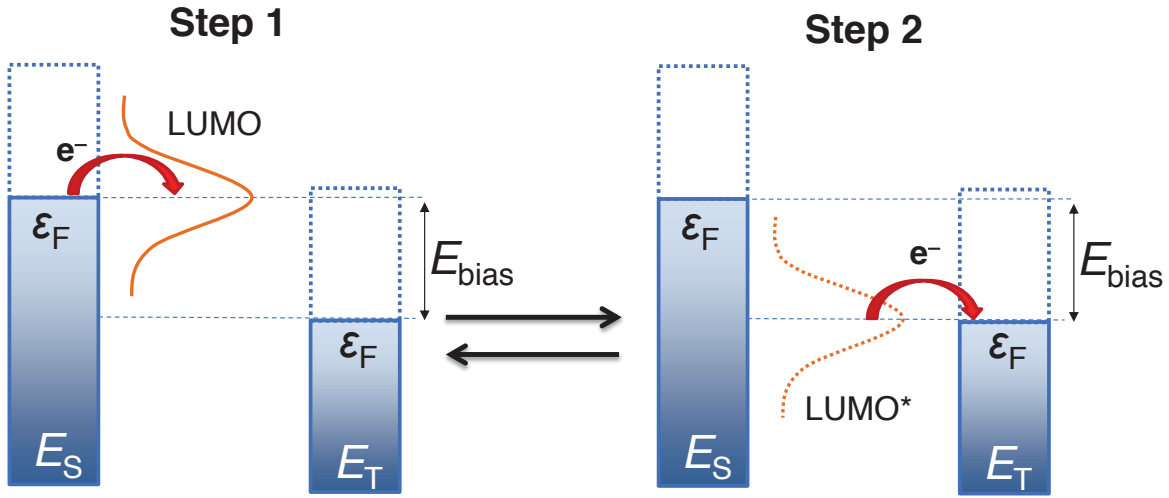
Figure 25: Schematic energy level diagram of a two-step ET process mediated by a redox-active radical molecule.

The curves can be fitted by using a numerical expression (Eq. 4) for the enhanced tunneling current obtained in the frameworks of the KU model.

$$I_{enh} = 1820E_{bias}\left[e^{\frac{9.73}{\lambda}(\lambda+\xi\eta+\gamma E_{bias})^2} + e^{\frac{9.73}{\lambda}(\lambda+E_{bias}-\xi\eta-\gamma E_{bias})^2}\right]^{-1} \tag{4}$$

Here, I_{enh} is enhanced tunneling current during constant-bias STS (in nA); the bias voltage (in V) $E_{bias} = (E_T - E_S)$ and overpotential (in V) $\eta = (E_S - E_0)$, where E_0 is the equilibrium potential for the electrochemical oxidation-reduction of a particular species; λ is reorganization energy (eV). ξ and γ, both ranging between 0 and 1, are model parameters describing the shift of η_{eff} with the variation of η and E_{bias}, respectively.

$$\eta_{eff} = \left(E_{eff} - E^0\right) = \xi\eta + \gamma E_{bias} = (\xi - \gamma) \cdot \eta + \gamma \cdot \eta T \tag{5}$$

6.2 Results and discussion

6.2.1 Electrochemical study

As we mentioned in the objectives, we want to analyze the fluctuations in the conductance of a SAM composed by PTM radical when we change the redox state of the PTM. For that purpose we employed a SAM of **HSC$_8$PTM^R** to be analyzed by electrogating approach using an electrochemical STS. However, before realizing the EC-STS experiments, it was required to optimize the electrochemical conditions to perform the experiment.

The cyclic voltammograms of the **HSC$_8$PTM^R** on Au(111) in acetonitrile showed a very stable and reproducible wave associated to the reduction of the PTM (PTM$^\bullet \rightleftharpoons$ PTM$^-$). Nevertheless the organic solvents are not appropriate for EC-STS experiments because their high volatility may destroy the STS cell, and also dissolve the coating polymer used to insulate the STM tips. One of the best options found for EC-STS measurements is to employ ionic liquids as a solvent.

Hence, we did an exhaustive study of the stability of the **HSC$_8$PTM^R** SAMs on Au (111) with different ionic liquids (which are summarized in the article "*Redox-active radical as an effective nanoelectronic component: stability and electrochemical tunnelling spectroscopy in ionic liquids*" in press). The problem that we found when we recorded the CV of the SAMs in these ionic liquids was that the intensity of the redox wave decreased after 20 cycles, even in neutral ionic liquids. This effect is associated to water traces present in the ionic liquids, which can protonate the α-carbon when the PTM anion is formed, and consequently the non-electroactive αH PTM is formed. To overcome this problem we decided to add a soft base, which does not reduce the PTM radical, in order to neutralize the traces of acidic protons, and dried the ionic liquids with molecular sieves. We concluded that the best conditions for realize the CVs in ionic liquids was to use a mixture of [Set$_3$][Tf$_2$N] and triethyl amine in a proportion 15:1 v/v, with molecular sieves. After that we performed the EC-STS measurements.

6.2.2 Electrochemical gating on PTM SAMs

The EC-STS experiments with **HSC$_8$PTM^R** SAMs were performed at constant bias voltage mode in the set-up shown in Figure 26. The STS curves (I_t vs E_s) obtained for those SAMs shows an increment of the tunneling current flowing between the substrate and the tip in the range of -0.8, -0.4 V forming a bell shaped curve with a maximum located to the equilibrium potential of the PTM$^\bullet \rightleftharpoons$ PTM$^-$ (Figure 27a and 27b). These bell-shaped STS curves are typical for redox mediated electron tunneling (REMET) processes showed for a variety of redox active molecules. Therefore, our system can also adjust to the K-U model (Figure 27c) described for other redox systems, with the difference that in our case the molecular orbital responsible of the electron transfer is the semi unoccupied molecular orbital (SUMO).

Our results ("*Redox-active radical as an effective nanoelectronic component: stability and electrochemical tunnelling spectroscopy in ionic liquids*") show that PTM radical is among the most efficient redox mediators in RMET, suggesting its applicability as an active electronic component in nanoelectronic devices and circuits.
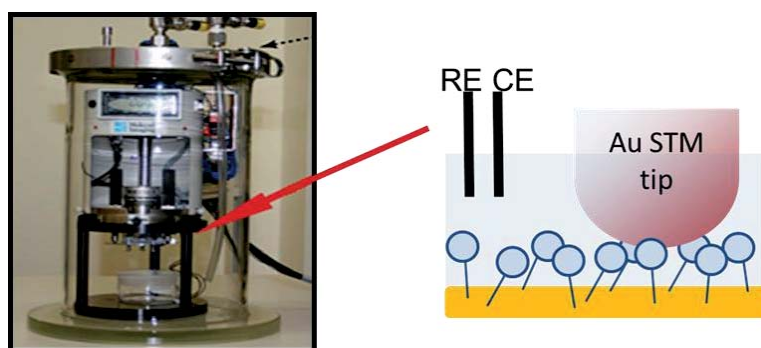
Figure 26: a) Set up of the STS cell employed.
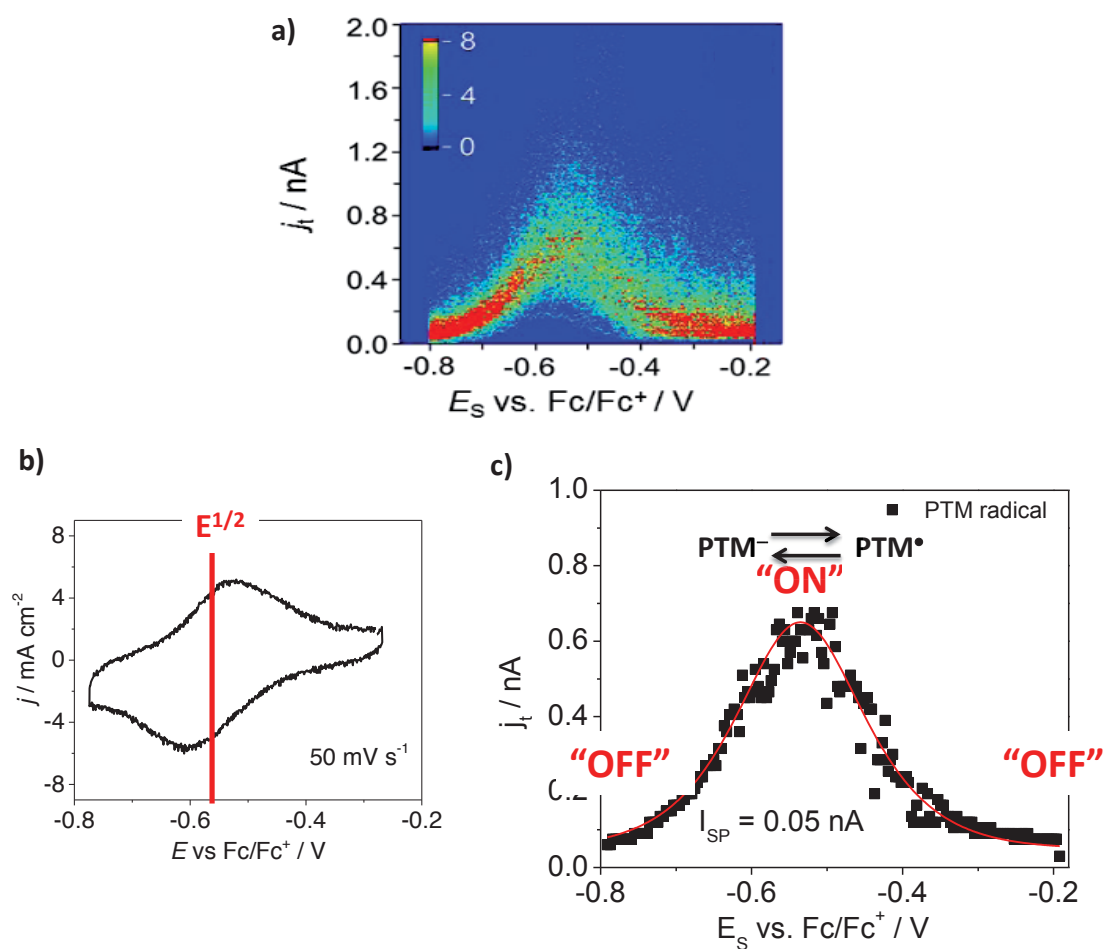
Figure 27: a) 2D occurrence histograms from 200 constant bias current-voltage traces for **HSC$_8$PTM^R** radical SAM on Au (111) b) CV of PTM SAM on Au (111) in [SEt$_3$][Tf$_2$N] recorded in a STM cell, where the half-wave potential is marked in red. c) Master current-voltage curves obtained for PTM radical SAM. The red line represents the fitting using the K-U model previously described.

7. Summary

We satisfactorily achieved the immobilization of PTM molecules on gold substrates, through which we were able to rationalize the charge transfer through PTM radicals and develop switching devices.

First we have developed a new synthetic strategy through which, we have obtained a new family of radical PTM and non-radical αH-PTM derivatives containing a thiol group connected to the PTM through an alkyl chain with different lengths (**HSC$_n$PTM^{NR}** and **HSC$_n$PTM^R** n = 8, 10 and 12). Also we have characterized all these compounds by different and complementary techniques: ^{1}H-NMR, ^{13}C-NMR, HPLC, Maldi-Tof for **HSC$_n$PTM^{NR}**; and CV, UV-Vis-NIR, HPLC, Maldi-Tof and EPR spectroscopy for **HSC$_n$PTM^R**.

With this family of compounds, we have been able to form well packed SAMs on Au (111), which were characterized by common techniques (CV, ARXPS and EPR spectroscopy) as well as by UPS and NEXAFS techniques that have permitted to determine the electronic structure of the SAMs, allowing us to build experimentally a scheme of the energetic levels.

We have studied the transport thorough the SAMs employing the EGaIn electrode as a contact testbed at different temperatures. Through these conductance measurements we have been able to determine the mechanism operating in these junctions, which is direct tunneling for both PTM radical and αH-SAMs. We also noticed that the PTM radical SAMs were 100 times more conductive than PTM αH-SAMs, proving thorough the energy orbital scheme, that the SUMO orbital of the PTM radicals have an important role in the electron transport in PTM SAMs junctions.

We have studied the electrochemical redox properties of the **HSC$_8$PTM^R** on Au (111) SAMs, demonstrating that the **HSC$_8$PTM^R** SAMs present a reversible and stable redox signal in ionic liquids, allowing us to exploit this SAMs as redox switch studied by electrochemical gating technique.

EC-STS experiments realized demonstrated that there is a current enhancement due to the redox-mediated electron tunneling mechanism. In comparison with other redox mediators studied so far, PTM radical is among the most efficient ones.

References

[1] B. A. Mantooth, P. S. Weiss. *Proceeding of the IEE*, 2003, **91**, 1785.

[2] S. Datta, W. Tian, S. Hong, R. Reifenberger, J. I. Henderson, C. P. Kubiak. *Phys. Rev. Lett.,* 1997, **79**, 2530.

[3] T. E. Kelley, E. L. Granstrom, C. D. Frisbie. *Adv. Mater.*, 1999, **11**, 261.

[4] J. Chen, M. A. Reed, A. M. Rawlett, J. M. Tour, *Science*, 1999, **286**, 1550.

[5] M. A. Reed, C. Zhou, C. J. Muller, T. P. Burgin, J. M. Tour, *Science*, 1997, **278**, 252.

[6] *Springer Handbook of Nanotechnology*, Ed:Bhushan, Germany, 2004.

[7] A. Ulman. *Academic Press: Boston*, 1991.

[8] a) G. K. Rowe, S. E. Creager, *Langmuir*, 1991, **7**, 2307-2312. b) L. A. Hockett, S. E. Creager, *Langmuir*, 1995, **11 (17)**, 2318-2321. c) H. C. Long, D. A. Buttry*, Society*, 1992, **17 (13)**, 2491-2496.

[9] R.F. Carvalhal, R. K. Mendes, L. T. Kubota, *Int. J. Electrochem. Sci.*, 2007, **2 (12)**, 973-985.

[10] M. T. Rojas, A. E. Kaifer, *J. Am. Chem. Soc.* 1995, **117 (12)**, 5883-5884.

[11] M. T. Rojas, R. Koniger, J. F. Stoddart, A. E. Kaifer, *J. Am. Chem. Soc.* 1995, **117 (7)**, 336-343.

[12] D. G. Walter, D. J. Campbell, C. A. Mirkin, *J. Phys. Chem. B*, 1999, **103**, 402-405.

[13] D. L. Feldheim, C. Keating. *Chem. Soc. Rev.*, 1998, **27**, 1.

[14] P.E. Laibinis, G. M. Whitesides, *J. Am. Chem. Soc.*, 1992, **114**, 9022-9028.

[15] G. K. Jennings, T.-H. Yong, J. C. Munro, P.E. Laibinis, *J. Am. Chem. Soc.*, 2003, **125 (10)**, 2950-2957.

[16] S. Steinberg, Y. Tor, E. Sabtani, I. Rubinstein*, J. Am. Chem. Soc.,* 1991, **113 (3)**, 5176-5182.

[17] D. Evans, R. Wampler, J. Phys. Chem. B, 1999, 103, 4666-4671.

[18] O. Chailapakul, R. M. Crooks, *Langmuir*, 1995, **11 (7)**, 1329-1340.

[19] P. D. Beer, P. A. Gale, *Supramolecular Chemistry, Oxford University Press*, 1999.

[20] I. Doy, E. Miyazaki, K. Takimiya, Y. Kunugi, *Chem. Mater.*, 2007, **19 (1)**, 5230-5237.

[21] J. C. Love, L. A. Estroff, J. K. Kriebel, *Self-Assembled Monolayers of Thiolates on Metals as a Form of Nanotechnology*, 2005, **Vol. 105**.

[22] R. G. Nuzzo, D. L. Allara, *J. Am. Chem. Soc.,* 1983, **105 (11)**, 4481-4483.

[23] M. D. Porter, T. B. Bright, D. L. Allara, D. E. D. Chidsey, *J. Am. Chem. Soc.,* 1987, **109 (6)**, 3559-3568.

[24] C. D. Bain, J. Evall, G. M. Whitesides, *J. Am. Chem. Soc.,* 1989, **111 (9)**, 7155-7164.

[25] H. Biebuyck, C. Bain, G. M. Whitesides, *Langmuir,* 1994, **10**, 1895-1831.

[26] P. Laibinis, G. M. Whitesides, *J. Am. Chem. Soc.,* 1991, **113**, 7152-7167.

[27] M. M. Walczak, C. Chung, S. M. Stole, C. Widrig, M. D. Porter, *J. Am. Chem. Soc.,* 1991, **113 (22)**, 2370-2378.

[28] J. C. Love, D. B. Wolfw, R. Haasch, M. L. Chabinyc, K. E. Paul, G. M. Whitesides, R. G. Nuzzo, *J. Am. Chem. Soc.,* 2003, **125**, 2597-2609.

[29] A. Carvalho, M. Geissler, H. Schmid, B. Michel, E. Delamarche, *Langmuir*, 2002, **18 (27)**, 2406-2412.

[30] Z. Li, S. C. Chang, R. S. Williams, *Langmuir*, 2003, **19 (15)**, 6744-6749.

[31] N. Muskal, I. Turyan. D. Mandler, *J. Electoanal. Chem.*, 1996, **409**, 131-136.

[32] T. Gupta, M. E. Van Der Boom, *J. Am. Chem. Soc.,* 2007, **129 (28)**, 12296-12303.

[33] J. Lee, B.-J. Jung, J.-I. Lee, H. Y. Chu, L.-M. Do, H.-K. Shim, *J. Mater Chem.*, 2012, **12 (12),** 3494-3498.

[34] M. Kawasaki, T. Sato, T. Tanaka, K. Takao, *Langmuir*, 2000, **16 (111)**, 1719-1728.

[35] C. D. Bain, E. B. Troughton, Y.-T. Tao, J. Evall, G. M. Whitesides, *J. Am. Chem. Soc.,* 1989, **111**, 321-335.

[36] F. Bensebaa, R. Voivu, L. Huron, T. Ellis, E. Kruus, Langmuir, 1997, **13 (9)**, 5335-5340.

[37] M. Kiguchi, S. Kaneko, *Chem. Phys. Chem*., 2012**, 13 (5)**, 1116-1126.

[38] Y. Qi, I. Ratera, J. Y. Park, P. D. Ashby, S. Y. Quek, J. B. Neaton, M. Salmeron, *Langmuir*, 2008, **24 (5)**, 2219-2223.

[39] T.- W. Kim, G. Wang, H. Lee, T. Lee, *Nanotechnology*, 2007, **18**, 315204.

[40] G. Binning H. Rohrer, C. Gerber, E. Weibel, *Appl. Phys. Lett*., 1982, **40,** 178-180.

[41] M. Celestin, S. Krishnan, S. Bhansali, E. Stefanakos, D. Y. Goswami*, Nano Research*, 2014, **7**, 589-625.

[42] a)S. Ho Choi, B. Kim, C. D. Frisbie, *Science*, 2008, **320**, 1482–1486. b) J. M. Beebe, B. Kim, J. W. Gadzuk, C. Daniel Frisbie, J. G. Kushmerick, *Phys. Rev. Lett*., 2006, **97**, 026801. c) D. J. Wold, R. Haag, M. A. Rampi, C. D. Frisbie, *J. Phys. Chem. B,* 2002, **106**, 2813–2816. d) J. M. Beebe, V. B. Engelkes, L. L. Miller, C. D. Frisbie, *J. Am. Chem. Soc.*, 2002, **124**, 11268–11269. e) V. B. Engelkes, J. M. Beebe and C. D. Frisbie, *J. Am. Chem. Soc.,* 2004, **126,** 14287–14296. f) B. Kim, J. M. Beebe, Y. Jun, X. Y. Zhu, C. D. Frisbie, *J. Am.Chem. Soc.,* 2006, **128**, 4970–4971. g) X. D. Cui, A. Primak, X. Zarate, J. Tomfohr, O. F. Sankey, A. L. Moore, T. A. Moore, D. Gust, G. Harris, S. M. Lindsay, *Science*, 2001, **294**, 571–574. h) X. D. Cui, X. Zarate, J. Tomfohr, O. F. Sankey, A. Primak, A. L. Moore, A. L. T. A. Moore, D. Gust, G. Harris, S. M. Lindsay, *Nanotechnology*, 2002, **13**, 5.

[43] a) T. D. Dunbar, M. T. Cygan, L. A. Bumm, G. S. McCarty, T. P. Burgin, W. A. Reinerth, L. Jones, J. J. Jackiw, J. M. Tour, P. S. Weiss, D. L. Allara, *J. Phys. Chem. B,* 2000, **104**, 4880– 4893. b) G. Yang, G.-y. Liu, *J. Phys. Chem.*

B, 2003, **107**, 8746–8759. c) P. A. Lewis, C. E. Inman, Y. Yao, J. M. Tour, J. E. Hutchison, P. S. Weiss, *J. Am. Chem. Soc.,* 2004, **126**, 12214–12215.

[44] L. A. Bumm, J. J. Arnold, T. D. Dunbar, D. L. Allara, P. S. Weiss, *J. Phys. Chem. B*, 1999, **103**, 8122–8127.

[45] B. Mann, H. Kuhn, L. V. Szentpaly, *Chem. Phys. Lett.*, 1971, **8**, 82-84.

[46] a) K. Slowinski, R. V. Chamberlain, C. J.Miller, M. Majda, *J. Am. Chem. Soc.,* 1997, **119**, 11910–11919. b) M. Duati, C. Grave, N. Tcbeborateva, J. Wu, K. Mullen, A. Shaporenko, M. Zharnikov, J. K. Kriebel, G. M. Whitesides, M. A. Rampi, *Adv. Mater.*, 2006, **18**, 329–333.

[47] N. Muskal, D. Mandler, *Electrochim. Acta*, 1999, **45**, 537-548.

[48] C. A. Nijhuis, W. F. Reus, G. M. Whitesides, *J. Am. Chem. Soc.,* 2009, **131**, 17814–17827

[49] M. Vasjari, Y. M. Shirshov, A. V. Samoylov, V. M. Mirsky, *J. Electroanal. Chem.,* 2007, **605**, 73–76.

[50] a) W. Wang, T. Lee, M. A. Reed, *Phys. E,* 2003, **19**, 117–125. b) W. Wang, T. Lee, M. A. Reed, *Rep. Prog. Phys.,* 2005, **68**, 523–544. c) N. Majumdar, N. Gergel, D. Routenberg, J. C. Bean, L. R. Harriott, B. Li, L. Pu, Y. Yao, J. M. Tour, J. *Vac. Sci. Technol., B: Microelectron. Nanometer Struct.–Process., Meas., Phenom.*, 2005, **23**, 1417–1421.

[51] B. de Boer, M. M. Frank, Y. J. Chabal, W. Jiang, E. Garfunkel, Z. Bao, *Langmuir*, 2004, **20**, 1539–1542.

[52] W. Wang, T. Lee, M. A. Reed, *Phys. Rev. B: Condens. Matter Mater. Phys.*, 2003, **68**, 035416.

[53] C. Zhou, M. R. Deshpande, M. A. Reed, L. Jones Ii, J. M. Tour, *Appl. Phys. Lett*., 1997, **71**, 611–613.

[54] P. A. Van Hal, E. C. P. Smits, T. C. T. Geuns, H. B. Akkerman, B. C. De Brito, S. Perissinotto, G. Lanzani, A. J. Kronemeijer, V. Geskin, J. Cornil, P. W. M. Blom, B. De Boer, D. M. De Leeuw, *Nat. Nanotechnol*., 2008, **3**, 749–754. b) H. B. Akkerman, A. J. Kronemeijer, J. Harkema, P. A. van Hal, E. C. P. Smits, D. M. de Leeuw, P. W. M. Blom, *Org. Electron*., 2009, **11**, 146–149.

[55] H. B. Akkerman, P. W. M. Blom, D. M. de Leeuw, B. de Boer, *Nature*, 2006, **441**, 69–72.

[56] a) G. Wang, H. Yoo, S.-I. Na, T.-W. Kim, B. Cho, D.-Y. Kim, T. Lee, *Thin Solid Films*, 2009, **518**, 824–828. b) H. B. Akkerman, B. de Boer, *J. Phys.: Condens. Matter*, 2008, **20**, 01300.

[57] S. A. DiBenedetto, A. Facchetti, M. A. Ratner, T. J. Marks, *Advanced Materials*, 2009, **21**, 1407–1433.

[58] a) J. G. Simmons, *J. Appl. Phys*., 1963, **34**, 1793-1803. b) J. G. Simmons, *J. Appl. Phys.,* 1964, **35**, 2655-2658.

[59] L. Luo, S. H. Choi, C. D. Frisbie, *Chem. Mater.,* 2011, **23**, 631–645.

[60] Y. A. Berlin, M. A. Ratner, *Radiat. Phys. Chem*., 2005, **74**, 124-131.

[61] a) A. Ulman, *An Introduction to Ultrathin Organic Films from Langmuir–Blodgett to Self-Assembly, Academic Press, Boston, CA,* 1991. b) J. C. Love, L. A. Estroff, J. K. Kriebel, R. G. Nuzzo, G. M. Whitesides, *Chem. Rev*., 2005, **105**, 1103–1170.

[62] A. Salomon, D. Cahen, S. Lindsay, J. Tomfohr, V. B. Engelkes, C. D. Frisbie, *Adv. Mater*., **2003**, 15, 1881–1890.

[63] G. Wang, T.-W. Kim, H. Lee, T. Lee, *Phys. Rev. B: Condens. Matter Mater. Phys.,* 2007, **76**, 205320

64 A. J. Kronemeijer, E. H. Huisman, H. B. Akkerman, A. M. Goossens, I. Katsouras, P. A. van Hal, T. C. T. Geuns, S. J. van der Molen, P. W. M. Blom, D. M. de Leeuw, *Appl. Phys. Lett.*, 2010, **97**, 173302–173303.

65 C. A. Nijhuis, W. F. Reus, G. M. Whitesides, *J. Am. Chem. Soc.*, 2009, **131**, 17814–17827.

66 G. Wang, T.-W. Kimb, T. Lee *J. Mater. Chem.*, 2011, **21**, 18117-18136.

67 C. A. Nijhuis, W. F. Reus, J. R. Barber, M. D. Dickey, G. M. Whitesides, *Nano Lett.*, 2010, **10**, 3611–3619.

68 A. Koitaho, R. Lahtienen, A. Efimov, H. K. Metsberg, E. Sariola, H. Lehtivuori, N. V. Tkachenko, H. Lemmetyinen, *J. Phys Chem*. C, 2001, **114**, 162-168.

69 A. J. Kronemeijer, H. B. Akkerman, T. Kudernac, B. J. Van Wees, B. L. Feringa, P. W. M. Blom, B. de Boer, *Adv. Mater.*, 2008, **20**, 1467-1473.

70 a) J. M. Mativetsky, G. Pace, M. Elbing, M. A. Rampi, M. Mayor, P. Samori, *J. Am. Chem. Soc.*, 2008, **130**, 9192–9193. b) G. Pace, V. Ferri, C. Grave, M. Elbing, C. von Hanisch, M. Zharnikov, M. Mayor, M. A. Rampi and P. Samori, *Proc. Natl. Acad. Sci. U. S. A.*, 2007, **104**, 9937–9942. c) U. Jung, O. Filinova, S. Kuhn, D. Zargarani, C. Bornholdt, R. Herges, O. Magnussen, *Langmuir*, 2010, **26**, 13913–13923.

71 J. Lee, H. Chang, S. Kim, G. S. Bang, H. Lee, *Angew. Chem. Int. Ed.*, 2009, **48**, 8501-8504.

72 a) R. L. Mc Creery, *Chem. Phys. Chem*. 2009, **10**, 2387–2391. b) R. L. McCreery, *Electrochemistry –The Electrochemical Society of Japan* 2010, **78**, 103.

73 E. Leary, S. J. Higgins , H. van Zalinge, W. Haiss, R. J. Nichols, S. Nygaard, J. O. Jeppesen, J. Ulstrup, *J. Am. Chem. Soc.*, 2008, **130**, 12204–12205.

74 W. Haiss, H van Zalinge, S. J. Higgins, D. Bethell, H. Hobenreich, D. J. Schiffrin, R. J. Nichols, *J. Am. Chem. Soc.*, 2003, **12**5, 15294–15295.

75 W. Han, E. N. Durantini, T. A. Moore, A. L. Moore, D. R. P. Gust, G. Leatherman, G. R. Seely, N. Tao, S. Lindsay, *J. Phys. Chem. B,* 1997, **101**, 10719–10725.

76 H. He, J. Zhu, N. J. Tao, L. A. Nagahara, I. Amlani, R. Tsui R, *J. Am. Chem. Soc.,* 2001, **123,** 7730–773.

77 T. Albrecht, A. Guckian, J. Ulstrup, J. G. Vos, *Nano. Lett.,* 2005, 5, 1451–1455.

78 I. Visoly-Fisher, K. Daie, Y. Terazono, C. Herrero, F. Fungo, L. Otero, E. Durantini, J. J. Silber, L. Sereno, D. Gust, T. A. Moore, A. L. Moore, S. M. Lindsay, *Proc. Natl. Acad. Sci. USA*, 2006, **103,** 8686–8690.

79 X. Xiao, D. Brune, J. He, S. Lindsay, C. B. Gorman, N. Tao, *Chem. Phys.,* 2006, **326**, 138–143.

80 X. Li, J. Hihath, F. Chen, T. Masuda, L. Zang, N. Tao, *J. Am. Chem. Soc.,* 2007, **129**, 11535–11542.

81 A. Alessandrini, M. Salerno, S. Frabboni, P. Facci, *Appl. Phys. Lett.,* 2005, **86**, 133902.

82 V. B. Engelkes, J. M. Beebe, C. Daniel Frisbie, *J. Phys. Chem*. *B,* 2005, **109**, 16801.

83 a) X.-S. Zhou, Z.-B. Chen, S.-H. Liu, S. Jin, L. Liu, H.-M. Zhang, Z.-X. Xie, Y.-B. Jiang, B.-W. Mao, *J. Phys. Chem. C* 2008, **112**, 3935. b) D. J. Wold, R. Haag, M. A. Rampi, C. D. Frisbie, *J. Phys. Chem. B* 2002, **106**, 2813.

[84] a) N. Crivillers, C. Munuera, M. Mas-Torrent, C. Simao, S. T. Bromley, C. Ocal, C. Rovira, J. Veciana, *Adv. Mater*. 2009, **21**, 1177–1181. b) N. Crivillers, M. Paradinas, M. Mas-Torrent, S. T. Bromley, C. Rovira, C. Ocal, C. Rovira, J. Veciana, *Chem. Commun.,* 2011, **47**, 4664-4666.

[85] R. C. Chiechi, E. A. Weiss, M. D. Dickey, G. M. Whitesides, *Angew. Chem. Int. Ed.*, 2008, **47**, 142-144.

[86] S. J. French, D. J. Saunders, G.W. Ingle, *J. Phys. Chem*. 1938, **42**, 265.

[87] D. Zrnic, D. S. Swatik, *J. Less-Common Met*. 1969, **18**, 67 .

[88] a) S. Kubatkin, A. Danilov, M. Hjort, J. Cornil, J. L. Bredas, N. Stuhr-Hansen, P. Hedegard, T. Bjornholm, *Nature*, 2003, **425**, 698. b) E. A. Osorio, T. Bjornholm, J. M. Lehn, M. Ruben, H. S. J. van der Zant, *J. Phys.: Condens. Matter*., 2008, **20**, 374121. c) H. S. J. van der Zant, Y. V. Kervennic, M. Poot, K. O'Neill, Z. de Groot, J. M. Thijssen, H. B. Heersche, N. Stuhr-Hansen, T. Bjornholm, D. Vanmaekelbergh, C. A. van Walree, L. L. W. Jenneskens, *Faraday Discuss.,* 2006, **131**, 347. d) E. A. Osorio, K. O'Neill, N. Stuhr-Hansen, O. F. Nielsen, T. Bjornholm, H. S. J. van der Zant, *Adv. Mater.,* 2007, **19**, 281. e) E. A. Osorio, K. O'Neill, M. Wegewijs, N. Stuhr-Hansen, J. Paaske, T. Bjornholm, H. S. J. van der Zant, *Nano Lett.,* 2007, **7**, 3336.

[89] N. J. Kay, S. J. Higgins, J. O. Jeppesen, E. Leary, J. Lycoops, J. Ulstrup, R. J. Nichols, *J. Am. Chem. Soc*., 2012, **134**, 16817-16826.

[90] Y. Yang, J.- Y. Liu, Z.- B. Chen, J.- H. Tian, X. Jin, B. Liu, X. Li, Z.- Z. Luo, M. Lu, F. Z. Yang, N. Tao, Z.- Q. Tian, *Nanotechnology*, 2011, **22**, 275313.

[91] a) C. Li, V. Stepanenko, M.-J. Lin, W. Hong, F. Wuerthner, T. Wandlowski, *Phys. Status Solidi B*, 2013, **250**, 2458–2467. b) N. Darwish, I. Diez-Perez, P. Da Silva, N. Tao, J. J. Gooding, M. N. Paddon-Row, *Angew. Chem., Int. Ed.,* 2012, **51**, 3203–3206.

[92] N. J. Tao, *Phys. Rev. Lett.,* 1996, **76**, 4066.

[93] Z. Li, B. Han, G. Meszaros, I. Pobelov, T. Wandlowski, A. Błaszczykzb, M. Mayor, *Faraday Discuss.,* 2006, **131**, 121–143.

[94] X. L. Li, B. Q. Xu, X. Y. Xiao, X. M. Yang, L. Zang, N. J. Tao, *Faraday Discuss.,* 2006, **131**, 111.

[95] C. Li, A. Mishchenko, Z. Li, I. Pobelov, T. Wandlowski, X. Q. Li, F. Wuerthner, A. Bagrets, F. J. Evers, *Phys.: Condens. Matter.,* 2008, **20**, 374122.

[96] J. He, F. Chen, S. Lindsay, C. Nuckolls, *Appl. Phys. Lett.*, 2007, **90**, 072112.

[97] E. Leary, S. J. Higgins, H. van Zalinge, W. Haiss, R. J. Nichols, S. Nygaard, J. O. Jeppesen, J. Ulstrup, *J. Am. Chem. Soc.,* 2008, **130**, 12204.

[98] a) A. M. Kuznetsov, I. G. Medvedev, J. Ulstrup, *J. Chem. Phys.,* 2007, **127**, 104708. b) J. Zhang, Q. Chi, A. M. Kuznetsov, A. G. Hansen, H. Wackerbarth, H. E. M. Christensen, J. E. T. Andersen, J. Ulstrup, *J. Phys. Chem. B,* 2002, *106*, 1131–1152. c) A. M. Kuznetsov, J. Ulstrup, *Chem. Phys.,* 1991, **157**, 25–33. d) A. M. Kuznetsov, J. Ulstrup, *Surf. Coat. Technol.*, 1994, **67**, 193–200. e) A. M. Kuznetsov, J. Ulstrup, *J. Phys. Chem. A,* 2000, **104**, 11531–11540. f) J. Zhang, A. M. Kuznetsov, J. Ulstrup, *J. Electroanal. Chem.,* 2003, **541**, 133–146. g) J. Zhang, Q. Chi, T. Albrecht, A. M. Kuznetsov, M. Grubb, A. G. Hansen, H. Wackerbarth, A. C. Welinder, J. Ulstrup, *Electrochim. Acta,* 2005, **50**, 3143–3159. h) A. M. Kuznetsov, J. *Chem. Phys.* 2007, **127**, 084710. i) A. M. Kuznetsov, J. Ulstrup, *J. Chem. Phys.,* 2002, **116**, 2149–2165. j) A. A. Kornyshev, A. M. Kuznetsov, J. U.

Nielsen, J. Ulstrup, *Phys. Chem. Chem. Phys*. 2000, **2**, 141–144. k) E. P. Friis, Y. I. Kharkats, A. M. Kuznetsov, J. Ulstrup, *J. Phys. Chem. A* 1998, **102**, 7851–7859. l) A. M. Kuznetsov, J. Ulstrup, *J. Electroanal. Chem.,* 2004, **564**, 209–222.

Publication 2

Title	Chemical control over the energy-level alignment in a two-terminal junction
Authors	Li Yuan, Carlos Franco, Núria Crivillers, Marta Mas-Torrent, Liang Cao, C. S. Suchand Sangeeth, Concepció Rovira, Jaume Veciana and Christian A. Nijhuis
Publication	*Nature Communications*, **2016**, *7*, 12066 doi:10.1038/ncomms1206

Chemical control over the energy-level alignment in a two-terminal junction

Li Yuan[1,*], Carlos Franco[2,*], Núria Crivillers[2,*], Marta Mas-Torrent[2], Liang Cao[1], C.S. Suchand Sangeeth[1], Concepció Rovira[2], Jaume Veciana[2] & Christian A. Nijhuis[1,3,4]

The energy-level alignment of molecular transistors can be controlled by external gating to move molecular orbitals with respect to the Fermi levels of the source and drain electrodes. Two-terminal molecular tunnelling junctions, however, lack a gate electrode and suffer from Fermi-level pinning, making it difficult to control the energy-level alignment of the system. Here we report an enhancement of 2 orders of magnitude of the tunnelling current in a two-terminal junction via chemical molecular orbital control, changing chemically the molecular component between a stable radical and its non-radical form without altering the supramolecular structure of the junction. Our findings demonstrate that the energy-level alignment in self-assembled monolayer-based junctions can be regulated by purely chemical modifications, which seems an attractive alternative to control the electrical properties of two-terminal junctions.

[1] Department of Chemistry, National University of Singapore, 3 Science Drive 3, Singapore 117543, Singapore. [2] Department of Molecular Nanoscience and Organic Materials, Institut de Ciència de Materials de Barcelona (ICMAB-CSIC) and Networking Research Center on Bioengineering, Biomaterials and Nanomedicine (CIBER-BBN), Campus de la UAB, Bellaterra 08193, Spain. [3] Centre for Advanced 2D Materials and Graphene Research Centre, National University of Singapore, 6 Science Drive 2, Singapore 117546, Singapore. [4] Solar Energy Research Institute of Singapore (SERIS), National University of Singapore, Singapore 117574, Singapore. * These authors contributed equally to this work. Correspondence and requests for materials should be addressed to J.V. (email: vecianaj@icmab.es) or to C.A.N. (email: christian.nijhuis@nus.edu.sg).

The possibility to integrate functional molecules into electronic devices is one of the promising approaches to miniaturize electronic circuits or to generate electronic function that is difficult to obtain using conventional semiconductors[1–3]. The advantage of molecular-based devices is, in principle, that the conductance can be tuned by designing molecules with the electronic and chemical structure tailored for the desired application. To achieve this 'chemical control' over transport characteristics, a good control over the energy-level alignment of the molecular frontier orbitals with respect to the Fermi level (E_F) of the electrodes is needed. For instance, control over the energy-level alignment has been used in thin film devices to lower charge injection barriers by either altering the work function of the metal-electrodes[4], or controlling the HOMO (highest-occupied molecular orbital) and/or LUMO (lowest unoccupied molecular orbital) levels with respect to the Fermi levels by chemical modification[5,6], or introducing charge injection layers[7,8]. In practical systems, however, chemical control over energy-level alignment proves to be challenging because of the so-called 'pillow effect' or Fermi-level pinning[7]. In molecular electronics, especially in the case of two-terminal devices, it remains difficult to predict how, if at all, certain chemical functionalities alter the junction characteristics[9–15]. Here we show how the tunnelling rates across molecular junctions can be increased by 2 orders of magnitude by tuning the energy levels of the system within the conduction window without the need for altering the molecular structure of the molecule–electrode interfaces by modifying the electronic structure of the molecules between the open- and closed-shell forms. Since the nature of the molecule–electrode interface is kept the same for both molecular forms, this approach is not limited by Fermi-level pinning.

The molecule bridging the two electrodes provides the molecular energy levels (E) in the solid-state device for conduction channels. The sum of the channels ($M(E)$) within the electrochemical potential window between μ_L and μ_R, will result in an effective current, as described by the Landauer formalism[16–18]:

$$I = \frac{2q}{h} \int_{\mu_L}^{\mu_R} T(E) M(E) \mathrm{d}E \qquad (1)$$

where h is Planck's constant, q is the electron charge and $T(E)$ is the transmission probability, which is inversely proportional to the square of zero-bias energy off-set between the molecular orbital and the Fermi level of the electrodes (δE_{ME}), equation (2),

$$T(E) = \frac{\Gamma_L \Gamma_R}{(\delta E_{ME})^2 + \frac{1}{4}(\Gamma_L + \Gamma_R)^2} \qquad (2)$$

where Γ_L and Γ_R are the degree of the coupling strength between the molecular frontier orbital and the Fermi level of the left (L) and the right (R) electrodes, respectively. Thus, the current (I) is proportional to the $M(E)$ and inversely proportional to (δE_{ME}) (ref. 2). Although in three-terminal devices the energy-level alignment of the systems, that is, the value of δE_{ME}, can be controlled via a gate electrode (or in a wet electrochemical environment gating via the electrolyte is possible)[19–22], in two-terminal devices, however, the molecular orbitals cannot be gated and therefore alternative approaches are needed.

One of these approaches is to control the energy-level alignment of the system by modifying the chemical structure of the molecules inside the junctions. In reality, it is difficult to predict how changes to the chemical structure of the junctions affect the electrical properties of the junctions and seemingly contradicting results have been reported. In SAM-based junctions, the difficulty of controlling the energy-level alignment due to Fermi-level pinning has been well-recognized.[7,23]

For example, Frisbie and co-workers[24] showed that changing the work function of the metal had a noticeable effect on the contact resistance (due to a large surface dipole at the metal–thiolate interface) but not on the energy-level alignment. Similarly, Blom and co-workers[25] found that introducing additional dipoles in the SAM structure results in large work function shifts. In contrast, Whitesides and co-workers[13–15] observed that the tunnelling rates across aliphatic SAMs in EGaIn junctions were independent of dipoles or acidity of small end groups of alkanethiolate SAMs. We confirmed these findings by Whitesides and co-workers[15] for a small subset of SAM structures, but Whitesides and co-workers and we also showed that other functionalities, such ferrocene (Fc) and redox-active aromatic groups[26–28], or polarizable groups (halogens)[29], did change the junction characteristics and induced rectification or changed the tunnelling rates, respectively. These studies show, as a group, that it is indeed difficult to predict which kind of chemical functionalities result in a noticeable change in the electrical characteristics of the junctions. One of the reasons is that changes in the molecular structure also result in changes of the molecule–electrode interactions and the supramolecular structure of the SAM making it difficult to isolate the factors that dominate the charge transport rates.

In this study, the charge transport rate across SAM-based tunnelling junctions with the same electrode–molecule interfaces and supramolecular structure but with different electronic structure modified by chemically switching the molecule between the open- and closed-shell forms is investigated. In particular, we incorporate SAMs of polychlorotriphenylmethyl radical (PTM^R) and of non-radical polychlorotriphenylmethane (PTM^{NR}) molecules tethered to the Au bottom electrode via an alkanethiolate linker into EGaIn junctions. The open-shell form contains a SOMO (single occupied molecular orbital), with one electron with an α spin configuration, and a SUMO (single unoccupied molecular orbital), and this results in a smaller molecular energy SOMO–SUMO gap than the HOMO–LUMO gap of the closed-shell form (ΔE values in Fig. 1). Similar observations have been made in an organic thin film in a wet electrochemical environment[25]. Thus, we change the electronic structure of the PTM while keeping the PTM—electrode interactions the same as the PTM is separated from the top-electrode via a van der Waals interface and the bottom-electrode via the alkyl group. Moreover, we show that not only the energy gap is lowered but also the value of δE_{ME} (or in other words, the energy-level alignment changed) which results in a low tunnelling barrier height and thereby a high-tunnelling current.

We investigated the mechanism of charge transport through a SAM of a free organic radical based on PTM radical because it is stable and can be readily grafted on gold[30,31], glass[32] and ITO[33], or as a single molecule linked between gold electrodes showing a Kondo effect at low temperatures[34]. The PTM radical has one unpaired electron located on the central carbon atom with a sp^2 hybridization, which is structurally shielded by the bulky o-chlorine atoms, leading to a high chemical and thermal stability[35]. This radical can be readily converted to the alpha-H non-radical derivative via reduction to the anion and protonation of the central carbon. Previously, the charge transport rates across PTM$^{R/NR}$ SAMs on gold were investigated by conductive probe atomic force microscopy (cpAFM), showing a higher tunnelling rate across junctions with PTM^R-based SAMs than those junctions with PTM^{NR}-based SAMs[36,37]. Theoretical calculations of the electronic structure of the gas phase molecules suggested SUMO-assisted transport in the case of the radical-based SAM. Based on these calculations, it was assumed that the mechanism of charge transport was coherent tunnelling without direct experimental evidence regarding the electronic
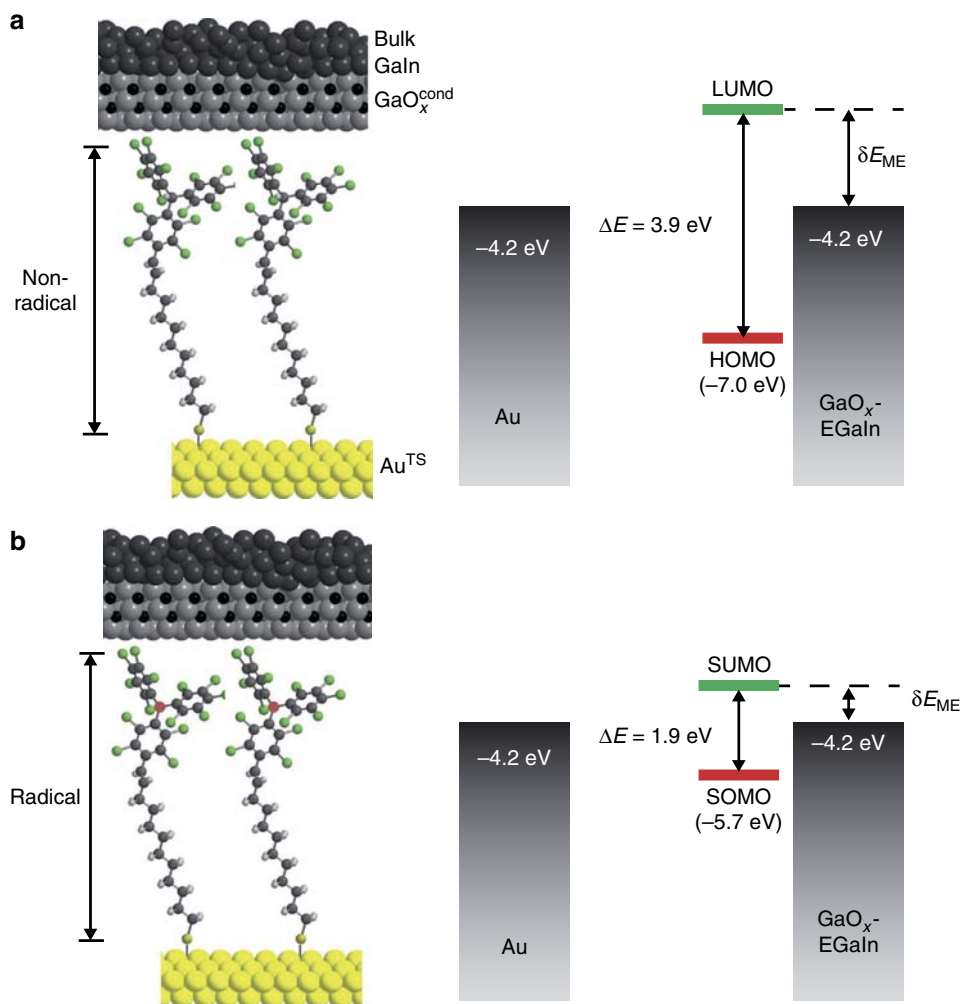
Figure 1 | Schematic illustrations of the junctions. Schematic representations of the junctions of Au^{TS}-$SC_{10}PTM^{R/NR}$//GaO_x^{cond}/EGaln and the corresponding energy level diagrams. The top-electrodes (**a**) are liquid metal GaO_x^{cond}/EGaln (where EGaln is the eutectic alloy of Ga and In, and GaO_x^{cond} is a 0.7-nm-thick self-limiting highly conductive oxide layer)[15–17]. The bottom electrodes (**b**) are template-stripped Au surfaces (~300-nm-thick, see fabrication methods in ref. 11 and Methods for details). The ΔE and δE_{ME} represent the molecular energy gap and zero-bias energy off-set between the LUMO (or SUMO) and the Fermi level of the electrodes, respectively. Red dots show the central C atoms of radical moieties. The distance (d) between two electrodes is about 2.1 nm.

structure of the junction- or temperature-dependent charge transport data. This assumption, however, may have been not correct because in these studies the PTM moiety was grafted to the bottom-electrode via a short-conjugated tether. Likely significant hybridization of the molecular frontier orbital with the gold electrode occurs and resonant transport cannot be excluded.

Here we demonstrate that the mechanism of charge transport is coherent tunnelling in both types of $PTM^{R/NR}$ SAMs bearing long (6 or more CH_2 units) non-conjugated alkyl tether, to ensure the molecular frontier orbitals remain localized on the PTM and that tunnelling rates across the junction can be increased by 2 orders of magnitude in the open-shell based SAMs with respect to the closed-shell ones without changing the tunnelling distance d or the nature of the molecule–electrode contacts. This increase in the tunnelling rates is because in junctions with the PTM^R SAMs, the SUMO participates in the transport and effectively lowers the tunnelling barrier height (see Fig. 1). Importantly, contrary to what we hypothesized in previous works[36,37], the findings reported here unambiguously demonstrate that the enhancement of the tunnelling rate transport across the radical-based SAMs is not due to a resonant tunnelling mechanism but instead due to a SUMO-assisted coherent non-resonant

tunnelling. We base our conclusions on statistically large numbers of $J(V)$ data and $J(V,T)$ measurements combined with a detailed physical-organic study of the electronic and supramolecular SAM structures using six newly designed PTM derivatives with different chain lengths. All SAMs are anchored on gold via a thiolate binding group and the $PTM^{R/NR}$ moieties are effectively decoupled from the electrode via the long alkyl chains. Hence, all types of SAMs yield similar work functions of gold. Here we show intramolecular control over the electronic structure of the junction, resulting in a large change in the value of δE_{ME} and, consequently, the observed tunnelling rates. In other words, we show a large modulation of the tunnelling rate of 2 orders of magnitude across junctions with the same supramolecular structure and work function of the electrodes.

Results

Molecular synthesis. Three PTM-CH=CH-$(CH_2)_{n-2}$SH radicals and three αH-PTM-CH=CH-$(CH_2)_{n-2}$SH non-radicals, with $n = 8$, 10 and 12, have been synthesized. We use the abbreviations $HSC_nPTM^{R/NR}$ for simplicity to follow the discussions. Figure 2 shows the synthetic route to the PTM-thiolated derivatives $HSC_nPTM^{R/NR}$. We aimed to couple the alkyl chain
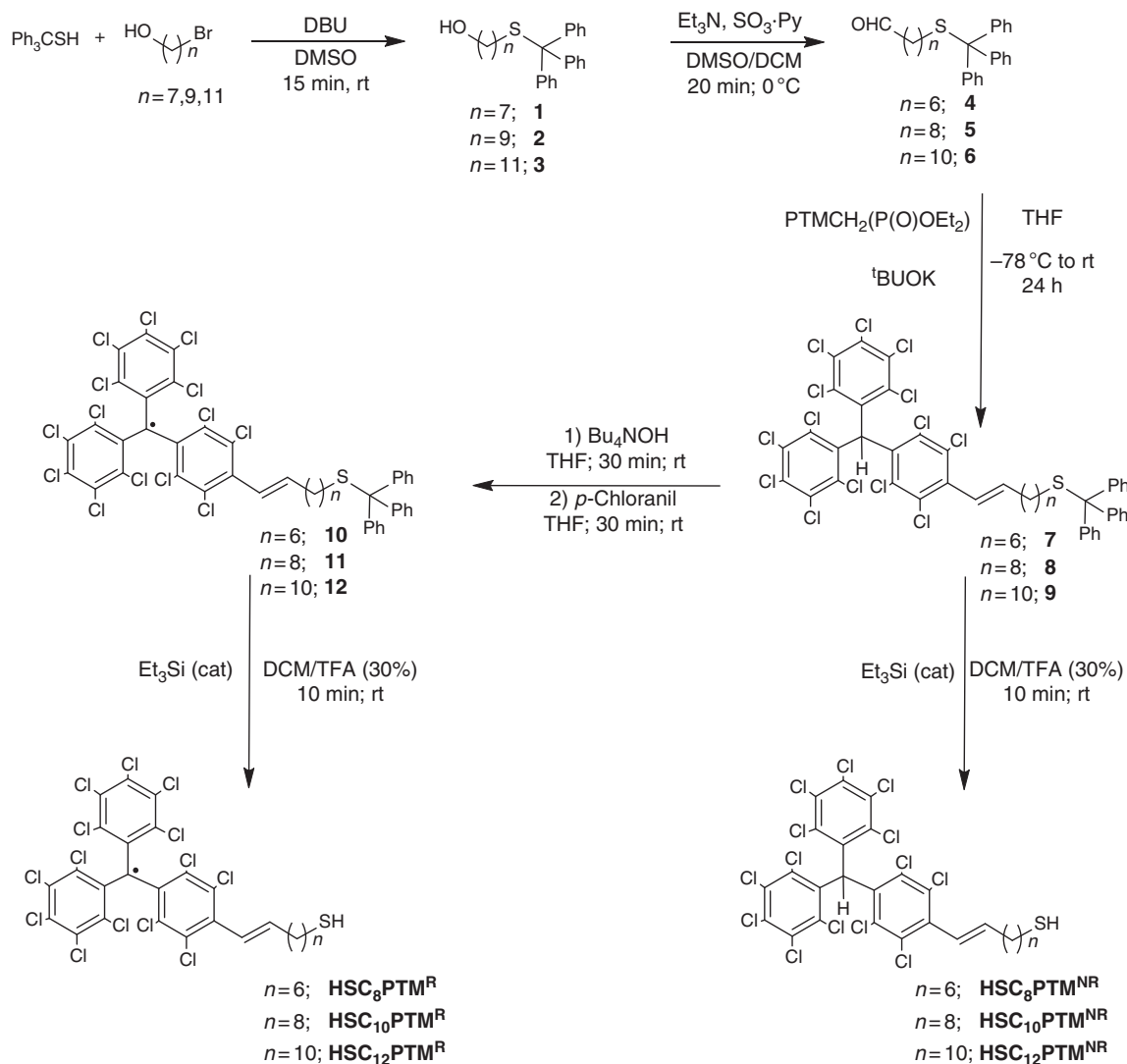
Figure 2 | Synthetic route to radicals HSC$_n$PTM^R and non-radicals HSC$_n$PTM^{NR}. DBU, 1, 8-diazabicycloundec-7-ene; ^{t}BuOK, potassium tert-butoxide; DMSO, dimtehylsulfoxide; DCM, dichloromethane; ET$_3$N, triethylamine; SO$_3$Py, sulfur trioxide pyridine; Bu$_4$NOH, tetrabutylammonium hydroxide; ET$_3$Si, triethylsilane; THF, tetrahydrofurane; TFA, trifluoroacetic acid; rt, room temperature.

with the thiol-anchoring group to the PTM unit using a C=C bond, because the double bond only causes a small modification to the electronic structure of the PTM (unlike electron donating/withdrawing groups such as amides or carbonyls) and it can be readily formed by a Wittig–Horner reaction between the PTM-phosphonate and an aldehyde bearing the corresponding alkyl chain and the thiol-precursor[38]. To overcome the instability of the thiol groups under the Wittig–Horner conditions, as well as under the oxidative conditions needed to generate the radical from the corresponding carbanion, we used a triphenylmethyl (trityl) as a protecting group. This protecting group was easily deprotected in acidic media in the last step of the synthesis to obtain the final thiolated compounds (Fig. 2). High-pressure liquid chromatography (HPLC) confirmed that, despite the reducing character of the thiol groups and the low-reduction potential of the PTM radicals[21], PTM-thiolated derivatives are stable for several weeks in ambient conditions. We note that storing for extended periods of time disulfide derivatives formed as a result of the oxidation of the thiol groups. The same was observed for the non-radical counterparts and, for this reason, all SAMs reported here were prepared using freshly deprotected thiolate derivatives.

SAM structural characterization. The SAMs were prepared using freshly template-stripped Au surfaces with ultra-flat topography[39–41], which were immersed in 0.5 mM solutions of the target compound in toluene. Before the fabrication of the top-electrode, the SAMs were characterized by cyclic voltammetry (CV) and angle-resolved X-ray photoelectron spectroscopy (ARXPS) to ensure that we used good-quality SAMs (See Supplementary Fig. 10 and Supplementary Figs 13–16 for the complete data sets). The ARXPS and element ratios (see more details in Method section 'Photoelectron spectroscopy' and 'Determination of the thickness of the SAMs from the S 2p spectra') analysis from XPS revealed that both radical and non-radical SAMs are in a standing-up phase rather than lying flat on the surface, the calculated layer thickness (d) scales with n and was similar for PTM^{NR} and PTM^R SAMs with the same number of n, and that all SAMs had very similar surface coverage ($1.4–1.6 \times 10^{-9}$ mol cm^{-2}) within experimental error (5%) (see Supplementary Table 1 and Methods). From our results, we conclude that the supramolecular structure of the SAM does not change when the PTM units are in the open- or closed-shell forms.
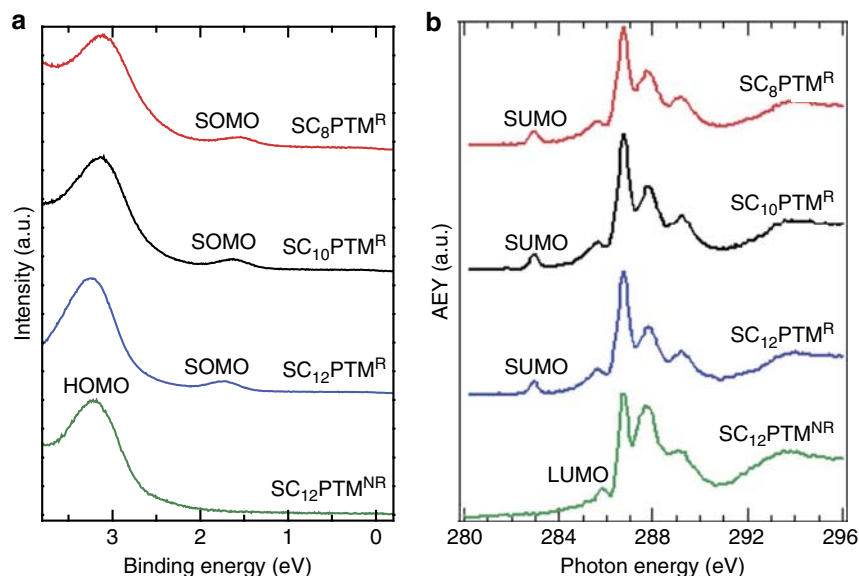
Figure 3 | Electronic structure of the PTM$^{R/NR}$ SAMs on Au^{TS}. (**a**) Ultraviolet photoemission spectroscopy (UPS) and (**b**) C K-edge X-ray absorption fine structure (NEXAFS) spectra of SAMs derived from HSC$_n$PTM^R with $n = 8$, 10, 12 and HSC$_{12}$PTM^{NR}.

SAM electronic structure characterization. The electronic structure of the SAMs on Au^{TS} was determined by ultraviolet photoelectron spectroscopy (UPS) and near edge X-ray adsorption fine structure spectroscopy (NEXAFS) to estimate the positions of the filled and empty states, respectively. The UPS spectra were recorded to determine their energy levels with respect to the Fermi level of a clean Au substrate for all PTM$^{R/NR}$-Au^{TS} SAMs. Figure 3a shows the UPS spectra of the HSC$_n$PTM^R SAMs. We found that the SOMO peak with a SOMO-onset value of ~ 1.45 eV is clearly visible in contrast to the spectra obtained from HSC$_n$PTM^{NR} SAM that do not show this peak (here only HSC$_{12}$PTM^{NR} SAM is shown as representative of the PTM^{NR} SAMs; see Supplementary Fig. 17 for $n = 8$ and 10) and only reveal the HOMO peak with the HOMO-onset value at ~ 2.45 eV. This is a clear evidence of the persistence of the unpaired electron once the molecules are covalently grafted on the surface.

The C K-edge NEXAFS spectra (Fig. 3b) show peaks at ~ 285.7 and ~ 286.5 eV, which are assigned to the C(Ph) $\rightarrow \pi^\star$ transitions in the perchlorinated phenyl rings of the PTM molecules[42]. These peaks are present in the spectra of PTM^R and PTM^{NR} SAMs, but in the case of the PTM^R SAMs there is an additional peak at ~ 282.9 eV. This peak indicates the presence of an empty state with an energy just above the Fermi level and it is attributed to the transition to the SUMO orbital[42,43]. We have calculated the SUMO (for the PTM^R SAMs) and LUMO (for the PTM^{NR} SAMs) energy position from the NEXAFS spectra (Table 1, see details in Methods). Thus, the molecular energy gap of the PTM$^{R/NR}$ SAMs could be calculated from UPS and NEXAFS spectra (Table 1) and the results are comparable with the optical band gap (~ 1.9 eV for R and ~ 3.9 eV for NR) determined by the ultraviolet–visible spectra (see Supplementary Figs 6 and 7).

We note that the energy levels determined by these techniques only involve SAMs. We believe that the energy levels shift once the SAMs form a contact with the GaO$_x^{cond}$/EGaIn top-electrodes, though we believe these shifts are small due to the non-covalent nature of the SAM//GaO$_x^{cond}$/EGaIn contact. Thus, the energy levels depicted in Fig. 1 give a good qualitative indication of the energy levels. Moreover these experimental data indicate that the SUMOs of radical and LUMOs of non-radical SAMs, are closer to the E_F of GaO$_x$/EGaIn (-4.2 eV)[44] and SAM-modified Au^{TS}

bottom electrodes (-4.1 to -4.2 eV) than the SOMO and HOMO. Therefore we believe the mechanism of charge transport involves tunnelling via the SUMO or LUMO orbitals. We note that the nature of the charge carrier cannot be directly measured in these two-terminal devices, but our results agree with the findings reported by Cahen and co-workers[45] for n-alkanethiolate SAMs that showed that transport is dominated by the unoccupied molecular orbitals.

Transport through the SAMs. For this study, we used liquid metal GaO$_x^{cond}$/EGaIn top-electrodes since they form non-invasive soft top-contacts with the SAMs[11,46,47]. To fabricate the molecular junctions, the HSC$_n$PTM$^{R/NR}$ derivatives were first self-assembled on ultra-smooth Au^{TS} bottom electrodes and followed by the formation of the top-electrodes following previously reported methods (see Methods)[48,49]. The Au^{TS}-SC$_n$PTM$^{R/NR}$//GaO$_x^{cond}$/EGaIn junctions were measured under the same experimental conditions and we biased the top-electrodes and grounded the bottom electrodes. We collected at least 21 traces on 20 different junctions for each type of junctions (see Table 1 for all statistics). The data were plotted in histograms of $\log_{10}|J|$ at each applied bias (voltage steps of 0.05 V), and then we fitted Gaussians to the histograms to obtain the mean values of $\log_{10}|J|$ ($<\log|J|>_G$), log-s.d. ($\sigma_{\log}$) and 95% confidence intervals. Figure 4 shows $<\log|J|>_G$ plotted against the applied bias with 95% confidence levels as error bars of the junctions and the histograms of $\log_{10}|J|$ at -1.0 V for the PTM$^{R/NR}$ SAMs (red corresponds to the radical and black to the alpha-H non-radical SAMs). In all cases, the values of $<\log|J|>_G$ measured for the PTM radical SAMs are consistently about 100 times higher than those values obtained for junctions with the non-radical SAMs in the whole measured bias range. The higher measured current across the radical SAMs is in agreement with our previous studies involving junctions based on cpAFM and electron transfer rate studies of different types of PTM-based SAMs[36,37]. Figure 4a also shows that $<\log|J|>_G$ values at $+1.0$ V are ~ 1.5 times higher than at -1.0 V; this small asymmetry in the $J(V)$ curves could be caused by the different electrode materials, different interfaces at top- and bottom-contact, or the negative dipole moment of the PTM

Table 1 | Statistics of electrical characterization of the PTM-based junctions and energy level determination by UPS and NEXAFS spectroscopy at room temperature.

SAM	Number of junctions	Traces	Short*	Yield (%)†	d (nm)‡	Work function (eV)§	SOMO/HOMO (eV)§	SUMO/LUMO (eV)‖	Energy gap (eV)¶	δE_{ME} (eV)#
R_8	20	424	2	90	1.83	4.12 ± 0.05	−5.65 ± 0.02	−3.72 ± 0.10	1.93 ± 0.12	0.40 ± 0.15
R_{10}	20	417	3	85	2.05	4.15 ± 0.05	−5.69 ± 0.02	−3.65 ± 0.10	2.04 ± 0.12	0.50 ± 0.15
R_{12}	20	424	2	90	2.20	4.20 ± 0.05	−5.72 ± 0.02	−3.51 ± 0.10	2.21 ± 0.12	0.69 ± 0.15
NR_8	20	420	2	90	1.79	4.28 ± 0.05	−6.95 ± 0.02	−3.08 ± 0.10	3.87 ± 0.12	1.20 ± 0.15
NR_{10}	20	420	2	90	2.08	4.26 ± 0.05	−7.02 ± 0.02	−3.00 ± 0.10	4.02 ± 0.12	1.26 ± 0.15
NR_{12}	20	424	1	95	2.22	4.26 ± 0.05	−6.95 ± 0.02	−2.86 ± 0.10	4.09 ± 0.12	1.40 ± 0.15

ARXPS, angle-resolved X-ray photoelectron spectroscopy; HOMO, highest-occupied molecular orbital; LUMO, lowest occupied molecular orbital; NEXAFS, near edge X-ray adsorption fine structure spectroscopy; NR, non-radical; SAM, self-assembled monolayer; SOMO, single occupied molecular orbital; SUMO, single unoccupied molecular orbital.
*A junction short was defined when the value of J exceeded 10^2 A cm^{-2} (the upper limit of J measurable by our instrument) while recording 20 J(V) scans.
†The yield of non-shorting junctions is defined as the percentage number of non-shorting junctions divided by the total number of junctions.
‡The thickness d was determined by ARXPS. The error bars were 0.2 nm (see Methods for details).
§The work function and the energy of the SOMO/HOMO were determined by UPS (see Methods for details).
‖The energy level of SUMO/LUMO was determined by NEXAFS spectroscopy (see Methods for details).
¶The energy gap was calculated by the difference between the HOMO and LUMO for the NR SAM and SOMO and SUMO for the R SAM.
#The value of δE_{ME} was calculated by the difference between the work function and SUMO/LUMO.
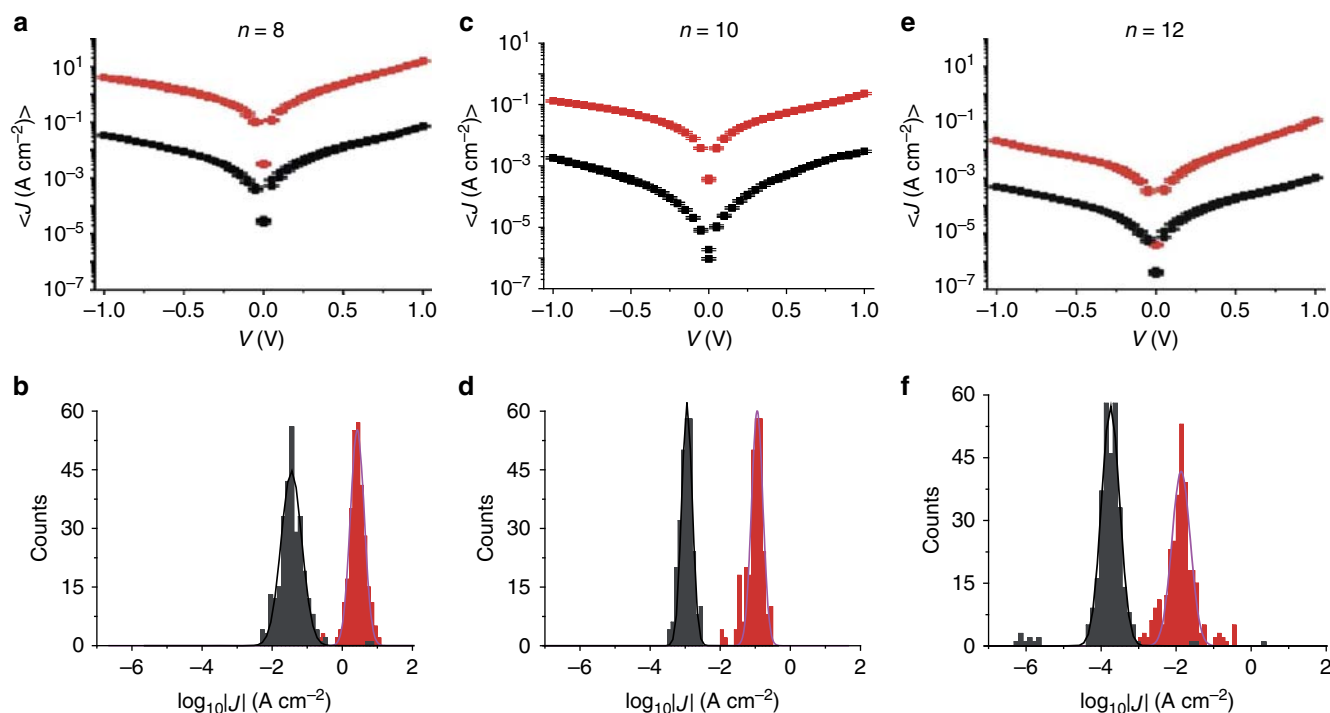
Figure 4 | Electrical characteristics of the tunnelling junctions at room temperature. (**a,c,e**) Plots of the $<\log|J|>_G$ against the applied bias for radical (red) and non-radical (black) junctions and (**b,d,f**) the histograms of $\log|J|$ measured at −1.0 V along with Gaussian fits to these histograms.

molecules due to electron-withdrawing character of chlorinated phenyl rings[30,50].

To investigate the charge transport mechanism in more detail, we carried out temperature-dependent charge transport measurements in the range of temperatures (T) from 340 to 210 K. We used a device made of a polymeric transparent polydimethylsiloxane (PDMS) mold having micro-channels that stabilize the GaO$_x^{cond}$/EGaIn (see ref. 51 and Methods for details). The GaO$_x^{cond}$/EGaIn formed contact with the SAM through small round-orifices present in the polymeric mold. These devices generate stable junctions over at least 1,000 traces (see Supplementary Fig. 12) and allow us to perform temperature-dependent measurements in the probestation. Figure 5a shows averaged J(V) curves from 10 J(V) traces at each temperature for the three radical SAM-based junctions, and Fig. 5b shows the Arrhenius plots for J at −1.0 V (see Supplementary Fig. 18 and Methods for temperature-dependent J(V) measurements of non-

radical SAM-based junctions, that is, NRs). For the whole measured temperature range, the measured values of J (A cm^{-2}) for the three radical SAMs are all temperature independent, which indicate the charge transport mechanism is in tunnelling regime.

To investigate the dependence of J as a function of tunnelling distance (d), here we used carbon number n as the equivalent for d and plotted $<\log|J|>_G$ (determined at −1.0 V) versus n (Fig. 6). To this plot, we fitted the general tunnelling equation (equation (3)):

$$J = J_0 e^{-\beta d} \tag{3}$$

where β is the tunnelling decay coefficient (in n^{-1}) and J_0 (A cm^{-2}) is a constant including the contact resistance and it measures the current density flowing through the electrode-SAM interface in the hypothetical case of zero separation between the electrodes[52]. The values of β only show a small difference
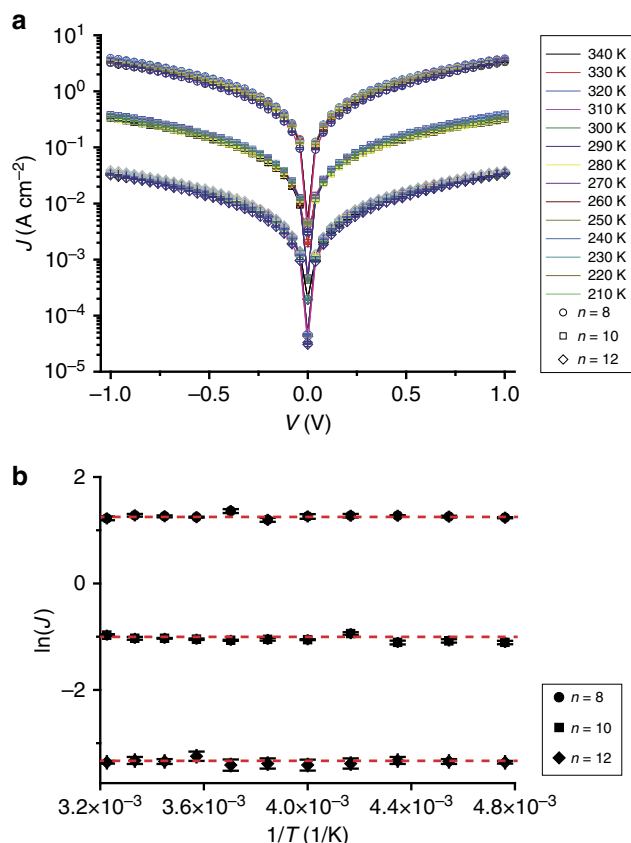
Figure 5 | Temperature dependence measurements. (**a**) Semi-log plots of the average $J(V)$ curves measured over the temperature range of 210–340 K at intervals of 10 K for Au^{TS}-SC_nPTM^R SAMs with $n = 8$, 10 and 12 and (**b**) Arrhenius plots of the average J at -1.0 V. The error bars represent the standard deviations of 10 $J(V)$ curves.

for both types of junctions ($\beta_R = 0.89 \pm 0.01\,n^{-1}$ and a $\beta_{NR} = 1.03 \pm 0.03\,n^{-1}$) but the values of J_0 differ strongly in the magnitude ($\log J_{0,R} = 3.0 \pm 0.2$ and $\log J_{0,NR} = 1.9 \pm 1.2$). Here, the error bar represents the 95% confidence level from least absolute deviation (LAD) fitting (see procedure of LAD fitting in ref. 26). These β values are similar in value to those reported for insulating organic molecules (n-alkanethiols), which have β values between 0.9 and 1.1 n^{-1} (refs 28,39,53). The magnitudes of the values of J_0 are in line with other SAM-based molecular junctions but at least 1,000 times lower than single molecular junctions due to the differences in effective contact area between the techniques[47,54]. It was reported before that the values of β are proportional to the square root of the δE_{ME} for coherent non-resonance tunnelling through a rectangular barrier, that is, $\beta \propto \sqrt{\delta E_{ME}}$ (refs 55,56). The δE_{ME} values of PTM^{NR} SAMs are consistently ~2 times higher than PTM^R SAMs, which leads to about a 1.4 times increase in β. This back of the envelope calculation is in line with our measured data that the β_{NR} at -1.0 V is about 1.2 times higher than β_R (this estimation does not take into account the shape of the barrier and the renormalization of the energy levels when bias is applied). This result also suggests that the decay rate is dominated by the length of the alkyl chain and the PTM moiety is effectively decoupled from the Au electrode by the long alkyl tether. This observation is supported by temperature-dependent measurements, which demonstrate that for over the entire measured temperature range, the values of J are independent of the temperature for the PTM^R junctions. Along with the exponential decay of J with d, we believe that the mechanism of charge transport is direct
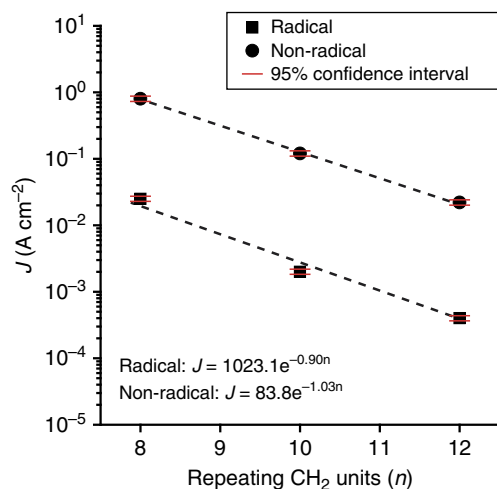
Figure 6 | General tunnelling equation fit. The average values of J (A cm^{-2}) at -1.0 V as a function of carbon number (n) for Au^{TS}-$SC_nPTM^{R/NR}//GaO_x^{cond}/EGaIn$ junctions. The dashed lines represented the fits to the general tunnelling equation. The red error bars represent the 95% confidence interval.

tunnelling[53,57]. This interpretation also agrees with equation (2) and the large difference in $J_{0,R}$ and $J_{0,NR}$ values relates to the difference in δE_{ME} values: the radical SAM-based junctions have smaller δE_{ME} values and thus larger higher transmission probabilities (T) than the non-radical analogues.

In previous reports some of us claimed that resonant tunnelling is important where the SOMO energy determines the tunnelling barrier height. These assumptions were based on electronic structure calculations using molecules in the gas phase without accounting for Fermi-level pinning as a result of the metal–thiolate bond. The energy level diagram shown in Fig. 1 is based on experimental data (Table 1) from which we conclude that the empty levels define the tunnelling barrier height and not the filled levels. Although the exact shape of the tunnelling barrier inside the junctions during charge transport is not known, we believe that the energy-level diagram represents our system well considering the non-covalent nature of SAM//top contact. Although the junctions are asymmetric and the empty levels of the PTM^R moieties are energetically and spatially very close to the Fermi level of the top-electrode and separated from the bottom electrode by the alkyl, we do not observe significant current rectification. In contrast, similar junctions but with Fc or bipyridyl (BIPY) end groups do rectify[26,58]. These diodes rectify currents because hopping (thermally activated charge transport) involving the Fc or BIPY is important. However, redox-active SAMs with p-quinone end groups resulted in rectifying EGaIn junctions with low rectification ratios of 3.5 (ref. 28). Although molecular asymmetry is needed to obtain rectification, the magnitude of rectification depends on many factors including the shape of the electrostatic potential profile[48], the terminal group coupling with the EGaIn top electrode[48,58] or relaxation time of the charge carrier on the molecule (or activation energy for hopping)[16,59]. Currently, we do not know why certain end groups facilitate hopping while others do not.

Discussion

In summary, a family of PTM radical (which have single-occupied molecular orbitals), and the corresponding non-radical (which have filled molecular orbitals), derivatives of different molecular lengths bearing a thiol group has been synthesized and successfully integrated in molecular junctions of the type of

Au^{TS}-$SC_nPTM^{R/NR}$/GaO_x^{cond}/EGaIn. Temperature- and chain length-dependent measurements indicate that the mechanism of charge transport across all the junctions is direct tunnelling. This work exemplifies that stable free organic radicals are interesting systems, in addition to others, in molecular junctions because they have small SOMO/SUMO or HOMO/LUMO gaps. In addition, the possibility of having the radical and non-radical junctions make it possible to re-align the molecular energy levels with respect to the Fermi-levels of the metal contacts without altering the nature of the molecule—metal contacts or the backbone of the molecule and, thus, avoiding issues such as Fermi-level pinning.

Our results demonstrate that intramolecular control over the energy-level alignment of molecular tunnelling junctions is a promising approach to control the electrical characteristics of two-terminal molecular junctions. We believe that in the future our findings may be extended to other types of junctions or to control, or perhaps induce, new electronic function.

Methods

Synthesis. The general procedure of the synthesis of PTM derivatives is outlined in Supplementary Fig. 1. The detailed synthesis and characterization of PTM derivatives are described in the Supplementary Methods. The representative infrared (IR), cyclic voltammetry (CV), ultraviolet–visible and electron paramagnetic resonance (EPR) spectra of radicals are shown in Supplementary Figs 2–9.

Fabrication of template-stripped bottom-electrode. We have reported before the procedure for template stripping using epoxy (EpoTek 353ND)[44,49,60]. Briefly, we deposited A 200-nm-thick Au (with a purity of 99.999% both from Super Conductor Materials Inc) film on clean Si(100) wafers by thermal deposition (Shen Yang Ke Yi, China). The evaporation rate was about $0.3 \, \text{Å s}^{-1}$ for the first 50 nm and then increased to $\sim 5 \, \text{Å s}^{-1}$ to deposit the remaining 150 nm and the deposition vacuum was about 2×10^{-6} mbar. We cut the glass slides into pieces of $1 \times 0.5 \, \text{cm}^2$ and then cleaned them in a solution of H_2SO_4:$H_2O_2 = 1{:}5$ (in volume) at 80 °C for 20 min, and then washed with H_2O to pH 7 and drying in a stream of N_2 gas. The glass slides were further cleaned by a plasma of air for 5 min at a pressure of 5 mbar. We dropped the epoxy on the Au surfaces and carefully added the glass slides on top of them. After the whole wafer was covered with glass slides, we cured the epoxy at 80 °C for 8 h in an oven (Epec). The final step was to lift off the glass slides with Au surfaces glued on them before immersion in the thiol solutions to minimize contamination of the Au^{TS} surfaces by air.

Formation of the SAMs. Au^{TS} surfaces were immersed in a freshly prepared solution of 0.5 mM of each compound in toluene (HPLC grade) for 24 h at 40 °C and then for an additional 24 h at room temperature. Always, before immersing the substrates, the solution was degassed with argon. During the SAM formation, the solution was kept in dark and under argon atmosphere to avoid the decomposition of the radical species. After the time indicated above, the substrates were removed from the solution and were washed with toluene and dichloromethane to remove any physisorbed materials. The modified substrates were characterized immediately after removal from the solution. The electrochemical characterization was performed using 300 nm Au evaporated on mica from Georg Albert (Germany). Before their use, the substrates were rinsed with acetone, dichloromethane and ethanol and then exposed to ozone for 20 min. Immediately after that the substrates were immersed in ethanol (HPLC grade) for at least 30 min. Before immersing the substrates in the PTM derivative solution, they were rinsed with ethanol and dried under nitrogen stream.

Electrochemical characterization of the SAMs. The three SAMs of Au-SC_nPTM were electrochemically characterized by using CV performed with an AUTOLAB 204 with NOVA 1.9 software. We used a custom built electrochemical cell with a Pt-wire as counter electrode, Ag-wire as pseudo reference electrode and the modified Au(111) on mica as working electrode. The area exposed to the tetra-butylammonium hexafluorophosphate ($TBAPF_6$) in dichloromethane electrolyte solution (0.1 M) was $0.26 \, \text{cm}^2$. The CVs were recorded in the range +0.1 V to −0.6 V. The electrochemical measurements were performed in a Faraday cage. CV depicted in Supplementary Fig. 10 shows the CV of the **R_{10}** SAM as representative for the different SAMs.

Fabrication of PDMS top-electrodes. We have reported the fabrication of the top-electrodes of Ga_2O_3/EGaIn stabilized in PDMS in detail elsewhere[51]. Since the fabrication methods are essentially the same, we only provide Supplementary Fig. 11, which shows the microscope image of the through-hole filled with

Ga_2O_3/EGaIn. A small gap of roughly 10 μm is present between the Ga_2O_3/EGaIn and the wall of the PDMS. In all the measurements reported here, we used electrodes with a geometrical contact area of about $7.1 \times 10^2 \, \mu\text{m}$.

Fabrication of Au^{TS}-$SC_nPTM^{R/NR}$/GaO_x^{cond}/EGaIn junctions. The fabrication of the SAM-based junctions with cone-shaped tips of GaO_x^{cond}/EGaIn were reported previously[11]. Briefly, in our experiments we grounded the bottom electrode with a gold probe penetrating the SAMs and the top-electrode of GaO_x^{cond}/EGaIn was biased from $0 \, \text{V} \rightarrow 1.0 \, \text{V} \rightarrow 0 \, \text{V} \rightarrow -1.0 \, \text{V} \rightarrow 0 \, \text{V}$, with a step size of 50 mV and a delay of 0.1 s, to record the $J(V)$ curves. The statistical analysis follows previous reported methods[11] and the results are listed in Table 1.

Stability measurement of Au^{TS}-$SC_8PTM^{R/NR}$//GaO_x^{cond}/EGaIn junctions. To investigate whether the junctions are stable and do not change during voltage cycling, we prepared junctions with the PDMS top-electrodes described in Methods section 'Fabrication of PDMS top-electrodes' and measured 1,000 $J(V)$ traces in the bias range of ± 1.0 V. All the $J(V)$ traces for both types of junctions (that is, with SAMs of R_8 (red) and NR_8 (black)) are plotted in Supplementary Fig. 12. The shape of the $J(V)$ traces did not change significantly and the values of J remained constant over 1,000 traces (plotted in Supplementary Fig. 12B for +1.0 V).

Photoelectron spectroscopy. We have reported the measurement procedures and analysis of synchrotron-based photoemission spectroscopy (PES) measurements (XPS and UPS) and NEXAFS spectroscopy at the SINS (Surface, Interface and Nanostructure Science) beamline of the Singapore Synchrotron Light Source (SSLS) elsewhere[54]. Briefly, the base pressure was kept at 1×10^{-10} mbar. We used the Au $4f_{7/2}$ core level peak at 84.0 eV measured from a sputter-cleaned gold foil in electrical contact with the sample to calibrate the photon energy. We chose 350 eV for the Cl $2p$, S $2p$ and C $1s$ for the XPS measurements, and 60 eV for the valence band measurements. To measure the work function, we applied –10 V bias to the sample to overcome the work function of the analyser. All UPS spectra were referenced to the Fermi edge of Au and all PES spectra were normalized by the photon current. For NEXAFS, we measured the photon energy from 270 eV to 330 eV. Two take-off angles (90° and 40°) were used to probe the angle-dependence. We performed the least-square peak fit analysis with Voigt functions (Lorentzian (30%) and Gaussian (70%)) using XPSpeak software, and the sloping background was modelled using Shirley plus linear background correction[61,62]. Supplementary Figs 13–16 show the high-resolution PES spectra with fits of Cl $2p$, C $1s$ and S $2p$ of the SAMs of Au^{TS}-$SC_nPTM^{R/NR}$ at two different take-off angles 90° and 40°, respectively. Supplementary Fig. 17 shows the UPS and NEXAFS spectra of Au^{TS}-SC_nPTM^{NR} ($n = 8$ and 10).

The C $1s$ high-resolution spectra show three components: (1) C–C single bond at ~ 284.2 eV labelled C_1, (2) the central C (αC) of the PTM moiety and the C=C group at ~ 285.2 to ~ 285.3 eV labelled C_2, and (3) aromatic C–Cl at ~ 286.4 eV labelled C_3 (ref. 62). The Cl $2p$ spectra show typical doublet peaks. The doublet peak of the S $2p$ spectra are solely (or mainly) contributed by the typical S–Au bond at the binding energy of 161.8 eV. The SAMs of R_8 and NR_8 show a small portion of low binding energy at ~ 160.8 eV, which has been reported before and is assigned to chemical absorption of the SAMs at grain boundaries[62]. We summarized the fitting results of the XPS spectra of C $1s$ and Cl $2p$ in the form of the elemental ratio in Supplementary Table 2. From Supplementary Table 2, we can make three conclusions: (1) the decrease of C_1/C_3 ratios from carbon number 8 to 12 indicate the SAMs are standing up; (2) the C_2/C_3 ratios are constant at 90° emission but slightly decrease at 40° due to the attenuation of the first C connected to the PTM group and (3) the Cl/C_3 ratios are constant for different SAMs and the difference between 90° and 40° emission angle is caused by the large attention of the central C signal compared with the Cl atom.

Determination of the surface coverage of the SAMs from the S $2p$ spectra. To calculate the surface coverage of the $PTM^{R/NR}$ SAMs, we determined the integrated intensity of Cl $2p$ spectra (I_{Cl}) of the $PTM^{R/NR}$ and $S(CH_2)_{10}CH_2Cl$ ($SC_{11}Cl$) SAMs (listed in the Supplementary Table 1). Since the Cl atoms were connected to the terminal groups of the SAMs, the I_{Cl} can be related to the surface coverage of the SAMs. The relative surface coverage was calculated by comparing the I_{Cl} of the $PTM^{R/NR}$ SAMs, which divided by 14 ($PTM^{R/NR}$ SAMs contains 14 Cl atoms), against that of $SC_{11}Cl$ SAMs. The surface coverage of $SC_{11}Cl$ SAMs on Ag has been reported before and is $1.1 \times 10^{-9} \, \text{mol cm}^{-2}$ (ref. 29). Thus, we compared the values of I_{Cl} of the $PTM^{R/NR}$ SAMs against those of the $SC_{11}Cl$ SAMs to calculate the relative surface coverage of the $PTM^{R/NR}$ SAMs (Supplementary Table 1). We estimated the uncertainties to be about 5% from the fitting errors of Cl $2p$ spectra. However, we note that not all of the 14 Cl atoms on the PTM moiety are located at the top of the SAMs, and the signal of at least 4 Cl atoms (connected to the phenyl ring with alkyl chain) are attenuated by half of the length (~ 6.3 Å) of the PTM moiety. Thus, the surface coverage calculated by XPS here was underestimated by at least 13% ($= 4/14 \times e^{-6.3\lambda}$). Nevertheless, the relative surface coverages are the same for all the PTM SAMs which support our conclusion that we did not change the supramolecular structure of the $PTM^{R/NR}$ SAMs.

We also estimated the theoretical surface coverage of these SAMs formed on the Au(111) surface, and the dimension of the PTM moiety was calculated from CPK model. Since the PTM moiety is a planer-triangle, its projection on the x–y plane changes between rectangles (or a parallelogram dependent on the molecular tilt angle which we do not know). We estimated a surface coverage of 1.8×10^{-10} mol cm^{-2} from the simple case of rectangle projection (side lengths: $a = 12.6$ Å and $b = 7.4$ Å). The surface coverage estimated from XPS is similar to the theoretical estimation.

Determination of the thickness of the SAMs from the S 2p spectra. We have reported the methods to fit the spectra and to calculate the SAM thickness from angle-dependent XPS measurements in ref. 48. We only give a short description here. The SAM thickness (d, nm) can be expressed as the sum of the Au–S bond ($d_{Au-S} = 1.8$ Å)[63] and the over layer thickness (the distance from the middle of the S atom to vacuum) d_2 in equation (4)

$$d = d_2 + d_{Au-S} \quad (4)$$

The different angles of the incident light (γ) result in different emission area on the samples. To normalize the footprint of incident light, we calculate the effective intensity (I_θ)

$$I_\theta = I\cos(90° - \gamma) \quad (5)$$

where I is the integrated intensity of the peak. The values of I_θ are exponentially dependent on d_2 and on the take-off angle

$$\frac{I_\theta(d, 90°)}{I_\theta(d, 40°)} = \frac{\left(1 - e^{-d_1/\lambda \sin 90°}\right)e^{-d_2/\lambda \sin 90°}}{\left(1 - e^{-d_1/\lambda \sin 40°}\right)e^{-d_2/\lambda \sin 40°}} \quad (6)$$

where the d_1 ($= 1.5$ Å) is estimated from the radius of S atoms and the S–C bond, and λ ($= 8$ Å) is the inelastic mean free path[62]. We can rewrite the equation (6) to calculate the value of d_2

$$d_2 = \frac{\lambda \sin 90° \sin 40° \left[\ln\left(\frac{I_{90°}}{I_{40°}}\right) + \ln\left(1 - e^{-\frac{d_1}{\lambda \sin 40°}}\right) - \ln\left(1 - e^{-\frac{d_1}{\lambda \sin 90°}}\right)\right]}{\sin 90° - \sin 40°} \quad (7)$$

The S 2p spectra along with fits are shown in Supplementary Figs 12–15, and the results are listed in Supplementary Table 3. The uncertainty of ± 2 Å takes into account the fitting errors and the angular misalignment due to sample mounting.

Calculation of LUMO energy level from NEXAFS spectra. We determined the SUMO or LUMO level with respect to the Fermi level of the electrode by the binding energy of the C 1s core level of the PTM from the XPS spectra (Supplementary Figs 13–18) and the SUMO or LUMO peak from the NEXAFS spectra with a correction of 0.5 eV for core–hole exciton-binding energy to take into account the core–hole attraction effect. Others have reported correction factors in the range of 0.1–2.0 eV (ref. 64), but we have used 0.5 eV also for other types of SAMs as described in the supporting information of ref. 60. Since we used for both types of junctions with NR and R SAMs the same correction factor, the energy levels for both types of junctions would shift equally in case one would chose different correction factors and hence will not affect our conclusions.

Temperature-dependent measurement of a junction with a SAM of NR$_8$. We used EGaIn top-electrodes stabilized in a through-hole in PDMS to form stable junctions, and measured the temperature-dependent J(V) in a probe station as mentioned in the main text. Supplementary Fig. 18 shows the J(V) traces recorded at 250–330 K at intervals of 10 K. Both the Arrhenius plots and the J(V) traces show that the junction characteristics are independent of temperature as expected, since the non-radical SAMs have larger molecular energy gaps than their radical counterparts and behave as tunnelling barrier.

LAD fitting. As mentioned in the manuscript, we performed LAD fitting of the tunnelling equation (equation (3) in the main text) to the full data set of $\log_{10}|J|$ at different applied bias (V) from -1.0 V to -0.1 V. The details of the LAD fitting have been reported in ref. 65. Supplementary Fig. 19 shows the plot of the tunnelling decay coefficient (β) against V. We found that the value of β of the junctions with SAMs of PTM^{NR} is consistently ~1.2 times higher than that of PTM^{R}.

Data availability. The data that support the findings of this study are available from the corresponding author upon request.

References

1. Akkerman, H. B. & de Boer, B. Electrical conduction through single molecules and self-assembled monolayers. *J. Phys. Condens. Matter* **20**, 013001 (2008).
2. Aviram, A. & Ratner, M. Molecular rectifiers. *Chem. Phys. Lett.* **29**, 277–283 (1974).
3. Cui, X. D. *et al.* Making electrical contacts to molecular monolayers. *Nanotechnology* **13**, 5–14 (2002).
4. Heimel, G., Romaner, L., Zojer, E. & Bredas, J.-L. The interface energetics of self-assembled monolayers on metals. *Acc. Chem. Res.* **41**, 721–729 (2008).
5. Malen, J. A. *et al.* Identifying the length dependence of orbital alignment and contact coupling in molecular heterojunctions. *Nano Lett.* **9**, 1164–1169 (2009).
6. Coughlin, J. E., Henson, Z. B., Welch, G. C. & Bazan, G. C. Design and synthesis of molecular donors for solution-processed high-efficiency organic solar cells. *Acc. Chem. Res.* **47**, 257–270 (2014).
7. Hung, L. S. & Chen, C. H. Recent progress of molecular organic electroluminescent materials and devices. *Mater. Sci. Eng. R* **39**, 143–222 (2002).
8. Scott, J. C. Metal-organic interface and charge injection in organic electronic devices. *J. Vac. Sci. Technol. A* **21**, 521–531 (2003).
9. Mativetsky, J. M. *et al.* Azobenzenes as light-controlled molecular electronic switches in nanoscale metal-molecule-metal junctions. *J. Am. Chem. Soc.* **130**, 9192–9193 (2008).
10. Liu, Y. *et al.* Giant enhancement in vertical conductivity of stacked CVD graphene sheets by self-assembled molecular layers. *Nat. Commun.* **5**, 5461 (2014).
11. Nerngchamnong, N. *et al.* The role of van der Waals forces in the performance of molecular diodes. *Nat. Nanotechnol.* **8**, 113–118 (2013).
12. Sayed, S. Y., Fereiro, J. A., Yan, H., McCreery, R. L. & Bergren, A. J. Charge transport in molecular electronic junctions: Compression of the molecular tunnel barrier in the strong coupling regime. *Proc. Natl Acad. Sci. USA* **109**, 11498–11503 (2012).
13. Yoon, H. J., Bowers, C. M., Baghbanzadeh, M. & Whitesides, G. M. The rate of charge tunnelling is insensitive to polar terminal groups in self-assembled monolayers in Ag^{TS}S(CH$_2$)$_n$M(CH$_2$)$_m$T//Ga$_2$O$_3$/EGaIn Junctions. *J. Am. Chem. Soc.* **136**, 16–19 (2014).
14. Liao, K.-C., Yoon, H. J., Bowers, C. M., Simeone, F. C. & Whitesides, G. M. Replacing Ag^{TS}SCH$_2$-R with Ag^{TS}O$_2$C-R in EGaIn-based tunnelling junctions does not significantly change rates of charge transport. *Angew. Chem. Int. Ed.* **53**, 3889–3893 (2014).
15. Yoon, H. J. *et al.* The rate of charge tunnelling through self-assembled monolayers is insensitive to many functional group substitutions. *Angew. Chem. Int. Ed.* **51**, 4658–4661 (2012).
16. Joachim, C. & Ratner, M. A. Molecular electronics: some views on transport junctions and beyond. *Proc. Natl Acad. Sci. USA* **102**, 8801–8808 (2005).
17. Landauer, R. Spatial variation of currents and fields due to localized scatterers in metallic conduction (and comment). *J. Math. Phys.* **37**, 5259–5268 (1996).
18. Datta, S. *Lessons from Nanoelectronics: A New Perspective on Transport* Vol. 1 (World Scientific Publishing Co. Pte. Ltd., 2012).
19. Díez-Pérez, I. *et al.* Rectification and stability of a single molecular diode with controlled orientation. *Nat. Chem.* **1**, 635–641 (2009).
20. Frisenda, R. *et al.* Kondo effect in a neutral and stable all organic radical single molecule break junction. *Nano Lett.* **15**, 3109–3114 (2015).
21. Fave, C. *et al.* Tunable electrochemical switches based on ultrathin organic films. *J. Am. Chem. Soc.* **129**, 1890–1891 (2007).
22. Capozzi, B. *et al.* Tunable charge transport in single-molecule junctions via electrolytic gating. *Nano Lett.* **14**, 1400–1404 (2014).
23. Lenfant, S. *et al.* Electron transport through rectifying self-assembled monolayer diodes on silicon: Fermi-level pinning at the molecule − metal interface. *J. Phys. Chem. B* **110**, 13947–13958 (2006).
24. Kim, B., Choi, S. H., Zhu, X. Y. & Frisbie, C. D. Molecular tunnel junctions based on pi-conjugated oligoacene thiols and dithiols between Ag, Au, and Pt contacts: Effect of surface linking group and metal work function. *J. Am. Chem. Soc.* **133**, 19864–19877 (2011).
25. de Boer, B., Hadipour, A., Mandoc, M. M., van Woudenbergh, T. & Blom, P. W. M. Tuning of metal work functions with self-assembled monolayers. *Adv. Mater.* **17**, 621–625 (2005).
26. Yuan, L., Thompson, D., Cao, L., Nerngchamnong, N. & Nijhuis, C. A. One carbon matters: The origin and reversal of odd–even effects in molecular diodes with self-assembled monolayers of ferrocenyl-alkanethiolates. *J. Phys. Chem. C* **119**, 17910–17919 (2015).
27. Nijhuis, C. A., Reus, W. F. & Whitesides, G. M. Molecular rectification in metal-SAM-metal oxide-metal junctions. *J. Am. Chem. Soc.* **131**, 17814–17827 (2009).
28. Reus, W. F., Thuo, M. M., Shapiro, N. D., Nijhuis, C. A. & Whitesides, G. M. The SAM, Not the electrodes, dominates charge transport in metal-monolayer// Ga$_2$O$_3$/gallium-indium eutectic junctions. *ACS Nano* **6**, 4806–4822 (2012).
29. Wang, D. *et al.* Tuning the tunnelling rate and dielectric response of sam-based junctions via a single polarizable atom. *Adv. Mater.* **27**, 6689–6695 (2015).
30. Crivillers, N., Mas-Torrent, M., Vidal-Gancedo, J., Veciana, J. & Rovira, C. Self-assembled monolayers of electroactive polychlorotriphenylmethyl radicals on Au(111). *J. Am. Chem. Soc.* **130**, 5499–5506 (2008).
31. Simão, C., Mas-Torrent, M., Veciana, J. & Rovira, C. Multichannel molecular switch with a surface-confined electroactive radical exhibiting tunable wetting properties. *Nano Lett.* **11**, 4382–4385 (2011).
32. Crivillers, N. *et al.* Self-assembled monolayers of a multifunctional organic radical. *Angew. Chem. Int. Ed.* **46**, 2215–2219 (2007).

33. Simão, C. et al. A robust molecular platform for non-volatile memory devices with optical and magnetic responses. Nat. Chem. **3,** 359–364 (2011).

34. Frisneda, R. et al. Kondo effect in a neutral and stable all organic radical single molecule break junction. Nano Lett. **15,** 3109–3114 (2015).

35. Ballester, M., Riera-Figueras, J., Castañer, J., Badfa, C. & Monso, J. M. Inert carbon free radicals. I. Perchlorodiphenylmethyl and perchlorotriphenylmethyl radical series. J. Am. Chem. Soc. **93,** 2215–2225 (1971).

36. Crivillers, N. et al. Dramatic influence of the electronic structure on the conductivity through open- and closed-shell molecules. Adv. Mater. **21,** 1177–1181 (2009).

37. Crivillers, N. et al. Negative differential resistance (NDR) in similar molecules with distinct redox behaviour. Chem. Commun. **47,** 4664–4666 (2011).

38. Rovira, C. et al. Influence of topology on the long-range electron-transfer phenomenon. Chem. Eur. J. **7,** 240–250 (2001).

39. Yuan, L., Jiang, L., Zhang, B. & Nijhuis, C. A. Dependency of the tunnelling decay coefficient in molecular tunnelling junctions on the topography of the bottom electrodes. Angew. Chem. Int. Ed. **53,** 3377–3381 (2014).

40. Weiss, E. A. et al. Influence of defects on the electrical characteristics of mercury-drop junctions: Self-assembled monolayers of n-alkanethiolates on rough and smooth silver. J. Am. Chem. Soc. **129,** 4336–4349 (2007).

41. Weiss, E. A. et al. Si/SiO₂-Templated formation of ultraflat metal surfaces on glass, polymer, and solder supports: Their use as substrates for self-assembled monolayers. Langmuir **23,** 9686–9694 (2007).

42. Shekhah, O. et al. Grafting of monocarboxylic substituted polychlorotriphenylmethyl radicals onto a COOH-functionalized self-assembled monolayer through copper (II) metal ions. Langmuir **24,** 6640–6648 (2008).

43. Mugnaini, V. et al. Looking inside the perchlorinated trityl radical/metal spinterface through spectroscopy. J. Phys. Chem. Lett. **6,** 2101–2106 (2015).

44. Wimbush, K. S. et al. Bias induced transition from an ohmic to a non-ohmic interface in supramolecular tunnelling junctions with Ga₂O₃/EGaIn top electrodes. Nanoscale **6,** 11246–11258 (2014).

45. Yaffe, O. et al. Charge transport across metal/molecular (alkyl) monolayer-Si junctions is dominated by the LUMO level. Phys. Rev. B **85,** 045433 (2012).

46. Chiechi, R. C., Weiss, E. A., Dickey, M. D. & Whitesides, G. M. Eutectic gallium–indium (EGaIn): a moldable liquid metal for electrical characterization of self-assembled monolayers. Angew. Chem. Int. Ed. **47,** 142–144 (2008).

47. Simeone, F. C. et al. Defining the value of injection current and effective electrical contact area for egain-based molecular tunnelling junctions. J. Am. Chem. Soc. **135,** 18131–18144 (2013).

48. Yuan, L. et al. Controlling the direction of rectification in a molecular diode. Nat. Commun. **6,** 7324 (2015).

49. Yuan, L., Jiang, L., Thompson, D. & Nijhuis, C. A. On the remarkable role of surface topography of the bottom-electrodes in blocking leakage currents in molecular diodes. J. Am. Chem. Soc. **136,** 6554–6557 (2014).

50. Nijhuis, C. A., Reus, W. F., Barber, J. R. & Whitesides, G. M. Comparison of SAM-based junctions with Ga₂O₃/EGaIn top electrodes to other large-area tunnelling junctions. J. Phys. Chem. C **116,** 14139–14150 (2012).

51. Wan, A., Jiang, L., Sangeeth, C. S. S. & Nijhuis, C. A. Reversible soft top-contacts to yield molecular junctions with precise and reproducible electrical characteristics. Adv. Funct. Mater. **24,** 4442–4456 (2014).

52. Nijhuis, C. A., Reus, W. F. & Whitesides, G. M. Mechanism of rectification in tunnelling junctions based on molecules with asymmetric potential drops. J. Am. Chem. Soc. **132,** 18386–18401 (2010).

53. Akkerman, H. B. et al. Electron tunnelling through alkanedithiol self-assembled monolayers in large-area molecular junctions. Proc. Natl Acad. Sci. USA **104,** 11161–11166 (2007).

54. Jiang, L., Sangeeth, C. S. S., Wan, A., Vilan, A. & Nijhuis, C. A. Defect scaling with contact area in egain-based junctions: impact on quality, joule heating, and apparent injection current. J. Phys. Chem. C **119,** 960–969 (2015).

55. Simmons, J. G. Generalized formula for electric tunnel effect between similar electrodes separated by a thin insulating film. J. Appl. Phys. **34,** 1793–1803 (1963).

56. Salomon, A. et al. Comparison of electronic transport measurements on organic molecules. Adv. Mater. **15,** 1881–1890 (2003).

57. Choi, S. H., Kim, B. S. & Frisbie, C. D. Electrical resistance of long conjugated molecular wires. Science **320,** 1482–1486 (2008).

58. Yoon, H. J. et al. Rectification in tunnelling junctions: 2,2'-bipyridyl-terminated n-alkanethiolates. J. Am. Chem. Soc. **136,** 17155–17162 (2014).

59. Moth-Poulsen, K. & Bjørnholm, T. Molecular electronics with single molecules in solid-state devices. Nat. Nanotechnol. **4,** 551–556 (2009).

60. Yuan, L., Breuer, R., Jiang, L., Schmittel, M. & Nijhuis, C. A. A molecular diode with a statistically robust rectification ratio of three orders of magnitude. Nano Lett. **15,** 5506–5512 (2015).

61. Tour, J. M. et al. Self-assembled monolayers and multilayers of conjugated thiols, alpha,omega-dithiols, and thioacetyl-containing adsorbates - understanding attachments between potential molecular wires and gold surfaces. J. Am. Chem. Soc. **117,** 9529–9534 (1995).

62. Ishida, T. et al. High-resolution X-ray photoelectron spectra of organosulfur monolayers on Au(111): S(2p) spectral dependence on molecular species. Langmuir **15,** 6799–6806 (1999).

63. Watcharinyanon, S. et al. Molecular orientation of thiol-derivatized tetraphenylporphyrin on gold studied by XPS and NEXAFS. Surf. Sci. **603,** 1026–1033 (2009).

64. Stohr, J. NEXAFS Spectroscopy (Springer–Verlag, 1992).

65. Reus, W. F. et al. Statistical tools for analyzing measurements of charge transport. J. Phys. Chem. C **116,** 6714–6733 (2010).

Author contributions

C.F. synthesized the compounds. N.C. prepared and electrochemically characterized the SAMs and participated in the J(V) measurements performed by L.Y., L.C. and L.Y. recorded and analysed the ARXPS, UPS and NEXAFS spectra. C.S.S.S. and L.Y. performed the temperature-dependent J(V) measurements. M.M.-T., C.R., J.V. and C.A.N. supervised the project. All authors contributed to writing the manuscript.

Additional information

Supplementary Information accompanies this paper at http://www.nature.com/naturecommunications

Competing financial interests: The authors declare no competing financial interests.

Reprints and permission information is available online at http://npg.nature.com/reprintsandpermissions/

How to cite this article: Yuan, L. et al. Chemical control over the energy-level alignment in a two-terminal junction. Nat. Commun. **7**:12066 doi: 10.1038/ncomms12066 (2016).
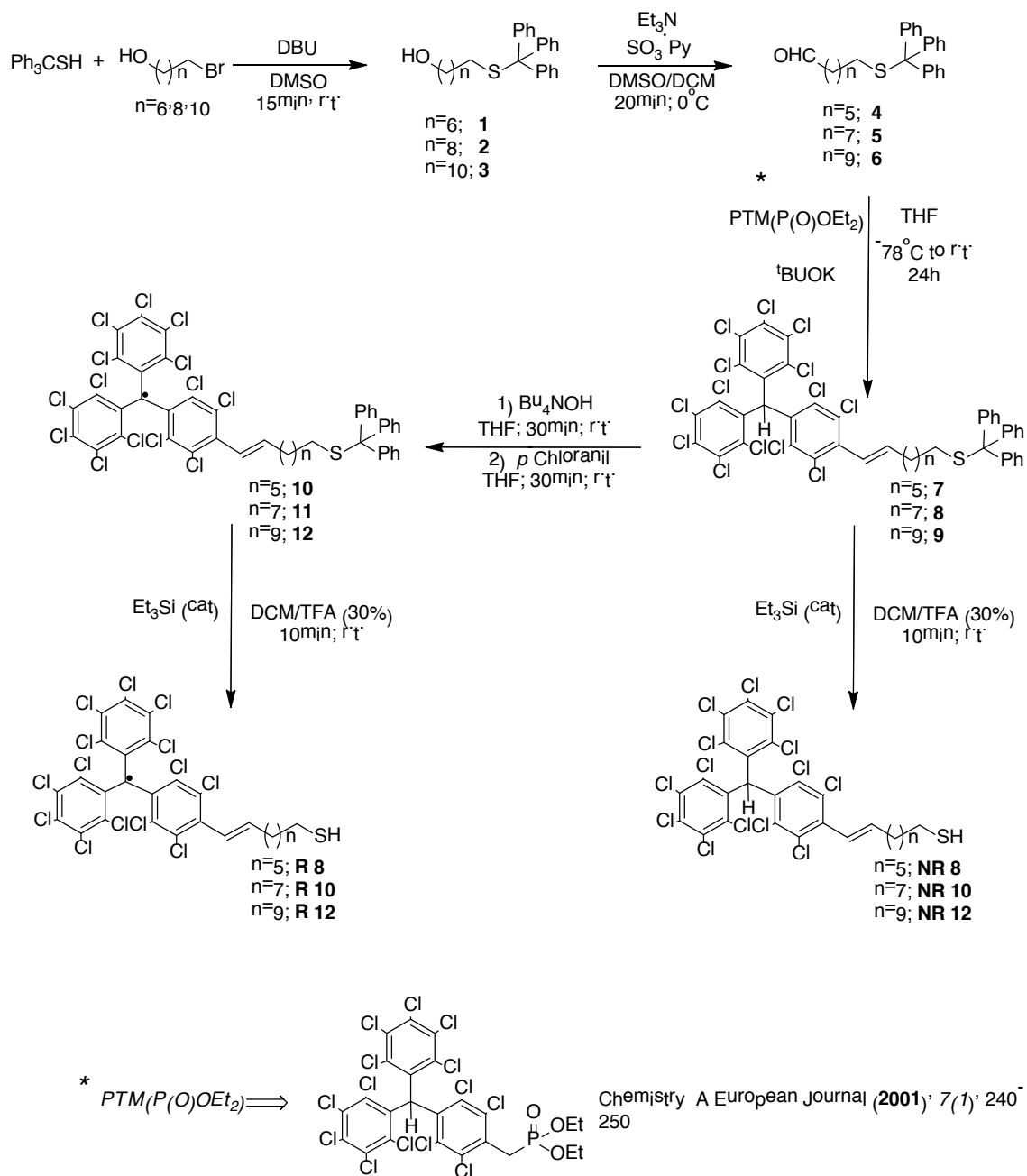
Supplementary Figure 1. General procedure for the synthesis of PTMC$_x$STrityl and PTMC$_x$SH.
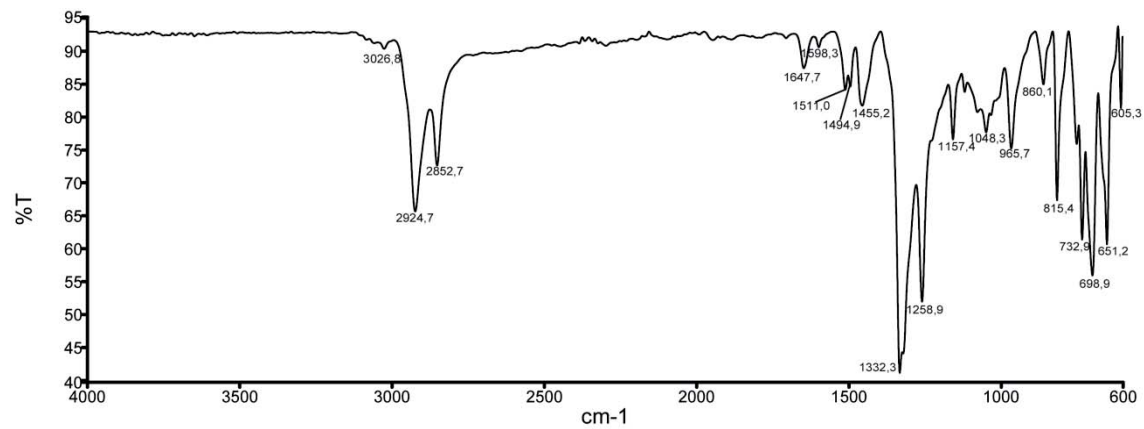
Supplementary Figure 2. IR-ATR spectrum of compound **R10**.
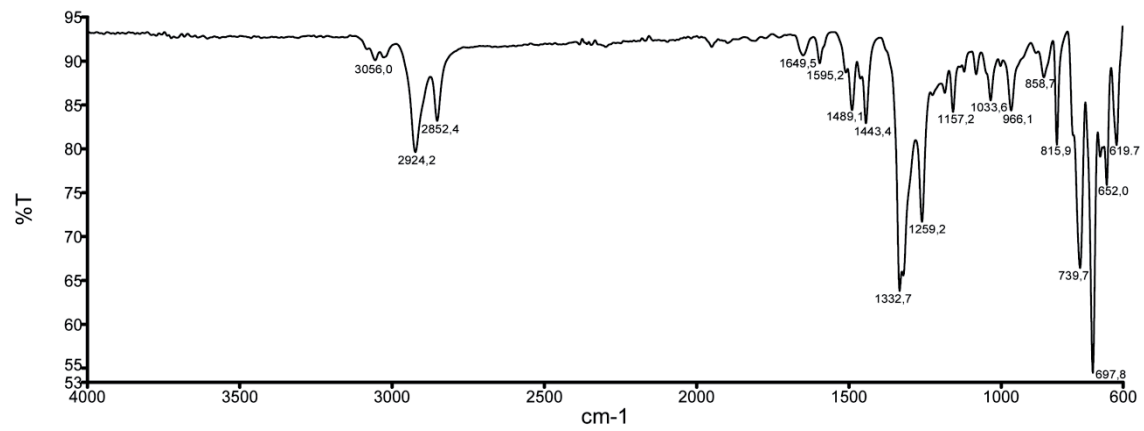
Supplementary Figure 3. IR-ATR spectrum of compound **11**.
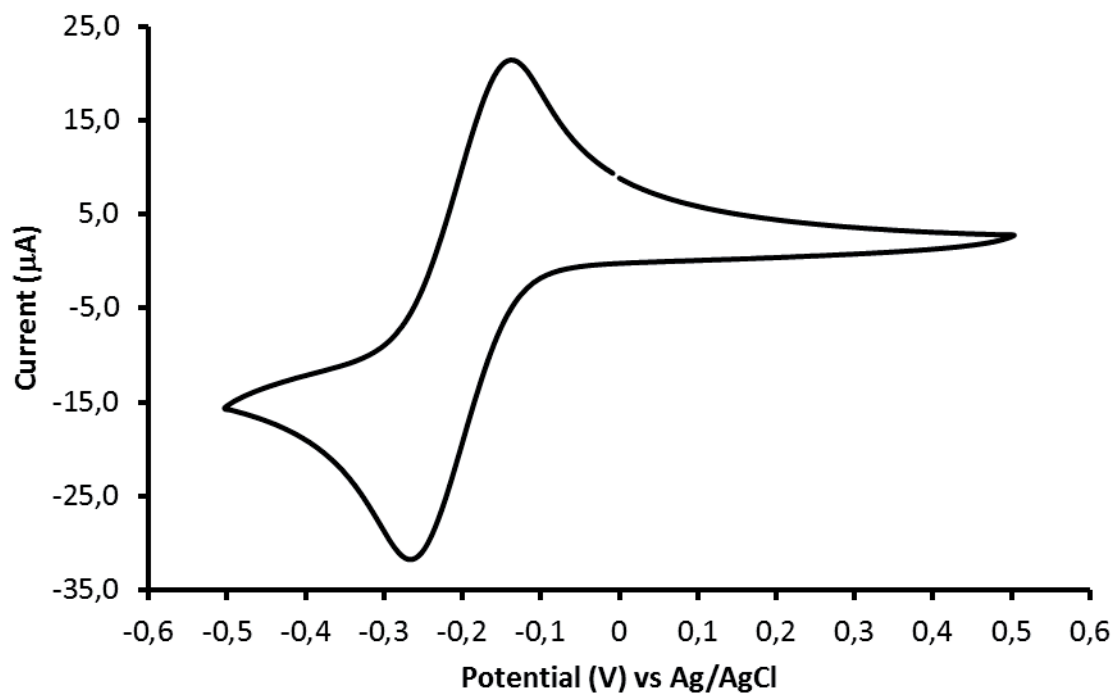
Supplementary Figure 4. Cyclic voltammogram of compound **R8.**
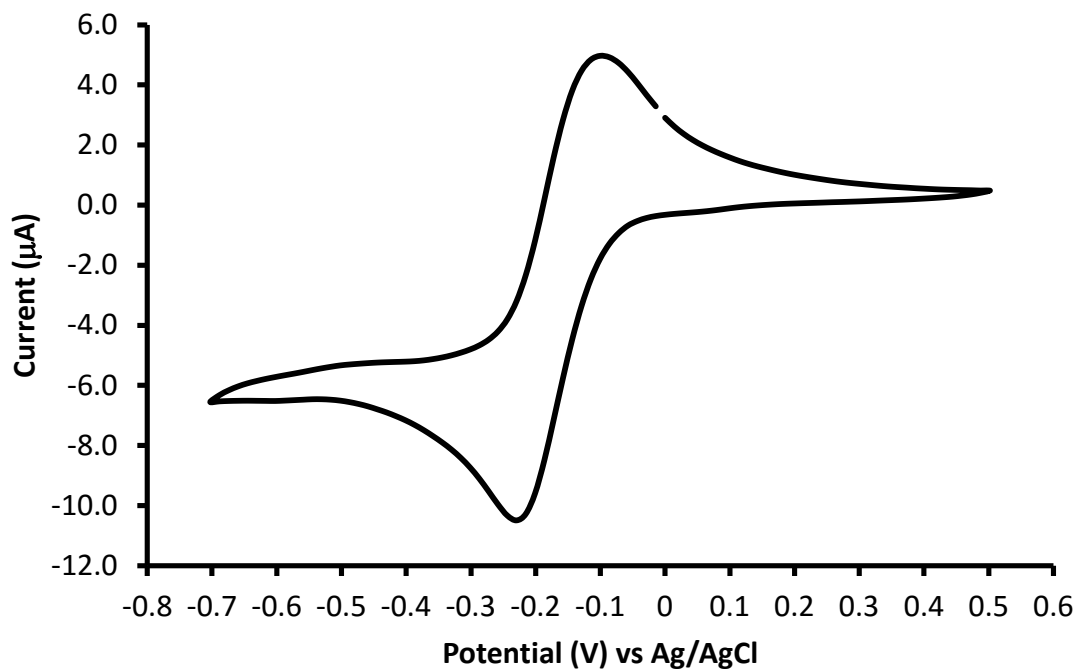
Supplementary Figure 5. Cyclic voltammogram of compound **11**.
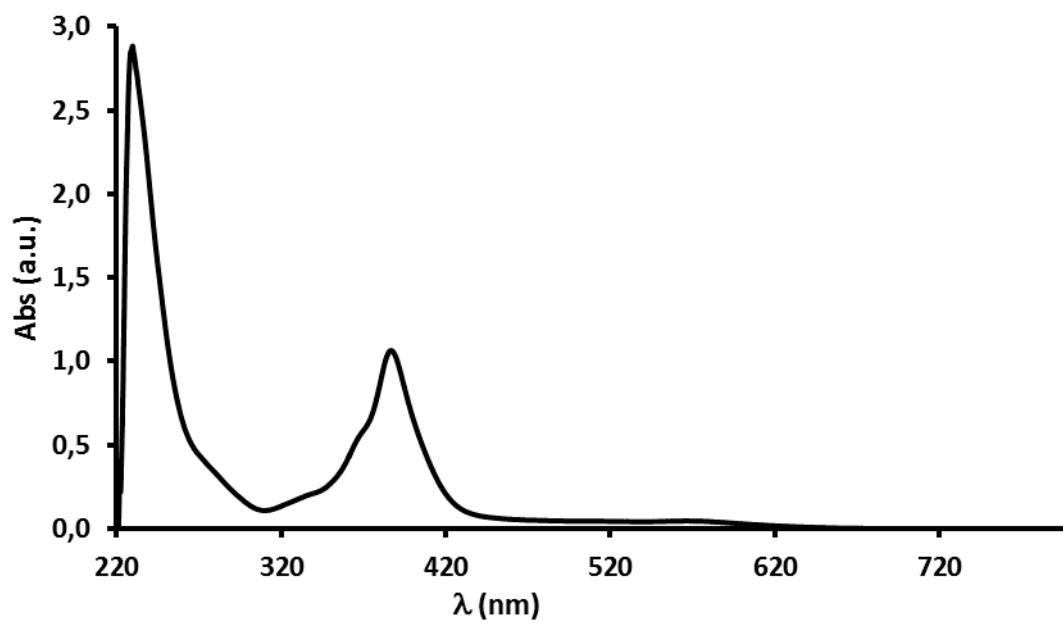
Supplementary Figure 6. UV-Vis spectrum of compound **10** in CH_2Cl_2 solution.
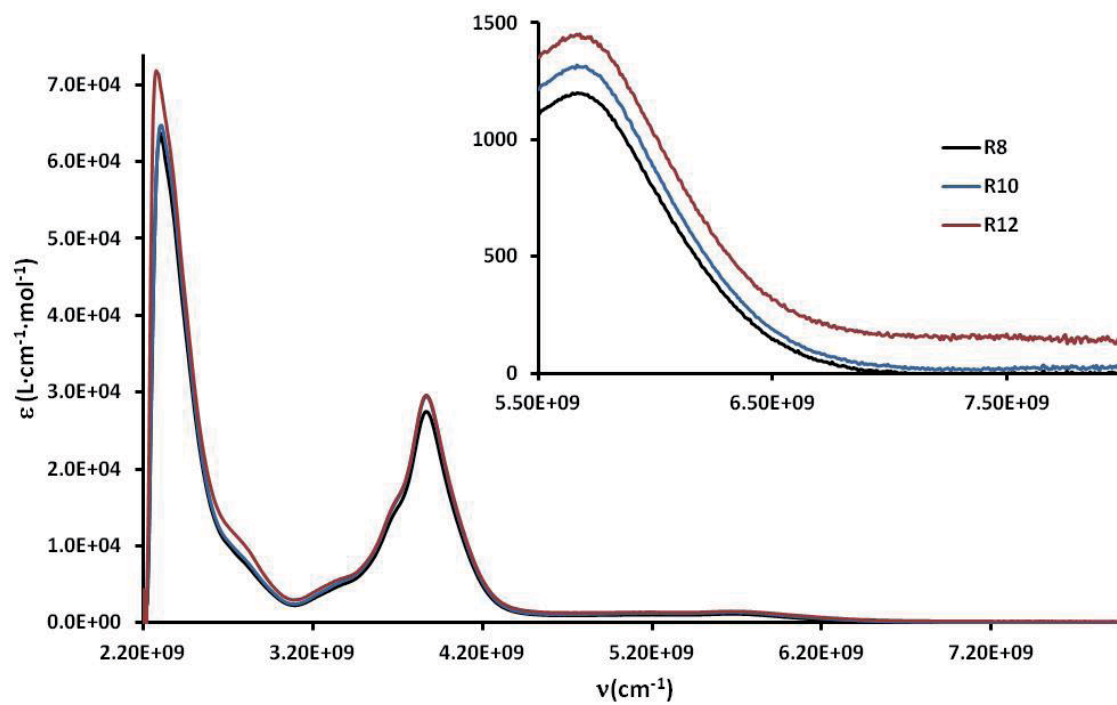
Supplementary Figure 7. UV-Vis spectra of radicals **R8**, **R10** and **R12** in CH_2Cl_2.
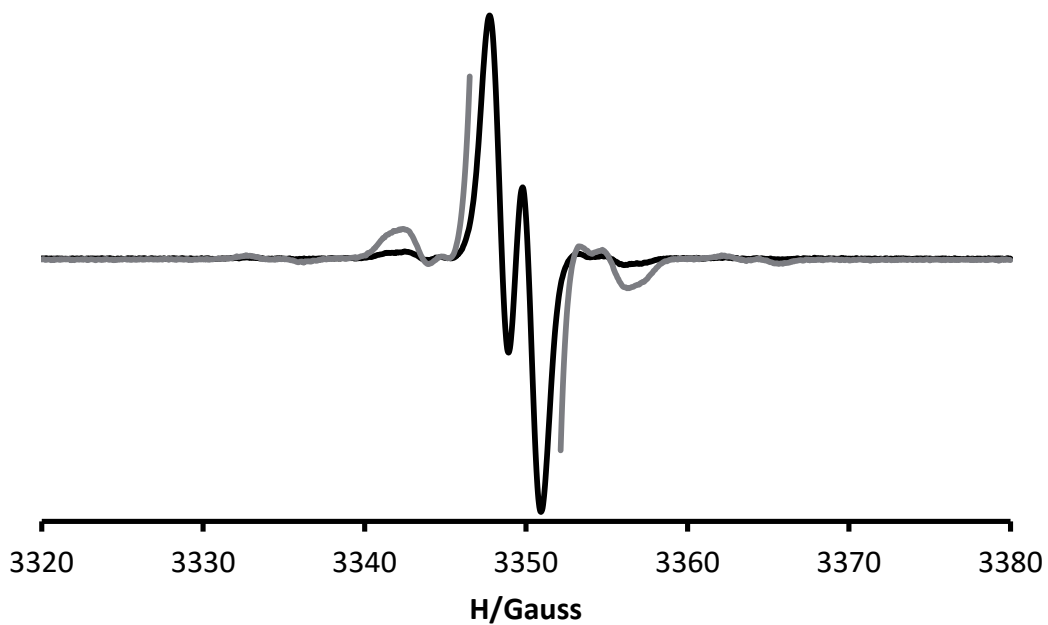
Supplementary Figure 8. EPR spectrum of compound **R10** in CH_2Cl_2 solution, at room temperature.
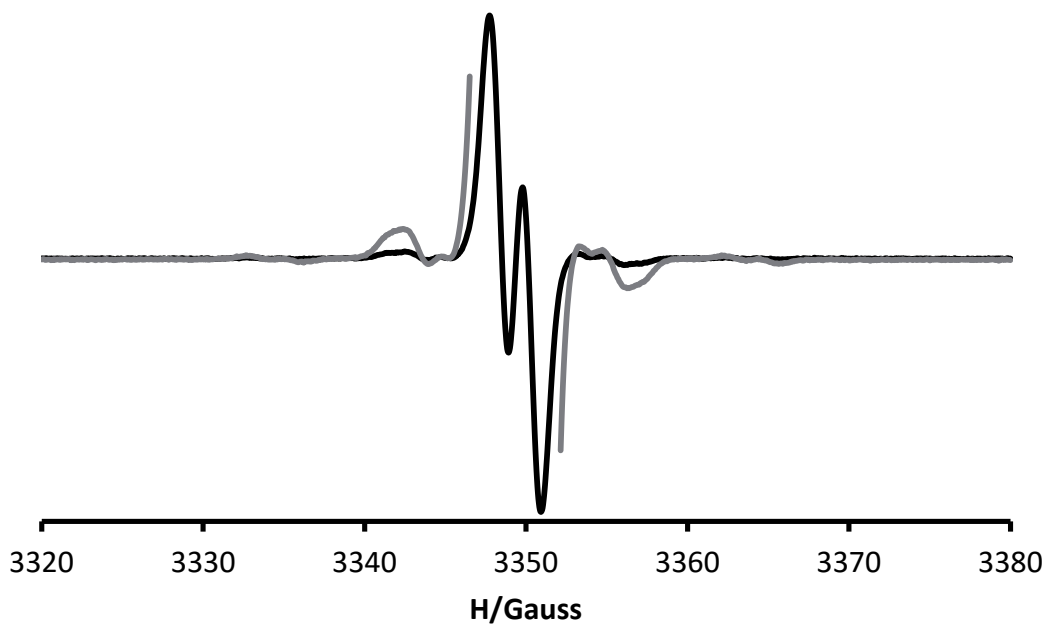
Supplementary Figure 9. EPR spectrum of compound **10** in CH$_2$Cl$_2$ solution, at room temperature.
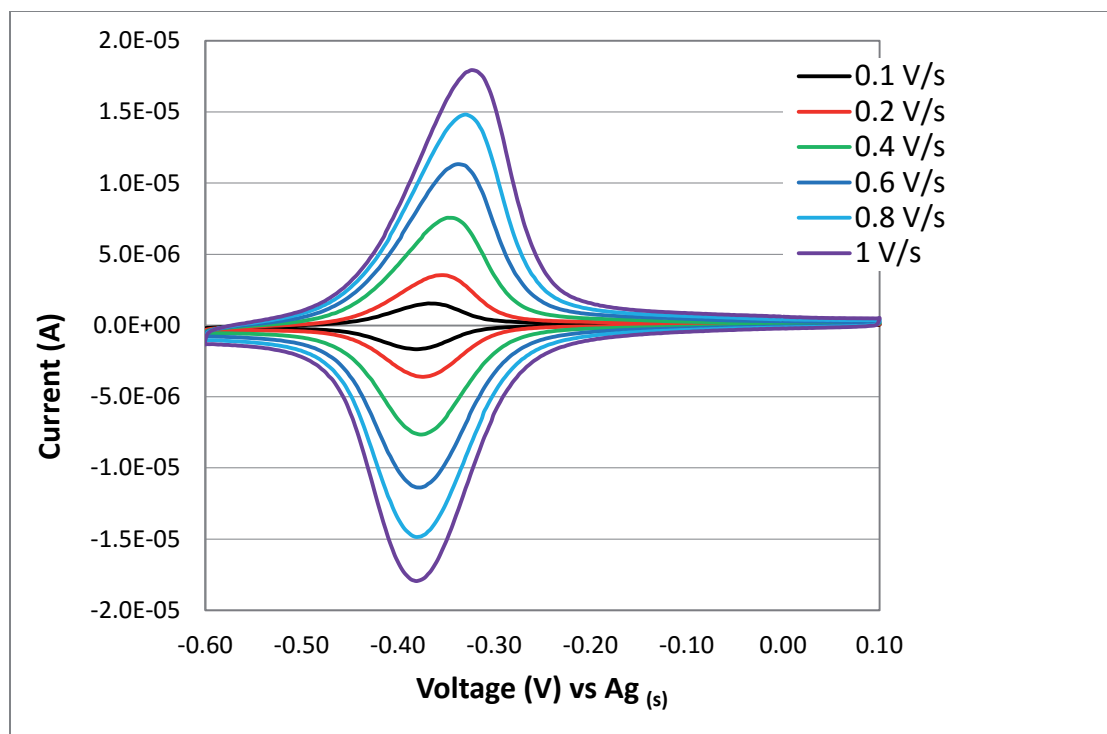
Supplementary Figure 10. Cyclic voltammogram of the **R$_{10}$** SAM on Au (111)/mica.
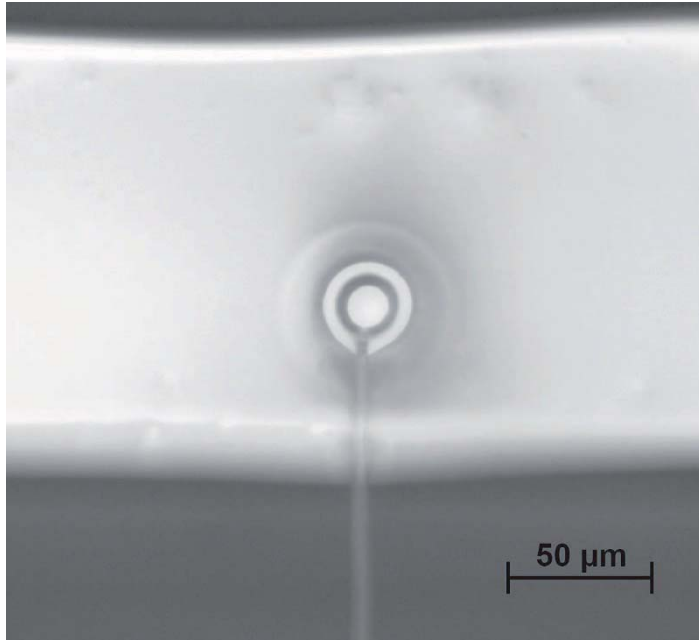
Supplementary Figure 11. Optical microscope image of the through-hole filled with Ga$_2$O$_3$/EGaIn.
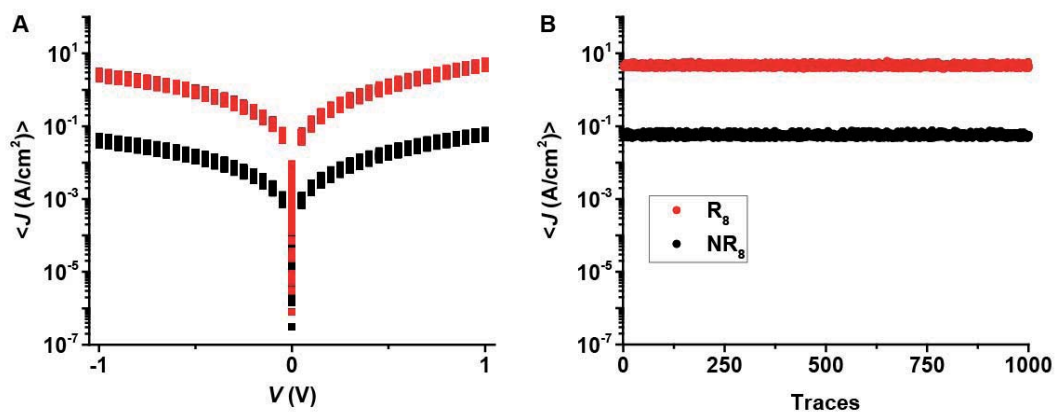
Supplementary Figure 12. A) The 1000 $J(V)$ traces of Au^{TS}-$SC_8PTM^{R/NR}$//GaO_x^{cond}/EGaIn junctions. B) The values of J as a function of trace number with R_8 and NR_8 SAMs at +1.0 V.
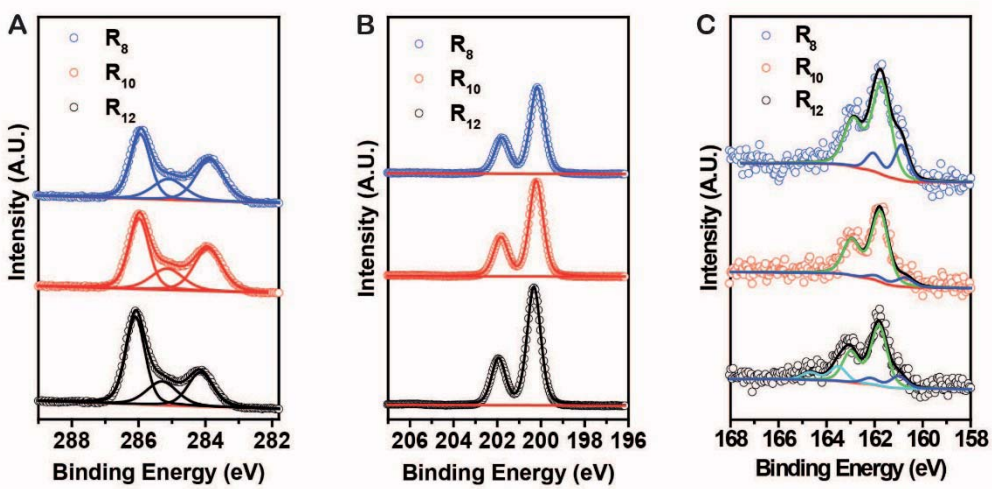
Supplementary Figure 13. The C $1s$ (A), Cl $2p$ (B), and S $2p$ (C) spectra of Au^{TS}-SC_nPTM^R (n= 8, 10, 12; R_8, R_{10} and R_{12} as indicated in the panels) with a take-off angle of 90°.
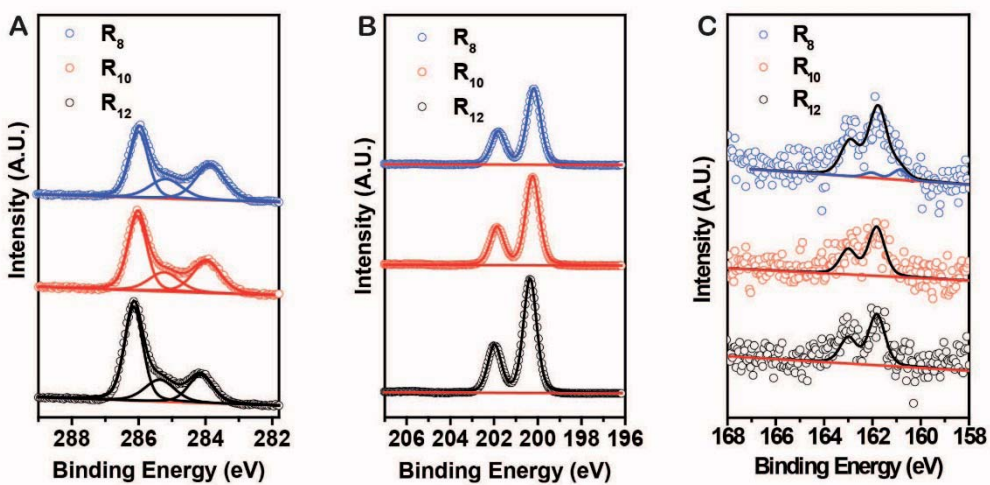
Supplementary Figure 14. The C 1s (A), Cl 2p (B), and S 2p (C) spectra of Au^{TS}-SC_nPTM^R (n= 8, 10, 12; R_8, R_{10} and R_{12} as indicated in the panels) with a take-off angle of 40°.
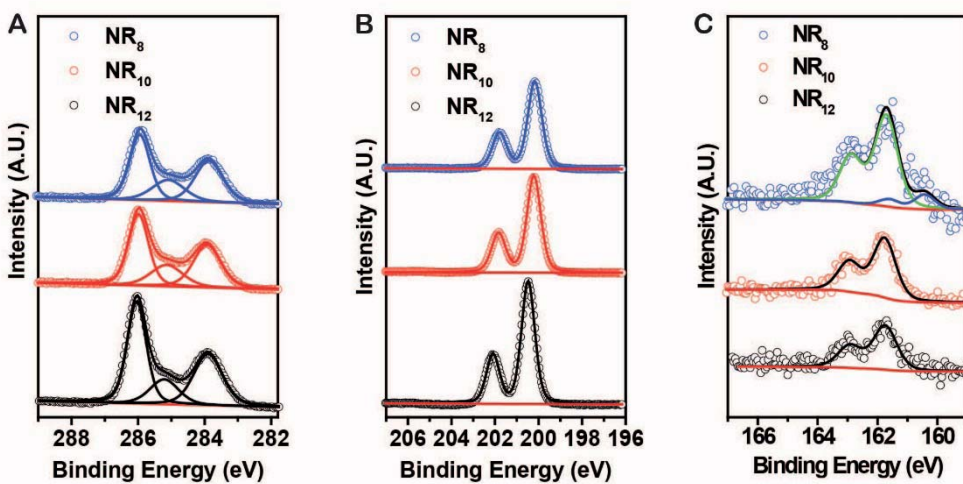
Supplementary Figure 15. The C 1s (A), Cl 2p (B), and S 2p (C) spectra of Au^{TS}-SC_nPTM^{NR} (n= 8, 10, 12; NR_8, NR_{10} and NR_{12} as indicated in the panels) with a take-off angle of 90°.
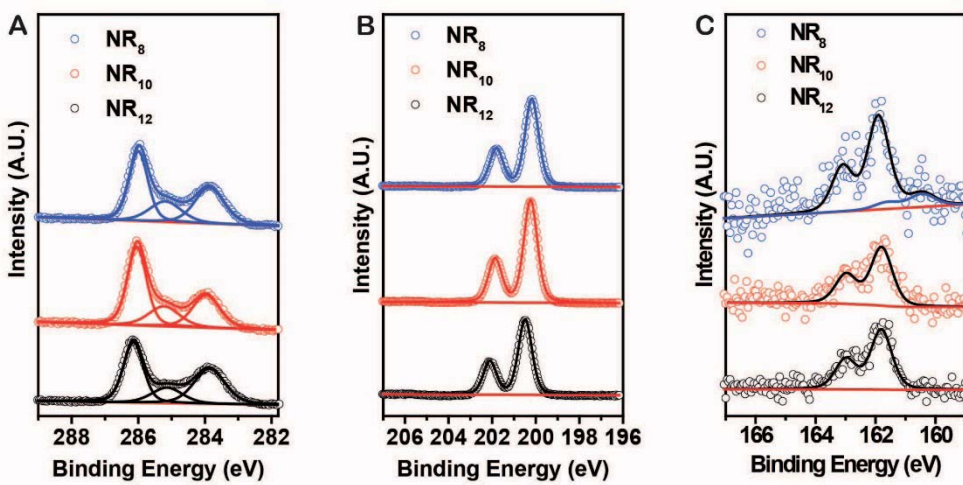
Supplementary Figure 16. The C 1s (A), Cl 2p (B), and S 2p (C) spectra of Au^{TS}-SC_nPTM^{NR} (n= 8, 10, 12; NR_8, NR_{10} and NR_{12} as indicated in the panels) with a take-off angle of 40°.
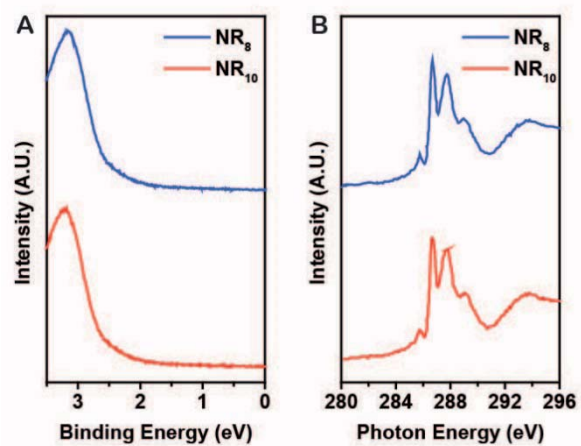
Supplementary Figure 17. UPS and NEXAFS spectra of Au^{TS}-SC_nPTM^{NR} (n= 8 and10; NR_8 and NR_{10} respectively in the figures).
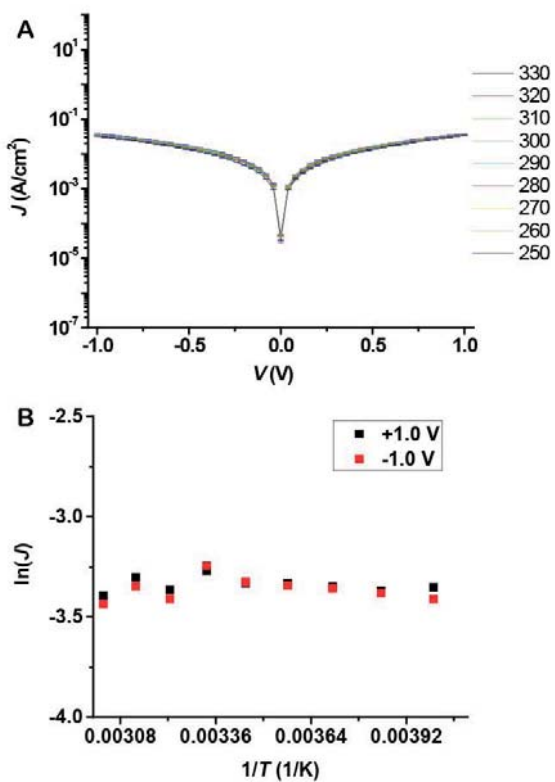
Supplementary Figure 18. Temperature dependent $J(V)$ curves and the corresponding

Arrhenius plot at $V = \pm 1.0$ V over the range of temperatures of 250 to 330 K of a junctions with

a SAMs of NR_8.
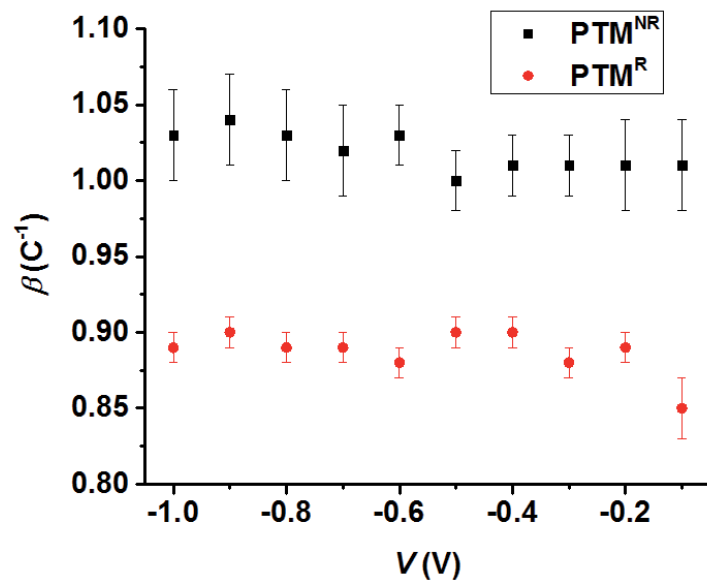
Supplementary Figure 19. The plot of tunneling decay coefficient (β) against V.

Supplementary Table 1. The values of I_{Cl}, relative surface coverage and absolute surface coverage.

SAMs	I_{Cl} at 90° take-off angle	Relative surface coverage[a]	Absolute surface coverage ($\times 10^{-9}$ mol/cm^2)
R_8	47997	0.13	0.14
R_{10}	49774	0.13	0.15
R_{12}	52305	0.14	0.16
NR_8	49225	0.13	0.15
NR_{10}	50556	0.14	0.15
NR_{12}	52907	0.14	0.16
$SC_{11}Cl$	26450	1	1.10

[a] The relative surface coverage is calculated from $I_{Cl}(SC_{11}Cl) / (I_{Cl}(PTM^{R/NR}) / 14)$.

Supplementary Table 2. The elemental ratios calculated from the high-resolution XPS spectra

| SAM | C 1s at 90° | | C 1s at 40° | | Cl/C$_3$ | |
	C$_1$/C$_3$	C$_2$/C$_3$	C$_1$/C$_3$	C$_2$/C$_3$	At 90°	At 40°
R$_8$	0.87	0.52	0.80	0.52	3.69	4.03
R$_{10}$	0.73	0.49	0.62	0.47	3.70	4.09
R$_{12}$	0.54	0.49	0.40	0.44	3.69	4.12
NR$_8$	0.87	0.51	0.80	0.51	3.68	4.06
NR$_{10}$	0.72	0.48	0.60	0.47	3.70	4.11
NR$_{12}$	0.57	0.51	0.39	0.44	3.68	4.20

Supplementary Table 3. The ratio of (I_θ) of S $2p$ between take-off angles of 90° and 40° of R-based SAMs on Au^{TS}.

	$I_\theta(90°)$ (%)	$I_\theta(40°)$ (%)	d (nm)
Au^{TS}-SC$_8$PTM^R	69.6	30.4	1.83
Au^{TS}-SC$_{10}$PTM^R	73.2	26.8	2.05
Au^{TS}-SC$_{12}$PTM^R	75.1	24.9	2.20
Au^{TS}-SC$_8$PTM^{NR}	68.9	31.1	1.79
Au^{TS}-SC$_{10}$PTM^{NR}	73.5	26.5	2.08
Au^{TS}-SC$_{12}$PTM^{NR}	75.2	24.8	2.22

Supplementary Methods

Synthesis and characterization of PTM derivatives

General procedure

Elemental analyses were performed on the CID (CSIC) services. NMR spectra were recorded on a Bruker Avance 400 MHz. EPR spectra were recorded in a Bruker ELEXYS E500 X-band spectrometer. The simulation of the EPR spectra was realised with software Simfonia. Electrochemical experiments were performed with a potensiostat/galvanostat Autolab/PGSTAT204 from Metrohm Autolab B.V. in a standard three-electrode cell, by using a platinum wire as working and counter electrode and Ag/AgCl as reference electrode. Tetrabutylammonium hexafluorophospate (Fluka, 99%) was used as the supporting electrolyte. UV-Vis spectra were recorded on a Varian Carey 5000 in double-beam mode. Mass Spectra were recorded with a Bruker Ultraflex LDI-TOF mass spectrometer. The liquid chromatography were performed in an Agilent 1100 series HPLC (Agilent Technologies) connected to with two (in parallel) detectord, a photodiode array working into 200nm and 800nm and a mass spectrometer (Esquire 3000 MS Trap (Bruker Daltonik) equipped with Electrospray source ionisation), the methodology used was a binary gradient of acetonitrile (with 5% of formic acid) and chloroform, from 90/10 to 60/40. The IR spectra were recorded with an ATR-IR Perkin Elmer Spectrum One. The manipulation of the radicals in solution was performed under red light.

General procedure for the synthesis of compounds tritylthio-alcohols 1, 2 and 3.
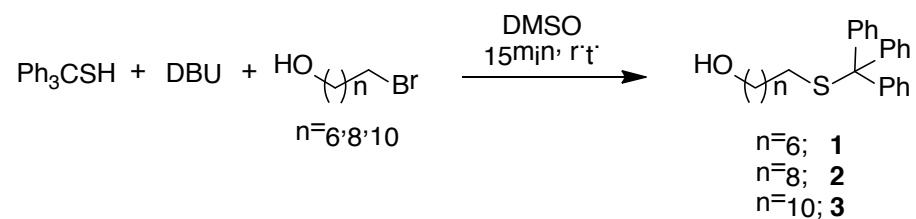
Triphenylmethane thiol (1Eq) was suspended in DMSO and DBU (1.14 Eq,) was added. After stirring at room temperature for 5 min, the corresponding bromo-alchol derivative (1.08 Eq, 0.96 mmol) was added, and the mixture was stirred for 10 min. The reaction mixture was diluted with ethyl acetate, quenched with 0.1M HCl (5 ml), extracted with ethyl acetate, dried over $MgSO_4$ and dried in vacum. The crude product was purified by flash chromatography (SiO_2, heptane/AcOEt 1/1).

General procedure for the synthesis of compounds tritylthio- aldehydes 4, 5 and 6.

The corresponding Triphenylmercapto-n-ol (1 Eq,) and triethylamine (3.5 Eq,) were dissolved in dichloromethane and DMSO, cooled to 0°C and added a suspension of sulfur trioxide pyridine complex (2.07 Eq, 408 mg, 2.57 mmol) in DMSO (400 µL). At the same temperature, the mixture was then stirred for 20 min at 0°C and after diluted with dichloromethane and quenched with 0.1M HCl (5ml) and extracted with dichloromethane. The combined organic phases were washed with brine and dried (MgSO₄) The crude product was purified by flash chromatography (heptane/AcOEt 1/1).

General procedure for the synthesis of PTM derivatives 7, 8 and 9.

Under Argon, potassium tert-butoxide (1.5 Eq) was added to a stirred solution of PTM-P(O)(OEt)₂ (1 Eq) in dry tetrahydrofuran (THF) at -78°C and the mixture was stirred at this temperature for 10min, then a solution of the corresponding triphenylmercapto-n-al (2 Eq) in dry THF was added and the mixture was allowed to warm to room temperature. The resulting mixture was stirred in the dark at room temperature for 24h. After evaporation of the solvent the crude was purified by column chromatography (SiO₂, Hexane/CH₂Cl₂ 80/20).

General procedure for the synthesis of PTM radical derivatives 10, 11 and 12.

To a solution of the corresponding αH PTM triphenylmercapto derivative in THF, 1.3 Eq of Bu$_4$NOH (1M in methanol) was added. The initial colorless solution turned to intense violet and the reaction mixture was stirred at room temperature for 30 min. and then, 1.5 Eq of *p*-chloranil was added. The color of the reaction mixture changed to red. After 30 min the solvent was removed under vacuum and the crude product was purified by flash chromatography (SiO$_2$, Hexane/CH$_2$Cl$_2$80/20). The resulting waxy compounds were washed with methanol to give a red solid in almost quantitative yield (96-98%).

General procedure to generation of the free thiol groups
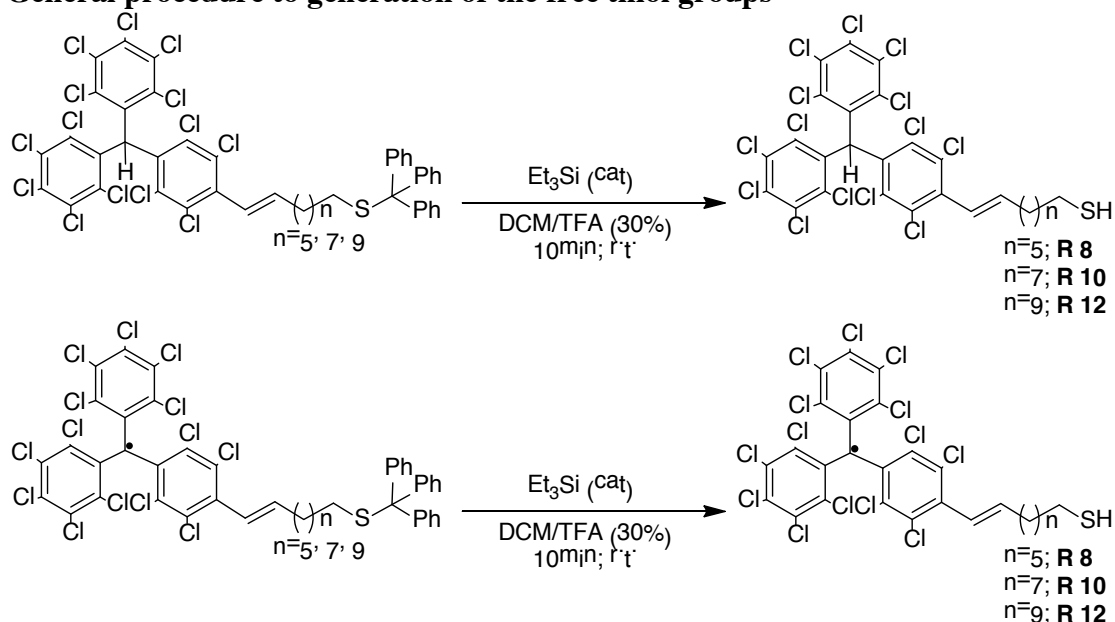
To a solution of trifluoroacetic acid (TFA) in DCM (30%) triethylsilyl (cat) was added under argon, and then the PTM triphenylmercapto derivative (either radical or αH) was added to the mixture. The solution was stirred at room temperature in the dark for 10 min. Then the solvent was evaporated in vacuum, and the crude product was purified by flash chromatography (silica gel, Hexane/CH$_2$Cl$_2$ 80/20). The product was washed with methanol in a sonicated bath and filtered several time, to yield a solid (red for radicals and withe for αHs) in almost quantitative yield (95%-97%)

7-(tritylthio)heptan-1-ol (1)
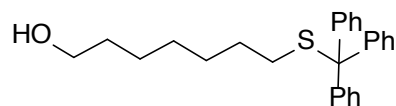
According to the general procedure, from triphenylmethane thiol (247 mg, 0.89 mmol), DBU (1.14 Eq, 152 μL, 1.02 mmol) and 7bromo-heptanol (187 mg, 0.96 mmol) in DMSO (1 mL), the compound **1** was obtained as a transparent oil (yield, 84%). **^{1}H-NMR** (400 MHz, CD$_2$Cl$_2$) δ/ppm: 7.49 (m, 6H), 7.35 (m, 6H), 7.28(m, 3H), 3.61 (t, J = 6.6 Hz, 2H), 2.21 (t, J = 7.4 Hz, 2H), 1.64 – 1.14 (m, 11H); **^{13}C- NMR** (101 MHz, CD$_2$Cl$_2$) δ/ppm: 145.17, 129.60, 127.79, 126.51, 70.74, 62.69, 32.75, 31.89, 28.97, 28.95, 28.54, 25.55. **FT-IR** v/cm^{-1}: 3345.9, 3085.0, 3055.8, 3024.1, 2927.5, 2853.9, 1594.7, 1488.5, 1443.4, 1183.3, 1079.6, 1054.8, 1033.9, 1001.6, 884.2, 850.1, 764.7, 741.3, 697.8, 676.3, 617.1; **EM (m/z)** (ESI): calculated for C$_{26}$H$_{30}$OS: 390.2; found: 413.2 (M+Na), 276.2(·SCPh3+1H$^+$), 243.11 (·CPh3+1H$^+$).
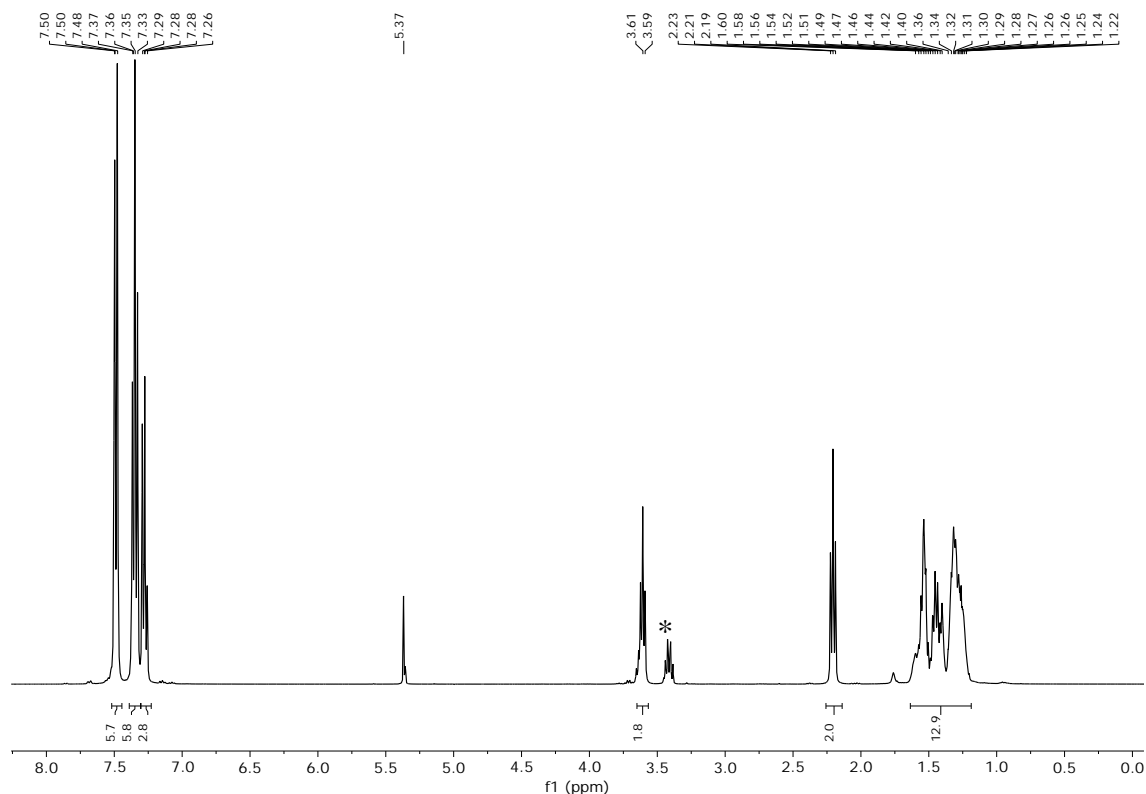
* Impurity that does not affect to the rest of the synthesis. Probably a fragment of the alkyl chain.
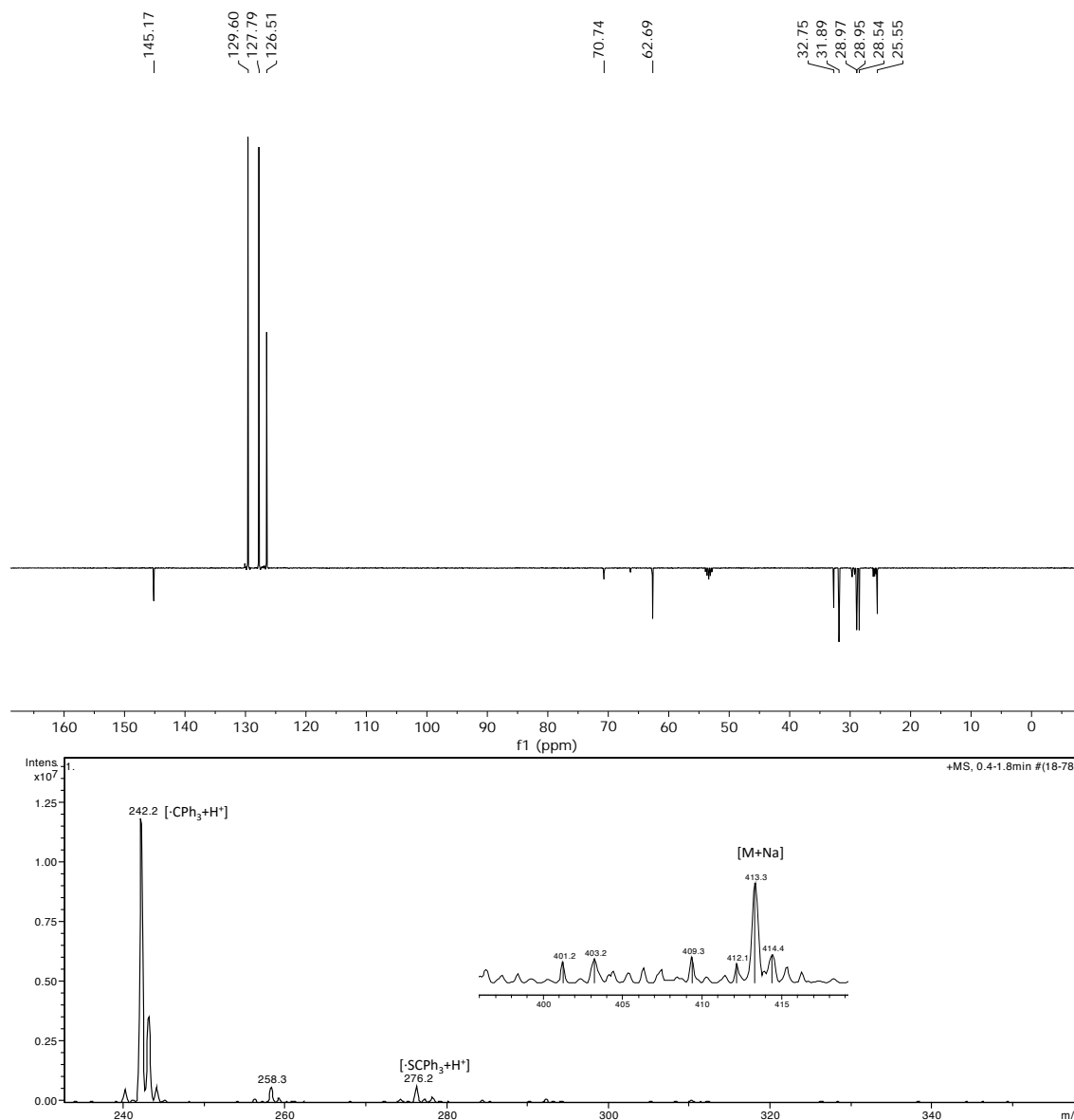
9-(tritylthio)nonan-1-ol (2)
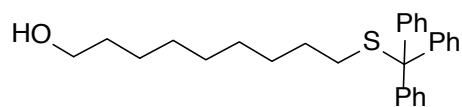
According to the general procedure, from triphenylmethane thiol (247 mg, 0.89 mmol), DBU (152 μL, 1.02 mmol) and 9-bromo-nonanol (214 mg, 0.96 mmol) in DMSO (1 mL) the compound **2** was obtained as a transparent oil (yield, 85%), **^{1}H-NMR** (400 MHz, CDCl$_3$) δ/ppm: 7.49 – 7.39 (m, 6H), 7.34 – 7.25 (m, 6H), 7.22 (t, J = 7.2 Hz, 3H), 3.63 (t, J = 6.6 Hz, 2H), 2.16 (t, J = 7.3 Hz, 2H), 1.56 (p, J = 6.6 Hz, 2H), 1.45 (s, 1H, OH), 1.40 (q, J = 7.5 Hz, 2H), 1.37 – 1.11 (m, 10H). **^{13}C-NMR** (101 MHz, CDCl$_3$) δ/ppm: 145.11, 129.64, 127.82, 126.53, 77.42, 77.10, 76.78, 66.40, 63.02, 32.79, 32.05, 29.38, 29.34, 29.13, 29.01, 28.62, 25.73; **FT-IR** v/cm^{-1}: 338.0, 3083.3, 3057.8, 3026.7, 2927.7, 2851.3, 1595.0, 1488.6, 1443.1, 1179.7, 1076.3, 1054.1,

1034.1, 1001.9, 885.2, 850.8, 765.2, 740.8, 697.5, 677.4. **EM (m/z)** (MALDI-TOF): calculated for $C_{28}H_{34}OS$: 418.23; found: 417.23 (M-H), 275.08($\cdot SCPh_3$), 243.11 ($\cdot CPh_3$) and 175.13 (M-CPh_3).
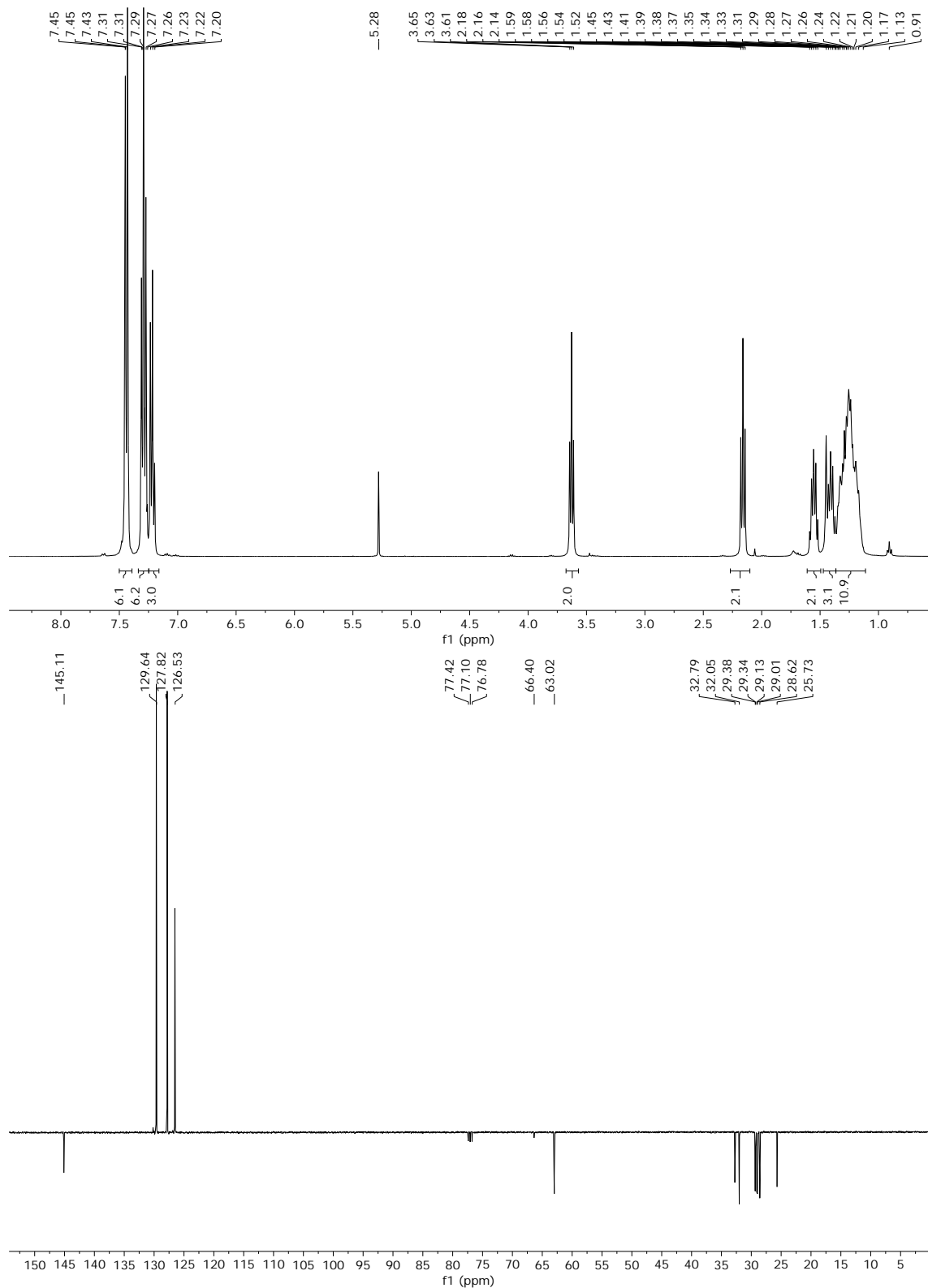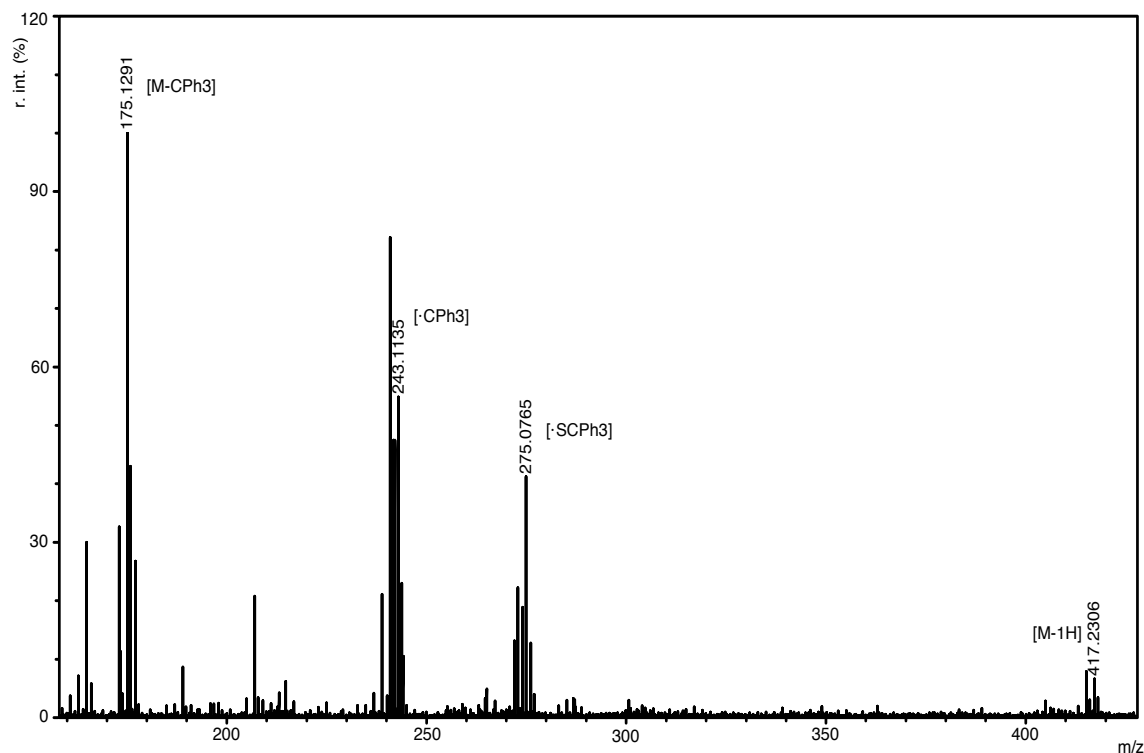
11-(tritylthio)undecan-1-ol (3)
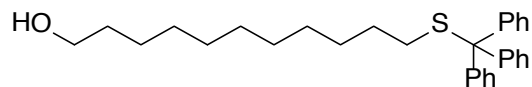
According to general procedure, from triphenylmethane thiol (247 mg, 0.89 mmol), DBU (152 µL, 1.02 mmol) and 11-bromo-undecanol (241 mg, 0.96 mmol) in DMSO (1 mL), the compound **3** was obtained as a transparent oil (yield, 79%). **^{1}H-NMR** (400 MHz, CD$_2$Cl$_2$) δ/ppm: 7.54 – 7.47 (m, 6H), 7.36 (t, J = 7.5 Hz, 6H), 7.29 (t, J = 7.2 Hz, 3H), 3.65 (t, J = 6.6 Hz, 2H), 2.22 (t, J = 7.4 Hz, 2H), 1.71 (s, 1H), 1.61 (q, J = 6.7 Hz, 2H), 1.53 – 1.16 (m, 16H); **^{13}C-NMR** (101 MHz, CD$_2$Cl2) δ/ppm: 145.20, 129.62, 127.81, 126.53, 66.35, 62.79, 53.46, 32.91, 31.95, 29.63, 29.54, 29.50, 29.45, 29.20, 29.06, 28.63, 25.83. **FT-IR** v/cm^{-1}: 3327.5, 3085.2, 3058.0, 3023.0, 2923.9, 2852.6, 1595.1, 1488.9, 1443.8 1183.5, 1077.4, 1055.3, 1033.9, 1001.7, 884.7, 852.1, 741.4, 967.8, 676.2, 617.3; **EM (m/z)** (MALDI-TOF): calculated for C$_{30}$H$_{38}$OS: 446.22; found: 445.29 (M-1H) and 243.13 ($\cdot$CPh$_3$).

¹H NMR (ppm): 7.54, 7.54, 7.52, 7.52, 7.50, 7.38, 7.36, 7.34, 7.32, 7.30, 7.29, 7.29, 7.27; 5.37; 3.67, 3.65, 3.64, 2.24, 2.22, 2.20, 1.71, 1.64, 1.62, 1.61, 1.59, 1.57, 1.50, 1.49, 1.47, 1.45, 1.43, 1.38, 1.35, 1.33, 1.32, 1.30, 1.30, 1.28, 1.26

Integrations: 6.26, 6.49, 3.07; 1.99; 2.09; 0.95, 2.24, 17.62

¹³C NMR (ppm): 145.20; 129.62, 127.81, 126.53; 66.35, 62.79; 53.46; 32.91, 31.95, 29.63, 29.54, 29.50, 29.45, 29.20, 29.06, 28.63, 25.83
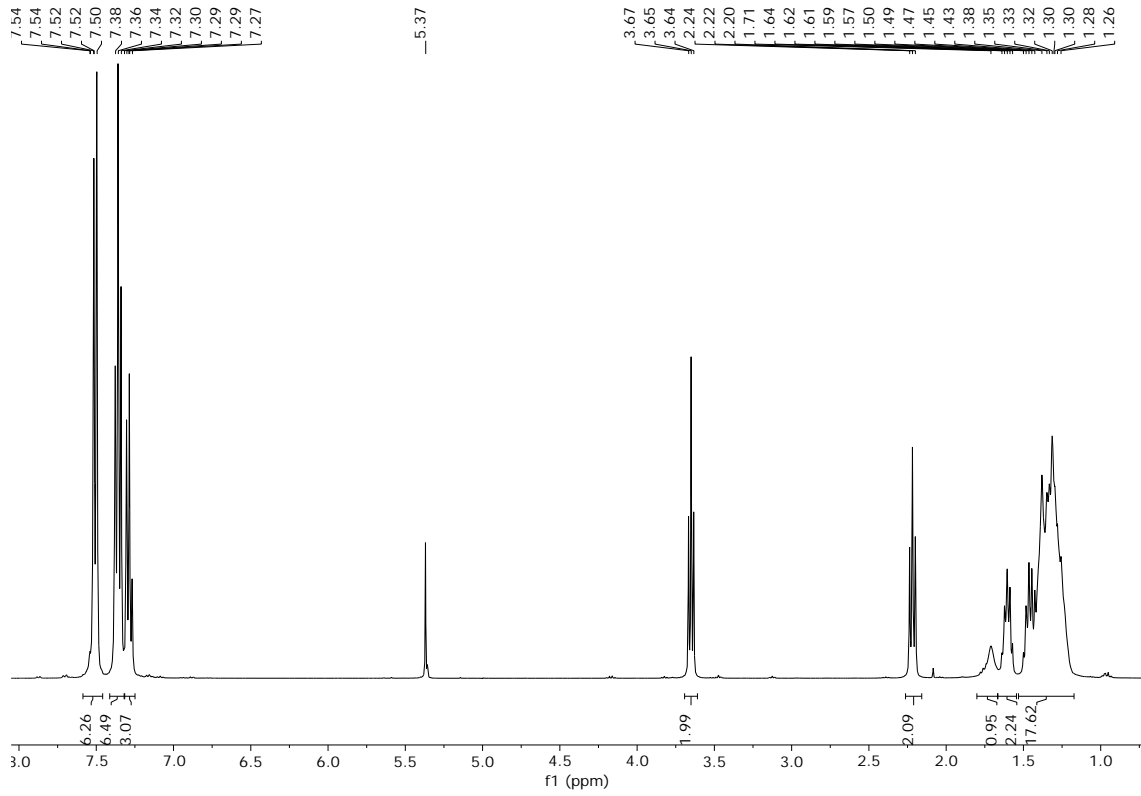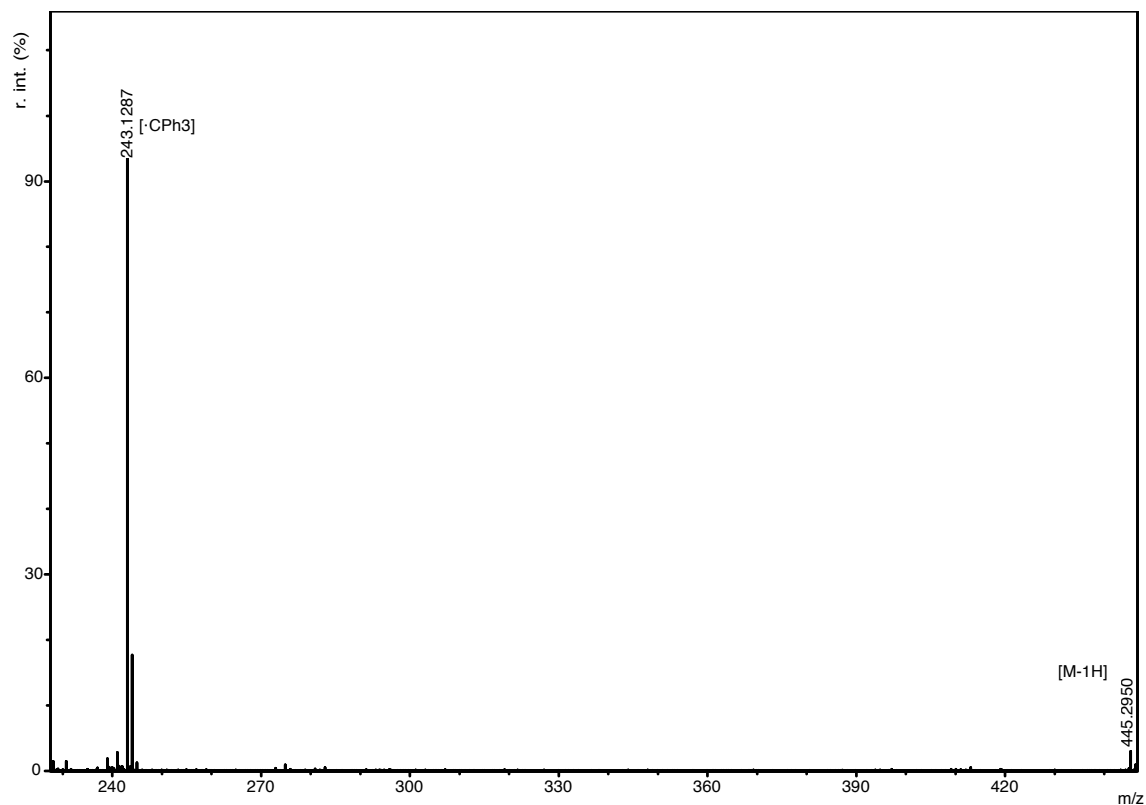
7-(tritylthio)heptanal (4)
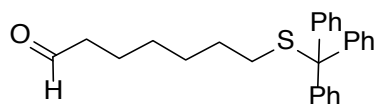
According to general procedure, from 7-triphenylmercapto-1-ol (**1**) (484 mg, 1.24 mmol) triethylamine (600 μL, 4.34 mmol) and sulfur trioxide pyridine complex (408 mg, 2.57 mmol) in mixture of DCM (3.5 mL) and DMSO (500 μL), the compound **4** was obtained as a transparent oil (yield, 66%). **^{1}H-NMR** (400 MHz, CD$_2$Cl$_2$) δ/ppm: 9.75 (t, J = 1.7 Hz, 1H), 7.56 – 7.43 (m, 6H), 7.35 (t, J = 7.5 Hz, 7H), 7.28 (t, J = 7.2 Hz, 3H), 2.40 (td, J = 7.4, 1.7 Hz, 2H), 2.21 (t, J = 7.3 Hz, 2H), 1.59 (p, J = 7.4 Hz, 2H), 1.51 – 1.38 (m, 2H), 1.38 – 1.19 (m, 4H). **^{13}C-NMR** (101 MHz, CD$_2$Cl$_2$) δ/ppm: 202.40, 145.14, 129.59, 127.80, 126.53, 70.75, 70.62, 43.71, 31.79, 28.68, 28.64, 28.40, 21.84; **FT-IR** v/cm^{-1}: 3083.7, 3056.6, 3028.8, 2929.2, 2855.5, 2721.2, 1721.9, 1593.5, 1485.6, 1440.8, 1238.1, 1079.6, 1033.9, 742.2, 698.3, 674.5, 625.5. **EM (m/z)** (ESI): calculated for C$_{26}$H$_{28}$OS: 388.2; found: 411.2 (M+Na), 243.11 (·CPh3+1H+).

¹H NMR:
9.75

7.50, 7.50, 7.48, 7.37, 7.36, 7.35, 7.33, 7.29, 7.28, 7.26

5.37

2.42, 2.41, 2.40, 2.39, 2.38, 2.38, 2.23, 2.21, 2.19, 2.07

1.60, 1.59, 1.57, 1.45, 1.43, 1.41, 1.32, 1.31, 1.30, 1.28, 1.27, 1.25

Integrations: 0.72, 5.79, 5.85, 2.79, 1.61, 2.00, 2.22, 2.77, 4.79

f1 (ppm)

¹³C NMR:
202.40

145.14

129.59, 127.80, 126.53

70.75, 66.39

43.71

31.79, 28.68, 28.64, 28.40, 21.84

f1 (ppm)

Intens
x10⁵

243.1 [·CPh₃+H⁺]

+MS, 2.4-3.3min #(107-142)

[M+Na]
411.3

262.9   301.2
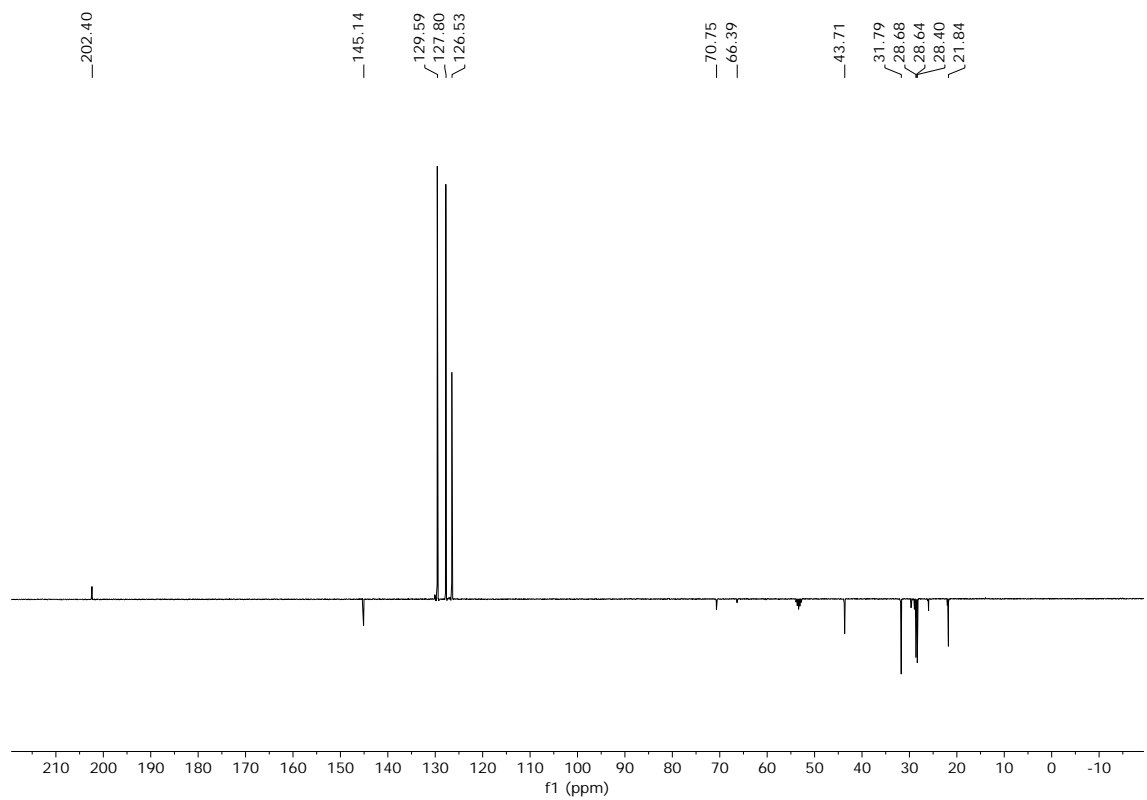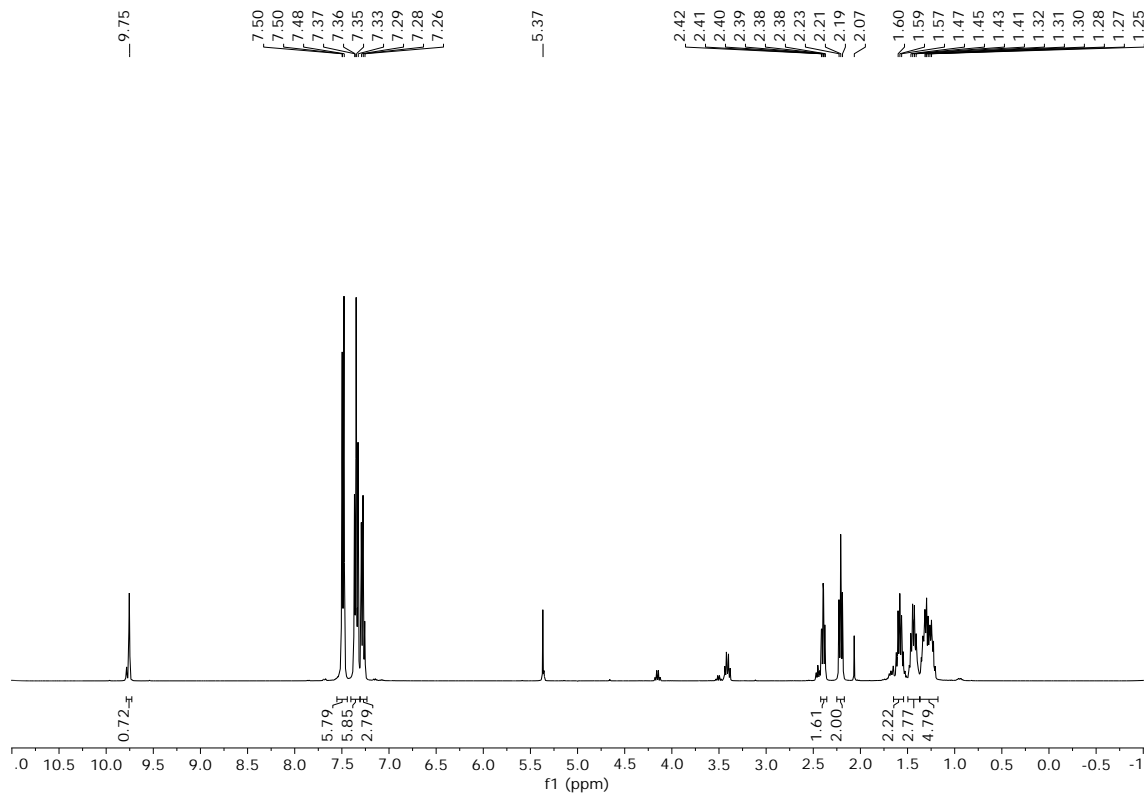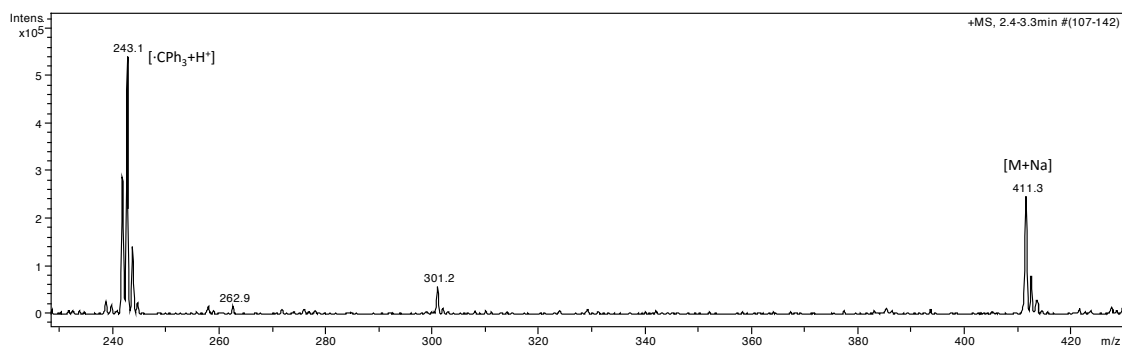
9-(tritylthio)nonanal (5)
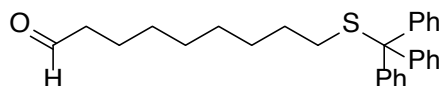
According to the general procedure, from 9-triphenylmercapto-1-ol (**2**) (1.24 mmol, 519 mg), triethylamine (600 μL, 4.34 mmol) and sulfur trioxide pyridine complex (408 mg, 2.57 mmol) in a mixture of DCM (3.5 mL) and DMSO (500 μL), the compound **5** was obtained as a transparent oil (yield, 71%). **¹H-NMR** (400 MHz, CDCl₃) δ/ppm: 9.84 (t, J = 1.6 Hz, 1H), 7.67 – 7.57 (m, 6H), 7.42 (t, J = 7.5 Hz, 6H), 7.35 (t, J = 7.2 Hz, 3H), 2.49 (td, J = 7.4, 1.6 Hz, 2H), 2.34 (t, J = 7.3 Hz, 2H), 1.72 (q, J = 7.2 Hz, 2H), 1.56 (q, J = 7.1 Hz, 2H), 1.50 – 1.26 (m, 8H); **¹³C-NMR** (101 MHz, CD₂Cl2) δ/ppm: 202.42, 145.31, 129.74, 127.95, 126.66, 66.52, 43.94, 32.04, 29.29, 29.19, 29.09, 29.06, 28.72, 22.16; **FT-IR** v/cm⁻¹: 3086.5, 3057.1, 3032.2, 2922.8, 2852.5, 1722.9, 1594.7, 1488.7, 1444.3, 155.5, 10841.1, 1034.1, 952.9, 887.2, 850.2, 164.3, 742.4, 697.8, 676.7; **EM (m/z)** (MALDI-TOF): calculated for C₂₈H₃₂OS: 416.22; found: 415.21 (M-H) and 243.08 (M-CPh₃).

NMR spectrum

^{1}H NMR (ppm): 9.8, 7.6, 7.6, 7.6, 7.4, 7.4, 7.4, 7.4, 7.3, 7.3, 5.4, 2.5, 2.5, 2.5, 2.5, 2.5, 2.4, 2.3, 2.3, 1.8, 1.7, 1.7, 1.7, 1.7, 1.6, 1.6, 1.6, 1.5, 1.5, 1.5, 1.5, 1.4, 1.4, 1.4, 1.4, 1.4, 1.4, 1.3

Integrations: 0.72, 6.62, 6.73, 3.30, 2.00, 2.20, 2.18, 2.49, 9.57

^{13}C NMR (ppm): 202.42, 145.31, 129.74, 127.95, 126.66, 66.52, 43.94, 32.04, 29.29, 29.19, 29.09, 29.06, 28.72, 22.16
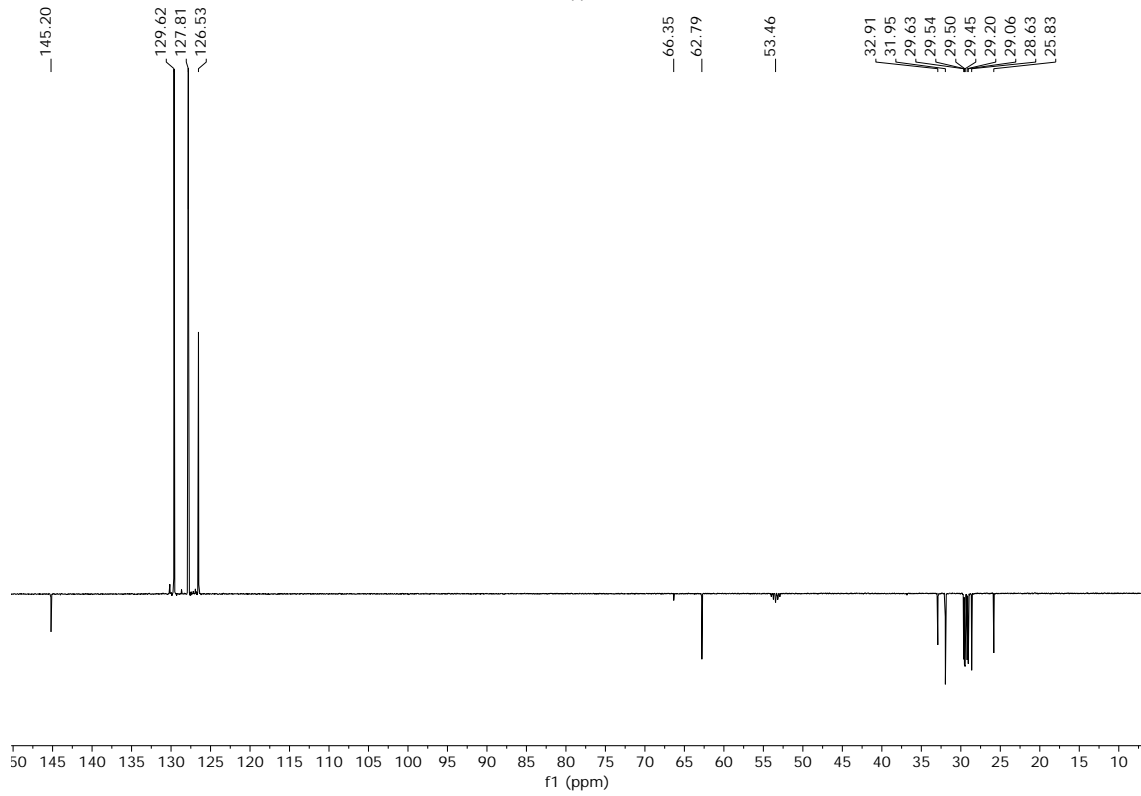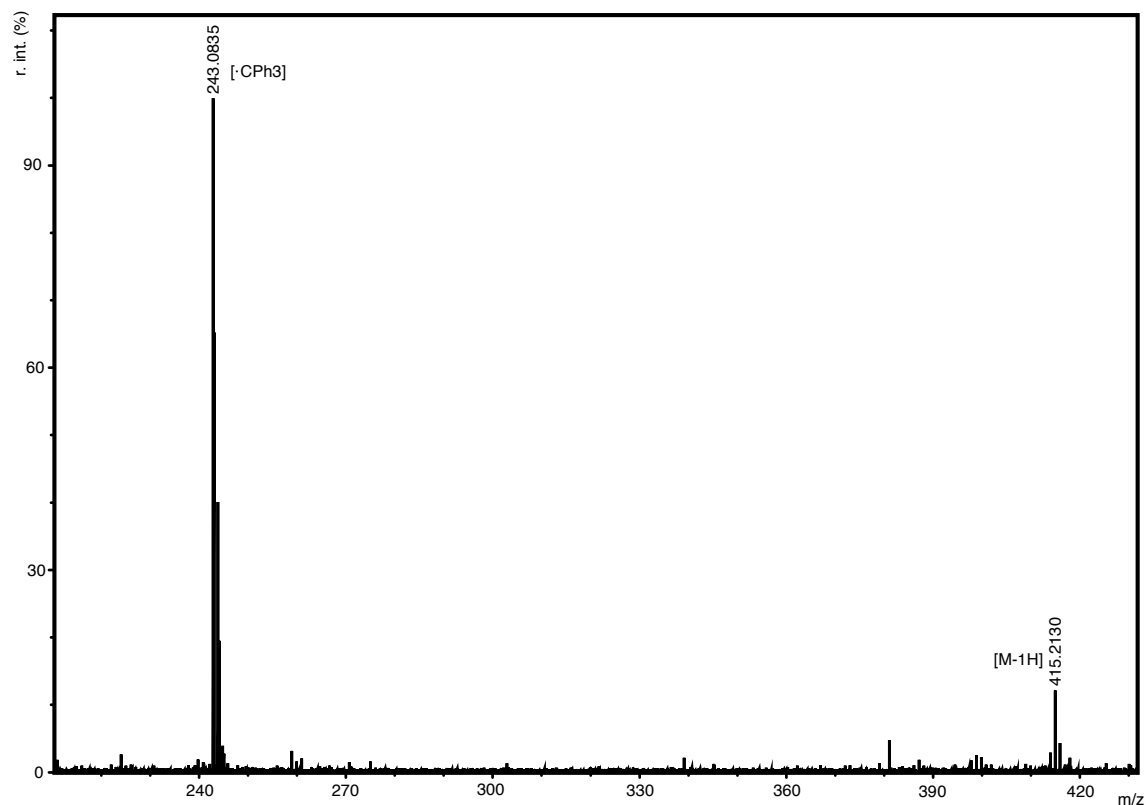
11-(tritylthio)undecanal (6)
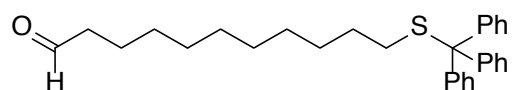
According to the general procedure, from 11-triphenylmercapto-1-ol (**3**) (1.24 mmol, 553 mg), triethylamine (600 μL, 4.34 mmol) and sulfur trioxide pyridine complex (408 mg, 2.57 mmol) in a mixture of DCM (3.5 mL) and DMSO (500 μL), the compound **6** was obtained as a transparent oil (yield, 68%). ^{1}**H-NMR** (400 MHz, CD$_2$Cl$_2$) δ/ppm: 9.77 (t, J = 1.8 Hz, 1H), 7.50 – 7.41 (m, 6H), 7.33 (t, J = 7.5 Hz, 6H), 7.26 (t, J = 7.2 Hz, 3H), 2.43 (td, J = 7.4, 1.8 Hz, 2H), 2.18 (t, J = 7.4 Hz, 2H), 1.64 (q, J = 7.3 Hz, 2H), 1.43 (q, J = 7.3 Hz, 2H), 1.38 – 1.12 (m, 12H). ^{13}**C-NMR** (101 MHz, CD$_2$Cl$_2$) δ/ppm: 202.64, 145.15, 129.57, 127.75, 126.47, 66.30, 53.41, 43.85, 31.89, 29.30, 29.12, 29.09, 28.98, 28.56, 22.06; **FT-IR** $(v$/cm$^{-1})$: 3058.1, 2924.9, 2853.2, 1723.2, 1595.5, 1489.3, 1444.1, 1276.2, 1262.1, 1081.4, 1033.4, 908.6, 851.1, 743.3; **EM (m/z)**: (MALDI-TOF): calculated for C$_{30}$H$_{36}$OS: 444.25; found: 445.43 (M+1H) and 243.21 (·CPh$_3$).

¹H NMR peaks: 9.77, 9.77, 9.76, 7.47, 7.47, 7.45, 7.36, 7.35, 7.34, 7.31, 7.29, 7.28, 7.26, 7.26, 7.25, 7.24, 5.36, 5.36, 5.36, 2.45, 2.44, 2.43, 2.43, 2.41, 2.41, 2.19, 2.18, 2.16, 1.68, 1.66, 1.64, 1.62, 1.60, 1.46, 1.44, 1.43, 1.41, 1.39, 1.32, 1.29, 1.29, 1.28, 1.26, 1.24, 1.23, 1.22

Integrations: 0.7, 6.1, 6.3, 2.9, 1.9, 2.1, 2.1, 2.4, 13.5

¹³C NMR peaks: 202.64, 145.15, 129.57, 127.75, 126.47, 66.30, 53.41, 43.85, 31.89, 29.30, 29.12, 29.09, 28.98, 28.56, 22.06
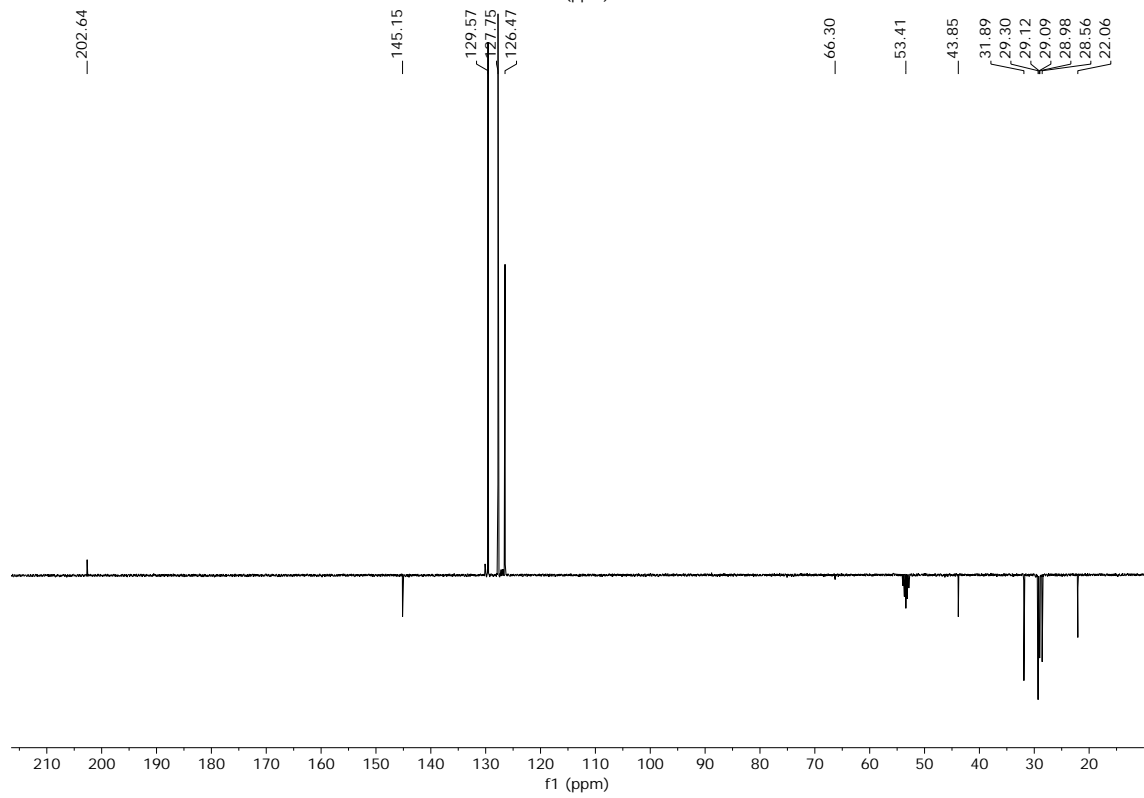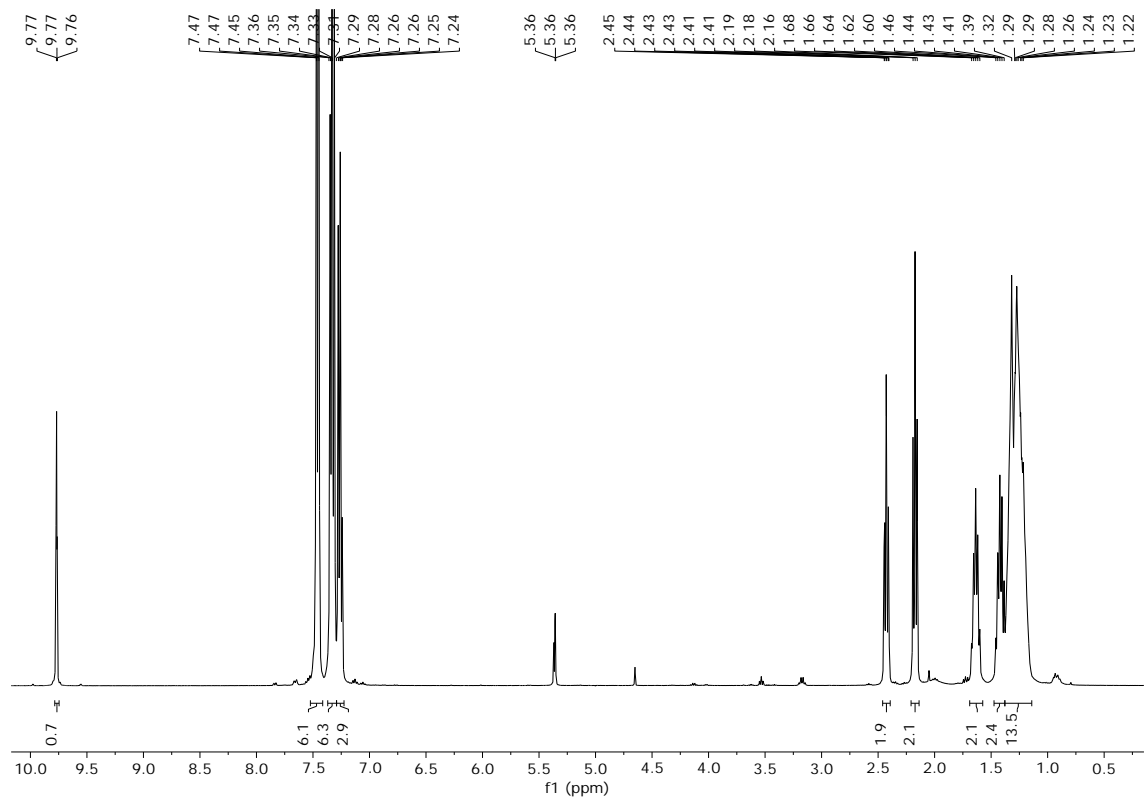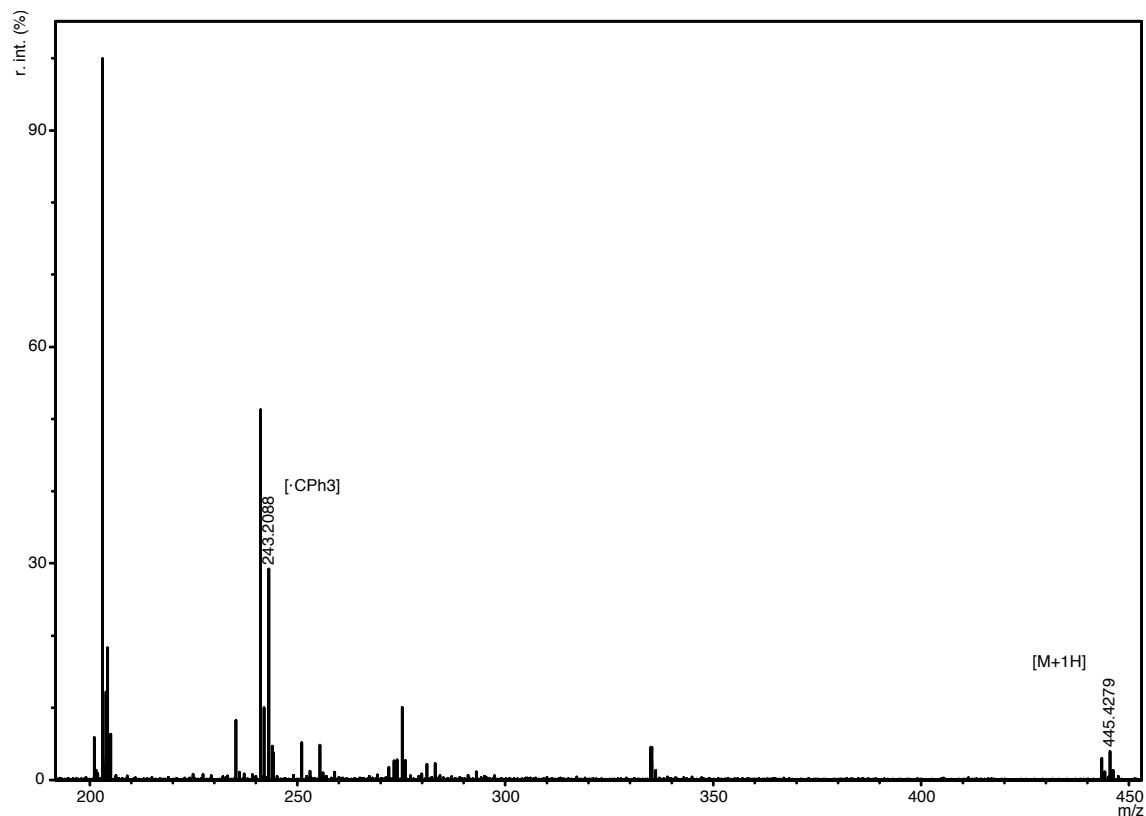
(E)-(8-(4-(bis(perchlorophenyl)methyl)-2,3,5,6-tetrachlorophenyl)oct-7-en-1-yl)(trityl)sulfane (7)
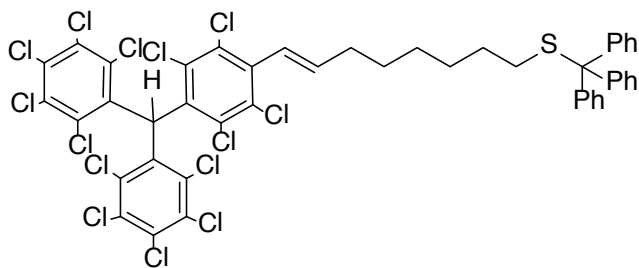
According to the general procedure, from potassium tert-butoxide (58 mg 051 mmol), PTM-P(O)(OEt)$_2$ (300 mg, 0.34 mmol) and 7-(tritylthio)heptanal (**4**) (263 mg, 0.68 mmol) in THF (10 mL), the compound **7** was obtained as a withe powder (yield, 67%). **^{1}H-NMR** (400 MHz, CD$_2$Cl$_2$) δ/ppm: 7.49 – 7.42 (m, 6H), 7.32 (t, J = 7.5 Hz, 6H), 7.25 (t, J = 7.2 Hz, 3H), 7.06 (s, 1H), 6.35 (d, J = 16.1 Hz, 1H), 6.16 (dt, J = 16.1, 6.9 Hz, 1H), 2.29 (q, J = 6.8 Hz, 2H), 2.19 (t, J = 7.3 Hz, 2H), 1.53 – 1.20 (m, 8H);); **^{13}C-NMR** (101 MHz, CD$_2$Cl$_2$) δ/ppm: 145.05, 141.22, 138.14, 136.67, 136.64, 135.38, 135.07, 134.96, 134.44, 133.95, 133.94, 133.56, 133.41, 133.38, 133.34, 133.23, 132.35, 132.31, 132.14, 129.49, 127.68, 126.40, 124.21, 66.27, 56.53, 53.33, 32.98, 31.77, 28.66, 28.46, 28.41, 28.32; **FT-IR** (v/cm^{-1}): 3057.4, 2926.1, 2852.6, 1594.5, 1488.4, 1442.7, 1362.6, 1334.9, 1295.2, 1238.3, 1137.8, 1238.3, 1137.8, 1032.6, 966.2, 852.7,

807.2, 741.5, 696.9. **EM (m/z)** (ESi): calculated for $C_{46}H_{30}Cl_{14}S$: 1109.76; found: 1108.8 (M-1H).
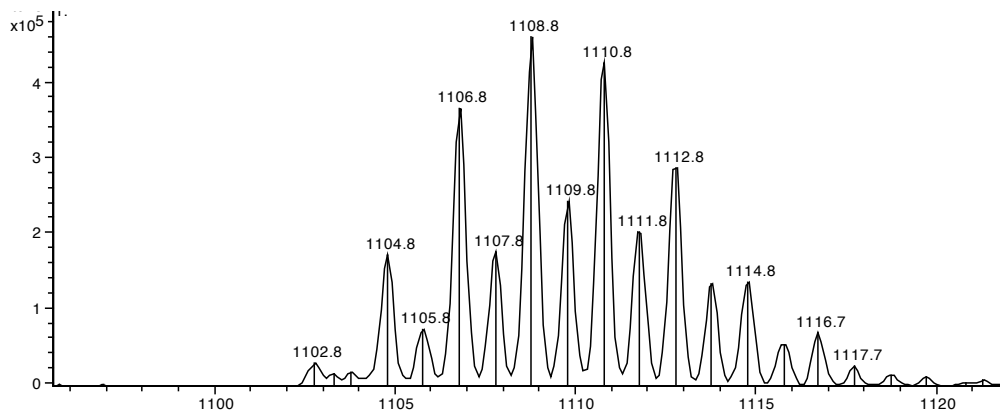
(E)-(10-(4-(bis(perchlorophenyl)methyl)-2,3,5,6-tetrachlorophenyl)dec-9-en-1-yl)(trityl)sulfane (8)
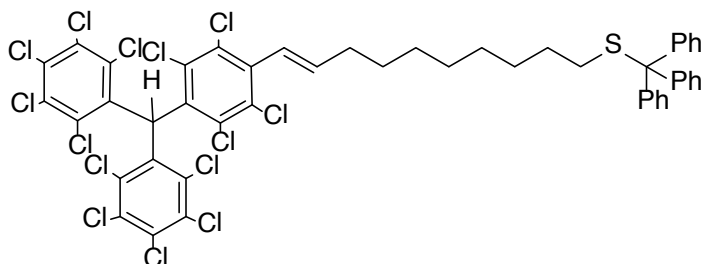
According to the general procedure, from potassium tert-butoxide (58 mg 051 mmol), PTM-P(O)(OEt)$_2$ (300 mg, 0.34 mmol) and 9-(tritylthio)nonanal (**5**) (283 mg, 0.68 mmol) in THF (10 mL), the compound **8** was obtained as a withe powder (yield, 65%).**^{1}H-NMR** (400 MHz, CD$_2$Cl$_2$) δ/ppm: 7.48 – 7.41 (m, 6H), 7.32 (t, J = 7.5 Hz, 6H), 7.25 (t, J = 7.2 Hz, 3H), 7.05 (s, 1H), 6.36 (d, J = 16.1 Hz, 1H), 6.19 (dt, J = 16.1, 6.9 Hz, 1H), 2.32 (q, J = 6.8 Hz, 2H), 2.16 (t, J = 7.4 Hz, 2H), 1.52 (p, J = 7.2 Hz, 2H), 1.46 – 1.16 (m, 10H); **^{13}C-NMR** (101 MHz, CD$_2$Cl$_2$) δ/ppm: 145.13, 141.46, 138.25, 136.74, 136.70, 135.42, 135.14, 135.03, 134.53, 134.50, 134.02, 134.00, 133.62, 133.47, 133.44, 133.40, 133.30, 132.41, 132.37, 132.21, 129.56, 127.75, 126.47, 124.21, 66.29, 56.59, 53.42, 33.18, 31.86, 29.17, 29.07, 28.96, 28.92, 28.61, 28.55; **FT-IR** (v/cm^{-1}): 3061.7, 2923.7, 2851.4, 1593.4, 1488.3, 1443.0, 1365.1, 1334.7, 1295.9, 1238.3, 1137.9, 1033.1, 965.1, 852.9, 807.5, 741.5, 967.7. **EM (m/z)** (ESI): calculated for C$_{48}$H$_{34}$Cl$_{14}$S: 1137.79; found: 1136.8 (M-1H).

¹H NMR spectrum (top): δ 7.46, 7.46, 7.44, 7.34, 7.32, 7.30, 7.26, 7.25, 7.05, 6.38, 6.34, 6.23, 6.21, 6.19, 6.17, 6.15, 5.36, 5.36; 2.35, 2.33, 2.31, 2.30, 2.18, 2.16, 2.15, 1.54, 1.52, 1.51, 1.49, 1.47, 1.44, 1.42, 1.40, 1.38, 1.36, 1.34, 1.31, 1.28, 1.27, 1.25, 1.24, 1.23, 1.22, 1.21

Integrations: 5.7, 5.7, 2.8, 0.7, 0.9, 0.9, 2.0, 2.0, 2.2, 11.5

¹³C NMR spectrum (bottom): δ 145.13, 141.46, 138.25, 136.74, 136.70, 135.42, 135.14, 135.03, 134.53, 134.00, 134.50, 134.02, 133.62, 133.47, 133.44, 133.40, 133.30, 132.41, 132.37, 132.21, 129.56, 127.75, 126.47, 124.21; 66.29; 56.59, 53.42; 33.18, 31.86, 29.17, 29.07, 28.96, 28.92, 28.61, 28.55

f1 (ppm)

(E)-(12-(4-(bis(perchlorophenyl)methyl)-2,3,5,6-tetrachlorophenyl)dodec-11-en-1-yl)(trityl)sulfane (9)

According to the general procedure, from potassium tert-butoxide (58 mg 051 mmol), PTM-P(O)(OEt)$_2$ (300 mg, 0.34 mmol) and 11-(tritylthio)undecanal (**6**) (302mg, 0.68 mmol) in THF (10 mL), the compound **9** was obtained as a withe powder (yield, 71%). **^{1}H-NMR** (400 MHz, CD$_2$Cl$_2$) δ/ppm: 7.45 (d, J = 7.6 Hz, 6H), 7.32 (t, J = 7.5 Hz, 6H), 7.25 (t, J = 7.2 Hz, 3H), 7.05 (s, 1H), 6.37 (d, J = 16.1 Hz, 1H), 6.20 (dt, J = 16.1, 6.8 Hz, 1H), 2.33 (q, J = 6.8 Hz, 2H), 2.16 (t, J = 7.4 Hz, 2H), 1.55 (p, J = 7.3 Hz, 2H), 1.48 – 1.11 (m, 14H); **^{13}C-NMR** (101 MHz, CD$_2$Cl$_2$) δ/ppm: 145.13, 141.51, 138.26, 136.74, 136.70, 135.41, 135.14, 135.02, 134.50, 134.01, 134.00, 133.62, 133.46, 133.43, 133.40, 133.29, 132.41, 132.37, 132.21, 129.55, 127.74, 126.46, 124.18, 66.27, 53.42, 33.21, 31.87, 29.47, 29.37, 29.11, 29.02, 28.98, 28.67, 28.55. **EM (m/z)** (ESI): calculated for C$_{50}$H$_{38}$Cl$_{14}$S: 1165.82; found: 1164.8 (M-1H).
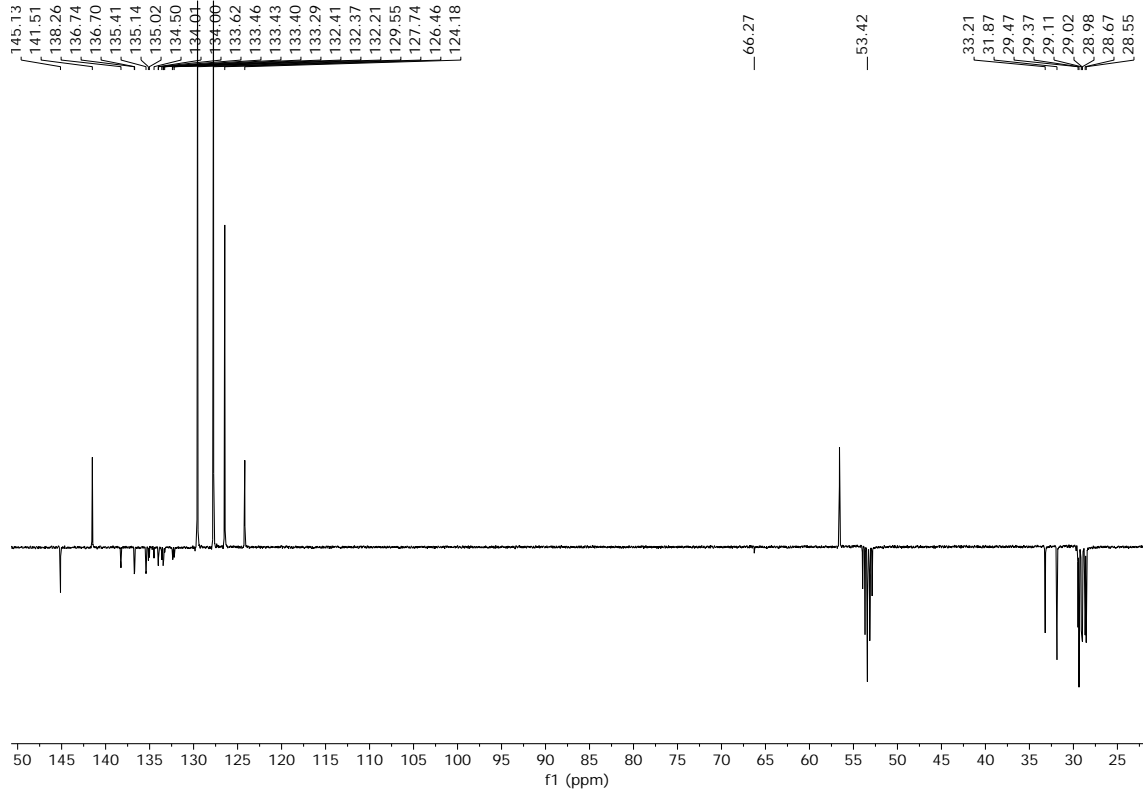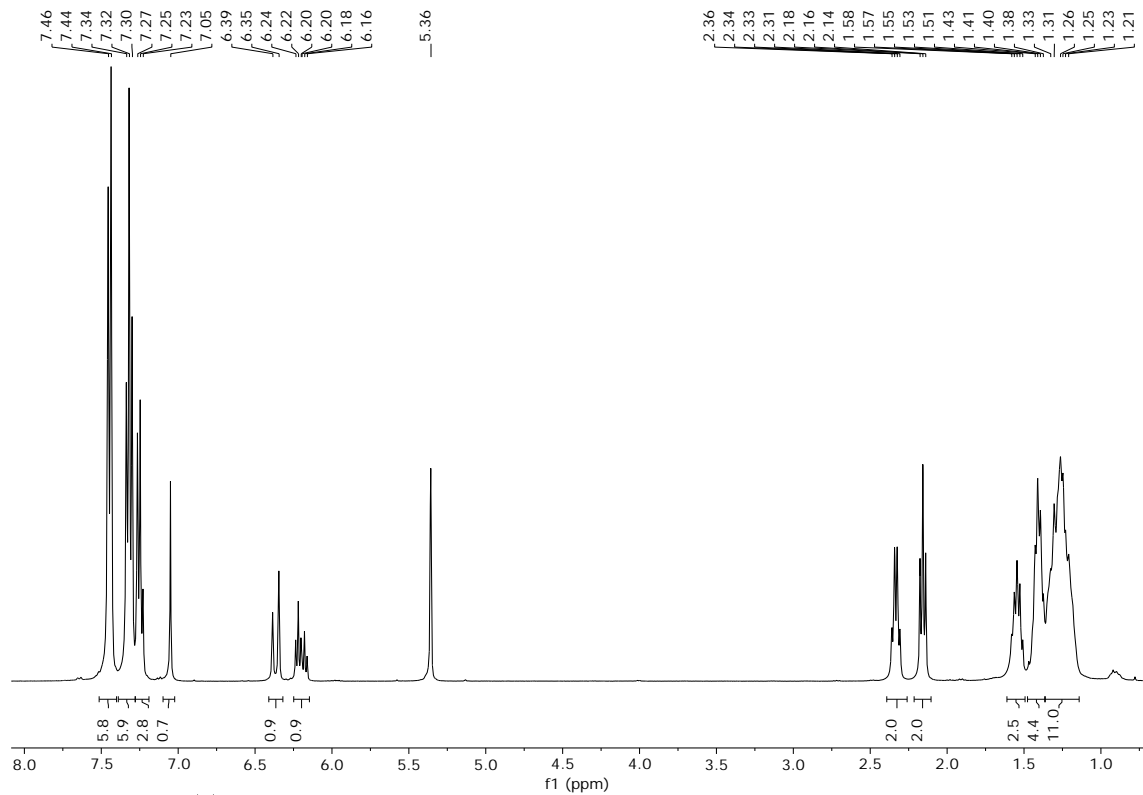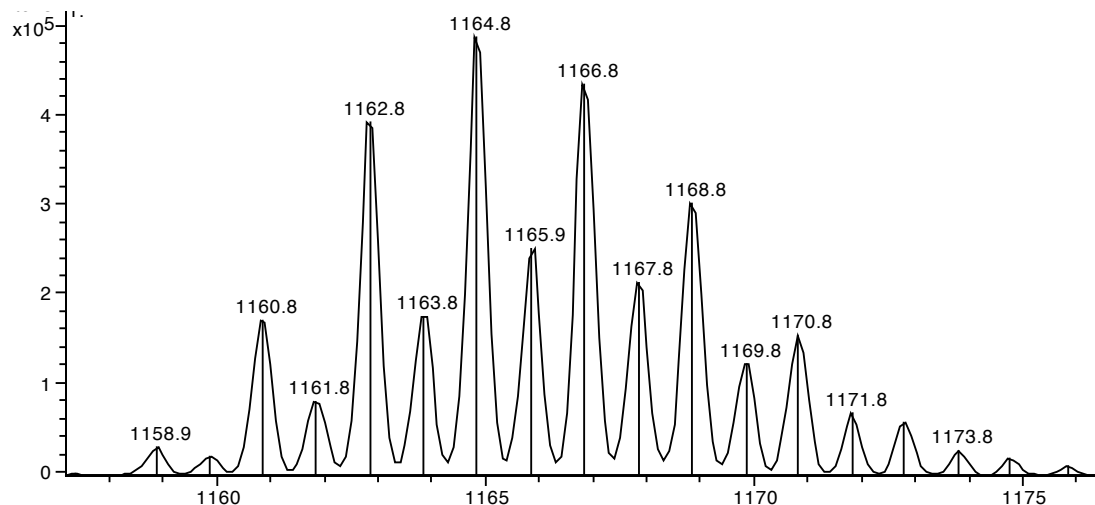
¹H NMR (ppm): 7.46, 7.44, 7.34, 7.32, 7.30, 7.27, 7.25, 7.23, 7.05, 6.39, 6.35, 6.24, 6.22, 6.20, 6.20, 6.18, 6.16, 5.36, 2.36, 2.34, 2.33, 2.31, 2.18, 2.16, 2.14, 1.58, 1.57, 1.55, 1.53, 1.51, 1.43, 1.41, 1.40, 1.38, 1.33, 1.31, 1.26, 1.25, 1.23, 1.21

Integrations: 5.8, 5.9, 2.8, 0.7, 0.9, 0.9, 2.0, 2.0, 2.5, 4.4, 11.0

¹³C NMR (ppm): 145.13, 141.51, 138.26, 136.74, 136.70, 135.41, 135.14, 135.02, 134.50, 134.01, 134.00, 133.62, 133.46, 133.43, 133.40, 133.29, 132.41, 132.37, 132.21, 129.55, 127.74, 126.46, 124.18, 66.27, 53.42, 33.21, 31.87, 29.47, 29.37, 29.11, 29.02, 28.98, 28.67, 28.55
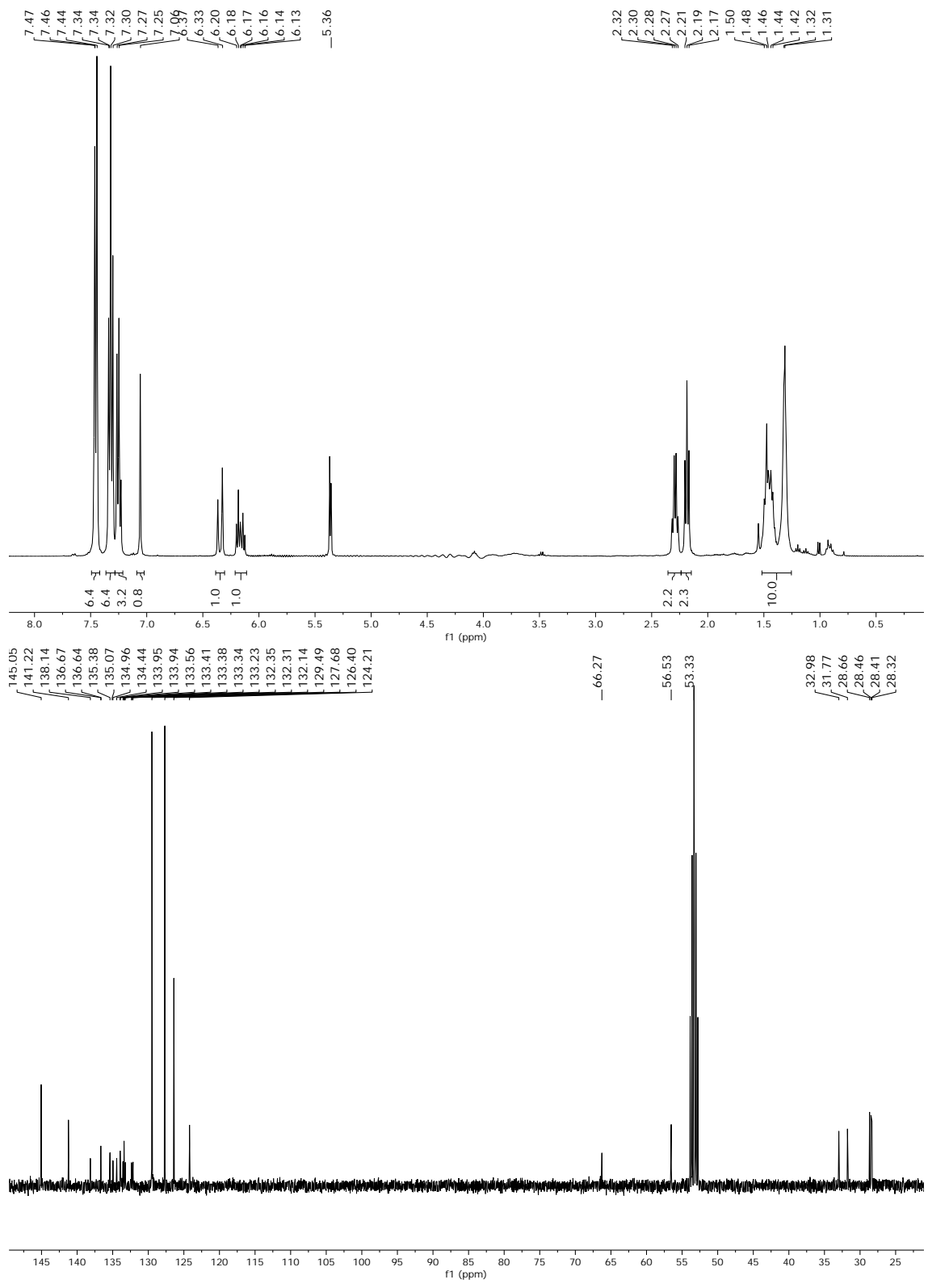
(E)-(8-(4-(bis(perchlorophenyl)methyl)-2,3,5,6-tetrachlorophenyl)oct-7-en-1-yl)(trityl)sulfane (radical) (10)
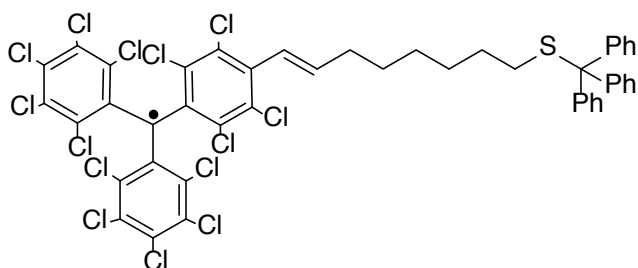
According to the general procedure, the compound **10** was obtained as a red powder in quantitative yield. **HPLC**: retention time: 14.9 (2.5% of cis isomer), 15.5min (95% of trans isomer), 16.9 (2.5% αH); **UV/Vis** (CH$_2$Cl$_2$): $\lambda(nm)$ (logε)= 388 (4.46), 515 (3.08), 567 (3.10). **CV**: E$^{1/2}$ = -0.16 V (PTM reduction); **FT-IR** (v/cm^{-1}): 3057.1, 2924.2, 2853.2, 1653.5, 1596.1, 1489.5, 144.4, 1333.0, 1259.6, 1157.3, 1081.6, 1033.9, 857.7, 816.4, 738.1, 697.9, 652.3, 620.5; **EPR** (CH$_2$Cl$_2$, r.t.): g = 2.002804; ΔH$_{PP}$ = 1.3 G, a$_{13C\alpha}$ = 29.6 G; a$_{13Co}$ = 13.2 G; a$_{13Cm}$ = 10.3 G; a$_{1H}$ = 1.8 G; **EM (m/z)** (ESI): calculated for C$_{46}$H$_{29}$Cl$_{14}$S$^{\cdot}$: 1108.75; found: 1108.8 (M*).
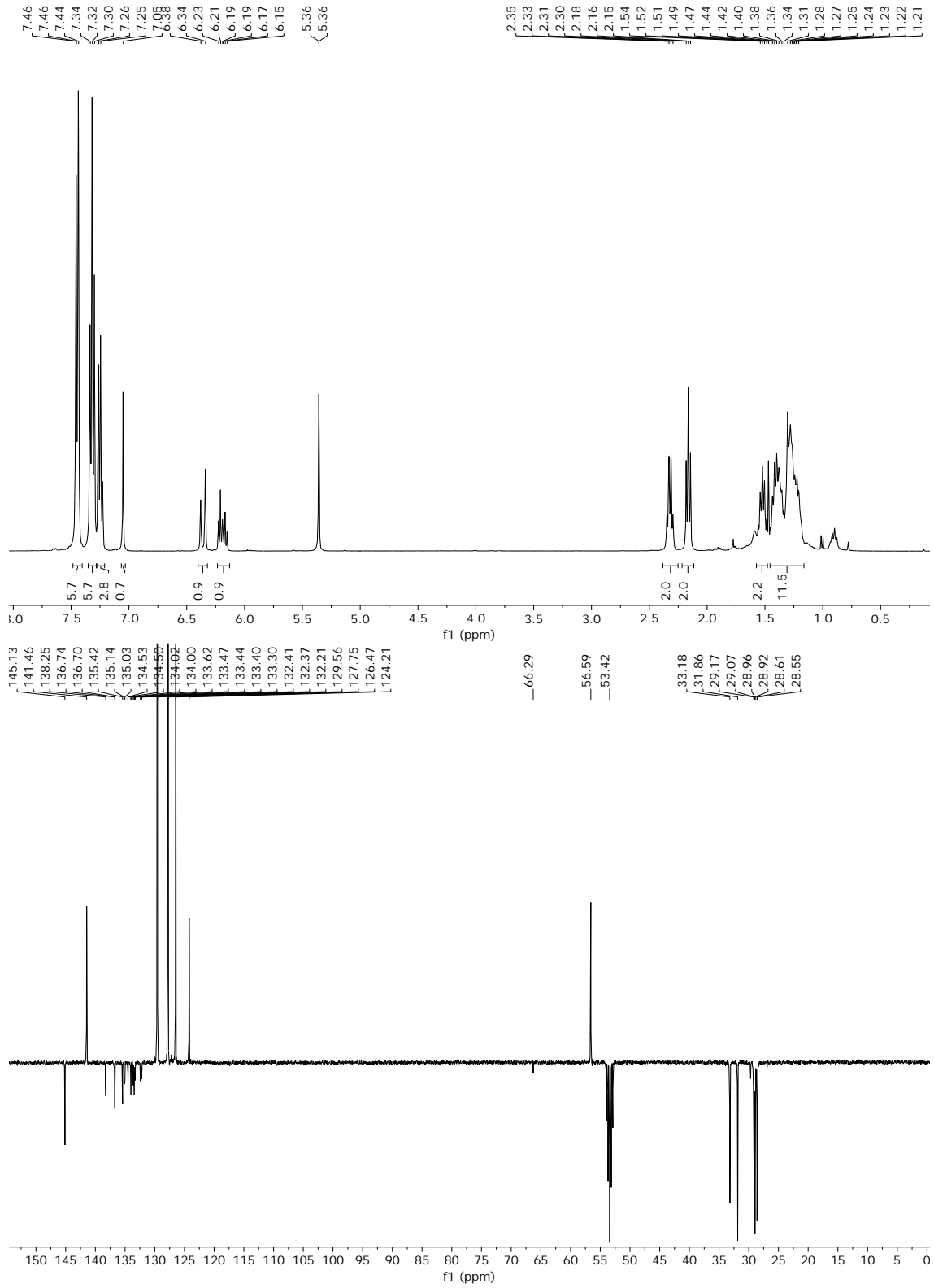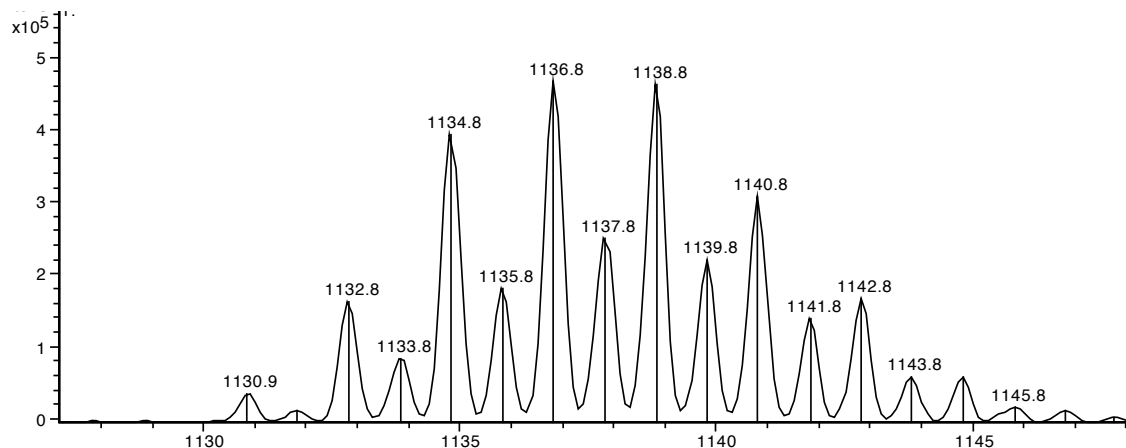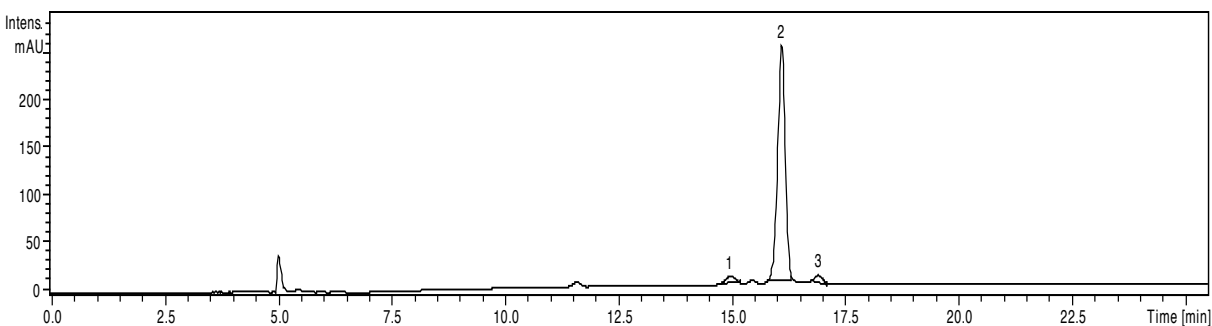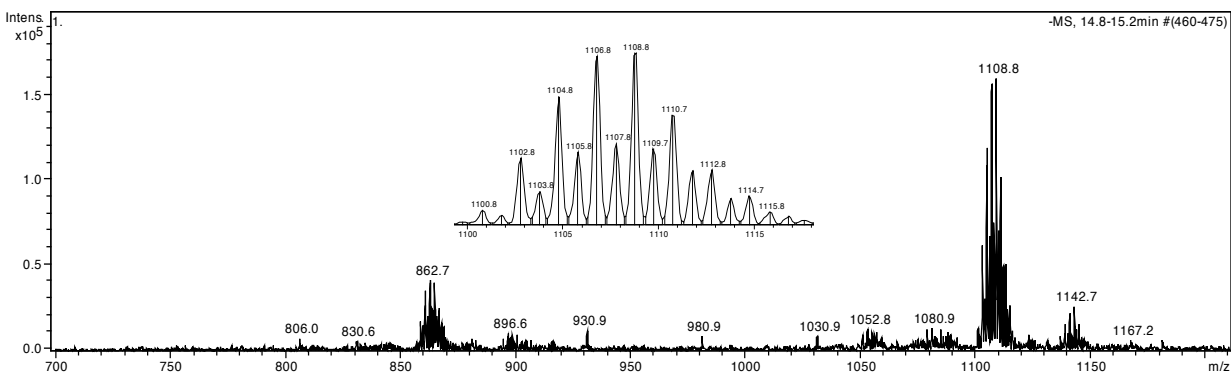
(E)-(10-(4-(bis(perchlorophenyl)methyl)-2,3,5,6-tetrachlorophenyl)dec-9-en-1-yl)(trityl)sulfane (radical) (11)

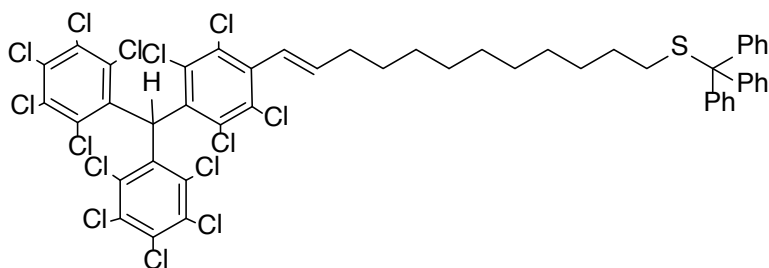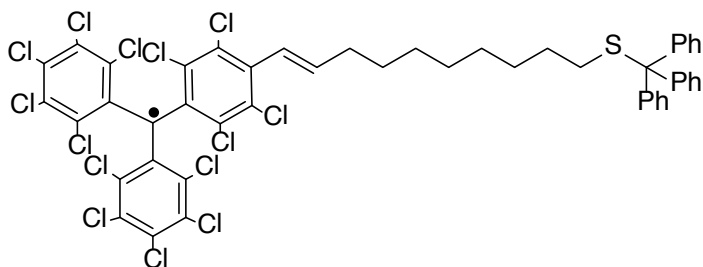According to the general procedure, the compound **11** was obtained as a red powder in quantitative yield. **HPLC**, retention time: 17.4min (98% of trans isomer); **UV/Vis** (CH$_2$Cl$_2$): $\lambda(nm)$ (logε)= 387 (4.49), 515 (3.11), 566 (3.13); **CV**: E$^{1/2}$ = -0.16 V (PTM reduction); **FT-IR** (ν/cm^{-1}): 3056.0, 2924.2, 2852.4, 1649.5, 1595.2, 1489.1, 1443.4, 1332.7, 1259.2, 1157.2, 1033.6, 966.06, 858.7, 815.9, 739.7, 697.8, 651.9, 619.7; **EPR** (CH$_2$Cl$_2$, r.t.): g = 2.002840; ΔH$_{PP}$ = 1.1 G, a$_{13C\alpha}$ = 29.6 G; a$_{13Co}$ = 13.2 G; a$_{13Cm}$ = 10.2 G; a$_{1H}$ = 1.8 G; **EM (m/z)** (Electrospray): calculated for C$_{48}$H$_{33}$Cl$_{14}$S$^{\cdot}$: 1136.78; found: 1136.8 (M*).
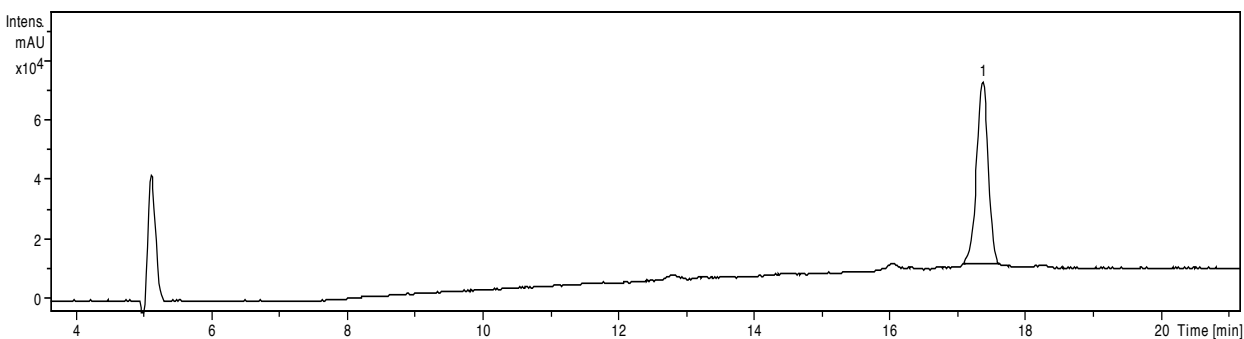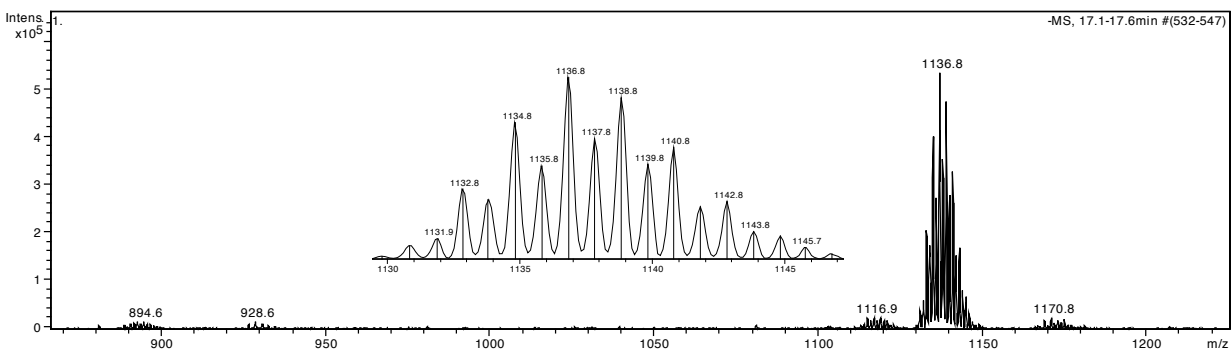
(E)-(12-(4-(bis(perchlorophenyl)methyl)-2,3,5,6-tetrachlorophenyl) dodec-11-en-1-yl)(trityl)sulfane (radical) (12)
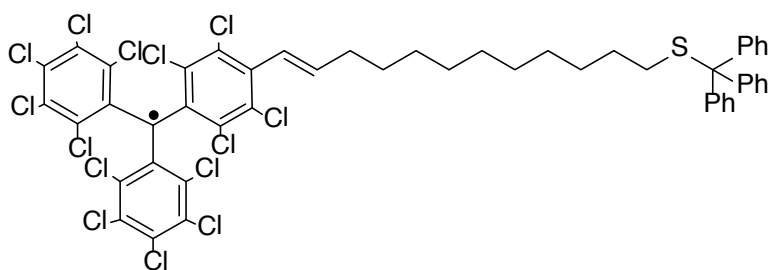
According to the general procedure, the compound **12** was obtained as a red powder in quantitative yield. **HPLC**, retention time: 18.8min (96% of trans isomer); **UV/Vis** (CH_2Cl_2): $\lambda(nm)$ ($\log\varepsilon$)= 388 (4.49), 515 (3.12), 566 (3.14); **CV**: $E^{1/2}$ = -0.16 V (PTM reduction); **FT-IR** (v/cm^{-1}):3055.7, 2924.2, 2852.3 1658.5, 1595.6, 1489.5, 1444.0, 1332.8, 1259.4, 1156.9, 1080.9, 1033.4, 967.2, 858.5, 816.0, 738.6, 697.8, 673.2, 651.8, 620.1; **EPR** (CH_2Cl_2, r.t.): g = 2.002945; ΔH_{PP} = 1.4 G, $a_{13C\alpha}$ = 29.6 G; a_{13Co} = 13.2 G; a_{13Cm} = 10.1 G; a_{1H} = 1.8 G; **EM (m/z)** (Electrospray): calculated for $C_{48}H_{32}Cl_{14}S^{.}$: 1164.81; found: 1164.8 (M*).
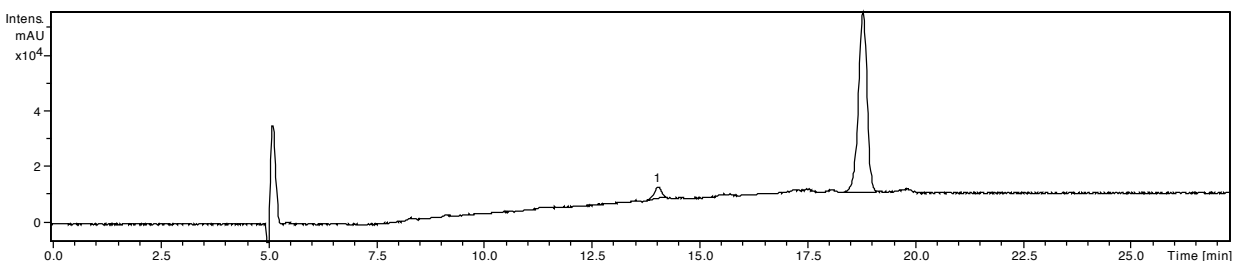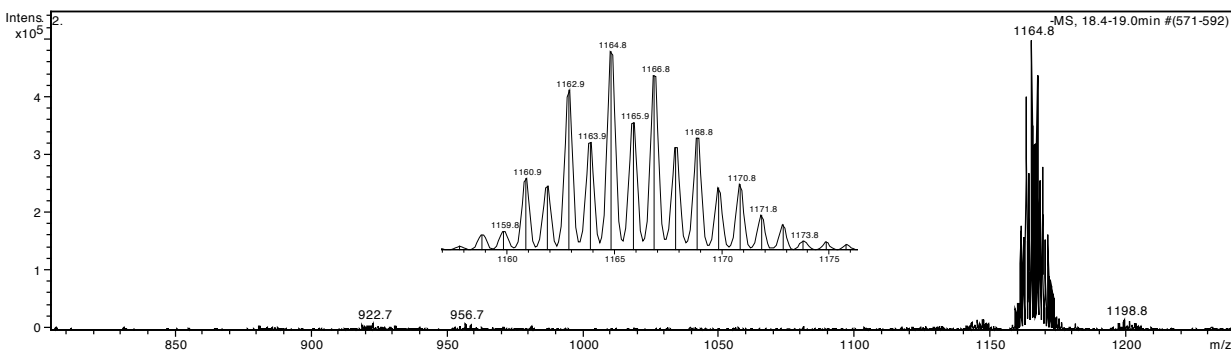
(E)-8-(4-(bis(perchlorophenyl)methyl)-2,3,5,6-tetrachlorophenyl)oct-7-ene-1-thiol (NR8)
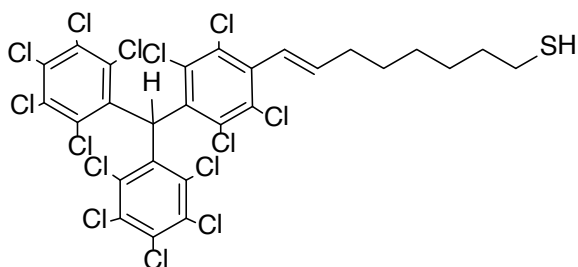
The compound **NR8** was obtained as withe powder in quantitative yield, using the general methodology described for the generation of free thiols. **^{1}H-NMR** (400 MHz, CD$_2$Cl$_2$) δ/ppm: 7.00 (s, 1H), 6.31 (d, J = 16.1 Hz, 1H), 6.14 (dt, J = 15.7, 6.7 Hz, 1H), 2.54 (q, J = 7.2 Hz, 2H), 2.31 (q, J = 6.3 Hz, 2H), 1.71 – 1.17 (m, 9H); **^{13}C-NMR** (101 MHz, CDCl$_3$) δ/ppm: 141.27, 138.19, 136.79, 136.76, 135.64, 135.28, 135.16, 134.71, 134.10, 134.08, 133.78, 133.70, 133.67, 133.64, 133.58, 133.41, 132.58, 132.54, 132.32, 124.55, 77.16, 56.71, 34.10, 33.33, 28.68, 28.63, 28.30, 24.77. **FT-IR** (v/cm^{-1}): 2927.0, 2853.9, 2343.8, 1654.2, 1533.8, 1461.7, 1363.7, 1335.5, 1298.7, 1241.0, 1139.2, 963.9, 855.3, 807.2, 752.8, 717.0, 675.2, 692.5. **EM (m/z)** (MALDI-TOF): calculated for C$_{27}$H$_{16}$Cl$_{14}$S: 867.65; found: 866.90 (M-1H) and 796.95 (M-2Cl).

¹H NMR (CDCl₃): δ 7.26 (CDCl₃), 7.00, 6.33, 6.29, 6.17, 6.16, 6.14, 6.12, 6.10, 2.57, 2.55, 2.53, 2.51, 2.32, 2.30, 2.28, 1.65, 1.64, 1.62, 1.54, 1.43, 1.42, 1.36, 1.34, 1.32, 1.26

¹³C NMR (CDCl₃): δ 141.27, 138.19, 136.79, 136.76, 135.64, 135.28, 135.16, 134.71, 134.10, 134.08, 133.78, 133.70, 133.67, 133.64, 133.58, 133.41, 132.58, 132.54, 132.32, 124.55, 77.16 (CDCl₃), 56.71, 34.10, 33.33, 28.68, 28.63, 28.30, 24.77

(E)-10-(4-(bis(perchlorophenyl)methyl-2,3,5,6-tetrachlorophenyl)dec-9-ene-1-thiol (NR10).

The compound **NR10** was obtained as withe powder in quantitative yield, using the general methodology described for the generation of free thiols. **^{1}H-NMR** (400 MHz, CDCl$_3$) δ/ppm: 6.99 (s, 1H), 6.31 (d, J = 16.1 Hz, 1H), 6.14 (dt, J = 16.1, 6.8 Hz, 1H), 2.52 (q, J = 7.4 Hz, 2H), 2.30 (q, J = 6.8 Hz, 2H), 1.61 (p, J = 7.2 Hz, 2H), 1.51 (p, J = 7.2 Hz, 2H), 1.43 – 1.21 (m, 9H); **^{13}C-NMR** (101 MHz, CDCl$_3$) δ/ppm: 141.47, 136.80, 136.77, 135.59, 135.28, 135.16, 134.70, 134.10, 134.08, 133.77, 133.69, 133.67, 133.64, 133.57, 132.58, 132.53, 132.32, 124.43, 77.16, 56.70, 34.17, 33.41, 29.86, 29.45, 29.18, 29.12, 28.79, 28.50, 24.81.; **FT-IR** (v/cm^{-1}): 2926.5, 2854.0, 1710.0, 1653.9, 1461.1, 1365.2, 1337.0, 1296.8, 1239.7, 1193.0, 1137.7, 1042.9, 966.8, 899.9, 855.2, 808.4, 739.0, 690.1, 648.4, 609.9; **EM (m/z)** (MALDI-TOF): calculated for C$_{29}$H$_{20}$Cl$_{14}$S: 895.68; found: 894.97 (M-1H) and 825.02 (M-2Cl).

^{1}H NMR (top) and ^{13}C NMR (bottom) spectra in CDCl$_3$.

^{1}H NMR peaks (ppm): 7.26 (CDCl$_3$), 6.99, 6.33, 6.29, 6.18, 6.16, 6.14, 6.12, 6.11, 2.55, 2.53, 2.52, 2.50, 2.32, 2.31, 2.29, 2.27, 1.61, 1.60, 1.55, 1.53, 1.51, 1.50, 1.39, 1.37, 1.35, 1.33, 1.31, 1.28, 1.25.

Integrations: 0.9, 1.1, 1.1, 2.0, 2.3, 2.2, 2.3, 15.1.

^{13}C NMR peaks (ppm): 141.47, 136.80, 136.77, 135.59, 135.28, 135.16, 134.70, 134.10, 134.08, 133.77, 133.69, 133.67, 133.64, 133.57, 132.58, 132.53, 132.32, 124.43, 77.16 (CDCl$_3$), 56.70, 34.17, 33.41, 29.86, 29.45, 29.18, 29.12, 28.79, 28.50, 24.81.
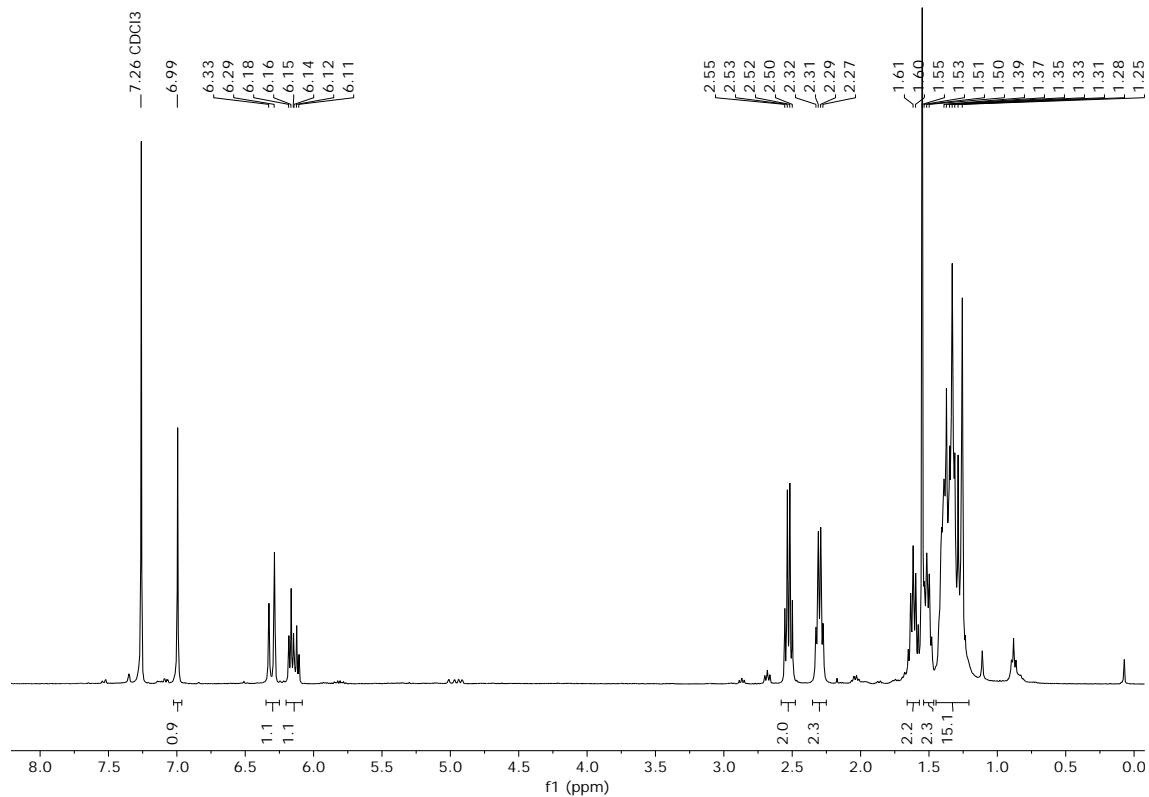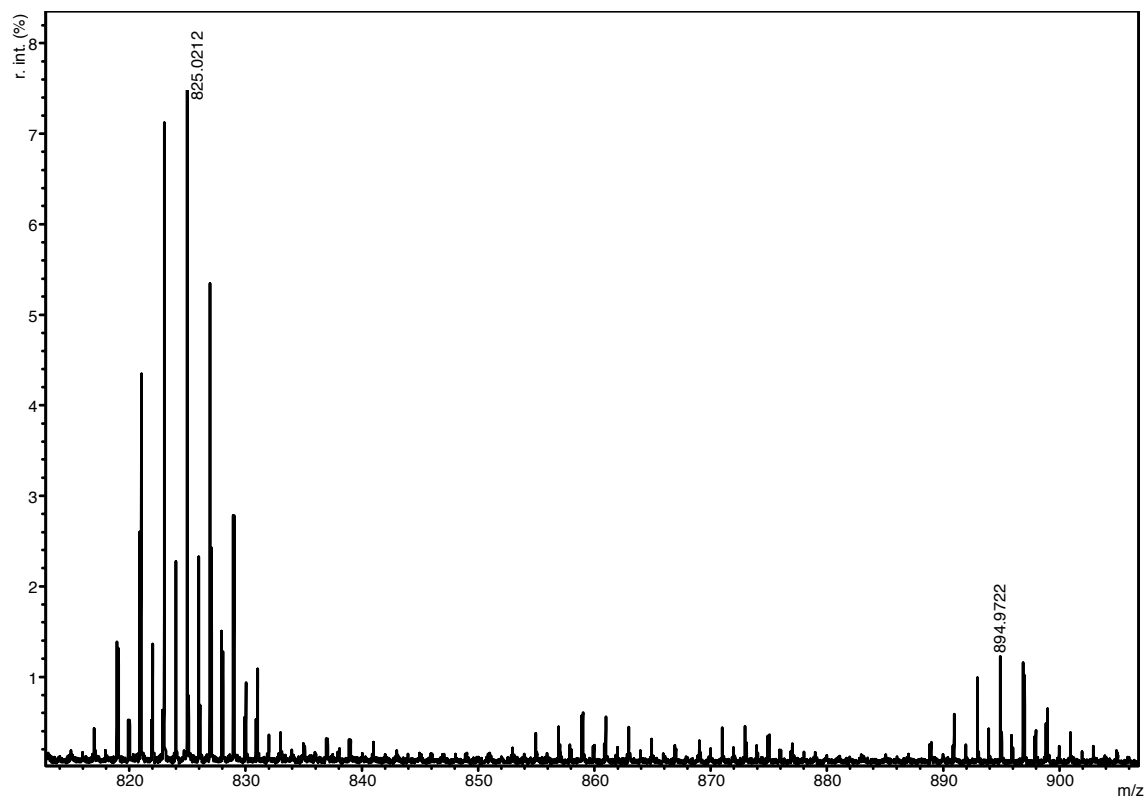
(E)-12-(4-(bis(perchlorophenyl)methyl)-2,3,5,6-tetrachlorophenyl) dodec-11-ene-1-thiol (NR12)
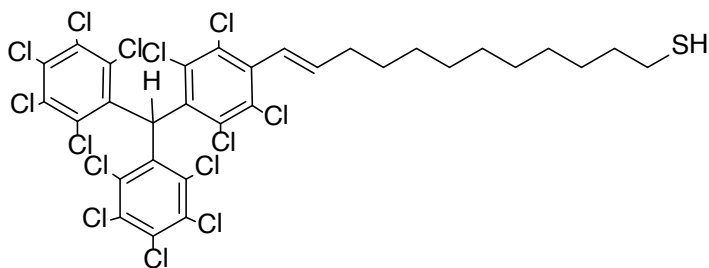
The compound **NR12** was obtained as withe powder in quantitative yield, using the general methodology described for the generation of free thiols. **^{1}H-NMR** (400 MHz, CDCl$_3$) δ/ppm: 7.00 (s, 1H), 6.31 (d, J = 16.2 Hz, 1H), 6.15 (dt, J = 16.1, 6.9 Hz, 1H), 2.52 (q, J = 7.4 Hz, 2H), 2.30 (q, J = 6.7 Hz, 2H), 1.67 – 1.45 (m, 5H), 1.45 – 1.12 (m, 16H); **^{13}C-NMR** (101 MHz, CDCl$_3$) δ/ppm: 141.54, 138.27, 136.80, 136.77, 135.58, 135.28, 135.17, 134.70, 134.10, 134.08, 133.77, 133.69, 133.67, 133.64, 133.58, 133.42, 132.58, 132.54, 132.33, 124.39, 77.16, 56.70, 34.20, 33.44, 29.86, 29.82, 29.68, 29.65, 29.56, 29.52, 29.22, 29.20, 28.83, 28.53, 24.81, 22.85; **FT-IR** (v/cm^{-1}): 2924.5, 2852.6, 1717.8, 1653.2, 1532.6, 1461.2, 1365.3, 1336.1, 1296.1, 1263.7, 1238.8, 1137.4, 966.7, 854.8, 807.6, 737.8, 717.6, 700.1, 674.9, 648.0, 606.9; **EM (m/z)** (MALDI-TOF): calculated for C$_{31}$H$_{24}$Cl$_{14}$S: 923.71; found: 922.93 (M-1H) and 852.99 (M-2Cl).

¹H NMR: 7.26 CDCl3, 7.00, 6.33, 6.29, 6.18, 6.17, 6.15, 6.13, 6.11, 2.55, 2.53, 2.51, 2.49, 2.32, 2.31, 2.29, 2.27, 1.64, 1.63, 1.61, 1.59, 1.57, 1.55, 1.53, 1.51, 1.49, 1.48, 1.38, 1.36, 1.34, 1.32, 1.29, 1.26, 0.88

Integrations: 0.9, 0.9, 0.9, 2.0, 2.0, 7.1, 32.5

¹³C NMR: 141.54, 138.27, 136.80, 136.77, 135.58, 135.28, 135.17, 134.70, 134.10, 134.08, 133.77, 133.69, 133.67, 133.64, 133.58, 133.42, 132.58, 132.54, 132.33, 124.39, 77.16 CDCl3, 56.70, 34.20, 33.44, 29.86, 29.82, 29.68, 29.65, 29.56, 29.52, 29.22, 29.20, 28.83, 28.53, 24.81, 22.85
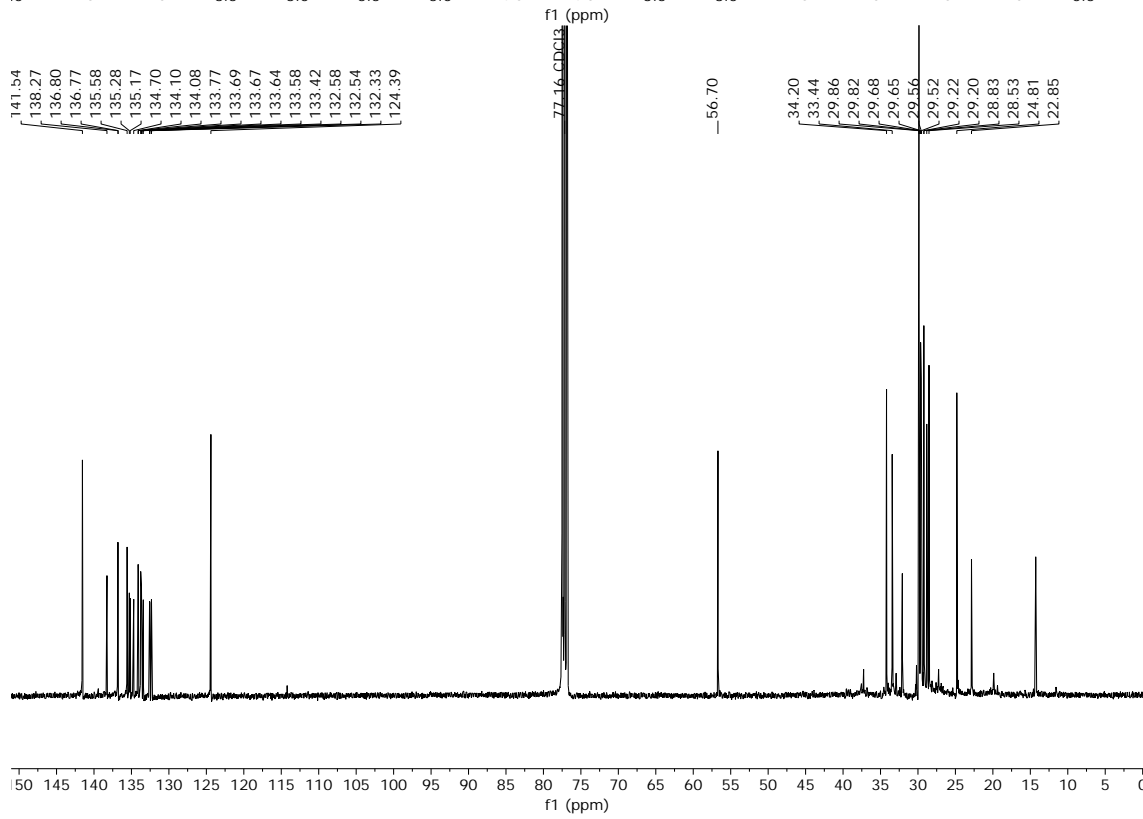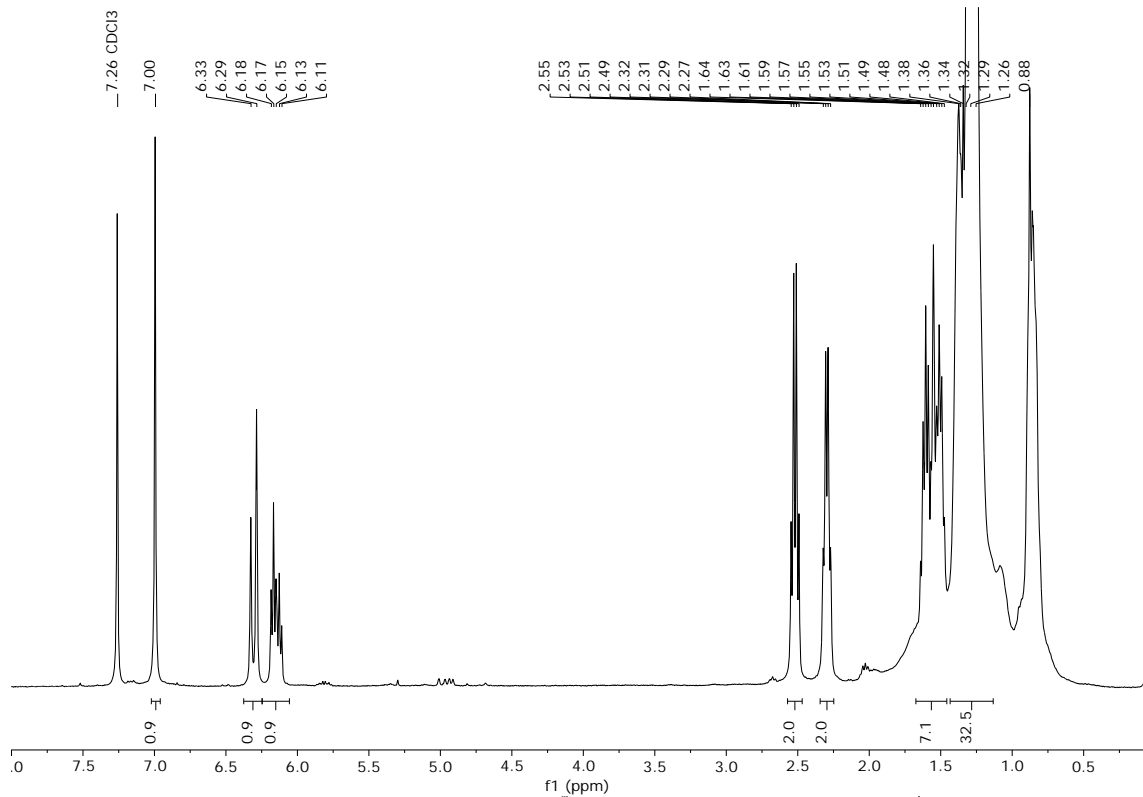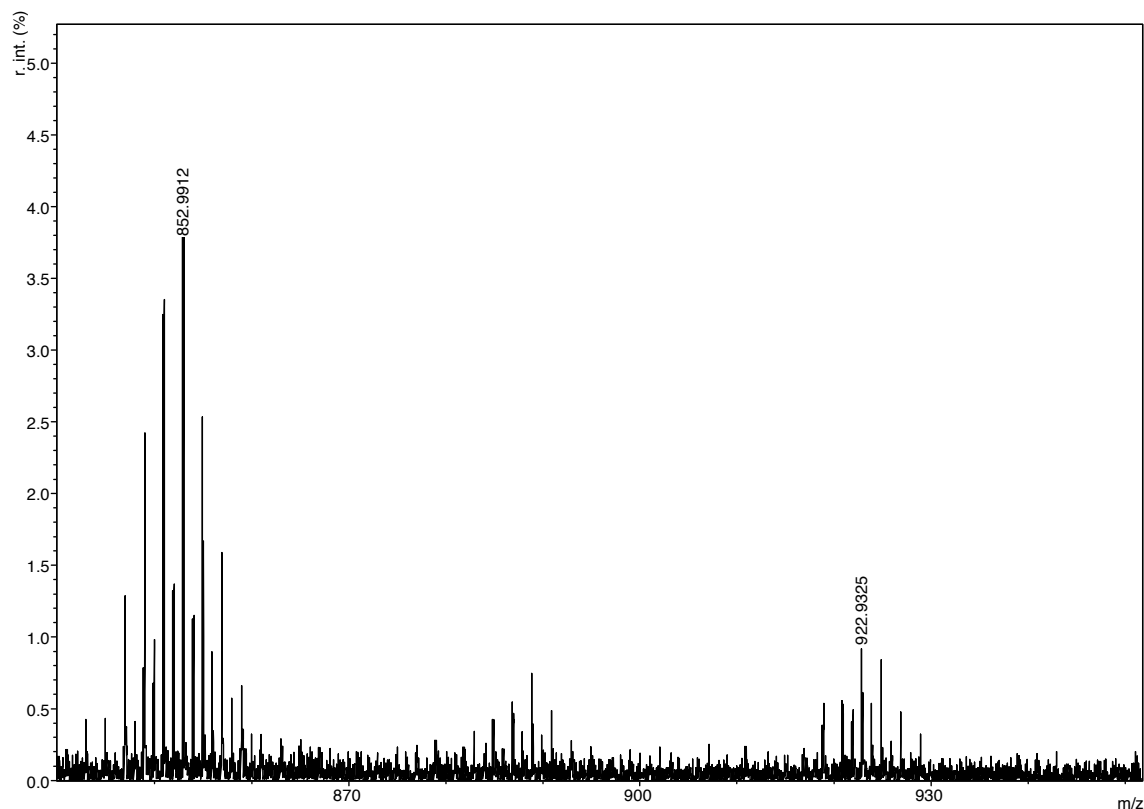
(E)-8-(4-(bis(perchlorophenyl)methyl)-2,3,5,6-tetrachlorophenyl)oct-7-ene-1-thiol radical (R8)
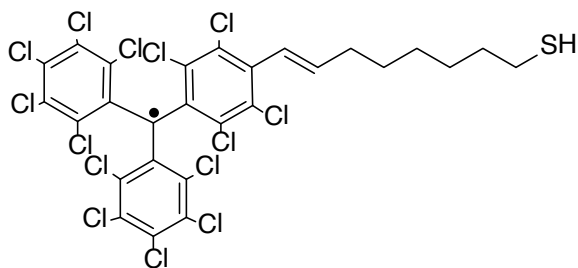
The compound **R8** was obtained as a red powder in quantitative yield, using the general methodology described for the generation of the free thiol groups. **HPLC**, retention time 13.8min: (97% of trans isomer); **UV/Vis** (CH$_2$Cl$_2$): λ*(nm)* (logε) = 387 (4.43), 515 (3.10), 566 (3.14); **CV**: E$^{1/2}$ = -0.18 V (PTM reduction); **FT-IR** (ν/cm^{-1}): 3025.5, 2926.1, 2853.6, 1647.8, 1597.7, 1511.2, 1494.2, 1450.8, 1332.3, 12594.4, 1157.4, 1120.1, 1078.6, 1049.1, 1031.4, 966.1, 860.2, 815.8, 752.9, 732.7, 698.1, 651.7, 605.1; **EPR** (CH$_2$Cl$_2$, r.t.): g = 2.002552; ΔH$_{PP}$ = 1.4 G, a$_{13C\alpha}$ = 29.8 G; a$_{13Co}$ = 13.1 G; a$_{13Cm}$ = 10.1 G; a$_{1H}$ = 1.8 G; EM (m/z) (ESI): calculated for C$_{27}$H$_{15}$Cl$_{14}$S$^{.}$: 866.6; found: 866.7 (M*).
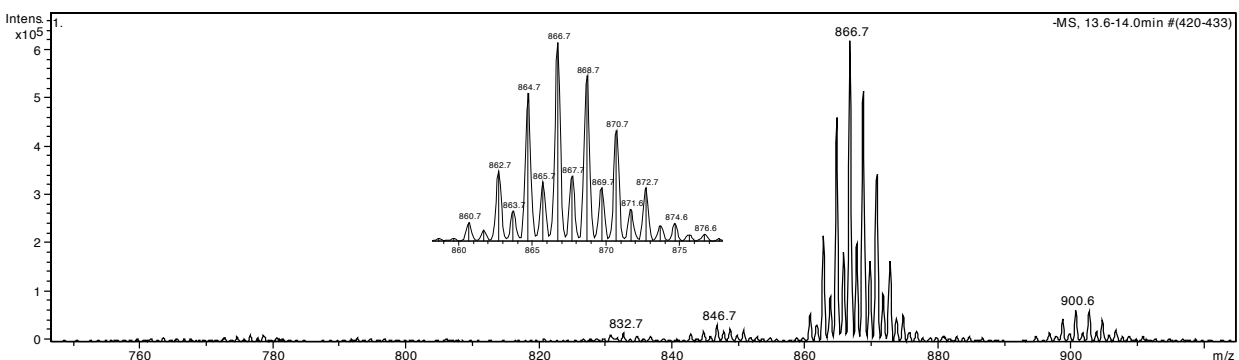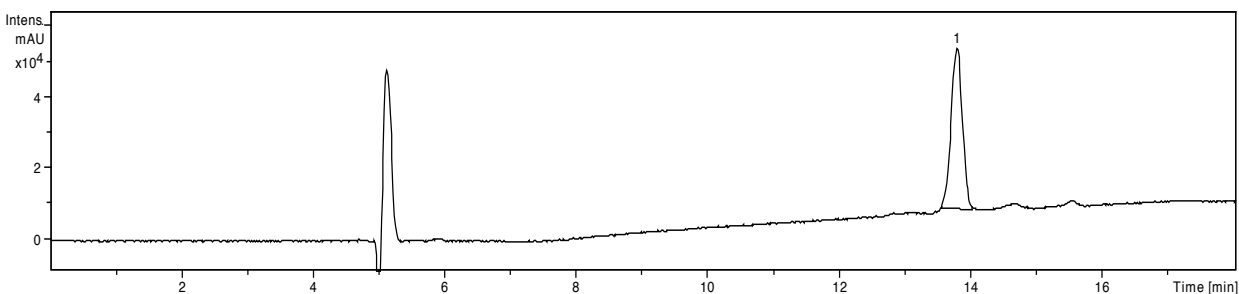
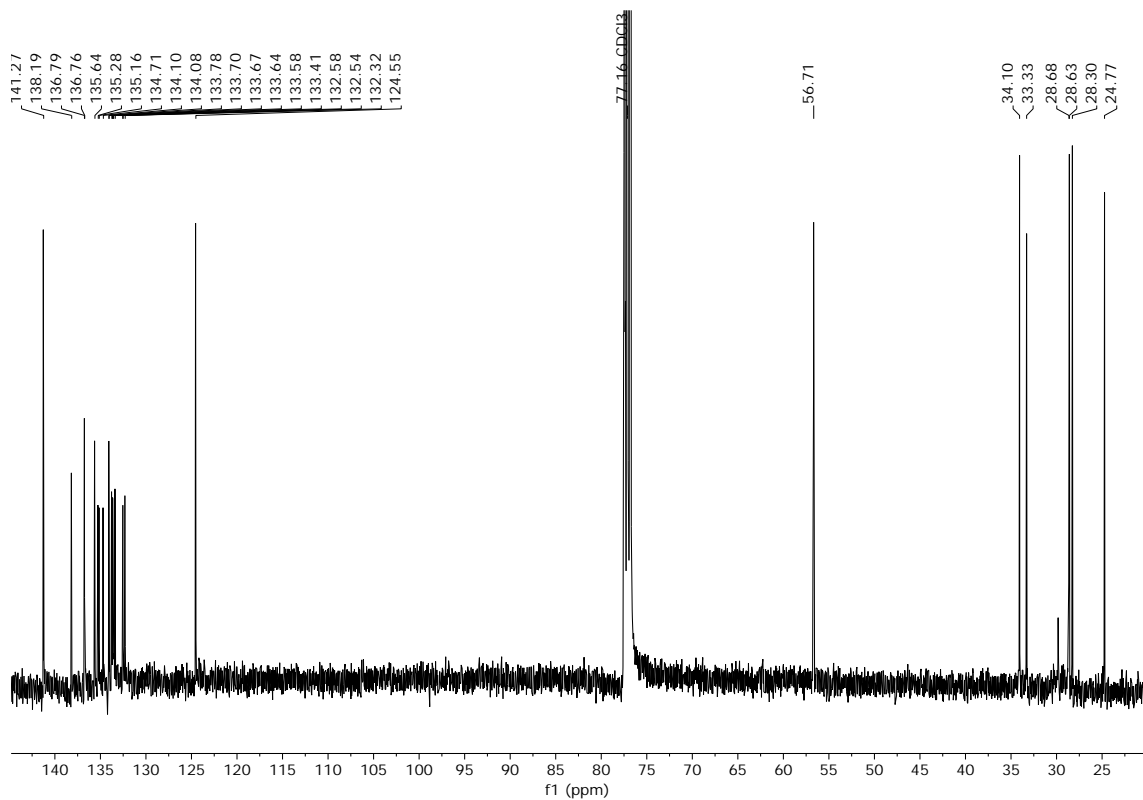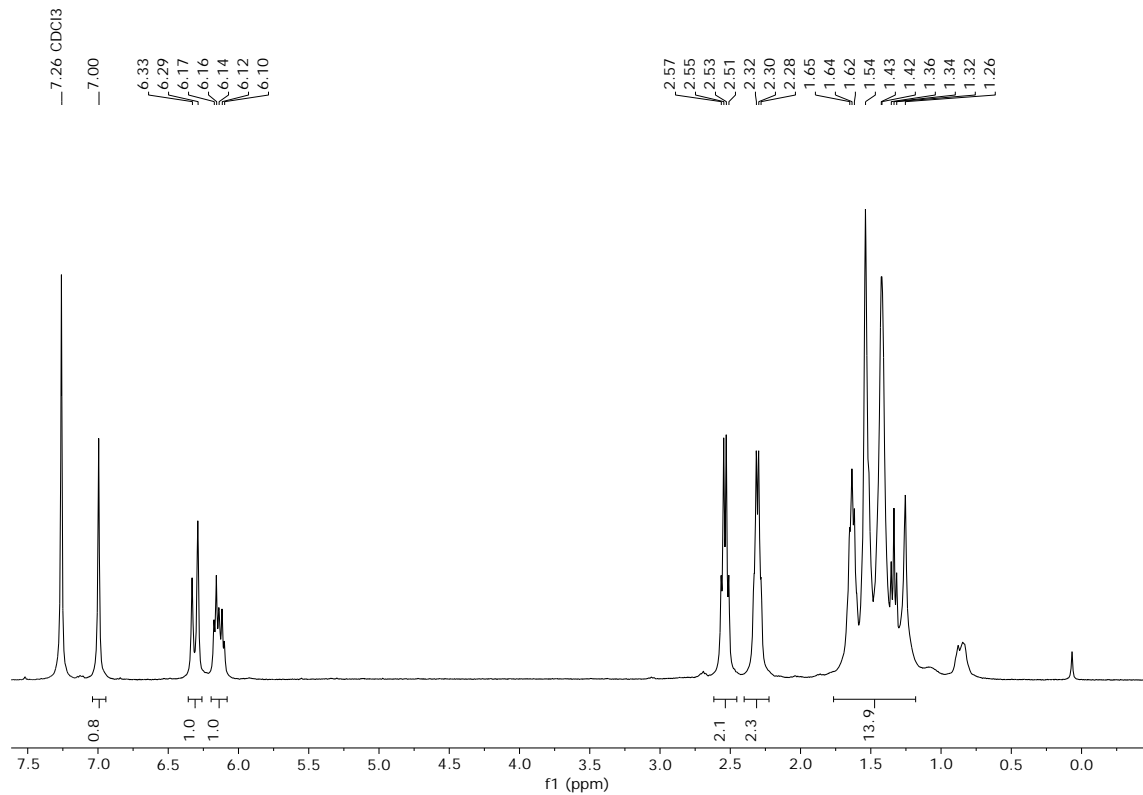## (E)-10-(4-(bis(perchlorophenyl)methyl)-2,3,5,6-tetrachlorophenyl)dec-9-ene-1-thiol radical (R10)
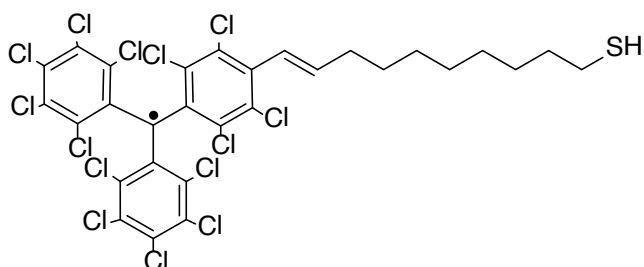
The compound **R10** was obtained as a red powder in quantitative yield, using the general methodology described for the generation of the free thiol groups. **HPLC** retention time: 15.2min (98% of trans isomer); **UV/Vis** (CH$_2$Cl$_2$): $\lambda(nm)$ (logε) = 388 (4.46), 515 (3.08), 566 (3.12); **CV**: E$^{1/2}$ = -0.18 V (PTM reduction); **FT-IR** (ν/cm^{-1}): 3026.8, 2924.7, 2852.7, 1647.37, 1598.3, 1511.0, 1494.9, 1455.2, 1332.3, 1258.9, 1157.4, 1118.9, 1048.3, 965.7, 860.1, 815.4, 750.7, 732.9, 698.9; **EPR** (CH$_2$Cl$_2$, r.t.): g = 2.002431; ΔH$_{PP}$ = 1.4 G, a$_{13C\alpha}$ = 29.5 G; a$_{13Co}$ = 13.0 G; a$_{13Cm}$ = 10.0 G; a$_{1H}$ = 1.8 G; **EM (m/z)** (ESI): calculated for C$_{29}$H$_{19}$Cl$_{14}$S$^{\cdot}$: 894.7; found: 894.7 (M*).
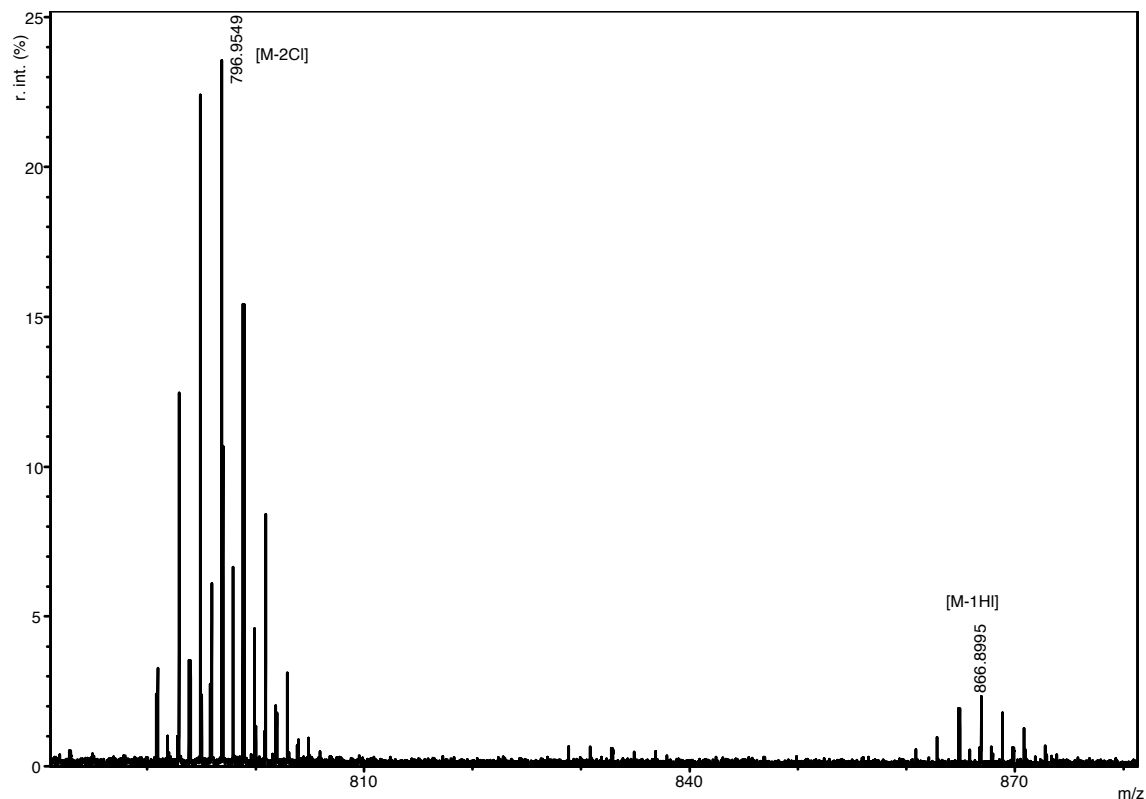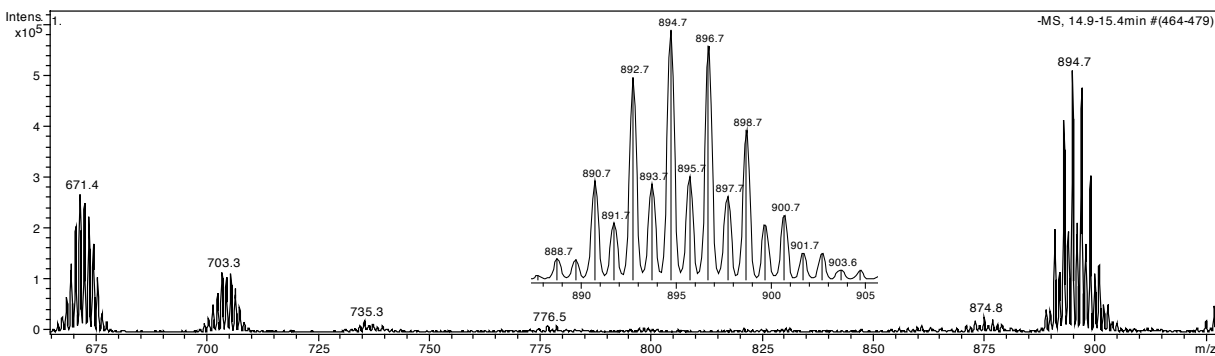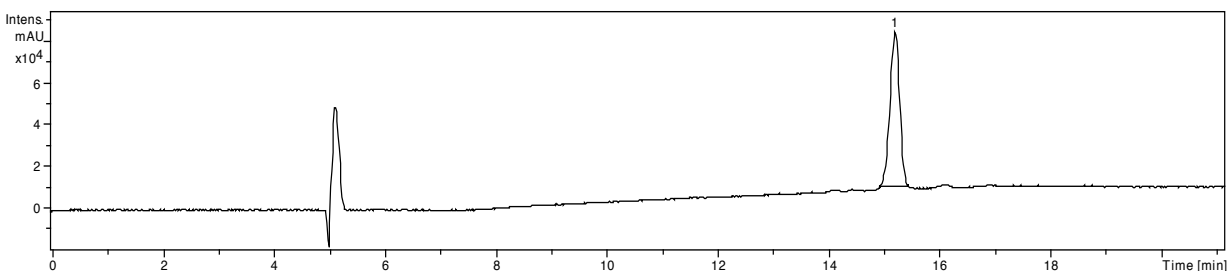
(E)-12-(4-(bis(perchlorophenyl)methyl)-2,3,5,6-tetrachlorophenyl) dodec-11-ene-1-thiol radical (R12)
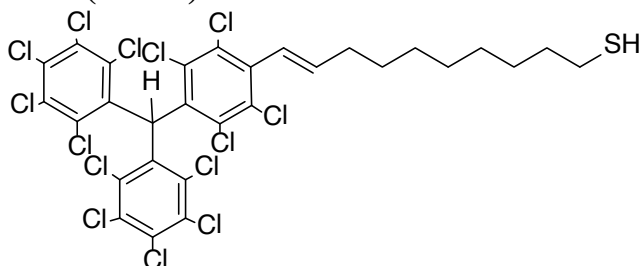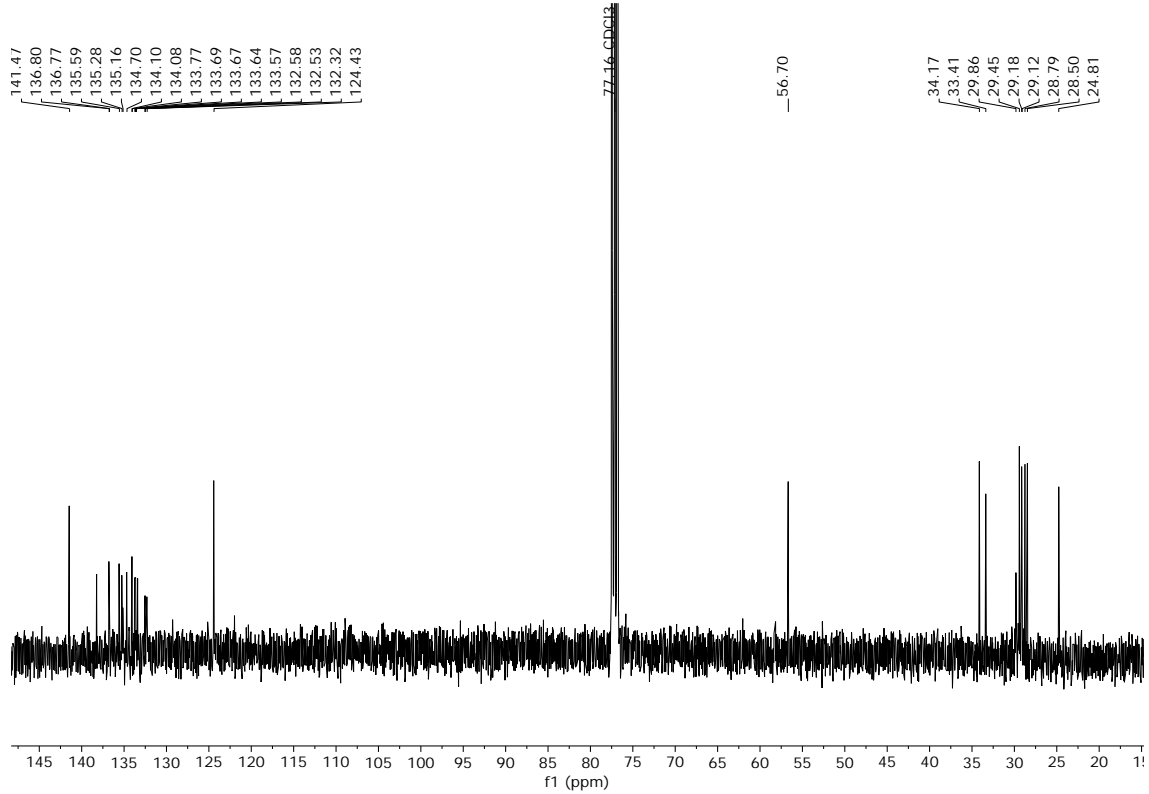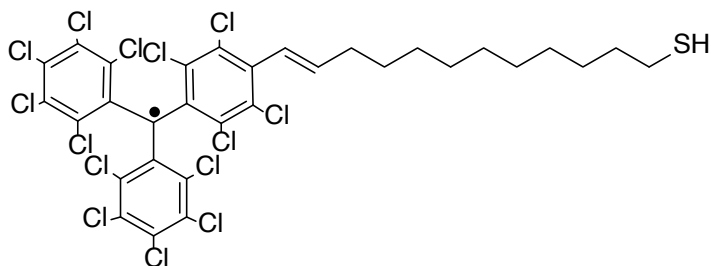

The compound **R12** was obtained as a red powder in quantitative yield, using the general methodology described for the generation of the free thiol groups. **HPLC** retention time: 21.1min (92% of trans isomer), 22.8 (8% of αH derivative); **UV/Vis** (CH$_2$Cl$_2$): λ*(nm)* (logε) = 387 (4.50), 515 (3.13), 566 (3.16); **CV**: E$^{1/2}$ = -0.18 V (PTM reduction); **FT-IR** (v/cm^{-1}):2924.4, 2852.4, 1648.6, 1510.6, 1460.7, 1332.3, 1259.1, 1157.1, 1119.7, 1048.3, 966.4, 860.2, 815.7, 752.1, 733.9, 707.0, 651.4, 606.1; **EPR** (CH$_2$Cl$_2$, r.t.): g = 2.002803; ΔH$_{PP}$ = 1.2 G, a$_{13C\alpha}$ = 29.8 G; a$_{13Co}$ = 13.2 G; a$_{13Cm}$ = 10.3 G; a$_{1H}$ = 1.8 G; **EM (m/z)** (ESI): calculated for C$_{31}$H$_{23}$Cl$_{14}$S$^{\cdot}$: 922.7; found: 922.7 (M*).
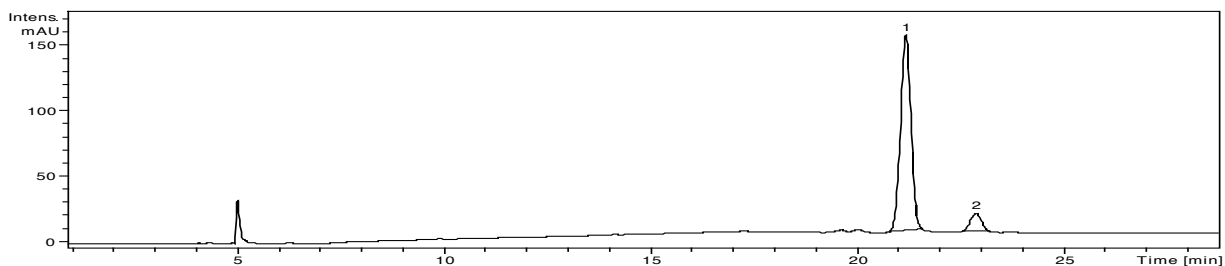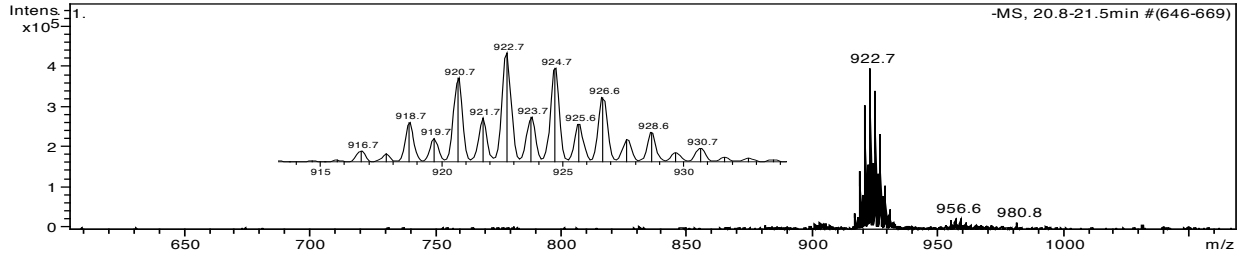
Publication 3

Title	Redox-active radical as an effective nanoelectronic component: stability and electrochemical tunnelling spectroscopy in ionic liquids
Authors	Alexander V. Rudnev, Carlos Franco, Núria Crivillers, Gonca Seber, Andrea Droghetti, Ivan Rungger, Ilya V Pobelov, Jaume Veciana, Marta Mas-Torrent, Concepció Rovira
Publication	*Physical Chemistry Chemical Physics*: In Press

Journal Name

COMMUNICATION

Redox-active radical as an effective nanoelectronic component: stability and electrochemical tunnelling spectroscopy in ionic liquids

Alexander V. Rudnev,[a,b]* Carlos Franco,[c] Núria Crivillers,[c]* Gonca Seber,[c] Andrea Droghetti,[d] Ivan Rungger,[e] Ilya V Pobelov,[a] Jaume Veciana,[c] Marta Mas-Torrent,[c]* Concepció Rovira[c]*

A redox-active persistent polychlorotriphenylmethyl (PTM) radical chemically linked to gold exhibits stable electrochemical activity in ionic liquids. Electrochemical tunnelling spectroscopy in this medium demonstrates that the PTM radical shows a highly effective redox-mediated current enhancement, demonstrating its applicability as an active nanoelectronic component.

Redox-active molecules have been shown to be promising active components for developing nanometer-scale electronic devices[1-3] capable to act as current rectifiers[4] and switches[5-7], mechanical switches[8] or active components in charge-storage devices.[9] In order to progress in this field, the control of the molecular redox state as well as the understanding of its influence on the charge transport properties is crucial. Experiments on electrochemically-gated charge transport across redox-active molecular junctions have demonstrated an effective current modulation.[10, 11] In these systems, the Marcus-type reorganization energy strongly influences the efficiency of the current enhancement due to redox mediated electron tunnelling.

Organic radical polychlorotriphenylmethyl (PTM) is persistent and stable, both chemically and thermally, due to the steric hindrance at the central carbon atom by the ortho-chlorine atoms of the phenyl rings (Fig. 1a).[12] Importantly, PTM radicals display a low reduction potential to the corresponding PTM anions,[13] which make them very interesting molecular redox switches.[14-16] The charge transport through self-assembled monolayers[17, 18] and single-molecule junctions[19] incorporating PTM radicals have been studied before, but the different redox states (radical and anion) were not addressed. Since the structure of both components of the redox pair is almost identical,[20] the inner reorganization energy associated with the structural change upon reduction/oxidation is expected to be low. In addition, bulky redox systems are expected to show low outer-sphere reorganization energy associated with the surrounding solvent, and indeed their current enhancement efficiency in redox-active molecular junctions is typically high.[21-23] In view of this, the bulky organic radical polychlorotriphenylmethyl (PTM) is expected to be a very good redox mediator.

Here, the electrochemical gating of the charge transport through a surface-bound PTM radical have been explored using the electrochemical scanning tunnelling spectroscopy (EC-STS) technique. We demonstrated current enhancement due to the redox-mediated electron tunnelling (RMET) mechanism[3, 22-39] involving PTM radical as the active redox-centre. Our results show that, in comparison with other redox-active moieties, PTM radical is among the most efficient redox mediators in RMET, demonstrating its applicability as an active electronic component in nanoelectronic devices, i.e. electronic devices of nanoscale size.
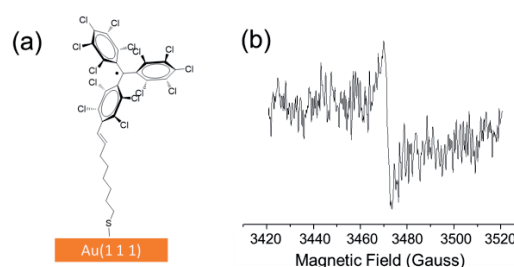
Fig. 1. (a) Schematics of PTM-C8-SH adsorbed on Au(111); (b) EPR spectrum of PTM-C8-SH SAM on Au(111) recorded at 300 K under ambient conditions.

a. *University of Bern, Department of Chemistry and Biochemistry, Freiestrasse 3, 3012 Bern, Switzerland.*
b. *Russian academy of sciences A.N. Frumkin Institute of Physical chemistry and Electrochemistry RAS, Leninskii pr. 31, Moscow, 119991, Russia*
c. *Department of Molecular Nanoscience and Organic Materials, Institut de Ciència de Materials de Barcelona (ICMAB- CSIC) and CIBER-BBN, Campus la Universitat Autonoma Barcelona (UAB), 08193 Bellaterra, Spain.*
d. *Nano-Bio Spectroscopy Group and European Theoretical Spectroscopy Facility (ETSF), Universidad del Pais Vasco CFM, CSIC-UPV/EHU-MPC & DIPC, Avenida Tolosa 72, 20018 San Sebastian, Spain.*
e. *Materials Division, National Physical Laboratory, Teddington, TW11 0LW, United Kingdom.*

Fig. 2. (a, b) CVs of PTM-C8-SH on Au(111): (a) in [Bmim][BF$_4$]; (b) in [Bmim][BF$_4$] + Et$_3$N (15:1 v/v) with molecular sieves at 2nd and 60th minutes from the beginning of potential cycling. Dashed curves are CVs of the redox-inactive αH-PTM-C8-SH on Au(111). Scan rate was 50 mV s^{-1}. The time from the beginning of continuous potential cycling is indicated.

Fig. 3. (a) CV of PTM-C8-SH on Au(111) in [Se$_3$][Tf$_2$N] + Et$_3$N (15:1 v/v) with molecular sieves as recorded in an STM cell and (b) EC-STM image recorded at E_S = -0.33 V, E_T = -0.03 V, $I_{SetPoint}$ = 40 pA.

A PTM radical bearing an alkenyl chain spacer with thiol anchoring group (PTM-C8-SH) was synthesised as described previously[17] and used to prepare self-assembled monolayers (SAM) on Au (111) (Fig. 1a). Figure 1a shows the schematics of PTM-C8-SH assembled on Au(111) (see ESI for characterization and assembly details). The Electron Paramagnetic Resonance spectrum of the SAM on Au(111) recorded at 300 K exhibited a signal with a g value of 2.0032 and a line width of 2.6 Gauss (Fig. 1b), which shows that the PTM radical character is preserved once the molecule is immobilized on the gold surface.

Cyclic voltammograms (CVs) of PTM-C8-SH SAM on Au(111) in acetonitrile solution (ESI, Fig. S1) showed the reduction and oxidation peaks assigned to the reversible reduction of PTM radical moieties (PTM$^{\bullet}$ ⇌ PTM$^-$). The redox response was stable during a repetitive potential cycling and the linear dependence of peak heights on potential scan rate indicates oxidation/reduction of a surface-confined species (ESI, Fig. S1). However, organic solvents are not suitable for electrochemical STM/STS experiments due to their high volatility and/or insufficient stability of coatings employed to electrochemically insulate STM tip. PTM anion can be readily protonated in an aqueous medium. Hence ionic liquids (ILs) appears to be the best media for EC-STM/STS measurements in our case.[10, 21]

First, the CVs of PTM-C8-SH on Au(111) were acquired using different ILs as electrolytes (ESI, Table S1). A decrease of the redox signal with time (Fig. 2a) was observed and after 20 cycles (20 min) the CV response indicated that the radical SAM became redox-inactive (dashed curve). However, the capacitance current did not change and remained much smaller than for bare Au(111) (ESI, Fig. S2a), demonstrating that the desorption of the monolayer does not take place. Figure S2b shows a representative EC-STM image of PTM-C8-SH on Au(111) in [Emim][EtSO$_4$] recorded after the disappearance of the redox peaks. As illustrated by a cross-section (Fig. S2c), the STM image shows a rather uniform corrugation height of ~0.8 nm, which confirms unambiguously the presence of the adlayer. The above mentioned results are in accordance with the well known acidic character of the imidazolium cation[40] (see ESI for more detailed explanation) which could promote the protonation of the electrochemically generated anion forming the non-electroactive αH-PTM-C8-SH
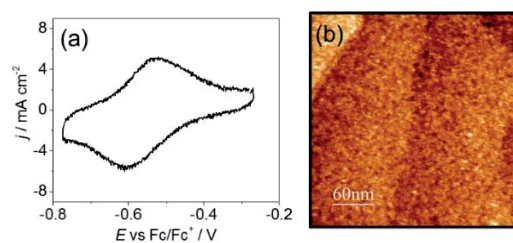
SAM on Au(111) (ESI, Scheme S1). In order to corroborate it, a solution of the non-functionalized PTM anion (PTM$^-$ K$^+$[18-Crown-6])[41] in [Emim][EtSO$_4$], was monitored by UV-vis spectroscopy. The characteristic band of the PTM$^-$ at 500nm was observed to decrease gradually with time (ESI, Fig. S3a), and completely disappeared after 24h confirming the protonation of the PTM anion in the IL, even after an exhaustive drying. The same CV experiment was performed with the PTM SAM using [SEt$_3$][Tf$_2$N] in which, although a higher stability of the layer was observed, the redox peaks also diminished with time. We believe that small traces of water in the ionic medium could also induce the protonation of the PTM anion. According to previous reports, drying ILs by using molecular sieves (3 Å) may significantly decrease the water content.[42, 43] We used the hot molecular sieves activated at 200 °C to dry ILs before an experiment and also added them directly into the electrochemical cell. Such a treatment considerably improved the stability of the SAM (ESI, Fig. S4 and S5), but did not solve the stability problem completely. For the purpose of comparison, the electrochemically inactive αH-PTM-C8-SH (ESI, Scheme S1) was isolated during the synthesis of the radical derivative and used to perform reference voltammetric and STS measurements.

In order to overcome this problem, a soft base like triethylamine (Et$_3$N) was added to the IL (1:15 v/v). According to the voltammetric and UV-Vis measurements, its presence greatly improved the stability of PTM anion in the IL media. The CVs of PTM-C8-SH on Au(111) did not change significantly after 1 h of potential cycling (Fig. 2b) and the absorption band of PTM$^-$ remained unaltered after 24 hours (ESI, Fig. S3b). We also notice that the redox peaks of PTM-C8-SH on Au(111) in ILs have a larger peak-to-peak separation as compared to that in acetonitrile (Fig. S1). We attribute such a behaviour to the slow ion pairing of PTM anion with the cations of ILs.[44] Moreover, the peak-to-peak separation differs for different ionic liquids, also suggesting that the shape of voltammograms is affected by the IL-cation and PTM anion interactions (cf Figs. 2, S4, S5).

Fig. 3 shows the CV of the PTM-C8-SH SAM on Au(111) in [SEt$_3$][Tf$_2$N] + Et$_3$N (15:1 v/v) recorded in the STM cell (Figure 3a) and a representative EC-STM image (Fig. 3b). The redox response was stable and nearly identical to that obtained in the standard glass electrochemical cell. As expected, a highly ordered monolayer was not observed due to the bulkiness of the PTM moiety, which hinders the formation of a well-

arranged molecular layer induced by the lateral interactions between alkyl chains. However, the STM image demonstrates the formation of a compact adlayer (see also Fig. S6 in ESI). The coverage estimated from the integration of CV peaks (with background current correction) was 1.2×10^{-10} mol·cm^{-2} which is $\approx 70\%$ of the theoretical maximum coverage calculated from the area of a single PTM-C8-S-Au (see ESI for details).

After the radical monolayer was assembled on Au(111) and confirmed to be stable, the electrochemical STS measurements in constant bias mode were performed.[22] In this mode, the
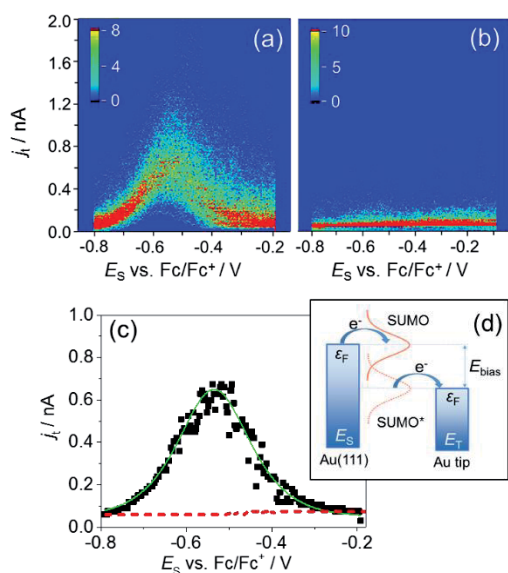
Fig. 4. 2D occurrence histograms constructed from (a) 200 and (b) 100 constant bias current-voltage traces for SAM on Au(111): (a) PTM-C8-SH radical and (b) αH-PTM-C8-SH. Set-point current $I_{SetPoint}$ = 50 pA, E_{bias} = 0.1 V (constant), starting E_S = -0.81 V and E_T = -0.71 V. No data selection was applied. (c) Master current-voltage curves obtained from the data in the panels (a,b): for radical (squares) and αH-PTM (dashed line) forms. Solid green line represents fitting using KU model (equations and fitting parameters are given in SI). (d) Schematic energy level diagram of a two-step ET process mediated by a redox-active radical molecule.

potentials of both working electrodes, i.e. substrate E_S and tip E_T were swept simultaneously while keeping the bias voltage E_{bias} = E_T - E_S constant. The STS curves (I_t vs. E_S) were recorded at a fixed geometry of the tunnelling junction with the feedback being temporarily switched off during the acquisition of each STS curve. Results obtained for the PTM-C8-SH on Au(111) are shown in Fig. 4a, in which a significant enhancement of the tunnelling current flowing between the substrate and the tip is observed. As expected, the control STS experiment with the redox-inactive αH-PTM-C8-SH monolayer showed constant current without tunnelling enhancement (Fig. 4b).

Fig. 4c shows the master curve obtained from the histogram where each data point corresponds to the value of tunnelling current measured with the highest probability at a given potential value. The curve has a bell shape with a maximum located close to the equilibrium potential of the PTM$^{\bullet}$/PTM^{-} redox pair (cf. the CV in Figure 3a). Such behaviour resembles a transistor like functionality. With the initial value $I_{SetPoint}$ of 0.05 nA at E_S = -0.80 V, the tunnelling current increases to ~0.65 nA

at the peak position, which corresponds to an on/off ratio of ~13. The bell-shaped STS curves are typical for redox-mediated electron tunnelling (RMET) processes, which have been reported for a variety of redox-active molecules placed between the conductive substrate and the STM tip,[21-30] as well as for single molecule junctions.[10, 45] However, it is the first time that a stable neutral free-radical is shown to mediate the tunnelling current enhancement under electrochemical conditions.

Similar to previous studies, the RMET phenomenon is rationalized by employing the Kuznetsov-Ulstrup (KU) model,[26] i.e., a two-step electron transfer with a partial vibrational relaxation. When the sample and the tip potentials are located before or after the redox peak, the Fermi levels of two electrodes are lower and higher than the Single-Unoccupied Molecular Orbital (SUMO) of the PTM radical (Fig. 4d). In the first electron transfer step, electron tunnels from the electrode with higher Fermi level to SUMO. Afterwards, the energy of the now occupied SUMO* decreases due to the vibrational relaxation. However, the second electron transfer occurs before a complete vibrational relaxation and before the energy of the molecular level passes the Fermi level of the second electrode. These electron-transfer steps are repeated causing a multitude of electrons being transferred between the tip and the sample through this pathway, which is additional to the direct (off-resonant) tip-substrate current. Thus, the tunnelling current through the junction can be modulated by tuning the potential of both electrodes around the equilibrium potential of the PTM$^{\bullet}$/PTM^{-} redox pair.

By fitting the experimental data (Fig. 4c) with the KU model the following model parameter values were obtained: total (inner- + outer-sphere) reorganization energy λ_T=0.39 eV, fractions of overpotential and of bias voltage at the redox site ξ=0.57 and γ=0.57, respectively (see ESI). These values allow us to evaluate the efficiency of the PTM radical as mediator compared to those reported in literature. It should be kept in mind that the direct comparison of the fitted KU parameters between different redox systems is not straightforward since not all mediators are measured at the same fixed junction geometry in the STS experiments. Practically, this is hardly possible in an STM configuration and it would require, for example, systematic measurements of a series of nanodevices (with different mediators) with fixed electrode separation and molecular assembly (see discussion in Ref.[3]). Instead, STS experiments are typically carried out at fixed starting E_{bias} and $I_{SetPoint}$ (or tunnelling conductance $I_{SetPoint}/E_{bias}$) which, via STM feedback mechanism, is expected to result in a reproducible junction geometry for the same "gap composition". Indeed, the established electrode separation will depend on the tunnelling efficiency through the gap in the absence of RMET (when the potentials of both electrodes are far from the equilibrium potential). Thus, diverse results attributed to a different gap geometry were obtained even for the same mediator in different starting redox states[22].

Judging solely on the basis of the on/off ratio, the most effective mediators studied appears to be Os bisterpyridine complex ($I_{max}/I_{SetPoint}$≈50).[21] This result was obtained in ionic

liquid using E_{bias} = 0.7 V and $I_{SetPoint}$ = 0.05 nA, which is also the lowest tunnelling conductance employed in EC-STS experiments. We cannot safely name this system *the* most efficient mediator, as the on/off ratio tends to increase at lower tunnelling conductances.[28] Formally, $I_{max}/I_{SetPoint} \approx 50$ was also obtained for viologens in one starting configuration (E_{bias} = 0.05 V, $I_{SetPoint}$ = 0.1 nA),[22] but the off-resonance current was asymmetric indicating contribution of non-RMET enhancement. Among the results obtained at spontaneously established standard settings for STS experiments, E_{bias} = 0.1 V and $I_{SetPoint}$ = 0.1 nA, the highest on/off ratios were obtained for perylene bisimide[23] ($I_{max}/I_{SetPoint} \approx 35$) and Fc(CO)(CH$_2$)$_7$SH[27] ($I_{max}/I_{SetPoint} \approx 12$). To the best of our knowledge, a ratio $I_{max}/I_{SetPoint}$ > 10 was not obtained for other mediators in either symmetric (covalently bounded to both contacts)[10, 45] or asymmetric (with a tunnelling gap)[3, 27, 28, 37] metal-molecule-metal junctions.

From the point of view of the KU model, an effective RMET mediator is characterized by the low total reorganization energy (λ), which depends on tunnelling resistance and therefore, electrode separation.[28] For example, in systems where λ was estimated from the fitting of STS results, the lowest values obtained were approximately 0.2 eV for mediators such as perylene bisimide[19] and λ≈0.35-0.4 eV for mediators such as the herein reported PTM and the Fc(CO)(CH$_2$)$_7$SH.[27] Interestingly, perylene bisimide and Os bisterpyridine complex are bulky structures, which is expected to decrease outer-sphere reorganization energy associated with the surrounding solvent, leading to higher $I_{max}/I_{SetPoint}$.

To get further information about the system presented in this work, the PTM inner-sphere reorganization energy (λ_i) has been calculated with Density Functional Theory by finite energy differences[46] giving a λ_i of 0.08eV (see ESI for further details). This value is comparable to λ_i calculated for perylene bisimide (0.10 eV, see ESI), but significantly higher than λ_i for ferrocene (~0.005 eV as estimated from spectroscopic data[47]). Nevertheless, with the on/off ratio 13 and estimated λ=0.39 eV, PTM radical is one of the best redox mediators in RMET mechanism reported. As expected, the outer-sphere reorganization energy (estimated from the difference between the calculated λ_i and the experimental λ_T) has a higher influence on the results.

In summary, in this work, we have prepared an organic radical based SAM on Au(111) exhibiting reversible and stable redox signal in ionic liquids. Electrochemical scanning tunneling spectroscopy experiments demonstrated current enhancement due to the redox-mediated electron tunnelling mechanism. In comparison with other redox mediators studied to date, PTM radical is among the most efficient ones, which indicates its potential applicability as an active electronic component in nanoelectronic devices.

Notes and references

1. L. Sun, Y. A. Diaz-Fernandez, T. A. Gschneidtner, F. Westerlund, S. Lara-Avila and K. Moth-Poulsen, *Chem. Soc. Rev.*, 2014, **43**, 7378.
2. S. Guo, J. M. Artés and I. Díez-Pérez, *Electrochim. Acta*, 2013, **110**, 741.
3. A. Alessandrini and P. Facci, *Eur. Polym. J.*, 2016.
4. C. A. Nijhuis, W. F. Reus and G. M. Whitesides, *J. Am. Chem. Soc.*, 2010, **132**, 18386.
5. M. Baghernejad, X. Zhao, K. Baruël Ørnsø, M. Füeg, P. Moreno-García, A. V. Rudnev, V. Kaliginedi, S. Vesztergom, C. Huang, W. Hong, P. Broekmann, T. Wandlowski, K. S. Thygesen and M. R. Bryce, *J. Am. Chem. Soc.*, 2014, **136**, 17922.
6. N. Darwish, I. Díez-Pérez, P. Da Silva, N. Tao, J. J. Gooding and M. N. Paddon-Row, *Angew. Chem. Int. Ed.*, 2012, **51**, 3203.
7. X. Xiao, L. A. Nagahara, A. M. Rawlett and N. Tao, *J. Am. Chem. Soc.*, 2005, **127**, 9235.
8. V. Kolivoska, M. Mohos, I. V. Pobelov, S. Rohrbach, K. Yoshida, W. J. Hong, Y. C. Fu, P. Moreno-Garcia, G. Meszaros, P. Broekmann, M. Hromadova, R. Sokolova, M. Valasek and T. Wandlowski, *Chem. Commun.*, 2014, **50**, 11757.
9. V. Kaliginedi, H. Ozawa, A. Kuzume, S. Maharajan, I. V. Pobelov, N. H. Kwon, M. Mohos, P. Broekmann, K. M. Fromm, M.-a. Haga and T. Wandlowski, *Nanoscale*, 2015, **7**, 17685.
10. H. M. Osorio, S. Catarelli, P. Cea, J. B. G. Gluyas, F. Hartl, S. J. Higgins, E. Leary, P. J. Low, S. Martín, R. J. Nichols, J. Tory, J. Ulstrup, A. Vezzoli, D. C. Milan and Q. Zeng, *J. Am. Chem. Soc.*, 2015, **137**, 14319.
11. C. Huang, A. V. Rudnev, W. Hong and T. Wandlowski, *Chem. Soc. Rev.*, 2015, **44**, 889.
12. M. Mas-Torrent, N. Crivillers, C. Rovira and J. Veciana, *Chem. Rev.*, 2012, **112**, 2506.
13. N. Crivillers, M. Mas-Torrent, J. Vidal-Gancedo, J. Veciana and C. Rovira, *J. Am. Chem. Soc.*, 2008, **130**, 5499.
14. C. Simão, M. Mas-Torrent, N. Crivillers, V. Lloveras, J. M. Artés, P. Gorostiza, J. Veciana and C. Rovira, *Nat Chem*, 2011, **3**, 359.
15. C. Simão, M. Mas-Torrent, J. Veciana and C. Rovira, *Nano Lett.*, 2011, **11**, 4382.
16. N. Crivillers, M. Paradinas, M. Mas-Torrent, S. T. Bromley, C. Rovira, C. Ocal and J. Veciana, *Chem. Commun.*, 2011, **47**, 4664.
17. L. Yuan, C. Franco, N. Crivillers, M. Mas-Torrent, L. Cao, C. S. S. Sangeeth, C. Rovira, J. Veciana and C. A. Nijhuis, *Nat. Comm.*, 2016, *accepted*.
18. N. Crivillers, C. Munuera, M. Mas-Torrent, C. Simão, S. T. Bromley, C. Ocal, C. Rovira and J. Veciana, *Adv. Mater.*, 2009, **21**, 1177.
19. R. Frisenda, R. Gaudenzi, C. Franco, M. Mas-Torrent, C. Rovira, J. Veciana, I. Alcon, S. T. Bromley, E. Burzurí and H. S. J. van der Zant, *Nano Lett.*, 2015, **15**, 3109.
20. J. Guasch, X. Fontrodona, I. Ratera, C. Rovira and J. Veciana, *Acta Crystallogr. Sect. C*, 2013, **69**, 255.
21. T. Albrecht, K. Moth-Poulsen, J. B. Christensen, J. Hjelm, T. Bjørnholm and J. Ulstrup, *J. Am. Chem. Soc.*, 2006, **128**, 6574.
22. I. V. Pobelov, Z. H. Li and T. Wandlowski, *J. Am. Chem. Soc.*, 2008, **130**, 16045.

23. C. Li, A. Mishchenko, Z. Li, I. Pobelov, T. Wandlowski, X. Q. Li, F. Würthner, A. Bagrets and F. Evers, *J. Phys.: Condens. Matter*, 2008, **20**, 374122.
24. I. Díez-Pérez, Z. Li, S. Guo, C. Madden, H. Huang, Y. Che, X. Yang, L. Zang and N. Tao, *ACS Nano*, 2012, **6**, 7044.
25. A. Mishchenko, M. Abdualla, A. Rudnev, Y. Fu, A. R. Pike and T. Wandlowski, *Chem. Commun.*, 2011, **47**, 9807.
26. J. Zhang, A. M. Kuznetsov, I. G. Medvedev, Q. Chi, T. Albrecht, P. S. Jensen and J. Ulstrup, *Chem. Rev.*, 2008, **108**, 2737.
27. A. V. Rudnev, I. V. Pobelov and T. Wandlowski, *J. Electroanal. Chem.*, 2011, **660**, 302.
28. Z. Li, Y. Liu, S. F. L. Mertens, I. V. Pobelov and T. Wandlowski, *J. Am. Chem. Soc.*, 2010, **132**, 8187.
29. P. Salvatore, A. Glargaard Hansen, K. Moth-Poulsen, T. Bjornholm, R. John Nichols and J. Ulstrup, *Phys. Chem. Chem. Phys.*, 2011, **13**, 14394.
30. J. M. Artés, I. Díez-Pérez and P. Gorostiza, *Nano Lett.*, 2012, **12**, 2679.
31. P. Petrangolini, A. Alessandrini and P. Facci, *J. Phys. Chem. C*, 2013, **117**, 17451.
32. A. Alessandrini, S. Corni and P. Facci, *Phys. Chem. Chem. Phys.*, 2006, **8**, 4383.
33. N. J. Tao, *Phys. Rev. Lett.*, 1996, **76**, 4066.
34. Li, J. Hihath, F. Chen, T. Masuda, L. Zang and Tao, *J. Am. Chem. Soc.*, 2007, **129**, 11535.
35. T. Albrecht, K. Moth-Poulsen, J. B. Christensen, A. Guckian, T. Bjornholm, J. G. Vos and J. Ulstrup, *Faraday Discuss.*, 2006, **131**, 265.
36. T. Albrecht, A. Guckian, J. Ulstrup and J. G. Vos, *Nanotechnology, IEEE Transactions on*, 2005, **4**, 430.
37. A. Alessandrini, M. Salerno, S. Frabboni and P. Facci, *Appl. Phys. Lett.*, 2005, **86**, 133902.
38. R. J. Nichols and S. J. Higgins, in *Electrocatalysis*, Wiley-VCH Verlag GmbH & Co. KGaA, 2013, pp. 99.
39. J. M. Artés, M. López-Martínez, A. Giraudet, I. Díez-Pérez, F. Sanz and P. Gorostiza, *J. Am. Chem. Soc.*, 2012, **134**, 20218.
40. D. R. MacFarlane, J. M. Pringle, K. M. Johansson, S. A. Forsyth and M. Forsyth, *Chem. Commun.*, 2006, 1905.
41. J. Veciana, J. Riera, J. Castañer and N. Ferrer, *J. Organomet. Chem.*, 1985, **297**, 131.
42. M. Gnahm and D. M. Kolb, *J. Electroanal. Chem.*, 2011, **651**, 250.
43. M. F. Suárez-Herrera, M. Costa-Figueiredo and J. M. Feliu, *Langmuir*, 2012, **28**, 5286.
44. S. F. L. Mertens, G. Meszaros and T. Wandlowski, *Phys. Chem. Chem. Phys.*, 2010, **12**, 5417.
45. N. J. Kay, S. J. Higgins, J. O. Jeppesen, E. Leary, J. Lycoops, J. Ulstrup and R. J. Nichols, *J. Am. Chem. Soc.*, 2012, **134**, 16817.
46. S. F. Nelsen, S. C. Blackstock and Y. Kim, *J. Am. Chem. Soc.*, 1987, **109**, 677.
47. A. S. Baranski, K. Winkler and W. R. Fawcett, *J. Electroan. Chem. Interfacial Electrochem.*, 1991, **313**, 367.

Supporting Information

Redox-active radical as an effective nanoelectronic component: stability and electrochemical tunnelling spectroscopy in ionic liquids

Alexander V. Rudnev,[a,b] Carlos Franco,[c] Núria Crivillers,[c] Gonca Seber,[c] Andrea Droghetti,[d] Ivan Rungger,[e] Ilya V Pobelov,[a] Jaume Veciana,[c] Marta Mas-Torrent,[c] Concepció Rovira[c]

[a] *University of Bern, Department of Chemistry and Biochemistry, Freiestrasse 3, 3012 Bern, Switzerland*
[b] *Russian academy of sciences A.N. Frumkin Institute of Physical chemistry and Electrochemistry RAS, Leninskii pr. 31, Moscow, 119991, Russia*
[c] *Department of Molecular Nanoscience and Organic Materials, Institut de Ciència de Materials de Barcelona (ICMAB-CSIC) and CIBER-BBN, Campus la Universitat Autonoma Barcelona (UAB), 08193 Bellaterra, Spain*
[d] *Nano-Bio Spectroscopy Group and European Theoretical Spectroscopy Facility (ETSF), Universidad del Pais Vasco CFM, CSIC-UPV/EHU-MPC & DIPC, Avenida Tolosa 72, 20018 San Sebastian, Spain.*
[e] *Materials Division, National Physical Laboratory, Teddington, TW11 0LW, United Kingdom*

Experimental details

Surface modification of the flame-annealed Au(1 1 1) electrodes was carried out according to the following protocol: PTM-C8-SH (Figure 1 in the main text) and αH-PTM-C8-SH (Scheme S1) SAMs were deposited on Au(1 1 1) by immersing a freshly prepared electrode in 0.3 mM solutions of the PTM derivatives in toluene (HPLC) at the temperature of 40 °C for 24 h. The samples were removed from the solution after incubation, rinsed with dichloromethane (DCM, HPLC), dried in a stream of argon, and subsequently transferred into the electrochemical or STM cell.
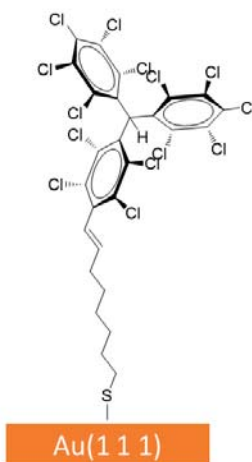
Scheme S1. αH-PTM-C8-SH SAM on Au(1 1 1)

As electrolytes we employed different ionic liquids: names, abbreviations, source and quality are given in Table S1. In some experiments we used trimethylamine (Et$_3$N, Sigma Aldrich, ≥99.5%) as an additive. Furthermore, we used an electrolyte solution prepared from tetrabutylammonium

hexafluorophosphate n-Bu$_4$NPF$_6$ in acetonitrile (Fisher Chemical, HPLC). The glassware and plastic parts were cleaned in piranha solution or boiling in 25% nitric acid followed by cooking and extended rinsing with Milli-Q water (18.2 MΩ, 2 ppb TOC) and overnight drying in an oven at 105°C.

A Clavillier-type Au(1 1 1) bead single crystal electrode with an oriented and polished surface (area 0.030 cm^2) served as a working electrode in the electrochemical studies. For in situ STM/STS experiments we used a disk Au(1 1 1) electrode of 10 mm diameter. Contact of the working electrode with the electrolyte was established under strict potential control. A platinum wires served as counter and quasi-reference electrodes in both electrochemical and STM studies.

The macroscopic electrochemical measurements in ionic liquids were performed in a dedicated all-glass cell employing an Autolab PGSTAT30 potentiostat. The STM/STS measurements were carried out with a PicoSPM system (Molecular Imaging) in a sealed, argon-filled chamber. The controlled environment ensures the long-term stability of the PTM radicals. The STM liquid cell was mounted on top of the Au(1 1 1) electrode via an O-ring (Kalrez). The STM tips were electrochemically etched gold wires (0.25 mm diameter) coated with polyethylene.

In situ STS measurements were carried out employing "electrolyte gating".[1] The potentials of both working electrodes (E_S and E_T for modified Au(1 1 1) substrate and coated gold tip, respectively) were swept simultaneously (with a constant bias voltage $E_{bias} = E_T - E_S$). Constant bias mode STS curves (I_t vs. E_S) were recorded at a fixed geometry of the tunneling junction with the feedback being temporarily switched off. First, the STM tip was brought into tunneling gap over PTM-C8-SH SAM with a preset current $I_{SetPoint}$ and bias E_{bias}, then the feedback was switched off and an STS curve is recorded. Afterwards, the feedback was switched on for a second to stabilize the junction, and further this cycle was repeated again. The data were collected automatically with a lab-written Visual Basic Script, which controlled the STM setup. The tip was repositioned after each 25 sweeps to a new area to ensure a better statistics. Usually around 200 spectra were recorded for each set of conditions. The data are presented as 2D histograms, which were constructed based on a LabVIEW program written by Dr. Artem Mishchenko. The following algorithm was applied: individual IV traces were first binned in 2D space (usually 200×200 bins) and the resulting individual 2D histograms were summed up. The results, plotted as intensity graphs, represent statistically significant in situ STS data. All electrochemical and *in situ* STM/STS experiments were performed under argon (5N) atmosphere at room temperature (295 K).

EPR spectra were recorded in a Bruker ELEXYS E500 X-band spectrometer. UV-Vis spectra were recorded on a Varian Carey 5000 in double-beam mode. The manipulation of the radicals in solution was performed under red light.

Characterization of PTM-C8-SH adlayers on Au(1 1 1) electrodes.

The CVs of the freshly prepared PTM-C8-SH SAM are shown in Figure S1a. CV results in acetonitrile and 0.1 M n-Bu$_4$NPF$_6$ as electrolyte (using silver wire as a reference electrode) showed one reversible pair of redox peaks with a formal potential $E_{1/2}$ of -0.08 V (vs. Ag) and a peak-to-peak separation ΔE = 27 mV at a scan rate of 1 Vs^{-1}. Start potential was 0.2 V, at which the radical form of PTM is stable. Cathodic (negative currents) and anodic (positive currents) peaks are assigned to the reduction of PTM radical moieties to anions and the reverse oxidation of the anions to the radicals, respectively. A small peak-to-peak separation and the linear dependence of peak heights on scan rate (top inset) indicate that the redox process is surface-confined. The redox signal was rather stable as tested by multiple potential cycling, during which no noticeable changes in CVs were detected (bottom inset). Electrochemical experiments in organic solvents were performed with a potensiostat/galvanostat Autolab/PGSTAT204 from Metrohm Autolab B.V. in a standard three-electrode cell.
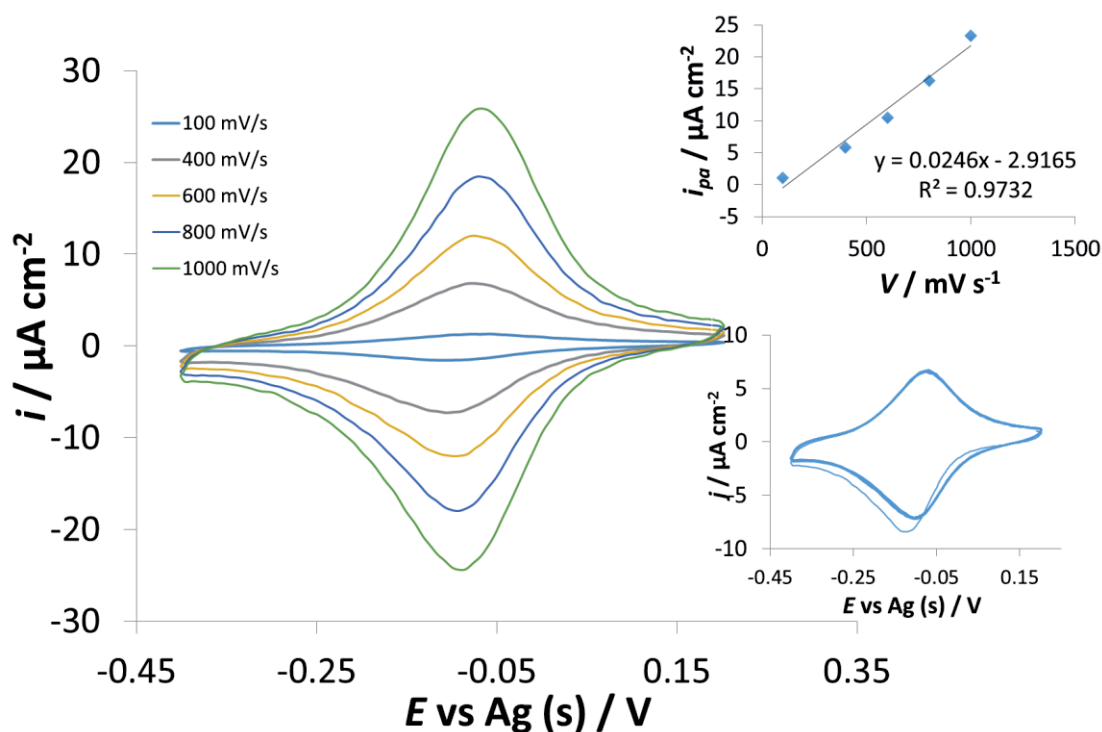
Figure S1. CVs of the radical PTM-C8-SH SAM in 0.1 M solution of n-Bu$_4$NPF$_6$ in acetonitrile, recorded at different scan rates. Top inset: Plot of the peak current vs scan rate. Bottom inset: Potential cycling (20cycles) at 0.4 Vs^{-1}.

Table S1. The list of different ionic liquids, in which PTM-C8-SH adlayer was tested. The stability time was estimated as a time of continuous potential cycling until the redox charge under peaks decreased to 10% of the initial value.

Abbreviation	Source and quality	Name	Structure	Stability
[Emim][Tf$_2$N]	Merck, for synthesis, ≥98.0%	1-ethyl-3-methylimidazolium bis(trifluoromethylsulfonyl)imide		< 10 min
[Emim][EtSO$_4$]	Alfa Aesar, 99%	1-ethyl-3-methylimidazolium ethyl sulfate		~10 min
[Bmim][BF$_4$]	Sigma Aldrich, HPLC, ≥97.0%	1-Butyl-3-methylimidazolium tetrafluoroborate		< 10 min
[Bmim][DCA]	Merck, for synthesis, ≥98.0%	1-Butyl-3-methylimidazolium dicyanamide		< 10 min
[Bmim][TfO]	Merck, high purity, ≥99.0%	1-butyl-3-methylimidazolium trifluoromethanesulfonate		< 10 min
[Hmim][PF$_6$]	Fluka, ≥97.0%	1-Hexyl-3-methylimidazolium hexafluorophosphate		< 10 min
[BMP][Tf$_2$N]	Merck, high purity, ≥99.0%	1-butyl-1-methylpyrrolidinium bis(trifluoromethylsulfonyl)imide		~ 30-60 min
[SEt$_3$]NTf$_2$	Fluka, for electrochem. ≥99.0%	Triethylsulfonium bis(trifluoromethylsulfonyl)imide		~30-60 min
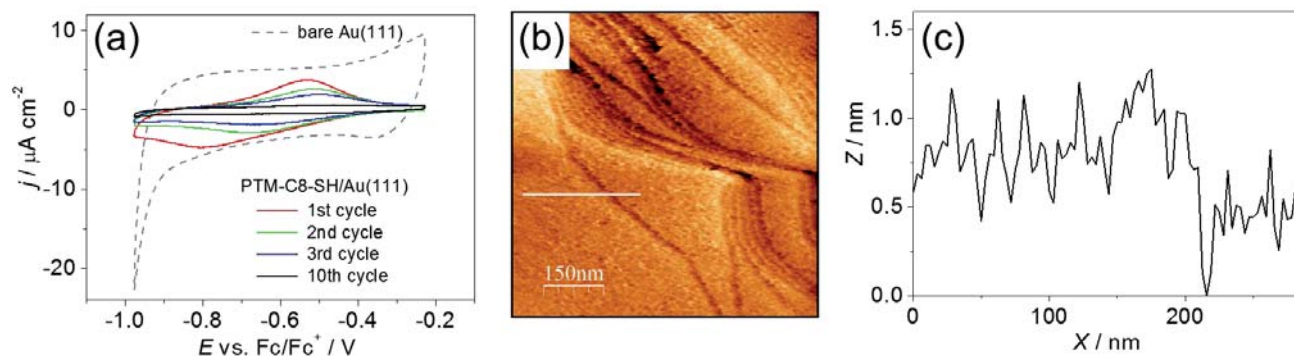
Figure S2. (a) Consecutive CVs of PTM-C8-SH/Au(111) in [Emim][EtSO$_4$]. The numbers of some cycles are indicated. Scan rate is 0.05 V s^{-1}. (b) A representative in situ STM image of PTM-C8-SH/Au(111). E_S = -0.20 V (vs. Pt), E_{bias} = 0.1 V, $I_{SetPoint}$ = 25 pA. (c) Cross-section along white line in the panel (b).

The mechanism of anion protonation in ILs is not clear. However, the following explanations can be proposed. With ILs containing imidazolium-based cations ([Emim], [Bmim], and [Hmim]) we observed a fast degradation of redox signal independently on the anion (Table S1). On the other hand, utilization of ILs with [BMP] and [SEt$_3$] cations led to a better stability of the PTM anion. It was reported that the slightly acidic C2 proton in the dialkyl imidazolium ring produces certain acid catalysis effects.[2] Furthermore, it seems that PTM anion displays strong proton-acceptor properties. Therefore, PTM anion can accept the C2 proton from an imidazolium-based cation and form the stable redox-nonactive αH-PTM moiety. This reaction is assisted by electrostatic interaction between the PTM anion and the dialkyl imidazolium cation. However, we notice that the protonation of PTM anion was also observed in dialkyl-imidazolium-free ionic liquids such as [BMP][Tf$_2$N] and [SEt$_3$][Tf$_2$N] (Table S1), although the degradation occurred proceeded slower. Furthermore, residual water may also serve as a source of protons for this reaction.
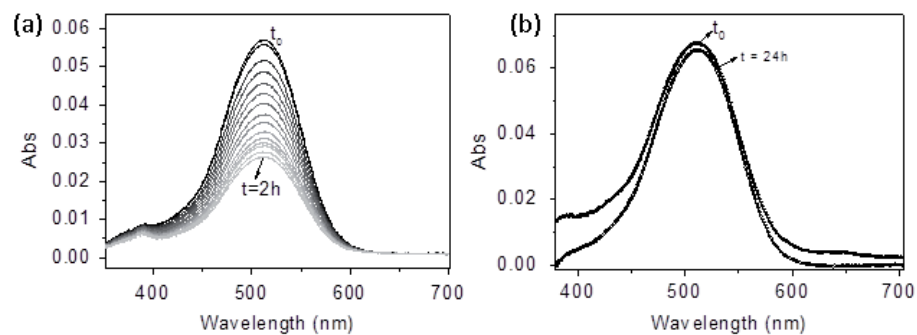
Figure S3. Evolution of the UV/Vis spectrum of PTM$^-$ K$^+$ [18-Crown-6] with time in (a) [Emim][EtSO$_4$] and (b) [Emim][EtSO$_4$] + Et$_3$N (15:1 v/v).
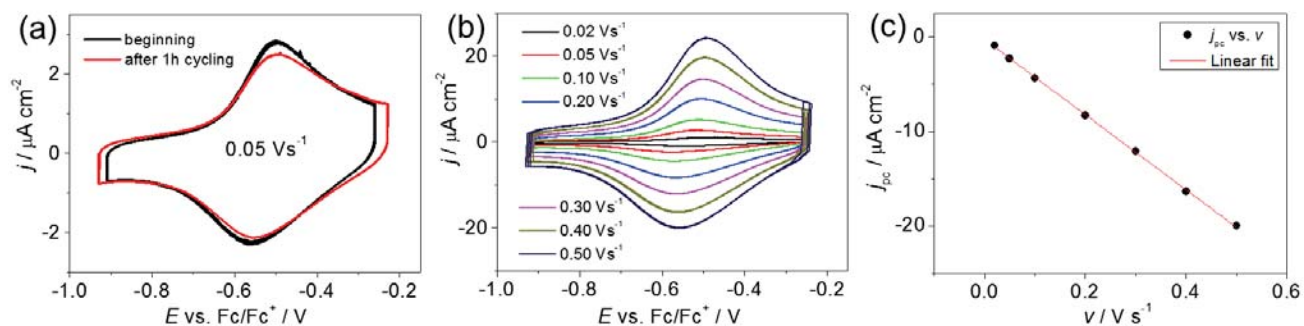
Figure S4. (a) Cyclic voltammograms of radical PTM-C8-SH/Au(111) in [Emim][EtSO$_4$] + Et$_3$N (15:1 v/v) with molecular sieves: at the beginning of the experiment and after 1 h of potential cycling. (b) CVs at different scan rates. (c) Plot of the cathodic current peak height vs. the scan rate and the linear fit.
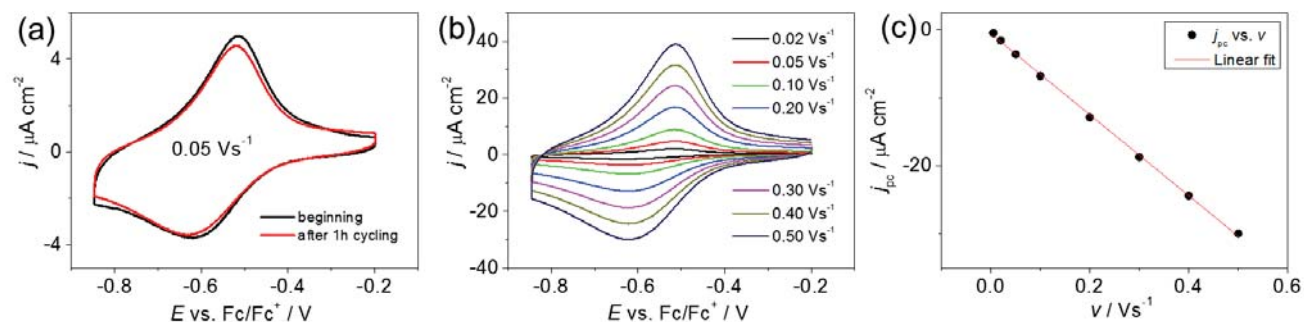
Figure S5. (a) Cyclic voltammograms of radical PTM-C8-SH/Au(111) in [SEt$_3$][Tf$_2$N] + Et$_3$N (15:1 v/v) with molecular sieves: at the beginning of the experiment and after 1 h of potential cycling. (b) CVs at different scan rates. (c) Plot of the cathodic current peak height vs. the scan rate and the linear fit.

The CV measurements in [Emim][EtSO$_4$] and [SEt$_3$][Tf$_2$N] ILs with addition of Et$_3$N demonstrated a high stability of voltammetric redox peaks. Examples are shown in Figures S4 and S5. CV shape does not change considerably even after cycling for 1 h, and linear dependence of peak height vs. scan rate indicates surface-confined redox process. We notice that usage of molecular sieves (added directly into the cell) also improves the redox-stability of the PTM-alkyl-SH SAM.

In situ STM images of PTM-C8-SH/Au(111) in [Emim][EtSO$_4$] + Et$_3$N (Figure S6) demonstrate that the SAM is compact, but disordered. Similar images were obtained in the [SEt$_3$][Tf$_2$N] ionic liquid (Figure 2 in the manuscript).
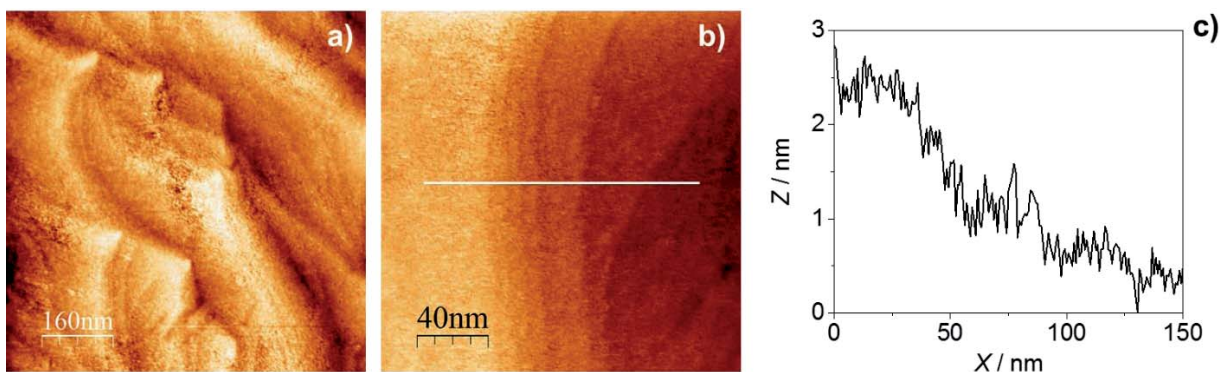
Figure S6. (a,b) *In situ* STM images of radical PTM-C8-SH/Au(111) in [Emim][EtSO$_4$] + Et$_3$N (15:1 v/v) with molecular sieves. E_S = -0.3 V, E_T = -0.2 V, I$_{SetPoint}$ = 0.06 nA. (c) Cross-section along the white line in the panel (b).

Estimation of maximal packing of PTM-C8-SH on Au(1 1 1)

The theoretical maximum of PTM-C8-SH coverage was estimated as follows. The bulky PTM moiety has a planar triangular shape. Hence, the closely-packed molecules attached vertically can be represented as rectangular parallelepipeds with the base edges 1.3 nm and 0.78 nm and projected area 1.014 nm^2 as depicted in Figure S7. Therefore, the maximal coverage is $9.86 \cdot 10^{13}$ molecules per cm^2, or $1.64 \cdot 10^{-10}$ mol cm^{-2}.
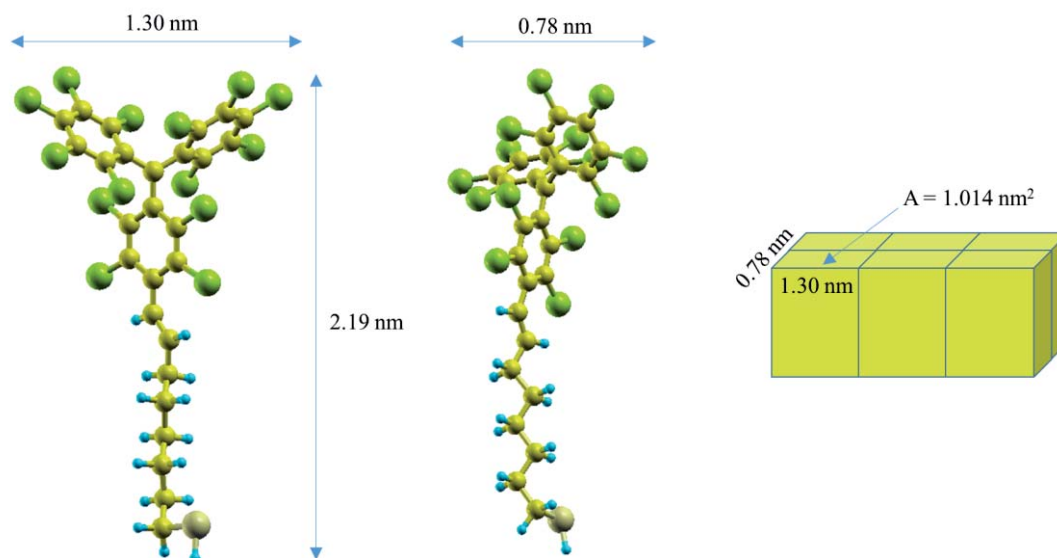
Figure S7. The representation of the closest packed adlayer of the PTM-C8-SH molecules as rectangular parallelepipeds with respective dimensions. The area of one molecule projected on a substrate is indicated in the figure.

Assuming the molecules lie on the surface as depicted in the left picture of Figure S7 (top view), one can suggest that the molecules have a triangular projection shape with the base of 13.0 Å and height of 21.9 Å. Then the area of such a triangle will be 1.424 nm^2, giving a maximal coverage 7.02 10^{13} molecules per cm^2, or 1.17 10^{-10} mol cm^{-2}. However, such a coverage suggests the very uniform arrangement of PTM triangles. More realistically they are oriented randomly and since the molecule is very long (21.9 Å), the coverage would decrease significantly. The arrangement of molecules on the Au(1 1 1) surface is difficult to deduce from our STM results, but relying on the coverage values of 1.1-1.2 10^{-10} mol cm^{-2} as obtained from CVs, we propose that the majority of the molecules are adsorbed in vertical-tilted configuration.

Redox-mediated electron tunneling (RMET): Kuznetsov-Ulstrup model.[3]

Several experimental works demonstrated a redox-mediated electron transfer (RMET)[4] trough different redox-active organic molecules,[1, 5-8] metal-organic complexes[9, 10] and biomolecules[11, 12] adsorbed on an electrode surface as well as through single molecule junction.[13, 14] Kuznetsov and Ulstrup treated the RMET process as a sequence of oxidation and reduction events occurring when the effective potential of the redox center lies between the potentials of two adjacent electrodes (a KU model), such as the tip of a STM (E_T) and the corresponding substrate (E_S). Assuming a strong electronic coupling between the molecule and both adjacent electrodes (adiabatic limit), we also rationalize RMET in our case by KU model, two-step electron transfer with partial vibrational relaxation. For further details we refer to previous reports.[1, 8, 14]

The master curve in Figure 4c was fitted by using a numerical expression[1, 10, 14] (1) for the enhanced tunneling current obtained in the frameworks of the KU model. The fitting parameters for the curve in Figure 4c are given in Table S2 ($E_{bias} = 0.1$ V and $I_{SetPoint} = 0.1$ nA).

$$I_{enh} = 1820E_{bias}\left\{exp\left[\frac{9.73}{\lambda}(\lambda + \xi\eta + \gamma E_{bias})^2\right] + exp\left[\frac{9.73}{\lambda}(\lambda + E_{bias} - \xi\eta - \gamma E_{bias})^2\right]\right\}^{-1} \qquad (1)$$

Here, I_{enh} is enhanced tunneling current during constant-bias STS (in nA); bias voltage (in V) E_{bias} = (E_T - E_S) and overpotential (in V) η = (E_S - E_0), where E^0 is the equilibrium potential for the electrochemical oxidation-reduction of a particular species; λ is reorganization energy (eV). ξ and γ, both ranging between 0 and 1, are model parameters describing the shift of η_{eff} with the variation of η and E_{bias}, respectively.

$$\eta_{eff}=(E_{eff}-E^0)=\xi\eta+\gamma E_{bias}=(\xi-\gamma)\cdot\eta+\gamma\cdot\eta_T \qquad (2)$$

The expression for the effective overpotential can be reformulated as a sum of the fractions of the sample overpotential η and of the tip overpotential $\eta_T = (E_T - E^0)$.[8]

Table S2. Model parameters obtained by fitting eq. 1 to the curve shown in Figure 3c in the main text.

λ / eV	ξ	γ
0.39	0.57	0.57

Calculation of the inner-sphere reorganization energy

The inner-sphere reorganization energy of the molecule[15] when going from neutral to the anion state, $\lambda_{i,an}$, is defined as the difference between the energy of the anion at the relaxed atomic structure of the neutral state, E_{an}, and the energy of the anion at its relaxed structure, E_a, so that $\lambda_{i,an}=E_{an}$ - E_a. The reorganization energy for the reverse transition from anion to neutral state, $\lambda_{i,na}$, is given by $\lambda_{i,na}=E_{na}-E_n$, where E_{na} is the energy of the neutral system at the anion relaxed geometry, and E_n is the energy of the neutral state at its relaxed geometry. Since usually for small deformations $\lambda_{i,an} \approx \lambda_{i,na}$, we can determine the average inner-sphere reorganization energy of a single molecule for both processes as $\lambda_i =(\lambda_{i,an} + \lambda_{i,na})/2$. These energies and atomic structures were calculated for the gas-phase PTM molecule by density functional theory (DFT) using the all-electron code FHI-AIMS[16]. The Perdew–Burke–Ernzerhof (PBE)[17,18] generalized gradient approximation to the exchange-correlation density functional was used together with numerical atom centered basis, where the free-atom-like radial orbitals are improved by adding further radial functions grouped in the tier 2 set. This corresponds to the pre-constructed "tight" default setting. Geometry optimization were performed until the ionic forces were smaller than 0.01 eV/Ang. The calculated values are then $\lambda_{i,an} = 0.082$ eV, and $\lambda_{i,na} = 0.077$ eV. These are indeed similar, and the average value is then $\lambda_i = 0.080$ eV.

We would like to compare the reorganization energy of PTM with that for perylene bisimide-type molecule, which also demonstrated RMET in STS configuration.[15] For this reason, we calculate the λ_i for perylene bisimide derivative (Scheme S2) in the same way as for PTM. The average value is $\lambda_i = 0.097$ eV.
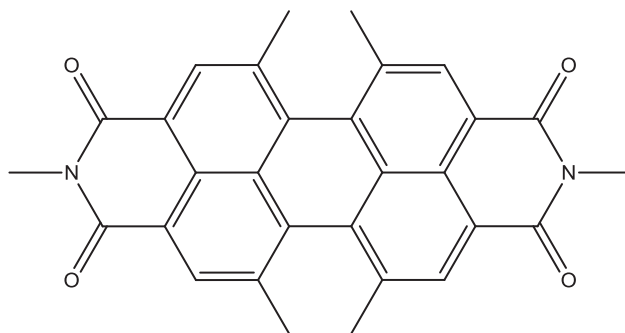
Scheme S2. Structure of perylene bisimide derivative used for the calculations of inner-sphere reorganization energy.

References

1.   I. V. Pobelov, Z. H. Li and T. Wandlowski, *J. Am. Chem. Soc.*, 2008, **130**, 16045-16054.
2.   D. R. MacFarlane, J. M. Pringle, K. M. Johansson, S. A. Forsyth and M. Forsyth, *Chem. Commun.*, 2006, 1905-1917.
3.   A. N. Kuznetsov and W. Schmickler, *Chem Phys*, 2002, **282**, 371-377.
4.   J. Zhang, A. M. Kuznetsov, I. G. Medvedev, Q. Chi, T. Albrecht, P. S. Jensen and J. Ulstrup, *Chem. Rev.*, 2008, **108**, 2737-2791.
5.   N. J. Tao, *Phys. Rev. Lett.*, 1996, **76**, 4066-4069.
6.   P. Salvatore, A. Glargaard Hansen, K. Moth-Poulsen, T. Bjornholm, R. John Nichols and J. Ulstrup, *Phys. Chem. Chem. Phys.*, 2011, **13**, 14394-14403.
7.   Z. Li, Y. Liu, S. F. L. Mertens, I. V. Pobelov and T. Wandlowski, *J. Am. Chem. Soc.*, 2010, **132**, 8187-8193.
8.   A. V. Rudnev, I. V. Pobelov and T. Wandlowski, *J. Electroanal. Chem.*, 2011, **660**, 302-308.
9.   T. Albrecht, K. Moth-Poulsen, J. B. Christensen, J. Hjelm, T. Bjørnholm and J. Ulstrup, *J. Am. Chem. Soc.*, 2006, **128**, 6574-6575.
10.   T. Albrecht, A. Guckian, J. Ulstrup and J. G. Vos, *Nanotechnology, IEEE Transactions on*, 2005, **4**, 430-434.
11.   J. Zhang, Q. Chi, A. G. Hansen, P. S. Jensen, P. Salvatore and J. Ulstrup, *FEBS Lett.*, 2012, **586**, 526-535.
12.   J. Zhang, Q. Chi, A. M. Kuznetsov, A. G. Hansen, H. Wackerbarth, H. E. M. Christensen, J. E. T. Andersen and J. Ulstrup, *J. Phys. Chem. B*, 2002, **106**, 1131-1152.
13.   H. M. Osorio, S. Catarelli, P. Cea, J. B. G. Gluyas, F. Hartl, S. J. Higgins, E. Leary, P. J. Low, S. Martín, R. J. Nichols, J. Tory, J. Ulstrup, A. Vezzoli, D. C. Milan and Q. Zeng, *J. Am. Chem. Soc.*, 2015, **137**, 14319-14328.
14.   N. J. Kay, S. J. Higgins, J. O. Jeppesen, E. Leary, J. Lycoops, J. Ulstrup and R. J. Nichols, *J. Am. Chem. Soc.*, 2012, **134**, 16817-16826.
15.   C. Li, A. Mishchenko, Z. Li, I. Pobelov, W. Th, X. Q. Li, F. Würthner, A. Bagrets and F. Evers, *J. Phys.: Condens. Matter*, 2008, **20**, 374122.

15.   S. F. Nelsen, S. C. Blackstock and Y. Kim, *J. Am. Chem. Soc.*, 1987, **109**, 677-682.

16.   V. Blum, R. Gehrke, F. Hanke, P. Havu, V. Havu, X. Ren, K. Reuter and M. Scheffler, *Comput. Phys. Commun.*, 2009, **180**, 2175-2196.

17.   J. P. Perdew, K. Burke and M. Ernzerhof, *Phys. Rev. Lett.*, 1996, **77**, 3865-3868.

18.   J. P. Perdew, K. Burke and M. Ernzerhof, *Phys. Rev. Lett.*, 1997, **78**, 1396.

Molecular Spintronics

The manipulation of electron spin made its appearance in the device world only few decades ago and because of its potential in different technological aspects, as for example magnetic data storage, strong efforts have been devoted to develop our skill in how the spin can be injected, manipulated and detected in the solid state. This new field is commonly known as Spintronics. Until now, spintronic devices have relied on bulk metals and inorganic semiconductors, but just a few years ago some new experimental and theoretical works suggested that organic materials can offer devices with superior performances. This is the concept of Molecular Spintronics, a growing research area aimed at exploring how the unique properties of the organic molecules can be exploited into spin devices. Molecular Spintronics is an interdisciplinary field where physicists, device engineers, synthetic chemists and theoreticians should work together to achieve the goals. In this chapter we will explain the most significant features of Molecular Spintronics focusing on single-molecule spintronics devices, and how PTM radicals can be interesting for this field.

1. Introduction

Most electronic devices work on the principle of detecting the variation of an electrical current with an external stimulus. Regardless, when the stimulus has a magnetic origin, the detection becomes more complicated, due to the fact that the magnetic field is less efficient than an electric one in moving electrons. For example to produce a Lorentz force equal to an electric field of 0.1 V/nm it is necessary a magnetic field of 10^3 T. So a different property from electrical charge must be used to detect the magnetism, this property is the spin.

The importance of the spin degree of freedom for the electron motion in transition metal magnets was first described by Mott[1] in 1936. He described that the current in a magnet is due to the interaction of two electron fluids characterized by opposite spin directions. That concept was confirmed 50 years later by the discovery of the giant magneto-resistance effect in magnetic multilayers,[2,3] that demonstrated that the electrical resistance of a magnetic device can be modified by changing its magnetic spin state. This discovery gave rise to the start of the magneto-electronics field, better known as Spintronics.[4]

Traditionally spin phenomena have been studied for transition metals and inorganic semiconductors.[5,6] But in the last 10 years, organic molecules have emerged as a revolutionary platform for spintronics. This emerging field, supported by spin-transport experiments[7] and theoretical[8] predictions, is known as Molecular Spintronics.[9]

The importance of this growing field is due to the unique properties of the organic molecules. They can be prepared in infinite combinations, their properties can be tuned and their degree of purity is, in general, higher than inorganic compounds. Also molecules can be synthesized and processed in soft conditions (low temperatures, atmospheric pressure, etc.). However, the most

important characteristic that differentiates organic molecules is that are made with the upper rows elements of the periodic table, thus the spin-orbit and hyperfine interaction are weak, favoring long spin relaxation times and coherent spin propagation. Hence, organic materials offer a versatile and unique playground for exploring new spintronics concepts and for implementing existing ones.

One of the most interesting concepts regarding molecular spintronics is the study of the transport properties through magnetic molecules. Recently some experimental advances have been reported related to the transport properties in junctions based on magnetic molecules. There are a variety of interesting charge transport phenomena that open the possibility of using these molecular materials for memory and logic applications related to spintronics. These phenomena are:[10]

Coulomb blockade[11] is the increased resistance at small bias voltages of an electronic device comprising at least of one low-capacitance tunnel junction which is in its simplest form an insulating barrier between tow conducting electrodes.

Magnetoresistance[12] is the property of a material to change the value of its electrical resistance when an external magnetic field is applied to it. In 1988 giant magneto-resistance was discovered,[2] understanding this as the increase of resistance in a system formed by two ferromagnetic layers separated by a nonmagnetic layer, when the magnetizations of magnetic layers are switched from parallel to antiparallel.

Negative differential Resistance[13] is the increase in resistance of a device when the voltage increased in a specific bias range, represented by al linear current peak in I-V curve. This phenomenon can be attributed to resonant tunneling between metal orbital and molecular orbitals, but its origin is still a matter of debate.

Spin polarization[14] is the degree to which the spins of conduction electrons are aligned with particular direction giving rise to spin-polarized currents. In this is based the use of the electron current, composed of spin up and spin down carriers, for encoding information in a binary language through the interaction with magnetic materials.[15]

Spin filtering.[16] This phenomenon allows to obtain highly spin-polarized charge carriers generated from nonmagnetic electrodes using magnetic tunnel barriers. The effect is based in the property whereby a magnetic material can filter electrons selectively according to their spins, polarizing the current flow in spin up/spin down selectivity.

Kondo effect[17] is the resistance increase of a metal at low temperature when magnetic impurities are present. This is due to the scattering of the conduction electrons that interact with the localized spins.

Concerning molecules, just a few examples of families of magnetic molecules in which conductance properties have been studied are reported in literature. These families have been

selected because their magnetic behavior and their properties in bulk are very well known. Those families and their characteristics are reported below:

1) Single molecule magnets (SMM), which are molecules, composed by transition metal clusters or lanthanide complexes. They are characterized by large spin at ground state and an easy-axis magnetic anisotropy, allowing a slow relaxation of their magnetic moment below the threshold temperature and magnetic hysteresis of purely molecular origin.[15,18,19]

2) Spin-crossover metal organic complexes. Their importance lies in the fact that the transition from low-spin to high-spin can be triggered by a variety of external stimuli.[20]

3) Endohedral fullerenes, in which magnetic atoms are captured into the fullerene cage. Within this group one of the most attractive is the endohedral fullerene N@C60, in which a ^{14}N is encapsulated into a fullerene molecule. The nitrogen is in ground state conferring to the system an electronic spin of 3/2.[21]

4) Different kind of organic free radicals with one or more unpaired electrons. Even though most of organic radical molecules are highly reactive, there are radicals such as verdazyls, nitroxides or polychlorotriphenylmethyl radicals that are good candidates for studies of electrons transport mechanism because of their elevated stability and persistence.[22]

One of the major challenges in the study of molecular electronics/spintronics is to have access at the molecular scale to visualize how the charge moves through the molecule. During the last decade, a number of techniques have been exploited for the fabrication of molecular organic devices. These techniques can be divided into two main categories: the techniques measuring molecular assemblies which contain tens to thousands[23,24] of individual molecules, and the ones to measure a single-molecule.[25,26] To achieve that purpose and study the conductance of molecules, two different configurations of single molecule devices have been commonly used: two-terminal and three-terminal devices (Figure 1).

-Two-Terminal devices.

In this kind of devices the molecules are immobilized by chemi- or physisorption on a conducting substrate, and a conducting tip acts as a second contact allowing the transport measurement. The most common techniques used are scanning tunneling spectroscopy (STS) and conducting scanning force microscopy (C-SFM). Besides, two electrode junctions (i.e., mechanically break junctions, electromigrated junctions, etc) where a molecule is trapped in between, are also used avoiding the use of the tip and hence, achieving a more symmetric device.

-Three-Terminal devices.

The difference with the previous one is that the *three-Terminal devices* consist in a single-molecule transistor, where the molecule is trapped between two electrodes (source and drain) while a third electrode, the gate, is used to create an electric field. The electrical characteristics of the molecule are determined by acquiring the current versus bias voltage (I-V) curves while the

gate voltage (Vg) is changed. The gate permits the control of the charge state of the molecule opening the possibility to tune its conductivity.
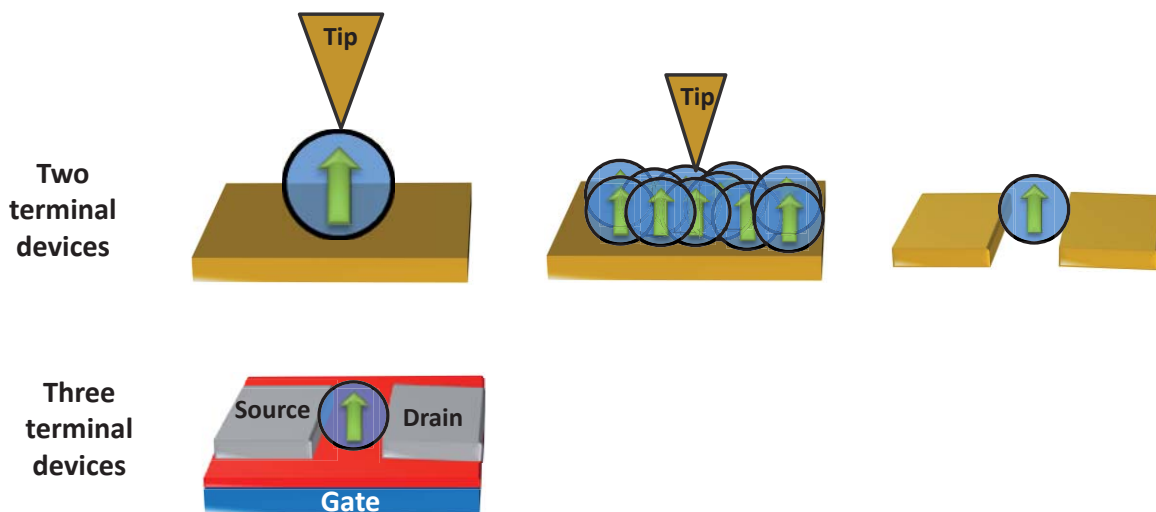
Figure 1: Representative scheme of two- and three-terminal devices used to measure the transport properties through magnetic molecules.

2. Single Molecule Devices: Break Junctions

Single-molecule break junctions are created by dynamic fabrication of nanogaps after rupture of a metallic contact. The break junction techniques provide a unique platform to access and study the charge transport through single-molecules.

2.1 Break junction fabrication

Mainly, there are three different methodologies to achieve this kind of single-molecule devices, STM break junction (STM-BJ), mechanically controllable break junction (MCBJ) and Electro-Migrated Break Junction (EMBJ).[27]

2.1.1 STM break junction (STM-BJ)

A STM-BJ (Figure 2a) is formed by a conductive substrate, where the molecules are deposited, and a conductive tip. The STM tip is repeatedly brought into contact with the substrate and then pulled away (withdrawn). This process forms a tip-substrate gap that is narrow enough to be bridged by a molecule. At a constant applied bias, the presence of a molecule in the break junction gives rise to a non-zero current that is manifested as a plateau in the current versus tip displacement curves. The magnitude of the current in the plateau is related to the conductance of the molecule in the junction.

2.1.2 Mechanically controllable break junction (MCBJ)

MCBJ (Figure 2b) is composed of a flexible substrate with two fixed nano-spaced electrodes, over which the target molecules are physisorbed from a solution. This substrate is pressed from the top by two clamping supports and has a movable pushing rod below. With the moving of the pushing rod, the thinnest part of the fixed metal wire is broken, and an adjustable nanometer-size gap is established. In this gap one molecule can be assembled, thus creating a single molecule device.

The MCBJ is interesting to investigate the conductance dependence with the electrode distance; since with this technique the gap can be precisely controlled. Other advantage is the mechanical stability and the easily modification of this methodology, thus enabling cheap device fabrication.[28]

2.1.3 Electro-Migrated Break Junction (EMBJ)

The fabrication of EMBJ is based on the breakage of metallic nanowires using a controlled passage of current (Figure 2c). The breaking process consistently produces two metallic wires with a nanometric separation where one molecule can be trapped.

The EMBJ technique presents some advantages in comparison with the other methods to achieve a single molecular junction. The EMBJ allows performing low noise temperature measurements; and also permits to apply a gate voltage and magnetic field allowing to study the magnetic field conductance dependence.[29]
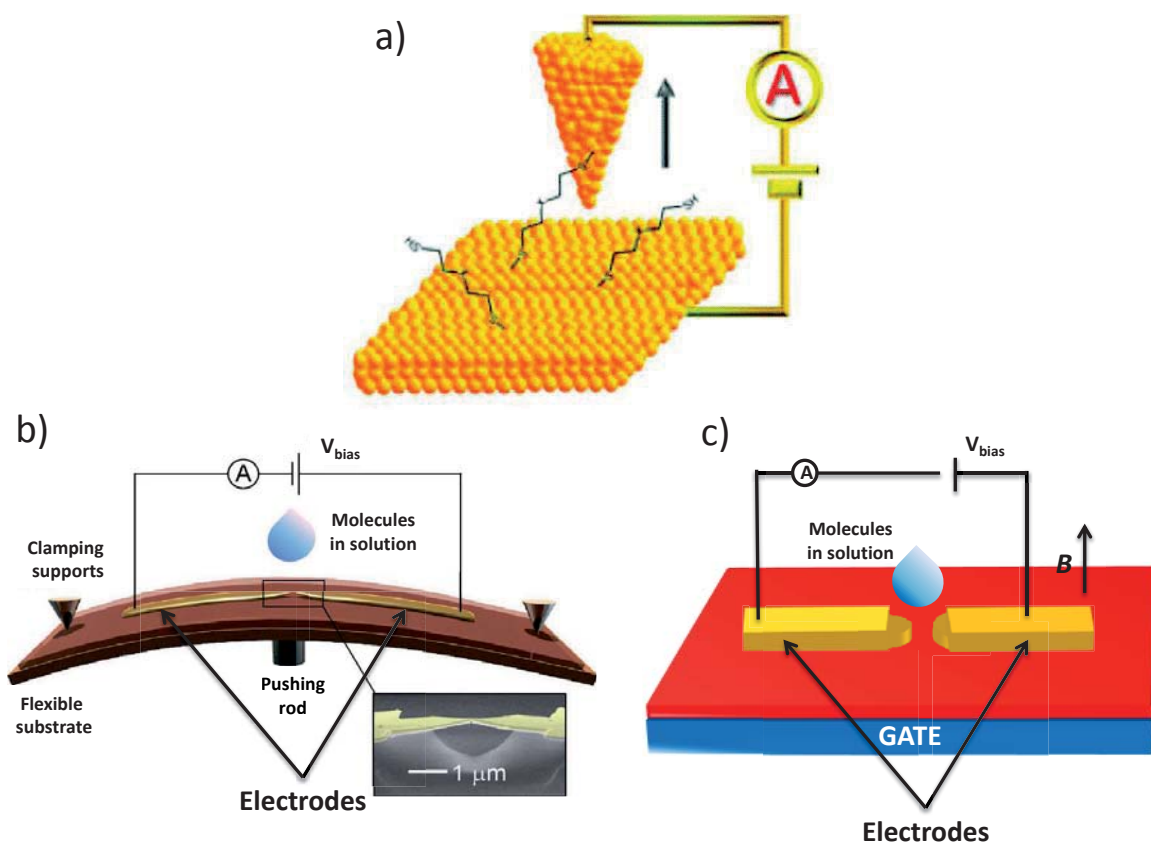
Figure 2: Schematic illustration of a) STM-BJ,[30] b) MCBJ,[50] and c) EMBJ.

2.2 Analysis of break junction measurement data

In an ideal break junction, the current flows through a fully stretched single-molecule junction by applying a constant bias voltage. However, break junctions measurements are dynamic processes where there are various possible molecular configurations with different geometry with respect to the electrodes. Thus, it is essential to understand the nature and the physics behind the conductance values extracted from break-junction experiments.

Besides, there are two factors to consider. The first one is that the conductance measured is a combination of molecular conductance and a through space tunneling conductance. Second, there is the existence of the snap-back phenomenon of the two electrodes. The snap-back takes place immediately after the rupture of de electrodes contact. This process is much faster than the displacement of the two electrodes and consequently it is not possible to measure the conductance in that point.

Considering these two points, the break junction can be schematically described as in Figure 3. The different molecular configurations are illustrated in part A, and the corresponding charge transports are described in part B. Here, the measured stretching trace is shown as solid light gray line, the direct tunneling conductance as a black dashed line and the molecule conductance as red dashed line. The complete process can be described as follows:

a) The electrodes are connected, and the measured conductance G is higher than a quantum conductance G_0.[*]

b) The electrodes form an atomic contact and the molecular conductance is significantly lower than G_0.

c) The snap-back of the atomic metallic connection occurs, and consequently the conductance cannot be measured.

d) An electrode-molecule-electrode junction is formed, but the molecular bridge is not extended. The contribution of through space tunneling (gray line) to G still prevails over the molecular conductance contribution, which only occurs when the distance between the two electrodes is shorter than the length of the molecular junction.

e) The electrode-molecule-electrode junction elongates, and G is mostly due to the molecular conductance. A conductance plateau is observed.

f) The molecule adopts a fully extended molecular configuration in the junction.

g) There is breaking of the molecule-electrode contact with a snap-back between the molecule and one electrode. The conductance decreases sharply.

h) The tunneling channel is formed between the electrode-molecule assembly and the other electrode (gray dashed line). The conductance is measurable until it approaches the current detection limit of the setup.

Finally a 1-dimensional histogram is obtained where numerous conductance traces are plotted, which may reveal a peak (or peaks) of the probable single-molecule conductance (Figure 3B right).

It should be mentioned that this technique of analysis has some limitations. The regions marked with number 1, 2, 3 and 4 in Figure 3B are areas that give problems in the conductance measurements. In region 1 the conductance cannot be resolved due to the snap-back process, which is faster than the conductance detection. In region 2 there is an overlap in conductance from direct tunneling and the molecule. The snap-back upon breaking of the molecular junction (region 3) should be analyzed in order to determine if there are one or more molecules attached,

---

[*] G_0 is the quantum unit of the conductance ($G_0 = 2e^2/h = 77.5$ μS).

since the shape of that region has a direct relationship with the intermolecular interactions such as π-π stacking, or extend hydrogen-bonded networks. Finally, in region 4, the conductance accuracy is limited by the sensitivity of the current detection in the experimental set-up, which common ranges between $10^{-5}\,G_0$-$10^{-9}\,G_0$.
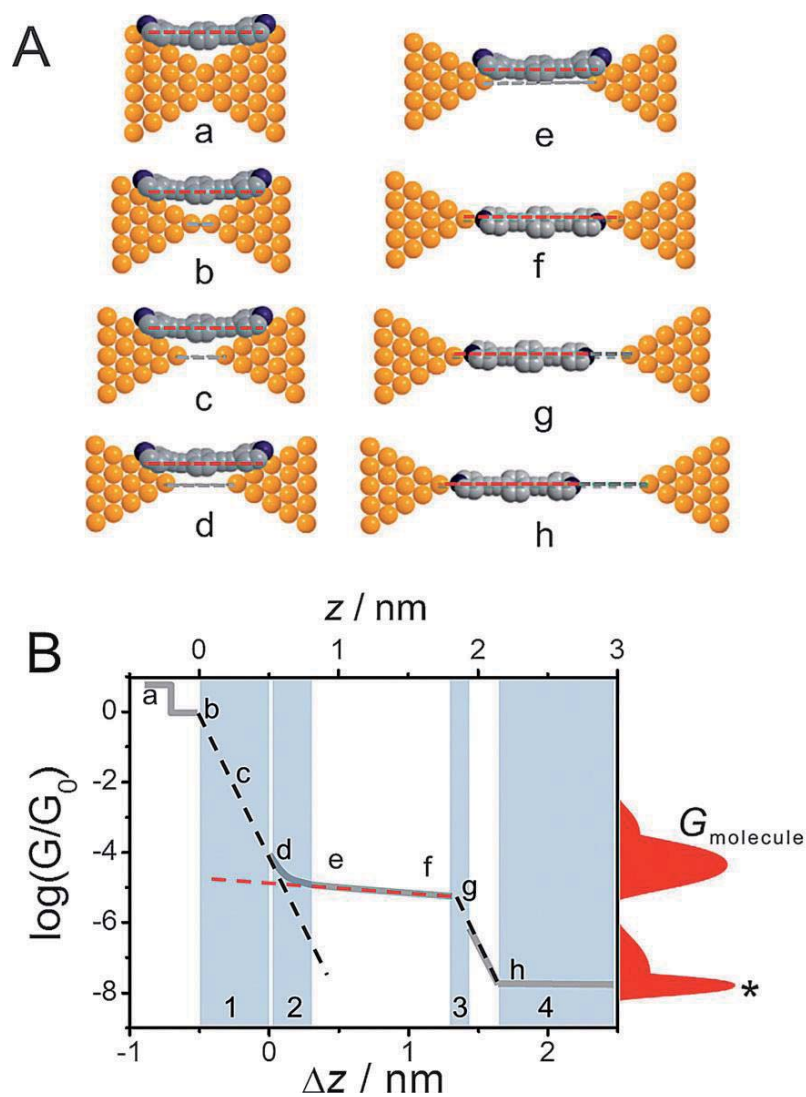
Figure 3: (A) Evolution of a molecular junction during break-junction measurements. (B) Simplified schematic representation of a measured conductance trace (solid light gray line) with conductance contributions from direct tunneling (black dashed lines) and from the molecule (red dashed line). A 1D conductance histogram is depicted in red color on the right side of panel B. *Indicates the noise level of the set-up.[31]

2.3 Influence of molecular structure on the nanojunction conductance

The charge transport in a molecular junction occurs through different molecular sub-units (Figure 4): the electrode-molecule interface and the molecular backbone comprising the functional molecular unit. So to design functional molecules able to create break junction devices, it is necessary to know the correlation between molecular structure and nano-junction conductance through the electrode-molecule interface and the molecular backbone.
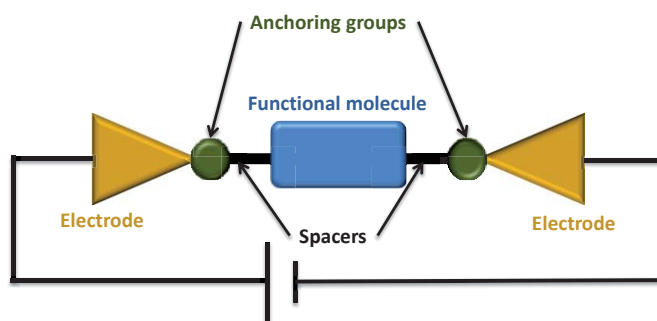
Figure 4: Scheme of a single molecular junction.

2.3.1 Electrode-molecule interface

The first step in the charge transport through a single-molecular junction is the charge flow through electrode-molecule interface. When a molecule is coupled to the electrodes, the discrete energy levels of the electrode-molecule interface are shifted and broadened.[32] Therefore, the charge transport through the single molecular junction depends strongly on (i) the energy barrier, E_{mol}, given by the energy difference between the frontier levels of the molecule (HOMO/LUMO) and the Fermi level in the electrodes and, (ii) the coupling strength, Γ, between the molecular state and the electrodes. (Figure 5).[33] For very large Γ, for example, H_2–Pt junctions,[34] the discrete levels are significantly broadened and coherent resonant transport occurs. For very small Γ, the lifetime of electrons on the molecule becomes longer, leading to incoherent transport and effects like Coulomb blockade, electron hopping, and the Kondo effect .[35] Between these two extremes, coherent, off-resonant tunneling occurs.[36]
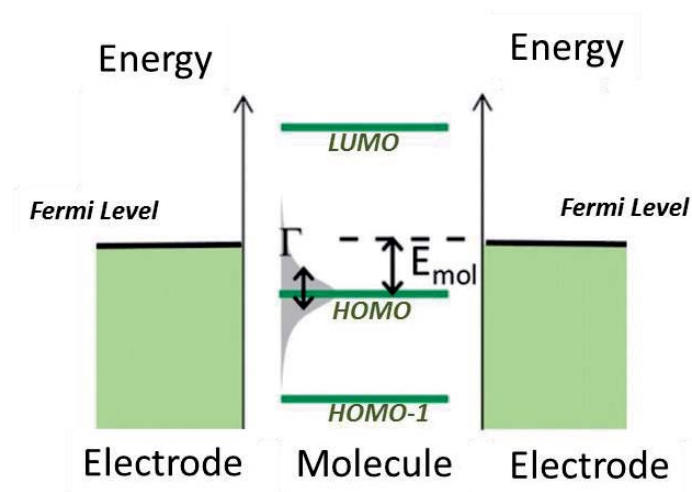
Figure 5: Energy level diagram for a single molecule junction where are represented the electrode Fermi level and the molecular orbital of the molecule. E_{mol}, corresponds to the energy barrier, and Γ to the coupling strength.[31]

Two major parameters are responsible for controlling the energy level alignment and adjusting the coupling strongly: one is the material of the electrodes and the other is the chemical nature of the anchoring groups.

In relation with the electrodes material, different metals are commonly used to perform the molecular junctions, such as Au, Ag, Pt and Pd, and non-metal materials principally carbon based ones. For metal materials, the Fermi level decrease in the order Ag > Au > Pd > Pt.[37] A few years ago, Venkataraman et al., published a study comparing the conductance of a series of amine-terminated oligophenyl and alkane molecular junctions formed with Ag and Au electrodes using the STM-BJ technique (Figure 6a).[38] Through DFT calculations, they demonstrated that the junctions conduct through the HOMO of the molecule, by injection of charge, from the electrode Fermi level. Experimentally, they found that Au molecular junctions have a higher conductance than those formed with Ag. So the Fermi level of Ag in comparison with Au Fermi level, leads a slower charge transport through the molecule-electrode interface and a lower junction conductance.

Another didactic example regarding the influence of the electrode material is the work reported by Ko *et al*.[39] They use $SCN(CH_2)_nNCS$ compounds as model molecules with a large HOMO-LUMO gap to study the conductance of the single molecule junctions with three different metal electrodes (Au, Pd and Pt) (Figure 6b). They found that the Pt and Pd junctions have higher conductance than the Au ones (about 2.5-3.5 times superior). In that case, the conductance's increase not only depends on the different Fermi level of the electrodes, but also they found that the d-orbital of Pt and Pd can play an important role. They suggest that Pt and Pd can promote junctions where the π character is significantly involved, while in Au contacts the union is predominantly of σ character. Therefore, Pt and Pd junctions cause a strong energy alignment in the interface resulting in the decrease of the energy barrier conductance in comparison with Au.
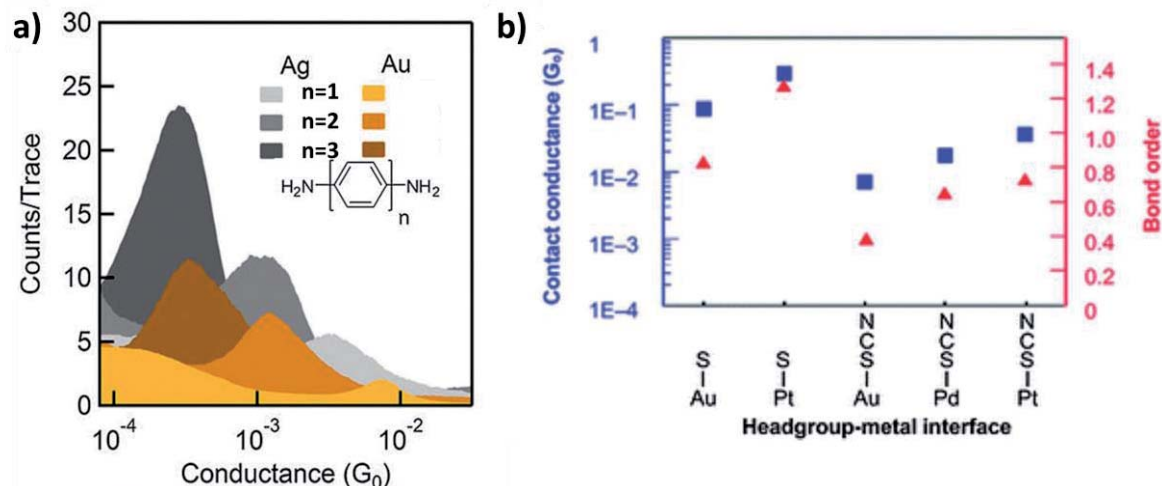
Figure 6: a) Long-binned conductance histograms for oligophenyls using Au and Ag electrodes. n=1-3 corresponds to the molecules with 1 to 3 benzene rings, respectively.[38] b) Correlation of the single-molecule conductance for different electrode materials and binding strength of the molecule-electrode contact.[39]

As we mentioned before, the anchoring groups of the molecules also play an important role in the charge transport process of molecular junctions. In the last years, many different anchoring groups have been widely investigated. Tao´s group studied and compared single molecule conductance of alkanes with –SH, -NH$_2$, and –COOH as anchoring groups, employing STM-BJ with gold electrodes.[40] They reported that conductance decreases in the order -SH > -NH$_2$ > -COOH. This distribution can be attributed to different electric coupling efficiencies between the electrode and anchoring groups, and alignments of the molecular energy levels relative to the Fermi energy level of the electrodes introduced by different anchoring groups. The measured length of the molecular junctions revealed that the binding strength decreased in the same order Au-S > Au-NH$_2$ > Au-COOH. So the strength of the electrode-molecule binding is responsible for the difference in the conductance.

Another factor to consider when comparing different anchoring groups is the deformation of the electrodes caused by the strong binding interaction between the anchoring group and the electrode. Arroyo *et al*.[41] explored this effect on gold break junctions employing thiols and amines as anchoring groups. They concluded that the thiol change the gold electrode more than amine. Therefore, to find an appropriate anchoring group, the molecule-junction conductance, stability and anchoring strength should be balanced.

2.3.2 Molecular length dependence and quantum interface

Besides the molecule-electrode interface, another requisite in order to design functional molecules for single molecule break junctions is to know the parameters that affect the transport through the molecular backbone. There are two factors which play an important role in charge transport through the molecular backbone: the molecular length and the quantum interface.

Length dependence

The mechanisms of charge transport associated to any system are mainly two: coherent transport via tunneling or superexchange and incoherent thermally activated hopping transport. As we mentioned in previous chapter, superexchange does not have a temperature dependence and has an exponential variation with the distance, while hopping has a strong temperature dependence and lower distance dependence.

Quantum interference effect

The wave nature of the electrons transferred through the energy levels provides a possibility to adjust the charge transport pathway by changing the wave functions of the molecule. The quantum interface concept, which is very well known in macro devices, also affects the transmission coefficient of charge transport at the single-molecule scale.[42] For example, if partial electron waves propagating through molecular orbital in a molecular junction interfere with each other destructively, conductance is suppressed, and if they interfere constructively, conductance is enhanced. The quantum interference concept can be used to tune the charge transport at the single-molecule scale by manipulation through for example redox process or a control of the single molecule conformation.

One of the most interesting examples where direct quantum interference was detected is in the cross-conjugated anthraquinone break junctions. M. Guedon *et al*.[43] compared the zero-bias conductance of anthraquinone (**AQ-DT**) and dihydroanthracene (**AC-DT**) molecules measured with conducting AFM (Figure 7). They observed that these two molecules, containing similar HOMO-LUMO gaps, exhibit different conductance values, being the one of anthraquinone almost two orders of magnitude lower than the one of the dihydroanthracene. This large difference in conductance is indicative of a destructive interference pathway in the anthraquinone junctions.
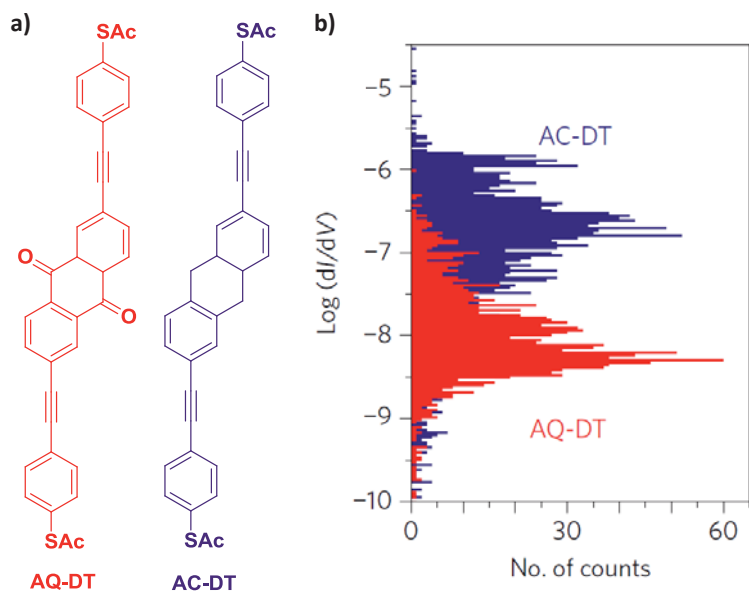
Figure 7: a) Chemical structure of the molecules. b) One-dimensional histogram at zero-bias conductance for **AC-DT** (purple) and for **AQ-DT** (red).[43]

The construction/destruction interference of the electron pathway could be employed for the development of single molecular switches. In this regard, M. Bahernejad *et al*. exploited the quantum interference effect in a redox pair anthraquinone/hydro-dianthraquinone break junction to create a single-molecule switch, under electrochemical control (Figure 8).[44] They observed an increase of conductance (of one order of magnitude) when reducing the anthraquinone to hydro-anthraquinone. The explanation of destructive/constructive interference is due to changes in the conjugation of the molecular pattern going from linear (hydro-anthraquinone) to cross-conjugated (anthraquinone).
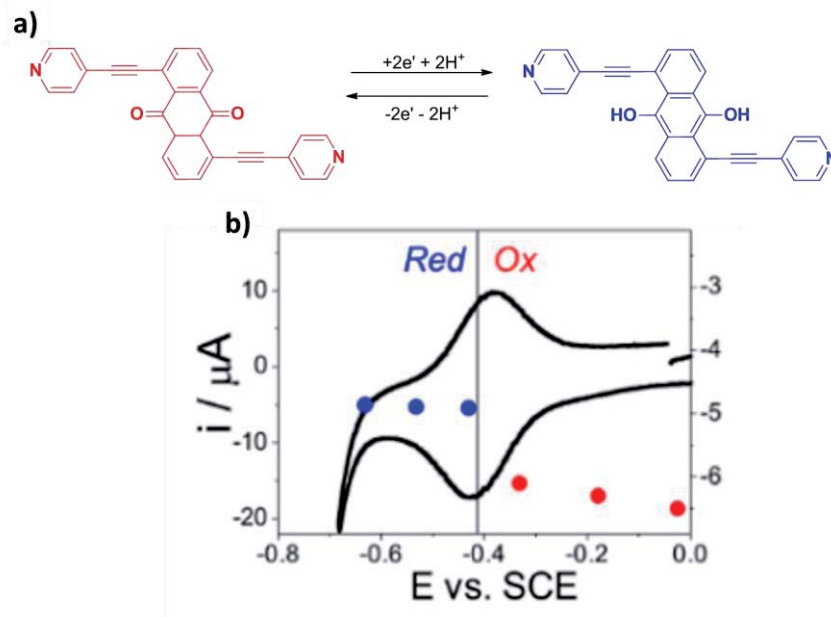
Figure 8: a) Anthraquinone (red)/hydro-anthrquinone (blue) redox pair studied. b) Experimental molecular conductance as function of the applied potential vs SCE. The vertical gray line indicates the measured redox potential.[44]

3. Precedents

Organic radicals are molecules having unpaired electrons, thus being paramagnetic in neutral state. As mentioned before, due to the light elements forming organic radicals, both the spin-orbit and hyperfine interactions are low. Therefore these families of molecules are good candidates to study the influence of the spin in the transport properties on single molecule devices. Nevertheless there are only a few examples of transport studies through organic radicals which is due to the fact that, in general, the organic radicals are very reactive and unstable. However, there are stable pure organic radicals as verdazyl, α,γ-bisdiphenyl-β-phenylallyl (BDPA), PTM, and N-oxide radicals that have recently attracted the attention in the field of spintronics.

In 2013 M. Yamashita and col., published a study of the spin properties of a verdazyl derivative TOV (Figure 9) adsorbed on Au (111) surface, using scanning tunneling spectroscopy (STS).[45] Also, in 2013, K. Kern and col. studied a nitronyl-nitroxide radical (2'-nitronilnitroxide-5'-methhyl-[1, 1'; 4, 1'']terphenyl-4, 4''-dicarbonitrile) adsorbed in Au (111) by differential conductance spectroscopy with scanning tunneling microscope (STM).[46] Another example of the conductance measurement through a single organic radical molecule was reported in 2013 by S. Müllegger *et al.*[47] In that work, they analyzed the conductivity of a monomer and a dimer of BDPA physisorbed on Au (111), by STS and STM.

The results (Figure 9) were in all cases the detection of Kondo effect at very low temperature (around 5 K), attributed to the interaction between the localized spin of the radical and the magnetic moment of the conducting mobile electrons. This interaction leads in the strong coupling regime, that is, at temperatures below characteristic Kondo temperatures (T_K) to a screening of the impurity magnetic moment and results in a stable, non-magnetic singlet ground state. That implies a dramatically decreases of the conductivity at T_K, resulting in a sharp peak in a conductance versus applied voltage measurements.

Also, some theoretically works predicts a spin filter behavior for different systems. For example, the calculated coherent transport properties of polyphenoxyl radical with four radicals centers sandwiched between two electrodes showed that the majority (α) and minority (β) spin components exhibit considerably different transmission spectra in the vicinity of the Fermi level. Therefore, if the magnetization axis is fixed by an external magnetic field, the molecular bridge would work as a spin filter.[48]

Furthermore, the transport properties of a family of 1,4-benzenediamines bridging two Au electrodes were also modeled.[49] The molecules were substituted in the 2-position with the radicals -CH2•, -NH•, and -O•. The spin filter efficiencies for these systems were calculated to be 49%, 27%, and 1%, respectively. The differences were attributed to the different electron affinities of the radicals, since they found that the radicals once connected to the electrodes can accept some charge, reducing the excess of spin, which, in turn, reduces the molecular orbitals splitting and the spin filter efficiency.
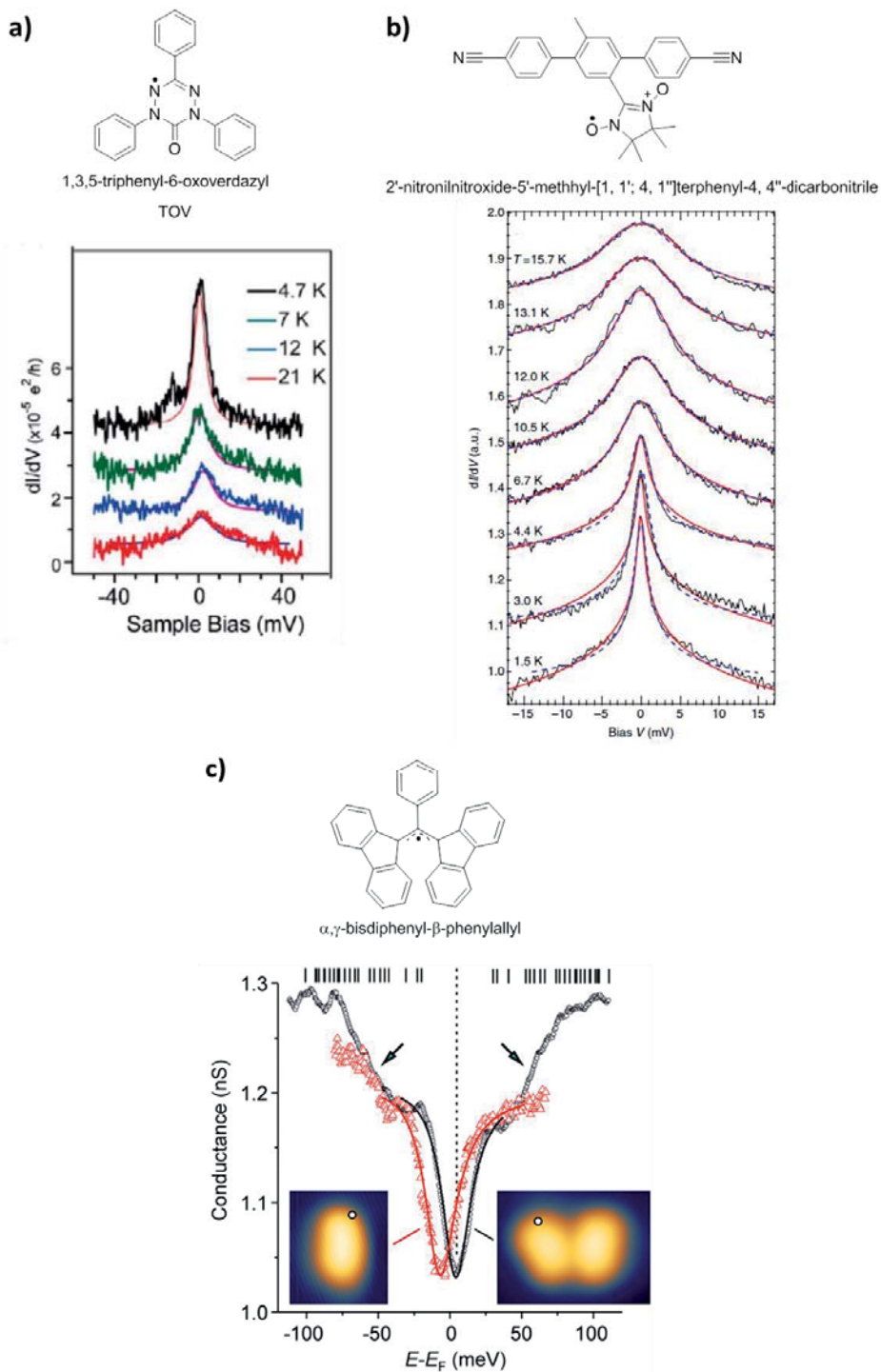
Figure 9: Differential conductance spectra taken at different temperatures for a) TOV radical;[45] b) (2'-nitronilnitroxide-5'-methhyl-[1, 1'; 4, 1'']terphenyl-4, 4''-dicarbonitrile radical;[46] and c) BDPA monomer (red) and a dimer (black) at 5 K, over positions marked by circles in the STM topographic insets.[47]

4. Objectives

All the conductance studies performed before with individual organic radicals were carried out with physisorbed systems using STM. However, to make these systems attractive for spintronics devices, it should be demonstrated that the magnetic moment of the organic radical can be retained when it is integrated in a solid-state device.

Considering these factors, our goal is to design and build single molecule devices by using a polycholortriphenylmethyl (PTM) radical as a central part of the device, and study the charge transport and the magnetic properties of the PTM in single molecule junctions (Figure 10).

In this thesis we proposed two different PTM derivatives to prepare single molecule break junctions: one PTM derivative with two linker groups able to be integrated in a single molecule break junction where the metallic electrodes are gold, and another PTM derivative with two appropriate linker groups to be integrated in single molecule break junctions using graphene as electrodes.
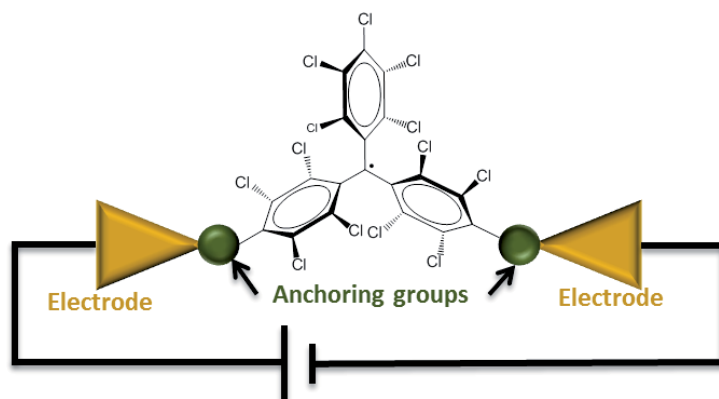
Figure 10: Scheme of a single molecule junction with a PTM as active molecule.

5. PTM integration on gold break junctions

5.1 Design and Synthesis of the molecule

The first step to design a PTM derivative for single molecule break junctions is to define the best group able to form a good metal-PTM binding giving rise to an appropriate molecular conformation. In this regard, van der Zant's group published a study on the effect of the quantum interference[50] on charge transfer through a single benzene ring on gold break junctions (figure 11, top), with different linkers. In this work, they analyzed four different molecules in which the central part is a benzene ring with acetylene spacer units connected in para- or meta-configuration. The anchoring groups consist of thiophene rings connected in two different positions (2 or 3 position) to examine the effect of the anchoring geometry and molecular conjugation.

They found that the conductance values of the derivatives where the thiophenes are linked through the position 3 are slightly higher than the derivatives where the thiophenes are linked in position 2. Furthermore, they observed a dramatical increase of conductance (more than 1 order of magnitude) for para-coupled benzene derivative compared to meta-coupled benzene (Figure 11, bottom). Based on calculation of the transmission functions, this result was explained by constructive interference of the molecule for para- derivatives and destructive interference for meta- derivatives.
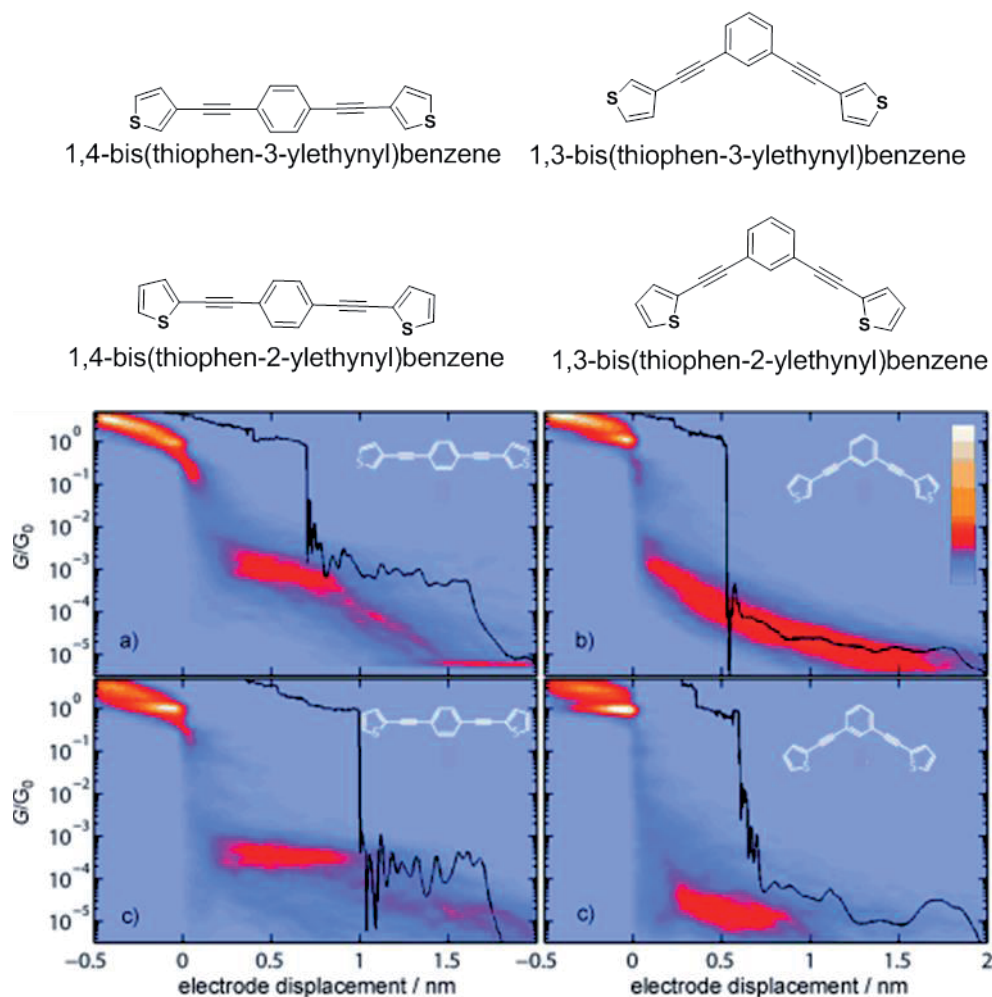
Figure 11: Top: studied molecules ; Bottom: two-dimensional break junction histograms taken at ambient conditions and 0.1 V bias for: a) 1,4-bis(thiophen-3-ylethynyl)benzene; b) 1,3-bis(thiophen-3-ylethynyl)benzene; c) 1,4-bis(thiophen-2-ylethynyl)benzene; d) 1,3-bis(thiophen-2-ylethynyl)benzene.[50]

Taking into account that results, we designed a molecule with a PTM core which contains two thiophene substituents in the para position of two chlorinated phenyl rings and that are connected to the PTM through position 3. But instead to use ethynyls groups to connect the thiophene rings to PTM, we proposed to use ethylene groups.

To obtain this bis-thiophene PTM radical molecule **1** we proposed the following retro-synthetic scheme (scheme 1). The molecule **13** could be obtained from the corresponding αH (αH-13) derivative in two steps: first the reaction with a strong base as tetrabutylammonium hydroxide to promote the elimination of the acidic proton in αH position and giving the corresponding carbanion. As second step the oxidation of this carbanion to the radical. The **αH-13** could be synthesized by Wittig-type coupling between 3-thiophene carboxaldehyde and the known PTM bis-phosphonate derivative.[51]
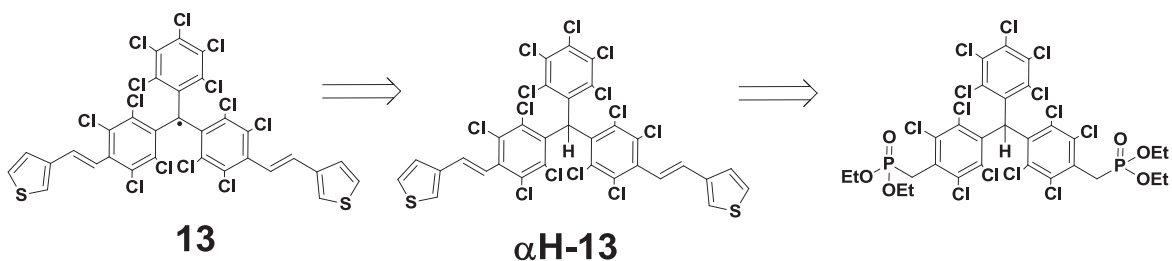
Scheme 1: Retro-synthetic pathway to synthesize the radical PTM-bis-thiophene **13** and the corresponding αH-13.

Following the proposed synthetic pathway, we obtained, in a good yield, a PTM molecule with a strong conjugation between anchoring groups and the central carbon of the PTM radical unit, where most of the spin density is located. This could provide relatively high conductance through the molecule. All new compounds were characterized by the usual techniques applied to organic molecules and, in addition, the electrical and magnetic properties of the radical also were also characterised by cyclic voltammetry (CV) and electron paramagnetic resonance spectroscopy (EPR), respectively.

Figure 12a corresponds to the EPR spectrum of the radical **13** in CH_2Cl_2. The spectrum with g = 2.0022 consists of three overlapped lines assigned to the coupling of the unpaired electron with two equivalent hydrogens from the two ethylene spacers closer to the thiophene rings (a_H = 1.95 G). The coupling with the other two hydrogens of the ethylene spacers is too small to be observed and contribute only to the enlargement of the line width. With more concentrated solutions it is observed the coupling with the alpha ^{13}C and with the ^{13}C from the phenyl rings ($a_{C\alpha}$= 29.9 G, a_{Carom} = 10.6 G The electrochemical characterization of radical **13** was performed by CV. In figure 12b the voltammogram of radical **13** using ferrocene (Fc) as internal reference is shown. The half-wave potential of **13** at -0.73 V (vs Fc) corresponds to the reduction to the PTM radical to PTM anion. However, the oxidation of the thiophene rings was not detected in that potential window.
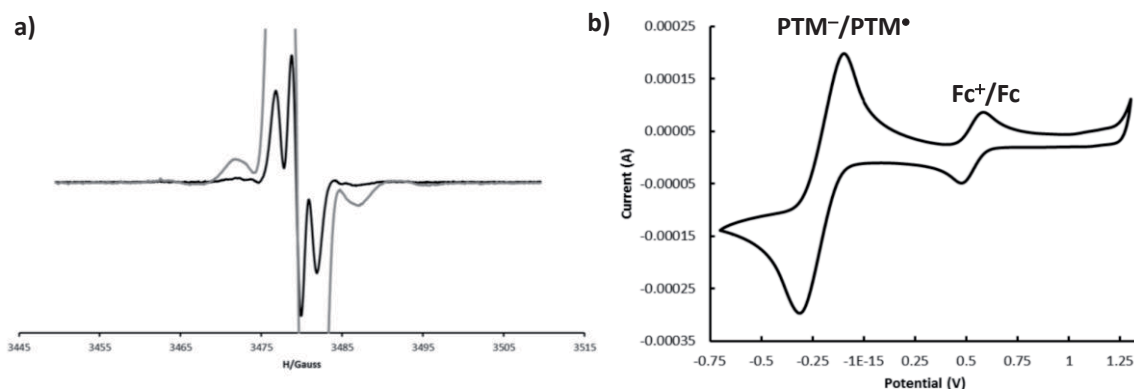
Figure 12: a) EPR spectrum of **13** in CH_2Cl_2 at room temperature. Black line corresponds to the spectrum of diluted solution of **13**, while grey line corresponds to the spectrum of concentrated solution of **13** b) Cyclic voltammogram of **1** in CH_2Cl_2 using n-Bu$_4$NPF$_6$ 0.1 M as supporting electrolyte, Ag wire as a pseudo-reference electrode, and platinum wires as the counter and working electrodes in the presence of Fc, as internal standard; $E^{1/2}$(**13**) =-073 V vs Fc.

Following, we performed a systematic investigation of the conductance of PTM derivative **1** in single molecule junctions by employing three complementary techniques, STM-BJ, EMBJ and MCBJ, and we rationalized our results by DFT calculations.

5.2 Break junctions

5.2.1 MCBJ and EMBJ

The target molecule **1** was integrated in gold MCBJ and gold EMBJ,[†] and the results obtained gave rise to a publication in Nano Letters ACS journal (*Nano. Lett*. 2015, **15**, 3109-3114).

In that paper we compare the conductance measurements performed whit PTM-bisthiophene (**13**) radical, an open-shell molecule, with the ones performed with the PTM-bisthiophene αH (**αH-13**) a close-shell molecule, in two and three terminal devices.

In the two terminal MCBJ devices, we detected for the radical **13** a zero-bias peak in the differential conductance *dI/dV*, which persists along the stretching junctions. Such stability suggests that the origin of the zero-bias peak is intrinsic of the PTM radical molecule. As a reference we measured the **αH-13**, showing that this system does not present a peak at zero-bias. In this way we can ensure that the origin of the zero-bias resonance is intrinsic of the radical molecule. In order to verify the Kondo character of this zero-bias resonance, we performed measurements at different temperatures and varying the magnetic field in a configuration of three terminal EMBJ devices.

The measurements performed in EMBJ configuration at different temperatures show temperature dependence typical from a Kondo resonance, ranging from a weak coupling (T = T_K ≈ 3 K) to a strong coupling regime (T<< T_K = 30mK). Furthermore, the experiments performed at variable magnetic field shows the expected onset of the Kondo resonance splitting. Besides, the DFT calculations exhibited that the SOMO orbital of the PTM radical **13** is the responsible for the Kondo-phenomena. Therefore, the measurement in EMBJ setup at variable temperature and magnetic field, and the DFT calculations, confirms that the zero-bias resonance is due to a Kondo state in the strong coupling regime.

These results prove, for the first time, the detection of the unpaired spin of an organic radical in a two and three terminal solid states configuration, and open the door to the utilization organic radical molecules as spintronic devices.

5.2.2 STM-BJ

The conductance of the PTM-bis-thiophene molecule was also measured by STM-BJ technique.[‡] The conductance histograms (Figure 13) were obtained form few thousand of conductance traces, and show two conductance peaks G_L and G_H (Low and High). These two peaks could be attributed

---

[†] In collaboration with the group of Prof.Herre van der Zant from Delft University of Technology.
[‡] In collaboration with Dr. Alexander Rudnev from Bern University.

to two different conformations of molecule **13** between the electrodes (Figure 14). The higher conductance is attributed to a structure when the S atom of the thiophene linkers is attached to a protruding Au atom, while when the thiophene linkers are placed on a rather flat Au region the conductance is lower. Notably, these conductance values are quite similar to the values obtained with MCBJ, proving that this molecule forms very robust and reproducible junctions so when measured under different techniques similar results are achieved.

These results are preliminary and now some DFT calculations are being performed[§] to understand more clearly the configuration of the molecules between the electrodes that can give rise to these two peaks.
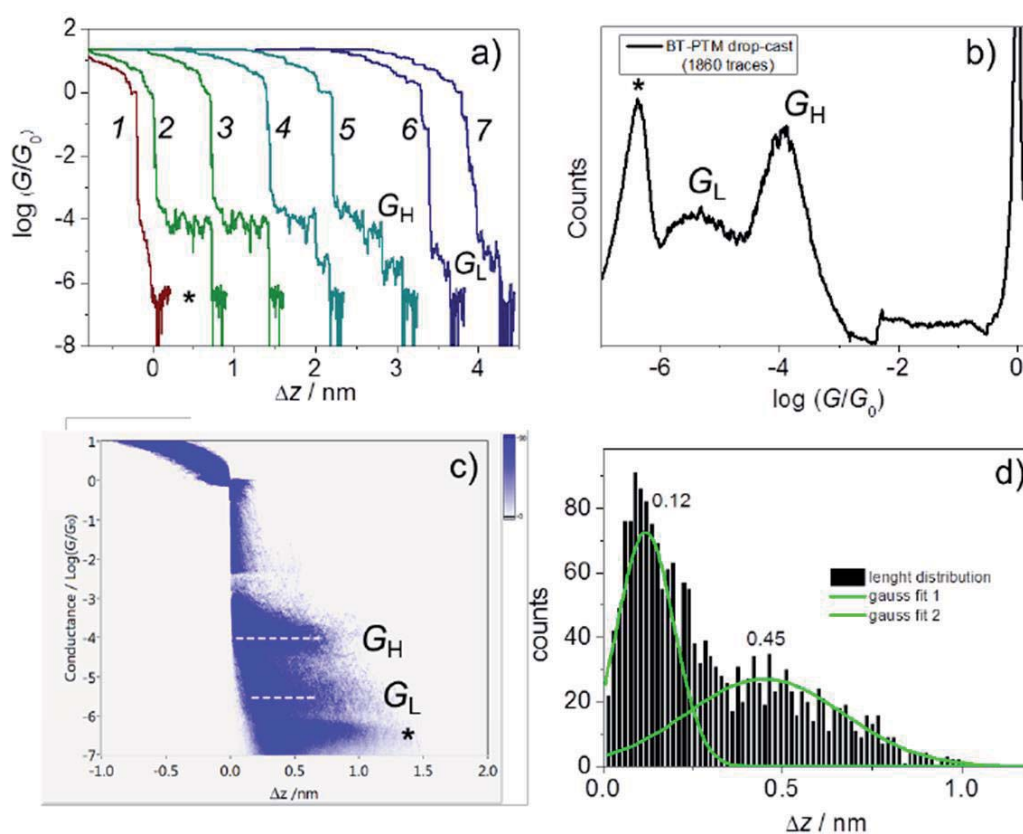
Figure 13: (a) Individual conductive traces without and with molecular plateaus for **13**, obtained by STM-BJ with V_{bias} = 0.1 V and a stretching rate of 87 nm s^{-1}. (b) 1D and (c) 2D conductance histograms for **13**. The asterisk indicates the noise level of the set-up. The small spike at $log(G/G_0) \sim -2.2$ in panel (b) is an artefact related to the switching of the amplifier stage. (d) Characteristic length distribution between $10^{-4.6}$ G_0 and $10^{-0.3}$ G_0. The measurements were done at room temperature in argon atmosphere after drop casting 20 µL of 0.08 mM **13** in dichloromethane and drying in a gentle argon stream.

[§] In collabortion with Dr. Ivan Rungger from Trinity College of Dublin, and Dr. Andrea Droghetii from University of the Basque Country.
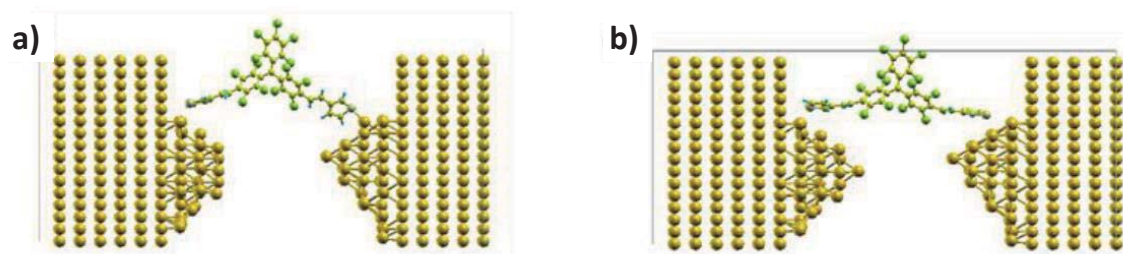
Figure 14: Calculated conformational structures for (a) High and (b) Low conductance for the radical **13**. The calculated conductance values are $10^{-3.7}$ G_0 for (a) and $10^{-4.4}$ G_0 for (b).

6. PTM integration on carbon break junctions.

An alternative strategy to the metallic electrodes in junctions is the use of carbon electrode-molecule junctions, where well structure carbon materials (carbon nanotubes and graphene) are used as a point of contact and electrode. The carbon electrodes are very promising due to their unique advantages: (i) they are entirely composed by sp^2-hybridized carbon atoms arranged in a honeycomb structure, thus giving stability up to high temperatures, and also offering a good compatibility with biological molecules; (ii) the carbon structures exhibit extraordinary electronic properties with high stability and chemical flexibility due to their π-conjugated skeletons; (iii) they are easily available in large areas through bottom-up chemical approaches and can be easily micro-/nanofabricated onto a large range of substrates with high accuracy; (iv) another advantage is that carbon electrodes allows for a large variety of possibilities to anchor diverse molecules as compared to metal electrodes. While with the metal electrodes mainly covalent unions with for example thiol and amine groups are used, the carbon-based materials can not only be functionalized covalently through organic chemistry techniques but also via physisorbed π–π stacking interactions of aromatic rings.

For all of these features, carbon materials are a very good choice to use as nanoscale electrode materials in molecular electronics and spintronics.[52]

6.1 Design and Synthesis of the molecule

Motivated by the advantages described before, van der Zant's group, reported in 2011 the fabrication of a break junction device, with two carbon electrodes generated by electroburning of graphene between which a curcuminoid molecule with two anthracene groups was trapped (Figure 15a and 15b).[53] The anthracene-groups are extended π-conjugated systems that interact strongly with the π-system of the top graphene layer, providing a strong anchoring to the electrodes, while the curcuminoid molecule has a high π-electron density that can mediate charge transport (Figure 15c)
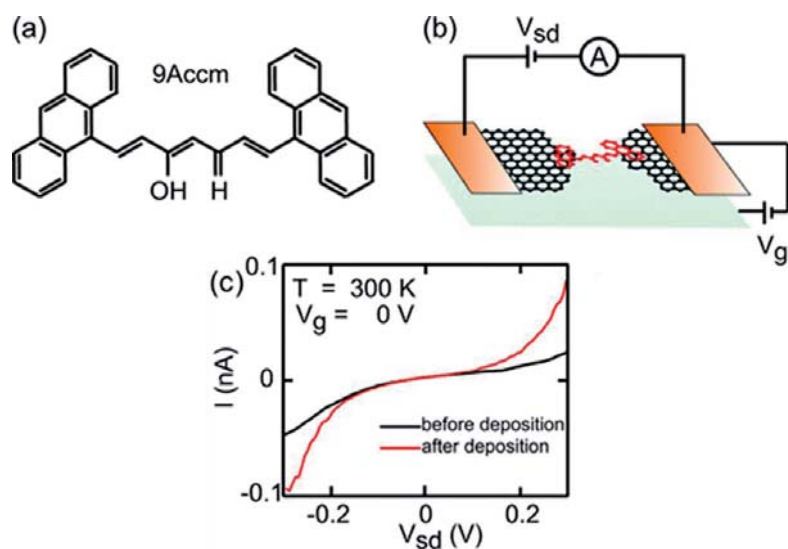
Figure 15: a) Chemical structure of the anthracene terminated curcuminoid wires (1,7-(di-9-anthracene)-1,6-heptadiene-3,5-dione). (b) Schematic representation of a single 9Accm molecule bridging a graphene nanogap. c) I–V-characteristics of the nanogapped electrodes before and after being bridged by the 9Accm molecules at 300 K. While the conductance at low bias superimposes with the empty gap characteristic, at higher bias a clear current increase is observed.[53]

Inspired by this work, we designed a PTM molecule to be integrated into carbon break-junction devices in order to study the conductance through the PTM molecule with this set up, and compare the results with the previous experiments performed with gold electrodes. Hence, we planned to synthesize a molecule with a PTM core containing two groups able to interact with the π-system of graphene.

We proposed a new PTM molecule with two pyrene groups able to get a strong π-interaction with carbon electrodes, and also conjugated with the PTM so then they can provide a high conductance through the molecule. The projected molecule **14**, could be obtained from the corresponding αH (**αH-14**) with the previously described procedure. The **αH-14** derivative was synthesized by Wittig-type coupling between 1-pyrene carboxaldehyde and PTM bis-phosphonate derivative (Scheme 2). Following this procedure, we obtained the radical 14 and **αH-14** molecules in good yield. These two molecules present excellent characteristics to be integrated in single-molecule devices for studying their transport properties with carbon-based devices.
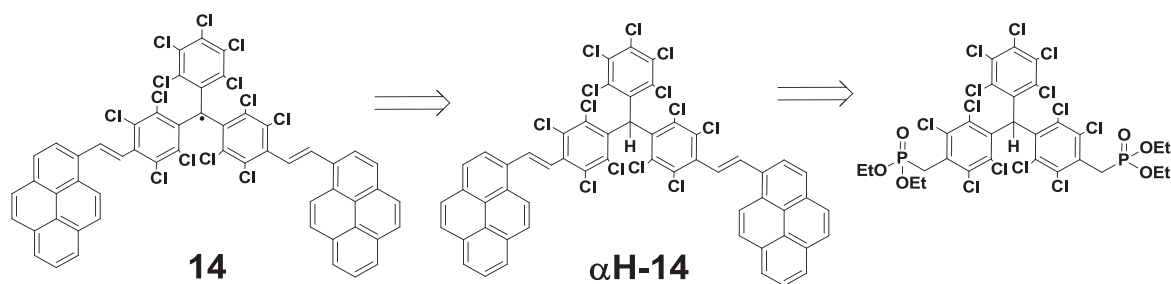
Scheme 2: Retro-synthetic pathway to synthesize the radical PTM-bis-pyrene **14** and the corresponding αH-14.

Compound **αH-14,** radical **14** and the reduced anionic form of **14,** also present very interesting and distinct optical properties. We have carefully studied the absorbance/fluorescence characteristics of these molecules, and also those of the PTM monosubstituted with just one pyrene, and shown that they can be exploited in logic gate devices. This study named "Pyrene-Based Dyad and Triad Leading to a Reversible Chemical and Redox Optical and Magnetic Switch" was published in *Chem. Eur. J*. **2015**, *21*, 5504 – 5509. In this work, we showed that the αH PTM-pyrene molecules (monosubstituted and bisubstituted) the fluorescence due to the pyrene is the same as in other pyrene-substituted derivatives, whereas in the radicals and the corresponding anions species there is a clear quenching of the fluorescence, which is more efficient in the case of the radicals. The quenching mechanism was attributed to the fact that the PTM-centred HOMO of the anionic species and the SUMO of the radicals lie on the middle of the HOMO-LUMO gap of pyrene. Furthermore, by a simple acid-base or redox reactions the compounds mimic the "AND" Boolean logic operations. Additionally, the redox activity of PTM radicals has been exploited to fabricate electrochemical switches with optical (i.e., absorption and fluorescence) and magnetic response.

6.2 Break Junctions

6.2.1 STM-BJ

Break-junction experiments with carbon-based electrodes were performed[**] with Highly Ordered Pyrolytic Graphite (HOPG) as a substrate and pyrolytic graphite tips.

The conductance of the PTM **14** integrated in a carbon junction was measured in STM-BJ experiments at room temperature. The results of the conductance experiments are shown in Figure 11. Two conductance plateaus were observed on some individual conductance traces (Figure 16), which corresponds to two conductance peaks G_H and G_L assigned to conductance of the PTM in contact with carbon electrodes. We think that G_H and G_L correspond to different junction configuration of the molecules with the electrodes.

[**] In collaboration with Dr. Alexander Rudnev from Bern University.

This promising investigation is in early stage, and it is necessary to perform more experiments to understand more clearly the conductance phenomena involved in these devices.
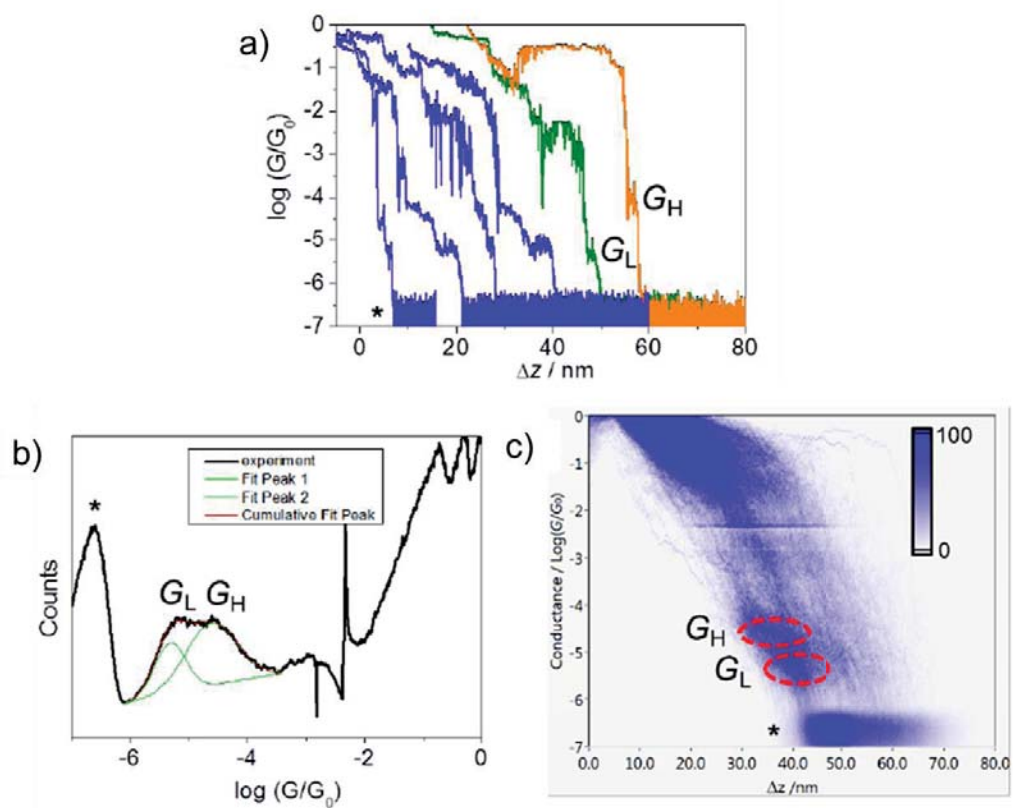
Figure 16: a) Individual conductive traces of the molecule **2** obtained by STM-BJ with V_{bias} = 0.1 V and a stretching rate of 435nm s-1. b) 1D and c) 2D conductance histograms for molecule **2**. The asterisk indicates the noise level of the set-up. The small spikes at log(G/G0) ~ -2.2 and -2.4 in panel b) are artifacts related to the switching of the amplifier stage. The measurements were done at room temperature: after drop casting 10 µL of 0.1 mM x in dichloromethane on HOPG and drying in gentle argon stream. STM tip was graphitic.

7. Summary

We successfully achieved the proposed objective of synthesizing molecules able to form single molecule devices which contain a PTM radical molecule. From these single molecule devices, we have studied the conductivity and the magnetic behaviour of the PTM free radical.

On one hand, we have designed synthesized and characterized the PTM radical derivative **13** that can be integrated in gold junctions due to the two thiophenes moieties acting as anchoring groups.

With this molecule, we were able to fabricate single molecule gold junctions through three different and complementary techniques (MCBJ, EMCBJ and STM-BJ) which allowed us to study the conductivity of a single PTM molecule, demonstrating that the PTM radical junction is two orders of magnitude more conductive that the one fabricated with the close-shell precursor α**H-13**. Through STM-BJ methodology, we could distinguish two different conductance regimes, which were associated to the fact that the radical **13** can adopt two conformations into the break-junction.

Importantly, through MCBJ and EMCBJ devices a Kondo peak was detected indicating that the localized magnetic moment of PTM radical interacts with conducting electrons. This is the first time that the Kondo effect has been observed for organic radicals in single molecule solid devices.

We have also synthesized a PTM radical derivative with two pyrene moieties (**14**), which can be integrated in carbon-based break-junctions through van der Walls interactions between the pyrene groups and the carbon electrodes.

With the PTM derivative **14** we were able to fabricate single molecule break-junctions by STM-BJ methodology using HOPG as substrate and pyrolytic graphite as STM tip, allowing to measure the conductivity of the radical **14** in carbon- based break-junctions. With these devices, we observed that the radical **14** have two different conductivity which was interpreted with the fact that the radical adopts two conformations within the carbon break- junctions.

References

[1] N. F. Mott, *Proc. R. Soc. London, Ser. A,* 1936, **153**, 699-717.

[2] M. N. Baibich, J. M. Broto, A. Fert, F. Nguyen Van Dau, F. Petroff, P. Etienne, G. Creuzet, A. Friederich and J. Chazelas, *Phys. Rev. Lett*., 1988, **61**, 2472–2475.

[3] G. Binasch, P. Gru¨ nberg, F. Saurenbach and W. Zinn, *Phys. Rev.B,* 1989, **39**, 4828–4830.

[4] I. Zutic, J. Fabian and S. Das Sarma, *Rev. Mod. Phys*., 2004, **76**, 323–410.

[5] *Semiconductor Spintronics and Quantum Computation*, ed. D. D. Awschalom, D. Loss and N. Samarth, Springer-Verlag, Berlin Heidelberg, Germany, 2002.

[6] D. D. Awschalom and M. E. Flatté, *Nat. Phys*., 2007, **3**,153–159.

[7] V. Dediu, M. Murgia, F. C. Matacotta, C. Taliani and S. Barbanera, *Solid State Commun*., 2002, **122**, 181–184.

[8] A. R. Rocha, V. Garcia Suarez, S. W. Bailey, C. J. Lambert, J. Ferrer and S. Sanvito, *Nat. Mater*., 2005, **4**, 335–339.

[9] S. Sanvito*, Chem. Soc. Rev.*, 2011, **40**, 3336-3355.

[10] N. Crivillers, M. Mas-Torrent, C. Rovira, J. Veciana, *J. Mater Chem.,* 2012, **22**, 13883-13890.

[11] (a) T. A. Fulton and G. J. Dolan, *Phys. Rev. Lett*., 1987, **59**, 109; (b) Y. M. B. Yuli and V. Nazarov, *Quantum transport. Introduccution to Nanoscience*, Cambridge University Press, 2009.

[12] G. Giuliani, *Europhys. Lett.*, 2008, **81**, 60002.

[13] J. Chen, M. A. Reed, A. M. Rawlett and J. M. Tour, *Science*, 1999, **286**, 1550.

[14] J. Kessler, *Polarized Electrons*, Springer Verlag, Berlin, Heidelberg, 1976.

[15] L. Bogani and W. Wernsdorfer, *Nat. Mater*., 2008, **7**, 179.

[16] J. S. Moodera, T. S. Santos, T. Nagahama, *J. Phys.: Condens. Matter,* 2007, **19**,165202.

[17] L. Kouwenhoven and L. Glazman, *Phys. World*, 2001, **14**, 33.

[18] D. Gatteschi and R. Sessoli, *Angew. Chem., Int. Ed*., 2003, **42**, 268.

[19] (a) J. R. Friedman, M. P. Sarachik, J. Tejada and R. Ziolo, *Phys. Rev. Lett*., 1996, **76**, 3830; (b) L. Thomas, F. Lionti, R. Ballou, D. Gatteschi, R. Sessoli and B. Barbara, *Nature*, 1996, **383**, 145.

[20] A. Bousseksou, G. Molnar, L. Salmon and W. Nicolazzi, *Chem. Soc. Rev*., 2011, **40**, 3313.

[21] (a) H. Mauser, N. Hommes, T. Clark, A. Hirsch, B. Pietzak, A. Weidinger and L. Dunsch, *Angew. Chem., Int. Ed. Engl.*, 1997, **36**, 2835. (b) Y. Yasutake, Z. J. Shi, T. Okazaki, H. Shinohara and Y. Majima, *Nano Lett.*, 2005, **5**, 1057.

[22] (a) R. G. Hicks, *Org. Biomol. Chem.*, 2007, **5**, 1321; (b) I. Ratera and J. Veciana, *Chem. Soc. Rev.*, 2012, **41**, 303.

[23] R. C. Chiechi, E. A.Weiss,M. D. Dickey and G. M. Whitesides, *Angew. Chem., Int. Ed.,* 2008, **47**, 142–144.

[24] S. Y. Sayed, J. A. Fereiro, H. Yan, R. L. McCreery and A. J. Bergren, *Proc. Natl. Acad. Sci. U. S. A.*, 2012, **109**, 11498–11503.

[25] J. Park, A. N. Pasupathy, J. I. Goldsmith, C. Chang, Y. Yaish, J. R. Petta, M. Rinkoski, J. P. Sethna, H. D. Abruna, P. L. McEuen, D. C. Ralph, *Nature*, 2002, **417**, 722.

[26] W. J. Liang, M. P. Shores, M. Bockrath, J. R. Long, H. Park, *Nature*, 2002, **417**, 725.

[27] M. Tsutsui, M. Taniquchi, *Sensor*, 2012, **12**, 7259-7298.

[28] A. M. Christian, M. v. R. Jan and S. J. v. d. Z. Herre, *Nanotechnology*, 2010, **21,** 265201.

[29] M. L. Perrin, C. J. O. Verzijl, C. A. Martin, A. J. Shaikh, R. Eelkema, J. H. van Esch, J. M. van Ruitenbeek, J. M. Thijssen, H. S. J. van der Zan, D. Dulic*, Nat. Nanotechnol.*, 2013, **8**, 282–287.

[30] E. Beall, X. Yin, D. H. Waldeck, E. Wierzbinski, *Nanoscale,* 2015, **7**, 14965-14973.

[31] C. Huang, A. V. Rudnev, w. Hong, T. Wandlowski, Chem. Soc. Rev. 2015, 44, 889-901.

[32] D. Cahen and A. Kahn, *Adv. Mater.*, 2003, **15**, 271–277.

[33] S. Y. Quek and K. H. Khoo, *Acc. Chem. Res*., 2014, **47**, 3250–3257.

[34] (a) K. S. Thygesen, K. W. Jacobsen, *Phys. Rev. Lett*. 2005, **94**, 036807. (b) K. H. Khoo, J. B. Neaton, H. J. Choi, S. G. Louie, *Phys. Rev. B.* 2008, **77**, 115326.

[35] (a) J. Park, A. N. Pasupathy, J. I. Goldsmith, C. Chang, Y. Yaish, J. R. Petta, M. Rinkoski, J. P. Sethna, H. D. Abruna, P. L. McEuen, D. C. Ralph, *Nature* 2002, **417**, 722–725. (b) S. H. Choi, B. Kim, C. D. Frisbie, *Science,* **008, 320**, 1482–1486.

[36] M. Galperin, M. A. Ratner, A. Nitzan, *J. Phys.: Condens. Matter.* 2007, **19**, 103201.

[37] D. Xiang, H. Jeong, T. Lee, D. Mayer, *Adv. Mater.*, 2013, **25**, 4845-4867.

[38] T. Kim, H. Vázquez, M. S. Hybertsen, L. Venkataraman, *Nano. Lett*., 2013, **13**, 3358-3364.

[39] C.-H. Ko, M.-J. Huang, M.-D. Fu, C.-H. Chen, *J. Am. Chem. Soc.*, 2009, **132**, 756-764.

[40] F. Chen, X. Li, J. Hihath, Z. Huang, N. Tao, *J. Am. Chem. Soc.*, 2006, **128**, 15874-15881.

[41] C. R. Arroyo, E. Leary, A. Castellanos-Gómez, G. Rubio-Bollinger, M. T. González, N. Agraït, *J. Am. Chem. Soc.*, 2011, **133**, 14313-14319.

[42] (a) T. Markussen, R. Stadler and K. S. Thygesen, *Nano Lett.*, 2010, **10**, 4260–4265. (b) C. J. Lambert, *Chem. Soc. Rev.*, 2015, **44**, 875—888.

[43] H. V. C. M. Guédon, T. Markussen, K. S. Thygesen, J. C. Hummelen, S. J. van der Molen, *Nat. Nanotechnol.*, 2012, **7**, 305-309.

[44] M. Baghernejad, X. Zhao, K. B Orson, M. Füeg, P. Moreno-García, A. V. Rudnev, V. Kaliginedi, S. Vesztergom, C. Huang, W. Hong, P. Broekmann, T. Wandlowski, K. S. Thygesen, M. Bryce. *J. Am. Chem. Soc.,* 2014, **136**, 17922–17925.

[45] J. L. Hironari Isshiki, K. Katoh, T. Morita, B. K. Breedlove, M. Yamashita and T. Komeda, *J. Am. Chem. Soc.,* 2013, **135**, 651-658.

[46] Y. Zahng, S. Kahle, T. Herden, C. Stroh, M. Mayor, U. Schlickum, M. Ternes, P. Wahl and K. Kern, *Nat. Comm*. 2013, **4**, 2110.

[47] S. Müllegger, M. Rashidi, M. Fattinger, R. Koch, *J. Phys. Chem. C*, 2013, **117**, 5718-5721.

[48] K. Tagami, M. J. Tsukada, *Phys. Chem. B* , 2004, **108**, 6441.

[49] M. Smeu, G. A. DiLabio, *J. Phys. Chem. C,* 2010, **114**, 17874.

[50] C. R. Arroyo, S. Tarkuc, R. Frisenda, J. S. Seldenthuis, C. H. M. Woerde, R. Eelkema, F. C. Grozema and H. S. J. van der Zant, *Angew. Chem., Int. Ed*., 2013, **52**, 3152–3155.

[51] C. Rovira, D. Ruiz-Molina, O. Elsner, J. Vidal-Gancedo, J. Bonvoisin, J.-P. Launay, J. Veciana, Chem. Eur. J. 2001, 7, 240.

[52] The Molecular Electronics Special Issue. *Nat. Nanotechol*. 2013, **8**, 377-467.

[53] F. Prins, A. Barreiro, J. W. Ruitenberg, J. S. Seldenthuis, N. Aliaga-Alcalde, L. M. K. Vandersypen and H. S. J van der Zant, *Nano. Lett.* 2011, **11**, 4607-4611.

Publication 4

Title	Kondo Effect in a Neutral and Stable All Organic Radical Single Molecule Break Junction
Authors	Riccardo Frisenda, Rocco Gaudenzi, Carlos Franco, Marta Mas-Torrent, Concepció Rovira, Jaume Veciana, Isaac Alcon, Stefan T. Bromley, Enrique Burzurí, and Herre S. J. van der Zant
Publication	*Nano Letters,* **2015**, *15(5),* 3109 DOI: 10.1021/acs.nanolett.5b00155

Kondo Effect in a Neutral and Stable All Organic Radical Single Molecule Break Junction

Riccardo Frisenda,[†] Rocco Gaudenzi,[†] Carlos Franco,[‡] Marta Mas-Torrent,[‡] Concepció Rovira,[‡] Jaume Veciana,[‡] Isaac Alcon,[§] Stefan T. Bromley,[§,∥] Enrique Burzurí,*[,†] and Herre S. J. van der Zant[†]

[†]Kavli Institute of Nanoscience, Delft University of Technology, Lorentzweg 1, 2628 CJ, Delft, The Netherlands
[‡]Institut de Ciéncia de Materials de Barcelona (ICMAB-CSIC) and CIBER-BBN, Campus de la UAB, 08193, Bellaterra, Spain
[§]Departament de Química Física and Institut de Química Teórica i Computacional (IQTCUB), Universitat de Barcelona, E-08028 Barcelona, Spain
[∥]Institició Catalana de Recerca i Estudis Avançats (ICREA), 08010 Barcelona, Spain

ⓢ *Supporting Information*

ABSTRACT: Organic radicals are neutral, purely organic molecules exhibiting an intrinsic magnetic moment due to the presence of an unpaired electron in the molecule in its ground state. This property, added to the low spin—orbit coupling and weak hyperfine interactions, make neutral organic radicals good candidates for molecular spintronics insofar as the radical character is stable in solid state electronic devices. Here we show that the paramagnetism of the polychlorotriphenylmethyl radical molecule in the form of a Kondo anomaly is preserved in two- and three-terminal solid-state devices, regardless of mechanical and electrostatic changes. Indeed, our results demonstrate that the Kondo anomaly is robust under electrodes displacement and changes of the electrostatic environment, pointing to a localized orbital in the radical as the source of magnetism. Strong support to this picture is provided by density functional calculations and measurements of the corresponding nonradical species. These results pave the way toward the use of all-organic neutral radical molecules in spintronics devices and open the door to further investigations into Kondo physics.

KEYWORDS: *Single molecule, break junction, electrical transport, Kondo effect, organic radical, magnetism*
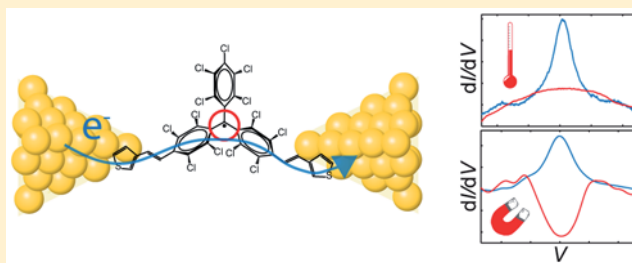
Organic free radicals were first synthesized in the 1900s and recently have been explored as building blocks for magnetic materials.[1−3] Thanks to the unpaired electron, these molecules are paramagnetic in their neutral state and have low spin—orbit coupling and weak hyperfine interactions due to their all-organic composition. Because of these properties, absent in transition metal-based magnetic compounds, organic radicals have recently attracted attention in molecular spintronics,[4,5] where long spin coherence times are required to preserve the information encoded in the electronic spin.

A number of studies on transport through organic radicals have lately appeared both on assemblies as well as individual molecules. An example of the first type can be found in refs 6−8, where a self-assembled monolayer of radical molecules is studied employing a conductive AFM. Investigations on individual molecules have been only focused on scanning tunneling spectroscopy studies of the Kondo effect in π-extended organic radical molecules physisorbed on surfaces.[9−11] However, a demonstration that a neutral organic radical molecule can retain its magnetic moment when integrated in a solid-state device, a crucial step toward future spintronics applications, is so far absent, which is in contrast to analogous results reported for molecules containing transition metals.[12]

In this Letter, we report on the detection of the unpaired spin of a neutral and stable polychlorotriphenylmethyl (PTM) radical molecule combining for the first time two and three-terminal solid-state devices. The detection is based on the observation of a Kondo resonance, arising from the many-body interaction between the conduction electrons and the magnetic impurity.[13,14] Kondo temperatures T_K of about 3 K are extracted and found to be rather independent of the elastic/inelastic conductance background and mechanical displacement of the junction, which is in contrast with other molecular families.[12,15] In addition, measurements on the nonradical PTM-αH counterpart show no Kondo signatures. These observations strongly support the picture that the magnetic impurity originates from the radical unpaired electron: a magnetic impurity well-protected against variations of the molecular arrangement and weakly coupled to the electron bath in the leads. This intrinsic Kondo effect in a neutral molecule

should be contrasted to the one observed in other organic molecules[15−19] where the magnetism is induced by a delocalized charge added with a gate voltage or by electron transfer from the leads, that is, in molecular systems that are charged and not intrinsically paramagnetic in their neutral state. This Kondo effect should also be contrasted with the one observed in transition metal-based molecules.[12,20,21] Kondo physics in these molecules arises from 3d orbitals making the Kondo temperature sensitive to external stimuli like stretching[12] or voltage.[21] Moreover, for spintronics purposes 3d orbitals of transition metals are expected to contribute more to the spin decoherence of the flowing electrons compared to the p orbitals of organic radicals.

A schematic of the PTM radical molecule is presented in Figure 1a. The unpaired electron is mainly located in the
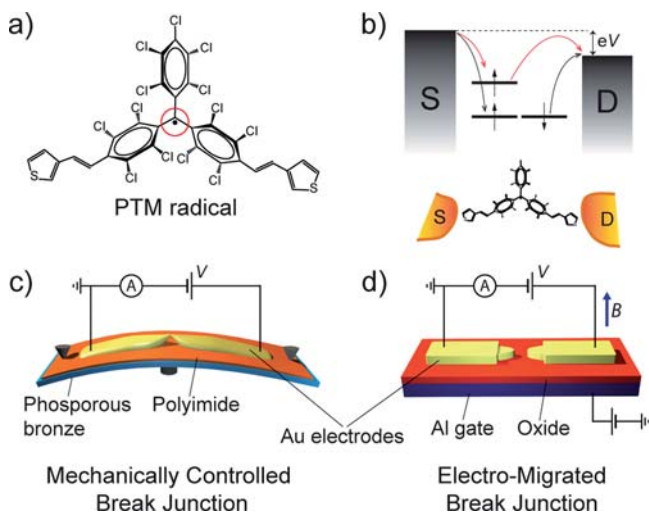

Figure 1. Two and three-terminal PTM radical-based devices. (a) Sketch of the neutral PTM radical molecule. The radical center resides on the carbon atom located in the middle of three chlorinated phenyl rings and is marked with a red circle. (b) Simple model of the energy levels/orbitals involved in the transport through the molecule. The HOMO orbital accounts for the spin-unpolarized background transport (black arrows), the radical-deriving SOMO orbital is the source of spin-correlated transport (red arrows). Below, the ideal arrangement of the molecule between source (S) and drain (D) electrodes is shown. (c) Two-terminal mechanically controlled break junction device. (d) Three-terminal electromigrated break junction transistor.

trivalent central carbon atom, shielded by three chlorinated phenyl rings arranged in a propeller-like configuration that provide stability against chemical reactions (see ref 22 and references therein). Two additional thiophene rings are bonded, through ethylene bridges, to the triphenylmethyl backbone and serve as linkers to the gold electrodes (Au−S interactions). The ideal physical arrangement of the molecule between the source and drain electrodes and the associated off-resonant transport schematic are depicted in Figure 1b. We can identify a spin-unpolarized background transport channel (black arrows) through the highest occupied molecular orbital (HOMO) and a spin-flipping Kondo-mediated transport channel (red arrows). This additional channel arises from the singly occupied molecular orbital (SOMO) and is responsible for the paramagnetism.

Measurements on the molecule were performed in two complementary setups: the two-terminal mechanically con-

trolled break junction (MCBJ) and the three-terminal electro-migrated break junction (EMBJ) setups, respectively depicted schematically in Figure 1c,d. MCBJs allowed for a study of the Kondo feature on a large number of samples as a function of electrode displacement. More extended detailed measurements as a function of temperature, magnetic field, and gate voltage were conducted with the EMBJs.

Results. *Mechanically Controlled Break Junctions.* Low-temperature I−V measurements are carried out on PTM molecular junctions formed with MCBJ nanoelectrodes. Here a large number of single-molecule junctions and different molecule−metal configurations can be studied by repeatedly breaking up the electrodes and pushing them together. We have measured in total 86 junctions in the presence of the PTM radical from which 31 formed molecular junctions. Interestingly, 20% of the molecular junctions showed a zero-bias peak in the differential conductance dI/dV. Figure 2a shows the
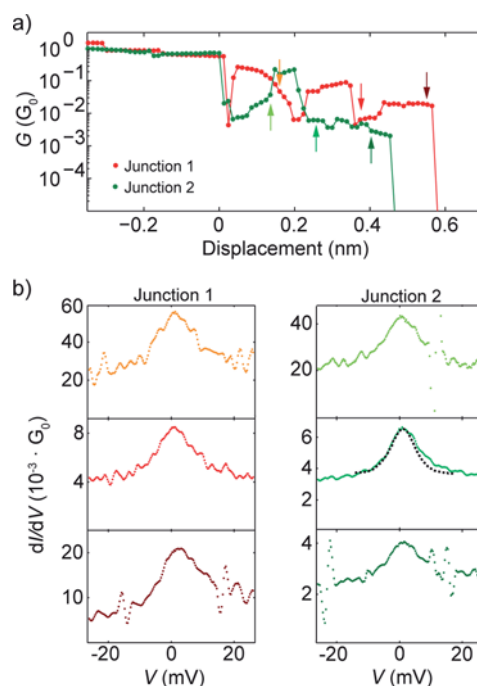
Figure 2. Two PTM radical samples showing a Kondo resonance investigated with mechanically controlled break junctions. (a) Conductance versus displacement traces for two different junctions measured with MCBJ. Each data point is extracted from an individual I−V. (b) Differential conductance traces measured at displacements indicated by the arrows in (a). Measurements are taken at $T \approx 6$ K. The dashed line corresponds to a different measurement on a PTM radical in EMBJ at $T \approx 4.5$ K. The trace is offset vertically. The FWHM and the conductance levels are comparable with both techniques. The slight variations in the peak width and the noise level may be due to coupling fluctuations at the molecule/metal interface while stretching.

zero-bias conductance, extracted from I−Vs at the corresponding position, as a function of the electrode displacement for two different PTM radical junctions. Both conductance traces show a plateau at 1 G_0 due to transport through a single Au atom, indicating atomically sharp electrodes. For conductance values below 1 G_0, the molecular junctions exhibit plateaus; this nonexponential decay with the interelectrode distance signals the presence of a molecule. At displacements of about 0.5 nm, both junctions exhibit an abrupt jump to conductance values

below the noise level of 10^{-6} G_0, indicating the rupture of the molecular junction. The fluctuations observed in conductance around the 10^{-2} G_0 value are to be assigned to atomic rearrangements at the metal/molecule interface or inside the molecule.[23,24] The current I is measured versus bias voltage V at every step of the junction stretching and thereafter dI/dV is obtained by taking the numerical derivative with respect to V. Figure 2b shows three examples at the positions marked by the colored arrows in Figure 2a. All traces show a zero-bias anomaly that persists along the stretching of the junction even if the average conductance background changes. Such mechanical stability indicates that the origin of the zero-bias anomaly is intrinsic to the PTM radical molecule and is not sensitive to stretching-dependent variations of the interface between the anchoring groups and the electrodes, in contrast to refs 12 and 15.

As a reference, we have also measured 95 junctions in the presence of the nonradical αH counterpart. Molecular junctions are formed in 30 cases, making the junction formation probability approximately the same for the radical and nonradical species and equal to 35%. In contrast to the radical molecule, the nonradical one shows no zero-bias peak in all the cases, see Supporting Information. In this way we can ascribe the origin of the zero-bias resonance to an intrinsic property of the radical molecule, as compared to the nonradical one. Provided that the only difference between radical and nonradical molecule lies in the open or closed shell electronic structure, it is reasonable to assign the zero-bias feature to the presence of the unpaired electron in the radical. In order to verify the Kondo character of this zero-bias resonance, measurements in temperature and magnetic field are carried out.

Electromigrated Break Junctions. To investigate in more detail the zero-bias resonance we have employed the EMBJ setup. With this setup, we perform low-noise measurements at temperatures ranging from $T \approx 30$ mK to $T \approx 4.5$ K, magnetic fields up to 8 T, and gate voltage. Nanojunctions are prepared following the electromigration method.[25,26] This technique, together with device fabrication, preparation, and deposition of the molecular solution, is described in Methods section. We record the formation of 25 molecular junctions out of the 126 measured devices. From those, a zero-bias peak in dI/dV appears in 11 samples. Differential conductance measurements as a function of the gate voltage showed off-resonant transport in the entire accessible gate window, see Supporting Information. This is a fingerprint of a substantial HOMO−LUMO gap. In Figure 3, the temperature and magnetic field characterization for two samples are presented. Figure 3a,b shows dI/dV spectra at different temperatures. A zero-bias resonance is clearly visible. In Figure 3c,d, the corresponding conductance at $V = 0$, $dI/dV|_{V=0}$, is plotted as a function of temperature on a logarithmic scale. The typical temperature dependence expected from a Kondo resonance is observed, ranging from the intermediate (weak coupling) $T \approx T_K$ to the low-energy (strong coupling) regime for $T \ll T_K$, where the asymptotic value of $dI/dV|_{V=0}$ is reached. For a direct comparison between traces shown here in the weak coupling regime and those measured with the MCBJ in Figure 2, we refer the reader to the Supporting Information. We notice here the three-order of magnitude difference in the conductance values observed between sample A and sample B. In addition, in Figure 3b two side shoulders weakly dependent on temperature are visible; such steplike features, occurring also
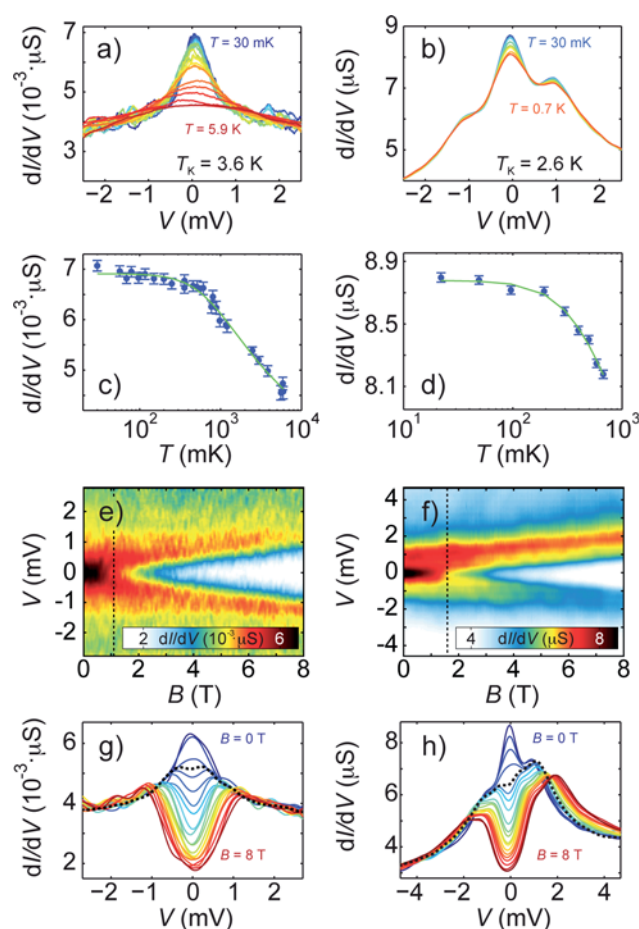
Figure 3. Two PTM radical samples exhibiting Kondo resonance investigated with electromigrated break junctions. (a,b) dI/dV traces ($1G_0 \approx 77$ μS) of the radical for temperatures indicated in the panels. (c,d) Peak height ($dI/dV|_{V=0}$), extracted from (a,b), as a function of temperature on a logarithmic scale. The solid lines are fits to a spin-1/2 Kondo with parameters $G_0 = 3.8$ nS, $G_b = 3.1$ nS, and $T_K = 3.6$ K for (c) and $G_0 = 3.1$ nS, $G_b = 5.6$ nS, and $T_K = 2.6$ K for (d) (see text). (e,f) dI/dV color map measured as a function of the magnetic field B and bias voltage V at $T = 590$ mK and $T = 25$ mK, respectively. Black dashed lines mark the onset of Kondo splitting. (g,h) dI/dV spectra extracted from (e,f) with a regular spacing of $\Delta B = 0.4$ T. The Kondo peak is seen splitting at $B_c \approx 1.2$ T and $B_c \approx 1.6$ T, respectively, as black dashed traces indicate.

at higher harmonically spaced bias values, are observed in about 50% of the measured samples. The harmonic spacing together with their nonexponential temperature dependence indicate a vibrational origin.[27,28]

A fit to the formula describing the conductance G as a function of the temperature for spin-1/2 Kondo[29]

$$G(T) = G_0 \left[1 + (2^{1/0.21} - 1) \left(\frac{T}{T_K} \right)^2 \right]^{-0.21} + G_b \tag{1}$$

yields $T_K = 3.6$ K and $T_K = 2.6$ K for the first and second samples, respectively. In 1, G_0 is the conductance in the $T \to 0$ limit, G_b is the background contribution, and T_K is defined so that $G(T_K) - G_b = G_0/2$. From the lower temperature spectra ($T \ll T_K$) of Figure 3a,b, that is, the data points in the flat region of Figure 3c,d, an independent estimation of the Kondo temperature can be obtained. Fitting the Kondo peak with a Lorentzian, the Kondo temperature is extracted from the full

width at half-maximum (Γ_K) of the Lorentzian according to $\Gamma_K \approx 2\sqrt{2}k_B\,T_K$.[30] The obtained values 3.0 and 3.1 K are in agreement with those deduced from the fit to 1.

In Figure 3e,f, the magnetic field dependence of dI/dV in the strong coupling regime ($T \ll T_K$) is shown. Suppression and subsequent Zeeman splitting of the Kondo resonance are observed. An estimation of the g-factor from the Zeeman energy in magnetic field yields $g \approx 2.0 \pm 0.2$. Figure 3g,h displays regularly spaced ($\Delta B = 0.4$ T) linecuts extracted from Figure 3e,f. At $B_c \approx 1.2$ T and $B_c \approx 1.6$ T, respectively, the onset of the Kondo resonance splitting is visible, as marked by the dashed lines in Figure 3e,f. These values are consistent with the expected critical magnetic field given by $B_c \approx 0.5k_B T_K/(g\mu_B)$,[31] above which splitting of the Kondo peak should be observed. Particularly insightful is the field-dependence in Figure 3h, where the Kondo resonance is observed evolving on top of the two side shoulders in an independent way. This behavior further supports the idea of a distinct origin for the two features.

The measurements in the EMBJ setup show a Kondo state in the strong coupling regime in which the three different perturbations all show the expected behavior.[10] This provides a sound estimation of the Kondo temperatures involved. Interestingly, the conductance levels dI/d$V|_{V=0}$ of the two samples shown in Figure 3 exhibit a three-order of magnitude difference due to an increase of the background conductance G_b with a similar G_0/G_b ratio in both cases.

Discussion. To corroborate the experimental findings, we carried out density functional theory (DFT) calculations to model the ground state electronic properties of the PTM radical. We employed the B3LYP hybrid functional[32] with a triple-ζ basis set incorporating polarization and diffuse functions for all atoms. Orbital energies were obtained after first optimizing the structure of the radical molecule in free space using spin-unrestricted calculations with no symmetry constrains. The Gaussian 09 code[33] was used throughout. Optimization of the molecule together with Au atoms to mimic the presence of the electrodes does not show significant variations in the geometric or electronic structure (see Methods). Figure 4 shows the calculated energy level diagram of the valence orbitals of the PTM radical molecule for the two spin channels α and β. HOMO and LUMO exhibit spin
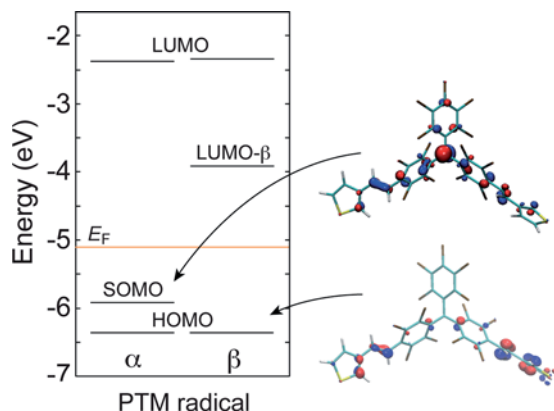
degeneracy, while SOMO and LUMO-β are spin-polarized. The experimental Fermi energy of gold lies close to the middle of the SOMO−LUMO-β energy gap (2 eV). The radical unpaired electron in the SOMO is therefore responsible for the magnetic properties of the system. The proximity of the Fermi level to the HOMO and SOMO occupied levels makes them the most relevant for transport, yielding an hole-mediated off-resonant conductance pathway. The large gap and the position of the Fermi energy are in agreement with the off-resonant transport experimentally observed in the whole gate voltage range, see Supporting Information. The large gap is also consistent with the stability of the Kondo resonance under external variations of the electrostatic environment.

A comparison between the iso-surfaces of the SOMO and the HOMO shows the former as mostly localized on the radical carbon atom with a small component on the backbone and the latter as fully delocalized over the molecular backbone with a considerable weight on the thiophene groups. Worth noticing is the two-lobed p-like shape of the SOMO, indicating a weak hybridization of the atomic orbital and its strong atomic character. Within this framework, we can propose a coherent picture to account for the transport through the PTM radical molecule observed in the experiments. The HOMO provides the spin-independent conductance background, while the SOMO is responsible for the Kondo-correlated phenomena. The strong localization of the SOMO in the carbon protected by the three chlorinated phenyl rings makes the Kondo resonance stable and reproducible in different samples and under stretching. To complete the analysis, DFT calculations using the same model were conducted for the PTM-αH nonradical molecule and the stretched PTM-radical molecule. The energy diagram and isosurfaces of the relevant orbitals are reported in the Supporting Information. The calculations for the PTM-αH nonradical reveal the presence of a fully occupied HOMO with the absence of a SOMO level and its unpaired electron spin. These findings are again in accordance with the experimental absence of Kondo features in the PTM-αH-formed junctions. For the stretched PTM-radical molecule, the energy of the SOMO varies only slightly throughout the stretching. This is in line with the localized character of the SOMO and the experimental findings (see Supporting Information).

Conclusion. Summarizing, we contacted a neutral organic radical molecule in both two and three-terminal solid-state devices. We demonstrate that the magnetic moment of the PTM-radical open-shell system is preserved upon interaction with the metal electrodes and robust against mechanical/electrostatical changes at the electrode-molecule interface. We do this by measuring in mechanically controlled break junctions as well as electro-migrated break junctions a statistically significant presence of fully screened spin-1/2 Kondo features that are insensitive to the electrode displacement and background conductance. We attribute the source of the paramagnetism to the unpaired electron located in the radical carbon center and we substantiate the picture with DFT calculations. Measurements on the closed-shell αH nonradical molecule show no Kondo correlations and therefore corroborate the relation between radical center and magnetic properties. The findings reported here open up the way toward the use of all-organic radical molecules in spintronics devices. From a more fundamental point of view, the overall stability of the unpaired electron of the radical molecule makes it an excellent platform for further investigation on Kondo physics.

Figure 4. Density functional theory calculations. DFT energy level diagram for the two spin channels α and β of the PTM-radical molecule. The orange line indicates the theoretical Fermi energy of gold. HOMO and SOMO levels are depicted together with their relative isosurfaces.

Methods. *Synthesis of PTM Radical and PTM-αH.* The PTM-αH molecule has been synthesized using a Wittig-type coupling between polychlorinated triphenylmethane bis-phosphonate and the 1-thiophenecarboxaldehyde. Treatment of PTM-αH with tetrabutylammonium hydroxide promotes the removal of the acidic proton at the αH position to give the corresponding carbanion that was subsequently oxidized with p-chloranil giving the desired PTM radical.

Preparation of the Solution. The molecular solutions are prepared in a glove-box dissolving 1.8 mg of PTM radical or PTM-αH in 2 mL of nitrogen saturated dichlorobenzene [$c = 1$ mM].

Mechanically Controlled Break Junctions (MCBJ). The mechanically controlled break junctions experiment is performed in vacuum ($p = 1.0 \times 10^{-7}$ mbar) at liquid He temperature. The molecular solution is drop-casted onto the MBCJ sample, whose fabrication is describe elsewhere,[34,35] and the setup is evacuated and cooled down to liquid He temperature. Measurements begin with a metallic constriction, characterized by a conductance of 10 G_0 that, by bending the substrate, can be stretched until it breaks in two nanoelectrodes facing each other, which can eventually be bridged by a molecule. The nanoelectrodes position can be controlled, and by uniting them one can form a new metallic constriction, allowing the exploration of many different junction configurations. During the stretching of the wire, performed in steps of 10 pm, we measure $I-V$ characteristics for each position and control the bending with a feedback on the current/conductance.

Electro-Migrated Break Junctions (EMBJ). Measurements in the electromigrated break junctions are carried out in vacuum ($p < 1.0 \times 10^{-3}$ mbar) in a dilution fridge with a base temperature of 30 mK. Magnetic fields up to 8 T can be applied to the sample. The molecular solution is drop-casted onto a Si/SiO$_2$ chip containing an array of 24 Au bridges 100 nm wide, 400 nm long, and 12 nm thick with an Al/Al$_2$O$_3$ local gate underneath. A nanogap is produced by feedback-controlled electromigration[25] of each of these bridges. As the bridge conductance reaches 3−4 G_0, electromigration is stopped and the wire is let self-break at room temperature.[26] The molecular solution is evaporated while evacuating the chamber and the sample is cooled down. All measurements are performed in dc with low-noise homemade electronics.

DFT Calculations. The molecular geometries of both the radical (spin unrestricted) and the H (closed shell) were optimized with no symmetry constraints using density functional theory as implemented in the Gaussian 09 code.[33] In all cases, the B3LYP[32] hybrid exchange-correlation functional and a triple-ζ 6-311++G(d,p) basis set including polarization functions on all atoms was employed. Different configurations of the PTM molecule, corresponding to different possible orientations of the C≡C-linked thyophene rings were tested in both its radical and αH forms. The lowest energy configurations were then used to extract the reported orbital energies. Optimizations of the PTM molecules with Au atoms placed near the two sulfur atoms to mimic the presence of gold contacts were found to very slightly stabilize all orbital energies by 0.05−0.1 eV. The significant dispersive contribution to the Au−S interaction was taken into account through use of the DFT-D2 method.[36] The interaction strength between a single Au atom and a S atom of the PTM was found to be 0.16 eV. Reported results are those from calculations without Au atoms.

ASSOCIATED CONTENT

Ⓢ Supporting Information

Further details about chemical synthesis, EMBJ and MCBJ measurements, and DFT calculations. Additional measurements with gate and on the αH nonradical molecule are provided. This material is available free of charge via the Internet at http://pubs.acs.org.

AUTHOR INFORMATION

Corresponding Author

*E-mail: e.burzurilinares@tudelft.nl.

Author Contributions

R.F. and R.G. contributed the same.

Notes

The authors declare no competing financial interest.

REFERENCES

(1) Gomberg, M. *J. Am. Chem. Soc.* **1900**, *22*, 757−771.

(2) Hicks, R. G. *Stable Radicals: Fundamentals and Applied Aspects of Odd-Electron Compounds*; John Wiley and Sons, Ltd: New York, 2010.

(3) Ratera, I.; Veciana, J. *Chem. Soc. Rev.* **2012**, *41*, 303−349.

(4) Rocha, A. R.; Garcia-Suarez, V. M.; Bailey, S. W.; Lambert, C. J.; Ferrer, J.; Sanvito, S. *Nat. Mater.* **2005**, *4*, 335−339.

(5) Mas-Torrent, M.; Crivillers, N.; Rovira, C.; Veciana, J. *Chem. Rev.* **2012**, *112*, 2506−2527.

(6) Crivillers, N.; Munuera, C.; Mas-Torrent, M.; Simao, C.; Bromley, S. T.; Ocal, C.; Rovira, C.; Veciana, J. *Adv. Mater.* **2009**, *21*, 1177−1181.

(7) Crivillers, N.; Paradinas, M.; Mas-Torrent, M.; Bromley, S. T.; Rovira, C.; Ocal, C.; Veciana, J. *Chem. Commun.* **2011**, *47*, 4664−4666.

(8) Simao, C.; Mas-Torrent, M.; Crivillers, N.; Lloveras, V.; Artes, J. M.; Gorostiza, P.; Veciana, J.; Rovira, C. *Nat. Chem.* **2011**, *3*, 359−364.

(9) Liu, J.; Isshiki, H.; Katoh, K.; Morita, T.; Breedlove, B. K.; Yamashita, M.; Komeda, T. *J. Am. Chem. Soc.* **2013**, *135*, 651−658.

(10) Zhang, Y. H.; Kahle, S.; Herden, T.; Stroh, C.; Mayor, M.; Schlickum, U.; Ternes, M.; Wahl, P.; Kern, K. *Nat. Commun.* **2013**, *4*, 2110.

(11) Mullegger, S.; Rashidi, M.; Fattinger, M.; Koch, R. *J. Phys. Chem. C* **2013**, *117*, 5718−5721.

(12) Parks, J. J.; Champagne, A. R.; Costi, T. A.; Shum, W. W.; Pasupathy, A. N.; Neuscamman, E.; Flores-Torres, S.; Cornaglia, P. S.; Aligia, A. A.; Balseiro, C. A.; Chan, G. K. L.; Abruna, H. D.; Ralph, D. C. *Science* **2010**, *328*, 1370−1373.

(13) Kondo, J. *Prog. Theor. Phys.* **1964**, *32*, 37−49.

(14) Goldhaber-Gordon, D.; Shtrikman, H.; Mahalu, D.; Abusch-Magder, D.; Meirav, U.; Kastner, M. A. *Nature* **1998**, *391*, 156−159.

(15) Parks, J. J.; Champagne, A. R.; Hutchison, G. R.; Flores-Torres, S.; Abruna, H. D.; Ralph, D. C. *Phys. Rev. Lett.* **2007**, *99*, 026601.

(16) Yu, L. H.; Natelson, D. *Nano Lett.* **2004**, *4*, 79−83.

(17) Osorio, E. A.; O'Neill, K.; Wegewijs, M.; Stuhr-Hansen, N.; Paaske, J.; Bjornholm, T.; van der Zant, H. S. J. *Nano Lett.* **2007**, *7*, 3336−3342.

(18) Scott, G. D.; Natelson, D. *ACS Nano* **2010**, *4*, 3560−3579.

(19) Scott, G. D.; Natelson, D.; Kirchner, S.; Munoz, E. *Phys. Rev. B* **2013**, *87*, 241104(R).

(20) Liang, W.; Shores, M. P.; Bockrath, M.; Long, J. R.; Park, H. *Nature* **2002**, *417*, 725−729.

(21) Wagner, S.; Kisslinger, F.; Ballmann, S.; Schramm, F.; Chandrasekar, R.; Bodenstein, T.; Fuhr, O.; Secker, D.; Fink, K.; Ruben, M.; Weber, H. B. *Nat. Nanotechnol.* **2013**, *8*, 575−579.

(22) Armet, O.; Veciana, J.; Rovira, C.; Riera, J.; Castaner, J.; Molins, E.; Rius, J.; Miravitlles, C.; Olivella, S.; Brichfeus, J. *J. Phys. Chem.* **1987**, *91*, 5608−5616.

(23) Hakkinen, H. *Nat. Chem.* **2012**, *4*, 443−455.

(24) Ratner, M. *Nat. Nanotechnol.* **2013**, *8*, 378−381.

(25) Park, H.; Lim, A. K. L.; Alivisatos, A. P.; Park, J.; McEuen, P. L. *Appl. Phys. Lett.* **1999**, *75*, 301−303.

(26) O'Neill, K.; Osorio, E. A.; van der Zant, H. S. J. *Appl. Phys. Lett.* **2007**, *90*, 133109.

(27) de la Vega, L.; Martin-Rodero, A.; Agrait, N.; Yeyati, A. L. *Phys. Rev. B* **2006**, *73*, 075428.

(28) Thijssen, W. H. A.; Djukic, D.; Otte, A. F.; Bremmer, R. H.; van Ruitenbeek, J. M. *Phys. Rev. Lett.* **2006**, *97*, 226806.

(29) Goldhaber-Gordon, D.; Gores, J.; Kastner, M. A.; Shtrikman, H.; Mahalu, D.; Meirav, U. *Phys. Rev. Lett.* **1998**, *81*, 5225−5228.

(30) Nagaoka, K.; Jamneala, T.; Grobis, M.; Crommie, M. F. *Phys. Rev. Lett.* **2002**, *88*, 077205.

(31) Costi, T. A. *Phys. Rev. Lett.* **2000**, *85*, 1504−1507.

(32) Stephens, P. J.; Devlin, F. J.; Chabalowski, C. F.; Frisch, M. J. *J. Phys. Chem.* **1994**, *98*, 11623−11627.

(33) Frisch, M. J.; Trucks, G. W.; Schlegel, H. B.; Scuseria, G. E.; Robb, M. A.; Cheeseman, J. R.; Scalmani, G.; Barone, V.; Mennucci, B.; Petersson, G. A.; Nakatsuji, H.; Caricato, M.; Li, X.; Hratchian, H. P.; Izmaylov, A. F.; Bloino, J.; Zheng, G.; Sonnenberg, J. L.; Hada, M.; Ehara, M.; Toyota, K.; Fukuda, R.; Hasegawa, J.; Ishida, M.; Nakajima, T.; Honda, Y.; Kitao, O.; Nakai, H.; Vreven, T.; Montgomery, J. A., Jr.; Peralta, P. E.; Ogliaro, F.; Bearpark, M.; Heyd, J. J.; Brothers, E.; Kudin, K. N.; Staroverov, V. N.; Kobayashi, R.; Normand, J.; Raghavachari, K.; Rendell, A.; Burant, J. C.; Iyengar, S. S.; Tomasi, J.; Cossi, M.; Rega, N.; Millam, N. J.; Klene, M.; Knox, J. E.; Cross, J. B.; Bakken, V.; Adamo, C.; Jaramillo, J.; Gomperts, R.; Stratmann, R. E.; Yazyev, O.; Austin, A. J.; Cammi, R.; Pomelli, C.; Ochterski, J. W.; Martin, R. L.; Morokuma, K.; Zakrzewski, V. G.; Voth, G. A.; Salvador, P.; Dannenberg, J. J.; Dapprich, S.; Daniels, A. D.; Farkas, Ö.; Ortiz, J. V.; Cioslowski, J.; Fox, D. J. *Gaussian 09*, revision A.08; Gaussian, Inc.: Wallingford, CT, 2009.

(34) van Ruitenbeek, J. M.; Alvarez, A.; Pineyro, I.; Grahmann, C.; Joyez, P.; Devoret, M. H.; Esteve, D.; Urbina, C. *Rev. Sci. Instrum.* **1996**, *67*, 108−111.

(35) Martin, C. A.; Smit, R. H. M.; Egmond, R. v.; van der Zant, H. S. J.; van Ruitenbeek, J. M. *Rev. Sci. Instrum.* **2011**, *82*, 053907.

(36) Grimme, S. *J. Comput. Chem.* **2006**, *27*, 1787−1799.

Supporting information: Kondo effect in a neutral and stable all organic radical single molecule break junction.

R. Frisenda,[†] R. Gaudenzi,[†] C. Franco,[‡] M. Mas-Torrent,[‡] C. Rovira,[‡] J. Veciana,[‡] I. Alcon,[¶] S. T. Bromley,[¶,§] E. Burzurí,[*,†] and H. S. J. van der Zant[†]

Kavli Institute of Nanoscience, Delft University of Technology, 2600 GA, The Netherlands, Institut de Ciència de Materials de Barcelona (ICMAB-CSIC) and CIBER-BBN, Campus de la UAB, 08193, Bellaterra, Spain, Departament de Química Física and Institut de Química Teòrica i Computacional, Universitat de Barcelona (IQTCUB), E-08028 Barcelona, Spain, and Institució Catalana de Recerca i Estudis Avançats (ICREA), 08010 Barcelona, Spain

E-mail: E.BurzuriLinares@tudelft.nl

In this supporting information we provide additional details on the Kondo physics in neutral PTM organic radicals embedded in two and three-terminal devices. Data on the non-radical counterpart species are also provided for comparison. In Section 1 we give details about the synthesis of the PTM-αH and the PTM radical. Section 2 is dedicated to MCBJs. There we describe the signatures accompanying the formation of a molecular

---

[*]To whom correspondence should be addressed
[†]Kavli Institute of Nanoscience, Delft University of Technology, 2600 GA, The Netherlands
[‡]Institut de Ciència de Materials de Barcelona (ICMAB-CSIC) and CIBER-BBN, Campus de la UAB, 08193, Bellaterra, Spain
[¶]Departament de Química Física and Institut de Química Teòrica i Computacional, Universitat de Barcelona (IQTCUB), E-08028 Barcelona, Spain
[§]Institució Catalana de Recerca i Estudis Avançats (ICREA), 08010 Barcelona, Spain

junction and we show the measurements performed on the PTM-αH non-radical molecule. Statistics for the two cases is provided in a graphical form. In section 3, we show gate-dependent measurements performed with the three-terminal EMBJs. A helpful comparison between exemplary dI/dV traces exhibiting Kondo in the two setups (MCBJ and EMBJ) is also shown. Section 4 is dedicated to the DFT calculations. There we include the energy levels and isosurfaces of the non-radical PTM molecule. We also include the levels and isosurfaces of the PTM-radical molecule under stretching.

1.-Synthesis and Characterization of the molecules.

General.

NMR spectra were recorded on a Bruker Avance 400 MHz. Chemical shifts are reported in parts per million (ppm) and are referenced to the residual solvent peak. Coupling constants (J) are given in hertz (Hz) and are quoted to the nearest 0.5 Hz spectrometers. EPR spectra were recorded in a Bruker ELEXYS E500 X-band spectrometer. Electrochemical experiments were performed with a potensiostat/galvanostat 263 from EG&G Princeton Applied Research, by using a platinum wire as working and counter electrode and Ag wire as quasi reference electrode. Tetrabutylammonium hexafluorophospate (Fluka, 99%) was used as the supporting electrolyte. UV-Vis spectra were recorded on a Varian Carey 5000 in double-beam mode. Mass Spectra were recorded with a Bruker Ultraflex LDI-TOF mass spectrometer. The IR spectra were recorded with an ATR-IR Perkin Elmer Spectrum One. Magnetic susceptibility data were measured from 4.2 to 200 K with a MPMS-XL7T Quantum design magnet. All manipulations of radicals in solution were performed under red light.

Synthesis of 3,3'-((1E,1'E)-(((perchlorophenyl)methylene)bis(2,3,5,6-tetrachloro-4,1-phenylene))bis(ethene-2,1-diyl))dithiophene (PTM-αH).

To a stirred solution of potassium tert-butoxide (104.4 mg; 0.93 mmol) in dry tetrahydrofuran (15 ml) under argon and cooled to -78°C, Bis-(diethylphosphonate)PTM[1] (300 mg; 0.31

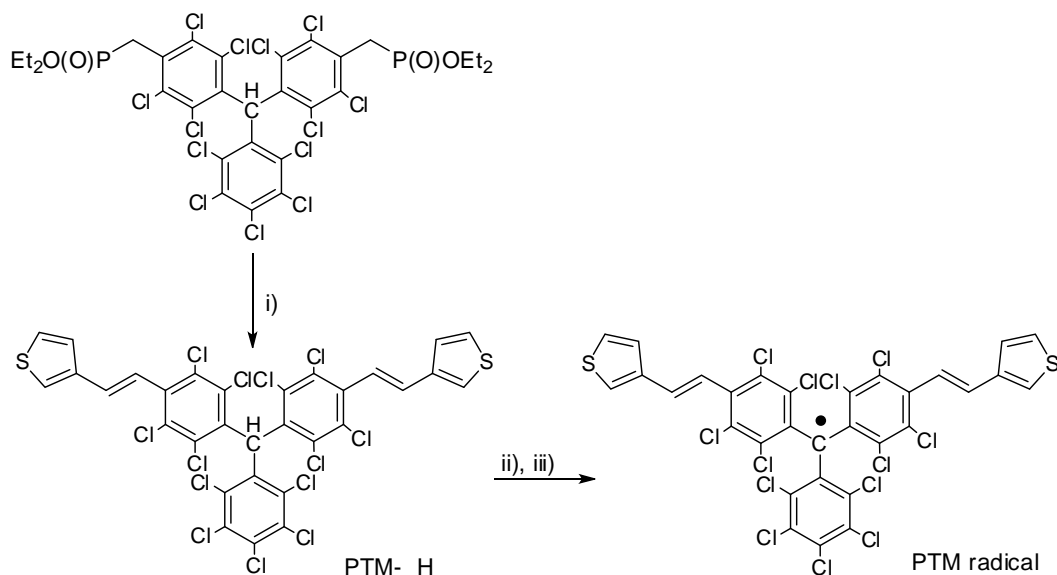Figure S1: **Synthetic route to PTM-αH and PTM radical.**(i) 3-thiophenecarboxaldehyde, tBuOK; -78°, THF, 48h; (ii)nBu$_4$NOH; r.t., THF, 20 min; (iii) chloranil; r.t., THF, 30 min.

mmol) was added. The yellow-orange ylide solution formed was stirred for 10 min and then 3-thiophenecarboxaldehyde (0.06 ml; 0.68 mmol) was added. The resulting mixture was allowed to reach room temperature, and stirred for 48 h. The yellow crude product was washed with water and extracted with CH$_2$Cl$_2$ and the organic layer was dried over MgSO$_4$, filtered and the solvent evaporated under reduced pressure. Chromatographic purification with silica gel (hexane/CH$_2$Cl$_2$ 90/10) yielded **PTM-αH** (196 mg 70%) as a pale yellow powder. ^{1}**H-RMN** (400 MHz, CDCl$_3$) δ (ppm) 7.41-7.37 (m, 6H$_{ar}$), 7.11 (d, $J = 16.5$ Hz, 2H$_{C=C}$), 7.05 (s, 1H$_{\alpha H}$), 6.92 (d, $J = 16.5$ Hz, 2H$_{C=C}$); ^{13}**C-RMN** (100.6 MHz, CDCl$_3$) δ (ppm): 138.84, 137.21, 137.19,136.99, 136.27, 136.24, 133.88, 132.45, 126.69, 124.74, 124.67, 122.81, 56.75 (1C$_{\alpha H}$); **UV/Vis** (THF): λ(nm) (ϵ)=285 (17800), 370 (22900); **ATR-IR** ν (cm^{-1}): 2922.2, 2854.4, 1631.4, 1543.3, 1459.9, 1361.4 1334.4, 1297.9, 1243.3, 1137.3, 1083.6, 960.9, 906.8, 867.4, 840.7, 808.1, 768.9; **UV/Vis (CH$_2$Cl$_2$)**: λ(nm) (ϵ)= 231.10 (77069.14), 307.87 (45859.58); **MALDI-TOF** (negative mode) (C$_{31}$H$_{11}$Cl$_{13}$S$_2$, M=908.4); m/z [M-1H] = 907.4; [M-2Cl] = 835,8.

3
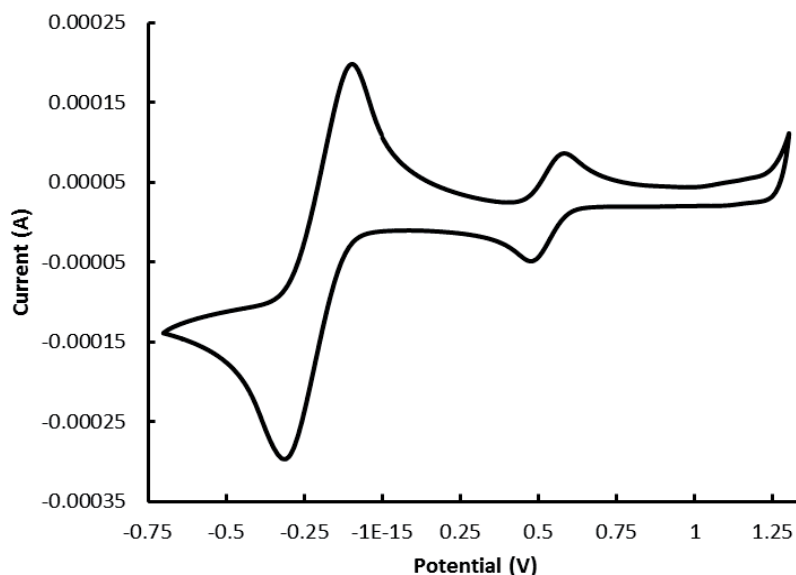
Figure S2: Cyclic voltammogram of PTM radical in CH_2Cl_2 using n-Bu$_4$NPF$_6$ 0.1 M as supporting electrolyte, Ag wire as a pseudo-reference electrode, and platinum wires as the counter and working electrodes in the presence of Fc, as internal standard; $E^{1/2}$(PTM)=-073 V vsFc.

Figure S3: **ESR characterization.** ESR spectrum of PTM radical in CH_2Cl_2 at room temperature: g=2.0022; ΔH_{pp}=1.19G; a$_H$=1.95G; a$_{13C\alpha}$=29.9 G; a$_{13C_{arom}}$=10.6 G.

Figure S4: **UV characterization.** UV-Vis spectrum of PTM radical in CH_2Cl_2.

Synthesis of radical (3,3'-((1E,1'E)-(((perchlorophenyl)methylene)bis(2,3,5,6-tetrachloro-4,1-phenylene))bis(ethene-2,1-diyl))dithiophene (PTM radical).
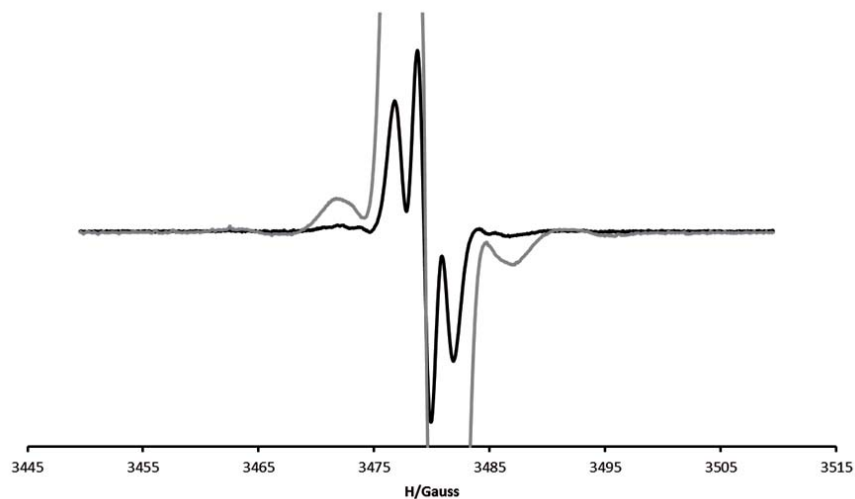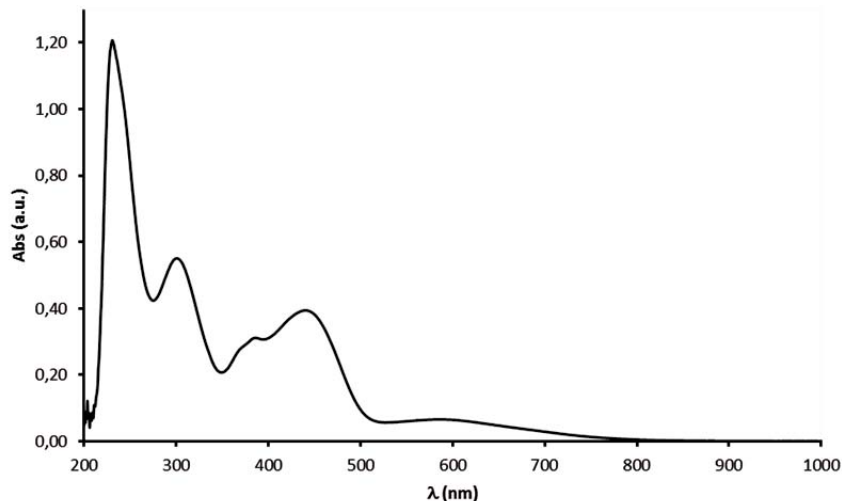
Tetrabutylammonium hydroxide (40% in water) (0.15 ml, 0.21 mmol) was added to a solution of **PTM-αH** (60 mg, 0.07 mmol) in THF (10 ml). The resulting violet mixture was stirred for 15 min and then p-chloranil (71.4 mg, 0.28 mmol) was added and the mixture was stirred for 30 min. Then, the crude was evaporated under reduced pressure and chormatographied through flash silica gel with Hexane/CH_2Cl_2 (8/2) as eluent to give **PTM radical** (58 mg, 96%) as a dark green powder. **ATR-IR** ν (cm^{-1}): 2922.7, 2853.7, 1622.5, 1507.1, 1333.8, 1265.2 1222.2 1167.3, 1083.4 1051.9 957.1 918.7 868.1, 842.6 769.3 734.3 693.9, 664.0; **UV/Vis (CH_2Cl_2)**: λ(nm) (ϵ)= 230.40 (52488.08), 300.79 (23934.52), 369.83 (12097.93), 386.17 (13509.08), 440.32 (17116.99), 586.36 (2833.72); $\mu_{eff} = 1.68$ μ_B mol^{-1}; **MALDI-TOF** (negative mode) ($C_{31}H_{10}Cl_{13}S_2$, M=907.4); m/z [M] = 907.7; [M-2Cl] = 836,1.

2. MCBJ: Molecular Signatures and Measurements on the non-radical Molecule

Figure S5a) reports the zero-bias conductance trace, extracted from the I-V characteristics, as a function of the electrode displacement for a PTM-αH molecular junction. Figure S5b)

shows three examples of dI/dV versus V, measured at the positions indicated by the arrows in a). From the differential conductance plots, one can see the absence of zero bias peaks, in contrast to the PTM-radical measurements discussed in the main text. Figure S6 shows the pie charts that summarize the statistics of the molecular junction formation probability and of the appearance of zero bias peaks in the dI/dV traces. As already discussed in the main text the two investigated molecules show a similar junction formation probability. The PTM-radical molecular junctions show in 22% of the cases a zero bias peak, in contrast to the PTM-αH non-radical molecular junction where the zero bias peak is completely absent.

The observation of the Kondo effect in transport is very sensitive especially to (i) the temperature, (ii) the molecule-electrode coupling and (iii) the level alignment to the electrodes Fermi energy. A well-known mesoscopic-physics expression for the Kondo temperature T_K is: $K_B T_K \approx \sqrt{\Gamma U} \exp\left(\pi \frac{\epsilon(\epsilon+U)}{\Gamma U}\right)$ (see for instance[2]), where Γ is the molecule/electrode coupling, ϵ is the level alignment and U is the charging energy. This formula shows that the Kondo effect, observed as a peak in the zero-bias differential conductance, and therefore the Kondo temperature is strongly dependent on the combination of the parameters described above. It is well known that those parameters change from junction to junction and some particular combinations of these prevents the observation of Kondo resonances at the experimental temperature of 6 K. We notice finally that the complete absence of Kondo features in the junctions formed with non-radical species supports the connection between the Kondo effect and the open-shell configuration in the radical molecule.

3. EMBJ: Gate Dependence and Comparison to MCBJ Measurements

In order to verify the stability of the radical against charging, we have performed conductance measurements as a function of bias and gate. Figure S7a shows the obtained differential conductance map related to the sample in Fig. 3a of the manuscript. At $V_g = 0$ V, value at which the Kondo peak in the manuscript is characterized, the expected Kondo peak is observed. Varying the gate voltage value, the peak height and width evolve. Moving from
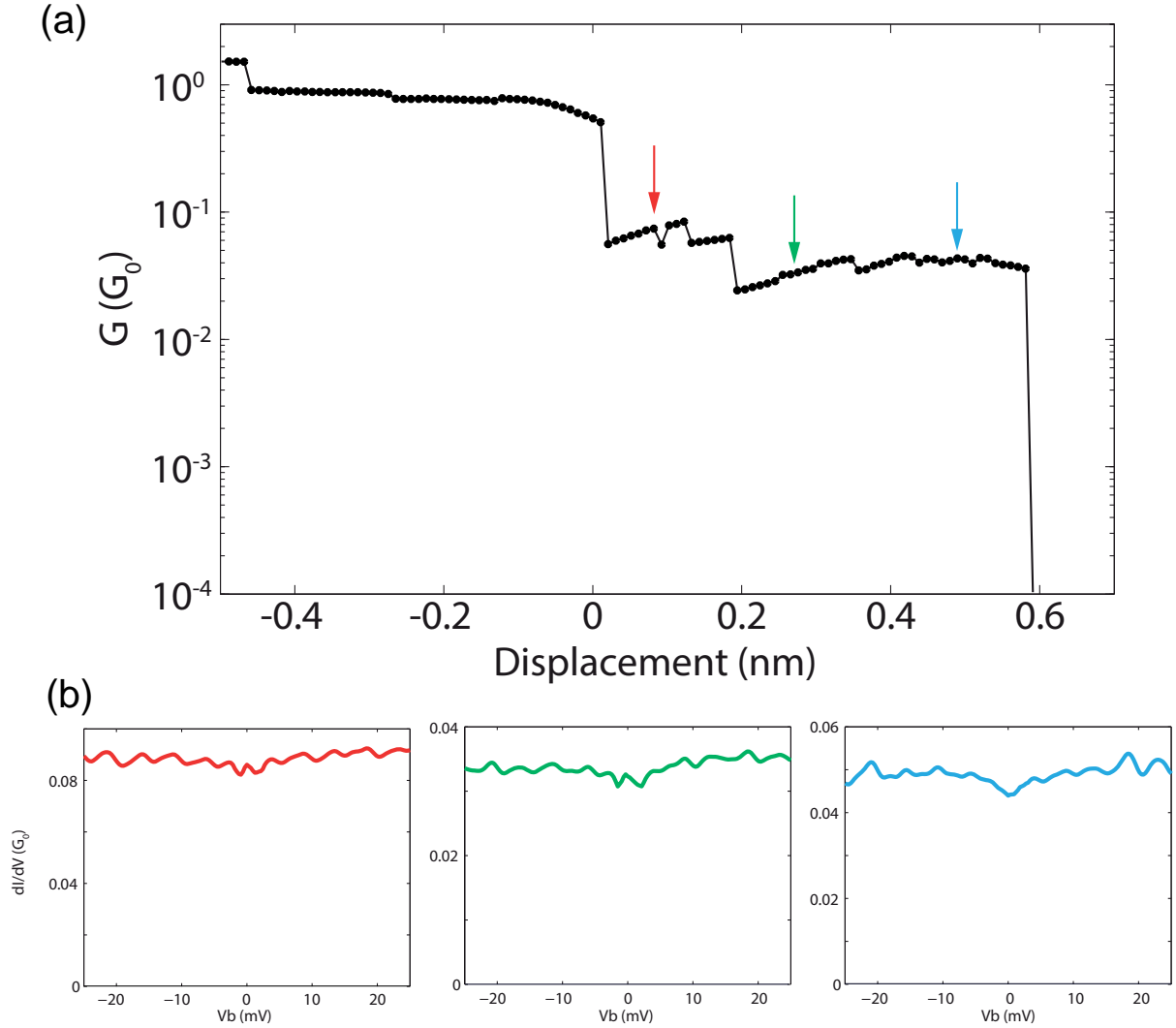
Figure S5: **Conductance trace and current-voltage of a non radical junction.** (a) Conductance versus displacement traces for a junction measured with MCBJ. Each data point is extracted from an individual IV. (b) Differential conductance traces measured at displacements indicated by the arrows in (a). Measurements are taken at a temperature of 6 K.

PTM Radical

Empty junctions

Molecular junctions

Zero bias peak

No features

55

31 36%

7

24

TM α-H

65

30 32%

30

Figure S6: **Statistics of radical and non radical junctions.** (a) Pie charts.

$V_\mathrm{g} = 0$ V towards positive (negative) values has the effect of increasing (decreasing) the Kondo peak height. However, from the symmetry point at $V_\mathrm{g} \approx -0.25$ V the peak width is seen slowly increasing both for more positive and more negative gate voltages. Figure S7b show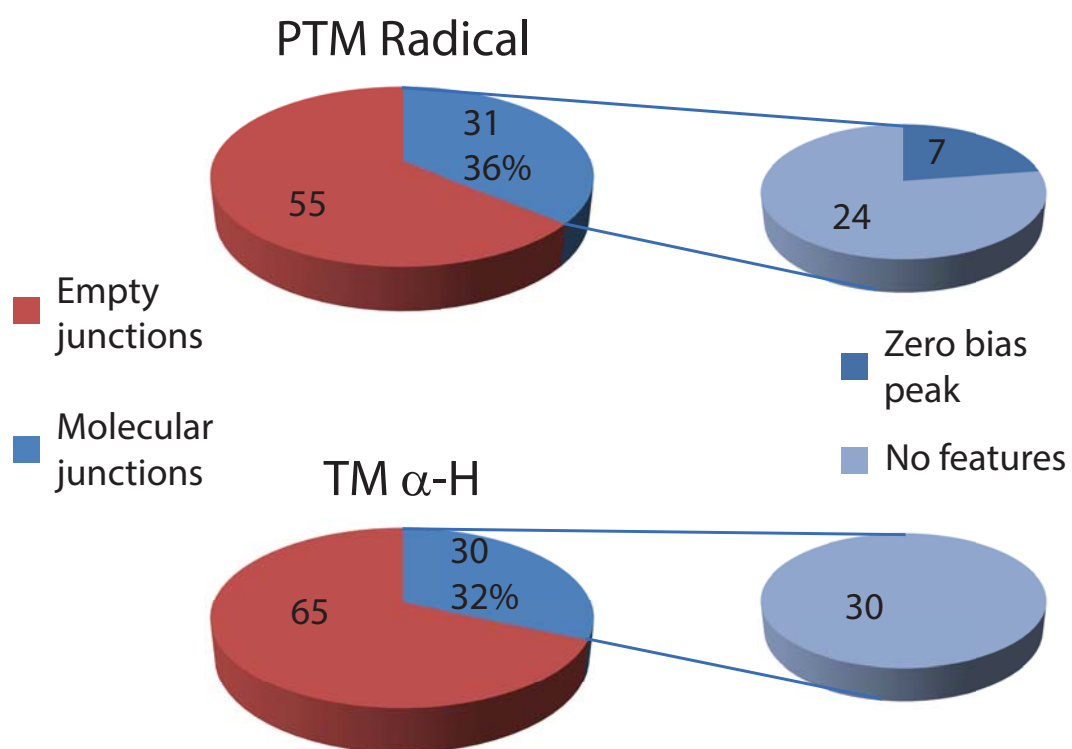s a similar characterization for another sample in which Kondo effect is observed. An increase of peak width for negative gate voltages is observed. Worth remarking is that in both sample no signatures of resonant transport are visible for the whole gate and bias range. These measurements provide strong indications that the Fermi level lies within a seemingly large HOMO-LUMO gap and above an half-filled orbital. As already mention in the main paper, DFT calculations allow us to associate the half-filled orbital to the radical SOMO and the LUMO to the spin-polarized LUMO-β, with a calculated gap of ~ 2 eV.

Here we also want to show how EMBJ measurements compare with MCBJ measurements. Figure S8 shows an exemplary trace measured with the former at temperatures $T \approx 4.5$ K against three traces obtained with the latter at $T \approx 6$ K for different displacements. The FWHM of the EMBJ trace is comparable to but slightly smaller than that of the MCBJ traces, consistently with the lower measuring temperature. Conductance levels are also comparable. As extensively shown in the manuscript, in the three MCBJ traces the Kondo peak is preserved despite changes in the conductance.

4. DFT calculations on the non-radical PTM

Figure S9 compares the eigenvalues of PTM-αH non-radical and the PTM radical calculated with DFT. The orbitals of the HOMO are included.

We have also performed DFT calculations to study the effect of stretching on the SOMO as seen in Figure S10. Stretched conformations of the PTM molecule were obtained by performing constrained optimisations whereby the two S atoms of the molecule were separated by increasing fixed displacements from their fully relaxed positions from 0-0.24 nm. The structural change and the isosurface of the SOMO for the PTM molecule stretched by 0.2 nm is shown in Figure S10a) and Figure S10b). Incrementally stretching the PTM-molecule

radical by up to 0.24 nm induces only very minor energy changes (0.02 eV) in the SOMO and LUMO, in line with their localised character and the experimental findings, see Figure S10c) and Figure S10d).

References

(1) Reitzenstein, D.; Quast, T.; Kanal, F.; Kullmann, M.; Ruetzel, S.; Hammer, M. S.; Deibel, C.; Dyakonov, V.; Brixner, T.; Lambert, C. *Chem. Mater.* **2010**, *22*, 6641.

(2) Scheer, E.; Cuevas, J. C. *Molecular Electronics: an introduction to theory and experiments* World Scientific, ISBN: 978-981-4282-58-1,2010).
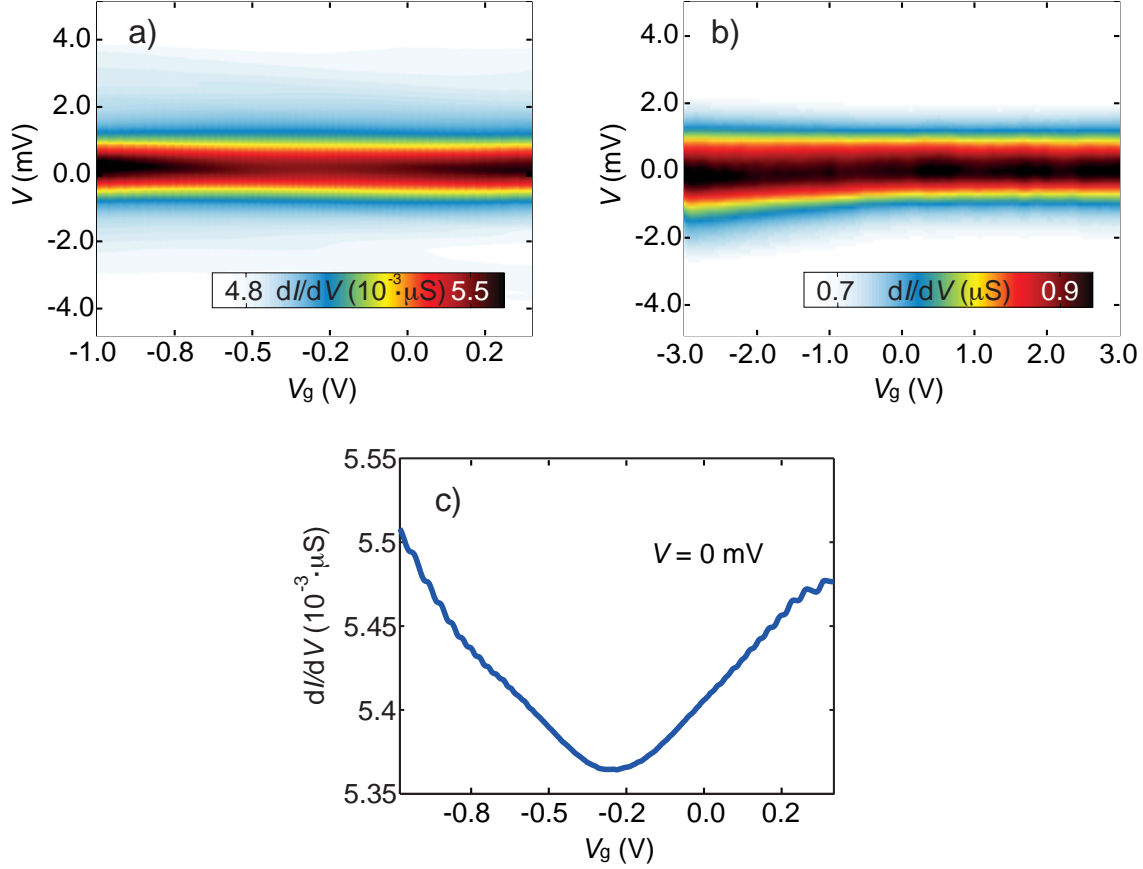
Figure S7: **Gate-dependent measurements on the PTM radical.** (a) Differential conductance map of the sample in Fig. 3a of the manuscript. The Kondo resonance can be seen to evolve with gate voltage. Peak height and width increase from $V_g \approx -0.25$ V towards both more positive and more negative gate voltages. No signatures of resonant transport and charging can be seen. (b) Differential conductance maps of another sample exhibiting Kondo correlations. Again the Kondo peak changes with gate voltage and no resonances are observed. (c) dI/dV zero bias linecut as a function of gate voltage extracted from (a). The Kondo peak height is clearly seen increasing in both gate voltage directions from the symmetry point at $V_g \approx -0.25$ V.
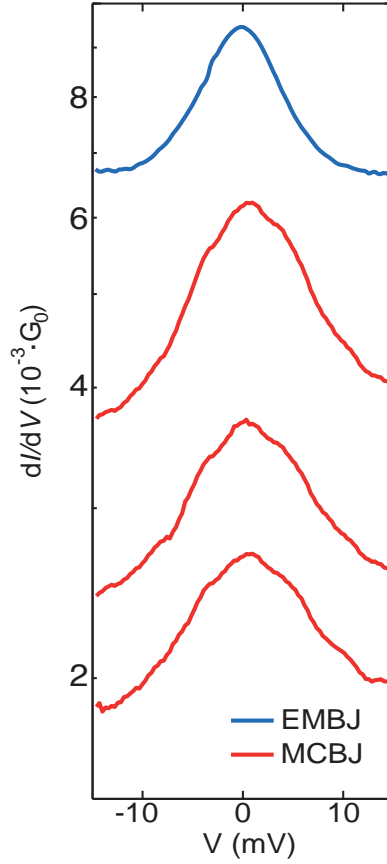
Figure S8: **Comparison between EMBJ and MCBJ measurements.** dI/dV spectra of the PTM radical obtained in the three-terminal EMBJ at $T \approx 4.5$ K (blue) against the series of the three spectra obtained in the two-terminal MCBJ for three different displacements at $T \approx 6$ K (red). The dI/dV is in a logarithmic scale.
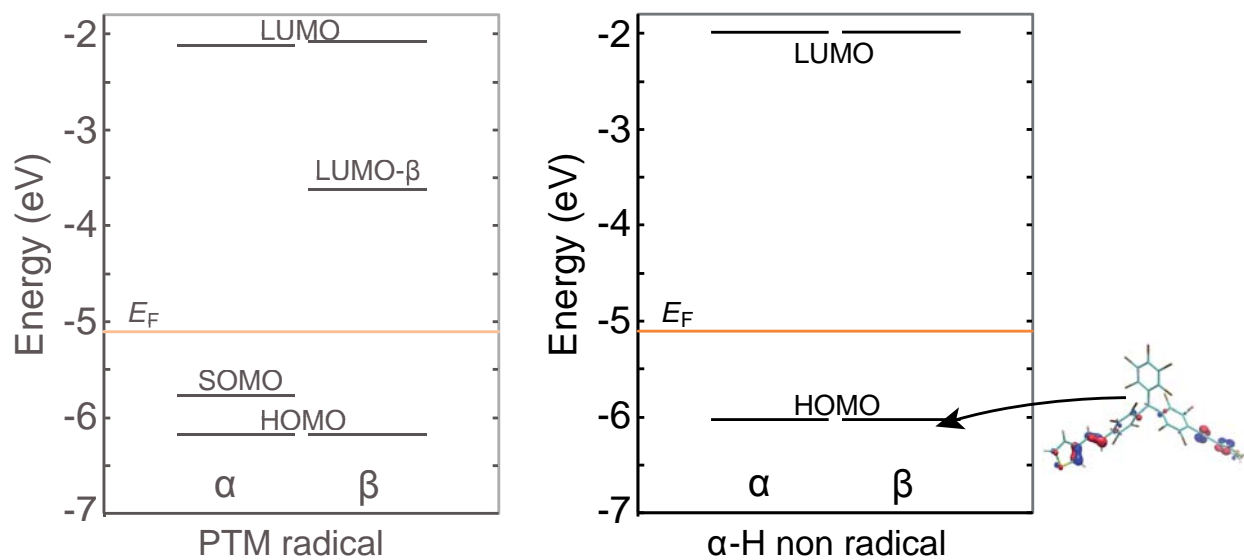
Figure S9: **DFT calculations.** Energy schemes for the PTM radical (left) and the PTM-αH (right).
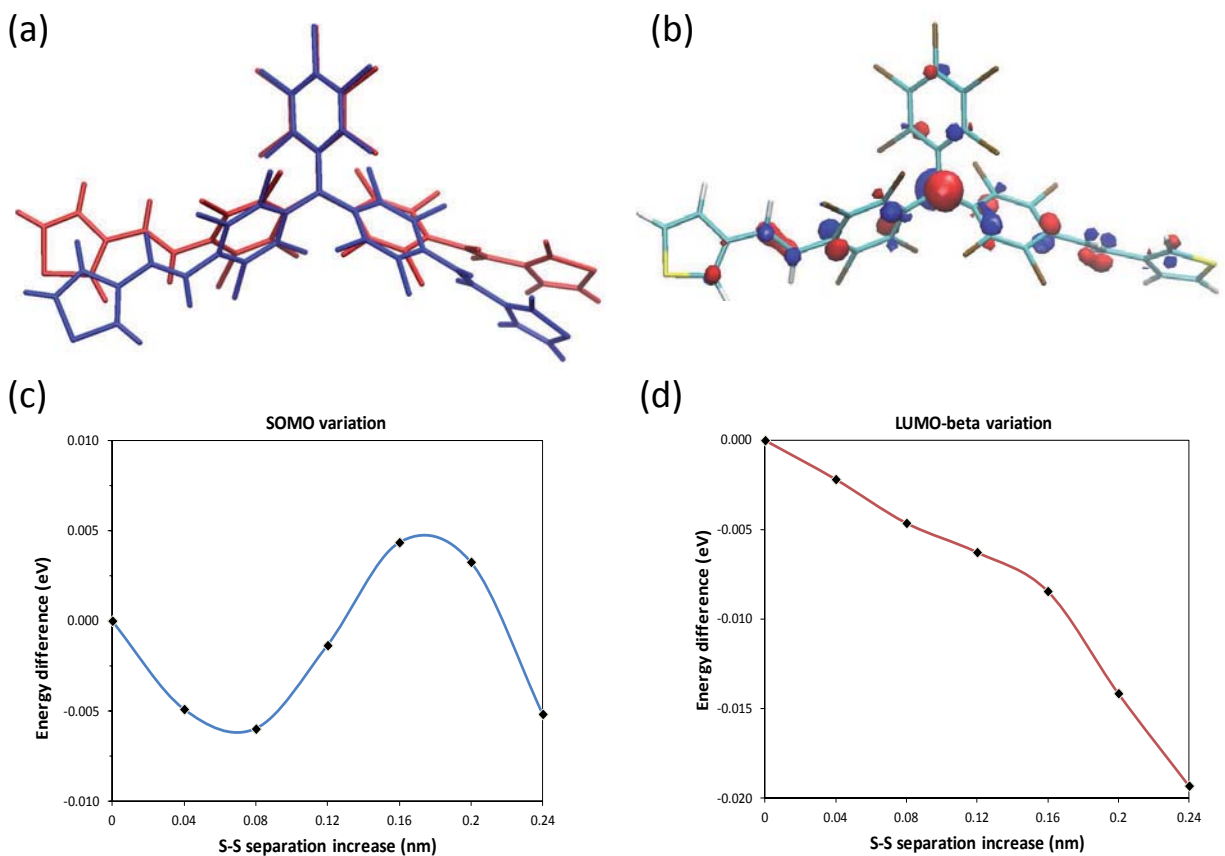
Figure S10: **DFT calculations.** (a) Comparison of the relaxed PTM radical molecule (blue) and the molecule stretched by 0.2 nm (red). (b) SOMO orbital of the PTM molecule stretched by 0.2 nm. (c) Variation of the energy of the SOMO with stretching relative to the SOMO energy of the relaxed molecule. (d) Variation of the energy of the β-LUMO with stretching relative to the β-LUMO energy of the relaxed molecule. Note that the molecule was stretched by by increasing the separation of the terminal S atoms (yellow in (b)) from their original positions in the relaxed molecule and reoptimising the structure while keeping the new positions of the S atoms fixed.

Publication 5

Title	Pyrene-Based Dyad and Triad Leading to a Reversible Chemical and Redox Optical and Magnetic Switch
Authors	Carlos Franco, Marta Mas-Torrent, Antonio Caballero, Arturo Espinosa, Pedro Molina, Jaume Veciana, and Concepciú Rovira
Publication	*Chemistry - A European Journal,* **2015***, 21(14),* 5504 DOI: 10.1002/chem.201405993

Donor–Acceptor Systems

Pyrene-Based Dyad and Triad Leading to a Reversible Chemical and Redox Optical and Magnetic Switch

Carlos Franco,[a, c] Marta Mas-Torrent,*[a, c] Antonio Caballero,[b] Arturo Espinosa,[b] Pedro Molina,[b] Jaume Veciana,[a, c] and Concepció Rovira*[a, c]

Abstract: Two new pyrene–polychlorotriphenylmethyl (PTM) dyads and triads have been synthesized and characterized by optical, magnetic, and electrochemical methods. The interplay between the different electronic states of the PTM moiety in the dyads and triads and the optical and magnetic properties of the molecules have been studied. The electronic spectra of the radicals 5˙ and 6˙ show the intramolecular charge-transfer transition at around 700 nm due to the acceptor character of the PTM radical. In the diamagnetic protonated derivatives 3 and 4 the fluorescence due to the pyrene is maintained, whereas in the radicals 5˙ and 6˙ and the corresponding anions 5⁻ and 6⁻ there is a clear quenching of the fluorescence, which is more efficient in the case of radicals. The redox activity of PTM radicals that are easily reduced to the corresponding carbanion has been exploited to fabricate electrochemical switches with optical and magnetic response.

Introduction

The design of novel molecules able to process information, such as the molecular systems involved in living organisms, is a current topic of research. Bistable molecules that can be externally interconverted between two or more states exhibiting different properties represent suitable platforms to fabricate molecular switches as a base of logic operations.[1, 2] Such processes can be visualized as a transformation of inputs into outputs. Fluorescence emission and optical absorption are highly attractive output signal responses due to the fact that they are very sensitive and involve easy and low-cost detection procedures.[3] Chemical inputs taking advantage, for instance, of host–guest interactions or acid–base reactions have been employed to trigger molecular transformations.[4] Further, optical and electrochemical stimuli have also been proved to be very efficient to reversibly interconvert photo- or electroactive molecules, respectively. In particular, in this work new dyads and triads based on pyrenyl (Pyr) and polychlorotriphenylmethyl

(PTM) radical moieties have been synthesized to be applied as molecular switches. Pyrenyl groups are well-known fluorescent cores, the fluorescence of which can be quenched by photoinduced electron-transfer processes.[5, 6] In addition, PTM derivatives show distinctive absorption characteristics and, in their radical form, their electroactive character can be used to modulate the magnetic and optical properties of the materials.[7] The PTM radicals have their open-shell centers sterically shielded by six bulky chlorine atoms, which ensure their persistency and thermal and chemical stabilities.[8] Thus, we show herein that the combination of these two functional moieties offers a promising approach to synthesize a novel class of switchable materials.

Results and Discussion

Synthesis of the pyrene-substituted PTM radicals 5˙ and 6˙ was performed following the synthetic approach depicted in Scheme 1. First, polychlorinated triphenylmethane (αH-PTM) bis-phosponate and bis-phosphonium bromide salt derivatives 1 and 2 were prepared from the corresponding αH-PTM bis-bromomethyl derivative.[9] Coupling of these compounds under Wittig conditions with 1-pyrenecarboxaldehyde leads to a mixture of αH-PTM mono- and bis-adducts 3 and 4 in different proportions depending on the starting compound used: bis-phosphonate 1 leads to a 1:9 proportion of 3:4, whereas with bis-phosphonium salt 2 the ratio was found to be 1:1. Treatment of 3 and 4 with an excess of tetrabutylammonium hydroxide promotes the removal of the acidic proton at the α position to give the corresponding carbanions, which were subsequently oxidized in situ using a concentrated solution of AgNO₃ in MeCN to yield the target radicals 5˙ and 6˙.

[a] C. Franco, Dr. M. Mas-Torrent, Prof. J. Veciana, Prof. C. Rovira
Institut de Ciència de Materials de Barcelona (ICMAB-CSIC)
Campus UAB, 08193 Bellaterra (Spain)
E-mail: mmas@icmab.es
cun@icmab.es

[b] Dr. A. Caballero, Dr. A. Espinosa, Prof. P. Molina
Departmento de Química Orgánica
Facultad de Química, Universidad de Murcia
Campus de Espinardo, 30100 Murcia (Spain)

[c] C. Franco, Dr. M. Mas-Torrent, Prof. J. Veciana, Prof. C. Rovira
Networking Research Center on Bioengineering Biomaterials and Nanomedicine (CIBER-BBN)
08193 Bellaterra (Spain)

Supporting information for this article is available on the WWW under http://dx.doi.org/10.1002/chem.201405993.
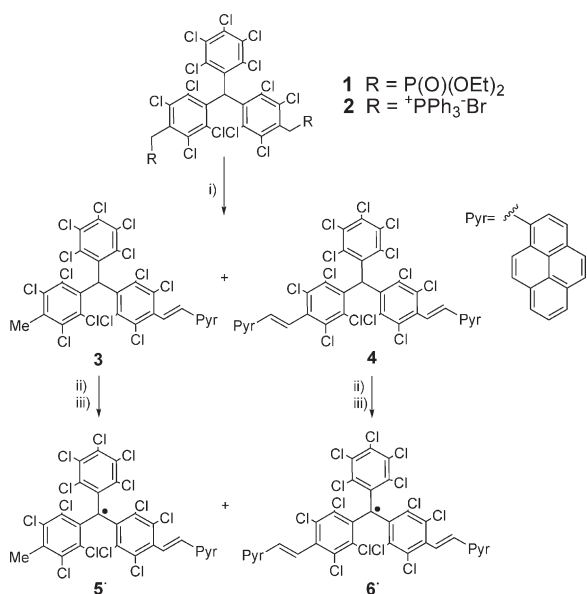
Scheme 1. Synthetic route to radicals **5·** and **6·**. Reaction conditions: i) 1-pyrenecarboxaldehyde, *t*BuOK; −78 °C, THF, 24 h; ii) *n*Bu$_4$NOH; RT, THF, 20 min; iii) AgNO$_3$; RT, MeCN, 10 min.

Figure 1. Cyclic voltammograms of radicals **5·** (gray) and **6·** (black) in CH$_2$Cl$_2$ using *n*Bu$_4$NPF$_6$ (0.05 M) as supporting electrolyte, Ag wire as a pseudo-reference electrode, and platinum wires as the counter and working electrodes in the presence of ferrocene (Fc) as internal standard.
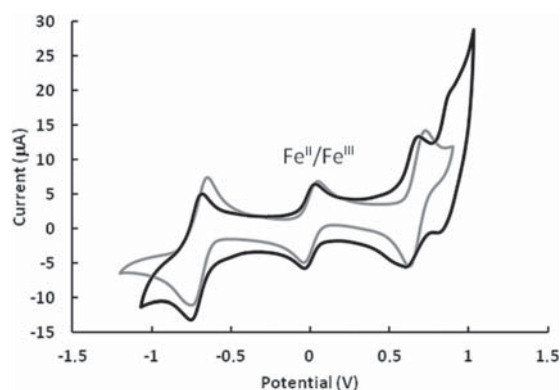
Both radicals show characteristic lines in the electron spin resonance (ESR) spectra corresponding to the coupling of the free electron with the protons of the vinylene bonds (Figure S1 in the Supporting Information).[10] The ESR spectrum of radical **5·** shows two principal broad lines with a coupling constant of $a_H = 1.95$ G. The coupling with the other vinylenic proton and the protons of the methyl group is small and contributes to the broadening of the lines. According to its structure, radical **6·** shows a three-line spectrum due to the coupling of the radical with two of the protons of the two vinylene bonds, with a coupling constant of $a_H = 1.90$ G.

The redox properties of all compounds in solution were studied by cyclic voltammetry (CV) (Table 1). As shown in

Table 1. Redox potentials of compounds **3–6** and radical PTM-CH$_3$[a] [V] versus Fc$^+$/Fc in CH$_2$Cl$_2$.

| Compound	$E_{1/2}^{red}$	$E_{1/2}^{ox1}$	$E_{1/2}^{ox2}$
5·	−0.70	0.68	–
6·	−0.72	0.64	0.85[b]
3	–	0.88[b]	–
4	–	0.78[b]	–
PTM-CH$_3$	−0.58	1.19	–

[a] Ref. [12]. [b] Quasi-reversible wave.

Figure 1 (gray line), the CV for compound **5·** displays two reversible processes at $E_{1/2} = −0.70$ and 0.68 V (versus ferrocenium/ferrocene, Fc$^+$/Fc). The cathodic process corresponds to the reduction of the PTM radical subunit to the corresponding anion[7,11] whereas the anodic peak is attributed to the oxidation of the pyrenyl subunit. In the corresponding αH compound **3**, the oxidation of the pyrenyl subunit is observed as a less reversible peak and at higher potential, $E_{1/2} = 0.88$ V (versus Fc$^+$/Fc; Figure S2 in the Supporting Information). CV of

compound **6·** (Figure 1, black line) shows the reduction wave at $E_{1/2} = −0.72$ V (versus Fc$^+$/Fc), and two oxidation processes at $E_{1/2} = 0.64$ and 0.85 V attributed to the stepwise oxidation of the two pyrenyl subunits.

The observation of two redox processes for the pyrenyl subunits of **6·** indicates a strong electronic interaction of the pyrenyl groups through the PTM radical bridge. To rationalize if the big splitting of the redox processes can be due to the formation of an intermediate species with a very strong spin–spin interaction when the cation radical of pyrene is formed, we have studied the ESR spectra of the one-electron oxidized species of radicals **5·** and **6·** generated "in situ". In both cases silent ESR spectra were obtained. In other words, the ESR signal corresponding to the PTM radical disappears and no new signals due to the pyrene cation radical appear, which means that the formed biradicals are in the singlet ground state possibly forming the closed-shell species depicted in Scheme 2. The formation of these species can also explain the lowering of the first oxidation potential in radicals **5·** and **6·** with respect to their αH counterparts **3** and **4** as well as the high reversibility of these processes, since it is known that the oxidation of pyrenyl units tends to result in not such reversible CV waves as in the case of **3** and **4**.
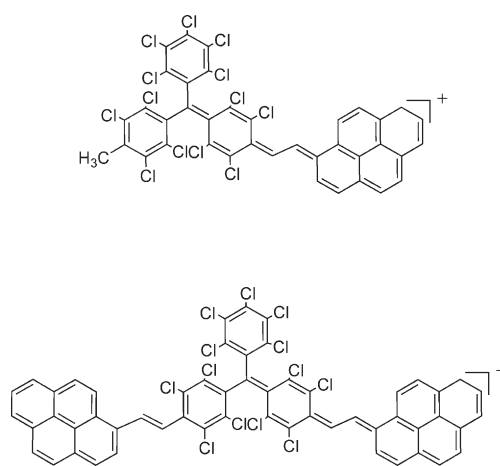
Scheme 2. Possible closed-shell forms derived from the 1 e$^−$ oxidation of radicals **5·** (top) and **6·** (bottom).

The UV/Vis spectrum of **3** in THF shows a broad absorption band in the visible range with an absorption maximum centered at 370 nm, assignable to the pyrenyl chromophore,[13] and that is in accordance with the pale green color of the solution (Figure 2a, Table S1 in the Supporting Information). Radi-
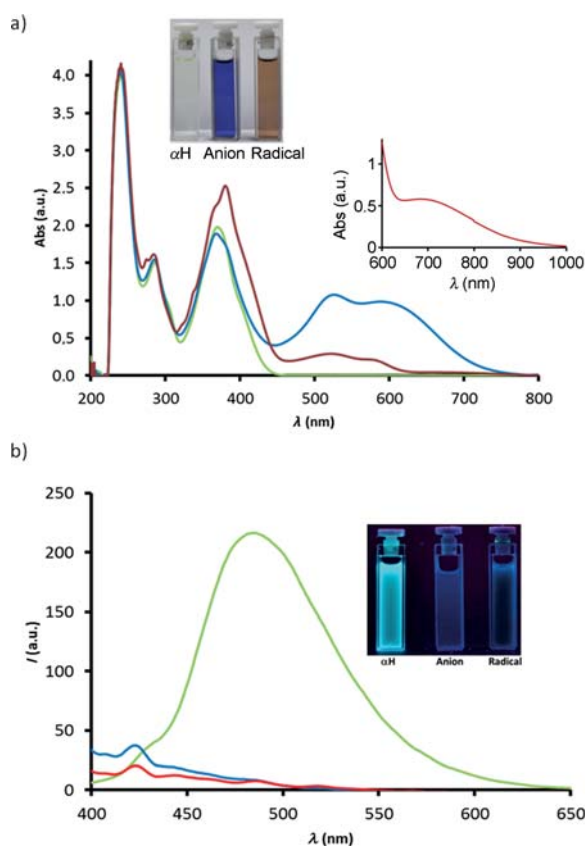

Figure 2. a) UV/Vis spectra of αH-PTM **3** (green line), anion **5⁻** (blue line), and radical **5·** (red line). Insets: photographs of cuvettes containing 7×10^{-5} M solutions of **3**, **5⁻**, and **5·** in THF and low-energy region spectrum of a more concentrated solution of radical **5·** showing the ICT band. b) Fluorescence spectra of αH-PTM **3** (green line), anion **5⁻** (blue line), and radical **5·** (red line). Inset: photographs of cuvettes under 366 nm light containing 2.5×10^{-5} M solutions of **3**, **5⁻**, and **5·** in THF.

cal **5·** solution has a brown color and accordingly displays four more bands in the visible region: an intense band at 380 nm, two broad and weak bands at 522 and 583 nm that are characteristic of conjugated PTM radical derivatives,[11] and a lower-energy very broad weak band centered around 700 nm that also follows the Lambert–Beer law and is attributed to the intramolecular charge transfer (ICT) from the electron-donating pyrenyl moiety to the electron-accepting PTM radical.[10,14] The UV/Vis spectrum of the corresponding anion **5⁻** was also studied after it was generated in situ from THF solutions of **3** or **5·** by adding excess nBu₄NOH, which acts as a base for removing the alpha proton of **3** or as reducing agent of radical **5·**. The carbanion solution shows an intense violet color and three bands in the visible region of the spectrum, one corresponding to the pyrenyl moiety at 365 nm and two broad and intense bands at 518 and 601 nm that are characteristic of the PTM

anion chromophore.[7] Similar spectral features are found in the analogous bis-substituted derivatives **4**, **6·**, and **6⁻**, the only difference arising from the relative intensities of the bands corresponding to the pyrenyl and PTM moieties (Figure S3 and Table S1 in the Supporting Information). Thus, it is clear that the three forms of the PTM derivatives (αH, radical, and anion) give distinct absorption properties.

The fluorescence characteristics of the synthesized materials were also explored, since it is well known that pyrene groups give a strong fluorescence (Table S1 in the Supporting Information). In agreement with this, the protonated derivative **3** shows an intense fluorescence. The emission spectrum in THF (Figure 2b) displays a typical excimer emission band at 484 nm ($\lambda_{exc} = 380$ nm) with high quantum yield ($\Phi = 0.0147$),[15] which is similar to those exhibited by pyrene derivatives in which the fluorescence emission is not quenched.[16] However, the emission spectra of radical **5·** and the corresponding reduced species **5⁻** in THF are completely different (Figure 2b). The fluorescence intensity decreases by one order of magnitude, and displays the typical monomer emission bands at 423, 444, 486, and 517 nm ($\lambda_{exc} = 380$ nm) with well-resolved vibronic features and low quantum yield ($\Phi = 0.0018$ for **5⁻** and $\Phi = 0.0009$ for **5·**). Both such spectra are similar to that of pyrene derivatives in which the fluorescence emission is quenched.[6] The difference between anion and radical spectra is only the intensity of the emission bands, the anion showing higher intensity than the radical, which implies that the pyrene fluorescence quenching is more effective with the radical moiety than with the anionic one. The same results were obtained with the bis-substituted derivatives **4**, **6·**, and **6⁻** (Figure S4 and Table S1 in the Supporting Information).

The observed fluorescence emission quenching in PTM–pyrene hybrids can occur through electron transfer following one of the two quenching pathways shown in Figure 3, similar to those previously described for the fluorescence quenching of phthalocyanine and anthracene by other electroactive molecules such as tetrathiafulvalenes.[17] In accordance with their electronic characteristics, PTM radical **5·** is a quite good electron acceptor, whereas PTM anion species **5⁻** is a very good electron donor. Therefore, electron transfer can occur easily from the HOMO of the anionic ground state to the HOMO of the excited pyrene (Pyr*) that due to photoexcitation increases
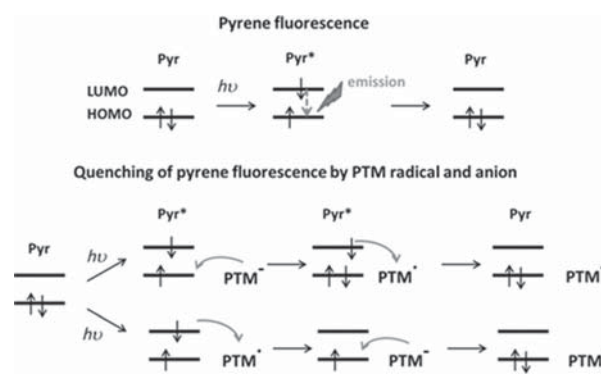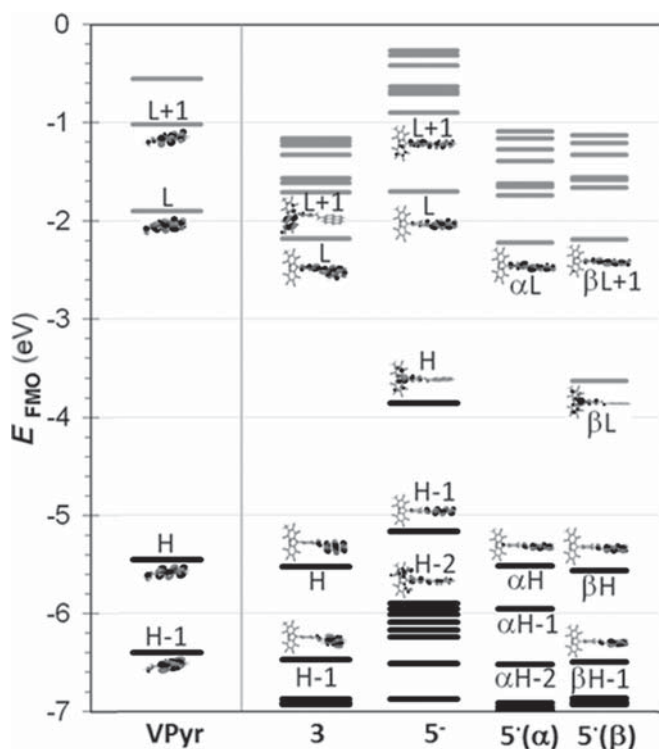

Figure 3. Molecular orbital scheme of pyrene emission and emission quenching pathways.
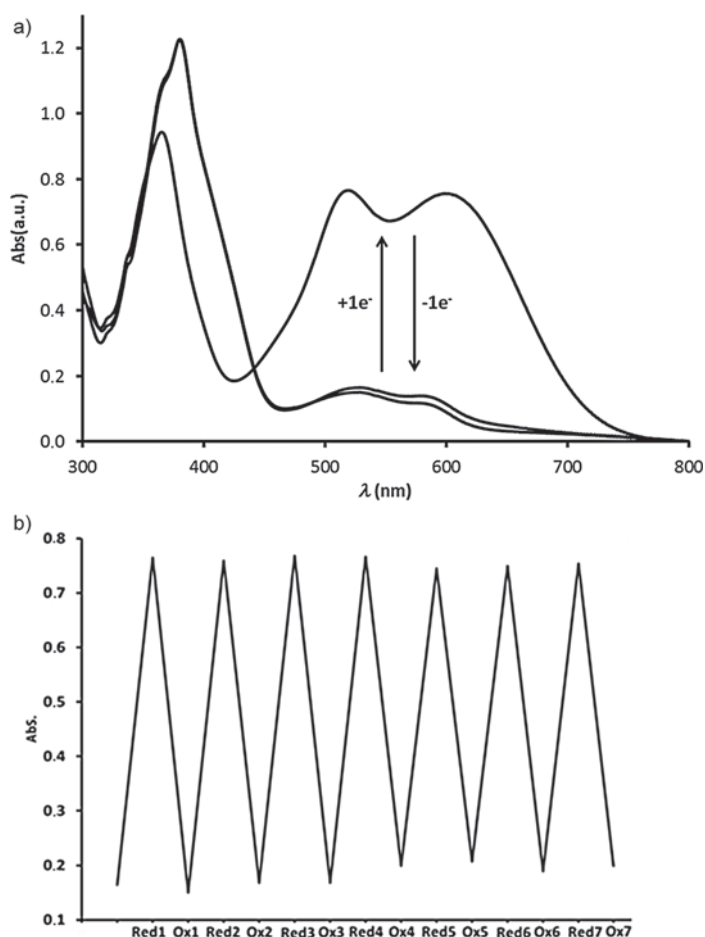
its acceptor strength, hence resulting in emission quenching. On the other hand, the photoexcitation of pyrene also results in an increase in its electron-donor character, and hence the electron-deficient PTM radical can accept electrons from Pyr*. Such electron transfer also results in emission quenching.

The above-described quenching mechanisms agree with the calculated frontier molecular orbitals (FMOs) in the ground state (Figure 4). For the αH-PTM compound **3**, the HOMO and LUMO levels are very similar to those of the isolated pyrene, in line with the fact that the fluorescence emission in **3** is similar to that of pyrene. However, the HOMO of the anionic species **5⁻** and the β-LUMO of the radical **5˙**, both centered in the PTM moiety (Figures S9–11 in the Supporting Information), lie in the middle of the HOMO–LUMO gap of pyrene. This is also in accordance with the fact that these orbitals can mediate the quenching mechanism through photoinduced electron-transfer processes.

As the oxidation/reduction between the radical-anion PTM pair can be reversibly carried out in radicals **5˙** and **6˙**, the possibility of fabricating a redox absorbance or fluorescence switch based on them arises. To elucidate this, spectroelectrochemical studies in UV/Vis absorption and fluorescence emission were performed. Applying a voltage potential step of −0.7 V (versus Ag/AgCl) during 15 min to a THF solution of radical **5˙** or **6˙** led to a reduction of radicals **5˙** and **6˙** to their corresponding

Figure 5. a) Changes in the UV/Vis spectra of radical **5˙** ($c = 3.6 \times 10^{-5}$ M in THF using $c = 0.05$ M Bu₄NPF₆) upon a chronoamperometric reduction experiment and subsequent oxidation step (15 min each step to reach the complete transformation). b) Evolution of the UV/Vis intensity at 518 nm during the stepwise reduction and oxidation cycles.

Figure 4. Calculated (COSMO_THF/B3LYP-D3/def2TZVPP//COSMO_THF/B3LYP-D3/def2-TZVP) energy diagram [eV] for FMOs in αH (**3**), anionic (**5⁻**), and radical (**5˙**) species. In the latter case, the α and β spin series are shown. The occupied FMOs are labeled in black and virtual ones in gray. For the most relevant FMOs, the corresponding Kohn–Sham isosurfaces (isovalue 0.04 a.u.) are also displayed. For the sake of comparison the energy levels of 1-vinyl-pyrene (VPyr) are included.

anions **5⁻** and **6⁻**, respectively. As expected, a change to the anion spectrum in absorbance (Figure 5 and Figure S6, left, in the Supporting Information) and enhancement of the fluorescence emission (Figure S5 and Figure S6, right, in the Supporting Information) was observed. Subsequent application of an oxidation potential of +0.5 V during 15 min resulted in the recovery of the radical absorbance spectrum and a decrease in the fluorescence intensity. After the electrochemical oxidation was completed, the initial parameters of absorbance and fluorescence of solutions of the radicals **5˙** and **6˙** were completely recovered. Reduction and subsequent oxidation were carried out for several cycles (Figure 5, Figures S5 and S7 in the Supporting Information). The absorbance spectrum and fluorescence intensity were recovered after each step, thus demonstrating the high reversibility of the switching process and the high stability of the involved species.

Such redox transformations can also be followed by ESR spectroscopy, since the paramagnetic radical species exhibit an ESR signal whereas the anionic forms are ESR silent due to their diamagnetic character. Therefore, the magnetic output is also a useful tool to follow the switching behavior.

Conclusion

The synthesis of new pyrene–PTM dyads and triads has been accomplished, which permitted study of the interplay between the different electronic states of the PTM moiety and the optical and magnetic properties of the molecules. In the diamagnetic protonated derivatives **3** and **4**, the fluorescence due to the pyrene is the same as in other pyrene-substituted derivatives, whereas in the radicals **5·** and **6·** and the corresponding anions **5⁻** and **6⁻** there is a clear quenching of the fluorescence, which is more efficient in the case of radicals. The fact that the PTM-centered HOMO of the anionic species and the β-LUMO of the radicals lie on the middle of the HOMO–LUMO gap of pyrene is in accordance with the mediation of those orbitals in the quenching mechanism. By simple acid–base or redox reactions the compounds mimic the "AND" Boolean logic operations. Further, the redox activity of PTM radicals has been exploited to fabricate electrochemical switches with optical (i.e., absorption and fluorescence) and magnetic response.

Experimental Section

General

Elemental analyses were performed on the CID (CSIC) services. NMR spectra were recorded on Bruker Avance 400 and 360 MHz spectrometers. Chemical shifts are reported in parts per million (ppm) and are referenced to the residual solvent peak. Coupling constants (J) are given in hertz (Hz) and are quoted to the nearest 0.5 Hz. ESR spectra were recorded on a Bruker ELEXYS E500 X-band spectrometer. Electrochemical experiments were performed with a potentiostat/galvanostat 263 from EG&G Princeton Applied Research, by using a platinum wire as working and counter electrode and Ag wire as quasi reference electrode. Bu_4NPF_6 (Fluka, 99%, 0.1 M) was used as the supporting electrolyte. UV/Vis spectra were recorded on a Varian Cary 5000 spectrometer in double-beam mode. Mass spectra were recorded with a Bruker Ultraflex LDI-TOF mass spectrometer. Fluorescence spectra were recorded with a Varian spectrophotometer (model Cary Eclipse). For both UV/Vis and fluorescence experiments, the concentration used was checked to be adequate to prevent the aggregation of molecules. FTIR spectra were recorded with an attenuated total reflection (ATR)-IR PerkinElmer Spectrum One spectrometer. All manipulations of radicals in solution were performed under red light.

Materials

Unless stated otherwise, all reagents were purchased from commercial sources and used without additional purification. αH-PTM bis(bromomethyl) and αH-PTM bis(diethylphosphonate) derivatives were prepared according to literature procedures.[9]

Syntheses

Synthesis of bis(bromotriphenylphosphine)-({[(perchlorophenyl)-methylene]bis(2,3,5,6-tetrachloro-4,1-phenylene)}bis(methylene)) salt (2): Triphenylphosphine (5.40 g, 20.60 mmol) was added to a solution of αH-PTM dibromomethyl derivative (1.50 g, 1.71 mmol) in dry benzene (150 mL) and the mixture was heated under reflux for 20 h. The formed precipitate was isolated by filtration, washed with benzene, and dried under vacuum to yield pure compound **2** (2.17 g, 90.1%). ¹H NMR (400 MHz, $CDCl_3$): $\delta = 7.82$–7.77 (m, $20 H_{Ph}$), 7.68–7.66 (m, $10 H_{Ph}$), 6.83 (s, $1 H_{\alpha H}$), 6.10–5.80 (m, 2H), 5.64 ppm (dd, $J = 25.7$, 15.3 Hz, 2H); ¹³C NMR (100.6 MHz, $CDCl_3$): $\delta = 138.22$, 138.04, 137.99, 135.83, 135.51, 135.23, 135.11, 134.94, 134.87, 134.80, 134.33, 134.23, 134.07, 132.13, 132.03, 131.93, 130.41, 130.29, 128.54, 128.43, 118.06, 117.20, 56.63 (αH), 32.07 (CH_2), 32.57 ppm (CH_2); IR (KBr): $\tilde{\nu} = 1585.4$, 1480.3, 1434.8, 1370.3, 1295.2, 1110.5, 995.1, 840.4, 810.2, 754.9, 684.7, 495.1 cm⁻¹; UV/Vis (THF): λ (ε) = 305 (1630), 295 (1606), 275 (10800), 219 nm (240000); elemental analysis calcd (%) for $C_{57}H_{35}Br_2Cl_{13}P_2$: C 48.81, H 2.52, Br 11.39, Cl 32.86; found: C 48.36, H 2.39, Br 11.08, Cl 31.85.

Synthesis of 2,2′-[(1E,1′E)-{[(perchlorophenyl)methylene]-bis(2,3,5,6-tetrachloro-4,1-phenylene)}bis(ethene-2,1-diyl)]dipyrene (4) and (E)-2-{2,3,5,6-tetrachloro-4-[(perchlorophenyl)(2,3,5,6-tetrachloro-4-methylphenyl)methyl]styryl}pyrene (3): Method A: Bis-triphenyl phosphonium salt **2** (200 mg, 0.14 mmol) was added to a stirred solution of potassium tert-butoxide (47 mg, 0.42 mmol) in dry THF (15 mL) under argon and cooled to −78 °C. The yellow-orange ylide solution formed was stirred for 10 min, then the temperature was increased to 0 °C with an ice bath, and 1-pyrenecarboxaldehyde (71.4 mg, 0.31 mmol) dissolved in dry THF (5 mL) was added. The resulting mixture was allowed to reach room temperature, and stirred for 48 h. The yellow crude product was washed with water, extracted with CH_2Cl_2, and the organic layer was dried over $MgSO_4$, filtered, and the solvent evaporated under reduced pressure. Flash chromatographic purification with silica gel (hexane/CH_2Cl_2 85:15) yielded compounds **3** (55 mg, 43%) and **4** (84 mg, 41%) as a yellow powders. Compound **3**: M.p. 264–266 °C; ¹H NMR (400 MHz, $CDCl_3$): $\delta = 8.42$ (d, $J = 9.3$ Hz, $1 H_{ar}$), 8.36 (d, $J = 8.1$ Hz, $1 H_{ar}$), 8.27–8.17 (m, $3 H_{ar} + 1 H_{C=C}$), 8.15 (d, $J = 9.3$ Hz, $1 H_{ar}$), 8.12–8.07 (m, $2 H_{ar}$), 8.03 (t, $J = 7.6$ Hz, $1 H_{ar}$), 7.28 (d, $J = 16.5$ Hz, $1 H_{C=C}$), 7.09 (s, $1 H_{\alpha H}$), 2.65 ppm (s, $3 H_{CH_3}$); ¹³C NMR (100.6 MHz, $CDCl_3$): $\delta = 136.03$, 128.20, 127.90, 127.42, 126.17, 125.94, 125.64, 125.40, 125.19, 123.95, 122.97, 56.70 (αH), 29.71 ppm (CH_3); UV/Vis (THF): λ (ε) = 285 (17800), 370 nm (22900); fluorescence (THF): λ ($\lambda_{exc} = 380$ nm) (φ) = 484 nm (0.0147); MALDI-TOF MS (negative mode) m/z calcd for $C_{38}H_{15}Cl_{13}$: 932.4; found: [M] = 932.1, [M−35] = 897.1. Compound **4**: M.p. 336–337 °C; ¹H NMR (400 MHz, $CDCl_3$): $\delta = 8.44$ (d, $J = 9.3$ Hz, $2 H_{ar}$), 8.38 (d, $J = 8.0$ Hz, $2 H_{ar}$), 8.29–8.19 (m, $6 H_{ar} + 2 H_{C=C}$), 8.16 (d, $J = 9.3$ Hz, $2 H_{ar}$), 8.13–8.07 (m, $4 H_{ar}$), 8.03 (t, $J = 7.6$ Hz, $2 H_{ar}$), 7.31 (d, $J = 16.4$ Hz, $2 H_{C=C}$), 7.18 ppm (s, $1 H_{\alpha H}$); ¹³C NMR (100.6 MHz, $CDCl_3$): $\delta = 137.71$, 137.11, 136.61, 136.18, 134.16, 133.51, 131.77, 131.49, 130.92, 130.70, 129.01, 128.23, 127.92, 126.18, 125.99, 125.66, 125.42, 125.20, 125.04, 124.85, 123.99, 123.00, 56.95 ppm (αH); UV/Vis (THF): λ (ε) = 285 (24700), 370 nm (32200); fluorescence (THF): λ ($\lambda_{exc} = 380$ nm) (φ) = 484 nm (0.0260); MALDI-TOF MS (negative mode) m/z calcd for $C_{55}H_{23}Cl_{13}$: 1144.6; found: [M] = 1144.1, [M−72] = 1072.0, [M−108] = 1036.0. Method B: The same procedure as in method A, but use of bis(diethylphosphonate) derivative **1** (300 mg, 0.31 mmol) yielded compounds **3** (34 mg, 9%) and **4** (265 mg, 75%).

Synthesis of radical (E)-2-{2,3,5,6-tetrachloro-4-[(perchlorophen-yl)(2,3,5,6-tetrachloro-4-methylphenyl)methyl]styryl} pyrene (5·): An excess (0.1 mL, 0.22 mmol) of tetrabutylammonium hydroxide (40% in water) was added to a solution of compound **3** (50 mg, 0,05 mmol) in THF (15 mL). The resulting violet mixture was stirred for 15 min and then $AgNO_3$ (56 mg, 0.33 mmol) was added and the mixture stirred for 10 min. The solution changed color to dark brown while silver (Ag^0) precipitated. Then the solution was filtered to eliminate the silver and evaporated under reduced pressure. The obtained compound was isolated by filtration through silica gel with CH_2Cl_2 and a dark brown powder was obtained (43 mg,

Synthesis of radical 2,2′-[(1E,1′E)-{[(perchlorophenyl)methylene]-bis(2,3,5,6-tetrachloro-4,1-phenylene)}bis(ethene-2,1-diyl)]dipyrene (6˙): The same procedure as before was used for the conversion of compound **4** to the corresponding radical **6** that was obtained as a dark brown powder, yield 92%. M.p. 320 °C dec.; ESR (CH$_2$Cl$_2$): $g = 2.0023$, $\Delta H_{pp} = 1.10$ G, $a_H = 1.90$ G, $a_{13Car} = 9.5$, 12.5 G, $a_{13C\alpha} = 29.6$ G; ATR-IR: $\tilde{v} = 2921.5$, 1616.4, 1509.3, 1336.8, 1319.2, 1264.5, 955.5, 838.5, 818.6, 716.1 cm^{-1}; UV/Vis (THF): $\lambda(\varepsilon) = 285$ (22 500), 370 (28 500), 397 (26 600), 536 (4700), 587 (4000), 687 nm (629); MALDI-TOF MS (negative mode) (C$_{55}$H$_{22}$Cl$_{13}$, $M = 1143.6$): m/z [M] = 1144.0, [M−72] = 1072.0, [M−108] = 1036.0.

Computational details

Quantum chemical calculations were performed with the ORCA electronic structure program package.[18] All geometry optimizations were run with tight convergence criteria using the B3LYP[19] functional together with the RIJCOSX algorithm[20] and the Ahlrichs segmented def2-TZVP basis set,[21] starting from preoptimized geometries obtained with the smaller def2-SVP basis set.[22] In all optimizations and energy evaluations, the latest Grimme's semiempirical atom-pairwise correction (DFT-D3 methods), which accounts for the major part of the contribution of dispersion forces to the energy, was included.[23] From these geometries obtained at the above-mentioned level, all reported electronic data were obtained by means of single-point calculations using the same functional as well as the more polarized def2-TZVPP basis set. Reported energies are uncorrected for the zero-point vibrational term. Solvent effects were taken into account by using the COSMO solvation model.[24] Molecular orbital diagrams (in Figure 4 of the main text and Figures S7, S8, and S9 in the Supporting Information) were drawn with VMD.[25]

Acknowledgements

[1] a) A. P. De Silva, H. Q. N. Gunaratne, C. P. McCoy, *Nature* **1993**, *364*, 42; b) U. Pischel, *Angew. Chem. Int. Ed.* **2010**, *49*, 1356; *Angew. Chem.* **2010**, *122*, 1396; c) M. Amelia, M. Baroncini, A. Credi, *Angew. Chem. Int. Ed.* **2008**, *47*, 6240; *Angew. Chem.* **2008**, *120*, 6336; d) J. Andréasson, S. D. Straight, T. A. Moore, A. L. Moore, D. Gust, *J. Am. Chem. Soc.* **2008**, *130*,

11122; e) F. M. Raymo, R. J. Alvarado, S. Giordani, M. A. Cejas, *J. Am. Chem. Soc.* **2003**, *125*, 2361; f) K. Szaciłowski, *Chem. Rev.* **2008**, *108*, 3481; g) T. Gupta, M. E. van der Boom, *Angew. Chem. Int. Ed.* **2008**, *47*, 5322; *Angew. Chem.* **2008**, *120*, 5402.

[2] a) M. Mas-Torrent, C. Rovira, J. Veciana, *Adv. Mater.* **2013**, *25*, 462; b) A. Coskun, J. M. Spruell, G. Barin, W. R. Dichtel, A. H. Flood, Y. Y. Botros, J. F. Stoddart, *Chem. Soc. Rev.* **2012**, *41*, 4827; c) S. Venkataramani, U. Jana, M. Dommaschk, F. D. Sönnichsen, F. Tuczek, R. Herges, *Science* **2011**, *331*, 445.

[3] F. M. Raymo, M. Tomasulo, *Chem. Soc. Rev.* **2005**, *34*, 327.

[4] a) J. Andréasson, U. Pischel, *Chem. Soc. Rev.* **2010**, *39*, 174; b) A. P. de Silva, S. Uchiyama, *Nature Nanotech.* **2007**, *2*, 399.

[5] a) H. Wang, D. Zhang, X. Guo, L. Zhu, Z. Shuai, D. Zhu, *Chem. Commun.* **2004**, 670; b) B. Balan, K. R. Gopidas, *Chem. Eur. J.* **2006**, *12*, 6701.

[6] R. Martínez, I. Ratera, A. Tárraga, P. Molina, J. Veciana, *Chem. Commun.* **2006**, *36*, 3809.

[7] a) C. Sporer, I. Ratera, D. Ruiz-Molina, Y. Zhao, J. Vidal-Gancedo, K. Wurst, P. Jaitner, K. Clays, A. Persoons, C. Rovira, J. Veciana, *Angew. Chem. Int. Ed.* **2004**, *43*, 5266; *Angew. Chem.* **2004**, *116*, 5378; b) C. Simão, M. Mas-Torrent, N. Crivillers, V. Lloveras, J. M. Artés, P. Gorostiza, J. Veciana, C. Rovira, *Nat. Chem.* **2011**, *3*, 359–364; c) C. Simão, M. Mas-Torrent, J. Veciana, C. Rovira, *Nano Lett.* **2011**, *11*, 4382.

[8] a) M. Ballester, *Adv. Phys. Org. Chem.* **1989**, *25*, 267; b) D. Maspoch, N. Domingo, D. Ruiz-Molina, K. Wurst, C. Tejada, C. Rovira, J. Veciana, *J. Am. Chem. Soc.* **2004**, *126*, 730.

[9] D. Reitzenstein, T. Quast, F. Kanal, M. Kullmann, S. Ruetzel, M. S. Hammer, C. Deibel, V. Dyakonov, T. Brixner, C. Lambert, *Chem. Mater.* **2010**, *22*, 6641.

[10] V. Lloveras, J. Vidal-Gancedo, T. M. Figueira-Duarte, J.-F. Nierengarten, J. J. Novoa, F. Mota, N. Ventosa, J. Veciana, C. Rovira, *J. Am. Chem. Soc.* **2011**, *133*, 5818.

[11] J. Guasch, L. Grisanti, M. Souto, V. Lloveras, J. Vidal-Gancedo, I. Ratera, A. Painelli, C. Rovira, J. Veciana, *J. Am. Chem. Soc.* **2013**, *135*, 6958.

[12] M. Ballester, J. Castañer, J. Riera, A. Ibáñez, J. Pujadas, *J. Org. Chem.* **1982**, *47*, 259.

[13] N. G. Connelly, W. E. Geiger, *Chem. Rev.* **1996**, *96*, 877.

[14] C. Rovira, D. Ruiz-Molina, O. Elsner, J. Vidal-Gancedo, J. Bonboisin, J. P. Launay, J. Veciana, *Chem. Eur. J.* **2001**, *7*, 240.

[15] The fluorescence quantum yields were measured with respect to anthracene as standard ($\Phi = 0.27$): W. R. Dawson, M. W. Windsor, *J. Phys. Chem.* **1968**, *72*, 3251.

[16] O. A. Khakhel, V. V. Nekrasov, T. V. Sakhno, N. N. Barashkov, R. N. Nurmukhametov, *J. Appl. Spectrosc.* **1994**, *60*, 66.

[17] C. Farren, C. A. Christensen, S. FitzGerald, M. R. Bryce, A. Beeby, *J. Org. Chem.* **2002**, *67*, 9130.

[18] ORCA—An ab initio, DFT and semiempirical SCF-MO package, written by F. Neese, Max Planck Institute for Bioinorganic Chemistry, D-45470 Mülheim/Ruhr, **2012**, version 3.0, webpage: http://www.cec.mpg.de/forum/portal.php. F. Neese, "The ORCA program system", *WIREs Comput Mol Sci.* **2012**, *2*, 73–78.

[19] a) A. D. Becke, *J. Chem. Phys.* **1993**, *98*, 5648–5652; b) C. T. Lee, W. T. Yang, R. G. Parr, *Phys. Rev. B* **1988**, *37*, 785–789.

[20] F. Neese, F. Wennmohs, A. Hansen, U. Becker, *Chem. Phys.* **2009**, *356*, 98–109.

[21] a) A. Schäfer, C. Huber, R. Ahlrichs, *J. Chem. Phys.* **1994**, *100*, 5829–5835; b) F. Weigend, R. Ahlrichs, *Phys. Chem.Chem. Phys.* **2005**, *7*, 3297–3305.

[22] A. Schäfer, H. Horn, R. Ahlrichs, *J. Chem. Phys.* **1992**, *97*, 2571–2577.

[23] S. Grimme, J. Antony, S. Ehrlich, H. Krieg, *J. Chem. Phys.* **2010**, *132*, 154104–154119.

[24] a) A. Klamt, G. Schüürmann, *J. Chem. Soc. Perkin Trans. 2* **1993**, 799–805; b) A. Klamt, *J. Phys. Chem.* **1995**, *99*, 2224–2235.

[25] VMD—Visual Molecular Dynamics: W. Humphrey, A. Dalke, K. Schulten, *J. Mol. Graphics* **1996**, *14*, 33–38, homepage: http://www.ks.uiuc.edu/Research/vmd/.

CHEMISTRY
A European Journal

Supporting Information

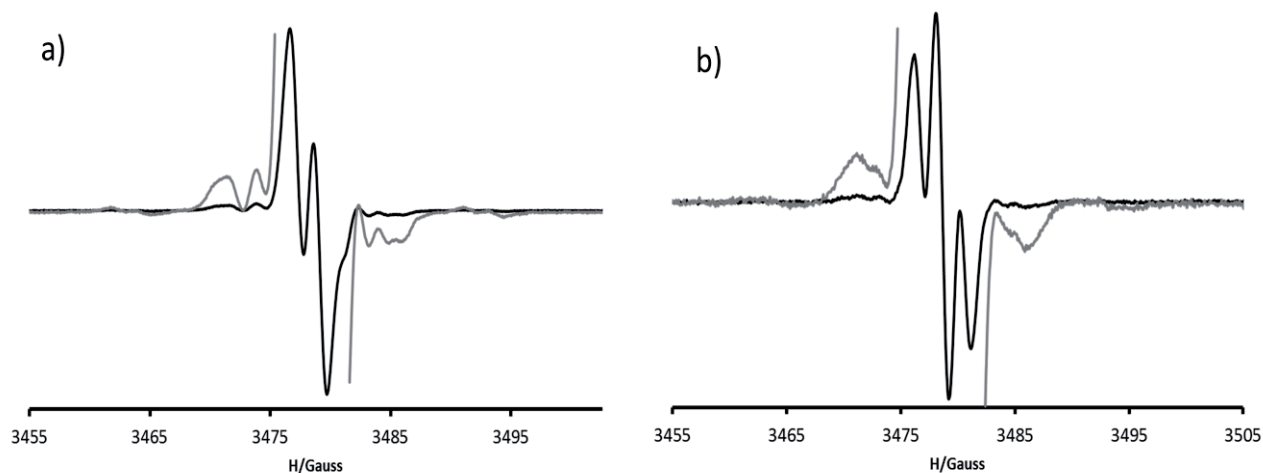# Pyrene-Based Dyad and Triad Leading to a Reversible Chemical and Redox Optical and Magnetic Switch

Carlos Franco,[a, c] Marta Mas-Torrent,*[a, c] Antonio Caballero,[b] Arturo Espinosa,[b] Pedro Molina,[b] Jaume Veciana,[a, c] and Concepció Rovira*[a, c]

chem_201405993_sm_miscellaneous_information.pdf

SUPPORTING INFORMATION

Content

Figure SI1: ESR spectra of radicals a) **5'** and b) **6'** in CH$_2$Cl$_2$ at room temperature.

c)
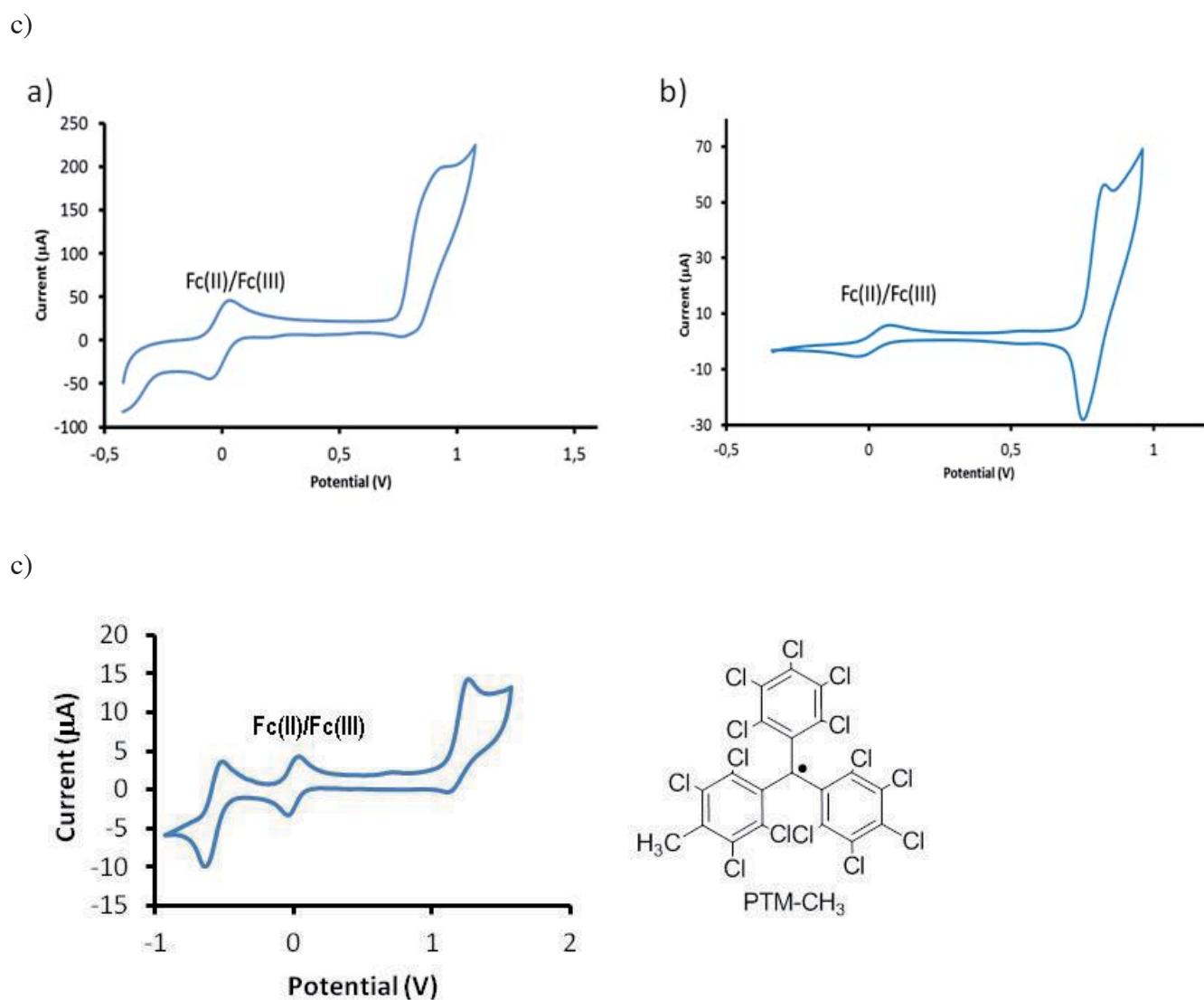
Figure SI2: Cyclic voltammograms of a) compound **3** b) compound **4** and c) Radical PTM-Me in CH$_2$Cl$_2$ using *n*-Bu$_4$NPF$_6$ 0.05 M as supporting electrolyte, Ag wire as a pseudoreference electrode, and platinum wires as the counter and working electrodes in the presence of Fc as internal standard.
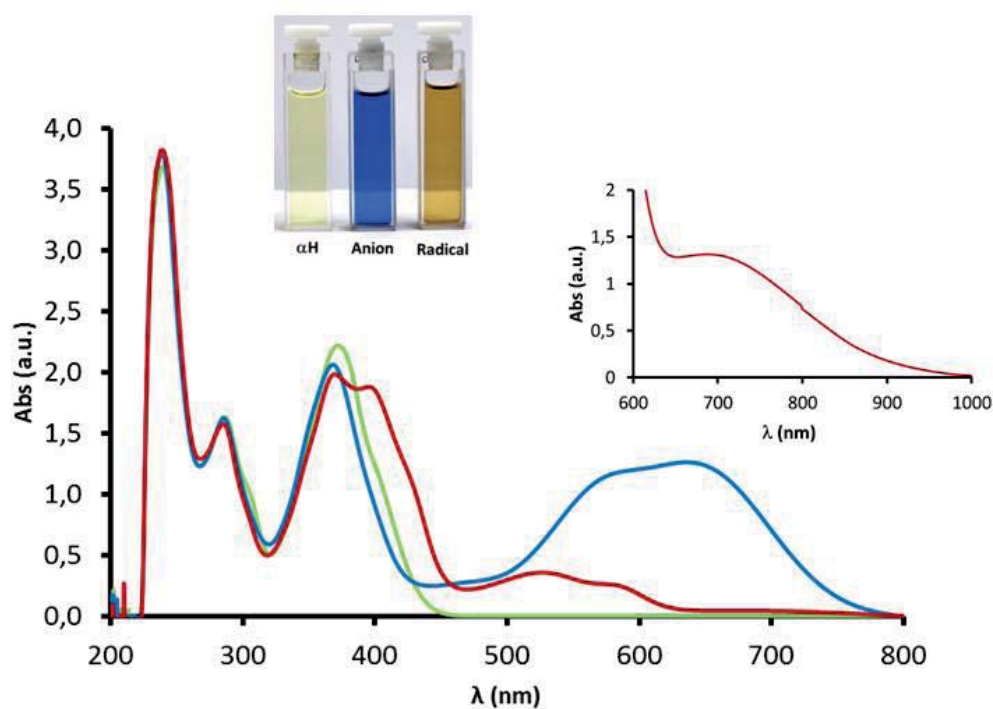
Figure SI3: UV-Vis spectra of αH-PTM **4** (blue line), anion **6⁻** (red line) and radical **6·** (green line). Insets: photographs of the cuvettes containing 7×10^{-5}M solutions of **4**, **6⁻** and **6·** in THF and low energy region spectrum of a more concentrated solution of radical **6·** showing the CT band.
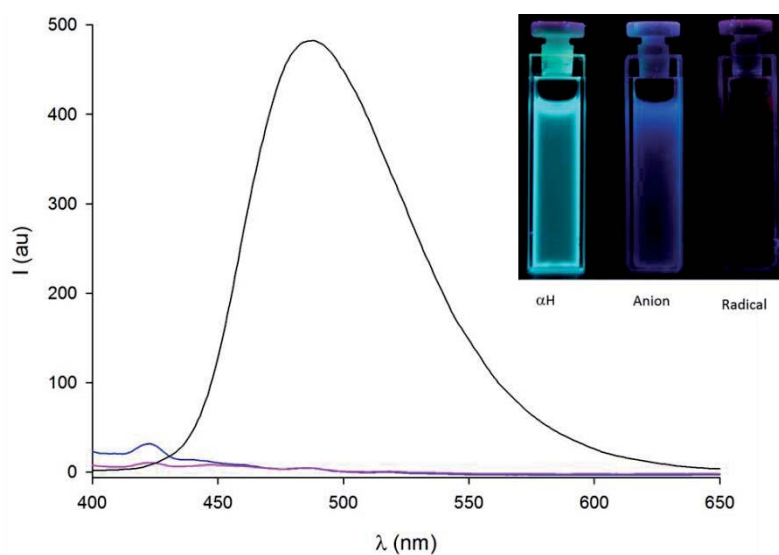
Figure SI4: Fluorescence spectra of αH-PTM **4** (black line), anion **6⁻** (blue line) and radical **6·** (pink line). Inset: photographs of cuvettes under 254 nm light, containing 2.5×10^{-5}M solutions of **4**, **6⁻** and **6·** in THF.

Table SI 1: Uv-Vis and Fluorescence data of compounds **3**, **4**, **5·**, **5⁻**, **6·** and **6⁻** in THF

| Compound	λ (nm) (ε (M⁻¹cm⁻¹)x 1·10⁻³)	Emission (λexc=380nm) (a.u.)	ϕ
PTM Anion **5⁻**	285 (18.8), 365 (20.1), 518 (16.3), 601 (16.1)	423 (37.2), 444 (18.1), 486 (7.4), 517 (1.9)	0.0018
PTM Radical **5·**	285 (16.6), 368 (23.5), 380 (26.3), 522 (3.5), 583 (2.9), 685 (0.45)	423 (20.4), 444 (12.5), 486 (7.8), 517 (3.5)	0.0009
αH-PTM **3**	285 (17.8), 370 (22.9)	484 (216)	0.0147
PTM Anion **6⁻**	284 (24.0), 367 (31.5), 596 (20.4), 636 (21.3)	423 (31.9), 444 (12.5), 486 (3.2)	0.0008
PTM Radical **6·**	285 (22.5), 370 (28.5), 397 (26.6), 536 (4.7), 587 (4.0), 687 (0.63)	423 (9.7), 444 (6.8), 486 (3.6)	0.0003
αH-PTM **4**	285 (24.7), 370 (32.2)	486(482)	0.026

A first attempt to follow the chemical oxidation processes of 3, 5·, 4, and 6· by UV- Vis spectroscopy resulted more complex than the formation of the anions from 5·, and 6·. A complex set of signals with almost no isosbestic points were obtained and was atributed to the low stability of the cationic species formed centered in the pyrenyl moieties.
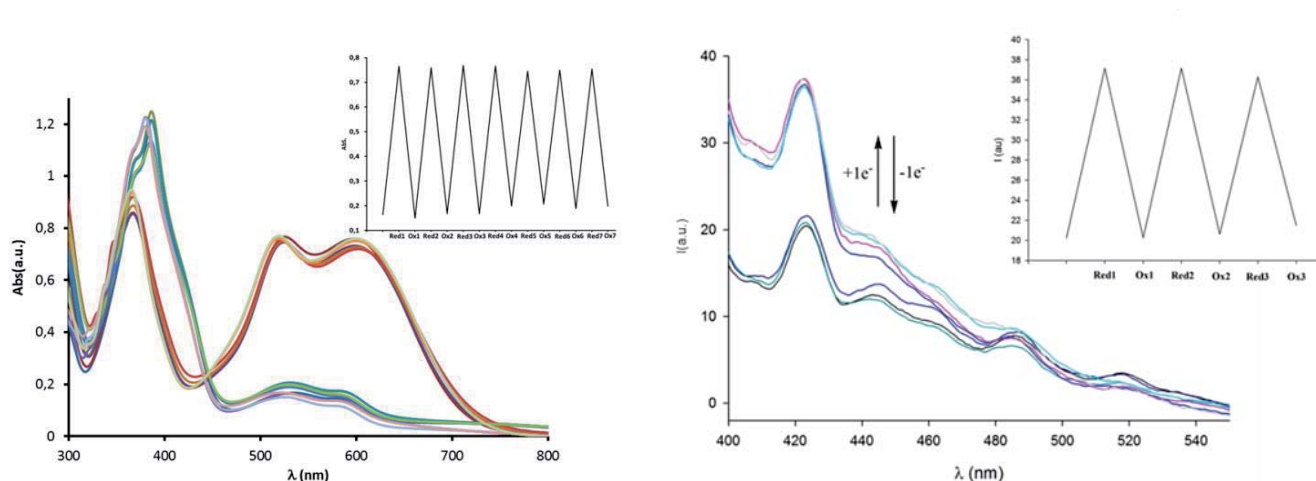
Figure SI5: Changes in UV-Vis spectra (left) and emission spectra (right) of radical **5·** in THF (electrolite 0.05 M of *n*-Bu₄NPF₆) upon several reduction and subsequent oxidation steps (15 minutes each step to reach the complete transformation). Insets: evolution of the UV-Vis intensity at 518 nm and emission intensity at 423 nm during the stepwise reduction an oxidation cycles.
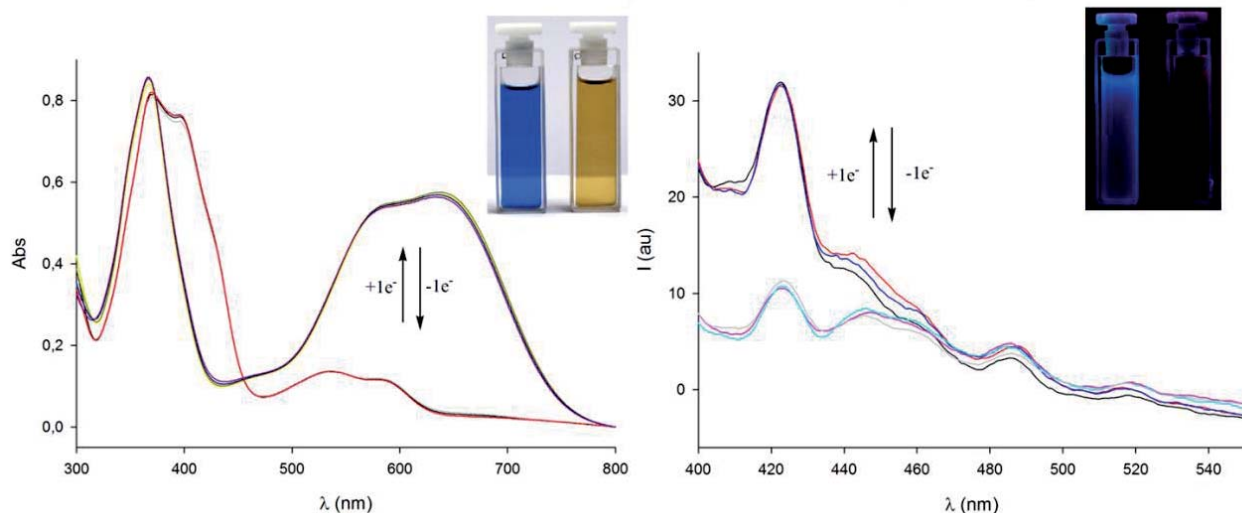
Figure SI 6: Changes in the UV-Vis spectra (left) and emission spectra (right) of radical **6·** (c = 2.5x10^{-5} M in THF using c = 0.05 M of *n*-Bu$_4$NPF$_6$) upon several reduction and subsequent oxidation steps (15 minutes each step to reach the complete transformation). Inset: visual changes in the absorption and fluorescence.
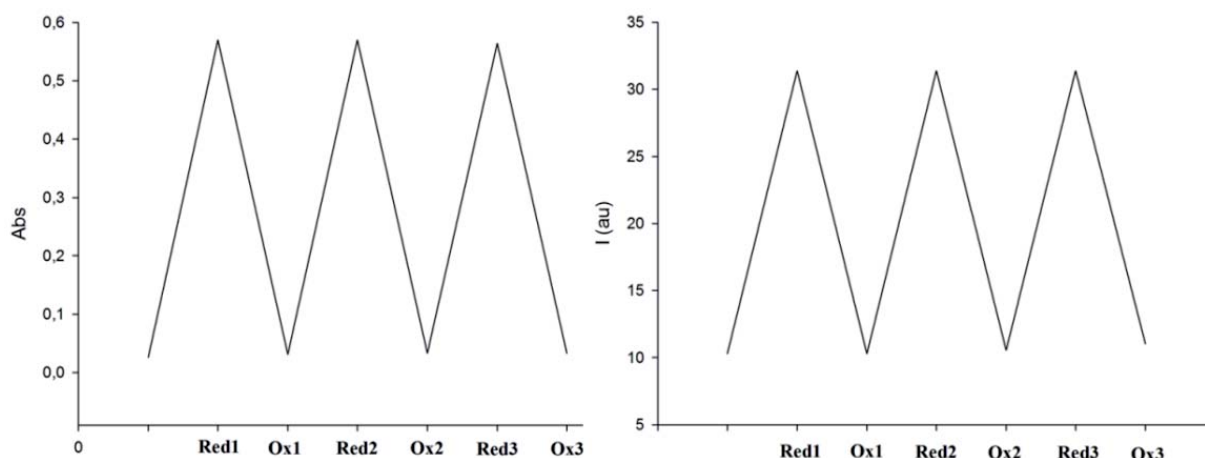
Figure SI 7: Evolution of the UV-Vis intensity at 518 nm (left) and fluorescence intensity at 423 nm (right) of the radical **6·** during the stepwise reduction an oxidation cycles.

Since it is demonstrated that the fluorescence of the synthesized compounds can be modulated by suitable chemical reagents, these systems can be exploited as platforms to mimic logic operations [R. J. Mitchell, *Microprocessor Systems: An Introduction*; Macmillan: London, 1995],where chemical reagents can be employed as input signals and the fluorescence at 484 nm as output. As an example, the addition of one equivalent of a reducing agent to a solution of radical **5·** or **6·** produces the reduction to the corresponding anions **5⁻** and **6⁻**, with only a modest increase in the fluorescence intensity. The reaction with one equivalent of acid (*I2*, Table 1), implies now a strong increase of the fluorescence intensity due to the formation of αH-PTM **3** and **4**. Applying the Boolean logic concepts, these operations can be interpreted as an "AND" gate.

		5·	6·
Reducing agent (*I1*)	H⁺ (*I2*)	O [*Φ*]	O (*Φ*)
0	0	0 [0.0009]	0 (0.0003)
1	0	0 [0.0018]	0 (0.0008)
0	1	0 [0.0009]	0 (0.0003)
1	1	1 [0.0147]	1 (0.0260)

Figure SI 8: The truth table for AND logic gate based on fluorescence of **5·** and **6·** in different conditions. The fluorescence quantum yields (Φ) are shown in the brackets. I1= reducing agent and I2=acid , where "1" and "0" refers to the presence or not of the chemical reagent, respectively; O= Fluorescence at 484 nm, where the binary code "1" is attributed to an emission above a pre-defined threshold level, and "0" below this level.

αLUMO

αHOMO

αHOMO-1

βLUMO+

βLUMO

βHOMO βHOMO-1
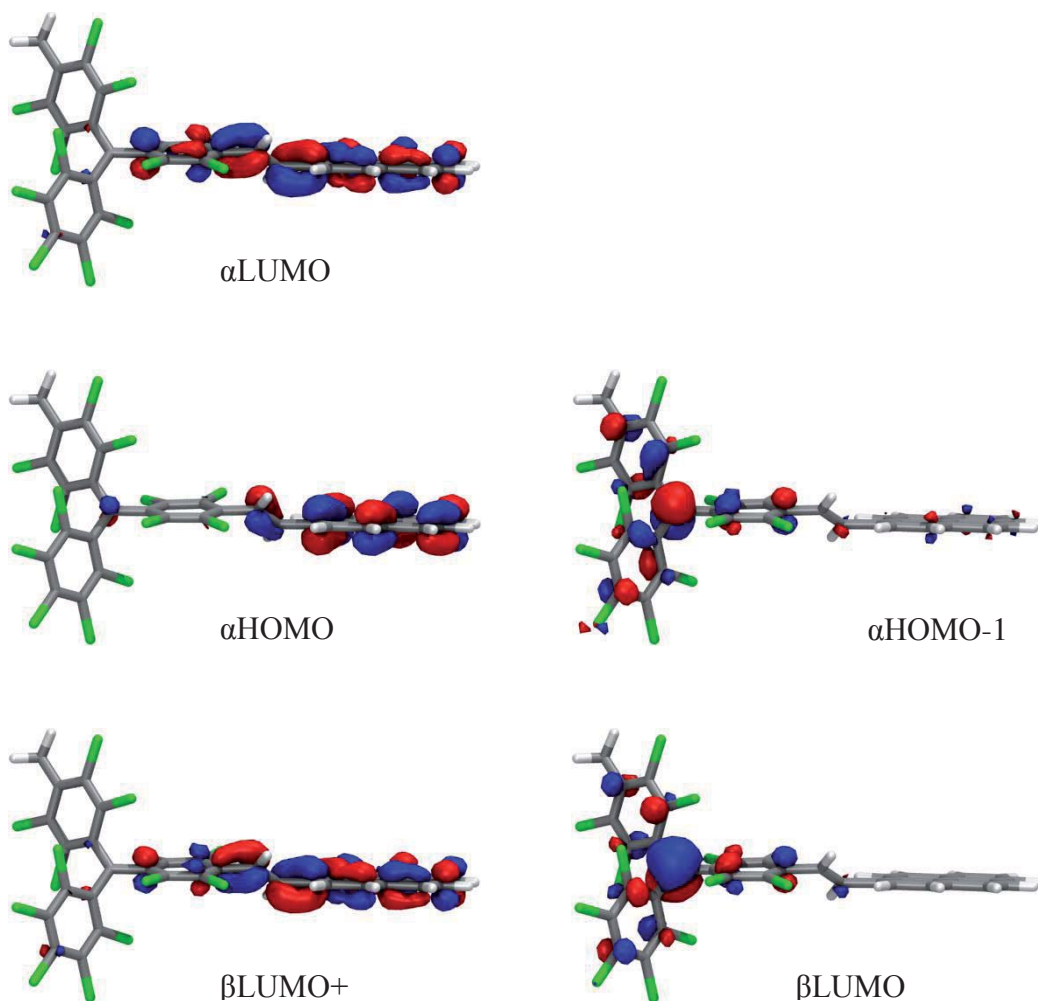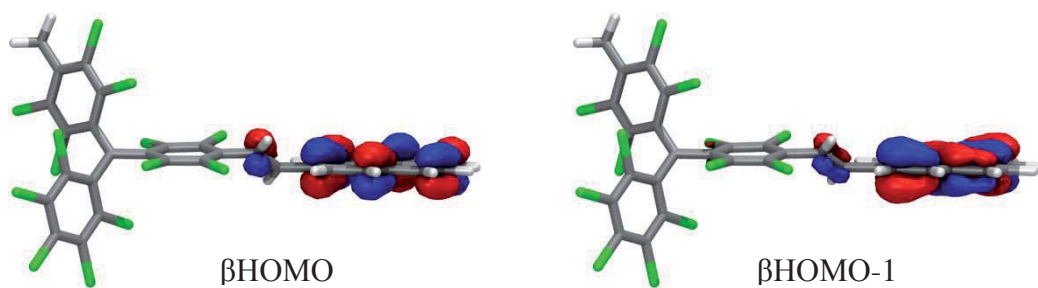
Figure SI 9: Calculated (COSMO$_{THF}$/B3LYP-D3/def2-TZVPP//COSMO$_{THF}$/B3LYP-D3/def2-TZVP) Kohn-Sham representative isosurfaces (isovalue 0.04 au) for radical **5**·.

LUMO

HOMO HOMO-1
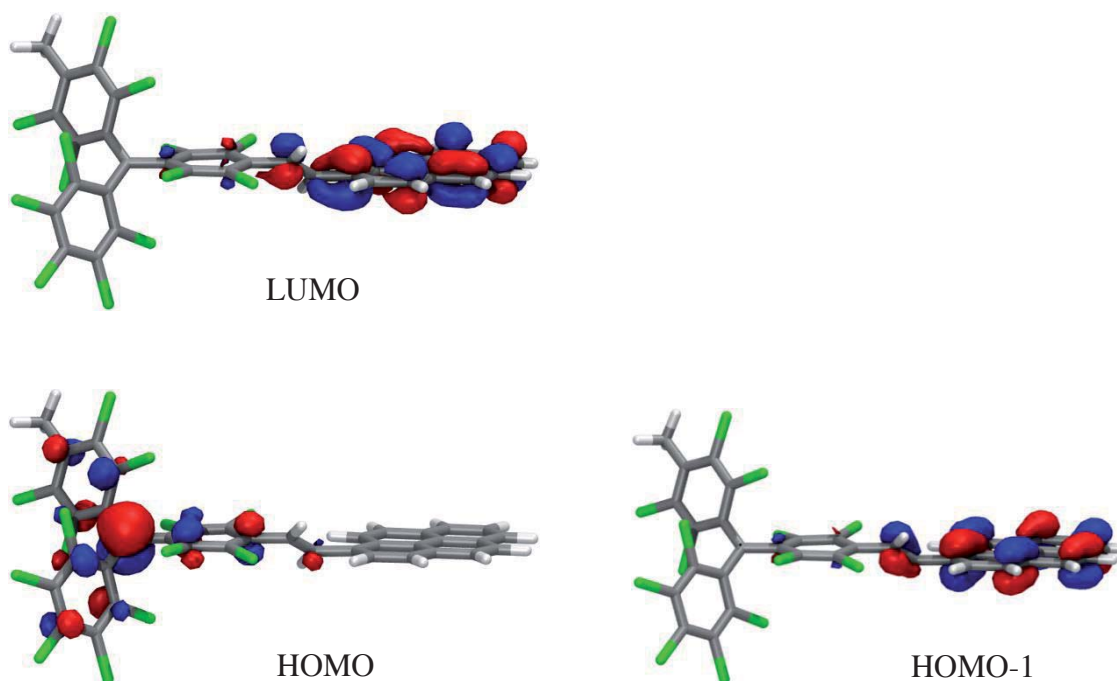
Figure SI 10: Calculated (COSMO$_{THF}$/B3LYP-D3/def2-TZVPP//COSMO$_{THF}$/B3LYP-D3/def2-TZVP) Kohn-Sham representative isosurfaces (isovalue 0.04 au) for anion **5**⁻.

LUMO

Figure SI 11: Calculated (COSMO_{THF}/B3LYP-D3/def2-TZVPP//COSMO_{THF}/B3LYP-D3/def2-TZVP) Kohn-Sham representative isosurfaces (isovalue 0.04 au) for **3**.

Cartesian coordinates (Å) and energies (hartree) for all computed species.

VPyr: E =-693.004418263285 au

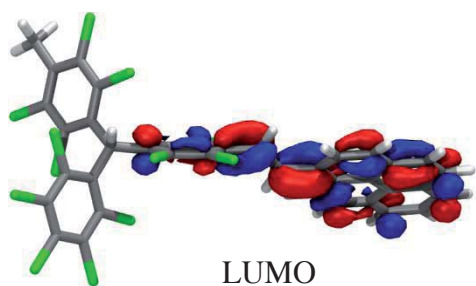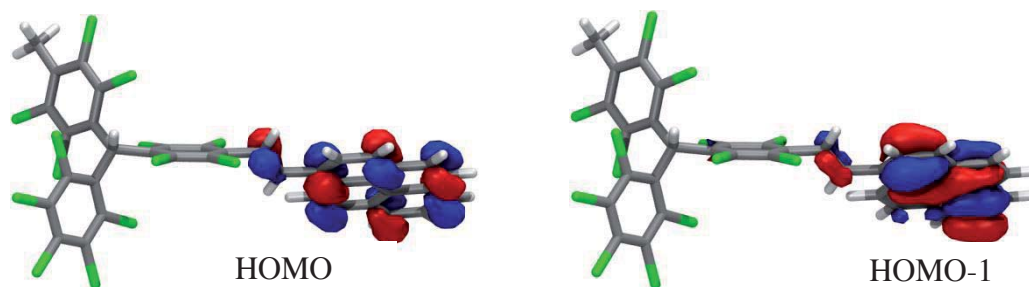|							
C	-0.077974	0.393658	0.072406	C	3.141049	-1.352584	6.473563
C	0.038660	-0.166415	1.276621	C	2.081685	-1.336911	5.626691
H	0.731758	0.930932	-0.405789	C	2.186224	-0.770183	4.313886
H	-1.006369	0.332199	-0.479732	C	1.109505	-0.734954	3.424312
H	-0.827909	-0.678505	1.686411	C	3.433659	-0.223783	3.908162
C	1.220775	-0.174333	2.148865	C	4.544305	-0.241869	4.792261
C	2.456073	0.355012	1.757478	H	2.571819	0.785168	0.770453
C	3.560276	0.342276	2.607429	H	4.929208	1.309180	1.227830
C	4.832833	0.881606	2.219082	H	6.844941	1.280573	2.752886
C	5.892939	0.865411	3.063047	H	7.820368	0.700140	4.961444
C	5.791955	0.306311	4.380496	H	7.576003	-0.275300	7.216437
C	6.869613	0.282152	5.270913	H	5.420198	-1.235926	7.938639
C	6.730479	-0.268158	6.539798	H	3.043084	-1.783945	7.463032
C	5.517991	-0.807680	6.947996	H	1.130082	-1.755836	5.932860
C	4.410404	-0.806997	6.091949	H	0.159062	-1.153205	3.737751

Compound **3**:   E = -7438.882775439215 au

C	0.014786	-0.021911	-0.123482	C	5.913571	-0.015851	-0.244380
H	-0.074568	0.108172	0.953211	H	6.282438	-1.042919	-0.267373
C	1.541440	-0.020256	-0.281898	H	6.345998	0.527288	-1.076988
C	2.270419	0.626097	-1.286363	H	6.268119	0.431469	0.686232
C	3.672549	0.640938	-1.277189	C	-0.736009	1.221042	-0.619304
C	4.411664	-0.004712	-0.283039	C	-1.633531	1.267844	-1.694130
C	3.681575	-0.662984	0.711392	C	-2.349188	2.431980	-2.003597
C	2.287540	-0.662463	0.721118	C	-2.162109	3.591572	-1.248726
Cl	1.463861	1.372887	-2.630000	C	-1.258646	3.579544	-0.183956
Cl	4.516767	1.476647	-2.552986	C	-0.571090	2.403043	0.123330
Cl	4.558117	-1.482355	1.971224	Cl	-1.843898	-0.091969	-2.746610
Cl	1.468561	-1.474856	2.026788	Cl	-3.456768	2.452472	-3.331451

Cl	-3.037114	5.030568	-1.629140	C	-3.342670	-8.538250	-4.626548
Cl	-1.014033	5.012653	0.749732	C	-3.937951	-9.836058	-4.539232
Cl	0.516162	2.428742	1.481621	C	-3.974726	-10.717076	-5.626931
C	-0.686197	-1.375459	-0.302144	C	-4.547618	-11.976546	-5.499168
C	-0.274163	-2.413769	-1.147531	C	-5.096267	-12.381712	-4.288507
C	-0.904133	-3.665612	-1.132105	C	-5.084757	-11.531611	-3.175028
C	-1.991348	-3.929081	-0.287908	C	-5.641170	-11.922761	-1.914229
C	-2.417210	-2.882241	0.539708	C	-5.617329	-11.083773	-0.847852
C	-1.782938	-1.641779	0.535100	C	-5.031287	-9.780907	-0.939753
Cl	1.001862	-2.166649	-2.297127	C	-4.996440	-8.905401	0.153053
Cl	-0.291860	-4.932730	-2.156413	C	-4.468491	-9.356395	-2.176197
Cl	-3.780121	-3.165206	1.581644	C	-4.498524	-10.238188	-3.295186
Cl	-2.373371	-0.404962	1.610199	H	-2.821387	-6.741425	-3.673419
C	-2.651410	-5.243311	-0.190677	H	-2.909458	-8.231117	-5.571377
H	-2.701624	-5.654694	0.811176	H	-3.546473	-10.406478	-6.572670
C	-3.183023	-5.904470	-1.224193	H	-4.564663	-12.648035	-6.348687
H	-3.117245	-5.443084	-2.200735	H	-5.540090	-13.365935	-4.195919
C	-4.412919	-7.658665	0.042397	H	-6.084133	-12.908036	-1.827848
C	-3.830610	-7.215258	-1.154114	H	-6.041990	-11.390435	0.100963
C	-3.868490	-8.065202	-2.289512	H	-5.440704	-9.212859	1.092343
C	-3.302349	-7.701997	-3.558574	H	-4.425051	-6.998581	0.900057

Radical **5·**:   E = -7438.256470934694 au

C	-0.065376	0.099712	0.005503	C	-0.484519	-0.870007	-2.277400
C	1.401854	-0.003986	0.033542	C	-1.176539	-1.719264	-3.142512
C	2.227893	1.136017	-0.041760	C	-2.303785	-2.442929	-2.713954
C	3.616565	1.021559	-0.041472	C	-2.667623	-2.299567	-1.361969
C	4.262170	-0.220630	0.010856	C	-1.952225	-1.491463	-0.482615
C	3.444848	-1.353734	0.089977	Cl	0.788568	0.117428	-2.926590
C	2.051984	-1.251836	0.117914	Cl	-0.590831	-1.905220	-4.771670
Cl	1.521681	2.708147	-0.249601	Cl	-4.063702	-3.166146	-0.788447
Cl	4.601241	2.452907	-0.138671	Cl	-2.396841	-1.491397	1.195757
Cl	4.179918	-2.930864	0.178725	C	-3.075131	-3.357594	-3.567265
Cl	1.116412	-2.694820	0.358044	H	-3.329829	-4.304845	-3.106514
C	5.761786	-0.289787	-0.019087	C	-3.509259	-3.094059	-4.805959
H	6.141347	0.189451	-0.923507	H	-3.258884	-2.140356	-5.252095
H	6.180320	0.252953	0.830784	C	-5.283496	-4.825578	-5.017254
H	6.122486	-1.311708	0.009518	C	-4.325370	-3.998361	-5.619261
C	-0.755854	1.044141	0.896807	C	-4.178546	-4.030713	-7.028632
C	-1.723966	1.943713	0.404680	C	-3.193899	-3.251736	-7.724211
C	-2.391710	2.835702	1.245341	C	-3.062333	-3.308721	-9.074221
C	-2.094458	2.861392	2.612274	C	-3.895809	-4.155254	-9.871922
C	-1.128549	1.989866	3.127253	C	-3.773503	-4.228347	-11.265405
C	-0.478994	1.091830	2.278589	C	-4.597608	-5.066718	-12.005995
Cl	-2.037396	2.029326	-1.297951	C	-5.558355	-5.848418	-11.375327
Cl	-3.562258	3.934710	0.605836	C	-5.713346	-5.810447	-9.983790
Cl	-2.914696	3.961219	3.658177	C	-6.688353	-6.610913	-9.304221
Cl	-0.769115	2.016037	4.817704	C	-6.813412	-6.567285	-7.953521
Cl	0.615466	-0.054215	2.980178	C	-5.981124	-5.717058	-7.156404
C	-0.836635	-0.744876	-0.916459	C	-6.092215	-5.664606	-5.761302

C	-5.011353	-4.895946	-7.798561	H	-6.197308	-6.500167	-11.959617
C	-4.874587	-4.952168	-9.215514	H	-7.325351	-7.260212	-9.893578
H	-2.527569	-2.613280	-7.160699	H	-7.551134	-7.181993	-7.450969
H	-2.308306	-2.709709	-9.571606	H	-6.834156	-6.279085	-5.265215
H	-3.025106	-3.622489	-11.762580	H	-5.417942	-4.779729	-3.944053
H	-4.490365	-5.112202	-13.082688				

Anion **5⁻**: E = -7438.394048586418 au

C	-0.090769	0.029914	0.015867	Cl	-4.279030	-3.075313	-0.426557
C	1.365058	-0.028660	-0.043926	Cl	-2.447499	-1.394248	1.395664
C	2.171794	1.128663	-0.180267	C	-3.335009	-3.606653	-3.179488
C	3.561617	1.061957	-0.226319	H	-3.683469	-4.463528	-2.613990
C	4.259928	-0.151268	-0.201525	C	-3.718462	-3.486817	-4.457475
C	3.475881	-1.303595	-0.085996	H	-3.384169	-2.628763	-5.025038
C	2.085475	-1.246940	0.023850	C	-5.626033	-5.089403	-4.508690
Cl	1.410485	2.681514	-0.404869	C	-4.572289	-4.442388	-5.168821
Cl	4.501100	2.532285	-0.373393	C	-4.366359	-4.705552	-6.545940
Cl	4.273499	-2.864320	-0.035804	C	-3.280761	-4.129067	-7.287147
Cl	1.216094	-2.726887	0.332498	C	-3.092836	-4.398864	-8.604134
C	5.760858	-0.169800	-0.300742	C	-3.967739	-5.277171	-9.319459
H	6.089284	0.310657	-1.224800	C	-3.792177	-5.565400	-10.678952
H	6.206493	0.388879	0.525253	C	-4.658218	-6.429634	-11.337707
H	6.153510	-1.180830	-0.282138	C	-5.713725	-7.025465	-10.657481
C	-0.726286	0.993018	0.893929	C	-5.925364	-6.769742	-9.296460
C	-1.804770	1.818020	0.473139	C	-6.999274	-7.374460	-8.565073
C	-2.423114	2.739699	1.315601	C	-7.177582	-7.120503	-7.243563
C	-1.954182	2.931187	2.619796	C	-6.306660	-6.235208	-6.530556
C	-0.877836	2.158813	3.067813	C	-6.471773	-5.964349	-5.166424
C	-0.308741	1.196297	2.236487	C	-5.238956	-5.603461	-7.228572
Cl	-2.324607	1.756741	-1.187846	C	-5.045158	-5.881388	-8.612600
Cl	-3.748709	3.710146	0.744769	H	-2.583524	-3.476425	-6.780198
Cl	-2.695676	4.102441	3.664646	H	-2.261220	-3.952069	-9.136641
Cl	-0.296795	2.378429	4.692073	H	-2.969250	-5.106324	-11.214103
Cl	0.887745	0.133217	2.923687	H	-4.509206	-6.641146	-12.389486
C	-0.887774	-0.862208	-0.793299	H	-6.384433	-7.699157	-11.177917
C	-0.584646	-1.159549	-2.151669	H	-7.667897	-8.046771	-9.090209
C	-1.323190	-2.060461	-2.914411	H	-7.990478	-7.588789	-6.700539
C	-2.494683	-2.668816	-2.425584	H	-7.286150	-6.434717	-4.627799
C	-2.822585	-2.360778	-1.091445	H	-5.801544	-4.870574	-3.462919
C	-2.040791	-1.533100	-0.295977				
Cl	0.713344	-0.293178	-2.934926				
Cl	-0.751088	-2.461030	-4.521635				
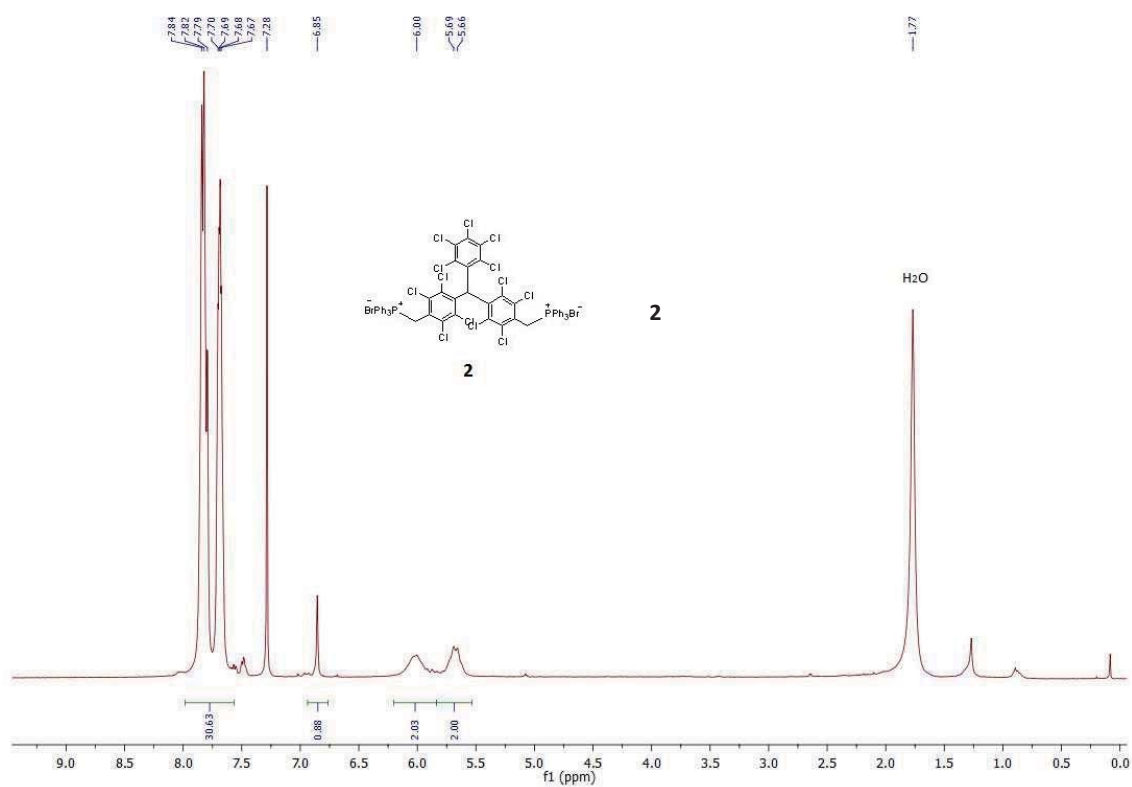
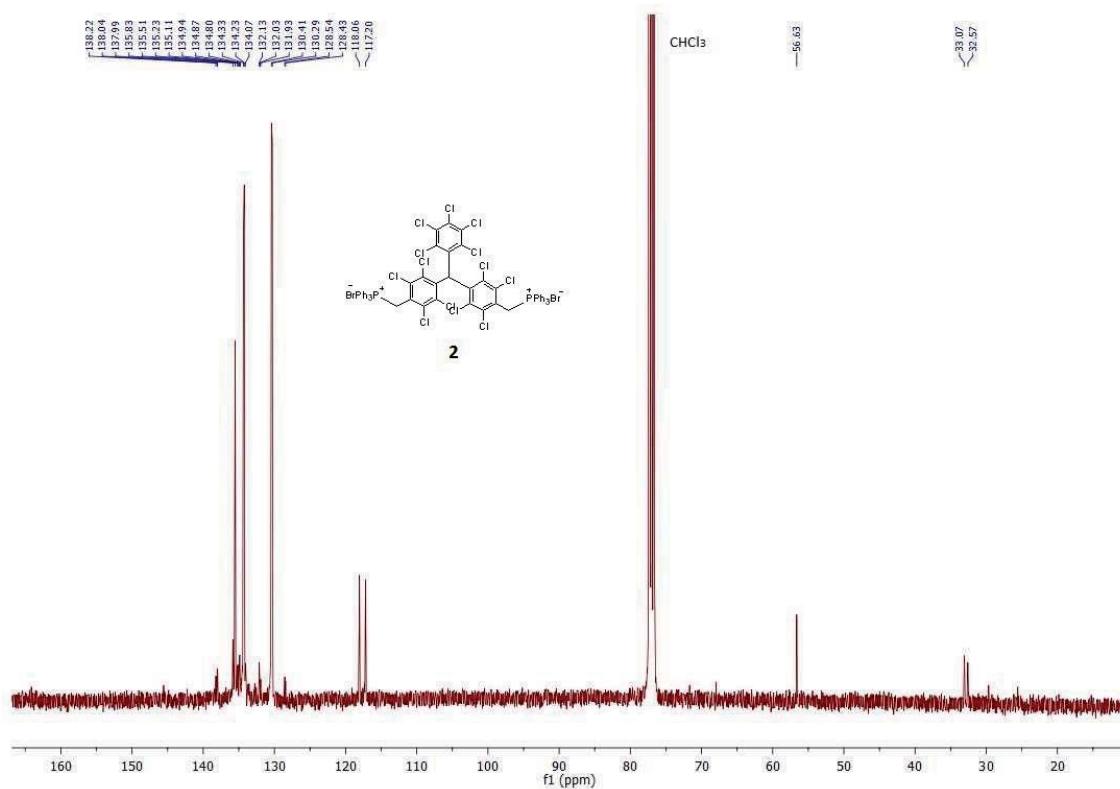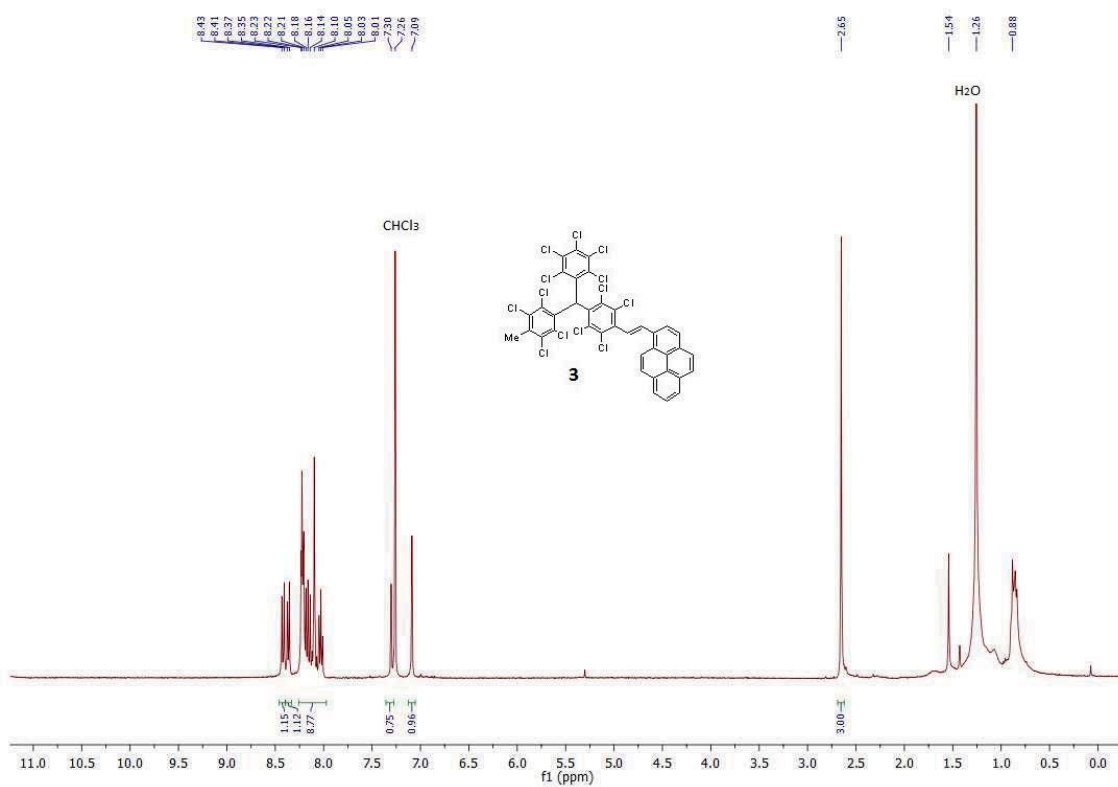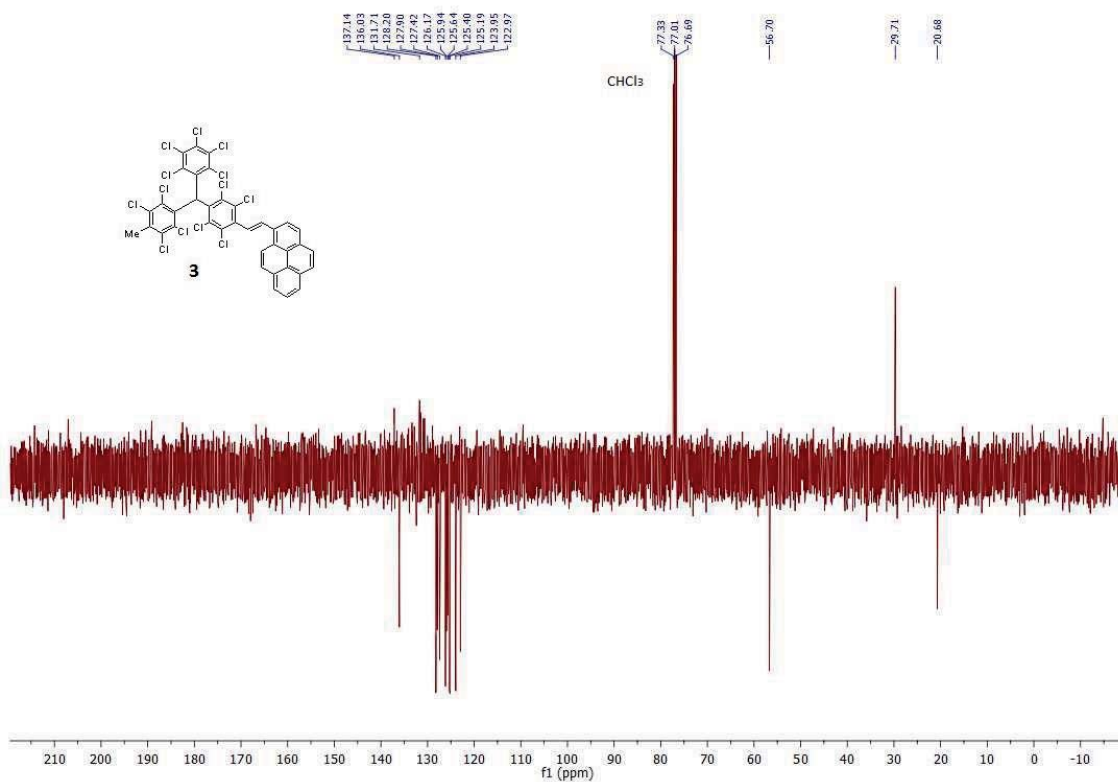**Figure SI 12:** ^{1}H-RMN (400 MHz, CDCl$_3$, r.t.) spectrum of **2.**

Figure SI 13: ^{13}C-RMN (100.6 MHz, CDCl$_3$, r.t.) spectrum of **2.**

Figure SI 14: ^{1}H-RMN (400 MHz, CDCl$_3$, r.t.) spectrum of **3.**

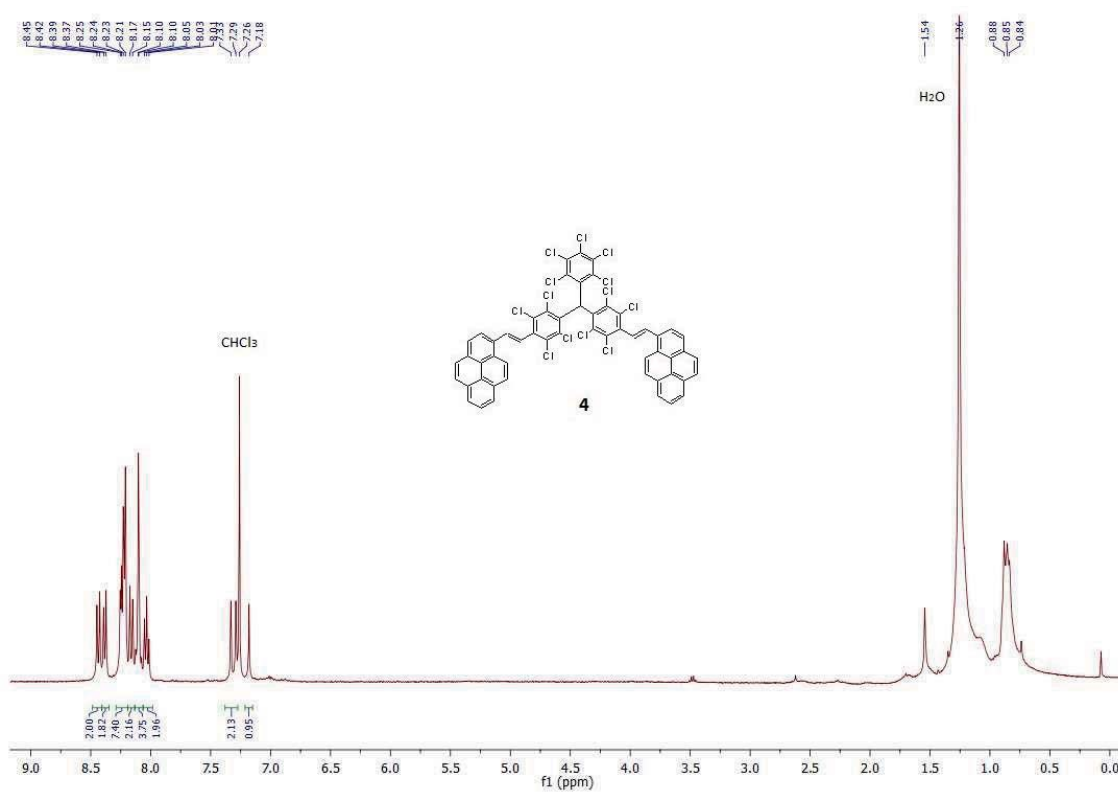**Figure SI 15:** ^{13}C-RMN-APT (100.6 MHz, CDCl$_3$, r.t.) spectrum of **3.**

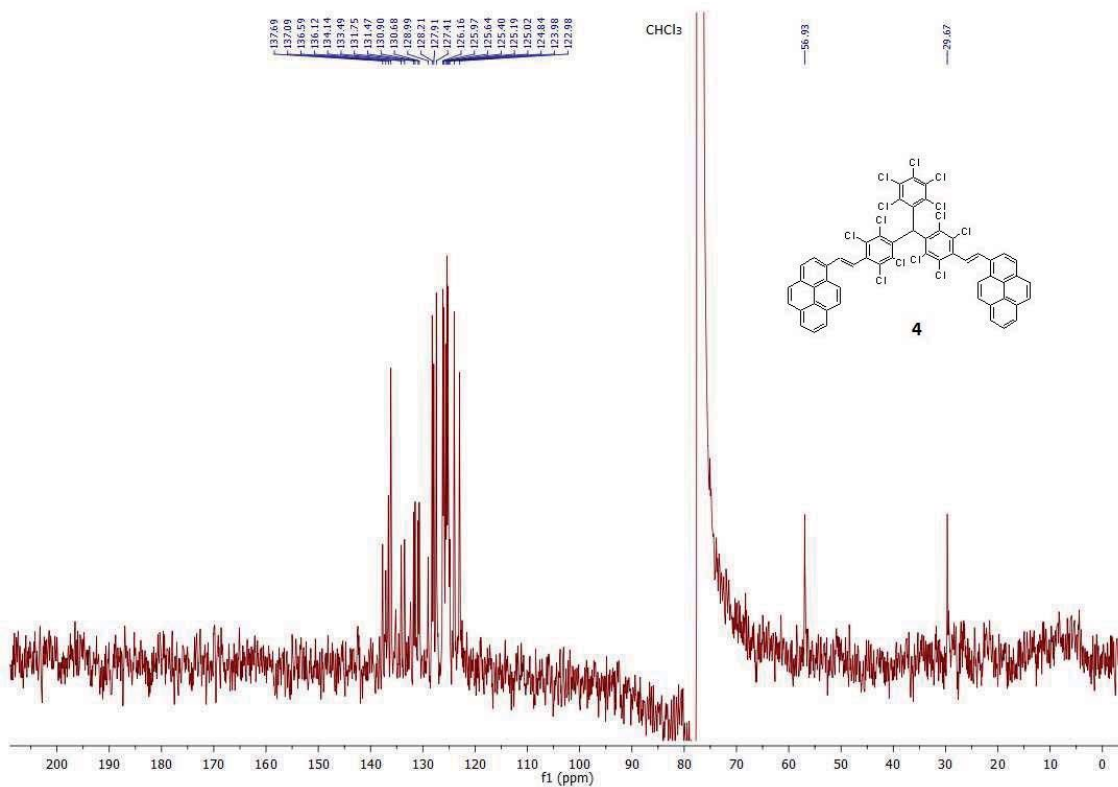**Figure SI 16:** ^{1}H-RMN (400 MHz, CDCl$_3$, r.t.) spectrum of **4.**

Figure SI 17: ^{13}C-RMN (75.45 MHz, CDCl$_3$, r.t.) spectrum.

Chapter 5:
Conclusions

Conclusions

From the work performed in this thesis on the synthesis and study of a variety of PTM derivatives as molecular electronics and spintronics components, we can conclude that the PTM radicals are good multifunctional materials, which, due to their interesting electrochemical, optical and magnetic properties, can be successfully exploited as building blocks in molecular electronics and spintronics devices.

1) We have demonstrated that the PTM radical, due to their redox properties, can be used to study the intramolecular electron transfer through different molecular wires by the mixed valence approximation. Thus, we have been able to determine the charge transfer mechanism operating through oligo-thiophene vinylene wires, and a new mechanism for the IET in PTM-OTVn-PTM anion radical mixed valence system has been proposed.

2) Also, thanks to the study of the intramolecular electron transfer in MV systems through rigidified oligo-*p*-phenylene vinylene wires, we can confirm that the IET is much more efficient in the conjugated OPPV planar wires than in the flexible ones.

3) The junctions formed by immobilized PTMs of different lengths forming SAMs on gold substrate and contacted by the liquid metal electrode EGaIn, allowed us to determine that the charge transfer mechanism operating through PTM molecules, is direct tunneling for both PTM radical non radical SAMs. We have also determined that the SUMO orbital of the PTM radical has a crucial role on enhancing the charge transport.

4) We have been able to form, for the first time, very stable single molecule break junctions with an organic radical. Importantly with these break junctions a Kondo peak was detected, demonstrating for the first time in single molecule solid devices that the localized magnetic moment of an organic free radical interacts with conducting electrons. This important result opens the door to use organic free radicals as molecular spitronics devices.